

Special Issue Reprint

Remote Sensing for Coastal and Aquatic Ecosystems' Monitoring and Biodiversity Management

Edited by
Simona Niculescu, Junshi Xia and Dar Roberts

www.mdpi.com/journal/remotesensing

Remote Sensing for Coastal and Aquatic Ecosystems' Monitoring and Biodiversity Management

Remote Sensing for Coastal and Aquatic Ecosystems' Monitoring and Biodiversity Management

Editors

Simona Niculescu

Junshi Xia

Dar Roberts

MDPI • Basel • Beijing • Wuhan • Barcelona • Belgrade • Manchester • Tokyo • Cluj • Tianjin



Editors

Simona Niculescu
Université de Brest
France

Junshi Xia
RIKEN Center for Advanced
Intelligence Project
Japan

Dar Roberts
University of California
USA

Editorial Office

MDPI
St. Alban-Anlage 66
4052 Basel, Switzerland

This is a reprint of articles from the Special Issue published online in the open access journal *Remote Sensing* (ISSN 2072-4292) (available at: https://www.mdpi.com/journal/remotesensing/special_issues/coastal_management).

For citation purposes, cite each article independently as indicated on the article page online and as indicated below:

LastName, A.A.; LastName, B.B.; LastName, C.C. Article Title. *Journal Name* **Year**, *Volume Number*, Page Range.

ISBN 978-3-0365-7520-9 (Hbk)

ISBN 978-3-0365-7521-6 (PDF)

© 2023 by the authors. Articles in this book are Open Access and distributed under the Creative Commons Attribution (CC BY) license, which allows users to download, copy and build upon published articles, as long as the author and publisher are properly credited, which ensures maximum dissemination and a wider impact of our publications.

The book as a whole is distributed by MDPI under the terms and conditions of the Creative Commons license CC BY-NC-ND.

Contents

About the Editors vii

Simona Niculescu, Junshi Xia and Dar Roberts

Editorial for Special Issue “Remote Sensing for Coastal and Aquatic Ecosystems’ Monitoring and Biodiversity Management”

Reprinted from: *Remote Sens.* **2023**, *15*, 766, doi:10.3390/rs15030766 1

Guanyao Xie and Simona Niculescu

Mapping Crop Types Using Sentinel-2 Data Machine Learning and Monitoring Crop Phenology with Sentinel-1 Backscatter Time Series in Pays de Brest, Brittany, France

Reprinted from: *Remote Sens.* **2022**, *14*, 4437, doi:10.3390/rs14184437 5

Wendy Diruit, Anthony Le Bris, Touria Bajjouk, Sophie Richier, Mathieu Helias, Thomas Burel, Marc Lennon, et al.

Seaweed Habitats on the Shore: Characterization through Hyperspectral UAV Imagery and Field Sampling

Reprinted from: *Remote Sens.* **2022**, *14*, 3124, doi:10.3390/rs14133124 33

Germán D. Silva, Dar A. Roberts, Joseph P. McFadden and Jennifer Y. King

Shifts in Salt Marsh Vegetation Landcover after Debris Flow Deposition

Reprinted from: *Remote Sens.* **2022**, *14*, 2819, doi:10.3390/rs14122819 59

Brian Timmer, Luba Y. Reshitnyk, Margot Hessing-Lewis, Francis Juanes and Maycira Costa
Comparing the Use of Red-Edge and Near-Infrared Wavelength Ranges for Detecting Submerged Kelp Canopy

Reprinted from: *Remote Sens.* **2022**, *14*, 2241, doi:10.3390/rs14092241 75

Stéphane Bertin, Pierre Stéphan and Jérôme Ammann

Assessment of RTK Quadcopter and Structure-from-Motion Photogrammetry for Fine-Scale Monitoring of Coastal Topographic Complexity

Reprinted from: *Remote Sens.* **2022**, *14*, 1679, doi:10.3390/rs14071679 93

Huachang Qiu, Zhaoning Gong, Kuinan Mou, Jianfang Hu, Yinghai Ke and Demin Zhou

Automatic and Accurate Extraction of Sea Ice in the Turbid Waters of the Yellow River Estuary Based on Image Spectral and Spatial Information

Reprinted from: *Remote Sens.* **2022**, *14*, 927, doi:10.3390/rs14040927 117

Mathilde Letard, Antoine Collin, Thomas Corpetti, Dimitri Lague, Yves Pastol and Anders Ekelund

Classification of Land-Water Continuum Habitats Using Exclusively Airborne Topobathymetric Lidar Green Waveforms and Infrared Intensity Point Clouds

Reprinted from: *Remote Sens.* **2022**, *14*, 341, doi:10.3390/rs14020341 141

Dorothee James, Antoine Collin, Antoine Mury and Rongjun Qin

Satellite-Derived Topography and Morphometry for VHR Coastal Habitat Mapping: The Pleiades-1 Tri-Stereo Enhancement

Reprinted from: *Remote Sens.* **2022**, *14*, 219, doi:10.3390/rs14010219 171

Alyson Le Quilleuc, Antoine Collin, Michael F. Jasinski and Rodolphe Devillers

Very High-Resolution Satellite-Derived Bathymetry and Habitat Mapping Using Pleiades-1 and ICESat-2

Reprinted from: *Remote Sens.* **2022**, *14*, 133, doi:10.3390/rs14010133 189

| | |
|--|------------|
| Marion Jaud, Guillaume Sicot, Guillaume Brunier, Emma Michaud, Nicolas Le Dantec, Jérôme Ammann, Philippe Grandjean, et al. Easily Implemented Methods of Radiometric Corrections for Hyperspectral-UAV—Application to Guianese Equatorial Mudbanks Colonized by Pioneer Mangroves Reprinted from: <i>Remote Sens.</i> 2021 , <i>13</i> , 4792, doi:10.3390/rs13234792 | 213 |
| Emma Gairin, Antoine Collin, Dorothée James, Tehani Maueau, Yoann Roncin, Lucas Lefort, Franck Dolique, et al. Spatiotemporal Trends of Bora Bora’s Shoreline Classification and Movement Using High-Resolution Imagery from 1955 to 2019 Reprinted from: <i>Remote Sens.</i> 2021 , <i>13</i> , 4692, doi:10.3390/rs13224692 | 231 |
| Lianna Gendall, Sarah B. Schroeder, Peter Wills, Margot Hessing-Lewis and Maycira Costa A Multi-Satellite Mapping Framework for Floating Kelp Forests Reprinted from: <i>Remote Sens.</i> 2023 , <i>15</i> , 1276, doi:10.3390/rs15051276 | 249 |

About the Editors

Simona Niculescu

Simona Niculescu received the PhD in geography-remote sensing from the Université de Paris IV-Sorbonne Paris, France, in 2002. In 2015 she obtained her degree of Habilitation of Research Direction (HDR) from the University of Sorbonne-Paris. Since 2005, she has been with the LETG-Géomer UMR 6554 CNRS Lab within the European Institute for Marine Studies, Brest, France. Her research interests include coastal areas and coastal wetlands, focusing on methodologies for exploiting the opportunities provided by new satellite imagery and machine learning methodologies. She was awarded a European Jean Monnet Chair in 2018.

Junshi Xia

Junshi Xia received the Ph.D. degree in photogrammetry and remote sensing from the China University of Mining and Technology, Xuzhou, China, in 2013 and the Ph.D. degree in image processing from the Grenoble Images Speech Signals and Automatics Laboratory, Grenoble Institute of Technology, Grenoble, France, in 2014. Since 2018, he has been a Senior Research Scientist with the RIKEN Center for Advanced Intelligence Project (AIP), Tokyo. His research interests include multiple classifier systems in remote sensing, hyperspectral remote sensing image processing, and deep learning in remote sensing applications.

Dar Roberts

Dar Roberts received his PhD in Geology from the University of Washington in 1991. Since 1994 he has been a professor in the Department of Geography at UC Santa Barbara. His research focuses on land-use/land-cover change, vegetation spectroscopy, urban remote sensing, all aspects of remote sensing of wildfire, mapping trace gasses such as methane, water vapor and carbon dioxide, drought impacts on vegetation, bathymetry, and sensor fusion using LiDAR, thermal and VSWIR sensors. He is a Fellow of the AGU and AAAS.



Editorial

Editorial for Special Issue “Remote Sensing for Coastal and Aquatic Ecosystems’ Monitoring and Biodiversity Management”

Simona Niculescu ^{1,*}, Junshi Xia ² and Dar Roberts ³¹ Department of Geography, University of Western Brittany, 3 Rue des Archives, 29238 Brest, France² Geoinformatics Unit, RIKEN Center for Advanced Intelligence Project (AIP), Tokyo 103-0027, Japan³ Department of Geography, University of California, Santa Barbara, CA 93106, USA

* Correspondence: simona.niculescu@univ-brest.fr

Abstract: Most of the papers published in this Special Issue were presented at the international conference EUCOMARE-2022 in the framework of the European Jean Monnet Chair European Spatial Studies of Sea and Coastal zones with the support of the ERASMUS+ Programme of the European Union.

Keywords: remote sensing; coastal and aquatic ecosystems; biodiversity management

1. Introduction

Environmental management and the preservation of biodiversity are widely considered priorities in the context of accelerating global changes affecting the physical and biological resources of our planet. This Special Issue focuses on “Coastal and Aquatic Ecosystems”. The coastal region is a transition area between terrestrial and marine ecosystems. This transition area is now considered an important component of the biosphere, in terms of ecosystem diversity, and the provision of resources and services. Moreover, the coastal region is home to a significant number of distinct biological communities, including coral reefs, mangroves, salt meadows and wetlands, phanerogam meadows, kelp forests, estuarine assemblages or coastal lagoons, forests, and grasslands. The diversity of coastal ecosystems is directly threatened by human activity. It is estimated that 60% of the world’s population lives on or near the coast, and economic development stresses the coastal environment. Coastal ecosystems are undergoing permanent changes in production rates, organism abundance, and community structure.

Achieving sustainable coastal zone management poses particularly significant challenges as the pressures of a growing human population, multiple development pressures, pollution from land-based sources, and unsustainable exploitation of natural resources are felt on many of the world’s coasts. Remote sensing meets this challenge by offering a wide range of standard products on environmental coastal conditions, thanks to various state-of-the-art sensors. The development of innovative methods based on integrating multi-source, multi-resolution, and multi-temporal images offers promising prospects for considering the different scales of ecosystems. Consequently, the products derived from remote sensing contribute to the development of temporal and spatial indicators for better knowledge and management of coastal and aquatic ecosystems. This Special Issue includes original environmental research using satellite data processing—optical or radar—addressing coastal and aquatic ecosystem monitoring on different spatial and temporal scales.

2. Overview of Contributions

The following is the synthesis of results obtained in each paper published in the SI “Remote Sensing for Coastal and Aquatic Ecosystems’ Monitoring and Biodiversity Management”.

Citation: Niculescu, S.; Xia, J.; Roberts, D. Editorial for Special Issue “Remote Sensing for Coastal and Aquatic Ecosystems’ Monitoring and Biodiversity Management”. *Remote Sens.* **2023**, *15*, 766. <https://doi.org/10.3390/rs15030766>

Received: 15 December 2022

Accepted: 13 January 2023

Published: 29 January 2023



Copyright: © 2023 by the authors. Licensee MDPI, Basel, Switzerland. This article is an open access article distributed under the terms and conditions of the Creative Commons Attribution (CC BY) license (<https://creativecommons.org/licenses/by/4.0/>).

G. Xie and S. Niculescu [1] propose a methodology to map two main winter crops (winter wheat and winter barley) in the northern Finistère region with high-resolution Sentinel-2 data and, in a second step, the monitoring of winter crop phenology with Sentinel-1 C-band SAR data using the Google Earth Engine (GEE) platform. In the first part of the research, pixel-based classification (PBC) and object-based classification (OBC) methods are proposed and evaluated. The results showed that OBC achieved better accuracy in mapping croplands, and PBC was more accurate in extracting winter crops. In the second part of the research, the objective was to synthesize the temporal behavior from sowing to harvesting, identifying three important phenological states (germination, heading and maturation, including harvesting) from the VV and VH polarizations as well as the VH/VV ratio.

W. Diruit et al. [2] focus their study on intertidal macroalgal habitats on the rocky coast of Porspoder (Western Brittany, France). The authors studied the distribution of macroalgae using field sampling and airborne hyperspectral mapping by drone over 17,000 m². Twenty-four sampling points, according to four bathymetric levels were proposed to characterize the dominant macroalgal cover and sessile fauna at low tide. These data were later used for comparison with the results of hyperspectral image processing (seven classes of algae, including five different species of Fucales). Two classification methods were implemented: the maximum likelihood method (MLC) and the spectral angle method (SAM). MLC was more accurate in classifying the main dominant species (overall accuracy (OA) 95.1%) than SAM (OA 87.9%) at the site scale.

G. Silva et al. [3] evaluate the impact of the January 2018 Montecito Debris Flow on the Carpinteria Salt Marsh Reserve California, a 93 ha reserve consisting of upland vegetation, high marsh, mid marsh, open channels, and mud flats. Using Sentinel-2 data, they calculated fractional cover, and two spectral vegetation indices prior to, immediately following and for several years after the debris flow. Fractional cover, SVIs and LiDAR data were used to train a Random Forest classifier to map changes in cover. Classification accuracies ranged from a Kappa of 0.911 in January 2018, immediately following a disturbance of 0.993 in November 2017, just prior to the disturbance. The most immediate impact of the debris flow was a decrease in both marsh classes and an increase in bare soil. Post-disturbance analysis demonstrated a rapid recovery with the vegetation extent approaching pre-disturbance levels by November 2020, but also showed a transition of high-marsh to mid-marsh vegetation in areas that showed initial increases in bare soil.

Timmer et al. [4] use a field spectrometer to evaluate the relative merits of Near-Infrared (NIR) and red-edge reflectance for the detection of submerged Bull kelp (*Nereocystis luetkeana*). Under clear-sky conditions, they measured kelp reflectance from 325–1075 nm at varying depths from the surface to a depth of 100 cm at 10 cm intervals. Field spectra were convolved to WorldView 3 bands and wavelengths sampled by the Micasense RedEdge-Mx sensor, a sensor deployed on an unoccupied aerial vehicle (UAV). Surface kelp showed higher NIR reflectance than red-edge reflectance. Submerged kelp resulted in two narrow peaks, one in the NIR, the other at the red edge, with higher reflectance observed in the red edge. SVIs calculated using red-edge bands were able to detect the presence of kelp deeper in the water column.

Bertin et al. [5] explore the potential of using a structure from motion (SfM) photogrammetry deployed from an RTK quadcopter to map the complex topographic variation typical of coastal beach environments in the rapidly changing intertidal zone. A key objective was to map topo-morphological features at submeter resolutions, while also being constrained to a two-hour period at low tide and using a minimum number of ground-control points (GCPs). Working at two coastal sites, they found that the addition of a single GCP produced global precision equivalent to traditional GCP-based photogrammetry; the highest accuracies were achieved using five GCPs and imagery at its native resolution. These findings offer promise for the rapid, accurate monitoring of coastal environments over large areas.

Qiu et al. [6] propose a new approach for mapping sea ice in the Yellow River Estuary, China, using multispectral data. They argue that sea ice map accuracies in this area are often low, due to the confounding effects of high variability in suspended particulate matter

(SPM) in the adjacent water. They developed a sea ice spectral information index that can be adapted to different levels of turbidity, combined with textural information and applied multi-scale image segmentation to map sea ice using the OTSU method. The approach was applied to Gaofen-1 (GF1), Sentinel-2 and Landsat 8 achieving accuracies above 93%, 5% higher than accuracies using Support Vector Machines (SVM) and K-Means.

Letard, M et al. [7] illustrate the usefulness of topo-bathymetric lidar data for mapping coastal and estuarine habitats by categorizing multispectral data to generate three-dimensional maps of 21 different types of land and sea cover at a very high resolution. To find characteristics that are unique to certain environments, the whole waveform data from a green lidar is analyzed. Random forest classifiers employ these characteristics as predictors with infrared intensities and altitudes, and their individual contributions to classification accuracy are evaluated. The research shows that combining green waveform information with infrared intensities and heights improves classification accuracy. Our segmentation accuracy on the dual-wavelength lidar dataset improves to 90.5% with this setup. In the end, we generate an original mapping of a coastal site in the form of a point cloud, which paves the way for the 3D categorization and administration of land and sea covers.

D. James et al. [8] improve very high resolution (VHR) habitat mapping/classification using Pleiades-1 derived topography, its morphometric by-products and Pleiades-1 derived images over the Emerald Coast in Brittany, France. In their study, the authors use a tri-stereo dataset to obtain nine 0.50 m pixel digital surface models (DSMs). Four morphometric predictors derived from the best of the nine generated DSMs were computed: slope, aspect, topographic position index (TPI) and TPI-based landform classification (TPILC). These morphometric predictors were added to the Red–Green–Blue reference. The best combination of TPILC added to RGB + DSM resulted in a 13% gain in OA, reaching 89.37%.

A. Le Quilleuc et al. [9] generated a very high-resolution (VHR) bathymetry and habitat mapping digital depth model (DDM) in Mayotte island waters (Indian Ocean) by fusing 0.5 m Pleiades-1 passive multispectral imagery and active ICESat-2 LiDAR bathymetry. In particular, along the ground track of the satellite ICESat-2, the RMSE of a DDM calibrated using ICESat-2 data was 0.89 m or around 6 percent of the maximum depth collected by ICESat-2. There was an overall accuracy of 96.62% and a coefficient of 0.94 for the classification performed by ML utilizing the Blue and Green spectral bands and the three geomorphic predictors. A slope geomorphic predictor was added to the SVM classification using blue, green, and red spectral bands, and the resulting model showed an overall accuracy of 96.50% and a coefficient of 0.95.

M. Jaud et al. [10] present light, easily-implemented, in-situ methods, using only two Spectralon[®] and a field spectrometer, to correct “vignetting effects” in the sensor and to convert digital numbers (DN) collected by the hyperspectral camera to reflectance, taking into account the time-varying illumination conditions. A portion of the dataset gathered above the pioneer mangrove-colonized mudflats in French Guiana is radiometrically corrected. The comparison of HyperDRELIO image spectra with an in situ spectrometer readings made high above the intertidal benthic biofilm and mangroves is used to evaluate the efficacy of the radiometric adjustments. Spectral angle mapper (SAM) distance was 0.039 above the benthic biofilm and 0.159 above the mangroves, and spectral shape remained similar throughout. Given the importance of benthic biofilm and mangroves in coastal food webs, biogeochemical cycles, and sediment stability, the results offer new perspectives for measuring and mapping these features at the scale of the Guianese intertidal mudbanks system.

E. Gairin et al. [11] investigate the historical evolution of the French Polynesian island of Bora Bora’s classification and position from 1955 to 2019. The evolution of the island’s shoreline was brought to light through the processing of a time series of ultra-high resolution aerial imagery. In the period between 1955 and 2019, the length of natural coastlines, which includes beaches, declined by 46%, while the length of man-made coasts, which includes seawalls, expanded by 476%, and now accounts for 61% of the coastline. This

research illustrates the effects of man-made buildings on erosional processes and highlights the need for sustainable coastal management strategies in French Polynesia by recording the changes to the Bora Bora shoreline over time.

Author Contributions: Conceptualization, S.N., J.X. and D.R.; writing—original draft preparation, S.N., J.X. and D.R.; writing—review and editing, S.N., J.X. and D.R.; visualization, S.N., J.X. and D.R.; supervision, S.N., J.X. and D.R.; project administration, S.N.; funding acquisition, S.N. All authors have read and agreed to the published version of the manuscript.

Institutional Review Board Statement: Not applicable.

Informed Consent Statement: Not applicable.

Data Availability Statement: The data presented in this study are available on request from the corresponding author.

Conflicts of Interest: The authors declare no conflict of interest.

References

1. Xie, G.; Niculescu, S. Mapping crop types using sentinel-2 data machine learning and monitoring crop phenology with sentinel-1 backscatter time series in pays de Brest, Brittany, France. *Remote Sens.* **2022**, *14*, 4437. [[CrossRef](#)]
2. Diruit, W.; Le Bris, A.; Bajjouk, T.; Richier, S.; Helias, M.; Burel, T.; Lennon, M.; Guyot, A.; Ar Gall, E. Seaweed habitats on the shore: Characterization through hyperspectral UAV imagery and field sampling. *Remote Sens.* **2022**, *14*, 3124. [[CrossRef](#)]
3. Silva, G.D.; Roberts, D.A.; McFadden, J.P.; King, J.Y. Shifts in salt marsh vegetation landcover after debris flow deposition. *Remote Sens.* **2022**, *14*, 2819. [[CrossRef](#)]
4. Timmer, B.; Reshitnyk, L.Y.; Hessing-Lewis, M.; Juanes, F.; Costa, M. Comparing the use of red-edge and near-infrared wavelengths for detecting submerged kelp canopy. *Remote Sens.* **2022**, *14*, 2241. [[CrossRef](#)]
5. Bertin, S.; Stephan, P.; Ammann, J. Assessment of RTK Quadcopter and structure-from-motion photogrammetry for fine-scale monitoring of coastal topographic complexity. *Remote Sens.* **2022**, *14*, 1679. [[CrossRef](#)]
6. Qiu, H.; Gong, Z.; Mou, K.; Hu, J.; Ke, Y.; Zhou, D. Automatic and accurate extraction of sea ice in the turbid waters of the yellow river estuary based on image spectral and spatial information. *Remote Sens.* **2022**, *14*, 927. [[CrossRef](#)]
7. Letard, M.; Collin, A.; Corpetti, T.; Lague, D.; Pastol, Y.; Ekelund, A. Classification of land-water continuum habitats using exclusively airborne topobathymetric lidar green waveforms and infrared intensity point clouds. *Remote Sens.* **2022**, *14*, 341. [[CrossRef](#)]
8. James, D.; Collin, A.; Mury, A.; Qin, R. Satellite-derived topography and morphometry for VHR coastal habitat mapping: The Pleiades-1 tri-stereo enhancement. *Remote Sens.* **2022**, *14*, 219. [[CrossRef](#)]
9. Le Quilleuc, A.; Collin, A.; Jasinski, M.F.; Devillers, R. Very high-resolution satellite-derived bathymetry and habitat mapping using pleiades-1 and ICESat-2. *Remote Sens.* **2022**, *14*, 133. [[CrossRef](#)]
10. Jaud, M.; Sicot, G.; Brunier, G.; Michaud, E.; Le Dantec, N.; Ammann, J.; Grandjean, P.; Launeau, P.; Thouzeau, G.; Fleury, J.; et al. Easily implemented methods of radiometric corrections for hyperspectral-UAV—Application to guianese equatorial mudbanks colonized by pioneer mangroves. *Remote Sens.* **2021**, *13*, 4792. [[CrossRef](#)]
11. Gairin, E.; Collin, A.; James, D.; Maueau, T.; Roncin, Y.; Lefort, L.; Doliq, F.; Jeanson, M.; Lecchini, D. Spatiotemporal trends of bora bora's shoreline classification and movement using high-resolution imagery from 1955 to 2019. *Remote Sens.* **2021**, *13*, 4692. [[CrossRef](#)]

Disclaimer/Publisher's Note: The statements, opinions and data contained in all publications are solely those of the individual author(s) and contributor(s) and not of MDPI and/or the editor(s). MDPI and/or the editor(s) disclaim responsibility for any injury to people or property resulting from any ideas, methods, instructions or products referred to in the content.



Article

Mapping Crop Types Using Sentinel-2 Data Machine Learning and Monitoring Crop Phenology with Sentinel-1 Backscatter Time Series in Pays de Brest, Brittany, France

Guanyao Xie ^{1,*} and Simona Niculescu ^{1,2}¹ Laboratory LETG-Brest, Géomer, UMR 6554 CNRS, IUEM UBO, 29200 Brest, France² Department of Geography, University of Western Brittany, 3 Rue des Archives, 29238 Brest, France

* Correspondence: guanyao.xie@univ-brest.fr

Abstract: Crop supply and management is a global issue, particularly in the context of global climate change and rising urbanization. Accurate mapping and monitoring of specific crop types are crucial for crop studies. In this study, we proposed: (1) a methodology to map two main winter crops (winter wheat and winter barley) in the northern region of Finistère with high-resolution Sentinel-2 data. Different classification approaches (the hierarchical classification and the classical direct extraction), and classification methods (pixel-based classification (PBC) and object-based classification (OBC)) were performed and evaluated. Subsequently, (2) a further study that involved monitoring the phenology of the winter crops was carried out, based on the previous results. The aim is to understand the temporal behavior from sowing to harvesting, identifying three important phenological statuses (germination, heading, and ripening, including harvesting). Due to the high frequency of precipitation in our study area, crop phenology monitoring was performed using Sentinel-1 C-band SAR backscatter time series data using the Google Earth Engine (GEE) platform. The results of the classification showed that the hierarchical classification achieved a better accuracy when it is compared to the direct extraction, with an overall accuracy of 0.932 and a kappa coefficient of 0.888. Moreover, in the hierarchical classification process, OBC reached a better accuracy in cropland mapping, and PBC was proven more suitable for winter crop extraction. Additionally, in the time series backscatter coefficient of winter wheat, the germination and ripening (harvesting) phases can be identified at VV and VH/VV polarizations, and heading can be identified in both VV and VH polarizations. Secondly, we were able to detect the germination phase of winter barley in VV and VH, ripening with both polarizations and VH/VV, and finally, heading in VV and VH polarizations.

Keywords: winter crops mapping; winter crops phenology; machine learning; hierarchical classification; object-based classification; pixel-based classification; Google Earth Engine (GEE); Sentinel-1; Sentinel-2

Citation: Xie, G.; Niculescu, S. Mapping Crop Types Using Sentinel-2 Data Machine Learning and Monitoring Crop Phenology with Sentinel-1 Backscatter Time Series in Pays de Brest, Brittany, France. *Remote Sens.* **2022**, *14*, 4437. <https://doi.org/10.3390/rs14184437>

Academic Editor: Jianxi Huang

Received: 1 August 2022

Accepted: 31 August 2022

Published: 6 September 2022

Publisher's Note: MDPI stays neutral with regard to jurisdictional claims in published maps and institutional affiliations.



Copyright: © 2022 by the authors. Licensee MDPI, Basel, Switzerland. This article is an open access article distributed under the terms and conditions of the Creative Commons Attribution (CC BY) license (<https://creativecommons.org/licenses/by/4.0/>).

1. Introduction

Crop supply is a global issue, particularly in the context of global climate change, rising population, and urbanization. With increasing food demand worldwide, agriculture production and food security should be guaranteed by ensuring biodiversity and limiting the environmental impacts [1]. This makes reliable information about crop spatial distribution and growing patterns crucial for studying regional agriculture production and supply, making political decisions, and facilitating crop management [2,3].

The classification of crop spatial distributions are valuable for agricultural monitoring and for the implementation and evaluation of crop management strategies [4,5]. Hence, crop type mapping is in high demand. Field research and remote sensing have always been the most important sources for obtaining agricultural information [6], and since the first launch of Earth observation satellites in 1972, continuous agriculture mapping and monitoring over large areas became possible with the Earth Observation (EO) data. Moreover, the new generation of EO data, nowadays, has increased the resolution of

sensors for agriculture uses, therefore since the last few decades, the science of agriculture mapping and monitoring has developed quickly, with diverse types of high spatial and temporal resolution EO data. For example, Sun et al. in 2019 [4] conducted a study of the crop types that were located at the lower reaches of the Yangzi River in China. They performed a classification of crop-type dynamics during the growing season by using three advanced machine learning algorithms (Support Vector Machine (SVM), Artificial Neural Network (ANN), and Random Forest (RF)) with a combination of three advanced sensors (Sentinel-1 backscatter, optical Sentinel-2, and Landsat-8). Arvor et al. in 2010 [7] provided a methodology for mapping the main crops and agricultural practices in the Mato Grosso state in Brazil; this study was performed by two successive, supervised classifications with the Enhanced Vegetation Index (EVI) time series from the MODIS sensor to create an agricultural mask and a crop classification of three main crops in the state. In another study by Forkuor et al. in 2014 [8], they found that an integration of multi-temporal optical RapidEye and dual-polarized Synthetic Aperture Radar (SAR) TerraSAR-X data can efficiently improve the classification accuracy of crops and crop group mapping in West Africa, in spite of excessive cloud cover, small sized fields, and a heterogeneous landscape. Furthermore, in the Finistère department, Xie and Niculescu 2021 [9] evaluated the multiannual change detections of different Land Cover Land Use (LCLU) regions, including agricultural land with accuracy indices between 70% and 90%, by using high-resolution satellite imagery (SPOT 5 and Sentinel-2) and three algorithms that were implemented: RF, SVM, and the Convolutional Neural Network (CNN).

More importantly, many studies of crop mapping focuses on winter crop mapping. Dong et al. in 2020 [10] proposed a method called phenology-time-weighted dynamic time warping (PT-DTW) for mapping winter wheat using Sentinel-2 time series data, and this new method may exploit phenological features in two periods, with a NDPI (Normalized Difference Phenology Index) providing more robust vegetation information and reducing the adverse impacts of soil and snow cover during the overwintering period. Zhou et al. in 2017 [11] studied the feasibility of winter wheat mapping in an urban agricultural region with a complex planting structure using three machine learning classification methods (SVM, RF, and neural network (NN)), and the possibility of improving classification accuracy by combining SAR and optical data.

Besides the contributions of the new generation of EO data, the diversity of the classification approaches and methods have provided more resources for agriculture mapping and monitoring. The classical, direct extraction approach is the traditional and most used classification approach that is used to extract single or multiple crop types directly from satellite images [12–14]. Moreover, we also propose the hierarchical classification approach for crops mapping in this study. Hierarchical classification is well known for its capacity to solve a complex classification problem by separating the problem into a set of smaller progressive classifications; it produces a series of thematic maps to progressively classify the image into detailed classes. Wardlow and Egbert [12] investigated the applicability of time-series Moderate Resolution Imaging Spectro-radiometer (MODIS) 250 m normalized difference vegetation index (NDVI) data for large-scale crop mapping in the Central Great Plains of the U.S. The hierarchical classification scheme was applied in this study with high classification accuracy, and instead of directly solving a complex irrigated crop mapping problem, a four-level hierarchical classification framework was implemented to produce a series of crop-related thematic maps that progressively classified cropland areas into detailed classes. Ibrahim et al. in 2021 [15] have also employed the hierarchical classification scheme to map crop types and cropping systems in Nigeria, using the RF classifier and Sentinel-2 imagery. Firstly, they produced a land cover map with five classes in order to eliminate other land cover types, then the next classification was performed only on cropland, where the specific crop types and cropping systems were mapped. The results indicated that the crop types were well classified with high accuracy, despite the study area being heterogeneous and smallholder-dominated.

In recent years, most studies in the agricultural field have explored the performance of different classification algorithms. Random Forest (RF) is one of the most well-known and widely used algorithms in the field for its optimal classification accuracy, effectiveness on large data bases, and its capability of estimating the importance of the variables in the classification [8,16–19]. The RF classification algorithm is traditionally run as a Pixel-Based Classification, which has proven efficient and accurate in agriculture fields by many studies [16,20–22]. On the other hand, the advantage of Object-Based Classification (OBC) is well documented and many recent studies have the conclusion that OBC usually outperforms PBC for its higher classification accuracy, better potential for extracting land cover information in a heterogeneous area with small size field, and the capacity to produce a more homogenous class [23,24]. However, even though Object-Based Classification is better developed and considered as more accurate than PBC, both classification methods are able to achieve a great degree of accuracy.

Aside from mapping and analyzing the crop spatial distribution, understanding agricultural growing patterns is also a key element for crop management. Crop phenology monitoring and the identification of the main phenological stages are highly necessary for agricultural production predicting, efficient interventions of farmers and decision-makers during the phenological phases such as fertilization, pesticide application, and irrigation [25]. In particular, germination is the most critical phase to be understood, and it is the starting point of the growing season. Based on the germination information, the farmer and decision-makers are able to make a future projection of the season, estimate the whole seasonal phenology for crop growth, and predict its production [25]. Furthermore, phenology is highly related to the seasonal dynamics of a growth environment, therefore, in the context of global warming, the phenology of many plants, especially crops, may have changed [6].

Crop phenology is usually monitored with optical satellite images using vegetation indices. For example, Pan et al. in 2015 [26] analyzed the phenology of winter wheat and summer corn in the Guanzhong Plain in the Shanxi Province, China by using Normalized Difference Vegetation index (NDVI) time series data and extracted seasonality information from the NDVI time series for measuring phenology parameters. The potential of another less-known index, the Normalized Difference Phenology Index (NDPI), is exploited by Gan et al. in 2020 [27] in order to detect winter wheat green-up dates. During the evaluation with three other indices (NDVI, EVI, and EVI2), the results indicate that NDPI outperforms the other indices with the highest consistency with the ground truth.

Compared to the optical data, SAR data is less used in agricultural areas. Nevertheless, lately, with the emergence of a new generation of high-resolution SAR data, in particular since the Copernicus program Sentinel-1 C-band high spatial–temporal resolution images became available, SAR data has begun to draw interest, especially for its advantage of having its own source of energy, making it nearly independent of weather conditions [8]. Thus, SAR backscattering coefficient time series data is now more frequently used for crop phenology monitoring. While optical data strongly depends on the chlorophyll content in the plants, SAR data can reveal the main changes in the canopy structure, identify significant phenological stages, and determine the main growing period with the signal that is received after interacting with the canopy of the plants. Therefore, studies of crop phenology monitoring using SAR data have increased considerably in recent years. Meroni et al. in 2020 [28] conducted a study of retrieving the crop-specific land surface phenology (LSP) of eight major European crops from Sentinel-1 SAR and Sentinel-2 optical data, where crop phenology was detected on the temporal profiles of the ratio of the backscattering coefficient VH/VV from Sentinel-1 and NDVI from Sentinel-2. They revealed that the crop phenology that was detected by Sentinel-1 and 2 can be complementary. Wali et al. in 2020 [29] introduced rice phenology monitoring in the Miyazaki prefecture of Japan by using Sentinel-1 dual polarization (VV and VH) time series data, and attempted to clarify the relationship between rice growth parameters and the backscattering coefficient using the combination of two linear-regression lines. Canisius et al. in 2018 [30] exploited SAR

polarimetric parameters that were derived from fully polarimetric RADARSAT-2 SAR time series data to predict the growth pattern and phenological stages of canola and spring wheat in the Nipissing agricultural district of Northern Ontario, Canada. Mandal et al. in 2020 [31] proposed a dual-pol radar vegetation index (DpRVI) from Sentinel-1 difference data (VV-VH) to characterize the vegetation growth of three crop types (canola, soybean, and wheat) from sowing to full canopy development, with the accumulation of the Plant Area Index (PAI) and biomass.

The feasibility and effectiveness of winter crop type mapping and phenology monitoring with optical or SAR satellite data has been proven by many studies in agricultural field, however, some limitations remain. For example, the potential of a vegetation index other than NDVI and EVI has rarely been explored, and the studies have never been performed in a coastal area with fragmented and small-scale fields. More importantly, almost all the research perform and evaluate a single classification approach or method, instead of comparing different approaches and methods for crop type mapping.

In this study, we introduce a methodology to map two winter crop types (winter wheat and winter barley) with Sentinel-2 optical data that was acquired during the growing season of the winter crops. Two different classification approaches (hierarchical classification and classical direct extraction) were performed using RF-supervised classification algorithms, and two classification methods (PBC and OBC) were operated and evaluated within the hierarchical classification framework. With the classification results of the winter crops, we are able to monitor their phenology with Sentinel-1 C-band SAR backscatter time series and precipitation data in order to understand their temporal behavior from sowing to harvesting, identify the three main phenological stages (germination, heading, and ripening, including harvesting), and study how crop phenology responds to weather conditions.

The main objectives of this study are listed as follows:

1. Study the feasibility of mapping winter crops with Sentinel-2 10 m spatial resolution data in a fragmented area that is dominated by small-size fields;
2. Perform hierarchical classification and classical direct extraction and evaluate the performance of both classification approaches;
3. Perform PBC and OBC and compare the performance in each level of the hierarchical classification structure;
4. Study the correlation between crop phenology and Sentinel-1 C-band SAR backscatter time series data and identify three phenological stages and the main growth period of the winter crops.

2. Study Area

The study area is located on the west coast of France in the north of the Finistère department and the region of Brittany (Figure 1).

The study area covers a land surface of 1034.41 km², and extends between the latitudes of 48°19′39″N and 48°40′41″N, and the longitudes of 4°12′50″W and 4°47′13″W. According to French National Institute of Geographic and Forest Information (IGN), the northern part of Finistère is mostly dominated by plains, and the elevation of the area ranges between 0 m and 100 m [32]. The study area is mostly occupied by cropland, temporal or permanent grasslands, small area of forests and shrubs, urban agglomeration in the south, and a wetland area in the north [33]. Climatically, the north of Finistère is classified as type Cfb (temperate oceanic climate), according to the Köppen climate classification, and it is characterized by warm winters and cool summers. On average, the northern region of Finistère receives 941 mm of total precipitation per year, with the annual average temperature being 12.1 °C (7.7 °C and 16.8 °C are the monthly average temperatures for the coldest and warmest months, respectively), and therefore the warm temperate climate with frequent rainfall provides very favorable conditions for agriculture activities.

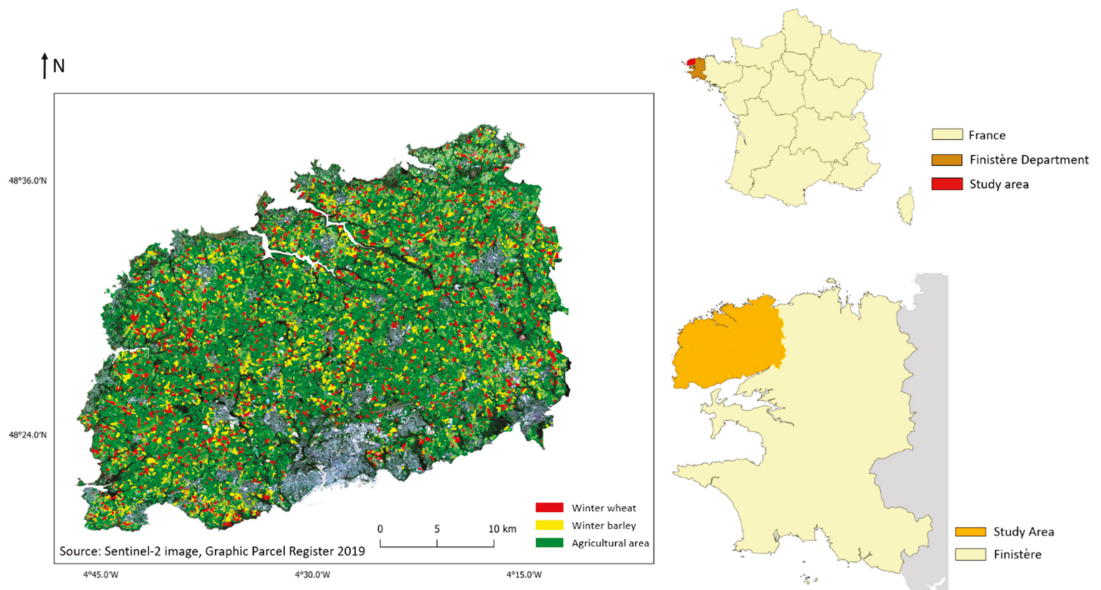


Figure 1. Location of study area, the north of the Finistère department, Brittany, France, as per the RGB band combination of a Sentinel-2 satellite image on 20 April 2019 and the distribution of agricultural land in 2019.

With such climate and topography conditions, agriculture is an important economic sector in the study area, and a considerable number of locals work in an agricultural or related sector in the department. There are 384,408 hectares of useful agricultural area in the department, so 57% of the department's surface is devoted to agricultural use [34]. One of main agricultural productions are crops, including corn, winter wheat, and winter barley, and vegetables [35].

Hence, it is important to develop a methodology to map one or several specific crop types and monitor their growth stages by using free access, high quality satellite images for crop production management. The north of the Finistère department was chosen as our first study area because of its favorable natural conditions, highly active agricultural activities, and its proximity, which facilitate the field research and interaction with farmers.

3. Data

The study was executed in the Finistère department in France during 2019, using open-access high-quality satellite data from the Sentinel platform. It is worth noting that the latest version of the graphic parcel register was published in 2019 by the French National Institute of Geographic and Forest Information, and this information was relevant to our study.

Due to the annual high-intensity precipitation there is frequent heavy cloud cover in the region, therefore, operable optical satellite images are very rare in the study area. Nevertheless, a Sentinel-2 optical satellite image was acquired in the spring, which is the growing season of the winter crops. In order to create a cloud-free time series of the study, the phenological phrases of winter crops from the SAR data were applied to the phenology monitoring process.

3.1. Sentinel-2 Optical Data

Sentinel-2 is an satellite imaging mission that is implemented by the European Commission (EC) and the European Space Agency (ESA) as a part of the Copernicus program [36]. The two identical satellites (Sentinel-2A and Sentinel-2B) provide continually

open-access, multispectral, wide swath (290 km), high spatial resolution (four bands at 10 m, six bands at 20 m, and three bands at 60 m), and high revisit frequency (five days with combined satellites) image data [36]. Due to frequent heavy cloud cover in the area, only one cloud-free level 2A atmospheric effect-corrected Sentinel-2 image from 20 April 2019 was acquired from the Theia platform (catalog.theia-land.fr) [37] (Table 1). Ten spectral bands (Table 2) were extracted for further processing and analysis.

Table 1. Sentinel-2 image used in the study.

| Date | Satellite | Platform | Processing Level | Tiles |
|---------------|------------|----------|------------------|--------|
| 20 April 2019 | Sentinel-2 | 2B | Level 2A | T30UUU |

Table 2. Sentinel-2 spectral bands used in the study.

| Sentinel-2 Bands | Spatial Resolution (m) | Wavelength Range (nm) |
|-----------------------------|------------------------|-----------------------|
| Band 2-Blue | 10 | 458–523 |
| Band 3-Green | 10 | 543–578 |
| Band 4-Red | 10 | 650–680 |
| Band 5-Vegetation red edge | 20 | 698–713 |
| Band 6-Vegetation red edge | 20 | 733–748 |
| Band 7-Vegetation red edge | 20 | 773–793 |
| Band 8-Near Infrared | 10 | 785–899 |
| Band 8A-Vegetation red edge | 20 | 855–875 |
| Band 11-Short-Wave Infrared | 20 | 1565–1655 |
| Band 12-Short-Wave Infrared | 20 | 2100–2280 |

3.2. Sentinel-1 SAR Data

The Sentinel-1 C-band SAR (Synthetic-aperture radar) is one of the ESA missions under the Copernicus program [38]. Sentinel-1 possesses two polar-orbiting satellites (Sentinel-1A and Sentinel-1B) sharing the same orbital plane, which are able to operate day and night using their own energy source in order to perform high spatial resolution (10 m), wide coverage, high repeat cycle (generally five days with two satellites), C-band SAR imaging in all weather conditions [38].

In this study, interferometric Wide Swath mode level-1 GRD (Ground Range Detected) Sentinel-1 data with an incidence angle ranging from 30 to 46 were acquired to create the time series of the growing period of the winter crops (winter wheat and winter barley) in 2019, from 1 October 2018 to 1 September 2019. Both polarizations (VV + VH) were used, but only the descending orbit was retained for the processing. In total, 109 Sentinel-1 C-band SAR images with descending orbit were acquired for this study.

3.3. Auxiliary Data

RPG (Graphic Parcel Register) was applied as the ground truth data in our study, used for creating training data and test data. RPG 2019 is the latest version of the very precise, geo-referenced agricultural land database that covers the entire France territory (except Mayotte) that was published by IGN. The databases show the precise crop types (e.g., wheat, corn, vegetables, sunflower) or temporary and permanent grasslands in that are in the recorded agricultural lands in each year [39].

4. Methods

The methodology of this paper is detailed in two parts, which relate to the two research subjects: mapping winter crop types using Sentinel-2 data, and monitoring crop phenology with Sentinel-1 backscatter time series. The data were processed in QGIS with Orfeo Toolbox, eCognition 10.0, and GEE (Google Earth Engine).

4.1. Winter Crop Types Mapping

A flow chart of the proposed global methodology is displayed below (Figure 2)

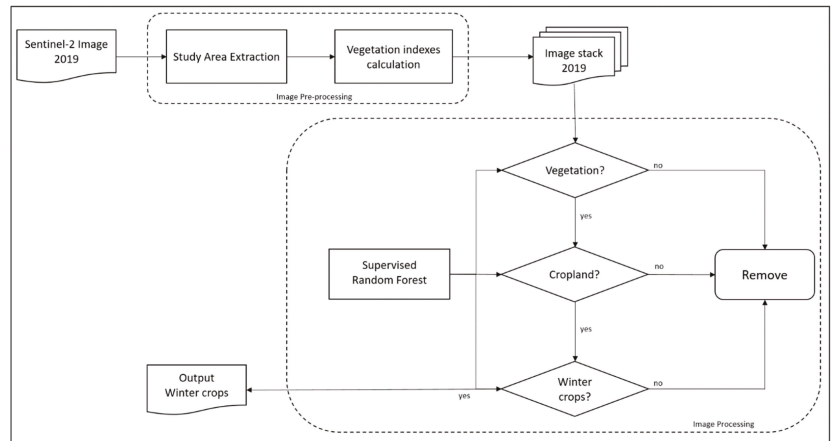


Figure 2. Hierarchical classification methodology used in the study for crop mapping.

4.1.1. Image Preprocessing

After the study area selection and satellite image acquisition, the boundary of the northern region of Finistère area was applied in order to extract our area of interest by subsetting the raw images for the purpose of reducing the image size and shortening the processing time.

In remote sensing fields, vegetation indices (VI) are the qualitative and quantitative evaluation of vegetation covers and their growth dynamics, using different combinations of spectral measurements. The results of the indices are different due to the different chemical and morphological characteristics of the surfaces of the organs or leaves of the plants [40], however the spectral responses are also affected by other factors, such as environmental effects, soil reflectance and its components, shadows, and atmospheric and topographic effects [41].

For this reason, over a hundred VIs have been developed and enhanced for various applications over the past three decades in order to enhance spectral responses, increase sensitivity for identifying vegetated areas, distinguish different vegetation types, evaluate the vegetation density, and provide data on the health of the vegetation [42], and also to minimize the effects of other factors that are described above [41]. In this study, six VIs are used with the aim of mapping winter crop types using Sentinel-2 data.

- The Normalized Difference Vegetation Index (NDVI), proposed in 1973 by [43], is the most known and widely used index in research related to vegetation monitoring. NDVI is the normalized difference between the visible red and near-infrared spectral reflectance of vegetation, as follows:

$$NDVI = \frac{NIR - RED}{NIR + RED} \quad (1)$$

Even though the index is often affected by atmospheric conditions and soil reflectance and its components, it remains a highly used index in agriculture-related fields to measure the rate of vegetation cover and evaluate the health of the crops.

- The Normalized Difference Water Index (NDWI), proposed by Gao in 1996 [44], is a vegetation index that is used to highlight the changes in the liquid water content of vegetation canopies with weak atmospheric aerosol scattering effects, while remaining independent of the soil background [44]. The index is the normalized ratio between visible red and short-wave infrared spectral bands, and the expression of this is displayed below:

$$NDWI = \frac{NIR - SWIR}{NIR + SWIR} \quad (2)$$

With its high sensitivity to water stress, NDWI is frequently used for the agricultural monitoring of drought and irrigation management. As well, some studies reveal the possibility of distinguishing crop types, especially winter crops, with NDWI [20,45–47].

- The Green Normalized Difference Water Index (GNDVI) was proposed in 1996 by Gitelson et al. [48], as NDVI; it is the index for evaluating the photosynthetic activity of the vegetation, except that the visible red band is replaced by the green band, ranging from 0.54 to 0.57 microns, and the expression of it is as follows:

$$GNDVI = \frac{NIR - Green}{NIR + Green} \quad (3)$$

Besides NDVI, the “Green” NDVI is more sensitive for assessing the chlorophyll concentration at the canopy level and it enables a precise estimation of the pigment concentration [48].

- The Enhanced Vegetation Index (EVI), developed by the MODIS Land Discipline Group [49], is aimed at optimizing the vegetation signal and correcting the imprecision of NDVI with improved sensitivity in high biomass regions by appending several additional spectral bands [50], and it is calculated by the following equation:

$$EVI = \frac{G * (NIR - Red)}{(NIR + C1 * Red - C2 * Blue + L)} \quad (4)$$

EVI is able to reduce the atmospheric conditions and canopy background noise with high sensitivity in densely vegetated areas and it is more responsive to canopy structural variations as compared to NDVI [50].

- The Soil-Adjusted Vegetation Index (SAVI), was proposed by Huete in 1988 [51] as an attempt to improve NDVI, which is frequently affected by the soil background conditions. Therefore, the index aims at minimizing the influence of soil brightness and eliminating the need for the additional calibration for different soils by using a soil-brightness correction factor [51]. It has an adjustment factor (L) in its calculation:

$$SAVI = \frac{(NIR - Red)}{(NIR + Red + L)}(1 + L) \quad (5)$$

SAVI was found to be helpful in separating different crop types, especially spring crops from winter ones [52].

- The Modified Soil Adjusted Vegetation Index (MSAVI) was developed by [53] in 1994 as an improved version of SAVI, with the constant soil adjustment factor L being replaced. It is proven to increase the dynamic range of the vegetation signal while further minimizing the soil backgrounds spatial and temporal variations, therefore resulting a greater vegetation sensitivity:

$$MSAVI = \frac{\left(2 * NIR + 1 - \sqrt{(2 * NIR + 1)^2 - 8 * (NIR - RED)}\right)}{2} \quad (6)$$

Studies have proven that MSAVI can be used in the agriculture field [54,55], and even more in winter crop monitoring [56].

After calculating the vegetation indices, an image stack with the ten original spectral bands and all of the indices was created for further image processing.

4.1.2. Image Processing

In this study, for the better extraction of winter wheat and winter barley in the study area from the satellite image, supervised image processing using different approaches was performed in order to make comparisons and attempt to reach the most adapted classification in this study (Figure 3).

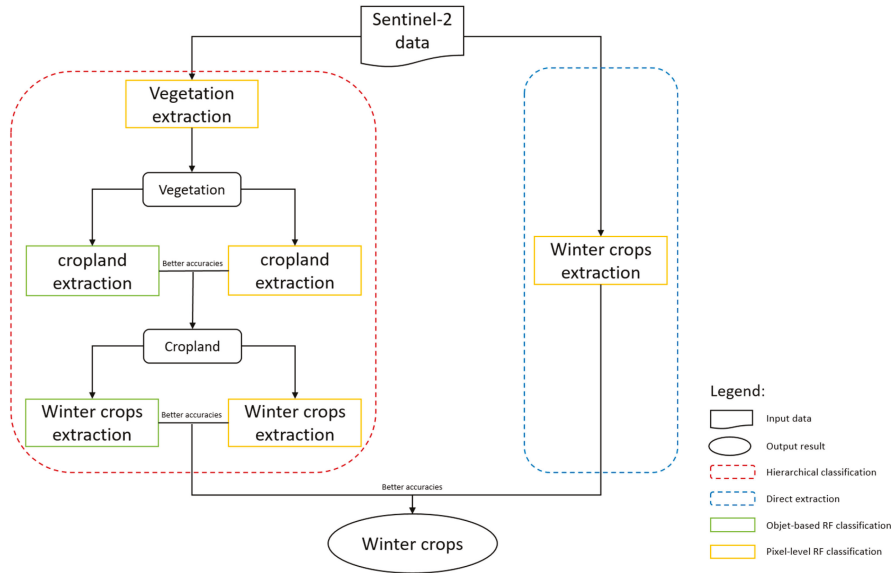


Figure 3. Proposed detail image processing methodology chart.

Compared to the direct extraction of winter crops with pixel-based RF algorithms, hierarchical classification methods are effectuated in three progressive levels, each with different objectives. The objectives from the first level of the hierarchy to the last one are extracting vegetation (including croplands) from raw images, extracting croplands from vegetated areas (trees, shrubs, and grassland), and finally, obtaining exclusively winter wheat and winter barley from all crop types detected in previous stages, respectively. Finally, the results of the two classification approaches were evaluated with accuracy indices, in order to distinguish which one had better agreement with the ground truth data.

In addition, inside the hierarchical classification structure, except for during the first step, separating vegetation and non-vegetation exclusively used the pixel-based RF algorithm and this reached a very close agreement with ground truth data. Each step has been performed using the two methods, pixel-based and object-based RF classification, in order to determine the result with better accuracies for further processing and analysis.

Pixel-Based Classification (PBC)

The traditional PBC is the most used method in remote sensing, especially for land use classification; therefore, this method was also widely employed in this study. The PBC was done on the pixel level, which is the smallest unit in an image, where only the spectral information of each single pixel was used. During the classification, each pixel was assigned predefined classes by using a model that was well trained with training data and a classification algorithm. In this paper, PBC is performed in both classification approaches.

Object-Based Classification (OBC)

OBC starts with an additional processing step before classification, which involves the segmentation of an image into numerous, non-overlapping, homogeneous objects [23],

hence, the OBC was done on the object level instead of the pixel level. At the same time, aside from the simple spectral information, the texture, color, form, and size of the objects are taken into account. Later the individual object that was generated by the segmentation algorithm was used for classification.

A Multiresolution Segmentation (MRS) algorithm was applied as the first step of the object-based image analysis (OBIA) in the current study. This relatively complex and user-dependent algorithm has proven to be one of the most successful image segmentation algorithms in the OBIA area [57]. At the beginning of the process, each pixel is considered as a segment; afterwards, pairs of adjacent image objects are merged to form larger segments [58]. The three main parameters of the algorithm: scale, shape, and compactness, can be adjusted by users. The scale parameter is able to define the maximum standard deviation of the heterogeneity in order to control the amount of spectral variation within objects and the size of their results [57,59]. Thereafter, there are also two homogeneity criteria, the shape criterion that defines the weight between the shape and the spectral information of the objects, and the compactness criterion which represents the compactness of the objects during segmentation [60].

In this study, several combinations of parameters were used, and the optimal ones were found on a trial-and-error basis. The scale, compactness, and shape parameters were assigned as follows: 15, 0.5, and 0.3, respectively, for cropland extraction, and 20, 0.5, and 0.1, respectively, for winter crops extraction.

Supervised RF Classification

Supervised RF classification was performed on the Sentinel-2 data. It is the most common procedure for the quantitative analysis of remote sensing imagery [61], and it involves the use of training data for machine-learning classification. The training data were selected with reference data, knowledge, and experience provided by the user, and the selected samples were considered representative of each class.

Training data and test data in our research were selected in this step, using the RPG 2019 map. For the purpose of comparing different methods of classification, training data that were selected for PBC and OBC were as similar as possible, such as using the same area and very approximate surfaces, in order to improve the global comparability of the two methods.

RF classification has been one of the most known and widely used classification algorithms, especially in the land cover classification field, over the past two decades. This powerful machine learning classifier has numerous key advantages, such as a low sensitivity to noise or overtraining, the ability to handle high-dimensional data, its high classification accuracy and non-parametric-nature, and its capacity to determine variable importance [19].

RF is also one of the ensemble learning algorithms that builds numerous classifiers that have been proven to improve classification accuracy considerably. For classification, RF forms an ensemble method using a tree-like classifier, where each tree in the forest contributes a single vote for the most popular class, and the majority of the vote determines the final prediction of the RF model [62].

The training and classification of the RF module were applied using the Orfeo toolbox with two user-defined parameters that were set on a trial-and-error basis: the number of decision trees grown in the forest and the maximum tree depth, which is the length of each tree in the forest. The two parameters that were used in this study were defined as 100 and 25, respectively.

4.1.3. Image Post Processing

After the classification, the accuracy assessment was performed with test data in order to evaluate the classification's degree of agreement with the reality and therefore assess the reliability of the classified results. In this study, in order to evaluate the classification quality and compare it amongst the different classification methods, five well-known

and highly promoted accuracy indices were calculated for each classification method and each class. Among them, overall accuracy (OA) and kappa were employed for the global accuracy assessment, otherwise, precision, recall, and F-score were computed to assess the classification results of each class.

The OA is one of the traditional measures of classification accuracy that is derived from the confusion matrix [63]. It indicates the probability that an individual pixel will be correctly classified by a classifier [64], hence, it is computed by dividing the number of correctly classified pixels by the total number of pixels in the confusion matrix. The popular kappa coefficient was first applied in the remote sensing community to express the classification accuracy in the early 1980s [65], and it is considered to be the assessment of the inter-classifier agreement and the accuracy of two classifiers; it usually gives a statistically more sophisticated measure of interclass agreement, also it gives a better interclass discrimination than OA does [66].

Among the per-class accuracy assessments, precision and recall were computed from the confusion matrix as well. Precision is also called the positive predictive value, which is related to the rate of correct positive predictions among the total predictions that are classified as positive, and the recall or sensibility represents the rate of the actual positive individual pixels that are correctly detected by the classifier. Furthermore, the F-score was generated from the precision and recall; it provides a single harmonic mean of the model's precision and recall.

In the hierarchical classification process, test data that were used for evaluating the classification of each step were generated as random points from the image that were used to perform classification, which is the result of the previous steps. Afterwards, the random points were labelled manually with the Graphic Parcel Register map as ground truth. However, with the aim of evaluating the performance of the proposed hierarchical classification approach by comparing with traditional direct extraction, a completely new test dataset was produced from the original Sentinel-2 image that was not classified.

4.2. Crops Phenology Monitoring

This second part of the study was performed, based on the mapped winter crops from the previous step. Due to limited climate conditions in the study area, winter crop phenology monitoring was performed with Sentinel-1 C-band SAR data using the Google Earth Engine (GEE) platform. GEE is an open-source, cloud computing platform with a fast, high-performance computation and visualization system and a large data catalog which hosts a large repository of publicly available geospatial datasets, including a variety of satellite imaging systems [67]. The platform is designed for global-scale geospatial big data storage, processing, and analyzing [68]. The utility of GEE has been examined in different fields, for vegetation mapping and monitoring, land cover change mapping, and agriculture applications [68].

The platform proposes a complete data process chain from a single or a collection of analysis-ready images to library functions or user-defined algorithms that are applied to achieve results generation and visualizing. One of its main advantages is allowing long-term monitoring using a user-defined period with free access to preprocessed time series data. Hence, in this study, the backscatter coefficient (σ°) in decibels (dB) of both polarizations (VV and VH) and their ratios of a Sentinel-1 image time series during a complete growing period of winter crops (from October to September) on a few chosen croplands was automatically generated in a line chart on the GEE platform. In order to study the scattering behavior of our target croplands, each image was preprocessed, and the backscatter coefficient was converted to dB by GEE using the Sentinel-1 Toolbox (Figure 4) A flow chart of the Sentinel-1 image time series process in GEE is displayed as follow (Figure 4):



Figure 4. Sentinel-1 image process in the GEE platform.

The first step in applying the orbit file aims at updating the orbit metadata with a restituted orbit file, then Ground Range Detected (GRD) border noise removal attempts were performed to remove the low intensity noise and invalid data on the scene edges. Afterward, a thermal noise removal function aims to remove the additive noise in sub-swaths to reduce the discontinuities between sub-swaths for scenes in different acquisition modes. Thereafter, radiometric calibration is applied to compute the backscatter intensity, and subsequently, a terrain correction, also called an orthorectification, was performed to convert the data from ground range geometry to σ° [69]. Lastly, dB was calculated from σ° with the equation $\text{dB} = 10 \times \log_{10}\sigma^\circ$. A series of line charts in dB were plotted for each polarization and ratio of each winter crop.

5. Results

5.1. Winter Crop Types Classification Methods Comparison

The classification results of the different approaches and methods of the winter wheat and winter barley and their accuracy analysis are presented in this part. Firstly, the results of PBC and OBC of each step in the hierarchical classification are demonstrated and evaluated through accuracy assessments, the more accurate results were retained for further processing and comparison with classical direct extractions. Then the final results of the hierarchical classification and classical direct extraction are displayed and compared with accuracy assessments as well.

5.1.1. PBC versus OBC

Vegetation Extraction

For vegetation extraction (including cropland), only PBC was performed since it achieved a great accuracy, approximately close to 1. From Figure 5 we see that the distribution of vegetation and cropland is coherent in the study area, apart from some urban environments, which are marked by intense non-vegetation pixels, in particular these areas are in the south and the northeast of the study area. According to Table 3, both global and interclass accuracy indices are very close to 1, this indicates a high probability of a correct classification of each individual pixel, and a great overall agreement level with the ground truth. Besides a good performance and good training of the PBC method, the distinction between the vegetated area and non-vegetation is very significant, and therefore, it is easy to classify.

Table 3. Accuracy assessment of PBC vegetation (including cropland) extraction.

| | Precision | Recall | F-Score |
|------------------------|-----------|--------|---------|
| Vegetation | 0.992 | 0.997 | 0.995 |
| Non-vegetation | 0.994 | 0.984 | 0.989 |
| Kappa: | 0.984 | | |
| Overall accuracy (OA): | 0.993 | | |

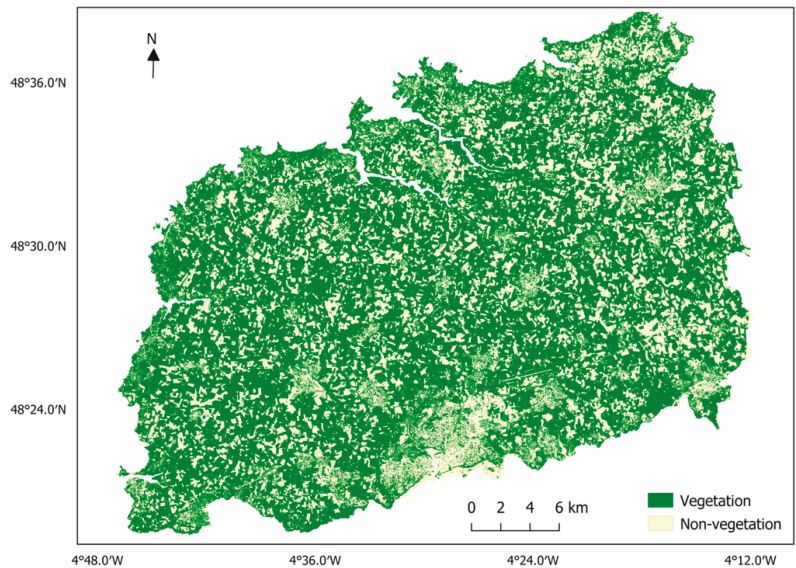


Figure 5. Level 1: PBC vegetation (including cropland) extraction results.

Croplands Extraction

Subsequently, based on the vegetated area that was extracted from the previous step, we aimed to distinguish and preserve only the croplands from all arboreal vegetation, shrub, and grasslands, including pasture. In this step, OBC and PBC were both performed and evaluated. Figure 6 demonstrates that the results of the two methods are almost identical, although more individual pixels were classified as cropland in PBC considering that PBC was operated on pixel-level.

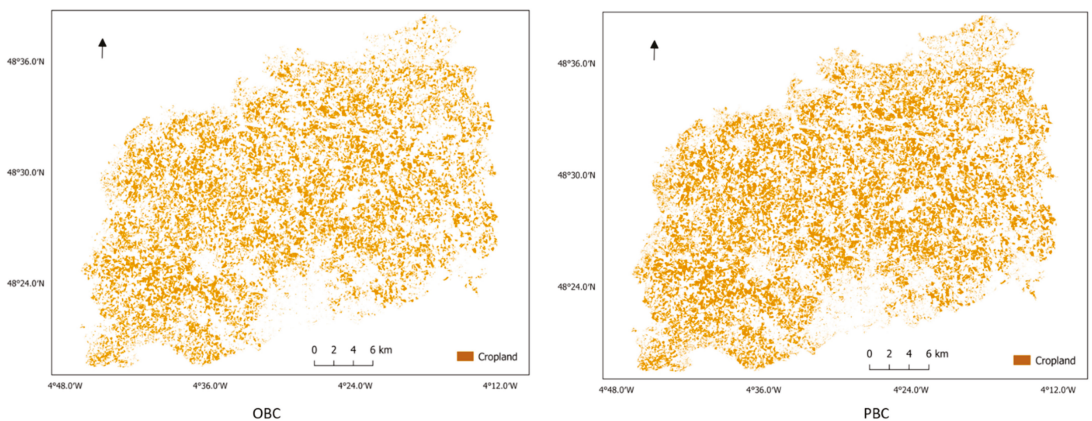


Figure 6. Level 2: PBC and OBC croplands extraction results.

Pursuant to Tables 4 and 5, even though the global accuracy indices of the results of OBC are slightly better than PBC with a difference of 0.024 in kappa and 0.004 in OA, the indices of the two results are still comparable. The tables below show that a large proportion of pixels are correctly predicted, in general, and that the level of agreement with the ground truth data is somewhat lower, but it is still acceptable. Furthermore, for the

interclass accuracy evaluation, cropland generally has the highest precision, recall, and F-score results, which are all around 0.90. The models were well trained to make a good prediction of the cropland class, especially for the OBC model, and most of the individual pixels belonging to the cropland class were correctly detected. This can be explained by the OBC taking into account the geometry, form, and texture elements, which are the key elements that are used to distinguish the croplands from other vegetation. The classification of the vegetation has a slightly lower accuracy of approximately 0.2 in comparison with croplands because of the mix of different kinds of vegetation and the uncertain form of the vegetated area, though OBC remains more precise when it is compared to PBC. Finally, the classes of the other pixels in our study area, which were mainly some isolated pixels that were left from the previous step due to some errors, were better classified with PBC since the non-vegetated area has highly different spectral behavior as compared to that of vegetation. Considering the better accuracy assessments of OBC, its classification result was preserved to perform the next step of classification.

Table 4. Accuracy assessment of OBC croplands extraction.

| | Precision | Recall | F-Score |
|------------------------|-----------|--------|---------|
| Vegetation | 0.786 | 0.746 | 0.765 |
| Cropland | 0.912 | 0.905 | 0.908 |
| Others | 0.700 | 0.875 | 0.778 |
| Kappa: | 0.716 | | |
| Overall accuracy (OA): | 0.861 | | |

Table 5. Accuracy assessment of PBC croplands extraction.

| | Precision | Recall | F-Score |
|------------------------|-----------|--------|---------|
| Vegetation | 0.769 | 0.678 | 0.721 |
| Cropland | 0.879 | 0.932 | 0.905 |
| Others | 0.929 | 0.813 | 0.867 |
| Kappa: | 0.692 | | |
| Overall accuracy (OA): | 0.857 | | |

Winter Crops Extraction

In this final step, two winter crop types were extracted, based on the results of the previous step, and the classification result of the cropland extraction was achieved by using OBC. The results of the two classification methods (Figure 7) are very close to identical in this level, wherein the differences between the two maps can hardly be noticed.

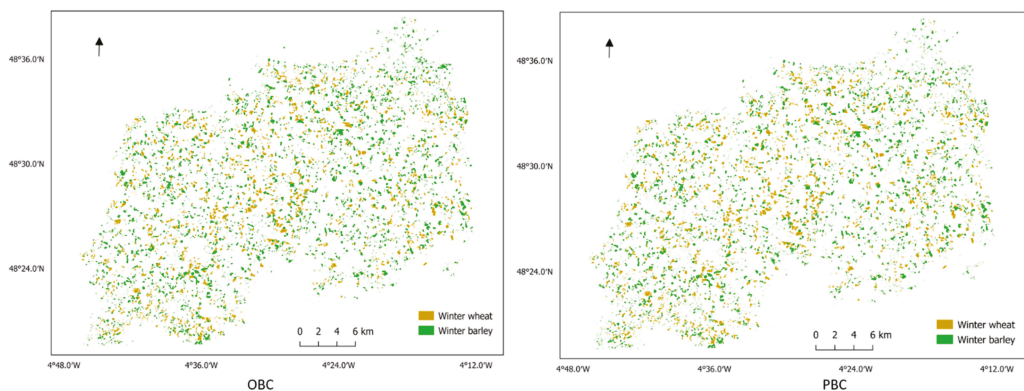


Figure 7. Level 3: PBC and OBC winter crops extraction results.

With the lack of a possibility to visually compare the two methods, they were evaluated and compared by using accuracy assessments (Tables 6 and 7). In regard to the global accuracy indices, all classes were stated as accurate when using the two methods, which signifies a good performance by both methods with a high accuracy and a strong level of agreement for the classification. Beyond that, it is worth noticing that PBC shows a better potential with about 0.03 higher value in the OA and 0.04 in kappa, moreover, PBC basically achieves a better accuracy indicator of three classes in comparison with that of the OBC. The results illustrate that the difference in spectral behavior was exploited to distinguish winter crops from other crops, since all the croplands share similar geometry, form, and texture characteristics. Nonetheless, among the different crop types that were presented in our area of study, winter wheat has the most distinctive spectral signature, thus it was found to be the class with the best accuracy indices in both results, with very strong reliability in terms of prediction and a high rate of precisely identifying winter wheat. In contrast, the classification of winter barley and other crops are somewhat less accurate with approximately 0.1–0.5, and the advantage of PBC is more significant, with higher accuracy indicators of around 0.04, which might be caused by the confusion of winter barley and other crops due to the similarity of their spectral behavior. In addition, the difference between these two classes were better detected by PBC with spectral information.

Table 6. Accuracy assessment of OBC winter crops extraction.

| | Precision | Recall | F-Score |
|------------------------|-----------|--------|---------|
| Winter wheat | 0.998 | 0.978 | 0.988 |
| Winter barley | 0.833 | 0.871 | 0.852 |
| Other crops | 0.870 | 0.848 | 0.859 |
| Kappa: | 0.848 | | |
| Overall accuracy (OA): | 0.899 | | |

Table 7. Accuracy assessment of PBC winter crops extraction.

| | Precision | Recall | F-Score |
|------------------------|-----------|--------|---------|
| Winter wheat | 0.994 | 0.976 | 0.985 |
| Winter barley | 0.876 | 0.913 | 0.894 |
| Other crops | 0.917 | 0.895 | 0.906 |
| Kappa: | 0.892 | | |
| Overall accuracy (OA): | 0.928 | | |

5.1.2. Hierarchical Classification versus Classical Direct Extraction

The results of the hierarchical classification, which is the classification approach that was proposed in this study, and the classical direct extraction for the winter crops mapping are presented in Figure 8. Generally, winter wheat and winter barley were well detected and extracted from the Sentinel-2 image; the results of two classification approaches are globally identical, with particular reference to the homogeneous distribution of the winter crops over the area of interest. Nevertheless, the classical direct extraction approach identified more winter croplands, especially winter barley, and the winter croplands that were detected are much more fragmented; many small pixels were classified as croplands. This could be explained by the fact that winter crops are directly extracted from the preprocessed image; in addition, there might be some confusion between winter barley, grasslands, and some different crops considering the resemblance of their spectral behavior.

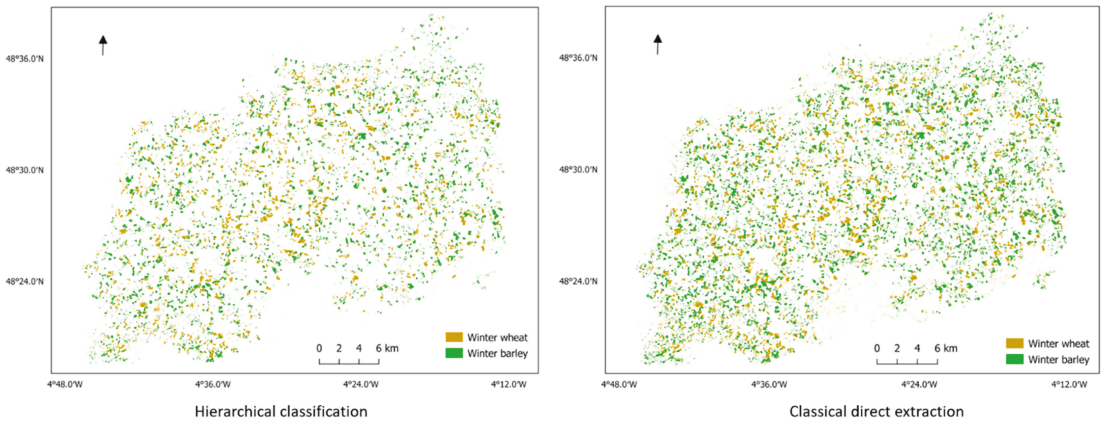


Figure 8. Classification results with hierarchical classification and classical direct extraction.

To make a better comparison, the accuracy assessments of the two approaches are displayed in Tables 8 and 9. According to the tables, both classification results are very satisfactory as mostly all of the accuracy indicators range from 0.8 to 1, specifically, with the hierarchical classification, almost all indices are superior to 0.9. This suggests a good performance and training of the models and also a strong agreement with ground truth of all classification approaches in the study. Still, it is worth noticing that the hierarchical classification shows a better potential for specific crop type mapping as compared to the classical direct extraction (approximately 0.1 higher in kappa and 0.07 in OA). Additionally, nearly every class achieved a higher accuracy in hierarchical classification, which indicates that the model is solid, and it is able to make a good prediction. Among the three classes, winter wheat is the most correctly classified class in both of the classification approaches, the indicators that range from 0.90 to 0.99 and with an F-score that is highly similar. Hierarchical classification reaches a better precision index, that means that the model is more exact, yet classical direct extraction achieved a finer recall, which means that the model returned more relevant results, and it can correctly and efficiently identify winter wheat. In addition, winter barley and the other classes were evaluated and less accurately classified, especially with the classical direct extraction approach. According to Table 8, the winter barley class obtained a high recall (0.960) and a relatively lower precision (0.683), which suggests a high false-positive rate; many individuals that were predicted as winter barley that the model returned were found misclassified when they were compared to the test data. On the contrary, the other class received a high precision index (0.955) and a comparatively low recall (0.797), and these indicators demonstrate that the pixels were correctly detected and labelled despite there being fewer results returned by the model. The comparably low accuracy of the two classes and the imbalance between the precision and recall indices might be explained by: (1) the similarity of the spectral behavior between winter barley and other crops and even grassland in the case of the classical direct extraction approach. (2) Since two winter crops are extracted directly from the Sentinel-2 image, the other class included not only non-vegetated urban areas, but also vegetation and other croplands which occupy a large area of our study site. Therefore, an imbalance between classes was caused, thus, more training datasets of the other class were acquired in consideration of its weak intraclass correlation.

Table 8. Accuracy assessment of hierarchical classification.

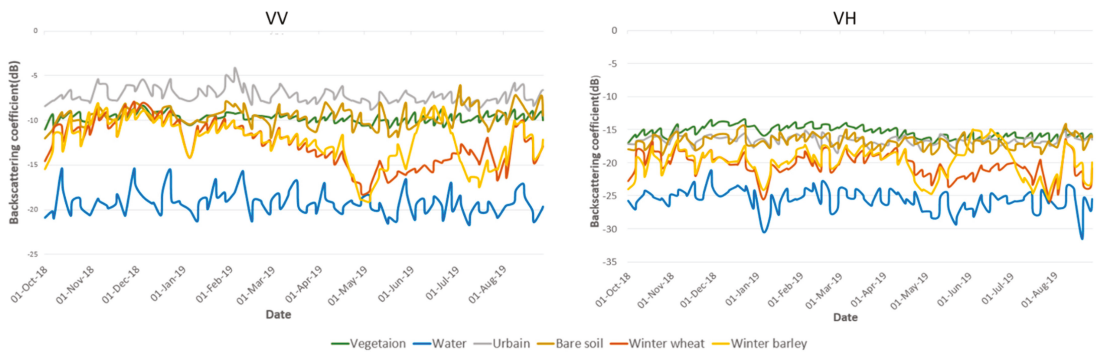
| | Precision | Recall | F-Score |
|-------------------------------|-----------|--------|---------|
| Winter wheat | 0.991 | 0.904 | 0.946 |
| Winter barley | 0.886 | 0.900 | 0.893 |
| Others | 0.929 | 0.959 | 0.944 |
| Kappa: | 0.888 | | |
| Overall accuracy (OA): | 0.932 | | |

Table 9. Accuracy assessment of classical direct extraction.

| | Precision | Recall | F-Score |
|-------------------------------|-----------|--------|---------|
| Winter wheat | 0.959 | 0.928 | 0.943 |
| Winter barley | 0.683 | 0.960 | 0.799 |
| Others | 0.955 | 0.797 | 0.869 |
| Kappa: | 0.789 | | |
| Overall accuracy (OA): | 0.866 | | |

5.2. Crops Phenology Monitoring

The Sentinel-1 temporal backscattering coefficient profiles of diverse land cover types at VV and VH dual-polarizations from the study area during the growing season of the winter crops (from 1 October 2018 to 1 September 2019) are shown in Figure 9; the temporal profiles of the mean σ_{vv} and σ_{vh} values of urban, vegetation (including other crops), water, bare soil, winter wheat, and winter barley land cover are displayed. As shown in Figure 9, besides the profiles of the water area, which fluctuate significantly due to the weather conditions, the temporal profiles of the vegetation, urban, and bare soil are much more stable than the profiles of winter crops are, which have a significant fluctuation according to their different growth stages. Especially in the σ_{vh} profile, the vegetation, urban, and bare soil profiles are generally close to their mean value, regardless of the season. Nonetheless, the variation of the backscattering coefficients of the two winter crops are clearly evident, for example, a peak is seen in early December, followed by a minimum value in early summer and a maximum value in midsummer. Thus, the results indicate that it is feasible to distinguish winter crops from other types of land cover, particularly vegetation and other crops, and furthermore, we are able to identify and study the main phenological stages from germination to ripening (harvesting) by using Sentinel-1 temporal profiles.

**Figure 9.** Sentinel-1 temporal backscattering coefficient profiles of different land covers (vegetation, water, urban area, bare soil, winter wheat, and winter barley) in the study area at VV and VH polarizations from 1 October 2018 to 1 September 2019.

Based on prior knowledge and field research with local farmers, winter wheat and winter barley are both cereal crop types that are planted from October to November. Generally, winter barley is sowed earlier than winter wheat in the Finistère department. Germination, which is the first growth stage of the crops, takes place three to four weeks after sowing, hence, this is in early December for winter wheat and in mid-November for winter barley. The crops remain in their vegetative stage during winter, and stem elongation begins in spring, and it lasts until the plants reach their maximum height, usually in early summer. Lastly, ripening, the final growth stage, and harvesting occur in summer (early summer for winter barley and mid-summer for winter wheat).

In Figure 10, both the raw signal and smoothed trend line of the temporal backscattering coefficient profiles of VV, VH, and the VH/VV ratio for the 2018–2019 growing season are displayed. Looking at the charts, it is shown that large variations occur before the germination due to the interaction between the bare soil and vegetation that is caused by stem-ground double scattering [6,70], while previous research suggests that the fluctuation in the backscattering profiles is mostly induced by changes in soil water content and roughness [6]. Pursuant to previous research, germination as the first stage of emergence of the plant can be recognized as the first maximum value of the profiles before they begin decreasing [25], therefore the germination stage is observed at around 1 December for winter wheat, and in early November for winter barley. Moreover, for winter wheat, this phase is best observed with VV and the VH/VV polarizations as they represent the first peak of the curves; however, the peak is better illustrated at VV and VH polarizations for winter barley. Afterwards the overwintering stage occurs, and the crops remain in their vegetative stage during winter (generally around 1 January); a gentle decreasing and a slight flattening can be observed in the VV polarization curves during this stage for both the crops. Furthermore, a fluctuation of the VV and VH curves of the two crops at around 1 January 2019 is driven by a short pause of rainfall, as the signals are highly affected by the soil water content. The stem elongation stage starts in spring, where the vertical development of the stems and leaves of the plants cause soil scattering attenuation, represented as a continuous and steadily decreasing line, until they reach the heading stage, where the plants achieve their maximum height. After a long decreasing phase, σ° reaches the minimum value of the temporal profiles at the heading stage at around 1 May 2019 for both winter crops, and this stage can be better observed in σ_{vv} and σ_{vh}/vv for winter wheat phenology, and in σ_{vh} and σ_{vh} for winter barley. However, the sharp decrease in σ_{vv} and σ_{vh} at the heading stage, specifically in the profiles of the winter barley might be the result of the relative lack of rainfall that occurred after early April. After heading, the inflorescence emergence, anthesis, grain development, and dough development stages occur. As seen on the graphs the curves start to increase during the flowering and grain development stages. These stages are illustrated by a sharp increase in the winter barley, regardless of the polarization, while by contrast the σ_{vv} and σ_{vh}/vv of the winter wheat shows a smooth increase. At last, the ripening stage, which is the maturation stage, occurs and the crops are ready to be harvested. This phase is shown as the last peak of the profiles during the growing season, followed by a sharp decrease which is caused by the absence of volume and multiple scattering after the harvesting [25]. As the results show, harvesting, which took place around 1 August 2019, is better demonstrated by σ_{vv} and σ_{vh} for winter wheat, while the harvesting stage was in late June for winter barley, and it is clearly shown by all polarizations, particularly in VV and VH.

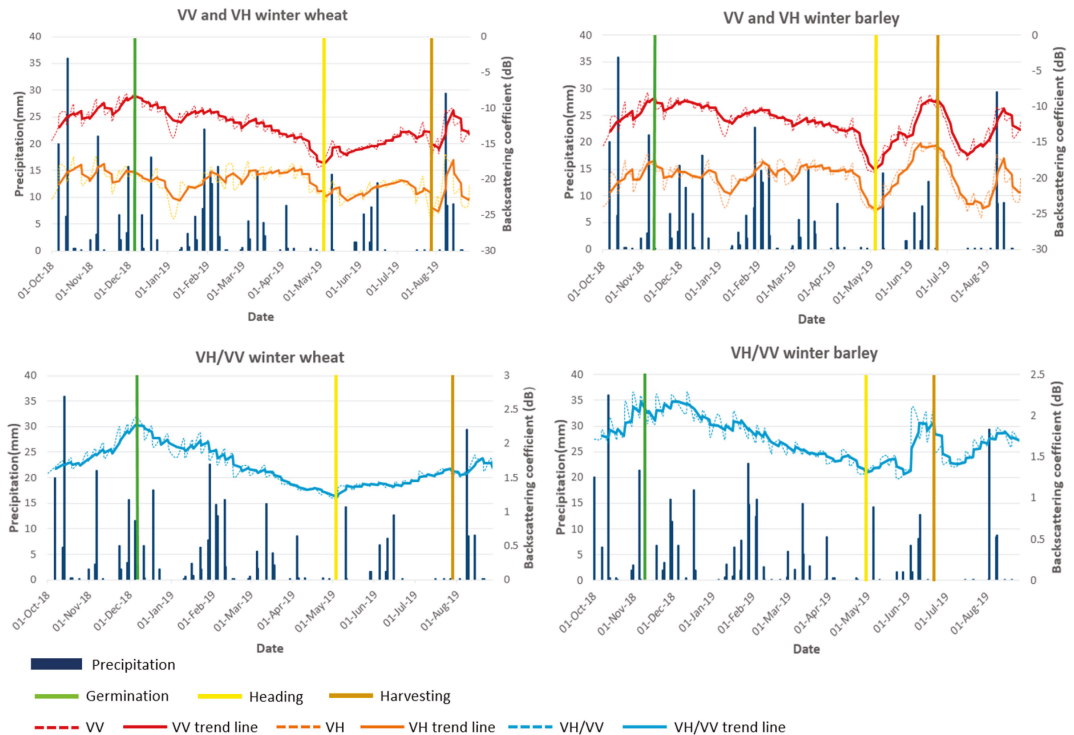


Figure 10. Winter wheat and winter barley Sentinel-1 temporal backscattering coefficient profiles at VV, VH, and VH/VV polarizations of the northern part of the Finistère region for the 2018–2019 growing season, with the daily precipitation data and three main phenological stages, which are presented by a vertical line as well.

The best polarization for each phenological stage (germination, heading, and ripening (harvesting)) are detailed as follows in Tables 10 and 11. The phenology monitoring of the winter wheat highly relies on VV polarization, while the VH/VV ratio is also very helpful in identifying the germination and heading stages. Otherwise, the VH polarization was used to detect the ripening stage and the harvesting event.

Table 10. The best polarization observed for each phenological stage of winter wheat in the study.

| Stage | Polarization | Date | Determination |
|-----------------------|--------------|-----------------|---|
| Germination | VH/VV, VV | Early December | First peak of the temporal series |
| Heading | VV, VH/VV | Early May | The minimum value after emergence |
| Ripening (Harvesting) | VV, VH | Around 1 August | Last maximum of the profiles, following by a sharp decrease |

Table 11. The best polarization observed for each phenological stage of winter barley in the study.

| Stage | Polarization | Date | Determination |
|-----------------------|---------------|----------------|---|
| Germination | VV, VH | Early November | First maximum of the temporal series |
| Heading | VV, VH | Around 1 May | The minimum after emergence |
| Ripening (Harvesting) | VV, VH, VH/VV | Around 1 July | Last maximum of the profiles, following by a sharp decrease |

Meanwhile, the phenology monitoring of the winter barley depends more on VV and VH polarizations, which are able to easily identify the three phenological statuses. In addition, VH/VV polarization is also effective for detecting the ripening and the harvesting stages.

6. Discussion

6.1. Hierarchical Classification for Winter Crops Mapping

In this study, two different classification approaches using Random Forest machine learning methods were performed on a Sentinel-2 high spatial resolution satellite image that was acquired in April 2019, which is the growing season of the winter crops, in order to detect and map winter wheat and winter barley in a fragmented area that was occupied by different land categories. One of the main objectives of this paper was to successfully extract winter crops data with the hierarchical classification that was proposed in this study, which allows an efficient winter crop type mapping for a study area with a complex landscape, and to easily distinguish winter crops from other land cover types, especially arboreal vegetation, shrubs, grassland, and other crop types. The results of the hierarchical classification were evaluated with different accuracy indicators (global or interclass) and were finally compared with the traditional direct extraction approach.

Both classification approaches achieved a good accuracy level despite the complex occupation and small cropland size in the region, with an overall accuracy of 0.866 and 0.932 and a kappa index of 0.789 and 0.888 for classical direct extraction and hierarchical classification, respectively. Even though the classical extraction method worked well for winter crop mapping, the accuracy assessment indicates that the hierarchical classification is clearly more accurate and better suited to our study by turning a complex multi-class classification problem into a series of smaller classifications. According to the results that are presented in Figure 8 and the accuracy indicators that are displayed in Tables 8 and 9, apart from the global accuracy indicators, the hierarchical classification has proven to be reliable, with outstanding performance in the classification of both winter crops classes, particularly the winter wheat.

The hierarchical classification approach is widely used in many different fields, such as for categorization problems [71], biological predictions [72,73], and music genre classification [74,75], meanwhile the concept of solving a complete classification problem step-by-step using agglomerative algorithms plays also an important role in image classification and its efficacy is well known and it is recognized by previous studies [76–79]. In this study, we proposed a hierarchical classification framework that was constituted by three smaller classifiers for extracting winter crop data, and we have clearly demonstrated the superiority of the hierarchical framework over the classical extraction method.

Additionally, both classifications in this study were performed with supervised RF machine learning methods and highly accurate results were acquired, regardless of the approach or the method. Therefore, RF has proven to be a feasible, well-suited classification algorithm for precisely mapping specific winter crop types from a small-sized field in a complex area.

6.2. Comparison of PBC and OBC

In this work, PBC and OBC were implemented in the two steps of the classification process within the hierarchical classification structure (croplands extraction from all vegetated area, and winter croplands extraction from all croplands). In addition, the two classification models were trained by a similar dataset, and then evaluated using the same test data. The two classification methods are widely known and used, and they are always compared in different fields. OBC provides a method to the satellite image classification, and numerous studies in the remote sensing field it is demonstrated that OBC usually achieves a better classification with different data and in different landscapes over PBC by bringing complementary information other than the spectral signal and turning classification units from pixels to image objects [80–83]. Whiteside et al. in 2011 [23] indicated that OBC has a better potential for extracting land cover information in a spatially heterogeneous land cover

area, while Weih and Riggan in 2010 [24] proposed that OBC produced more homogeneous classes, as the classes that were produced by PBC are more fragmented. Furthermore, many studies have also pointed out that OBC regularly outperforms PBC for crop type mapping and they noted that it has a more efficient calculation time [84–86]. However, OBC is limited by segmentation errors, such as over-segmentation and under-segmentation, which bring negative impacts to the classification; consequently, low segmentation accuracy leads to low classification accuracy [79,86,87]. Furthermore, some studies have also revealed that the difference in accuracy values between the two methods decreases or even disappears when the same classification algorithms are applied, or the spatial resolution of the image is increased [88–90].

In this work, the results illustrate that each method has its advantage in the classification process. OBC slightly outperformed PBC in cropland extraction as the complementary texture, geometry, and shape information are helpful for cropland detecting. On the other hand, PBC reaches a higher accuracy in winter crops extraction, since all croplands have a similar shape, but winter crops can be easily distinguished from other crops with direct spectral information. Additionally, the statistical difference between the results of PBC and OBC is not particularly significant. In conclusion, small differences that are induced by several factors between the two methods can be noticed, yet both methods are equally useful for our classification.

6.3. Potential of Sentinel-1 Data in Crops Phenology Monitoring

Optical satellite data are well developed and have traditionally been used for different crop phenology monitoring by using vegetation indices time series [91–93], with NDVI being the most used vegetation index for crop phenology mapping [26,94,95]. However, Sakamoto et al. in 2005 [96] proposed rice phenology detection with time-series EVI data with fewer errors between the estimated phenological dates and the statistical data. Dong et al. in 2020 [10] have exploited the potentialities of a newly developed vegetation index, the Normalized Difference Phenology Index (NDPI), to provide more robust vegetation information and to reduce the adverse impacts of soil and snow cover for winter wheat mapping. In recent years, with the emergence of the new generation of high spatial and temporal resolution SAR data, a particular interest in radar data for crop phenology monitoring was found, especially for its “all weather” capacity, which leads directly to an increased role of SAR data in the field [97–99]. This study proved that Sentinel-1 C-band SAR-polarized backscatter time series data has great potential to monitor winter crop phenology in a coastal area that is marked by frequent precipitation, and some important considerations of the behavior of different polarizations in regard to different phenological stages are worth discussing.

Firstly, despite the σ° of both polarizations and their ratios being relatively similar, the curves of the VH and VV polarizations are sharper when they are compared to those of the ratio, due to the fact that the ratio is less sensitive to varying conditions like moisture and incidence angle variations. This can be explained by such effects having certain impacts in both polarizations, where the impacts would be reduced in the ratio [1]. As seen in Figure 10, the curves of the ratio VH/VV of winter wheat and winter barley are smoother in comparison with those of the single polarization and they are less impacted by continuous rainfalls or drought due to absence of precipitation.

Secondly, the timing of the phenological stages or growing periods of the crops based on the field knowledge are in agreement with the observations of the results. Based on prior knowledge, the sowing takes place between October and November, and winter barley is usually planted earlier than winter wheat is, and the germination occurs 3–4 weeks after sowing. This period can be confirmed by noting the large variations of the curves in the beginning which are induced by the interaction between the bare soil and the vegetation that is caused by the stem-ground double scattering [6], afterwards the germination is represented by the first peak of the curves, and this is especially well demonstrated in the polarization ratio for winter wheat and in the single polarizations for winter barley. After

the overwintering period, the stem elongation, which begins in spring, can be recognized on the curves as a decreasing period that is caused by the attenuation of the signal when the vegetation cover occurs. Thereafter, the heading stage, where the crops attain their maximum height, occurs in early summer. This stage was confirmed with a minimum value on the curves at around 1 May, which can be well observed in the polarization ratio for winter wheat and in single polarization for winter barley. After heading, the volume backscattering was increased due to the increase of the plant biomass [1], and the winter barley is harvested in early summer, and the winter wheat is harvested in midsummer. This is illustrated by the curves in all polarizations decreasing as expected with large variations post-harvesting, depending on the soil conditions.

This leads to the conclusion that it is feasible to map crop phenology with high accuracy by using SAR data, which is highly sensitive to the phenology of agriculture crops. In addition, unlike many methods which exclusively use the single polarization or the ratio [31,100,101], our study shows that the combination of both is able to provide a better observation of agriculture phenology. Further studies can investigate the feasibility and performance of combining SAR and optical data for crop phenology monitoring.

6.4. Limitations and Perspectives

Some limitations were revealed during the process of result analyzing. Despite the fact that the hierarchical classification approach acquired a better accuracy (0.099 in kappa and 0.066 in OA), this classification approach required more complicated processing steps and was more costly when one is comparing it to the direct extraction, for a slight enhancement in the results. Moreover, the confusion between winter barley and grassland was nonnegligible. For increasing classification accuracy, extra data such as SAR or Sentinel-2 time series data can be applied. Additionally, even though the three main phenological statuses were successfully extracted from Sentinel-1 backscatter time series, more field research and expert knowledge is required for identifying some others important phenological stages (e.g., tillering, flowering, soft dough and hard dough).

7. Conclusions

Three issues surrounding winter crops have been studied and discussed in this paper. Firstly, two types of winter crops (winter wheat and winter barley) were mapped by using a Sentinel-2 high-resolution image, and two different classification approaches were performed. Both the hierarchical classification, which turns a complex classification problem into a series of smaller classifications, and the classical direct extraction, which extracts the winter crops directly from the original satellite image, were carried out. The hierarchical classification was composed of three smaller classifications: vegetation extraction from the original image, cropland extraction from the vegetation, and finally the winter crop extraction from other crops. Additionally, PBC and OBC were both performed in the last two steps and evaluated in order to keep the most accurate classification for further processing and analysis. Subsequently, crop phenology monitoring was performed, based on the results of the previous step by using Sentinel-1 C-band SAR time series data, and the three important phenological stages (germination, heading, and ripening (harvesting)) and the main growing periods were identified as well.

To respond to the objectives of the study and as the contribution of this paper, our results showed that winter crops in a fragmented landscape with heterogeneous land cover were successfully detected with high accuracy by using a Sentinel-2 image and the classification approaches that have been proposed. In particular, the hierarchical classification framework significantly improved the classification accuracy (0.1 and 0.06 increase in the kappa and OA, respectively, against classical direct extraction), moreover the classification of winter barley is also enhanced by reducing the confusion between winter barley and grassland with the hierarchical classification framework (0.094 increase in the F-score). Within the hierarchical classification, each classification method has its advantage; OBC slightly outperformed PBC in cropland extraction, yet PBC achieved higher accuracy in

winter crops mapping. Although some small differences can be noticed, however there is no significant statistical divergence between the two classification methods.

The results also lead to the conclusion that Sentinel-1 C-band SAR-polarized backscatter time series has great potential to monitor winter agriculture phenology in a coastal area with frequent rainfall. Three phenological stages and main growing periods could be easily identified from the time series in a single polarization or from the ratio, and furthermore the timing of the stages and the growing periods of the crops that are observed in the results highly conform to the field knowledge.

Although very satisfactory results were acquired in this study, some recommendations can be made for further studies, such as applying Sentinel-2 time series or SAR data for crop mapping in order to increase the classification accuracy, and in particular to reduce the confusion between winter barley and grasslands or other crop types. Exploring the potential of the combination of SAR and optical data for identifying more phenological stages and growth periods from the time series is advocated by us.

Author Contributions: G.X.: Conceptualization, methodology, software, investigation, resources, data curation, writing—original draft preparation; S.N.: Conceptualization, validation, formal analysis, writing—review and editing, visualization, supervision, project administration, funding acquisition. All authors have read and agreed to the published version of the manuscript.

Funding: This research was funded by Fondation de France and the French Space Agency (CNES).

Data Availability Statement: Publicly available datasets were analyzed in this study. The data can be found here: theia.cnes.fr/ (accessed on 31 July 2022) for Sentinel-2 image, earthengine.google.com for Sentinel-1 image, www.geoportail.gouv.fr/ (accessed on 31 July 2022) for RPG 2018 data.

Acknowledgments: We would like to thank the French Space Agency (CNES) and the project CNES/Tosca for funding the publication.

Conflicts of Interest: The authors declare no conflict of interest.

References

- Schlund, M.; Erasmi, S. Sentinel-1 Time Series Data for Monitoring the Phenology of Winter Wheat. *Remote Sens. Environ.* **2020**, *246*, 111814. [[CrossRef](#)]
- Yin, H.; Prishchepov, A.V.; Kuemmerle, T.; Bleyhl, B.; Buchner, J.; Radeloff, V.C. Mapping Agricultural Land Abandonment from Spatial and Temporal Segmentation of Landsat Time Series. *Remote Sens. Environ.* **2018**, *210*, 12–24. [[CrossRef](#)]
- Song, X.-P.; Potapov, P.V.; Krylov, A.; King, L.; Di Bella, C.M.; Hudson, A.; Khan, A.; Adusei, B.; Stehman, S.V.; Hansen, M.C. National-Scale Soybean Mapping and Area Estimation in the United States Using Medium Resolution Satellite Imagery and Field Survey. *Remote Sens. Environ.* **2017**, *190*, 383–395. [[CrossRef](#)]
- Sun, C.; Bian, Y.; Zhou, T.; Pan, J. Using of Multi-Source and Multi-Temporal Remote Sensing Data Improves Crop-Type Mapping in the Subtropical Agriculture Region. *Sensors* **2019**, *19*, 2401. [[CrossRef](#)]
- Birrell, S.J.; Sudduth, K.A.; Borgelt, S.C. Comparison of Sensors and Techniques for Crop Yield Mapping. *Comput. Electron. Agric.* **1996**, *14*, 215–233. [[CrossRef](#)]
- Song, Y.; Wang, J. Mapping Winter Wheat Planting Area and Monitoring Its Phenology Using Sentinel-1 Backscatter Time Series. *Remote Sens.* **2019**, *11*, 449. [[CrossRef](#)]
- Arvor, D.; Jonathan, M.; Meirelles, M.S.P.; Dubreuil, V.; Durieux, L. Classification of MODIS EVI Time Series for Crop Mapping in the State of Mato Grosso, Brazil. *Int. J. Remote Sens.* **2011**, *32*, 7847–7871. [[CrossRef](#)]
- Forkuor, G.; Conrad, C.; Thiel, M.; Ullmann, T.; Zoungrana, E. Integration of Optical and Synthetic Aperture Radar Imagery for Improving Crop Mapping in Northwestern Benin, West Africa. *Remote Sens.* **2014**, *6*, 6472–6499. [[CrossRef](#)]
- Xie, G.; Niculescu, S. Remote Sensing Mapping and Monitoring of Land Cover/Land Use (LCLU) Changes in the Crozon Peninsula (Brittany, France) from 2007 to 2018 by Machine Learning Algorithms (Support Vector Machine, Random Forest, and Convolutional Neural Network) and by Post-Classification Comparison (PCC). *Remote Sens.* **2021**, *13*, 3899. [[CrossRef](#)]
- Dong, Q.; Chen, X.; Chen, J.; Zhang, C.; Liu, L.; Cao, X.; Zang, Y.; Zhu, X.; Cui, X. Mapping Winter Wheat in North China Using Sentinel 2A/B Data: A Method Based on Phenology-Time Weighted Dynamic Time Warping. *Remote Sens.* **2020**, *12*, 1274. [[CrossRef](#)]
- Zhou, T.; Pan, J.; Zhang, P.; Wei, S.; Han, T. Mapping Winter Wheat with Multi-Temporal SAR and Optical Images in an Urban Agricultural Region. *Sensors* **2017**, *17*, 1210. [[CrossRef](#)] [[PubMed](#)]
- Wardlow, B.D.; Egbert, S.L. Large-Area Crop Mapping Using Time-Series MODIS 250 m NDVI Data: An Assessment for the U.S. Central Great Plains. *Remote Sens. Environ.* **2008**, *112*, 1096–1116. [[CrossRef](#)]

13. Jiang, Y.; Lu, Z.; Li, S.; Lei, Y.; Chu, Q.; Yin, X.; Chen, F. Large-Scale and High-Resolution Crop Mapping in China Using Sentinel-2 Satellite Imagery. *Agriculture* **2020**, *10*, 433. [CrossRef]
14. Del Frate, F.; Ferrazzoli, P.; Guerriero, L.; Strozzi, T.; Wegmuller, U.; Cookmartin, G.; Quegan, S. Wheat Cycle Monitoring Using Radar Data and a Neural Network Trained by a Model. *IEEE Trans. Geosci. Remote Sens.* **2004**, *42*, 35–44. [CrossRef]
15. Ibrahim, E.S.; Rufin, P.; Nill, L.; Kamali, B.; Nendel, C.; Hostert, P. Mapping Crop Types and Cropping Systems in Nigeria with Sentinel-2 Imagery. *Remote Sens.* **2021**, *13*, 3523. [CrossRef]
16. Ok, A.O.; Akar, O.; Gungor, O. Evaluation of Random Forest Method for Agricultural Crop Classification. *Eur. J. Remote Sens.* **2012**, *45*, 421–432. [CrossRef]
17. Tatsumi, K.; Yamashiki, Y.; Canales Torres, M.A.; Taibe, C.L.R. Crop Classification of Upland Fields Using Random Forest of Time-Series Landsat 7 ETM+ Data. *Comput. Electron. Agric.* **2015**, *115*, 171–179. [CrossRef]
18. Son, N.-T.; Chen, C.-F.; Chen, C.-R.; Minh, V.-Q. Assessment of Sentinel-1A Data for Rice Crop Classification Using Random Forests and Support Vector Machines. *Geocarto Int.* **2018**, *33*, 587–601. [CrossRef]
19. Rodriguez-Galiano, V.F.; Ghimire, B.; Rogan, J.; Chica-Olmo, M.; Rigol-Sanchez, J.P. An Assessment of the Effectiveness of a Random Forest Classifier for Land-Cover Classification. *ISPRS J. Photogramm. Remote Sens.* **2012**, *67*, 93–104. [CrossRef]
20. Hao, P.; Zhan, Y.; Wang, L.; Niu, Z.; Shakir, M. Feature Selection of Time Series MODIS Data for Early Crop Classification Using Random Forest: A Case Study in Kansas, USA. *Remote Sens.* **2015**, *7*, 5347–5369. [CrossRef]
21. Li, H.; Zhang, C.; Zhang, S.; Atkinson, P.M. Crop Classification from Full-Year Fully-Polarimetric L-Band UAVSAR Time-Series Using the Random Forest Algorithm. *Int. J. Appl. Earth Obs. Geoinf.* **2020**, *87*, 102032. [CrossRef]
22. Saini, R.; Ghosh, S.K. Crop classification on single date sentinel-2 imagery using random forest and support vector machine. *Int. Arch. Photogramm. Remote Sens. Spatial Inf. Sci.* **2018**, *XLII-5*, 683–688. [CrossRef]
23. Whiteside, T.G.; Boggs, G.S.; Maier, S.W. Comparing Object-Based and Pixel-Based Classifications for Mapping Savannas. *Int. J. Appl. Earth Obs. Geoinf.* **2011**, *13*, 884–893. [CrossRef]
24. Weih, R.; Riggan, N. Object-Based Classification vs. Pixel-Based Classification: Comparative Importance of Multi-Resolution Imagery. *Int. Arch. Photogramm. Remote Sens. Spat. Inf. Sci. ISPRS Arch.* **2010**, *38*, C7.
25. Nasrallah, A.; Baghdadi, N.; El Hajj, M.; Darwish, T.; Belhouchette, H.; Faour, G.; Darwich, S.; Mhawej, M. Sentinel-1 Data for Winter Wheat Phenology Monitoring and Mapping. *Remote Sens.* **2019**, *11*, 2228. [CrossRef]
26. Pan, Z.; Huang, J.; Zhou, Q.; Wang, L.; Cheng, Y.; Zhang, H.; Blackburn, G.A.; Yan, J.; Liu, J. Mapping Crop Phenology Using NDVI Time-Series Derived from HJ-1 A/B Data. *Int. J. Appl. Earth Obs. Geoinf.* **2015**, *34*, 188–197. [CrossRef]
27. Gan, L.; Cao, X.; Chen, X.; Dong, Q.; Cui, X.; Chen, J. Comparison of MODIS-Based Vegetation Indices and Methods for Winter Wheat Green-up Date Detection in Huanghuai Region of China. *Agric. For. Meteorol.* **2020**, *288–289*, 108019. [CrossRef]
28. Meroni, M.; d'Andrèmont, R.; Vrieling, A.; Fasbender, D.; Lemoine, G.; Rembold, F.; Seguíni, L.; Verhegghen, A. Comparing Land Surface Phenology of Major European Crops as Derived from SAR and Multispectral Data of Sentinel-1 and -2. *Remote Sens. Environ.* **2021**, *253*, 112232. [CrossRef]
29. Wali, E.; Tasumi, M.; Moriyama, M. Combination of Linear Regression Lines to Understand the Response of Sentinel-1 Dual Polarization SAR Data with Crop Phenology—Case Study in Miyazaki, Japan. *Remote Sens.* **2020**, *12*, 189. [CrossRef]
30. Canisius, F.; Shang, J.; Liu, J.; Huang, X.; Ma, B.; Jiao, X.; Geng, X.; Kovacs, J.M.; Walters, D. Tracking Crop Phenological Development Using Multi-Temporal Polarimetric Radarsat-2 Data. *Remote Sens. Environ.* **2018**, *210*, 508–518. [CrossRef]
31. Mandal, D.; Kumar, V.; Ratha, D.; Dey, S.; Bhattacharya, A.; Lopez-Sanchez, J.M.; McNairn, H.; Rao, Y.S. Dual Polarimetric Radar Vegetation Index for Crop Growth Monitoring Using Sentinel-1 SAR Data. *Remote Sens. Environ.* **2020**, *247*, 111954. [CrossRef]
32. Géoportail. Available online: <https://www.geoportail.gouv.fr/> (accessed on 21 August 2022).
33. Rouault, S. Observer L'occupation des Sols Pour Guider les Politiques D'aménagement (MOS). Available online: <https://www.adeupa-brest.fr/nos-publications/observer-l'occupation-des-sols-pour-guider-les-politiques-damenagement-mos-0> (accessed on 21 August 2022).
34. Agence d'Urbanisme Brest Bretagne | ADEUPa Brest. Available online: <https://adeupa-brest.fr/> (accessed on 21 August 2022).
35. Chambres d'Agriculture de Bretagne. Available online: <http://www.chambres-agriculture-bretagne.fr/synagri/accueilRegion> (accessed on 22 August 2022).
36. Sentinel-2—Missions—Sentinel Online—Sentinel Online. Available online: <https://sentinel.esa.int/web/sentinel/missions/sentinel-2> (accessed on 18 August 2022).
37. Sentinel-1—Missions—Sentinel Online—Sentinel Online. Available online: <https://sentinels.copernicus.eu/web/sentinel/missions/sentinel-1> (accessed on 18 August 2022).
38. Registre Parcellaire Graphique (RPG). Available online: <https://artificialisation.developpement-durable.gouv.fr/bases-donnees/registre-parcellaire-graphique> (accessed on 18 August 2022).
39. Xue, J.; Su, B. Significant Remote Sensing Vegetation Indices: A Review of Developments and Applications. *J. Sens.* **2017**, *2017*, 1–17. [CrossRef]
40. Bannari, A.; Morin, D.; Bonn, F.; Huete, A.R. A Review of Vegetation Indices. *Remote Sens. Rev.* **1995**, *13*, 95–120. [CrossRef]
41. Campbell, J.B.; Wynne, R.H. *Introduction to Remote Sensing*, 5th ed.; Guilford Press: New York, NY, USA, 2011; ISBN 978-1-60918-177-2.
42. Rouse, J.W.; Haas, R.H.; Scheel, J.A.; Deering, D.W. Monitoring Vegetation Systems in the Great Plains with ERTS. In Proceedings of the 3rd Earth Resource Technology Satellite (ERTS) Symposium, Washington, DC, USA, 10–14 December 1973; Volume 1, pp. 48–62.

43. Gao, B. NDWI—A Normalized Difference Water Index for Remote Sensing of Vegetation Liquid Water from Space. *Remote Sens. Environ.* **1996**, *58*, 257–266. [CrossRef]
44. Mulianga, B.; Bégué, A.; Clouvel, P.; Todoroff, P. Mapping Cropping Practices of a Sugarcane-Based Cropping System in Kenya Using Remote Sensing. *Remote Sens.* **2015**, *7*, 14428–14444. [CrossRef]
45. Valero, S.; Arnaud, L.; Planells, M.; Ceschia, E. Synergy of Sentinel-1 and Sentinel-2 Imagery for Early Seasonal Agricultural Crop Mapping. *Remote Sens.* **2021**, *13*, 4891. [CrossRef]
46. Yin, L.; You, N.; Zhang, G.; Huang, J.; Dong, J. Optimizing Feature Selection of Individual Crop Types for Improved Crop Mapping. *Remote Sens.* **2020**, *12*, 162. [CrossRef]
47. Gitelson, A.A.; Kaufman, Y.J.; Merzlyak, M.N. Use of a Green Channel in Remote Sensing of Global Vegetation from EOS-MODIS. *Remote Sens. Environ.* **1996**, *58*, 289–298. [CrossRef]
48. Matsushita, B.; Yang, W.; Chen, J.; Onda, Y.; Qiu, G. Sensitivity of the Enhanced Vegetation Index (EVI) and Normalized Difference Vegetation Index (NDVI) to Topographic Effects: A Case Study in High-Density Cypress Forest. *Sensors* **2007**, *7*, 2636–2651. [CrossRef]
49. Huete, A.; Didan, K.; Miura, T.; Rodriguez, E.P.; Gao, X.; Ferreira, L.G. Overview of the Radiometric and Biophysical Performance of the MODIS Vegetation Indices. *Remote Sens. Environ.* **2002**, *83*, 195–213. [CrossRef]
50. Huete, A.R. A Soil-Adjusted Vegetation Index (SAVI). *Remote Sens. Environ.* **1988**, *25*, 295–309. [CrossRef]
51. Palchoudhuri, Y.; Valcarce-Diñeiro, R.; King, P.; Sanabria-Soto, M. Classification of Multi-Temporal Spectral Indices for Crop Type Mapping: A Case Study in Coalville, UK. *J. Agric. Sci.* **2018**, *156*, 24–36. [CrossRef]
52. Qi, J.; Chehbouni, A.; Huete, A.R.; Kerr, Y.H.; Sorooshian, S. A Modified Soil Adjusted Vegetation Index. *Remote Sens. Environ.* **1994**, *48*, 119–126. [CrossRef]
53. Samasse, K.; Hanan, N.P.; Anchang, J.Y.; Diallo, Y. A High-Resolution Cropland Map for the West African Sahel Based on High-Density Training Data, Google Earth Engine, and Locally Optimized Machine Learning. *Remote Sens.* **2020**, *12*, 1436. [CrossRef]
54. Wyawahare, M.; Kulkarni, P.; Kulkarni, A.; Lad, A.; Majji, J.; Mehta, A. Agricultural Field Analysis Using Satellite Surface Reflectance Data and Machine Learning Technique. In *International Conference on Advances in Computing and Data Sciences*; Singh, M., Gupta, P.K., Tyagi, V., Flusser, J., Ören, T., Valentino, G., Eds.; Springer: Singapore, 2020; pp. 439–448.
55. Li, Z.; Chen, Z. Remote Sensing Indicators for Crop Growth Monitoring at Different Scales. In Proceedings of the 2011 IEEE International Geoscience and Remote Sensing Symposium, Vancouver, BC, Canada, 24–29 July 2011; pp. 4062–4065.
56. Witharana, C.; Civco, D.L. Optimizing Multi-Resolution Segmentation Scale Using Empirical Methods: Exploring the Sensitivity of the Supervised Discrepancy Measure Euclidean Distance 2 (ED2). *ISPRS J. Photogramm. Remote Sens.* **2014**, *87*, 108–121. [CrossRef]
57. Darwish, A.; Leukert, K.; Reinhardt, W. Image Segmentation for the Purpose of Object-Based Classification. In Proceedings of the 2003 IEEE International Geoscience and Remote Sensing Symposium, Toulouse, France, 21–25 July 2003; Volume 3, pp. 2039–2041.
58. Benz, U.C.; Hofmann, P.; Willhauck, G.; Lingenfelder, I.; Heynen, M. Multi-Resolution, Object-Oriented Fuzzy Analysis of Remote Sensing Data for GIS-Ready Information. *ISPRS J. Photogramm. Remote Sens.* **2004**, *58*, 239–258. [CrossRef]
59. ECognition Suite Documentation. Available online: https://docs.ecognition.com/v9.5.0/Page%20collection/eCognition%20Suite%20Documentation.htm?tocpath=Documentation%20eCognition%20Suite%7C_____0 (accessed on 14 April 2021).
60. Richards, J.A.; Jia, X. Supervised Classification Techniques. In *Remote Sensing Digital Image Analysis: An Introduction*; Richards, J.A., Jia, X., Eds.; Springer: Berlin/Heidelberg, Germany, 1999; pp. 181–222. ISBN 978-3-662-03978-6.
61. Gislason, P.O.; Benediktsson, J.A.; Sveinsson, J.R. Random Forests for Land Cover Classification. *Pattern Recognit. Lett.* **2006**, *27*, 294–300. [CrossRef]
62. Foody, G.M. Status of Land Cover Classification Accuracy Assessment. *Remote Sens. Environ.* **2002**, *80*, 185–201. [CrossRef]
63. Alberg, A.J.; Park, J.W.; Hager, B.W.; Brock, M.V.; Diener-West, M. The Use of “Overall Accuracy” to Evaluate the Validity of Screening or Diagnostic Tests. *J. Gen. Intern. Med.* **2004**, *19*, 460–465. [CrossRef]
64. Foody, G.M. Explaining the Unsuitability of the Kappa Coefficient in the Assessment and Comparison of the Accuracy of Thematic Maps Obtained by Image Classification. *Remote Sens. Environ.* **2020**, *239*, 111630. [CrossRef]
65. Fitzgerald, R.W.; Lees, B.G. Assessing the Classification Accuracy of Multisource Remote Sensing Data. *Remote Sens. Environ.* **1994**, *47*, 362–368. [CrossRef]
66. Gorelick, N.; Hancher, M.; Dixon, M.; Ilyushchenko, S.; Thau, D.; Moore, R. Google Earth Engine: Planetary-Scale Geospatial Analysis for Everyone. *Remote Sens. Environ.* **2017**, *202*, 18–27. [CrossRef]
67. Mutanga, O.; Kumar, L. Google Earth Engine Applications. *Remote Sens.* **2019**, *11*, 591. [CrossRef]
68. Sentinel-1 Algorithms | Google Earth Engine. Available online: <https://developers.google.com/earth-engine/guides/sentinel1> (accessed on 4 July 2022).
69. Picard, G.; Le Toan, T.; Mattia, F. Understanding C-Band Radar Backscatter from Wheat Canopy Using a Multiple-Scattering Coherent Model. *IEEE Trans. Geosci. Remote Sens.* **2003**, *41*, 1583–1591. [CrossRef]
70. Koller, D.; Sahami, M. Hierarchically Classifying Documents Using Very Few Words. In Proceedings of the 14th International Conference on Machine Learning (ICML), San Francisco, CA, USA, 28 June–1 July 2001; Volume 223.

71. Costa, E.P.; Lorena, A.C.; Carvalho, A.C.P.L.F.; Freitas, A.A. A Review of Performance Evaluation Measures for Hierarchical Classifiers. In *Evaluation Methods for Machine Learning II: Papers from the AAAI-2007 Workshop, AAAI Technical Report WS-07-05*; Drummond, C., Elazmeh, W., Japkowicz, N., Macskassy, S.A., Eds.; AAAI Press: Palo Alto, CA, USA, 2007; pp. 1–6. ISBN 978-1-57735-332-4.
72. Costa, E.P.; Lorena, A.C.; Carvalho, A.C.P.L.F.; Freitas, A.A.; Holden, N. Comparing Several Approaches for Hierarchical Classification of Proteins with Decision Trees. In *Proceedings of the Advances in Bioinformatics and Computational Biology, Angra dos Reis, Brazil, 29–31 August 2007*; Sagot, M.-F., Walter, M.E.M.T., Eds.; Springer: Berlin/Heidelberg, Germany, 2007; pp. 126–137.
73. Silla, C.N.; Freitas, A.A. A Survey of Hierarchical Classification across Different Application Domains. *Data Min. Knowl. Disc.* **2011**, *22*, 31–72. [[CrossRef](#)]
74. Burred, J.J.; Lerch, A. A Hierarchical Approach to Automatic Musical Genre Classification. In *Proceedings of the 6th international Conference on Digital Audio Effects, London, UK, 8–11 September 2003*; pp. 8–11.
75. Guo, Y.; Liu, Y.; Bakker, E.M.; Guo, Y.; Lew, M.S. CNN-RNN: A Large-Scale Hierarchical Image Classification Framework. *Multimed Tools Appl.* **2018**, *77*, 10251–10271. [[CrossRef](#)]
76. Fan, J.; Gao, Y.; Luo, H. Hierarchical Classification for Automatic Image Annotation. In *Proceedings of the 30th Annual International ACM SIGIR Conference on Research and Development in Information Retrieval, Amsterdam, The Netherlands, 23–27 July 2007*; Association for Computing Machinery: New York, NY, USA, 2007; pp. 111–118.
77. Uca Avci, Z.D.; Karaman, M.; Ozelkan, E.; Kumral, M.; Budakoglu, M. OBIA Based Hierarchical Image Classification for Industrial Lake Water. *Sci. Total Environ.* **2014**, *487*, 565–573. [[CrossRef](#)]
78. Gerylo, G.; Hall, R.J.; Franklin, S.E.; Roberts, A.; Milton, E.J. Hierarchical Image Classification and Extraction of Forest Species Composition and Crown Closure from Airborne Multispectral Images. *Can. J. Remote Sens.* **1998**, *24*, 219–232. [[CrossRef](#)]
79. Liu, D.; Xia, F. Assessing Object-Based Classification: Advantages and Limitations. *Remote Sens. Lett.* **2010**, *1*, 187–194. [[CrossRef](#)]
80. Estoque, R.C.; Murayama, Y.; Akiyama, C.M. Pixel-Based and Object-Based Classifications Using High- and Medium-Spatial-Resolution Imagery in the Urban and Suburban Landscapes. *Geocarto Int.* **2015**, *30*, 1113–1129. [[CrossRef](#)]
81. Fu, B.; Wang, Y.; Campbell, A.; Li, Y.; Zhang, B.; Yin, S.; Xing, Z.; Jin, X. Comparison of Object-Based and Pixel-Based Random Forest Algorithm for Wetland Vegetation Mapping Using High Spatial Resolution GF-1 and SAR Data. *Ecol. Indic.* **2017**, *73*, 105–117. [[CrossRef](#)]
82. Blaschke, T. Object Based Image Analysis for Remote Sensing. *ISPRS J. Photogramm. Remote Sens.* **2010**, *65*, 2–16. [[CrossRef](#)]
83. Castillejo-González, I.L.; López-Granados, F.; García-Ferrer, A.; Peña-Barragán, J.M.; Jurado-Expósito, M.; de la Orden, M.S.; González-Audicana, M. Object- and Pixel-Based Analysis for Mapping Crops and Their Agro-Environmental Associated Measures Using QuickBird Imagery. *Comput. Electron. Agric.* **2009**, *68*, 207–215. [[CrossRef](#)]
84. Belgiu, M.; Csillik, O. Sentinel-2 Cropland Mapping Using Pixel-Based and Object-Based Time-Weighted Dynamic Time Warping Analysis. *Remote Sens. Environ.* **2018**, *204*, 509–523. [[CrossRef](#)]
85. Devadas, R.; Denham, R.J.; Pringle, M. Support vector machine classification of object-based data for crop mapping, using multi-temporal landsat imagery. *Int. Arch. Photogramm. Remote Sens. Spat. Inf. Sci.* **2012**, *XXXIX-B7*, 185–190. [[CrossRef](#)]
86. Möller, M.; Lyburner, L.; Volk, M. The Comparison Index: A Tool for Assessing the Accuracy of Image Segmentation. *Int. J. Appl. Earth Obs. Geoinf.* **2007**, *9*, 311–321. [[CrossRef](#)]
87. Kampouraki, M.; Wood, G.A.; Brewer, T.R. Opportunities and Limitations of Object Based Image Analysis for Detecting Urban Impervious and Vegetated Surfaces Using True-Colour Aerial Photography. In *Object-Based Image Analysis: Spatial Concepts for Knowledge-Driven Remote Sensing Applications*; Lecture Notes in Geoinformation and Cartography; Blaschke, T., Lang, S., Hay, G.J., Eds.; Springer: Berlin/Heidelberg, Germany, 2008; pp. 555–569. ISBN 978-3-540-77058-9.
88. Duro, D.C.; Franklin, S.E.; Dubé, M.G. A Comparison of Pixel-Based and Object-Based Image Analysis with Selected Machine Learning Algorithms for the Classification of Agricultural Landscapes Using SPOT-5 HRG Imagery. *Remote Sens. Environ.* **2012**, *118*, 259–272. [[CrossRef](#)]
89. Gao, Y.; Mas, J. A Comparison of the Performance of Pixel Based and Object Based Classifications over Images with Various Spatial Resolutions. *Online J. Earth Sci.* **2008**, *2*, 27–35.
90. Berhane, T.M.; Lane, C.R.; Wu, Q.; Anenkhonov, O.A.; Chepinoga, V.V.; Autrey, B.C.; Liu, H. Comparing Pixel- and Object-Based Approaches in Effectively Classifying Wetland-Dominated Landscapes. *Remote Sens.* **2018**, *10*, 46. [[CrossRef](#)]
91. Bolton, D.K.; Friedl, M.A. Forecasting Crop Yield Using Remotely Sensed Vegetation Indices and Crop Phenology Metrics. *Agric. For. Meteorol.* **2013**, *173*, 74–84. [[CrossRef](#)]
92. Gao, F.; Zhang, X. Mapping Crop Phenology in Near Real-Time Using Satellite Remote Sensing: Challenges and Opportunities. *J. Remote Sens.* **2021**, *2021*, 1–14. [[CrossRef](#)]
93. Boschetti, M.; Stroppiana, D.; Brivio, P.A.; Bocchi, S. Multi-Year Monitoring of Rice Crop Phenology through Time Series Analysis of MODIS Images. *Int. J. Remote Sens.* **2009**, *30*, 4643–4662. [[CrossRef](#)]
94. De Castro, A.I.; Six, J.; Plant, R.E.; Peña, J.M. Mapping Crop Calendar Events and Phenology-Related Metrics at the Parcel Level by Object-Based Image Analysis (OBIA) of MODIS-NDVI Time-Series: A Case Study in Central California. *Remote Sens.* **2018**, *10*, 1745. [[CrossRef](#)]
95. De Bernardis, C.; Vicente-Guijalba, F.; Martínez-Marin, T.; Lopez-Sanchez, J.M. Contribution to Real-Time Estimation of Crop Phenological States in a Dynamical Framework Based on NDVI Time Series: Data Fusion with SAR and Temperature. *IEEE J. Sel. Top. Appl. Earth Obs. Remote Sens.* **2016**, *9*, 3512–3523. [[CrossRef](#)]
96. Sakamoto, T.; Yokozawa, M.; Toritani, H.; Shibayama, M.; Ishitsuka, N.; Ohno, H. A Crop Phenology Detection Method Using Time-Series MODIS Data. *Remote Sens. Environ.* **2005**, *96*, 366–374. [[CrossRef](#)]

97. Bargiel, D. A New Method for Crop Classification Combining Time Series of Radar Images and Crop Phenology Information. *Remote Sens. Environ.* **2017**, *198*, 369–383. [[CrossRef](#)]
98. Steele-Dunne, S.C.; McNairn, H.; Monsivais-Huertero, A.; Judge, J.; Liu, P.-W.; Papathanassiou, K. Radar Remote Sensing of Agricultural Canopies: A Review. *IEEE J. Sel. Top. Appl. Earth Obs. Remote Sens.* **2017**, *10*, 2249–2273. [[CrossRef](#)]
99. McNairn, H.; Shang, J. A Review of Multitemporal Synthetic Aperture Radar (SAR) for Crop Monitoring. In *Multitemporal Remote Sensing: Methods and Applications*; Ban, Y., Ed.; Remote Sensing and Digital Image Processing; Springer International Publishing: Cham, Switzerland, 2016; pp. 317–340. ISBN 978-3-319-47037-5.
100. Son, N.-T.; Chen, C.-F.; Chen, C.-R.; Toscano, P.; Cheng, Y.-S.; Guo, H.-Y.; Syu, C.-H. A Phenological Object-Based Approach for Rice Crop Classification Using Time-Series Sentinel-1 Synthetic Aperture Radar (SAR) Data in Taiwan. *Int. J. Remote Sens.* **2021**, *42*, 2722–2739. [[CrossRef](#)]
101. Van de Voorde, T.; Vlaeminck, J.; Canters, F. Comparing Different Approaches for Mapping Urban Vegetation Cover from Landsat ETM+ Data: A Case Study on Brussels. *Sensors* **2008**, *8*, 3880–3902. [[CrossRef](#)]



Article

Seaweed Habitats on the Shore: Characterization through Hyperspectral UAV Imagery and Field Sampling

Wendy Diruit ^{1,*}, Anthony Le Bris ², Touria Bajjouk ³, Sophie Richier ², Mathieu Helias ¹, Thomas Burel ¹, Marc Lennon ⁴, Alexandre Guyot ⁴ and Erwan Ar Gall ¹

¹ Univ Brest, CNRS, IRD, Ifremer, LEMAR, 29280 Plouzané, France;

mathieu.helias@etudiant.univ-brest.fr (M.H.); thomas.burel@univ-brest.fr (T.B.); erwan.argall@univ-brest.fr (E.A.G.)

² Centre d'Etude et de Valorisation des Algues (CEVA), 22195 Pleubian, France; anthony.lebris@ceva.fr (A.L.B.); sophie.richier@ceva.fr (S.R.)

³ Ifremer, Dynamiques des Ecosystèmes Côtiers (DYNECO)/Laboratoire d'Ecologie Benthique Côtière (LEBCO), 29280 Plouzané, France; touria.bajjouk@ifremer.fr

⁴ Hytech-Imaging, 115 Rue Claude Chappe, 29280 Plouzané, France; marc.lennon@hytech-imaging.fr (M.L.); alexandre.guyot@hytech-imaging.fr (A.G.)

* Correspondence: wendy.diruit@univ-brest.fr

Abstract: Intertidal macroalgal habitats are major components of temperate coastal ecosystems. Their distribution was studied using field sampling and hyperspectral remote mapping on a rocky shore of Porspoder (western Brittany, France). Covers of both dominating macroalgae and the sessile fauna were characterized in situ at low tide in 24 sampling spots, according to four bathymetric levels. A zone of ca. 17,000 m² was characterized using a drone equipped with a hyperspectral camera. Macroalgae were identified by image processing using two classification methods to assess the representativeness of spectral classes. Finally, a comparison of the remote imaging data to the field sampling data was conducted. Seven seaweed classes were distinguished by hyperspectral pictures, including five different species of Fucales. The maximum likelihood (MLC) and spectral angle mapper (SAM) were both trained using image-derived spectra. MLC was more accurate to classify the main dominating species (Overall Accuracy (OA) 95.1%) than SAM (OA 87.9%) at a site scale. However, at sampling points scale, the results depend on the bathymetric level. This study evidenced the efficiency and accuracy of hyperspectral remote sensing to evaluate the distribution of dominating intertidal seaweed species and the potential for a combined field/remote approach to assess the ecological state of macroalgal communities.

Keywords: seaweeds; hyperspectral; UAVs; intertidal ecology; rocky shores; supervised classification; vegetation cover

Citation: Diruit, W.; Le Bris, A.; Bajjouk, T.; Richier, S.; Helias, M.; Burel, T.; Lennon, M.; Guyot, A.; Ar Gall, E. Seaweed Habitats on the Shore: Characterization through Hyperspectral UAV Imagery and Field Sampling. *Remote Sens.* **2022**, *14*, 3124. <https://doi.org/10.3390/rs14133124>

Academic Editor: Stuart Phinn

Received: 29 April 2022

Accepted: 26 June 2022

Published: 29 June 2022

Publisher's Note: MDPI stays neutral with regard to jurisdictional claims in published maps and institutional affiliations.



Copyright: © 2022 by the authors. Licensee MDPI, Basel, Switzerland. This article is an open access article distributed under the terms and conditions of the Creative Commons Attribution (CC BY) license (<https://creativecommons.org/licenses/by/4.0/>).

1. Introduction

The intertidal zone hosts considerable diversity together with a great abundance of benthic organisms [1,2] and has long been monitored as a control ecosystem in ecological processes. Seaweeds are the major component of flora on temperate rocky shores, where they can commonly form extensive canopies, structuring macroalgal communities comparable to terrestrial forest systems in their arrangement [3,4]. Seaweed species are vertically distributed on the shore according to several abiotic factors such as desiccation, hydrodynamics, light and salinity, themselves largely influenced by tide oscillations [5,6]. Temperate rocky shores are globally dominated by fucoids (i.e., large Phaeophyceae from the order Fucales), from high to low levels of the shore and by kelps (i.e., large Phaeophyceae from the order Laminariales *sensu lato*) in the lower intertidal fringe and the subtidal area [7]. Along the north east Atlantic coastline, up to six successive macroalgal communities may be found [8,9], which can be reduced to 2–5 depending on the geographical area, the substratum or the hydrodynamic conditions [10].

Brittany is a long-term monitored area for macroalgal diversity (approximately 650 species [11]) and resources (e.g., Benthic Network research program since 2005). These characteristics are examples of a prime area to fully describe seaweed-dominated habitats through remote sensing. Therefore, remote sensing for macroalgal covers has undergone early development since the 1960s [12–17].

Seaweed communities have been recognized as a quality element for the classification of coastal water bodies as part of the European Water Framework Directory (WFD, 2000/60/EC; E.C., 2000 [18]) and several metrics based on the good ecological state of macroalgal communities have been developed along the European coasts [6,9,19–24]. On rocky shores, the occurrence and abundance of vegetation can easily be estimated visually through the cover-abundance scale, or percentage-cover indices, without damaging the habitat [5]. Even if these estimations are easy to implement, they may be time consuming and some locations remain difficult to reach. In this context, using remote sensing imagery for spatialization is an interesting alternative to a site-specific scale [25,26], and could help survey shifting ecosystems [27].

Both multispectral and hyperspectral imagery are routinely used on terrestrial vegetation, for instance, to estimate crop yields [28–31]. By contrast with other plants, seaweeds have a larger phylum-specific diversity of pigments, which can be discriminated by analyzing spectral characteristics at different wavelengths [32]. Pigment diversity in algae contributed to the early development of seaweed detection through airborne remote sensing [33]. Later, mapping of macroalgal communities was processed using satellite imagery (IKONOS, SPOT, Sentinel-2), with scale refining depending on the sharpness of the sensors aboard [34–37], and promoted combined airborne/ground spectra acquisition for macroalgal mapping. Another powerful tool to study coastal environments is the use of free-access satellite images, which could help to produce extensive habitat mapping, in order to observe natural variations in habitats overtime [38].

These methods enable the collection of homogeneous data over broad spatial scales but are inaccurate when applied to heterogeneous habitats, varying at a centimeter in scale [39]. Such approaches are complexified in coastal areas due to tidal variations and highly mosaic environments [40]. Furthermore, data acquisition is generally altered by the occurrence of a water layer [41] and often disturbed by atmospheric conditions (noticeably, cloud cover and light reflection). The development and easy access to both unmanned aerial vehicles (UAVs) and hyperspectral sensors further promoted the remote mapping and characterization of intertidal habitats [42–44]. Since the 1970s, automated methods (i.e., classification algorithms) have been developed to classify multi-/hyper-spectral images [45–47]. The present work focuses on an easy habitat classification through high spatial resolution pictures, obtained by a UAV and by applying commonly used algorithms. To characterize seaweed-dominated habitats, maximum likelihood (MLC) is currently the most widely used method of supervised classifications [48], along with the spectral angle mapper (SAM) [49–52].

To date, there are still few studies comparing both mapping intertidal seaweed using multispectral [38,42,53] or hyperspectral sensors on UAVs, and an accurate spatial resolution (less than 5 cm). Indeed, the majority of studies focus on kelp beds at lower resolution (spatial and/or spectral) [54–57]. Rossiter et al. (2020) [49,58] successfully classified shores using both multispectral and hyperspectral sensors focusing on the Fucales *Ascophyllum nodosum*, but did not compare sensor data with macroalgal in situ covers.

To fill these gaps existing between remote sensing and field sampling, a two-way approach was conducted: on the one hand, in situ sampling of macroalgal communities, and on the other hand, hyperspectral UAV imagery acquisition and automated classifications. In that prospect, several objectives were defined:

1. Distinguishing macroalgae from seawater, substratum and associated non-algal organisms based on classification results from hyperspectral imagery.
2. Using hyperspectral data to discriminate the main species of fucooids from green and red macroalgae.

3. Testing the accuracy of supervised classification algorithms.
4. Comparing field and remotely estimated cover-abundance data.

The working hypothesis of this study is that the two classifications, obtained from hyperspectral images, would yield similar results between the two, successfully differentiating macroalgae and would correspond to those obtained in the field. The present experiment was performed on a seaweed-dominated shore of western Brittany to test the complementarity between both approaches and to study the distribution of seaweed habitats. The aim of the study is to evaluate the correspondence between the distribution of species in macroalgal habitats obtained by both in situ sampling on the shore and hyperspectral imagery by a UAV.

2. Materials and Methods

2.1. Studied Site and Communities

The study was performed on the coasts of north-west Brittany, on the site of Porspoder (48°28.88' N/4°46.29' W) (Figure 1). The site is about 230 m long and 100 m wide, with a maximal tidal range of 8.15 m and mainly exhibiting dense macroalgal canopies with some pools, boulder fields and bedrock. The six macroalgal communities typically found in the north-east Atlantic were vertically distributed on the shore [8] and were grouped into 4 bathymetric levels for the study. These levels correspond to either single or mixed communities named by the dominating Fucales and Laminariales: (1) *Pelvetia canaliculata* plus *Fucus spiralis* communities, (2) *Ascophyllum nodosum*/*Fucus vesiculosus* community, (3) *Fucus serratus* community and (4) *Himanthalia elongata*/*Bifurcaria bifurcata* plus *Laminaria digitata* communities. These levels are referred to, respectively, as Pc-Fspi, An, Fser and He-Ld hereafter.

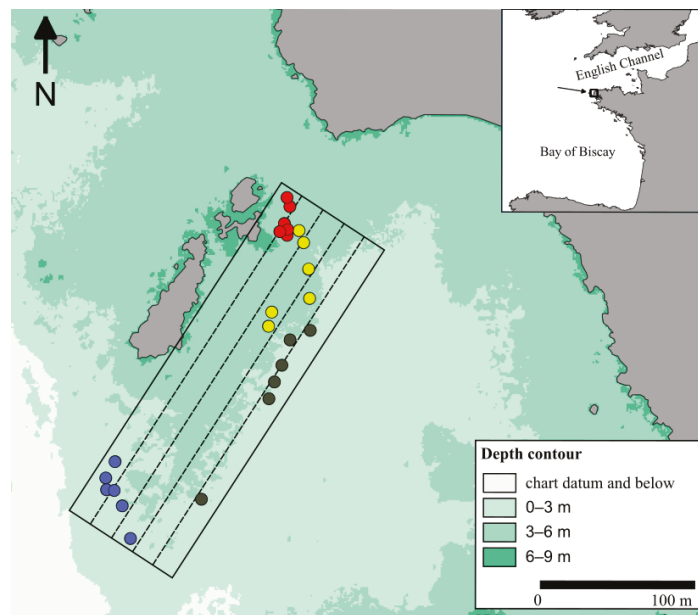


Figure 1. Study site of Porspoder (Brittany, France: 48°28.88' N/4°46.29' W) showing the 24 in situ sampling spots surveyed during the study. The color of the circles indicates the intertidal level considered: red circles, *P. canaliculata*—*F. spiralis*; yellow circles, *A. nodosum*; black circles, *F. serratus*; blue circles, *H. elongata*. The dotted lines correspond to the UAV flight lines.

2.2. Sampling Method

Field sampling was conducted in Spring 2021 (28 April to 1 June). A total of 24 sampling spots (i.e., 6 for each of the 4 levels) were monitored at low tide. The sampling spots were referenced using pictures and GPS positioning (Garmin GPS 73, ± 3 m). The sampling protocol followed the methodology described in Burel et al. (2019b) [59]. A mobile plastic grid structure of 1.65 m \times 1.65 m divided into 25 quadrats of 33 cm \times 33 cm was used to delimit each sampling spot. Covers of benthic fauna, flora and bare rock were estimated visually on the entire surface delimited by the plastic structure from 0 to 100 percent, with a 5 percent pace. That approach, known as ‘undisturbed sampling’, describes the distribution of the main groups of benthic organisms plus the substratum during emersion.

2.3. Remote Sensing Acquisition

Acquisitions were made by Hytech-Imaging (Plouzané, Brittany, France) using a NEO HysPex Mjolnir V-1240 sensor (Oslo, Norway) (Table 1). The sensor was set on an octocopter UAV based on Gryphon Dynamics X8 architecture (Figure 2), with a gStabi H16 stabilization, containing an Applanix APX15 inertial unit with an L1/L2 GPS receiver and a GPS L1/L2 Tallysman enabling geolocation. The UAV and the central acquisition unit of the sensor were remotely controlled by a radio link.

Table 1. Characteristics of the hyperspectral visible near infrared (VNIR) Mjolnir_V-1240 sensor. FOV = field of view.

| Spectral Range | Spatial Pixels | Spectral Resolution | Spectral Sampling | Number of Bands | FOV Across Track | iFOV Across/3Along Track | Coding |
|---------------------|----------------|---------------------|-------------------|-----------------|------------------|--------------------------|---------|
| 0.4–1 μm | 1240 | 4.5 nm | 3 nm | 200 | 20° | 0.27/0.27 mrad | 12 bits |



Figure 2. UAV octocopter used for the acquisitions.

Acquisitions were performed on the 24 June 2021 at a 64 m height to obtain a resolution of 2 cm (Table 2). To perform the image acquisition, two technicians were involved to pilot the UAV and to operate the hyperspectral sensor. The acquisition lasted about 30 min. The flight plan was designed to cover a subsection of the site of Porspoder, including all of the field sampling spots (Figure 1).

Table 2. Parameters of the aerial survey.

| Flight Altitude | Ground Sampling Distance | Swath | Mapped Area | Viewing Angle | Flight Lines |
|-----------------|--------------------------|-------|-------------|---------------|--------------|
| 64 m | 2 cm | 23 m | 1.76 ha | 20° | 4 |

Images (Figure 3) were collected between 09h28 and 09h47 UTC at low tide (tidal coefficient 92 corresponding to tidal range of 6.1 m). During the acquisitions, light was diffused due to cloud cover.

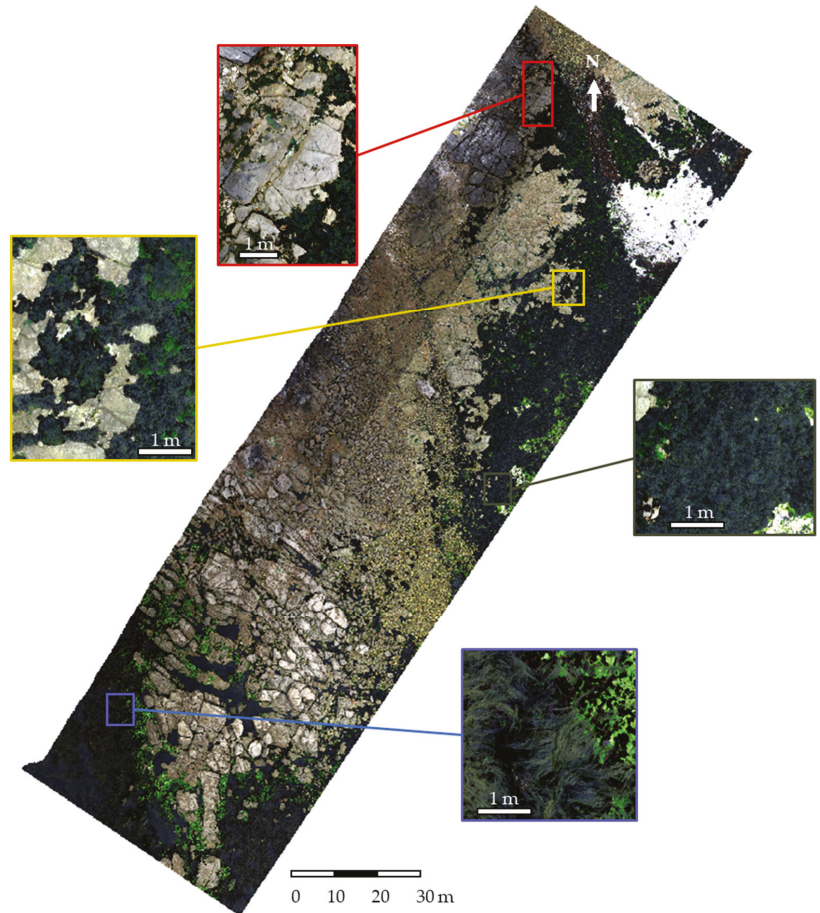


Figure 3. Porspoder orthophoto (RGB) obtained during the flight on the 24 June 2021. Detailed sections of the color image illustrating the different bathymetric levels on the shore are represented: Pc-Fspi (red square), An (yellow square), Fser (black square) and He-Ld (blue square).

2.4. Pre-Processing

To obtain a georeferenced image in spectral radiance ($W \cdot m^{-2} \cdot sr^{-1} \cdot \mu m^{-1}$), the hyperspectral image was processed from raw data (level 0) to a radiometrically and geometrically calibrated image (level 1c) using the HYPIP (HYPPerspectral Image Preprocessing) chain of Hytech-imaging that includes ATCOR/PARGE software applications (ReSe Applications, Wil, Switzerland). To calculate the surface reflectance, atmospheric corrections were

performed in a two-step process: first, using the ATCOR-4 software, and then empirically adjusting each spectrum. To adjust each spectrum, coefficients of gain and bias were calculated per spectral band, by linear regression between surface reflectance data and the reflectance signature. This reflectance signature was obtained by positioning pre-calibrated targets (tarps) near the area of interest overflown during the survey.

2.5. Data Classification

For this study, supervised classifications were performed, where categories (classes) correspond to spectral signatures defined by the user. A class contains a characteristic spectral signature for each dominating fucoid species, macroalgal group or an abiotic component and corresponds to homogeneous regions delineated on the UAV image. The software then assigns each pixel of the image into a cover type to which its signature is most comparable [60]. The supervised classifications were performed after defining regions of interests (ROIs) which are training data. ROIs were created for each class using 'ROI tool' in ENVI version 5.6.1 (Exelis Visual Information Solutions, Boulder, CO, USA) by manually circling pixel areas on the image. More than one training ROI were usually used to represent a particular class (ROIs = multiple polygons) (Table 3). The number of polygons and pixels per class depend on the surface occupied by each species. For example, covers of *P. canaliculata* and *F. spiralis* are low compared to those of *F. serratus* or *H. elongata*, which represent more homogeneous and larger classes. Classes were selected in agreement with the hyperspectral image and pictures taken during field sampling.

Table 3. Number of ROIs and pixels for each class.

| Class | Number of ROIs | Number of Pixels |
|------------------------|----------------|------------------|
| <i>P. canaliculata</i> | 76 | 29,899 |
| <i>F. spiralis</i> | 10 | 551 |
| <i>A. nodosum</i> | 233 | 334,002 |
| <i>F. serratus</i> | 227 | 894,910 |
| <i>H. elongata</i> | 145 | 353,825 |
| Green | 482 | 73,592 |
| Red | 509 | 41,808 |
| Substratum | 408 | 1,834,496 |
| Water | 235 | 1,073,044 |

Nine classes were thus defined for the site of Porspoder (Figure 4), including five classes of dominating Fucales ('*Pelvetia canaliculata*', '*Fucus spiralis*', '*Ascophyllum nodosum*', '*Fucus serratus*' and '*Himanthalia elongata*'), and two classes related to green and red seaweeds (respectively, 'Green' and 'Red') were created. A 'Substratum' class was defined grouping bedrock, boulders, gravel and sand, and, finally, a 'Water' class was also created, gathering immersed parts of the shore (pools or subtidal zone). The 'Substratum' and 'Water' classes were classified in the same way as the other classes and have subsequently been removed from the maps to improve their clarity and interpretation. Due to the complexity of accurately identifying benthic fauna on the UAV image, no appropriate class was created, and these data were grouped together as the 'Substratum' class.

Training data (i.e., ROIs mean spectra) were checked for class separability using the Jeffries–Matusita distance [61]. The values of the resulting output between each pair of classes ranged between 0 and 2, with values greater than 1.9 indicating almost perfect separability between them [46]. A large class separability indicates that accurate training areas have been selected, whereas values approaching zero suggest either the need for more training areas or classes that are inherently similar in their spectral properties.

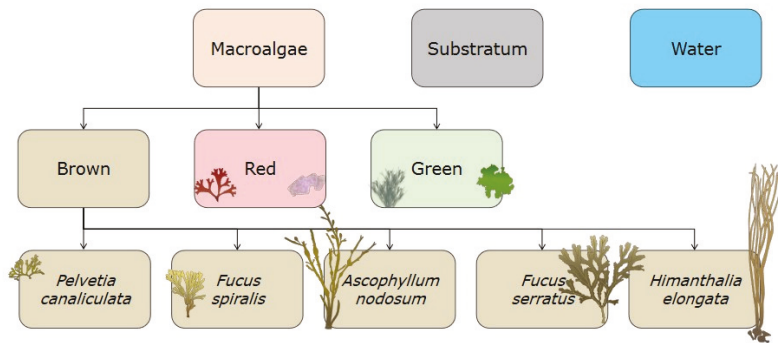


Figure 4. Hierarchical tree of decision to make classes, inspired from Congalton et al. (1999) [62].

Two supervised classification methods were performed to test the representativeness of the spectral classes running the software ENVI version 5.6.1 (Exelis Visual Information Solutions, Boulder, CO, USA), i.e., the algorithms maximum likelihood classification (MLC) and spectral angle mapper (SAM).

MLC calculates the probability that an individual pixel belongs to a specific class and is based on an estimated probability density function derived from the defined reference classes [63]. MLC is a popular classifier [64]. The use of spectral profiles by this method requires ROIs based on multiple pixels. Following this method, the classification is based on the selection of the most representative spectral profiles in ROIs of the same class upon different flight lines. The MLC classifier assumes a Gaussian distribution for each input training class [65] and it can be expressed by the following equation:

$$g_i(x) = \ln p(\omega_i) - \frac{1}{2} \ln |\Sigma_i| - \frac{1}{2} (x - m_i)^T \Sigma_i^{-1} (x - m_i) \quad (1)$$

where i is a given spectral class, x equals n -dimensional data, $p(\omega_i)$ is the probability that class ω_i occurs in the image and it is assumed the same for all classes, $|\Sigma_i|$ is the determinant of the covariance matrix of the data in class ω_i , Σ_i^{-1} is the inverse matrix and m_i is the mean vector. The advantage of MLC as a parametric classifier is that it considers the variance-covariance within the class distributions and, for normally distributed data, MLC performs better than the other known parametric classifiers [66]. However, for data with a non-normal distribution, the results may be unsatisfactory.

SAM identifies the spectral similarity between two spectra collected from an image or distributed from a spectral library [67]. The resulting classification is rather based on the angular orientations of spectral vectors [29]. Similarities within pairs of spectra (reference and classification) can be compared regardless of differences in brightness, and the pairs are treated as vectors in an n -dimensional space [68]. SAM is expressed by the following equation, taken from Kruse et al. 1993 [67]:

$$\alpha = \cos^{-1} \left[\frac{\sum_{i=1}^{nb} t_i r_i}{\left(\sum_{i=1}^{nb} t_i r_i \right)^{\frac{1}{2}} \left(\sum_{i=1}^{nb} t_i r_i \right)^{\frac{1}{2}}} \right] \quad (2)$$

where t is the spectra for a pixel, r is for the reference spectrum pixel, α is the spectral angle between t and r (measured in radians or degrees) and n is the number of bands.

The average spectral reflectance curves from the ROIs were extracted since SAM requires endmember spectra. If two ROIs were identical, they were averaged in order to obtain one curve with the maximum possible data. The use of spectra derived directly from

the image is usually better than using ground or library spectra due to better inclusions of errors related to atmospheric corrections, calibration and effects of sensor responses [29].

For both classifications (SAM and MLC), no detection threshold was selected, so that all pixels could be classified.

2.6. Data Analysis

Accuracy assessment for classification was checked using ground truth (or reference) ROIs based on the same method as the training data [63,69]. These polygons were independent of the training ROIs and their number represented one third of training ROIs. The accuracy assessment tool was used to create the confusion matrix and derive quantitative measures of accuracy (i.e., kappa coefficient, overall accuracy, user/producer accuracy, errors of commission/omission) using ENVI version 5.6.1 (Exelis Visual Information Solutions, Boulder, CO, USA). User accuracy is the probability of correct class assignment, calculated by dividing the number of correctly classified pixels by the total number of pixels in the class, and producer accuracy is the correctly classified reference pixels, calculated by dividing the number of correctly classified pixels by the total number of pixels that should be in a class.

Each grid structure was replaced using ‘Advanced Digitizing toolbar’ (‘Move Feature’ and ‘Rotate Feature’ options) on Qgis. Corresponding polygons were accurately positioned using pictures taken during the field sampling, in order to decrease the potential GPS error and to compare the exact same position.

To compare in situ data and classification data, vectors of the grid structure were replaced on the Porspoder image using the ‘Vector to ROI’ tool, and the percentage of pixels for each class in ROIs was extracted with the ROI statistics tool on ENVI.

Statistical analyses were conducted using the R environment [70]. Normality and homoscedasticity were first tested on each biological and classification variable, corresponding to seaweed species and substratum covers, with Shapiro–Wilk and F Test/Levene tests, respectively. These tests then determined what analyses were the most suitable (parametric or not). In order to represent the distribution of the replicates described by the three approaches, a distance-based redundancy analysis (db-RDA) was constructed, based on the method described by Escobar-Briones et al. (2008) [71]. Values for each class (apart from ‘Water’) were first converted into a distance matrix by calculating the Hellinger distance for each class in the whole dataset. Then, a principal coordinates analysis (PCoA) was performed on this matrix. The PCoA allows to convert the distance between items (distance matrix) into a map-based visualization (each item is assigned a location in a low-dimensional space, materialized by its eigenvector) in order to better understand the relation between each object. All the PCoA eigenvectors were used as input into an RDA in order to build the db-RDA. The db-RDA represents on a single plot the position of the different replicates using the PCoA eigenvalues, as well as the species (classes) and the explanatory variables (level and method).

To compare more precisely the cover of each of the classes for the three methods and for each bathymetric level, Kruskal–Wallis tests (non-parametric) were performed followed by a post-hoc Dunn test to identify variables that were statistically different.

3. Results

3.1. In Situ Vegetation Cover

Large discrepancies were observed in the covers between bathymetric levels, the lowest levels being characterized by a dominance of seaweeds, whereas bare rock showed a large occurrence in the upper level. Covers of macroalgal classes differed between the four levels (Figure 5). The Pc-Fspi level, corresponding to the upper shore (5.2–6.1 m above chart datum (CD)), was lightly vegetated, with bare rock occupying 55% of the surface. The level was dominated by the Fucales *P. canaliculata* for about 32.5%. The remaining covers were well distributed between *F. spiralis* and red seaweeds (5% each), whereas benthic fauna (barnacles and limpets) corresponded to a cover of 2.5%.

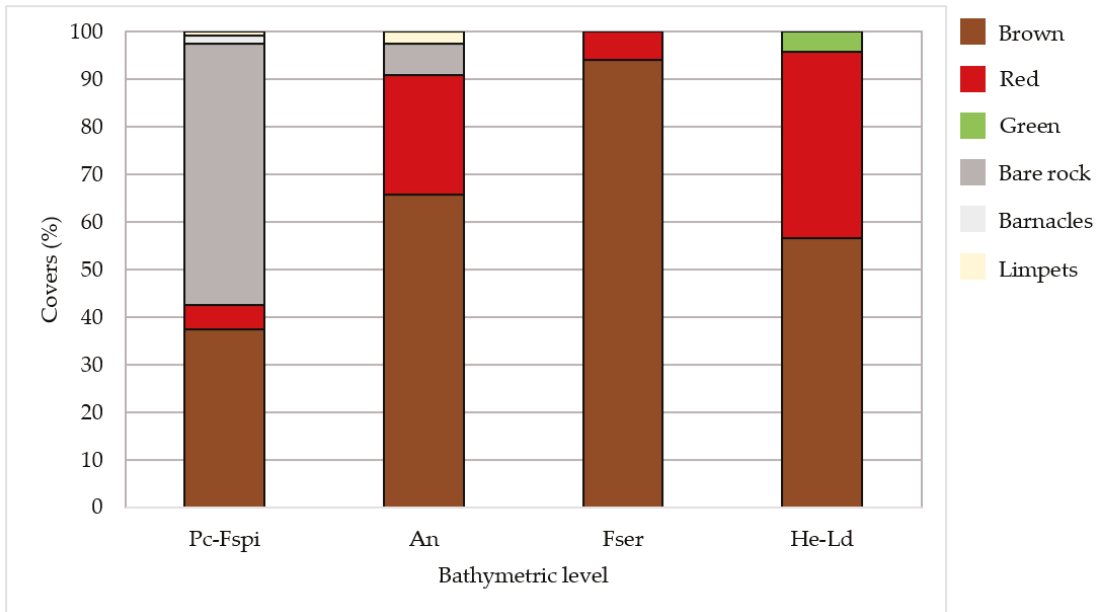


Figure 5. Average covers of macroalgal groups and sessile fauna, and percentage of bare rock observed in situ at each bathymetric level. Covers are given in percentages. Fucoids and other brown species are grouped in the 'Brown' class, and erect and crustose red algae are grouped in the 'Red' class.

The An level (middle shore, 3.4–4.4 m above CD) was largely dominated by the Fucales *A. nodosum* (60%) and *F. serratus* (5.9%). Red seaweeds then covered about 25% of the surface (22.5% erect and 2.5% crustose). Bare rock and limpets completed the remaining surface (6.7% and 2.5%, respectively).

In the Fser level (lower shore, 3.1–2.3 m above CD), macroalgal covers became conspicuously dominant compared to bare rock and sessile fauna. Indeed, the cover of *F. serratus* was close to 100% (94.2%), while the rest corresponded to erect red algae (5.8%).

In the He-Ld level (2.8–1.6 m ab. CD), the distribution between macroalgal groups was equilibrated, with a co-dominance of *H. elongata* (39.2%) and erect red seaweeds (36.7%). The Laminariales *L. digitata* also presented large covers (17.5%), and in addition, there were little covers of crustose red and green seaweeds (2.5% and 4.2%, respectively).

Thus, An, Fser and He-Ld had a higher cover of Phaeophyceae (more than one half compared to the other macroalgal groups of species (65.8%, 94.2% and 56.7% of cover, respectively). By contrast, Pc-Fspi showed only a bit more than one third of cover by Phaeophyceae (37.5%).

3.2. Classifications Results

3.2.1. MLC Results

The results from the class separability test of image-derived spectra showed that all of the class pairs had values greater than 1.90, indicating globally a good class separation (Figure 6) [72].

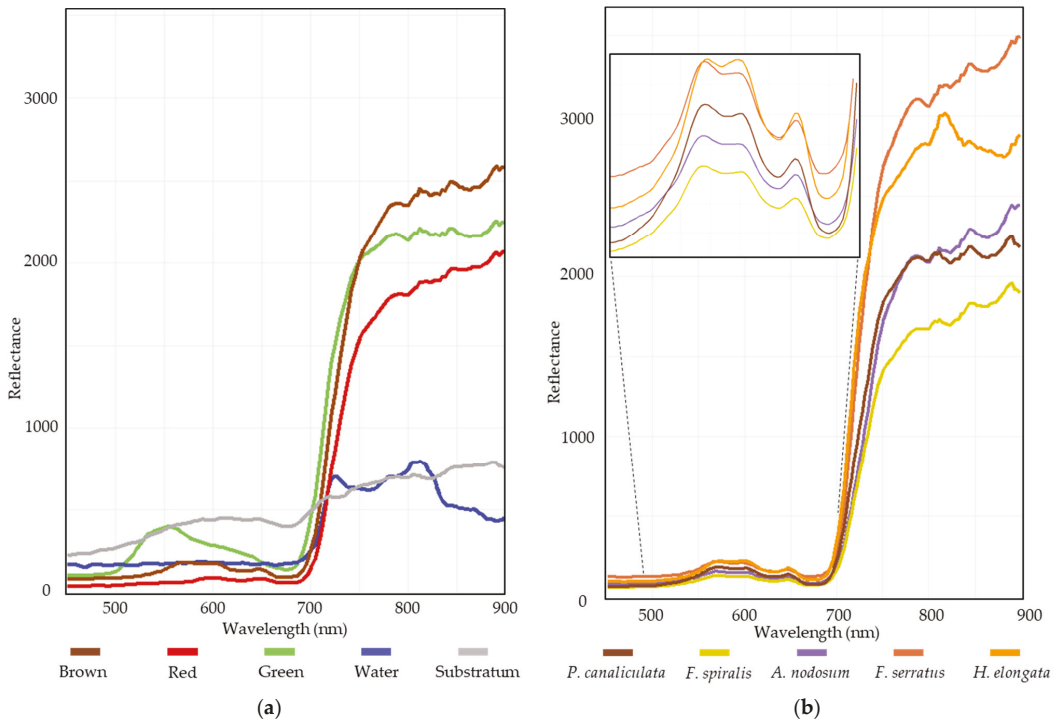


Figure 6. Average reflectance of the different spectral classes between 450 and 900 nm: (a) macroalgal groups, water and substratum mean reflectance; (b) detailed spectra of each Fucal species.

The MLC classifier, trained using image-derived spectra, revealed a dense cover of intertidal Fucal species (26.9% of the site) (Figure 7). The overall classification accuracy for the MLC was 95.1% and the kappa coefficient was 0.93. The four bathymetric/vegetation levels appeared clearly, forming four distinctive bands. The Pc-Fspi level (upper shore) was dominated by a thin band of both *P. canaliculata* and *F. spiralis* (1.3% and 0.1% of total pixels, respectively). The An and Fser levels (mid-shore) were dominated by a large band of *A. nodosum* and of *F. serratus* (5.6% and 6.8% of total pixels, respectively). The He-Ld level (lower shore) was characterized by the important development of *H. elongata* (9.7% of total pixels) and a cover of red macroalgae greater than in higher levels (1.7% for all of the site). Green algae were mainly present in the lower shore (1.7% of total pixels). The 'Substratum' and 'Water' classes represented the majority of the site (51.8% and 21.3% of total pixels for the site, respectively). The macroalgal classes '*A. nodosum*', '*F. serratus*' and '*H. elongata*' showed the highest producer/user accuracies (Table 4). There were some misclassifications between the Fucal species '*A. nodosum*' and '*F. serratus*' (1.56%), and between '*A. nodosum*' and '*P. canaliculata*' (7.04%). The lowest producer/user accuracy was for '*F. spiralis*', with some misclassifications between '*F. spiralis*' and '*P. canaliculata*' (44.13%) and between '*F. spiralis*' and '*A. nodosum*' (14.81%). 'Green' and 'Red' algae were also well classified (96.92% and 90.54%, respectively) but there were some misclassifications between 'Red' algae and the Fucal species '*P. canaliculata*' (3.04%) and '*H. elongata*' (2.06%).

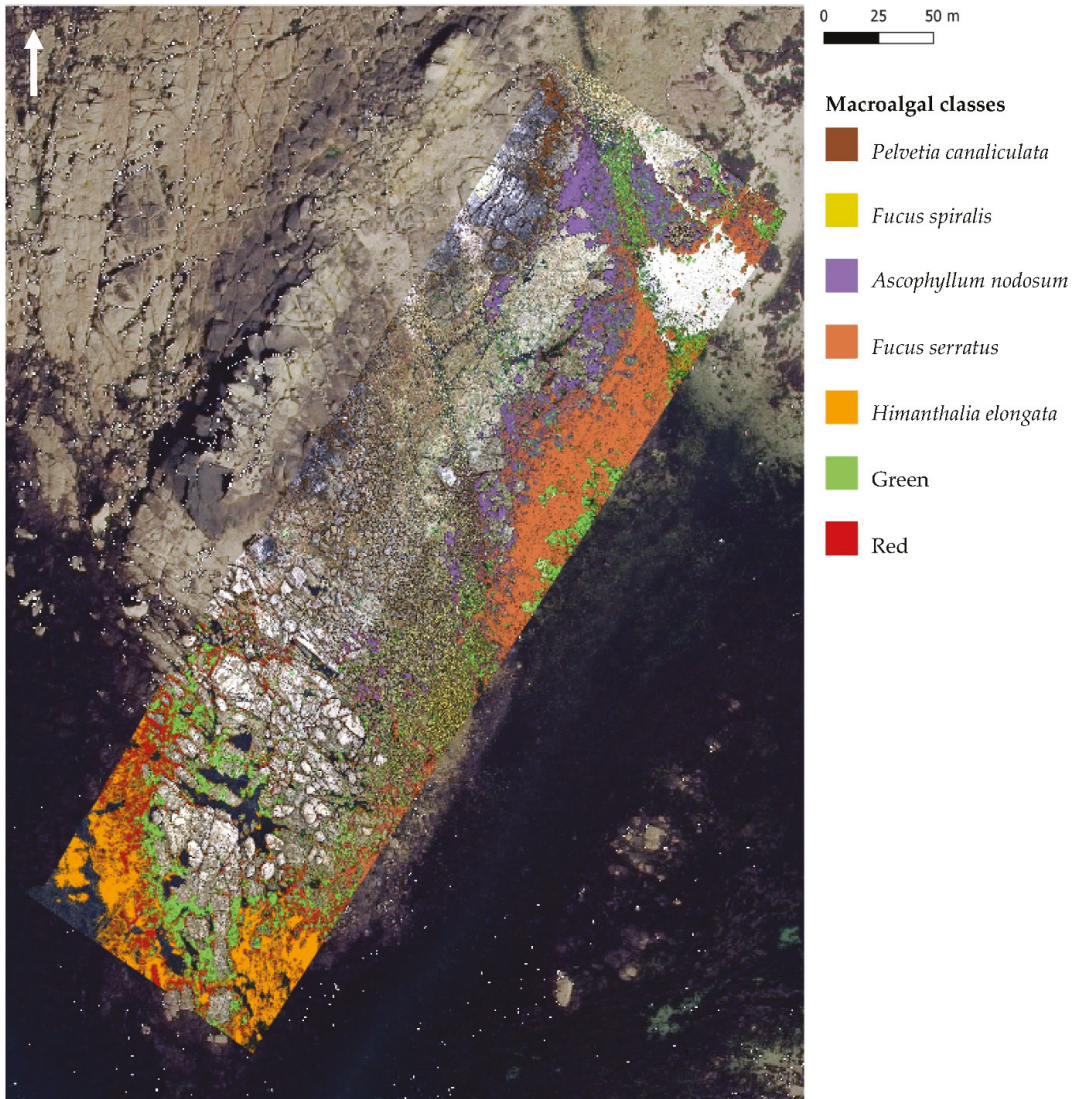


Figure 7. Maximum likelihood classification (MLC), trained using image-derived spectra resulting from the hyperspectral UAV survey at Porspoder. Seven macroalgal cover classes are displayed over the UAV RGB imagery and an orthophotography (Mégalis Bretagne et collectivités territoriales bretonnes—2015), giving an overview of the site. The ‘Substratum’ and ‘Water’ classes are not represented on the map. Class codes ‘Green’ and ‘Red’ represent grouped green and red macroalgal species, respectively.

Table 4. Maximum likelihood classification (MLC) confusion matrix, calculated, using ENVI 5.6.1, by comparing pixels of known class locations to those predicted by the classification workflow for each of the nine cover classes. Results are displayed as percentages of pixels assigned, correctly or incorrectly, to each class. User/producer accuracies (User Acc. and Prod. Acc., respectively) are also presented.

| Class | <i>P. canaliculata</i> | <i>F. spiralis</i> | <i>A. nodosum</i> | <i>F. serratus</i> | <i>H. elongata</i> | Green | Red | Substratum | Water | Total | User Acc. |
|------------------------|------------------------|--------------------|-------------------|--------------------|--------------------|-------|-------|------------|-------|-------|-----------|
| Unclassified | 0 | 0 | 0 | 0 | 0 | 0 | 0 | 0 | 0 | 0 | - |
| <i>P. canaliculata</i> | 97.82 | 44.13 | 7.04 | 0.01 | 0.02 | 0 | 3.04 | 0.90 | 0.03 | 1.28 | 26.04 |
| <i>F. spiralis</i> | 0.13 | 39.00 | 0.23 | 0 | 0.07 | 0 | 0.85 | 0.09 | 0.24 | 0.14 | 6.23 |
| <i>A. nodosum</i> | 0.79 | 14.81 | 89.32 | 5.59 | 0.03 | 0.27 | 0.78 | 0.04 | 0.02 | 5.63 | 91.93 |
| <i>F. serratus</i> | 0.01 | 0 | 1.56 | 91.71 | 0.03 | 0.01 | 0.04 | 0 | 0 | 6.80 | 98.61 |
| <i>H. elongata</i> | 0.09 | 0.15 | 0.08 | 0.38 | 93.53 | 0.18 | 2.60 | 0 | 4.00 | 9.69 | 90.72 |
| Green | 0.17 | 0.15 | 0.73 | 0.35 | 0.07 | 96.92 | 0.70 | 0.11 | 0.21 | 1.66 | 88.85 |
| Red | 0.01 | 1.76 | 0.75 | 1.78 | 3.14 | 1.64 | 90.54 | 0.02 | 0.22 | 1.68 | 67.03 |
| Substratum | 0.67 | 0 | 0.14 | 0.03 | 0 | 0.22 | 0.25 | 96.59 | 0.15 | 51.78 | 99.90 |
| Water | 0.30 | 0 | 0.15 | 0.15 | 3.10 | 0.75 | 1.20 | 2.25 | 95.15 | 21.34 | 92.76 |
| Total | 100 | 100 | 100 | 100 | 100 | 100 | 100 | 100 | 100 | 100 | - |
| Prod. Acc. | 97.82 | 39.00 | 89.32 | 91.71 | 93.53 | 96.92 | 90.54 | 96.59 | 95.15 | - | - |

3.2.2. SAM Results

The SAM classifier, trained using image-derived spectra, revealed a similar cover of intertidal Fucales (27.6% of the site) (Figure 8). The overall classification accuracy for the SAM was 87.9% and the kappa coefficient was 0.82. By contrast with MLC, the four bathymetric levels appeared less distinct. The Pc-Fspi level was dominated by a thin band of both *P. canaliculata* and *F. spiralis* (1.4% and 1.3% of total pixels, respectively) with a better cover of *F. spiralis* than for MLC. The An and Fser levels (mid-shore) were dominated by a large band of *A. nodosum* and of *F. serratus* (5.5% and 3.5% of total pixels, respectively), but the cover of *F. serratus* was less important than for MLC. The He-Ld level (lower shore) was characterized by the important development of *H. elongata* (11.8% of total pixels). The cover of red macroalgae was distributed on all of the site (2.2% of total pixels) and was more present in the Fser level compared to the MLC results. Green algae were mainly present in the lower shore (1.9% of total pixels). The 'Substratum' and 'Water' classes represented the majority of the site (54.8% and 17.5% of the site, respectively). The macroalgal classes '*H. elongata*' and 'Green' showed the highest producer/user accuracies (Table 5). As for MLC, there was some misclassification. First, 18% of '*P. canaliculata*' pixels had been classified as '*F. spiralis*' (9.44%) and '*H. elongata*' (9.49%). The lowest producer/user accuracy was for '*F. spiralis*', with the largest misclassification (37.54%) in '*A. nodosum*' and 14.37% of pixels in '*P. canaliculata*'. Of the '*A. nodosum*' pixels, 18.76% were misclassified as '*F. spiralis*', but also 7.35% and 4.62% of '*A. nodosum*' pixels were misclassified as '*F. serratus*' and '*P. canaliculata*', respectively. Of the '*F. serratus*' pixels, 18.86% were misclassified as 'Red', and 17.37% of pixels should have been classified as '*F. serratus*', when they were in fact classified as '*A. nodosum*'. 'Green' and 'Red' algae were globally well classified, but there was some misclassification between 'Red' algae and some Fucales, such as '*A. nodosum*'. 'Substratum' and 'Water' classes had the highest producer/user accuracy and so were well classified on the entire image.

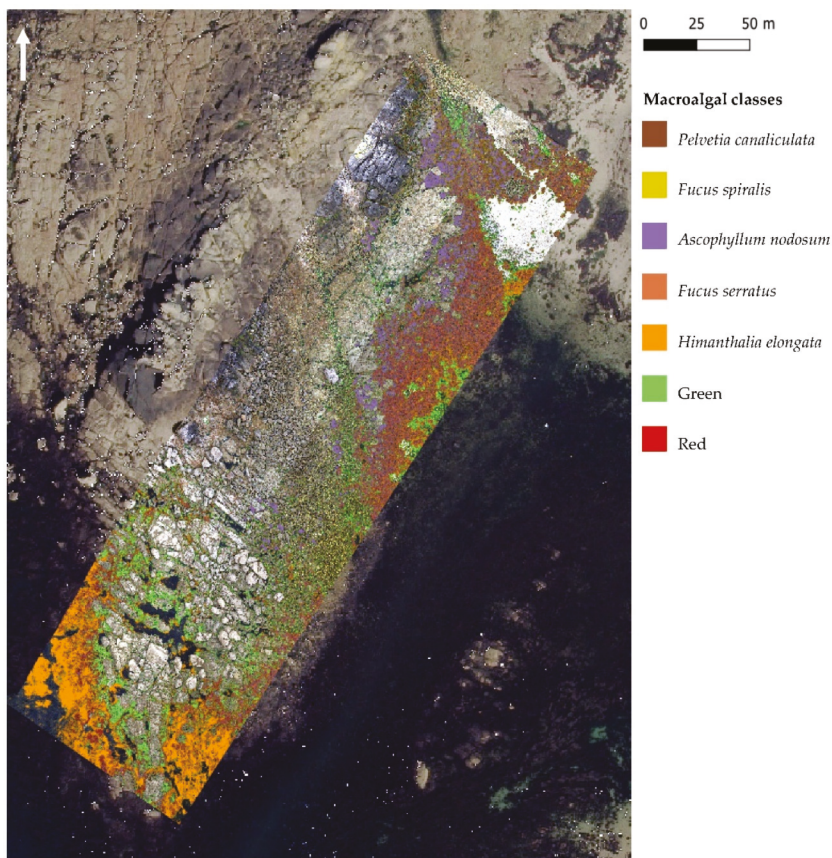


Figure 8. Spectral angle mapper (SAM), trained using image-derived spectra resulting from the hyperspectral UAV survey at Porspoder. Seven macroalgal cover classes are displayed over the UAV RGB imagery and an orthophotography (Mégalis Bretagne et collectivités territoriales bretonnes—2015), giving an overview of the site. The ‘Substratum’ and ‘Water’ classes are not represented on the map. Class codes ‘Green’ and ‘Red’ represent grouped green and red macroalgal species, respectively.

Table 5. Spectral angle mapper (SAM) confusion matrix, calculated, using ENVI 5.6.1, by comparing pixels of known class locations to those predicted by the classification workflow, for each of the nine cover classes. Results are displayed as percentages of pixels assigned, correctly or incorrectly, to each class. User/producer accuracies (User Acc. and Prod. Acc., respectively) are also presented.

| Class | <i>P. canaliculata</i> | <i>F. spiralis</i> | <i>A. nodosum</i> | <i>F. serratus</i> | <i>H. elongata</i> | Green | Red | Substratum | Water | Total | User Acc. |
|------------------------|------------------------|--------------------|-------------------|--------------------|--------------------|-------|-------|------------|-------|-------|-----------|
| Unclassified | 0 | 0 | 0 | 0 | 0.06 | 0 | 0 | 0 | 0.24 | 0.06 | - |
| <i>P. canaliculata</i> | 65.22 | 14.37 | 4.62 | 9.604 | 0.72 | 6.32 | 3.97 | 0.03 | 0.04 | 1.44 | 15.44 |
| <i>F. spiralis</i> | 9.44 | 25.95 | 18.76 | 2.78 | 0 | 0.33 | 0.70 | 0.01 | 0 | 1.35 | 0.43 |
| <i>A. nodosum</i> | 3.02 | 37.54 | 67.06 | 17.37 | 0.04 | 0.32 | 22.84 | 0.01 | 0.01 | 5.48 | 70.97 |
| <i>F. serratus</i> | 1.97 | 8.80 | 7.35 | 38.80 | 1.36 | 1.44 | 8.21 | 0.01 | 0.04 | 3.54 | 80.26 |
| <i>H. elongata</i> | 9.49 | 1.47 | 0.44 | 11.78 | 95.01 | 10.76 | 7.26 | 0.01 | 7.92 | 11.76 | 75.96 |
| Green | 7.72 | 6.45 | 0.77 | 0.75 | 0.86 | 77.33 | 1.42 | 0.64 | 0.73 | 1.89 | 62.07 |
| Red | 2.56 | 5.13 | 0.93 | 18.86 | 0.60 | 0.23 | 54.82 | 0 | 0.02 | 2.19 | 31.09 |
| Substratum | 0.29 | 0 | 0.05 | 0.01 | 0 | 0.43 | 0.06 | 99.04 | 8.41 | 54.81 | 96.79 |
| Water | 0.30 | 0.29 | 0.02 | 0.02 | 1.35 | 2.82 | 0.72 | 0.24 | 82.60 | 17.49 | 98.23 |
| Total | 100 | 100 | 100 | 100 | 100 | 100 | 100 | 100 | 100 | 100 | - |
| Prod. Acc. | 65.22 | 25.95 | 67.06 | 38.8 | 95.01 | 77.33 | 54.82 | 99.04 | 82.6 | - | - |

3.3. Comparison of Field Sampling and Hyperspectral Classification

Covers determined by field sampling are compared here to the classification results by both MLC and SAM. A visual representation of the comparison between in situ sampling, an infrared picture and the two methods is provided in Figure 9 and Appendix A Figures A1–A3.

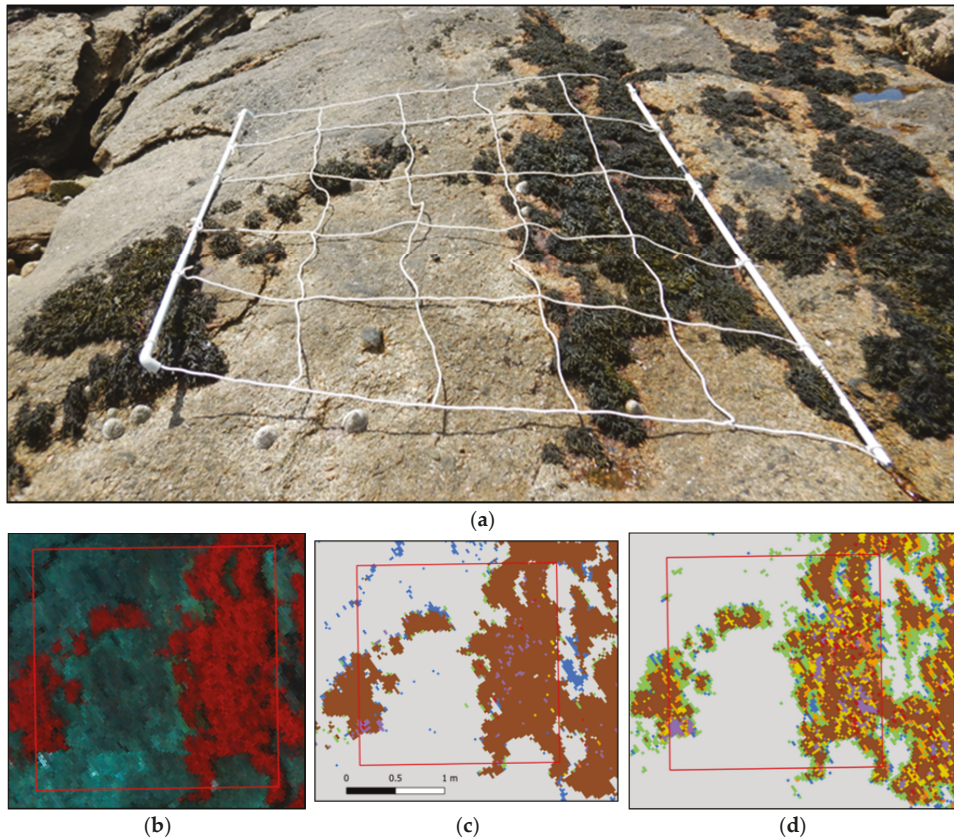


Figure 9. (a) Picture of a sampling spot on the Pc-Fspi level at Porspoder taken during field sampling in June 2021. (b) NIR-G-B image of the same sampling spot. (c) Result of the MLC classification. (d) Result of the SAM classification. The red square corresponds to the mobile grid structure used for field sampling. Color code in (c,d) corresponds to the following classes: ‘*P. canaliculata*’ (brown), ‘*F. spiralis*’ (yellow), ‘*A. nodosum*’ (purple), ‘*F. serratus*’ (coral), ‘*H. elongata*’ (orange), ‘Red’ algae (red), ‘Green’ algae (green), ‘Substratum’ (grey) and ‘Water’ (blue).

To compare covers estimated in situ to those obtained through hyperspectral classification, in situ erect and crustose red algae on one side, and *H. elongata* and *L. digitata* on the other side, have been mixed up in order to attain classes similar to remote classification (Figures 10 and 11).

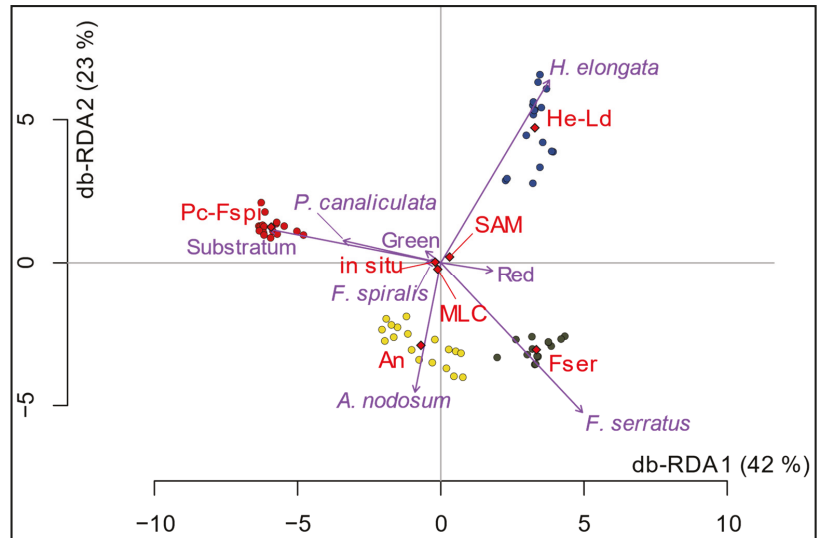


Figure 10. Db-RDA (scaling 1) performed from the macroalgal and pixels covers data for the in situ and the two classifications algorithms. Sampling spots are indicated by circles (Pc-Fspi = red circles, An = yellow circles, Fser = black circles and He-Ld = blue circles), variables (classes used in situ and for classifications: *Pelvetia canaliculata*, *Fucus spiralis*, *Ascophyllum nodosum*, *Fucus serratus*, *Himanthalia elongata*, Red, Green and Substratum) appear in purple, and the explanatory variables (level: Pc-Fspi, An, Fser and He-Ld; method: in situ, MLC and SAM) in red.

The results of the db-RDA are shown in Figure 10. Only the distance between objects (replicates) is considered; therefore, Scaling 1 has been chosen. The model is significant, with an R^2 of 91% (F-value of 117.89, p -value < 0.001). Axes 1 and 2 explain a significant portion of the total variability, with 42% and 23%, respectively. The points, corresponding to the replicates, are grouped into four homogeneous clusters, in agreement to the four bathymetric levels, with no significant distinction between the three methods. The explanatory variable 'level' is obviously correlated to the four clusters, with 'Pc-Fspi', 'An', 'Fser' and 'He-Ld' associated with the clusters corresponding to these four levels while the variable 'method' appears to have no significant influence on the distribution of replicates within each level. The results obtained from the three methods thus appear similar.

When looking in detail at the classes, the methods appeared broadly similar (Figure 11).

In Pc-Fspi (Figure 11a), the cover of the dominating Fucales '*P. canaliculata*' estimated by the in situ sampling was 32.5%, showing no significant difference to those obtained from MLC (39.9%) and SAM (20.9%) (Kruskal–Wallis, $p > 0.05$). On the contrary, for the other dominating Fucales '*F. spiralis*', the test showed no significant difference between in situ sampling (5.0%) and both methods, but a significant difference was observed between the two models (0.6% for MLC and 5.5% for SAM, Kruskal–Wallis, $p < 0.04$). In contrast, the cover of 'Red' macroalgae was 5.0% in situ, showing a single significant difference with the method MLC (0.2%, Kruskal–Wallis, $p < 0.001$). The estimation performed by SAM (1.4%) did not show any significant difference with the other two methods. Bare rock represented about half of the surface of sampling spots in this level, whatever the method considered, showing no significant differences (Kruskal–Wallis, $p > 0.05$).

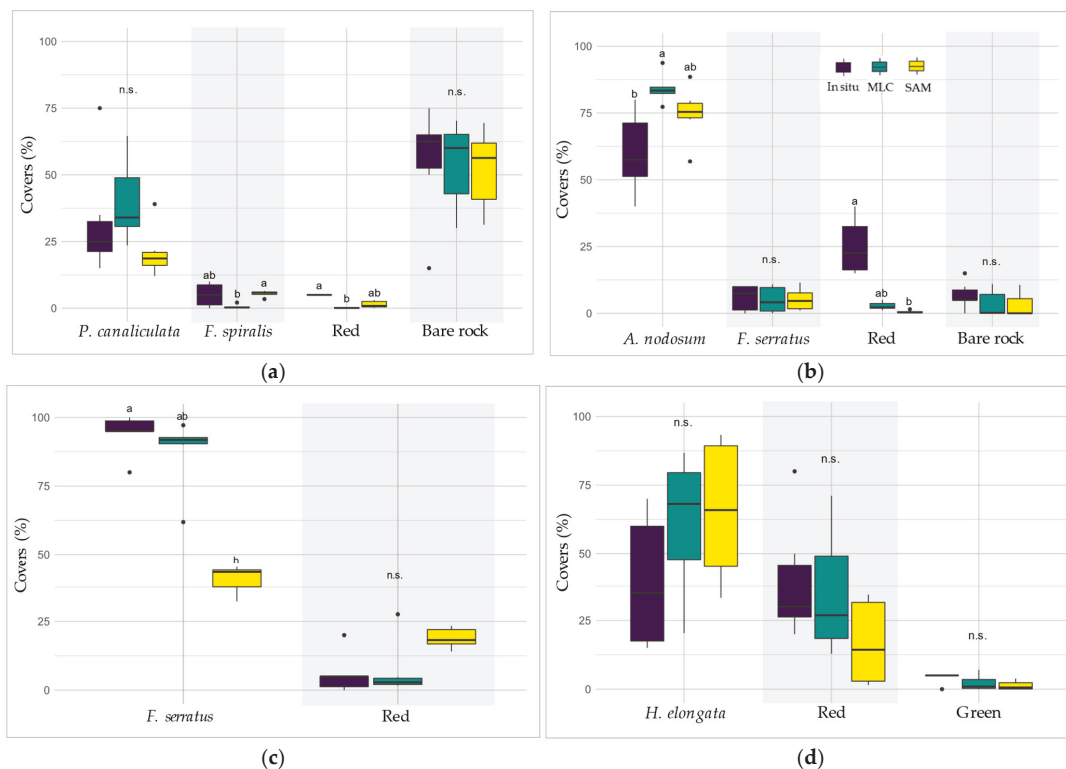


Figure 11. (a) Comparison of in situ (violet boxes), MLC (green boxes) and SAM (yellow boxes) determined covers of main Fucales species, macroalgal classes and bare rock found in Pc-Fspi (a), An (b), Fser (c) and He-Ld (d) levels. Covers are given in percentages. In the boxplots, only the classes showing covers for all three methods are represented. Letters refer to statistical differences (Kruskal–Wallis).

In An (Figure 11b), the cover of '*A. nodosum*' for SAM and MLC was higher (74.7% and 84.1%, respectively) than the in situ cover (60%). However, there was no significant difference in its covers between in situ and SAM, but a significant difference appeared between in situ and MLC (Kruskal–Wallis, $p < 0.05$). The '*F. serratus*' cover showed no significant difference between the three methods, i.e., circa 5% (Kruskal–Wallis, $p > 0.05$). The percentage of 'Substratum' was also close and did not show significant differences, with 6% in situ and ca. 3% for MLC/SAM (Kruskal–Wallis, $p > 0.05$). However, covers of 'Red' were significantly higher in the in situ field sampling (25%) than in the MLC method (Kruskal–Wallis, $p < 0.005$). The SAM method was not different for either of the two.

In the Fser level (Figure 11c), the cover of '*F. serratus*' was significantly greater in situ, with 94.2%, than in SAM with an estimated cover of 40.5% (Kruskal–Wallis, $p < 0.05$). MLC method did not show significant differences with either method (87.6%).

In He-Ld (Figure 11d), the '*H. elongata*' covers were 56.7% in situ, 61.3% with MLC and 65.5% with SAM and were statistically the same (Kruskal–Wallis, $p > 0.05$). 'Red' covers showed nearly similar values (39.2% and 34.9%, respectively). Even though SAM 'Red' covers were lower (16.8%), no significant difference was observed between the three methods (Kruskal–Wallis, $p > 0.05$). 'Green' covers were also not significantly different between in situ (4.2%), MLC (2.3%) and SAM (1.3%) (Kruskal–Wallis, $p > 0.05$).

To summarize these results, no generalization can be applied, both methods showed contrasted results according to the level and/or class considered. For instance, the cover of 'Red' is better estimated by the SAM in Pc-Fspi, and, on the contrary, better estimated by the MLC in An. The same observation can be made for the dominating Fucales, which are better represented by the SAM method in An, and by the MLC in Fser.

4. Discussion

Seaweeds are ecosystem engineers and key habitat-formers in temperate marine coastal ecosystems [73,74]. The use of satellite sensors to monitor populations of large temperate macroalgal species is well documented [54,75,76]. Such techniques have been used mainly to characterize the extension of macroalgal communities and related habitats [37]. However, the accurate classification of closely related macroalgal species (e.g., different species within the same Genus) and groups of species in remote sensing analysis remain a key point that still needs to be investigated. Using a high spatial and spectral resolution technology could be part of the solution [44].

In this study, heterogeneous seaweed habitats vertically distributed were successfully differentiated using both field and remote techniques. The 'undisturbed' sampling method [59] was used in situ to describe the structure of macroalgal communities and was then directly compared with the remote sensing imagery.

4.1. Habitats Characterization through Remote Sensing and Field Sampling

Orthophotos are often sufficient to remotely describe a habitat dominated by a single species, forming homogeneous populations, such as mussels [77,78] or polychaete reefs [79] that can be identified on a large scale. Eventually, species groups can be discriminated (brown, red and green seaweeds) [43], but this differentiation is quickly overtaken when studying complex ecosystems, showing an intricate microtopography, such as the European rocky shores. In the present study, using hyperspectral imagery, seaweed habitats were successfully differentiated (1) between them, (2) from substratum and (3) from seawater; the spectral signature allowed a clear differentiation between them (Figure 6a) as already reported in previous studies [13,42,75]. Moreover, the spectral signatures of five Fucales species were also differentiated, allowing an accurate mapping of the study site and its habitats. Here, two species of Fucus (*F. serratus* and *F. spiralis*), previously often gathered as a single class [35,44,58], were also discriminated. Indeed, the rocky shore surveyed during the present study showed a succession of several dominant fucoid species, with a conspicuous increase of red seaweeds abundance in the low intertidal zone, as already reported from previous studies in the area, using only field sampling [80,81]. However, technical limitations were spotted: limpets and barnacles were impossible to discriminate (although large limpets can be guessed) because of their heterogeneous distribution on rocky shore and close spectral signature with substratum. The same issue was observed for distinguishing red and green seaweed species, which were heterogeneously distributed and can present similar spectra, or variations of spectra according to their health conditions (e.g., pigment degradation, grazing, occurrence of epi/endophytes) [42,82,83].

In this study, we assigned several subclasses in the 'Red' one because of the dominance in He-Ld by an assemblage of *Mastocarpus stellatus*/*Chondrus crispus*. That assemblage masked the occurrence of several filamentous or turf red algae which were not identified on hyperspectral images, but with the use of existing spectral libraries [82], it may be an option [44]. In the same way, crustose and erect red macroalgae were also assigned in the 'Red' class for the same reasons, but with distinguishable patches, it could be possible to create two different classes [42]. For further analysis, it would be interesting to refine classes and to include more identified red species to the classification. The kelp *Laminaria digitata* was not added to the classification due to residual seawater on the images. However, it would be useful to separate that species as a spectral class due to its dominance in the upper sublittoral zone [44,58]. It would also be interesting to transfer the spectral library created for other study sites to check if the method is interoperable.

4.2. Comparison of the Two Classifiers

Our results showed that remote classification data were in agreement with covers calculated from field sampling inside sampling spots, in spite of an approximation of 5% for in situ estimations, and whatever spectral properties of brown macroalgae, which are very similar [82,84] (Figure 6b).

MLC provided the best producer/user accuracies for dominating algae of three levels (An, Fser and He-Ld) (Table 4) and SAM for two levels (An and He-Ld) (Table 5). Pc-Fspi provided the lowest producer/user accuracy, with the lowest values for '*F. spiralis*' for the two classifications. This could be a site effect due to the lower extension of these two species compare to the others in Porspoder, especially *F. spiralis*, which results in a reduced pixels selection for the algorithms. Moreover, the fact that *F. spiralis* is found in more shaded environments/crevices on this site could affect the data since shadows cause serious difficulties for remote shooting [85]. There is also a clear misclassification between *P. canaliculata* and *F. spiralis*, especially for MLC, which might be explained because of forming confused communities with small size species, and similar colors, in this site.

In An, MLC was less accurate than SAM for *A. nodosum*. Due to the presence of the red alga *Vertebrata lanosa*, which was not taken into account for the classifications, the '*A. nodosum*' class was not considered as a 'pure class' and SAM had confusion overestimating 'Red' seaweed in An and Fser levels. There was also a little confusion in '*A. nodosum*' with *P. canaliculata*, as in Rossiter et al. (2020) [58]. This confusion appeared in the upper limit of *A. nodosum* distribution, where *A. nodosum* appeared brighter due to a stronger light stress [86], with a color close to that of *P. canaliculata*. Not surprisingly, *P. canaliculata* was also classified as *A. nodosum* when it was darker than usual.

The 'Red' class had a lower producer/user accuracy for the SAM classification, with an overestimation in Fser to the detriment of *F. serratus*, which is underestimated (Table 5). For that level, SAM is not a good descriptor at the site level.

On the processed images (Figures 7 and 8), many pixels were classified as 'Green', despite a reduced cover of green seaweeds in the field data. This is mainly due to the positioning of the spots on the shore, chosen because of a clear dominance by brown macroalgae.

Both SAM and MLC misclassified pixels of *H. elongata*, with some occurrence in Pc-Fspi, An and Fser, whereas this species does not develop in higher intertidal zones [7,87]. On the contrary, the high-level species *F. spiralis* could appear in An with both MLC and SAM. An approach taking into account the bathymetric range (strongly affecting certain species) could be determined using a lidar approach [88] and could solve such a problem, considering the vertical zonation of species [17].

The MLC classification was found to be more accurate than SAM at the site level due to better management of spatial heterogeneity of habitats by the MLC, and because SAM does not consider the magnitude of pixels' vectors. Moreover, groups of macroalgal species, Fucales in particular, have close spectral similarities, which could partially explain the lower accuracy of SAM [47,89]. Nevertheless, both supervised classifications mapped the four bathymetric levels sampled in this study and both classifiers were able to separate brown, red and green algae. At sampling spots scale, they provided similar results, so, they can be used to compare macroalgal covers with accuracy. To refine the results, it could be interesting to test an object-based classification that takes into account not only spectral information but also the shape, size, texture, tone and the compactness [90,91] of objects. In that prospect, macroalgae could be an interesting model due to various morphologies and textures.

4.3. Consistency of Specific Identification and Perspectives

Automated macroalgal classification applied to shores dominated by a single fucooid species is currently manageable [43]. However, discriminating and mapping *Fucus* spp. remain a challenge, as seen in previous studies, in which *Fucus* spp. have been gathered in a single mixed class [35,44,58]. Overall accuracy, used to estimate the quality of the

classification [62,92], presented values indicating a clear distinction between *F. spiralis* and *F. serratus*. Even though the final classification of the entire site of Porspoder pointed out some pixels which were not correctly attributed, the entire distribution of pixels on the site was consistent. The analysis by db-RDA did not show a significant influence by the method in the distribution of the sampling spots, unlike the level. This may be related to the nature of the site studied, with the Pc-Fspi level having much lower macroalgal covers than the An and Fser levels, and to the spectral properties of each species. Moreover, the comparison between in situ covers with MLC and SAM data showed no significant difference for most classes (Figure 11), therefore, validating the algorithms as good descriptors for intertidal macroalgal covers at sampling spots scale. This also confirms the db-RDA results; efficiency does not depend on the method but on the studied bathymetric level. However, there were more differences (at the site scale) with SAM which resulted in more misclassified pixels on images (Figures 9 and A1–A3). So, the use of common algorithms could be perfectible, but it does answer the problem of the study by classifying correctly macroalgal communities. Other algorithms such as random forests or support vector machines might be considered to estimate entire shores, as for coastal/terrestrial objects [93–97].

Indeed, the routine use of the hyperspectral method could be the subject of a long-term study in an ecosystem monitoring context, particularly in the context of Fucales regression on European coasts [98,99]. Indeed, since the last century, covers of some Fucales species have decreased under the action of various factors such as the intensification of grazing [100]. This trend is also well known and studied in various marine phanerogam species [101], and also in kelp species, submitted to increasing grazing and/or heat waves related to global change [102–104]. Indeed, hyperspectral imagery is already being used in many ecosystems in the context of conservation biology [105,106]. Thus, the promising results obtained in this work could serve as a basis for a conservation/monitoring program of intertidal habitats.

5. Conclusions

In light of the results, MLC seems to be a better classifier for mapping a seaweed-dominated rocky shore, with a more realistic achievement. To better assess the impact of global change on coastal ecosystems, there is an increasing interest in remote sensing data to evaluate the ecological state of corresponding habitats [107]. Otherwise, the community approach in ecological surveys gives a good opportunity to better understand functional traits of marine vegetation, including relationships with primary production [108,109]. In that context, this study gives for the first time a comparison of cover data for macroalgal habitats obtained by both in situ sampling on the shore and hyperspectral imagery at a centimeter resolution, and a consistent cartography of a site using well-known algorithms.

Our results go beyond the global distribution of macroalgal covers as inferred from indices such as NDVI, VCI or IP [35,110,111], but rather provide information on the fine scale repartition of species/groups of species on the shore.

Since coastal rocky shores integrate various and imbricated habitats, the UAVs approach developed here seems to be an adequate tool to evaluate the distribution of macroalgal communities/habitats at the site to geographical area level. Moreover, hyperspectral imaging at the centimeter scale allows for a precise analysis of the seaweed habitat structure in parallel to field monitoring.

Author Contributions: Collected field sampling data, methodology, analyzed and interpreted field and remote sensing data, wrote the article, W.D.; remote sensing methodology, made critical revisions for important intellectual content, A.L.B., T.B. (Touria Bajjouk) and S.R.; data analysis, made critical revisions for important intellectual content, M.H.; collected field sampling data, data analysis, made critical revisions for important intellectual content, T.B. (Thomas Burel); hyperspectral acquisition and pre-treatment, made critical revisions for important intellectual content, M.L. and A.G.; conceived and designed the study, supervision, collected field sampling data, funding acquisition, made critical revisions for important intellectual content, E.A.G. All authors have read and agreed to the published version of the manuscript.

Funding: This study was funded by the DREAL (Direction régionale de l'environnement, de l'aménagement et du logement) and the Regional Council of Brittany (Rebent Network), the Office Français de la Biodiversité and the Agence de l'Eau Loire-Bretagne (European Water Framework Directive and Marine Strategy Framework Directive). Wendy Diruit received a fellowship from the Doctoral School of Marine Sciences (Ecole Doctorale des Sciences de la Mer et du Littoral).

Data Availability Statement: The data presented in this study are available on request from the corresponding author.

Acknowledgments: Authors thank Sara Terrin and Alain Guenneguez for helping with the field sampling, and Marion Jaud for her valuable advice in hyperspectral analysis and the use of ENVI.

Conflicts of Interest: The authors declare no conflict of interest.

Appendix A

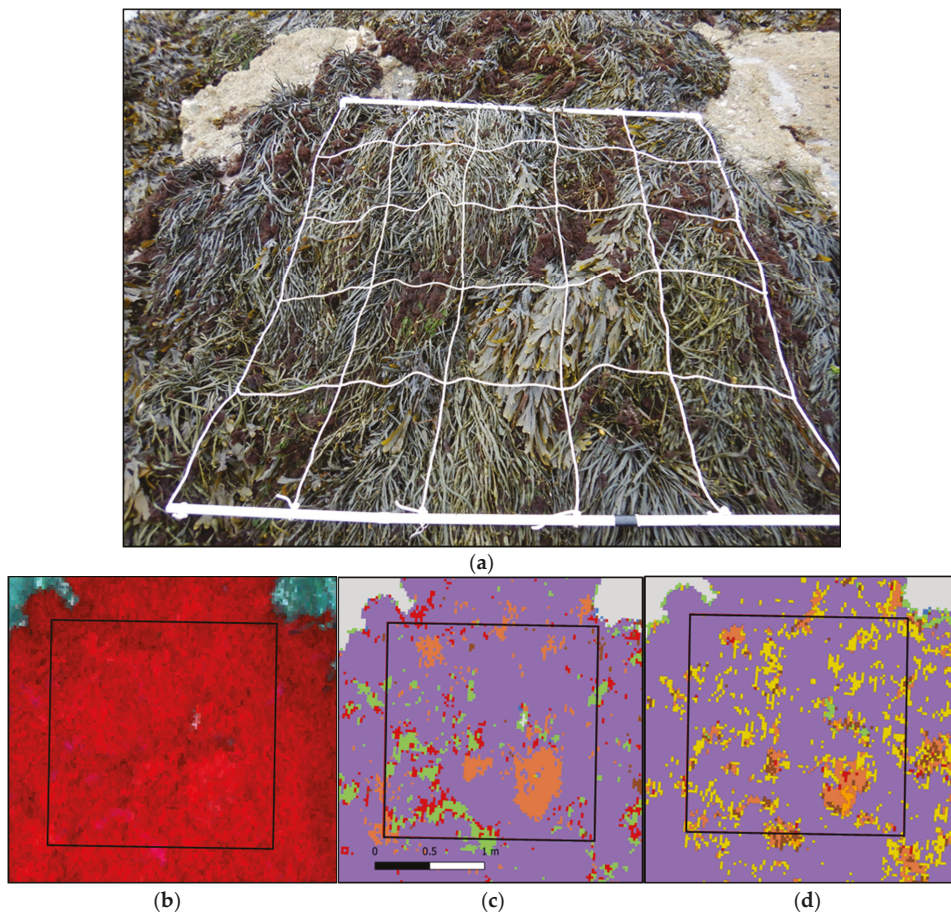


Figure A1. (a) Picture of a sampling spot on the An level at Porspoder taken during field sampling in May 2021. (b) NIR-G-B image of the same sampling spot. (c) Result of the MLC classification. (d) Result of the SAM classification. The black square corresponds to the mobile grid structure used for field sampling. Color code in (c,d) corresponds to the following classes: '*P. canaliculata*' (brown), '*F. spiralis*' (yellow), '*A. nodosum*' (purple), '*F. serratus*' (Coral), '*H. elongata*' (orange), 'Red' algae (red), 'Green' algae (green), 'Substratum' (grey) and 'Water' (blue).

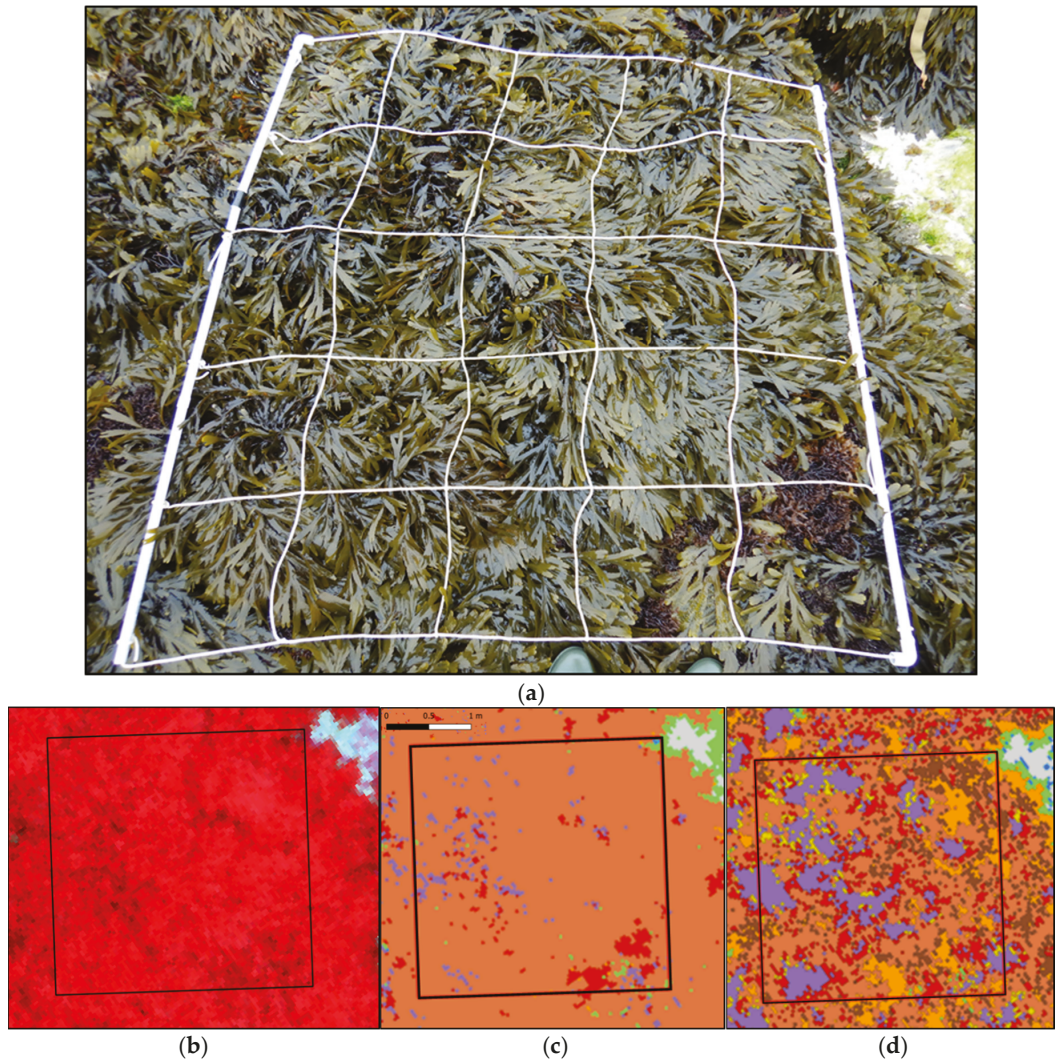


Figure A2. (a) Picture of a sampling spot on the Fser level at Porspoder taken during field sampling in June 2021. (b) NIR-G-B image of the same sampling spot. (c) Result of the MLC classification. (d) Result of the SAM classification. The black square corresponds to the mobile grid structure used for field sampling. Color code in (c,d) corresponds to the following classes: '*P. canaliculata*' (brown), '*F. spiralis*' (yellow), '*A. nodosum*' (purple), '*F. serratus*' (Coral), '*H. elongata*' (orange), 'Red' algae (red), 'Green' algae (green), 'Substratum' (grey) and 'Water' (blue).

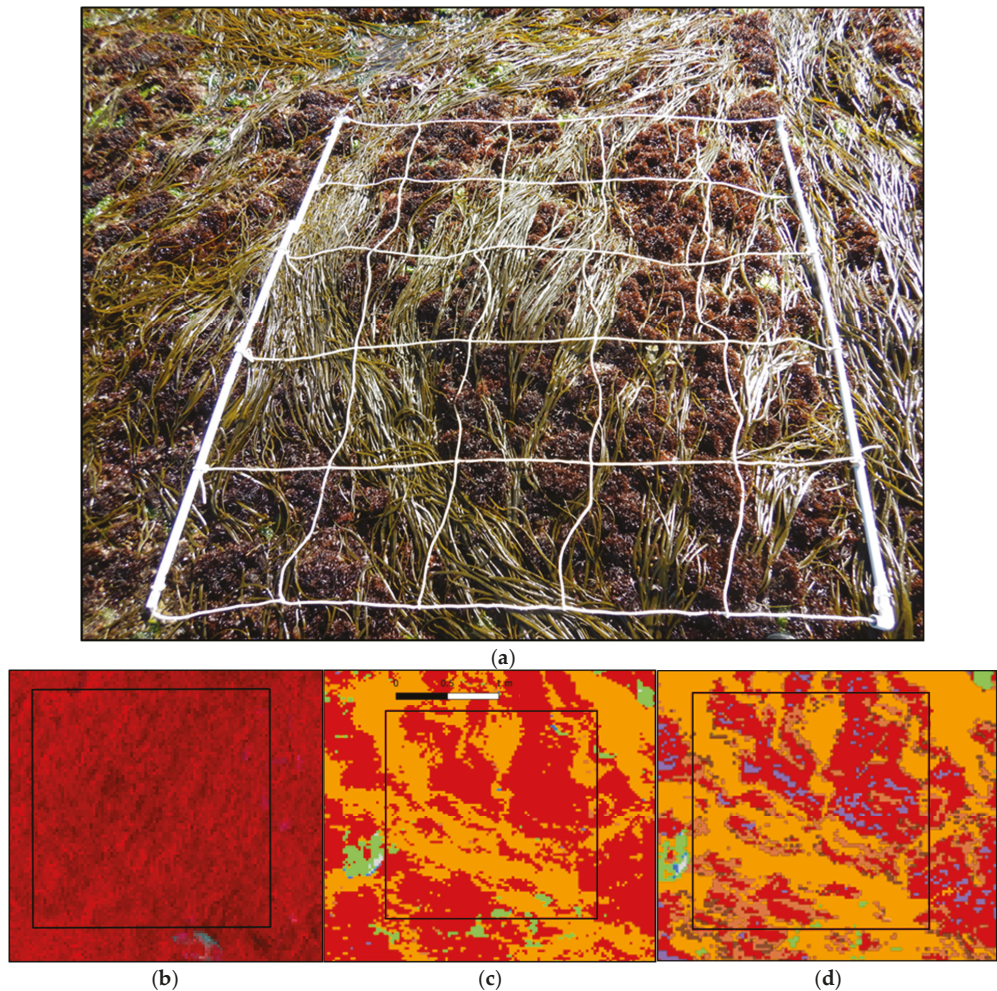


Figure A3. (a) Picture of a sampling spot on the He-Ld level at Porspoder taken during field sampling in April 2021. (b) NIR-G-B image of the same sampling spot. (c) Result of the MLC classification. (d) Result of the SAM classification. The black square corresponds to the mobile grid structure used for field sampling. Color code in (c,d) corresponds to the following classes: ‘*P. canaliculata*’ (brown), ‘*A. nodosum*’ (purple), ‘*F. serratus*’ (Coral), ‘*H. elongata*’ (orange), ‘Red’ algae (red), ‘Green’ algae (green), ‘Substratum’ (grey) and ‘Water’ (blue).

References

1. Hawkins, S.J.; Pack, K.E.; Hyder, K.; Benedetti-Cecchi, L.; Jenkins, S.R. Rocky shores as tractable test systems for experimental ecology. *J. Mar. Biol. Assoc. UK* **2020**, *100*, 1017–1041. [[CrossRef](#)]
2. Hawkins, S.J.; Bohn, K.; Firth, L.B.; Williams, G.A. *Interactions in the Marine Benthos*; Cambridge University Press: Cambridge, UK, 2019; ISBN 110841608X.
3. Boaventura, D.M. *Patterns of Distribution in Intertidal Rocky Shores: The Role of Grazing and Competition in Structuring Communities*; University of Faro: Faro, Portugal, 2000.
4. Graham, L.E.; Graham, J.M.; Cook, M.E.; Wilcox, L.W. *Algae*; LJLM Press: Madison, WI, USA, 2016.
5. Raffaelli, D.G.; Hawkins, S.J. *Intertidal Ecology*, 2nd ed.; Kluwer Academic Publishers: Alphen aan den Rijn, The Netherlands, 1999; ISBN 9780412299506.

6. Juanes, J.A.; Guinda, X.; Puente, A.; Revilla, J.A. Macroalgae, a suitable indicator of the ecological status of coastal rocky communities in the NE Atlantic. *Ecol. Indic.* **2008**, *8*, 351–359. [CrossRef]
7. Lüning, K. *Seaweeds: Their Environment, Biogeography, and Ecophysiology*; John Wiley & Sons: Hoboken, NJ, USA, 1990; ISBN 0471624349.
8. Cabioch, J.; Floc'h, J.-Y.; Le Toquin, A.; Boudouresque, C.F. *Guide des Algues des mers d'Europe*; Delachaux & Niestlé: Paris, France, 2006; ISBN 260301384X.
9. Ar Gall, E.; Le Duff, M. Development of a quality index to evaluate the structure of macroalgal communities. *Estuar. Coast. Shelf Sci.* **2014**, *139*, 99–109. [CrossRef]
10. Ar Gall, E.; Le Duff, M.; Sauriau, P.G.; de Casamajor, M.N.; Gevaert, F.; Poisson, E.; Hacquebart, P.; Joncourt, Y.; Barillé, A.L.; Buchet, R.; et al. Implementation of a new index to assess intertidal seaweed communities as bioindicators for the European Water Framework Directive. *Ecol. Indic.* **2016**, *60*, 162–173. [CrossRef]
11. Burel, T.; Le Duff, M.; Ar Gall, E. Updated check-list of the seaweeds of the French coasts, Channel and Atlantic Ocean. *An Aod-Les Cahiers Naturalistes de l'Observatoire Marin* **2019**, *7*, 1–38.
12. Floc'h, J.-Y. Cartographie de la végétation marine dans l'archipel de Molène (Finistère). *Revue des Travaux de l'Institut des Pêches Maritimes* **1970**, *34*, 89–120.
13. Moussa, H.B.; Viollier, M.; Belsher, T. Télédétection des algues macrophytes de l'Archipel de Molène (France) Radiométrie de terrain et application aux données du satellite SPOT. *Remote Sens.* **1989**, *10*, 53–69. [CrossRef]
14. Rossi, N.; Daniel, C.; Perrot, T. Suivi de la Couverture en Macroalgues Intertidales de Substrat dur dans le Cadre du Projet REBENT. 2009, p. 76. Available online: <http://www.rebent.org/> (accessed on 20 September 2021).
15. Bajjouk, T. Soutien aux Actions NATURA 2000 de la Région Bretagne-Cahier des Charges Pour la Cartographie D'habitats des sites Natura 2000 Littoraux: Guide Méthodologique; RST/IFREMER/DYNECO/AG/09-01/TB/NATURA2000: 107 p.+ Annexes pp. 2009. Available online: <https://www.ifremer.fr/natura2000/> (accessed on 20 September 2021).
16. Bajjouk, T.; Rochette, S.; Laurans, M.; Ehrhold, A.; Hamdi, A.; Le Niliot, P. Multi-approach mapping to help spatial planning and management of the kelp species *L. digitata* and *L. hyperborea*: Case study of the Molène Archipelago, Brittany. *J. Sea Res.* **2015**, *100*, 2–21. [CrossRef]
17. OF Hytech Imaging. TBM Environment Réalisation d'une Cartographie des Habitats Intertidaux de L'archipel de Molène et de la Côte Nord du parc. 2020. Available online: <https://parc-marin-iroise.fr/> (accessed on 20 September 2021).
18. EC Council. Directive for a legislative frame and actions for the water policy, 2000/60/EC. *Off. J. L* **2000**, *327*, 1–73.
19. Guinda, X.; Juanes, J.A.; Puente, A.; Revilla, J.A. Comparison of two methods for quality assessment of macroalgae assemblages, under different pollution types. *Ecol. Indic.* **2008**, *8*, 743–753. [CrossRef]
20. Guinda, X.; Juanes, J.A.; Puente, A. The Quality of Rocky Bottoms index (CFR): A validated method for the assessment of macroalgae according to the European Water Framework Directive. *Mar. Environ. Res.* **2014**, *102*, 3–10. [CrossRef] [PubMed]
21. Neto, J.M.; Gaspar, R.; Pereira, L.; Marques, J.C. Marine Macroalgae Assessment Tool (MarMAT) for intertidal rocky shores. Quality assessment under the scope of the European Water Framework Directive. *Ecol. Indic.* **2012**, *19*, 39–47. [CrossRef]
22. Kuhlenskamp, R.; Schubert, P.; Bartsch, I. Water Framework Directive Monitoring-Component Macrophytobenthos N5 Helgoland, EQE Evaluation 2010. Final Report March 2011. Investigation Period: July 2010 February 2011. MMH-Report 17 for Landesamt für Landwirtschaft, Umwelt und Ländliche Räume des Landes Schleswig-Holstein; Germany (LLUR-SH). LLUR Reference number: LLUR-AZ 0608.451013. 2011, pp. 1–62. Available online: <https://epic.awi.de/id/eprint/24229/> (accessed on 9 February 2022).
23. Wells, E.; Wilkinson, M.; Wood, P.; Scanlan, C. The use of macroalgal species richness and composition on intertidal rocky seashores in the assessment of ecological quality under the European Water Framework Directive. *Mar. Pollut. Bull.* **2007**, *55*, 151–161. [CrossRef] [PubMed]
24. Derrien-Courtel, S.; Le Gal, A. Suivi des Macroalgues Subtidales de la Façade Manche-Atlantique-Rapport Final-Convention 2010-Action 5. 2011. Available online: <https://archimer.ifremer.fr/doc/00036/14735/> (accessed on 9 February 2022).
25. Pauly, K.; De Clerck, O. *GIS-Based Environmental Analysis, Remote Sensing, and Niche Modeling of Seaweed Communities BT—Seaweeds and their Role in Globally Changing Environments*; Seckbach, J., Einav, R., Israel, A., Eds.; Springer: Dordrecht, The Netherlands, 2010; pp. 93–114. ISBN 978-90-481-8569-6.
26. Smale, D.A.; Burrows, M.T.; Moore, P.; O'Connor, N.; Hawkins, S.J. Threats and knowledge gaps for ecosystem services provided by kelp forests: A northeast Atlantic perspective. *Ecol. Evol.* **2013**, *3*, 4016–4038. [CrossRef] [PubMed]
27. Hawkins, S.J.; Sugden, H.E.; Mieszowska, N.; Moore, P.J.; Poloczanska, E.; Leaper, R.; Herbert, R.J.H.; Genner, M.J.; Moschella, P.S.; Thompson, R.C.; et al. Consequences of climate-driven biodiversity changes for ecosystem functioning of North European rocky shores. *Mar. Ecol. Prog. Ser.* **2009**, *396*, 245–260. [CrossRef]
28. Senay, G.B.; Ward, A.D.; Lyon, J.G.; Fausey, N.R.; Nokes, S.E. Manipulation of high spatial resolution aircraft remote sensing data for use in site-specific farming. *Trans. ASAE* **1998**, *41*, 489. [CrossRef]
29. Yang, C.; Everitt, J.H.; Bradford, J.M. Yield estimation from hyperspectral imagery using spectral angle mapper (SAM). *Trans. ASABE* **2008**, *51*, 729–737. [CrossRef]
30. Steneck, R.S.; Watling, L. Feeding capabilities and limitation of herbivorous molluscs: A functional group approach. *Mar. Biol.* **1982**, *68*, 299–319. [CrossRef]
31. Plant, R.E.; Munk, D.S.; Roberts, B.R.; Vargas, R.L.; Rains, D.W.; Travis, R.L.; Hutmacher, R.B. Relationships between remotely sensed reflectance data and cotton growth and yield. *Trans. ASAE* **2000**, *43*, 535. [CrossRef]

32. Viollier, M.; Belsher, T.; Loubersac, L. Signatures spectrales des objets du littoral. In Proceedings of the 3th International Colloquium on Spectral Signatures of Objects in Remote Sensing, Les Arcs, France, 16–20 December 1985.
33. Floc'h, J.-Y. Cartographie de la Végétation Marine et Observations Écologiques dans L'archipel de MOLÈNE (Finistère). Ph.D. Thesis, Université de Rennes, Rennes, France, 1967.
34. Andrefouet, S.; Zubia, M.; Payri, C. Mapping and biomass estimation of the invasive brown algae *Turbinaria ornata* (Turner) J. Agardh and *Sargassum mangarevense* (Grunow) Setchell on heterogeneous Tahitian coral reefs using 4-meter resolution IKONOS satellite data. *Coral Reefs* **2004**, *23*, 26–38. [CrossRef]
35. Guillaumont, B.; Callens, L.; Dion, P. Spatial distribution and quantification of *Fucus* species and *Ascophyllum nodosum* beds in intertidal zones using spot imagery. In *Fourteenth International Seaweed Symposium*; Springer: Dordrecht, The Netherlands, 1993; pp. 297–305.
36. Zoffoli, M.L.; Gernez, P.; Rosa, P.; Le Bris, A.; Brando, V.E.; Barillé, A.-L.; Harin, N.; Peters, S.; Poser, K.; Spaias, L. Sentinel-2 remote sensing of *Zostera noltei*-dominated intertidal seagrass meadows. *Remote Sens. Environ.* **2020**, *251*, 112020. [CrossRef]
37. Bajjouk, T.; Guillaumont, B.; Populus, J. Application of airborne imaging spectrometry system data to intertidal seaweed classification and mapping. In *Fifteenth International Seaweed Symposium*; Springer: Dordrecht, The Netherlands, 1996; pp. 463–471.
38. Brodie, J.; Ash, L.V.; Tittley, I.; Yesson, C. A comparison of multispectral aerial and satellite imagery for mapping intertidal seaweed communities. *Aquat. Conserv. Mar. Freshw. Ecosyst.* **2018**, *28*, 872–881. [CrossRef]
39. Anderson, K.; Gaston, K.J. Lightweight unmanned aerial vehicles will revolutionize spatial ecology. *Front. Ecol. Environ.* **2013**, *11*, 138–146. [CrossRef]
40. Hamylton, S.M. *Spatial Analysis of Coastal Environments*; Cambridge University Press: Cambridge, UK, 2017; ISBN 1107070473.
41. Crawford, C.; Harwin, S. *Reassessment of Intertidal Macroalgal Communities Near to and Distant from Salmon Farms and an Evaluation of Using Drones to Survey Macroalgal Distribution*; Fisheries Research and Development Corporation: Canberra, Australia, 2018.
42. Tait, L.; Bind, J.; Charan-Dixon, H.; Hawes, I.; Pirker, J.; Schiel, D. Unmanned Aerial Vehicles (UAVs) for Monitoring Macroalgal Biodiversity: Comparison of RGB and Multispectral Imaging Sensors for Biodiversity Assessments. *Remote Sens.* **2019**, *11*, 2332. [CrossRef]
43. Murfitt, S.L.; Allan, B.M.; Bellgrove, A.; Rattray, A.; Young, M.A.; Ierodiakonou, D. Applications of unmanned aerial vehicles in intertidal reef monitoring. *Sci. Rep.* **2017**, *7*, 10259. [CrossRef] [PubMed]
44. Oppelt, N.M.; Schulze, F.; Doernhoefer, K.; Eisenhardt, I.; Bartsch, I. Hyperspectral classification approaches for intertidal macroalgae habitat mapping: A case study in Heligoland. *Opt. Eng.* **2012**, *51*, 111703. [CrossRef]
45. Davis, S.M.; Swain, P.H. *Remote Sensing: The Quantitative Approach*; McGraw-Hill International Book Company: New York, NY, USA, 1978.
46. Richards, J.A. *Remote Sensing Digital Image Analysis*; Springer: Berlin, Germany, 1986; p. 281.
47. Shafri, H.Z.M.; Suhaili, A.; Mansor, S. The Performance of Maximum Likelihood, Spectral Angle Mapper, Neural Network and Decision Tree Classifiers in Hyperspectral Image Analysis. *J. Comput. Sci.* **2007**, *3*, 419–423. [CrossRef]
48. Bolstad, P.; Lillesand, T.M. Rapid maximum likelihood classification. *Photogramm. Eng. Remote Sens.* **1991**, *57*, 67–74.
49. Rossiter, T.; Furey, T.; McCarthy, T.; Stengel, D.B. Application of multiplatform, multispectral remote sensors for mapping intertidal macroalgae: A comparative approach. *Aquat. Conserv. Mar. Freshw. Ecosyst.* **2020**, *30*, 1595–1612. [CrossRef]
50. Bartsch, I.; Oppelt, N.; Bochow, M.; Schulze, F.; Geisler, T.; Eisenhardt, I.; Nehring, F.; Heege, T. Detection and Quantification of Marine Vegetation by Airborne Hyperspectral Remote Sensing: Case Study Helgoland. 2011. Available online: <https://epic.awi.de/id/eprint/25251/> (accessed on 20 September 2021).
51. Uhl, F.; Oppelt, N.; Bartsch, I. Spectral mixture of intertidal marine macroalgae around the island of Helgoland (Germany, North Sea). *Aquat. Bot.* **2013**, *111*, 112–124. [CrossRef]
52. Brodie, J.; Hayes, P.K.; Barker, G.L.; Irvine, L.M. Molecular and morphological characters distinguishing two *Porphyra* species (Rhodophyta: Bangiophycidae). *Eur. J. Phycol.* **1996**, *31*, 303–308. [CrossRef]
53. Casal, G.; Kutser, T.; Domínguez-Gómez, J.A.; Sánchez-Carnero, N.; Freire, J. Assessment of the hyperspectral sensor CASI-2 for macroalgal discrimination on the Ría de Vigo coast (NW Spain) using field spectroscopy and modelled spectral libraries. *Cont. Shelf Res.* **2013**, *55*, 129–140. [CrossRef]
54. Cavanaugh, K.C.; Siegel, D.A.; Reed, D.C.; Dennison, P.E. Environmental controls of giant-kelp biomass in the Santa Barbara Channel, California. *Mar. Ecol. Prog. Ser.* **2011**, *429*, 1–17. [CrossRef]
55. Deysher, L.E. Evaluation of remote sensing techniques for monitoring giant kelp populations. *Hydrobiologia* **1993**, *260*, 307–312. [CrossRef]
56. D'Archino, R.; Piazzini, L. Macroalgal assemblages as indicators of the ecological status of marine coastal systems: A review. *Ecol. Indic.* **2021**, *129*, 107835. [CrossRef]
57. Volent, Z.; Johnsen, G.; Sigernes, F. Kelp forest mapping by use of airborne hyperspectral imager. *J. Appl. Remote Sens.* **2007**, *1*, 11503.
58. Rossiter, T.; Furey, T.; McCarthy, T.; Stengel, D.B. UAV-mounted hyperspectral mapping of intertidal macroalgae. *Estuar. Coast. Shelf Sci.* **2020**, *242*, 106789. [CrossRef]
59. Burel, T.; Schaal, G.; Grall, J.; Le Duff, M.; Chapalain, G.; Schmitt, B.; Gemin, M.; Boucher, O.; Ar Gall, E. Small-scale effects of hydrodynamics on the structure of intertidal macroalgal communities: A novel approach. *Estuar. Coast. Shelf Sci.* **2019**, *226*, 106290. [CrossRef]

60. Eastman, J.R. IDRISI Kilimanjaro: Guide to GIS and Image Processing. 2003. Available online: <https://www.academia.edu/24202322> (accessed on 7 April 2022).
61. Carrasco-Escobar, G.; Manrique, E.; Ruiz-Cabrejos, J.; Saavedra, M.; Alava, F.; Bickersmith, S.; Prussing, C.; Vinetz, J.M.; Conn, J.E.; Moreno, M. High-accuracy detection of malaria vector larval habitats using drone-based multispectral imagery. *PLoS Negl. Trop. Dis.* **2019**, *13*, e0007105. [[CrossRef](#)]
62. Congalton, R.G.; Green, K. *Assessing the Accuracy of Remotely Sensed Data: Principles and Practices*; CRC Press: Boca Raton, FL, USA, 1999; ISBN 0429629354.
63. Foody, G.M. Status of land cover classification accuracy assessment. *Remote Sens. Environ.* **2002**, *80*, 185–201. [[CrossRef](#)]
64. Colombo, P.M.; Orsenigo, M. Sea depth effects on the algal photosynthetic apparatus II. An electron microscopic study of the photosynthetic apparatus of *Halimeda tuna* (Chlorophyta, Siphonales) at -0.5 m and -6.0 m sea depths. *Phycologia* **1977**, *16*, 9–17. [[CrossRef](#)]
65. Jia, X.; Richards, J.A. Efficient maximum likelihood classification for imaging spectrometer data sets. *IEEE Trans. Geosci. Remote Sens.* **1994**, *32*, 274–281.
66. ERDAS Inc. *Erdas Field Guide*; Erdas Inc.: Atlanta, GA, USA, 1999; Volume 672.
67. Kruse, F.A.; Lefkoff, A.B.; Boardman, J.W.; Heidebrecht, K.B.; Shapiro, A.T.; Barloon, P.J.; Goetz, A.F.H. The spectral image processing system (SIPS)—Interactive visualization and analysis of imaging spectrometer data. *Remote Sens. Environ.* **1993**, *44*, 145–163. [[CrossRef](#)]
68. Yuhas, R.H.; Goetz, A.F.H.; Boardman, J.W. Discrimination among semi-arid landscape endmembers using the spectral angle mapper (SAM) algorithm. In Proceedings of the JPL, Summaries of the Third Annual JPL Airborne Geoscience Workshop, Pasadena, CA, USA, 1–5 June 1992; Volume 1, pp. 147–149.
69. Rwanga, S.S.; Ndambuki, J.M. Accuracy assessment of land use/land cover classification using remote sensing and GIS. *Int. J. Geosci.* **2017**, *8*, 611. [[CrossRef](#)]
70. R Core Team. *R: A Language and Environment for Statistical Computing*; Foundation for Statistical Computing: Vienna, Austria, 2021. Available online: <https://www.R-project.org/> (accessed on 12 January 2022).
71. Escobar-Briones, E.G.; Díaz, C.; Legendre, P. Meiofaunal community structure of the deep-sea Gulf of Mexico: Variability due to the sorting methods. *Deep Sea Res. Part II Top. Stud. Oceanogr.* **2008**, *55*, 2627–2633. [[CrossRef](#)]
72. Marçal, A.R.S.; Borges, J.S.; Gomes, J.A.; Da Costa, J.F.P. Land cover update by supervised classification of segmented ASTER images. *Int. J. Remote Sens.* **2005**, *26*, 1347–1362. [[CrossRef](#)]
73. Jones, C.G.; Lawton, J.H.; Shachak, M. Organisms as ecosystem engineers. In *Ecosystem Management*; Springer: Berlin/Heidelberg, Germany, 1994; pp. 130–147.
74. Teagle, H.; Hawkins, S.J.; Moore, P.J.; Smale, D.A. The role of kelp species as biogenic habitat formers in coastal marine ecosystems. *J. Exp. Mar. Bio. Ecol.* **2017**, *492*, 81–98. [[CrossRef](#)]
75. Belsher, T. Apport du Satellite SPOT à la Cartographie des Végétaux Marins. Halieutique, Océanographie Télédétection Contrib. Française aux Colloq. Fr. Thème Télédétection, 3–13 Octobre 1988, Tokyo Shimizu, Japan. 1990, Volume 6, p. 61. Available online: https://horizon.documentation.ird.fr/exl-doc/pleins_textes/divers/20-07/31498.pdf#page=65 (accessed on 20 September 2021).
76. Bell, T.W.; Allen, J.G.; Cavanaugh, K.C.; Siegel, D.A. Three decades of variability in California's giant kelp forests from the Landsat satellites. In Proceedings of the AGU Fall Meeting Abstracts, San Francisco, CA, USA, 5–9 December 2011; Volume 2018, p. B31L-2645.
77. Gomes, I.; Peteiro, L.; Bueno-Pardo, J.; Albuquerque, R.; Pérez-Jorge, S.; Oliveira, E.R.; Alves, F.L.; Queiroga, H. What's a picture really worth? On the use of drone aerial imagery to estimate intertidal rocky shore mussel demographic parameters. *Estuar. Coast. Shelf Sci.* **2018**, *213*, 185–198. [[CrossRef](#)]
78. Barbosa, R.V. Assessing the Effect of Microhabitat Features on the Dynamics of a Benthic Intertidal Species: Use of Remote Sensing and Biophysical Modeling. Université de Bretagne Occidentale. 2022. Available online: <http://www.theses.fr/s210110> (accessed on 8 March 2022).
79. Brunier, G.; Oiry, S.; Gruet, Y.; Dubois, S.F.; Barillé, L. Topographic Analysis of Intertidal Polychaete Reefs (*Sabellaria alveolata*) at a Very High Spatial Resolution. *Remote Sens.* **2022**, *14*, 307. [[CrossRef](#)]
80. Connan, S. Etude de la Diversité Spécifique des Macroalgues de la Pointe de Bretagne et Analyse des Composés Phénoliques des Phytophycées Dominantes. Ph.D. Thesis, Université de Bretagne Occidentale, Brest, France, 2004.
81. Burel, T. Effet de L'hydrodynamisme sur la Structure des Communautés Macroalgales et sur les Interactions Macroflore/Macrofaune en Zone Intertidale. Ph.D. Thesis, Université de Bretagne Occidentale, Brest, France, 2020.
82. Douay, F.; Verpoorter, C.; Duong, G.; Spilmont, N.; Gevaert, F. New Hyperspectral Procedure to Discriminate Intertidal Macroalgae. *Remote Sens.* **2022**, *14*, 346. [[CrossRef](#)]
83. Olmedo-Masat, O.M.; Raffo, M.P.; Rodríguez-Pérez, D.; Arijón, M.; Sánchez-Carnero, N. How Far Can We Classify Macroalgae Remotely? An Example Using a New Spectral Library of Species from the South West Atlantic (Argentine Patagonia). *Remote Sens.* **2020**, *12*, 3870. [[CrossRef](#)]
84. Kutser, T.; Miller, I.; Jupp, D.L.B. Mapping coral reef benthic substrates using hyperspectral space-borne images and spectral libraries. *Estuar. Coast. Shelf Sci.* **2006**, *70*, 449–460. [[CrossRef](#)]
85. Zhou, W.; Huang, G.; Troy, A.; Cadenasso, M.L. Object-based land cover classification of shaded areas in high spatial resolution imagery of urban areas: A comparison study. *Remote Sens. Environ.* **2009**, *113*, 1769–1777. [[CrossRef](#)]

86. Stengel, D.B.; Dring, M.J. Seasonal variation in the pigment content and photosynthesis of different thallus regions of *Ascophyllum nodosum* (Fucales, Phaeophyta) in relation to position in the canopy. *Phycologia* **1998**, *37*, 259–268. [CrossRef]
87. Stengel, D.B.; Wilkes, R.J.; Guiry, M.D. Seasonal growth and recruitment of *Himantalia elongata* (Fucales, Phaeophycota) in different habitats on the Irish west coast. *Eur. J. Phycol.* **1999**, *34*, 213–221. [CrossRef]
88. Burel, T.; Grall, J.; Schaal, G.; Le Duff, M.; Ar Gall, E. Wave height vs. elevation effect on macroalgal dominated shores: An intercommunity study. *J. Appl. Phycol.* **2020**, *32*, 2523–2534. [CrossRef]
89. Petropoulos, G.P.; Vadrevu, K.P.; Kalaitzidis, C. Spectral angle mapper and object-based classification combined with hyperspectral remote sensing imagery for obtaining land use/cover mapping in a Mediterranean region. *Geocarto Int.* **2013**, *28*, 114–129. [CrossRef]
90. Zheng, Y.; Wu, J.; Wang, A.; Chen, J. Object- and pixel-based classifications of macroalgae farming area with high spatial resolution imagery. *Geocarto Int.* **2017**, *33*, 1048–1063. [CrossRef]
91. Liu, D.; Xia, F. Assessing object-based classification: Advantages and limitations. *Remote Sens. Lett.* **2010**, *1*, 187–194. [CrossRef]
92. Foody, G.M. Explaining the unsuitability of the kappa coefficient in the assessment and comparison of the accuracy of thematic maps obtained by image classification. *Remote Sens. Environ.* **2020**, *239*, 111630. [CrossRef]
93. Hobbey, B.; Arosio, R.; French, G.; Bremner, J.; Dolphin, T.; Mackiewicz, M. Semi-Supervised Segmentation for Coastal Monitoring Seagrass Using RPA Imagery. *Remote Sens.* **2021**, *13*, 1741. [CrossRef]
94. Kumar, P.; Gupta, D.K.; Mishra, V.N.; Prasad, R. Comparison of support vector machine, artificial neural network, and spectral angle mapper algorithms for crop classification using LISS IV data. *Int. J. Remote Sens.* **2015**, *36*, 1604–1617. [CrossRef]
95. Otukei, J.R.; Blaschke, T. Land cover change assessment using decision trees, support vector machines and maximum likelihood classification algorithms. *Int. J. Appl. Earth Obs. Geoinf.* **2010**, *12*, S27–S31. [CrossRef]
96. Zheng, Y.; Duarte, C.M.; Chen, J.; Li, D.; Lou, Z.; Wu, J. Remote sensing mapping of macroalgal farms by modifying thresholds in the classification tree. *Geocarto Int.* **2019**, *34*, 1098–1108. [CrossRef]
97. Chen, J.; Li, X.; Wang, K.; Zhang, S.; Li, J.; Sun, M. Assessment of intertidal seaweed biomass based on RGB imagery. *PLoS ONE* **2022**, *17*, e0263416. [CrossRef]
98. Thibaut, T.; Pinedo, S.; Torras, X.; Ballesteros, E. Long-term decline of the populations of Fucales (*Cystoseira* spp. and *Sargassum* spp.) in the Albères coast (France, North-western Mediterranean). *Mar. Pollut. Bull.* **2005**, *50*, 1472–1489. [CrossRef]
99. Jonsson, P.R.; Kotta, J.; Andersson, H.C.; Herkül, K.; Virtanen, E.; Sandman, A.N.; Johannesson, K. High climate velocity and population fragmentation may constrain climate-driven range shift of the key habitat former *Fucus vesiculosus*. *Divers. Distrib.* **2018**, *24*, 892–905. [CrossRef]
100. Le Roux, A. Les patelles (*Patella vulgata* L.), agents de la destruction de la couverture algale des estrans rocheux du Golfe du Morbihan. *Bull. De La Société Des Sci. Nat. De L'ouest De La Fr.* **2008**, *30*, 162–180.
101. Richardson, J.P.; Lefcheck, J.S.; Orth, R.J. Warming temperatures alter the relative abundance and distribution of two co-occurring foundational seagrasses in Chesapeake Bay, USA. *Mar. Ecol. Prog. Ser.* **2018**, *599*, 65–74. [CrossRef]
102. Thomsen, M.S.; Mondardini, L.; Alestra, T.; Gerrity, S.; Tait, L.; South, P.M.; Lilley, S.A.; Schiel, D.R. Local extinction of bull kelp (*Durvillaea* spp.) due to a marine heatwave. *Front. Mar. Sci.* **2019**, *6*, 84. [CrossRef]
103. Beas-Luna, R.; Micheli, F.; Woodson, C.B.; Carr, M.; Malone, D.; Torre, J.; Boch, C.; Caselle, J.E.; Edwards, M.; Freiwald, J. Geographic variation in responses of kelp forest communities of the California Current to recent climatic changes. *Glob. Chang. Biol.* **2020**, *26*, 6457–6473. [CrossRef]
104. Smale, D.A. Impacts of ocean warming on kelp forest ecosystems. *New Phytol.* **2020**, *225*, 1447–1454. [CrossRef]
105. Jones, T.G.; Coops, N.C.; Sharma, T. Exploring the utility of hyperspectral imagery and LiDAR data for predicting *Quercus garryana* ecosystem distribution and aiding in habitat restoration. *Restor. Ecol.* **2011**, *19*, 245–256. [CrossRef]
106. Valle, M.; Pala, V.; Lafon, V.; Dehouck, A.; Garmendia, J.M.; Borja, A.; Chust, G. Mapping estuarine habitats using airborne hyperspectral imagery, with special focus on seagrass meadows. *Estuar. Coast. Shelf Sci.* **2015**, *164*, 433–442. [CrossRef]
107. Israel, A.; Einav, R.; Seckbach, J.; Israel, A.; Einav, R.; Seckbach, J. *Seaweeds and Their Role in Globally Changing Environments*; Springer Science & Business Media: New York, NY, USA, 2010; Volume 15. ISBN 9048185696.
108. Bordeyne, F.; Migné, A.; Plus, M.; Davout, D. Modelling the annual primary production of an intertidal brown algal community based on in situ measurements. *Mar. Ecol. Prog. Ser.* **2020**, *656*, 95–107. [CrossRef]
109. Golléty, C.; Migné, A.; Davout, D. Benthic metabolism on a sheltered rocky shore: Role of the canopy in the carbon budget. *J. Phycol.* **2008**, *44*, 1146–1153. [CrossRef]
110. Dugdale, S.J. An Evaluation of Imagery from an Unmanned Aerial Vehicle (UAV) for the Mapping of Intertidal Macroalgae on Seal Sands, Tees Estuary, UK. Master's Thesis, Durham University, Durham, UK, 2007.
111. Ben Moussa, H. Contribution de la Télédétection Satellitaire à la Cartographie des Végétaux Marins: Archipel de Molène (Bretagne/France). 1987. Available online: <https://archimer.ifremer.fr/doc/00104/21524/> (accessed on 24 January 2022).



Article

Shifts in Salt Marsh Vegetation Landcover after Debris Flow Deposition

Germán D. Silva *, Dar A. Roberts, Joseph P. McFadden and Jennifer Y. King

Department of Geography, University of California, Santa Barbara, CA 93106-4060, USA; dar@geog.ucsb.edu (D.A.R.); mcfadden@ucsb.edu (J.P.M.); jyking@ucsb.edu (J.Y.K.)

* Correspondence: german.silva@geog.ucsb.edu

Abstract: On 9 January 2018, Carpinteria Salt Marsh Reserve received a large quantity of sediment following debris flows in Montecito, California. Because disturbances potentially impact the ecosystem services and functions that wetlands provide, an understanding of how the ecosystem responded to the debris flows is important for the management of salt marsh systems. However, a lack of field data before and after this disturbance makes this task impossible to complete by field methods alone. To address this gap, we used Sentinel-2 satellite imagery to calculate landcover fractions and spectral indices to produce maps of landcover before, during, and after the debris flow using a random forest classifier. Change detection showed that vegetation extent in November 2020 approached pre-debris flow conditions. While total vegetated area experienced little net change (0.15% decrease), there was a measurable change in the areal extent of vegetation type, with high marsh vegetation transitioning to mid marsh vegetation in regions that initially showed an increase in bare soil cover. These results are uniquely quantifiable using remote sensing techniques and show that disturbance due to debris flows may affect ecosystem function via plant community change. These impacts will need to be taken into consideration when managing wetlands prone to depositional events.

Keywords: remote sensing; wetland change; change detection; random forest classifier; *Salicornia pacifica*

Citation: Silva, G.D.; Roberts, D.A.; McFadden, J.P.; King, J.Y. Shifts in Salt Marsh Vegetation Landcover after Debris Flow Deposition. *Remote Sens.* **2022**, *14*, 2819. <https://doi.org/10.3390/rs14122819>

Academic Editor: Nicholas Murray

Received: 28 April 2022

Accepted: 7 June 2022

Published: 12 June 2022

Publisher's Note: MDPI stays neutral with regard to jurisdictional claims in published maps and institutional affiliations.



Copyright: © 2022 by the authors. Licensee MDPI, Basel, Switzerland. This article is an open access article distributed under the terms and conditions of the Creative Commons Attribution (CC BY) license (<https://creativecommons.org/licenses/by/4.0/>).

1. Introduction

Coastal salt marshes are dynamic ecosystems found at the interface between marine and terrestrial environments. These productive ecosystems play important roles in coastal resilience via a variety of ecosystem services, such as accreting sediments, sequestering carbon, and providing habitat for a rich range of biota [1,2]. However, as little as 10% of California's historical wetland cover remains today [3]. This decrease in wetland cover is likely to worsen with the potential increased frequency of disturbances that further reduce and degrade wetland cover, such as sea level rise, coastal erosion, deposition, and anthropogenic marine debris [4–6]. In Santa Barbara County, CA, a series of large debris flows known as the Montecito Debris Flows exemplify a large-scale depositional disturbance to both built and natural environments, including wetlands. The increasing frequency of events related to climate change, such as fires, hurricanes, and altered hydrology, will likely increase the potential for further debris flows, both locally and globally [7]. To mitigate the impacts of disturbance, management should include the effects of disturbances from debris flows in the understanding of marsh form and function. For instance, sediment deposition is a common and important process in many marshes, with deposition due to hurricanes frequently studied and found to provide sediment important for nutrient delivery and the ability to offset sea level rise [2,5]. In contrast, anthropogenic marine debris, such as fishing gear and wooden poles, has been found to damage plant tissues in marshes [4]; meanwhile, oiling has been found to temporarily increase shoreline loss of affected wetlands [8].

Debris flows are an episodic depositional disturbance event; however, there is little literature studying them in wetlands. Furthermore, many studies examining disturbance

events in salt marshes have focused on the Gulf of Mexico and the east coast of the U.S. [4,5,8–11]. However, the disturbances that are common in those regions, such as hurricanes, are not common on the west coast of the U.S., where debris flows are more common. As such, the question of how the Montecito Debris Flows impacted the marsh is of interest. However, addressing this question with field methods is complicated by the fact that the unpredictability of the event meant that field data could not be collected prior to the event. Furthermore, a combination of manager-led mechanical dredging and inundation by exceptionally high tides, also known as king tides, removed sediment from the marsh and limited the ability to collect field data following the event. Remotely sensed data, however, were collected before and following the event and could be used to assess impacts of the debris flow on the marsh.

Remote sensing has been used for change detection, biomass estimation, and land cover classification in wetlands with a large range of applications [9,12]. Due to recent advances in sensor design and data analysis, remote sensing is becoming more practical for monitoring natural and anthropogenic changes in coastal systems [12]. Prior studies have recommended a variety of sensors (e.g., Landsat, imaging spectrometers, LiDAR, PlanetScope, and drone data), techniques (e.g., maximum likelihood classification, Multiple Endmember Spectral Mixture Analysis (MESMA), reclassification, random forest, and post-classification change detection), and indices (e.g., normalized difference vegetation index) to monitor coastal wetland conditions [6,8,9,11,13–17]. Sensor and spectral vegetation index recommendations vary depending on the wetland type and the characteristics that are being assessed. Index recommendations are more dependent on the type of wetland being assessed.

Several approaches have been used to classify land cover in wetlands. One study implemented the use of fractional cover of different endmembers—spectra from pixels that are representative of a land cover, obtained by spectral mixture analysis (SMA) and MESMA [18]—in the classification of a marsh in the southern San Francisco Bay [12]. While both MESMA and SMA have challenges, MESMA was found to provide a more accurate representation of fractional cover, especially if 4- or 5-endmember models were used with more than one endmember per class [12]. Peterson et al. (2015) used MESMA on airborne visual/infra-red imaging spectrometer (AVIRIS) data to detect oil-impacted regions of coastal salt marsh in Barataria Bay, Louisiana with high accuracy of detecting oiled vs. non-oiled marshes (87.5% to 93.3%) [11]. Beland et al. (2017) used these maps and image change analysis to determine that oiling temporarily accelerated land loss in coastal marshes [8]. These studies highlight the effectiveness of MESMA as a technique for classifying wetland landcover and detecting areas affected by disturbance.

Other classification methods have also been used for tracking change. Tuxen et al. (2008) used NDVI to track vegetation colonization in Petaluma River Marsh after tidal restoration via post-classification change detection [19]. They concluded that NDVI can be used to discriminate vegetated and non-vegetated portions of marshes and is robust to human interpretations of NDVI [19]. Another study used Breaks For Seasonal and Trend (BFAST) and random forest classification on monthly NDVI products made from Landsat (5, 7, 8) and MODIS/Landsat fill-in images to perform change detection in forested wetlands with a classification accuracy of 92.96% and change detection accuracy of 87.8% [17]. Parihar et al. (2012) used maximum likelihood classification on Landsat MSS and TM data to track changes in the East Kolkata Wetlands in the absence of ground data, although the accuracy of this method was between 73.80% and 79.33% [14]. Im et al. (2008) showed that object-based land cover classification with high accuracies (>90%) can be achieved with solely using a high point density LiDAR data [20].

In this study, we use random forest classification and change detection to assess how the Montecito Debris Flows impacted landcover in Carpinteria Salt Marsh Reserve. Our main objectives were: (1) classification of marsh landcover before and after the debris flows, (2) identification of what change in landcover had occurred and possible implications,

(3) identification of important classification variables, and (4) assessment of how accurately random forest classification could map marsh landcover.

2. Materials and Methods

2.1. Event and Site Description

In December 2017, the Thomas Fire burned an area of 1140 km² in the Santa Ynez Mountains, making it the largest fire in California's history at the time [21,22]. Following the fire, the burned areas experienced an increased risk of debris flows, and, in early January 2018, a heavy rain event mobilized soils from the burn area and triggered a depositional event known as the Montecito Debris Flows [22]. The debris flows deposited approximately 680,000 m³ of sediment across urban and natural areas along the Santa Barbara Coast [22]. In addition to at least 3 fatalities, 167 injuries, and 408 damaged homes, the Carpinteria Salt Marsh Reserve, an ecological study reserve operated by the University of California, received a large deposition of sediment.

Carpinteria Salt Marsh Reserve (CSMR), located in Carpinteria, CA (34.4012° N, 119.5379° W), is situated between California Highway 101, downtown Carpinteria, and the Pacific Ocean (Figure 1). The wetland is a heterogeneous landscape made up of 93 hectares of annual and perennial herbs and grasses, transitional upland habitat, water channels, and mud flats [6]. The plant community can be split into two main categories: mid marsh, primarily dominated by *Salicornia pacifica* (formerly *Salicornia virginica*, pickleweed), and high marsh, which is a mix of *Salicornia pacifica*, *Jaumea carnosa* (marsh jaumea), *Distichlis littoralis* (shore grass), *Arthrocnemum subterminale* (Parish's glasswort), *Frankenia salina* (alkali heath), and a few other less abundant species [6,23]. Water inputs come largely from tidal inundation and from water inlets in the eastern portion of the marsh that allow for input from further inland [24].



Figure 1. Carpinteria Salt Marsh Reserve with study extent outlined. Imagery courtesy of USDA National Agriculture Inventory Program.

2.2. Data Description and Correction

The imagery used in this study is Sentinel-2 A and B data produced by the European Space Agency. The mission is composed of two multispectral satellites that collect images that cover a large spatial extent, have a fine spatial resolution (up to 10 m for half the electromagnetic bands they detect), and a five day revisit time using both sensors. Both

satellites carry optical sensors that sample in 13 spectral bands at varying spatial resolutions (Table 1) [25,26]. The high temporal resolution of the two satellites allowed us to assemble a time series for quantifying marsh change despite the variable cloud cover and inundation of CSMR which would prevent accurate image analysis. Imagery dates were selected to represent similar times of year, tide, and cloud cover. Four dates were selected to establish pre-flow, immediate, and post-flow conditions (approximately one and three years after the initial Montecito Debris Flows). Imagery from 13 November 2017 was used for pre-flow conditions as it was the date closest to the debris flow in which the marsh was not flooded or covered by clouds. Imagery from 12 January 2018 represented the immediate conditions as the data were collected three days after the flow occurred and before mechanical clean up and king tides occurred. Lastly, 3 November 2018 and 12 November 2020 imagery represented two recovery steps and were chosen to be consistent with the pre-flow November image. No November 2019 imagery was selected, as all available images were collected when there was either dense cloud cover or the marsh was inundated by high tide. All Sentinel-2 imagery was downloaded from the USGS Earth Explorer portal [27].

Table 1. Sentinel-2 band descriptions.

| Band | Resolution (m) | Central Wavelength (nm) | Bandwidth (nm) | Description |
|------|----------------|-------------------------|----------------|----------------------------------|
| B1 | 60 | 443 | 21 | Ultra blue (Coastal and Aerosol) |
| B2 | 10 | 490 | 66 | Blue |
| B3 | 10 | 560 | 36 | Green |
| B4 | 10 | 665 | 31 | Red |
| B5 | 20 | 705 | 15 | Visible and Near Infrared (VNIR) |
| B6 | 20 | 740 | 15 | Visible and Near Infrared (VNIR) |
| B7 | 20 | 783 | 20 | Visible and Near Infrared (VNIR) |
| B8 | 10 | 842 | 106 | Visible and Near Infrared (VNIR) |
| B8a | 20 | 865 | 21 | Visible and Near Infrared (VNIR) |
| B9 | 60 | 940 | 20 | Short Wave Infrared (SWIR) |
| B10 | 60 | 1375 | 31 | Short Wave Infrared (SWIR) |
| B11 | 20 | 1610 | 91 | Short Wave Infrared (SWIR) |
| B12 | 20 | 2190 | 175 | Short Wave Infrared (SWIR) |

Imagery was preprocessed in the Sentinel Application Platform (SNAP) prior to being implemented in ENVI Classic 5.5.3 [28,29]. First, the Sen2Cor SNAP add-on was used to perform atmospheric correction to obtain bottom of atmosphere L2A imagery from the top of atmosphere L1C imagery downloaded from the USGS [30]. This process produced 12 atmospherically-corrected L2A bands. Once corrected, bands 1, 9, and 10 were removed as they are primarily used for atmospheric properties and are too coarse (60 m resolution) to be used in assessment of the fine scale change in the marsh. The remaining 20 m resolution bands (bands 5, 6, 7, 8A, 11, and 12) were then resampled using pixel replication to match the 10 m resolution of bands 2, 3, 4, and 8. Resampled and native 10 m resolution bands were layer stacked for further processing in ENVI.

High density LiDAR was also used in addition to Sentinel-2 imagery to assess conditions immediately after the debris flows occurred (January 2018). The LiDAR data were collected over the areas affected by the debris flows soon after the event by the Federal Emergency Management Agency (FEMA) at a density of at least 4 points per square meter [31]. LiDAR data were corrected and processed using the BCAL add-on for ENVI [29,32]. Data were height filtered at a threshold of 30 m with a 10 m search window. Height filtered

data were then processed using last returns into a digital terrain model (DTM) with 10 m resolution to match Sentinel-2 data.

2.3. Spectral Analysis

Before classification, corrected Sentinel-2 images were processed to obtain fractional cover and to calculate the normalized difference vegetation index (NDVI) and modified anthocyanin reflectance index (mARI).

Fractional cover was obtained via MESMA using the following steps. First, two spectral libraries were generated using the November 2017 and January 2018 processed images. Endmembers were selected based on site knowledge and similarity of spectra to those that would be expected for each landcover class (November endmember spectra are shown in Figure 2). Both libraries had endmembers selected to represent four broad landcovers that are expected in the marsh: non-photosynthetic vegetation (NPV), green vegetation, bare soil, and subtidal (water). Libraries were optimized using the endmember average root mean square error (RMSE) (EAR) [33], minimum average spectral angle (MASA) [34] and count-based endmember selection (CoB) [35], or the EMC option in VIPER Tools, and included a minimum of four sample endmembers per landcover class [36]. The November library was used for the pre-debris and two recovery images. The January 2018 image had a separate spectral library for the unique conditions that were expected around the debris flow.

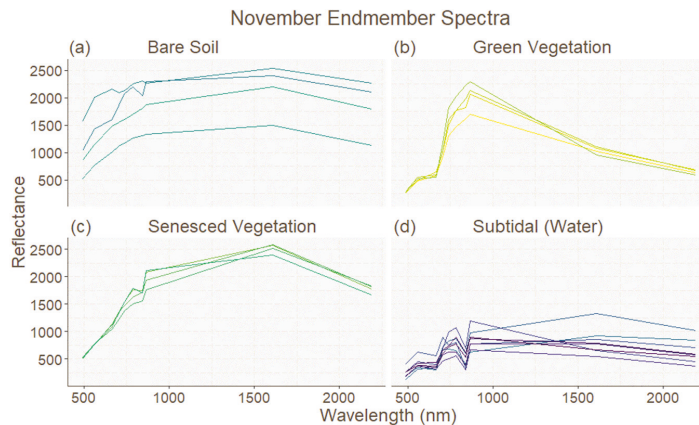


Figure 2. Spectral library for November 2017. Axes are (*x*-axis) wavelength in nm and (*y*-axis) reflectance values. Spectral signatures for (a) bare soil, (b) green vegetation, (c) non-photosynthetic vegetation (senesced), and (d) subtidal cover classes. Colors used for visual differentiation of the different endmembers.

With the libraries generated, MESMA was performed to obtain fractional cover for all four dates. Endmember models used were 2-, 3-, 4-, and 5-endmember models to ensure the inclusion of the model approaches recommended by Rosso et al. (2005) [12]. All models were constrained to fractional cover between 0.0 and 1.0, shade fraction between 0.0 and 0.8, and a maximum RMSE of 0.025. This process produced fractional cover for the four endmember classes for each date (Figure 3 for example).

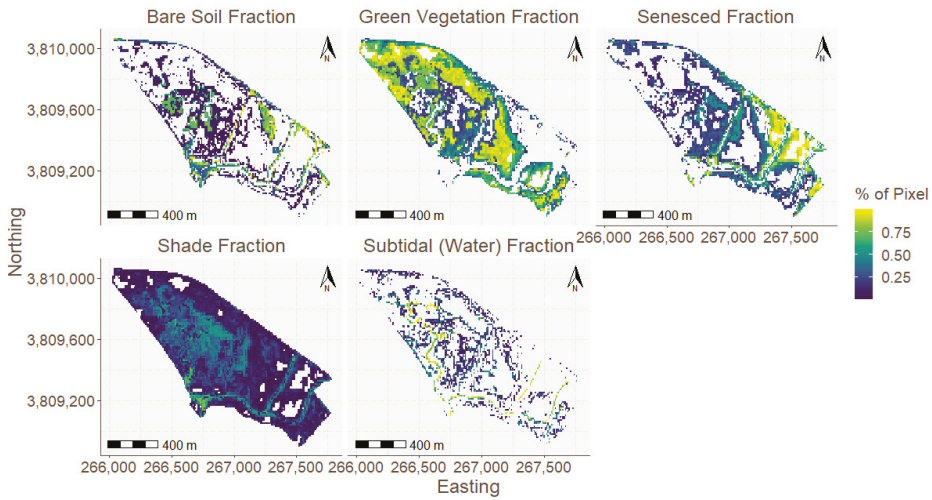


Figure 3. Fractional cover for November 2020 shown as an example of MESMA results. Scale indicates proportion of pixel that is made up of respective endmembers or shade. Pixels with a 0% cover were removed for visual clarity.

To further build on the data that would guide the classification of CSMR, two vegetation indices were calculated from the Sentinel-2 imagery: NDVI (Equation (1)) [37] and mARI (Equation (2)) [38,39].

$$\text{NDVI} = \frac{(\text{NIR} - \text{RED})}{(\text{NIR} + \text{RED})} = \frac{(\text{Band8} - \text{Band4})}{(\text{Band8} + \text{Band4})} \quad (1)$$

NDVI is one of the vegetation indices recommended in the literature for wetland analysis and was found to be one of the more important factors in classifying landcover classes in CSMR in prior work [6,9,10,19].

$$\text{mARI} = 800 \text{ nm} \cdot \left(\frac{1}{550 \text{ nm}} - \frac{1}{700 \text{ nm}} \right) = \text{Band8} \cdot \left(\frac{1}{\text{Band3}} - \frac{1}{\text{Band5}} \right), \quad (2)$$

mARI is used to detect the levels of anthocyanins, a family of red pigments that can be related to stress and senescence in plants [40]. Anthocyanin content in *Salicornia pacifica* has been found to increase in the fall and winter [41]. Therefore, mARI has the potential to further help the classification of both senesced vegetation and a dominant marsh plant in CSMR.

Once the Sentinel-2 and LiDAR products were produced, data were layer stacked prior to the creation of training data. Training data were produced for five landcover classes—bare soil, high marsh, mid marsh, senesced, and subtidal—by selecting reference polygons that matched regions of corresponding landcover from an expert map and from a report of landcover prior to the debris flow developed by Myers et al. (2017) (see Table 2) [23]. The high marsh class represents a mixed plant community of *Salicornia pacifica*, *Arthrocnemum subterminale*, *Frankenia salina*, and *Distichlis spicata*. Mid marsh represents portions of the marsh dominated by *S. pacifica*. The senesced landcover is composed of upland regions dominated by non-native shrubs and grasses [23]. Training data were collected for each date by creation of rectangular polygons in ArcGIS (Table 2 and Supplementary Materials Table S1) [42]. Training data and layer stacked images were analyzed in R [43].

Table 2. Polygon counts and decision metrics for training data generation.

| Class | Polygon Counts | | | | Metric |
|------------|----------------|--------------|---------------|---------------|--|
| | November 2017 | January 2018 | November 2018 | November 2020 | |
| Bare soil | 10 | 11 | 17 | 13 | High Bare Soil Fractions, Low NDVI, Low mARI |
| High Marsh | 5 | 5 | 10 | 7 | High Green Vegetation Fraction, High NDVI, High mARI |
| Mid Marsh | 12 | 7 | 16 | 13 | Moderate-High NDVI, Mixed Green Vegetation Fractions and Bare Soil Fractions |
| Senesced | 8 | 5 | 8 | 5 | High Non-photosynthetic Vegetation Fractions, Low NDVI, High mARI |
| Subtidal | 20 | 7 | 21 | 19 | High Subtidal Fractions, Low NDVI |

2.4. Random Forest and Change Detection

We used a random forest classifier to assign landcover class to each pixel. Random forest is a machine learning technique that automates the categorization of data by running a datapoint (e.g., a pixel) through a set number of decision trees and picking a finalized landcover class via majority vote. Pixel values were first extracted from the layer stacked images with the values and associated landcover recorded into a data frame, which was then filtered to remove variables with NA/NULL values. The data frame was then read into the random forest algorithm, with $n = 500$ decision trees. This process produced classified maps of the five landcover classes. Additional outputs include: (1) variable importance, a measure that identifies which layer stack inputs were important in the landcover classification; (2) mtry accuracy, an accuracy assessment metric of the final model; and (3) kappa values, a secondary accuracy assessment metric. Final model selection and accuracy assessment were done via k-fold cross validation. Post-classification change detection was performed in ENVI using the change detection statistics option. Dates were compared to each other in both chronological order (i.e., November 2017 to January 2018, November 2018 to November 2020) and net order (November 2017 to November 2020). Comparing the dates this way allowed us to track landcover and to obtain extent for all five classes as time progressed, thus obtaining net change for each landcover class in the system. ENVI reported change statistics in terms of pixel count, area in square meters, and percentage change. These statistics include class differences and image differences. Percentage change was recalculated using both pixel count and area and used in place of the ENVI reported percentages.

3. Results

3.1. Random Forest

Variable importance was used to determine which of the random forest inputs were most important in the landcover classification of CSMR. Variable importance was measured by the mean decrease in Gini index (Gini value), a measure in which higher values indicate higher importance in the model (Table 3) [44]. From this measure, NDVI and green vegetation fraction were the most important variables in three of the four years. NDVI and green vegetation fractions did not have the highest importance in January 2018 and November 2020, respectively. Secondary variables that also had high importance were mARI, bare soil fractions, and senesced vegetation. Recovery time steps had greater mARI importance compared to the earlier dates. Shade fractions and subtidal fractions had the lowest amount of importance in many of the dates. The bare surface model (digital elevation) was only available and used for January 2018 but had moderate importance in

the model. LiDAR was not used for other dates due to expected differences in surface from time of the debris flow to later dates. Additionally, January 2018 had the lowest values for decrease in Gini index, and this could be linked to having more variables to use and/or high solar zenith angle.

Table 3. Variable importance across dates (mean decrease in Gini index).

| Date | Soil Fraction | Green Veg Fraction | Senesced Fraction | Subtidal Fraction | Shade Fraction | NDVI | mARI | Digital Terrain |
|---------------|---------------|--------------------|-------------------|-------------------|----------------|--------|-------|-----------------|
| November 2020 | 62.24 | 58.33 | 45.79 | 31.21 | 46.56 | 109.52 | 99.69 | |
| November 2018 | 55.01 | 63.01 | 25.91 | 50.83 | 20.55 | 60.63 | 17.14 | |
| January 2018 | 31.07 | 43.72 | 41.79 | 28.53 | 8.96 | 17.28 | 4.87 | 23.17 |
| November 2017 | 40.61 | 94.05 | 60.13 | 23.08 | 34.99 | 83.23 | 21.95 | |

Final model selection was done via k-fold cross validation where models with the lowest error were selected as the final model, with accuracies being reported for each number of splits tested. The number of splits that occur at each node within a decision tree is indicated by mtry; the random forest model then selects the mtry with the highest accuracy as the final prediction. The final mtry accuracy values (mtry = 2, 8, 2, and 2 respectively, Table 4) were high for all four dates—99.5%, 93%, 95.6%, and 97.1%, respectively—with similar kappa values—99.3%, 91.1%, 94.3%, and 96.3%.

Table 4. Class error and final model accuracy across dates.

| Class | November 2017 | | January 2018 | | November 2018 | | November 2020 | |
|----------------------|---------------|------------------|--------------|------------------|---------------|------------------|---------------|------------------|
| | User's Error | Producer's Error | User's Error | Producer's Error | User's Error | Producer's Error | User's Error | Producer's Error |
| Bare Soil | 0.103 | 0.062 | 0.038 | 0.05 | 0.020 | 0 | 0.061 | 0.013 |
| High Marsh | 0 | 0 | 0.017 | 0.048 | 0 | 0 | 0.006 | 0.011 |
| Mid Marsh | 0.030 | 0.072 | 0.171 | 0.105 | 0 | 0.024 | 0.071 | 0.064 |
| Senesced Veg. | 0.019 | 0.088 | 0 | 0 | 0.018 | 0 | 0 | 0.009 |
| Subtidal/Water | 0.12 | 0.029 | 0.1 | 0.1 | 0 | 0 | 0.061 | 0.089 |
| | Accuracy | Kappa | Accuracy | Kappa | Accuracy | Kappa | Accuracy | Kappa |
| Final Model Accuracy | 0.995 | 0.993 | 0.930 | 0.911 | 0.956 | 0.943 | 0.971 | 0.963 |

Landcover class accuracy was measured via producer's and user's error and allows for the assessment of the mapping of individual landcover classes (Table 4). High marsh vegetation was most accurately mapped with low user's and producer's error across all dates. Subtidal and mid marsh had the greatest amount of user's and producer's error, especially in January 2018. Subtidal cover had the greatest confusion with mid marsh vegetation and bare soil, while mid marsh was confused with bare soil and subtidal. Error within the subtidal and mid marsh classes was below 10% for most dates, and classification for the two classes remained relatively accurate.

3.2. Post-Classification Change Detection

The random forest classifier produced four landcover maps for CSMR (Figure 4). Each map shows the extent of the five landcover classes—bare soil, high marsh, mid marsh, senesced, and subtidal—and represents different states of disturbance and recovery. The high marsh landcover had the most area in November 2017 and January 2018, and mid marsh vegetation was the largest landcover class in November 2018 and 2020 (Figures 5

and 6). Senesced vegetation and subtidal landcover experienced little change compared to bare soil, high marsh, and mid marsh vegetation (Figures 5 and 6).

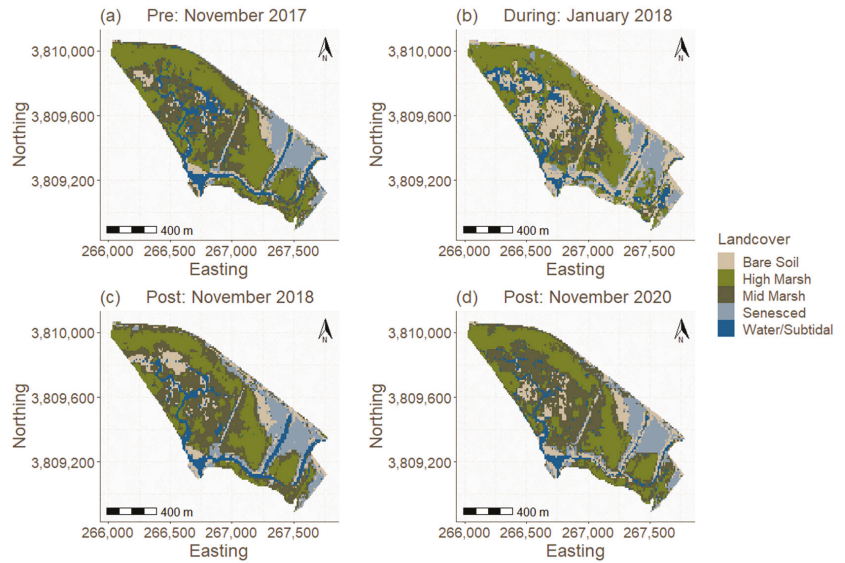


Figure 4. Maps produced by the random forest classification. Maps depict the extent of bare soil, high marsh, mid marsh, senesced vegetation, and subtidal/water landcover. Top to bottom, left to right: (a) November 2017, (b) January 2018, (c) November 2018, and (d) November 2020. (Projection: NAD 84 UTM Zone 11).

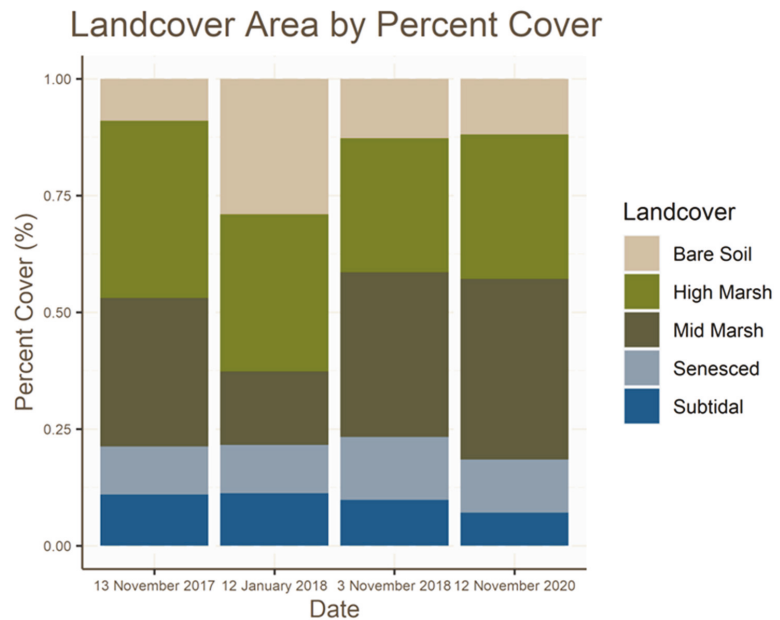


Figure 5. Percent cover for each landcover class in CSMR stacked by date.

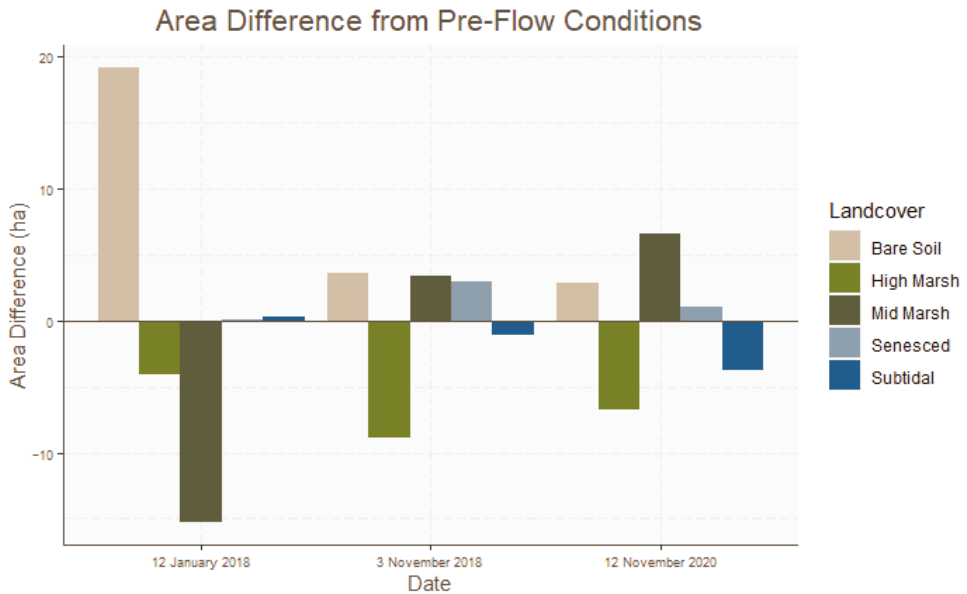


Figure 6. Difference of landcover class area (ha) compared to pre-flow conditions (November 2017). Bars are clustered by date.

The post-classification change detection showed a 19.1 ha increase in bare soil coverage between November 2017 and January 2018 (Figure 6). This amounted to 27.69 ha (~29%) of the marsh being covered in bare soil immediately following the debris flow (Figure 5). In November 2020, bare soil coverage decreased by 15.52 ha when compared to January 2018, a decrease of bare soil coverage to 12.17 ha (~16%) of total marsh area (Figure 5). Between November 2017 and November 2020, there was a 2.66 ha (~31%) net increase in bare soil coverage in the marsh (Figure 6).

On the other hand, overall marsh vegetation (high marsh + mid marsh) coverage experienced little change, with only a 0.1 ha (0.15%) net decrease in total vegetation coverage between November 2017 and November 2020 (Figure 5). However, when split into the two respective vegetation landcover classes, we find that high marsh vegetation coverage decreased as mid marsh vegetation increased (Figure 6). There were a few areas where change in landcover was prominently seen in the landscape, especially areas that were high marsh vegetation and/or near areas covered by bare soil that changed to mid marsh vegetation, such as near the salt pan in the northeast (Figure 7c) and some of the mudflat region in the western portion of the marsh (Figure 7a,b).

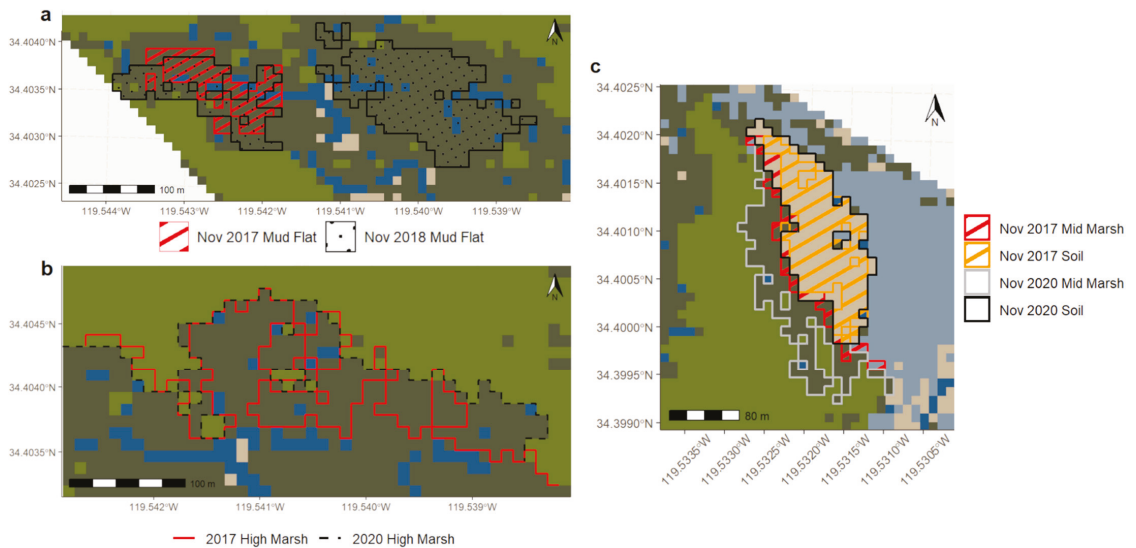


Figure 7. Maps highlighting areas where landcover change is most prominent. (a) High marsh to mid marsh conversion, (b) difference in mudflat extent, and (c) difference in salt pan (soil) and vegetated (mid marsh) perimeter. (Projection: NAD 84 UTM Zone 11, converted to lat/long).

4. Discussion

4.1. Model Accuracy

The accuracy metrics (mtry accuracy, kappa, producer's and user's error) suggested that landcover was accurately mapped by the random forest classifier and that the produced maps were reliable for use in change detection. The accuracy of the random forest classification is comparable to that of other wetland classifications. For example, Wu et al. (2020) also performed a random forest classification for a subtropical wetland that had a similar overall accuracy value of 92.96% compared to this study's average of 96.3% [17]. The model also performed as well as or better than classifications done using other methods such as maximum likelihood classification, iso-cluster unsupervised classification, or reclassification/recoding of vegetation indices [14,16,19]. The random forest classification done here was more accurate than the maximum likelihood classification done by Parihar et al. (2012), with an average accuracy of 96.3% vs. 76.5%, respectively [14]. When compared to Tuxen et al. (2007), the random forest did approximately the same or slightly better than reclassification, with reclassification having accuracy values of 81.4% and 96.3% compared to our average accuracy of 96.3% [19]. Iso-cluster classification on NDVI did somewhat better than the random forest, with accuracy values of 97.3%, 97.5%, 97.6%, and 98.0% for the respective dates [16].

High marsh had the highest accuracy, while the mid marsh class had high user's and producer's errors. As mid marsh is one of the classes that experienced the most change following the debris flow, any error present in its classification presents a problem; however, this error only exceeds 10% in January 2018 (user's: 17.1%, producer's: 10.5%) and is within acceptable margins for all other dates. Possible sources for the error include: (1) training data may have included misclassified pixels and introduced error to the corresponding landcover class, (2) pixels may have had values similar to that of multiple landcover classes, (3) resampled 20 m resolution Sentinel-2 bands may have still been too coarse to assess changes in the marsh, and (4) the use of a different spectral library for January 2018 may have led to lower accuracies for this date. To remedy this, the use of data from higher spatial resolution sensors may be useful in reducing the frequency of mixed pixels and the need for fractional cover. Additionally, higher spectral resolution may improve the building

of spectral libraries that can better differentiate between endmember classes, which then improves inputs into the random forest model.

4.2. Landcover Change and Ecological Implications

A majority of the landcover change occurred in bare soil, high marsh, and mid marsh vegetation. Bare soil area increased by 222% following the debris flows and dropped considerably in area by November 2018, likely due to the mechanical clean-up effort and king tides which removed a large amount of the sediment. Bare soil continued to decrease until there was only a net 31% increase in bare soil by November 2020. This may indicate that the marsh was still recovering from the debris flows and would continue to change over time.

Total vegetated area in the marsh showed little change over the 3 years, with only a 0.15% decrease in total marsh vegetation between November 2017 and November 2020. However, change was occurring, which is apparent when total vegetation is broken down into community types (high vs. mid marsh) and compared. High marsh (a mixed community of *Salicornia pacifica*, *Arthrocnemum subterminale*, *Frankenia salina*, and *Distichlis spicata*) area decreased by about the same amount that mid marsh (primarily only *S. pacifica*) area increased, creating the illusion of little change in vegetated area. The post-classification change detection showed that this shift from high to mid marsh community primarily occurred near areas that had been covered by bare soil following the debris flow.

The conversion to mid marsh vegetation from high marsh vegetation signifies a decrease in plant biodiversity as the community shifts from a mixed community to one that is largely composed solely of *S. pacifica*. This change in diversity poses some ecological challenges important to long-term wetland management. Studies have shown that a less diverse community is less resilient to the effects of disturbance, and spatial heterogeneity is important in the enhancement of the resilience of ecosystem functions [45]. Less resilience may dictate a need for more management intervention following disturbances, especially as the frequency of disturbances, such as wildfire, sea level rise and flooding, and landslide and mudslide damage, are predicted to increase with global climate change [7]. Studies have found that the addition of sediment via depositional events can promote plant growth by the delivery of mineral nutrients [5]. These nutrients may promote increased primary productivity by providing limiting nutrients. However, biodiversity has also been found to be positively linked to primary productivity and its temporal stability [46]. A trend of conversion from a mixed community of several plant species to one made of primarily only one plant species may have harmful repercussions for marsh productivity and other ecosystem services and functions. Determining whether this change to a less diverse community is a permanent change or only a short-term condition as the marsh recovers from the debris flow would require analysis of a longer time series of imagery over several years following the debris flows.

Sea level rise (SLR) is a challenge for the conservation of coastal wetlands, especially in developed regions, as rising sea levels contribute to coastal squeeze, leading to landcover change, fragmentation, and eventual loss of coastal marshes [47]. Sediment deposition and soil accretion are viewed as important processes for the offsetting of SLR [5,48]. However, our results imply that debris flow deposition is also leading to landcover and plant community change. While there are not clear policy implications from this work, beyond possibly assisted restoration, landcover change may become an important consideration when planning for the management of coastal wetlands that can be prone to depositional events; this study is an important example of how to inform those plans in the absence of field data.

4.3. Limitations and Challenges

As discussed above, the resolution of remotely sensed data is important in the assessment of the fine scale changes that occur in marsh ecosystems. Some Sentinel-2 bands do not have a native 10 m resolution and, therefore, have pixels that represent an average

of a larger mix of landcover types. Resampling, as conducted in this study, only splits this coarser data into smaller pixels and not into its disaggregated components. Therefore, landcover classification would benefit from a sensor where all bands have the same fine spatial resolution, such as unmanned aerial vehicles. High density LiDAR for more dates would also help in the assessment of biomass and vertical landcover differences such as water in channels vs. plants in upland regions. In addition, the baseline landcover prior to the debris flow was limited to a single date due to cloud cover, tide, and the length of historical record. Baseline assessments could be improved by using a sensor with a longer history or by using multiple dates per year. Ground reference data were also scarcely available due to the lack of prior field data to compare against classification of historical imagery and due to the COVID-19 pandemic limiting ability to go into the field to collect such data, hence the emphasis on other accuracy metrics. The results are also limited in their predictive power. For example, the rate at which sediment is being removed from the system or identification of whether the recently mapped sediment was the same sediment that had been deposited during the debris flow cannot be properly ascertained from these data. The processes leading to the conversion of high marsh to mid marsh vegetation also cannot be directly detected from these data.

5. Conclusions

Post-classification change detection tracked change in the five different landcover types in CSMR and found that mid marsh, high marsh, and bare soil landcover changed most dramatically in the dates studied. Total marsh vegetation (high marsh + mid marsh) cover returned to similar levels to those before the debris flows; however, assessing change as total marsh vegetation, as was the initial frame of the research question, does not lead to a robust conclusion. Areas that were covered in debris transitioned from high marsh vegetation to mid marsh vegetation despite total vegetated area remaining relatively unchanged. This transition has important ecological implications for marsh productivity and resilience to disturbance that continue after the debris is removed from the system.

The method used here shows promise in being applied to other depositional disturbances to wetland systems. For example, the random forest model identified important classification variables that can be used to classify marsh landcover without field-based data. The method can also serve as an important first step in the identification of regions of interest that can be used to inform field campaigns to address further questions that arise from the use of remote sensing (e.g., a field campaign to assess the factors that are leading to the transition from high marsh to mid marsh vegetation).

The Montecito Debris Flows provided a unique opportunity to study debris interactions with marshes in a context different than what is known from previous studies which more commonly focused on hurricane deposition. Data and information are an important part of making informed management decisions, and this study provides a successful demonstration of the use of post-classification change detection to assess wetland landcover response to an episodic event and the data that can be expected from such an assessment.

Supplementary Materials: The following supporting information can be downloaded at: <https://www.mdpi.com/article/10.3390/rs14122819/s1>, Table S1. Descriptive Statistics for Training Data Parameters, including min. and max. values, mean, and standard deviation for all variables used.

Author Contributions: G.D.S., D.A.R., J.P.M., and J.Y.K. contributed to study conception and design. Material preparation, data collection, and analyses were performed by G.D.S. The first draft of the manuscript was written by G.D.S., and all authors commented on previous versions of the manuscript. All authors have read and agreed to the published version of the manuscript.

Funding: This work was supported by the National Science Foundation Graduate Research Fellowship to GDS (Grant number: 2139319).

Data Availability Statement: Original Sentinel-2 data obtained from USGS Earth Explorer, available here: <https://earthexplorer.usgs.gov/> (accessed on 2 February 2021). Code and end products

generated during this study, such as layered images, classified maps, etc., available here: https://github.com/German-Sil/carpinteria_debris_thesis (accessed on 10 November 2021).

Acknowledgments: The authors would like to acknowledge a few individuals and organizations: First, Kristin Morell for providing the FEMA LiDAR data set used in the January 2018 assessment and Andy Brooks for providing helpful insight into the landscape and work being done at Carpinteria Salt Marsh Reserve. Second, Alex Feldwinn for his computer support through the duration of the pandemic. And last, but certainly not least, the National Science Foundation Graduate Research Fellowship Program for funding the graduate work of G.D.S. that this manuscript is derived from.

Conflicts of Interest: The authors declare no conflict of interest. The funder had no role in the design of the study; in the collection, analyses, or interpretation of data; in the writing of the manuscript, or in the decision to publish the results.

References

- Gibbs, J.P. Wetland Loss and Biodiversity Conservation. *Conserv. Biol.* **2000**, *14*, 314–317. [[CrossRef](#)]
- Callaway, J.C.; Borgnis, E.L.; Turner, R.E.; Milan, C.S. Carbon Sequestration and Sediment Accretion in San Francisco Bay Tidal Wetlands. *Estuaries Coast* **2012**, *35*, 1163–1181. [[CrossRef](#)]
- California Department of Fish and Wildlife. Coastal Wetlands-Emergent Marshes. California’s Living Marine Resources: A Status Report. 2001. Available online: <https://nrm.dfg.ca.gov/FileHandler.ashx?DocumentID=34250> (accessed on 16 May 2021).
- Uhrin, A.V.; Schellinger, J. Marine Debris Impacts to a Tidal Fringing-Marsh in North Carolina. *Mar. Pollut. Bull.* **2011**, *62*, 2605–2610. [[CrossRef](#)] [[PubMed](#)]
- Tweel, A.W.; Turner, R.E. Landscape-Scale Analysis of Wetland Sediment Deposition from Four Tropical Cyclone Events. *PLoS ONE* **2012**, *7*, e50528. [[CrossRef](#)] [[PubMed](#)]
- Doughty, C.L.; Cavanaugh, K.C. Mapping Coastal Wetland Biomass from High Resolution Unmanned Aerial Vehicle (UAV) Imagery. *Remote Sens.* **2019**, *11*, 540. [[CrossRef](#)]
- Erwin, K. Wetlands and Global Climate Change: The Role of Wetland Restoration in a Changing World. *Wetl. Ecol. Manag.* **2009**, *17*, 71–84. [[CrossRef](#)]
- Beland, M.; Biggs, T.; Roberts, D.; Peterson, S.; Koklay, R.; Piazza, S. Oiling Accelerates Loss of Salt Marshes, Southeastern Louisiana. *PLoS ONE* **2017**, *12*, e0181197. [[CrossRef](#)]
- Klemas, V. Remote Sensing of Coastal Wetland Biomass: An Overview. *J. Coast. Res.* **2013**, *29*, 1016–1028. [[CrossRef](#)]
- Klemas, V. Remote Sensing of Emergent and Submerged Wetlands: An Overview. *Int. J. Remote Sens.* **2013**, *34*, 6286–6320. [[CrossRef](#)]
- Peterson, S.H.; Roberts, D.A.; Beland, M.; Kokaly, R.F.; Ustin, S.L. Oil Detection in the Coastal Marshes of Louisiana Using MESMA Applied to Band Subsets of AVIRIS. *Remote Sens. Environ.* **2015**, *159*, 222–231. [[CrossRef](#)]
- Rosso, P.H.; Ustin, S.L.; Hastings, A. Mapping Marshland Vegetation of San Francisco Bay, California, Using Hyperspectral Data. *Int. J. Remote Sens.* **2005**, *26*, 5169–5191. [[CrossRef](#)]
- Eastwood, J.A.; Yates, M.G.; Thomson, A.G.; Fuller, R.M. The Reliability of Vegetation Indices for Monitoring Saltmarsh Vegetation Cover. *Int. J. Remote Sens.* **1997**, *18*, 3901–3907. [[CrossRef](#)]
- Parihar, S.M.; Sarkar, S.; Dutta, A.; Sharma, S.; Dutta, T. Characterizing Wetland Dynamics: A Post-Classification Change Detection Analysis of the East Kolkata Wetlands Using Open Source Satellite Data. *Geocarto Int.* **2013**, *28*, 273–287. [[CrossRef](#)]
- Miller, G.J.; Morris, J.T.; Wang, C. Estimating Aboveground Biomass and Its Spatial Distribution in Coastal Wetlands Utilizing Planet Multispectral Imagery. *Remote Sens.* **2019**, *11*, 2020. [[CrossRef](#)]
- Nasser Mohamed Eid, A.; Olatubara, C.O.; Ewemoje, T.A.; Farouk, H.; Talaat El-Hennawy, M. Coastal Wetland Vegetation Features and Digital Change Detection Mapping based on Remotely Sensed Imagery: El-Burullus Lake, Egypt. *Int. Soil Water Conserv. Res.* **2020**, *8*, 66–79. [[CrossRef](#)]
- Wu, L.; Li, Z.; Liu, X.; Zhu, L.; Tang, Y.; Zhang, B.; Xu, B.; Liu, M.; Meng, Y.; Liu, B. Multi-Type Forest Change Detection Using BFAST and Monthly Landsat Time Series for Monitoring Spatiotemporal Dynamics of Forests in Subtropical Wetland. *Remote Sens.* **2020**, *12*, 341. [[CrossRef](#)]
- Roberts, D.A.; Gardner, M.; Church, R.; Ustin, S.; Scheer, G.; Green, R.O. Mapping Chaparral in the Santa Monica Mountains Using Multiple Endmember Spectral Mixture Models. *Remote Sens. Environ.* **1998**, *65*, 267–279. [[CrossRef](#)]
- Tuxen, K.; Schile, L.; Kelly, M.; Siegel, S. Vegetation Colonization in a Restoring Tidal Marsh: A Remote Sensing Approach. *Restor. Ecol.* **2008**, *16*, 313–323. [[CrossRef](#)]
- Im, J.; Jensen, J.R.; Hodgson, M. Object-Based Land Cover Classification Using High-Posting-Density LiDAR Data. *GISci. Remote Sens.* **2008**, *45*, 209–228. [[CrossRef](#)]
- Andone, D. The Largest Wildfire in California’s Modern History is Finally Out, More Than 6 Months After It Started. CNN. Cable News Network. 2018. Available online: <https://www.cnn.com/2018/06/02/us/thomas-fire-officially-out/index.html> (accessed on 16 May 2021).

22. Kean, J.W.; Staley, D.M.; Lancaster, J.T.; Rengers, F.K.; Swanson, B.J.; Coe, J.A.; Hernandez, J.L.; Sigman, A.J.; Allstadt, K.E.; Lindsay, D.N. Inundation, Flow Dynamics, and Damage in the 9 January 2018 Montecito Debris-Flow Event, California, USA: Opportunities and Challenges for Post-Wildfire Risk Assessment. *Geosphere* **2019**, *15*, 1140–1163. [CrossRef]
23. Myers, M.R.; Cayan, D.R.; Iacobellis, S.F.; Melack, J.M.; Beighley, R.E.; Barnard, P.L.; Dugan, J.E.; Page, H.M. Santa Barbara Area Coastal Ecosystem Vulnerability Assessment. CASG-17-009 2017. California. Available online: <https://casegrant.ucsd.edu/sites/default/files/SBA-CEVA-final-0917.pdf> (accessed on 13 January 2021).
24. Brooks, A. (University of California, Santa Barbara, Santa Barbara, CA, USA). Personal communication, 2019.
25. Drusch, M.; Del Bello, U.; Carlier, S.; Colin, O.; Fernandez, V.; Gascon, F.; Hoersch, B.; Isola, C.; Laberinti, P.; Martimort, P.; et al. Sentinel-2: ESA's Optical High-Resolution Mission for GMES Operational Services. *Remote Sens. Environ.* **2012**, *120*, 25–36. [CrossRef]
26. European Space Agency. Overview—Sentinel Online. Available online: <https://sentinel.esa.int/web/sentinel/missions/sentinel-2/overview> (accessed on 16 May 2021).
27. U.S. Geological Survey. Earth Explorer. Geological Survey (U.S.) FS 083-00. 2000. Available online: <https://earthexplorer.usgs.gov/> (accessed on 15 November 2020).
28. SNAP—ESA Sentinel Application Platform v8.0. Available online: <https://step.esa.int> (accessed on 15 November 2020).
29. Harris Geospatial. *Exelis Visual Information Solutions*; Harris Geospatial: Boulder, CO, USA, 2013. Available online: <https://www.l3harrisgeospatial.com/> (accessed on 15 November 2020).
30. Main-Knorr, M.; Pflug, B.; Louis, J.; Debaecker, V.; Müller-Wilm, U.; Gascon, F. Sen2Cor for Sentinel-2. *Proc. SPIE* **2017**, *10427*, 1042704. [CrossRef]
31. Federal Emergency Management Agency. *Montecito Debris Flow LiDAR*; Federal Emergency Management Agency: San Francisco, CA, USA, 2018.
32. Streutker, D.R.; Glenn, N.F. LiDAR Measurement of Sagebrush Steppe Vegetation Heights. *Remote Sens. Environ.* **2006**, *102*, 135–145. [CrossRef]
33. Dennison, P.E.; Roberts, D.A. Endmember Selection for Multiple Endmember Spectral Mixture Analysis using Endmember Average RSME. *Remote Sens. Environ.* **2003**, *87*, 123–135. [CrossRef]
34. Dennison, P.E.; Halligan, K.Q.; Roberts, D.A. A Comparison of Error Metrics and Constraints for Multiple Endmember Spectral Mixture Analysis and Spectral Angle Mapper. *Remote Sens. Environ.* **2004**, *93*, 359–367. [CrossRef]
35. Roberts, D.A.; Dennison, P.E.; Gardner, M.; Hetzel, Y.; Ustin, S.L.; Lee, C. Evaluation of the Potential of Hyperion for Fire Danger Assessment by Comparison to the Airborne Visible/Infrared Imaging Spectrometer. *IEEE Trans. Geosci. Remote Sens.* **2003**, *41*, 1297–1310. [CrossRef]
36. Roberts, D.; Halligan, K.; Dennison, P.; Dudley, K.; Somers, B.; Crabbé, A. VIPER Tools. 2019. Available online: <https://drive.google.com/drive/folders/0B0zkcpjAaSqFbUVacVJCSURtSzQ> (accessed on 15 November 2020).
37. Rouse, J.W.; Haas, H.R.; Deering, D.W.; Schell, J.A.; Harlan, J.C. *Monitoring the Vernal Advancement and Retrogradation (Green Wave Effect) of Natural Vegetation*; NASA/GSFC Type III Final Rep.; The Goddard Space Flight Center: Greenbelt, MD, USA, 1974; 371p.
38. Gitelson, A.A.; Keydan, G.P.; Merzlyak, M.N. Three-Band Model for Noninvasive Estimation of Chlorophyll Carotenoids and Anthocyanin Contents in Higher Plant Leaves. *Geophys. Res. Lett.* **2006**, *33*, L11402. [CrossRef]
39. Gitelson, A.A.; Chivkunova, O.B.; Merzlyak, M.N. Non-Destructive Estimation of Anthocyanins and Chlorophylls in Anthocyanic Leaves. *Am. J. Bot.* **2009**, *96*, 1861–1868. [CrossRef] [PubMed]
40. Gitelson, A.A.; Merzlyak, M.N.; Chivkunova, O.B. Optical Properties and Nondestructive Estimation of Anthocyanin Content in Plant Leaves. *Photochem. Photobiol.* **2001**, *74*, 38–45. [CrossRef]
41. Farrens, G. Color Change and Succulence in *Salicornia pacifica*. Master's Thesis, San Jose State University, San Jose, CA, USA, 1971.
42. Environmental Systems Research Institute. *ArcGIS. Version 10.7.1*; Environmental Systems Research Institute, Inc.: Redlands, CA, USA, 2019.
43. R Core Team. R: A Language and Environment for Statistical Computing; R Foundation for Statistical Computing, Vienna, Austria. 2019. Available online: <https://www.R-project.org/> (accessed on 15 November 2020).
44. Lee, C. Feature Importance Measures for Tree Models—Part 1. 2017. Available online: <https://medium.com/the-artificial-impostor/feature-importance-measures-for-tree-models-part-i-47f187c1a2c3> (accessed on 11 December 2020).
45. Oliver, T.H.; Heard, M.S.; Issac, N.J.B.; Roy, D.B.; Procter, D.; Eigenbrod, F.; Freckleton, R.; Hector, A.; Orme, C.D.L.; Petchey, O.L. Biodiversity and Resilience of Ecosystem Functions. *Trends Ecol. Evol.* **2015**, *30*, 673–684. [CrossRef]
46. Oehri, J.; Schmid, B.; Schaepman-Strub, G.; Niklaus, P.A. Biodiversity Promotes Primary Productivity and Growing Season Lengthening at the Landscape Scale. *Proc. Natl. Acad. Sci. USA* **2017**, *114*, 10160–10165. [CrossRef] [PubMed]
47. Torio, D.D.; Chmura, G.L. Assessing Coastal Squeeze of Tidal Wetlands. *J. Coast. Res.* **2013**, *29*, 1049–1061. [CrossRef]
48. Rosencranz, J.A.; Ganju, N.K.; Ambrose, R.F.; Brosnahan, S.M.; Dickhudt, P.J.; Guntenspergen, G.R.; MacDonald, G.M.; Takekawa, J.Y.; Thorne, K.M. Balanced Sediment Fluxes in Southern California's Mediterranean-Climate Zone Salt Marshes. *Estuaries Coast* **2016**, *39*, 1035–1049. [CrossRef]



Article

Comparing the Use of Red-Edge and Near-Infrared Wavelength Ranges for Detecting Submerged Kelp Canopy

Brian Timmer^{1,*}, Luba Y. Reshitnyk², Margot Hessing-Lewis², Francis Juanes³ and Maycira Costa¹

¹ Spectral Lab, University of Victoria, 3800 Finnerty Road, Victoria, BC V8P 5C2, Canada; maycira@uvic.ca

² Hakai Institute, Heriot Bay, BC VOP 1H0, Canada; luba.reshitnyk@hakai.org (L.Y.R.); margot@hakai.org (M.H.-L.)

³ Department of Biology, University of Victoria, 3800 Finnerty Road, Victoria, BC V8P 5C2, Canada; juanes@uvic.ca

* Correspondence: brianzimmer@uvic.ca

Abstract: Kelp forests are commonly classified within remote sensing imagery by contrasting the high reflectance in the near-infrared spectral region of kelp canopy floating at the surface with the low reflectance in the same spectral region of water. However, kelp canopy is often submerged below the surface of the water, making it important to understand the effects of kelp submersion on the above-water reflectance of kelp, and the depth to which kelp can be detected, in order to reduce uncertainties around the kelp canopy area when mapping kelp. Here, we characterized changes to the above-water spectra of *Nereocystis luetkeana* (Bull kelp) as different canopy structures (bulb and blades) were submerged in water from the surface to 100 cm in 10 cm increments, while collecting above-water hyperspectral measurements with a spectroradiometer (325–1075 nm). The hyperspectral data were simulated into the multispectral bandwidths of the WorldView-3 satellite and the Micasense RedEdge-MX unoccupied aerial vehicle sensors and vegetation indices were calculated to compare detection limits of kelp with a focus on differences between red edge and near infrared indices. For kelp on the surface, near-infrared reflectance was higher than red-edge reflectance. Once submerged, the kelp spectra showed two narrow reflectance peaks in the red-edge and near-infrared wavelength ranges, and the red-edge peak was consistently higher than the near-infrared peak. As a result, kelp was detected deeper with vegetation indices calculated with a red-edge band versus those calculated with a near infrared band. Our results show that using red-edge bands increased detection of submerged kelp canopy, which may be beneficial for estimating kelp surface-canopy area and biomass.

Keywords: kelp; hyperspectral; multispectral; red-edge; near-infrared; satellite; unoccupied aerial vehicle; remote sensing

Citation: Timmer, B.; Reshitnyk, L.Y.; Hessing-Lewis, M.; Juanes, F.; Costa, M. Comparing the Use of Red-Edge and Near-Infrared Wavelength Ranges for Detecting Submerged Kelp Canopy. *Remote Sens.* **2022**, *14*, 2241. <https://doi.org/10.3390/rs14092241>

Academic Editors: Simona Niculescu, Junshi Xia and Dar Roberts

Received: 11 March 2022

Accepted: 5 May 2022

Published: 7 May 2022

Publisher's Note: MDPI stays neutral with regard to jurisdictional claims in published maps and institutional affiliations.



Copyright: © 2022 by the authors. Licensee MDPI, Basel, Switzerland. This article is an open access article distributed under the terms and conditions of the Creative Commons Attribution (CC BY) license (<https://creativecommons.org/licenses/by/4.0/>).

1. Introduction

Kelp forests are highly productive three-dimensional coastal marine habitats [1,2] that provide a number of environmental services and contribute substantial economic value to coastal communities globally [3]. In the northeast Pacific, the two dominant surface-canopy forming kelp species, *Nereocystis luetkeana* and *Macrocystis pyrifera* [4], stabilize shorelines via wave dampening [5,6], support economically important fisheries [7,8], and are commercially harvested for various purposes [9,10]. However, both kelp species are subject to high spatial and temporal variability, correlated with biotic and abiotic drivers of change [11,12]. As such, resource managers are incentivized to monitor the status of these kelp forests, and the corollary effects of the ecosystem services they provide [10,12,13], a task that has been facilitated by remote sensing since the mid-20th century [12,14].

Generally, the remote sensing of surface-canopy forming kelp forests aims to detect the portion of the kelp that forms a canopy, floating at the water's surface; using sensors

aboard Earth Observation Satellites (EOS) [15,16], piloted aircraft [10,12], and Uncrewed Aerial Vehicles (UAVs) [17]. In order to use the data provided by remote sensing platforms effectively, it is crucial to understand factors that influence the spectral signature of kelp canopy in water [16]. Floating kelp canopy has high reflectance in the near-infrared wavelength range (NIR) (700–1000 nm), which contrasts with the high NIR absorption by the surrounding water, allowing for binary classification of floating kelp canopy and water within an image [14]. However, there are numerous considerations (e.g., sun glint, bathymetry, turbidity; see [13,16]) that can reduce the separability between the spectral values of kelp canopy and water. One crucial factor that can affect the ability to detect kelp canopy is the submersion of the canopy by tides and associated tidal currents, which can dampen the NIR reflectance of kelp and lead to potential errors when estimating kelp area or biomass [17,18].

In an attempt to minimize classification errors associated with kelp submergence, remote sensing imagery is often acquired at low tides during the peak growing season (mid-late summer) when the majority of the kelp canopy is floating at the water's surface [10,18,19]. However, there are multiple reasons why a remote sensor may also want to detect the submerged portion of the kelp canopy. For example, the northeast Pacific coastline often experiences non-ideal weather conditions for remote sensing data acquisition, leading to imagery being opportunistically collected at higher than ideal tidal heights when more kelp canopy is more likely to be submerged compared to ideal low tide conditions [13,16]. Further, the fixed rate of EOS orbits may result in some regions only having imagery available during high tides even if acquisition conditions are otherwise ideal [13]. Even if remote sensing imagery is captured during ideal tide and weather conditions, portions of kelp canopy may also be continuously submerged depending on the species being targeted. Specifically, if a remote sensor is targeting detection of *Nereocystis luetkeana* (hereafter, *Nereocystis*) surface canopy, one has to consider the two distinct structures with varying buoyancy, the bulb and blades. The bulb is a roughly cylindrical gas-filled structure that floats on the surface of the water and is anchored to the sea floor by a stipe and holdfast [9]. The blades are long thin structures that trail from the end of the bulb, often with many individuals around four meters long per bulb [9]. The blades are not buoyant and are likely to remain submerged below the water's surface regardless of tidal height [16,20]. In addition, floating portions of kelp canopy may be periodically submerged in areas with especially strong currents [20]. Therefore, it is important to understand how submersion of kelp canopy affects the reflectance in the NIR range, as well as whether certain spectral features may allow for higher detectability of kelp when collecting remote sensing imagery from different platforms.

In the past, the red-edge (RE) spectral region (670–750 nm), which includes a range of the shortest NIR wavelengths, has traditionally been used to determine health characteristics of terrestrial plants [21]. However, these wavelength ranges also penetrate deeper into the water column than longer NIR wavelength ranges [22], resulting in the potential for higher above water reflectance in the RE than the longer NIR for submerged vegetation [23–26]. Therefore, given the spectral similarities between kelps and other types of vegetation, it is reasonable to assume that the RE wavelength range may also be beneficial for detecting submerged kelp canopy. Hereafter, the term NIR will refer to only the longer wavelength range above 751 nm, to avoid confusion with the NIR wavelength range that overlaps the RE wavelength range.

To date, there have been no direct comparisons of the ability to detect submerged kelp when using RE or NIR wavelength ranges. Additionally, while the submersion kelp canopy due to tides and currents is well documented using various sensors with different spatial and spectral resolutions [11,17–20,27], there has been no characterization of the changes to the above water spectra of kelp as the canopy is submerged, nor any investigation of the band combinations used in vegetation indices in relationship to accurate detection of the submerged kelp canopy. With this in mind, our goal was to characterize changes to above-water reflectance of different *Nereocystis* canopy structures as they were submerged and to

relate those changes to depth detection limits. To accomplish this goal, we performed (1) an experiment that documents the effects of kelp submersion on the above-water hyperspectral reflectance of both *Nereocystis* bulb and blade structures. We also compared (2) the detection limits of submerged kelp using RE and NIR vegetation indices, which were calculated from the simulated multispectral bands of high spatial-resolution air- and space-borne sensors.

2. Materials and Methods

2.1. Spectral Data Acquisition and Processing

The kelp submergence experiment took place on a marina dock in Victoria BC, on a sunny, cloudless day in September 2020. The Secchi depth during the time of the experiment was 7.5 m, showing relatively clear water, similar to general conditions for the coastal waters of the Salish Sea at the same time of year with low influence from riverine discharge, and low levels of total suspended-matter, chlorophyll-a, and colored dissolved organic matter present in the water column [28]. While the ranges of both *Nereocystis* and *Macrocystis* overlap on the British Columbia coast, only *Nereocystis* is found around the southern tip of Vancouver Island where this study occurred. The location and timing of the experiment allowed for the control of four criteria that we required: (1) controlled sea-state; with the dock acting as a shelter from any slight breezes, thereby minimizing variability in glint or light refraction due to ripples or waves on the water [29]; (2) platform stability, which minimized the potential errors during spectral acquisition due to the movement of both kelp and sensor that might occur in situ from a boat; (3) maintained environmental conditions expected in situ during peak biomass for local kelp, such as the inherent optical properties of water and optical constituents within the water column that would be difficult to reproduce in vitro; (4) a water depth (12 m) greater than the Secchi depth to minimize the influence of substrate reflectance on the above-water reflectance signal [30,31].

The experiment consisted of four separate trials. For each trial, a sample of *Nereocystis* was attached to a black frame made of high-density polyethylene (a plastic with low reflectance across the visual and near-infrared wavelength ranges), which was submerged from the surface to 100 cm in 10 cm increments on the sunlit side of the dock (Figure 1). Before each trial, radiance measurement of a Spectralon white-reference panel ($L_{\text{spec}}(\lambda)$) and an internal dark-current reading were taken to calculate reflectance (Table 1; Equation (1)) and reduce noise in the spectral data [32]. During each trial, ten individual above-water hyperspectral radiance measurements ($L_T(\lambda)$) of kelp were collected at each incremental depth. Two of the four trials used the *Nereocystis* bulb, and two trials used the *Nereocystis* blades. Therefore, in total, 20 measurements of $L_T(\lambda)$ were collected for each kelp structure (bulb or blades) at each depth. After each trial, 10 radiance measurements were taken of the sky ($L_{\text{sky}}(\lambda)$) to be used in sky glint corrections [33]. Additionally, a total of 60 $L_T(\lambda)$ measurements were taken of water with no kelp within the field of view as a baseline for comparison with submerged kelp.

Table 1. Spectral parameters used to calculate above-water reflectance, as per Equation (1). All spectral measurements were collected using a calibrated ASD Fieldspec Handheld2 spectroradiometer with a one-degree fore optic (full viewing-angle), which detects a wavelength range from 325–1075 nm at 1 nm increments.

| Symbol | Name | Units | Angle from Nadir | Sun-Sensor Azimuthal Angle |
|-------------------|------------------------|---|------------------|----------------------------|
| λ | Wavelength | nm | - | - |
| L_T | Above-water radiance | $\mu\text{W cm}^{-2}\text{sr}^{-1}\text{nm}^{-1}$ | 5° | 135° |
| L_{spec} | White panel radiance | $\mu\text{W cm}^{-2}\text{sr}^{-1}\text{nm}^{-1}$ | 5° | 135° |
| L_{sky} | Sky radiance | $\mu\text{W cm}^{-2}\text{sr}^{-1}\text{nm}^{-1}$ | 175° | 135° |
| ρ' | Proportionality factor | - | - | - |

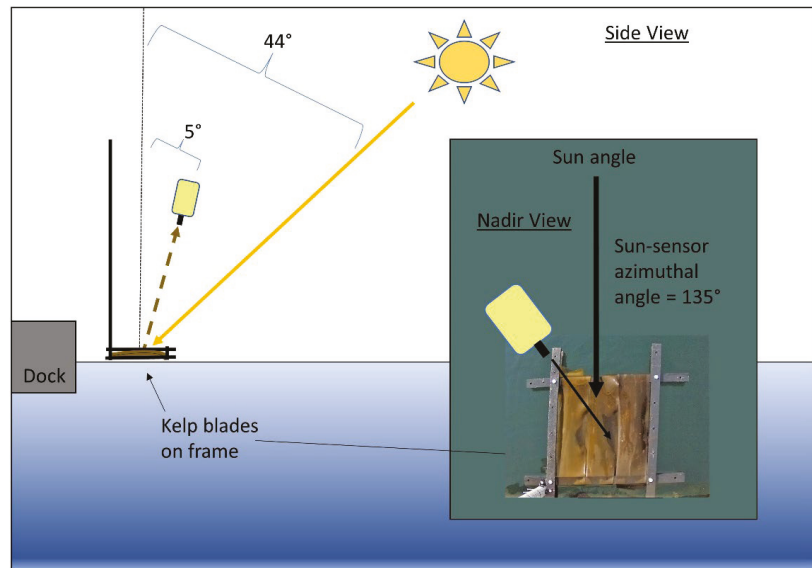


Figure 1. Side view of submergence experiment showing the geometry of acquisition for spectroradiometer and angle of zenith for the sun. Inset shows nadir view of the experiment with the azimuthal angle between spectroradiometer and sun and kelp blades inside the black frame. Diagrams are not to scale.

The solar elevation angle during the experiment was 46°, which ensured sun-glint did not contaminate the spectra based on our geometry of acquisition [33,34]. $L_T(\lambda)$ measurements were taken at 5° from a nadir viewing angle to avoid reflection of the white spectroradiometer in the field of view on the water surface, and a sensor-sun azimuthal angle of 135° was used to minimize specular reflection in the field of view (FOV) [33]. $L_{sky}(\lambda)$ measurements were taken at 5° from zenith at the same azimuthal angle as $L_T(\lambda)$. The spectroradiometer was held one meter above water, giving a footprint ranging from about 1.6 cm at the surface to 3.8 cm when the target was 100 cm deep. This small footprint was meant to ensure that the $L_T(\lambda)$ measurements contained 100% kelp, avoiding mixed pixel considerations [35].

$$R(\lambda)_{0+}(\%) = \left(\frac{L_T(\lambda)}{L_{spec}(\lambda)} - \frac{(\rho' \cdot L_{sky}(\lambda))}{L_{spec}(\lambda)} \right) \times 100 \quad (1)$$

Here, ρ' was the proportionality factor of 0.0211, which relates the radiance measured directly from the sky to the estimated amount of sky radiance reflected off the sea surface based on wind, cloud cover, and geometry of acquisition [33]. $R(\lambda)_{0+}(\%)$ for kelp at the surface (0 cm) was not subjected to the sky glint correction. Hereafter, $R(\lambda)_{0+}(\%)$ values for kelp on the surface, submerged kelp, and water with no kelp are referred to as R_{0+} for brevity.

The R_{0+} spectra were first smoothed using a mean filter with a window of 5 nm to reduce noise while maintaining spectral features, and all spectra were then manually inspected for quality control. All bulb spectra were highly consistent, however, some blade spectra showed deviations in both the blue-green and NIR regions; likely due to water movement between blades as kelp was submerged, causing opened gaps in the “canopy” of blades attached to the platform. These spectra likely did not contain 100% blades within the field of view and were therefore removed from further analysis (Table 2). Despite the

removal of some blade spectra, the smallest sample size at any depth after quality control was at 90 cm with $n = 10$ spectral samples. Therefore, we do not expect that these removals biased the results of this study.

Table 2. Total number of each class of spectra before and after quality control was performed.

| Spectral Sample Type | Samples Collected | Samples Removed during Quality Control | Samples Used in Analysis |
|-------------------------|-------------------|--|--------------------------|
| Bulbs (surface-100 cm) | 220 | 0 | 220 |
| Blades (surface-100 cm) | 220 | 51 | 169 |
| Water | 60 | 0 | 60 |
| Sky | 40 | 0 | 40 |

2.2. Simulation of Micasense and WorldView Band R_{0+} and Indices

After sky-glint correction, smoothing, and quality control of the spectra, R_{0+} measurements were simulated into bands of the WorldView-3 (R_{0+WV3}) and the Micasense RedEdge-MX (R_{0+MSRE}) sensors [36,37]. These sensors were chosen because both have a relatively high spatial resolution (WV3: 1.84 m; MSRE: ~1–10 cm), which is ideal for mapping kelp canopy in nearshore regions where it is likely to be submerged by tides and currents [16]. The R_{0+} at the bands of these sensors were simulated using Gaussian functions to estimate the sensor's spectral response for each band, based on full-width half maximum values of each sensor's band (Figure 2; Table 3). For a direct comparison, only the VNIR bands shared by both sensors were used for simulations.

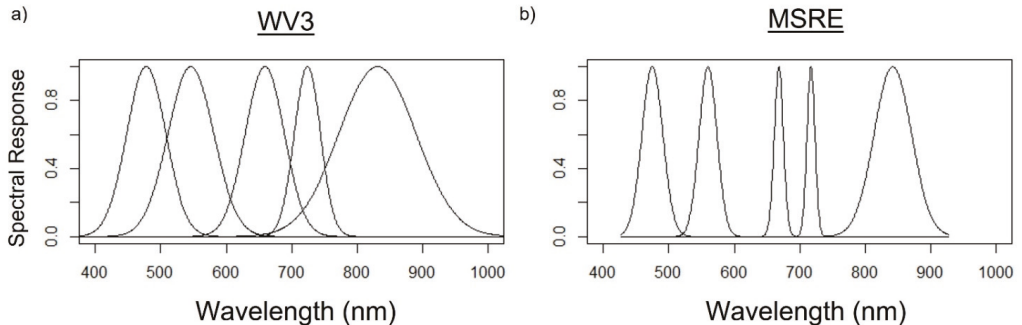


Figure 2. Relative spectral responses at each band according to Gaussian functions were used to simulate the shared bands of (a) WorldView-3 (WV-3) earth observation satellite and (b) Micasense RedEdge-MX (MSRE) uncrewed aerial vehicle sensors—from left to right: blue, green, red, red-edge, and near-infrared band locations are shown.

Table 3. The effective bandwidths of the overlapping bands for both WorldView-3 (WV3) and Micasense RedEdge-MX (MSRE) sensors.

| Band | WV3 | MSRE |
|---------------|------------|----------------|
| Blue | 445–517 nm | 459–491 nm |
| Green | 507–586 nm | 546.5–573.5 nm |
| Red | 626–696 nm | 661–675 nm |
| Red-edge | 698–749 nm | 711–723 nm |
| Near-infrared | 765–899 nm | 813.5–870.5 nm |

2.3. Normalized Vegetation Indices

Once the hyperspectral data were simulated into the respective sensor bands, the R_{0+} at these bands were used to calculate normalized vegetation indices (VI_n ; Equation (2)), which are commonly used to enhance spectral features of interest and reduce sensitivity to environmental influences within remote sensing imagery [38,39]. We tested several band combinations for VI_n as different band combinations may increase or decrease the separability between kelp and water in an image [40].

$$VI_n = \frac{\text{band 2} - \text{band 1}}{\text{band 2} + \text{band 1}} \quad (2)$$

Because naming conventions for different VI_n combinations are not ubiquitous across published literature, here, we referred to each VI_n as the order in which bands appeared in the numerator of the VI_n equation, separated by an underscore (Table 4).

Table 4. Vegetation indices calculated from simulated multispectral data.

| Vegetation Index (VI_n) | VI_n Equation |
|-----------------------------|-----------------------------------|
| RE_R | RE−red |
| RE_G | RE+red RE−green |
| RE_B | RE+green RE−blue |
| NIR_R | RE+blue NIR−red |
| NIR_G | NIR+red NIR−green |
| NIR_B | NIR+green NIR−blue NIR+blue |

One of the most commonly used VI_n for kelp mapping is NIR_R, which was originally used to detect terrestrial vegetation because of the high NIR and low red signal [38], but has since been used for kelp canopy detection due to the similar spectral characteristics between kelp canopy and terrestrial vegetation [14]. More recently, NIR_R has been positively correlated with both the areal extent and biomass of kelp canopy [15,18,19]. However, various other combinations of visible and NIR bands have been used for kelp canopy detection with multispectral sensors. For instance, Schroeder et al. (2019b) used NIR_R and NIR_G for kelp detection with the WorldView-2 imagery. The NIR_G combination may be more accurate for detecting a wide range of chlorophyll levels [41] and has generally been found comparable with NIR_R in the detection of both floating and submerged vegetation [26]. Stekoll et al. (2006) found that NIR_B and NIR_G both provided higher kelp canopy and water separability in aerial imagery than NIR_R. Further, recent comparisons with multi-spectral UAV and satellite imagery have shown that RE indices can improve separability of *Macrocystis* canopy and water when compared with NIR based indices [17,42], although this improvement was not specifically attributed to improved detection of submerged portions of the kelp canopy in either study.

Here, we compared the statistical differences in NIR and RE-based VI_n values. R_{0+MSRE} and R_{0+WV3} bands were used to calculate NIR_B, NIR_G, NIR_R, and RE_B, RE_G, and RE_R for both bulb and blades separately, for each depth. The statistical analysis was comprised of (i) VI_n values compared with one another at each depth from the surface to 100 cm, and (ii) VI_n values for water (with no kelp) compared to one another. First, the dataset was tested for normality, and while quantile–quantile plots suggested reasonable normality of the data distributions, Levene’s test showed nearly all groupings for comparison displayed heterogeneity in variance. Therefore a non-parametric test was used in the analysis [43]. The Welch’s ANOVA test was used to determine whether significant differences between VI_n existed at each depth, and the Games–Howell post hoc test was used to determine which indices were significantly different from one another [44,45]. As part of the analysis, we focused on the statistical results comparing the RE and NIR counterpart indices only (e.g., NIR_R & RE_R, or NIR_B & RE_B) at each depth.

2.4. Threshold Selection and Depth Limits for Kelp Detection

Once a VI_n has been selected for classifying kelp in remote sensing imagery, a VI_n value is then chosen as a threshold to classify the kelp and water within the imagery. For example, Cavanaugh et al. (2010) selected a threshold based on the 99.98th percentile highest NIR_R value from a histogram of known ‘deep water’ pixels, and Nijland et al. (2019) determined a NIR_R value of 0.05 to be a reasonable threshold by comparing pixel values of sparse kelp and open water. Since the R_{0+} values of water vary spatially and temporally according to optical constituents and inherent optical properties of water, as well as the characteristics of local substrate and bathymetry [28,46,47], these thresholds are often ‘dynamic’, and are therefore determined on an image-by-image basis. For satellite or airborne imagery covering a large regional scale, it may even be appropriate to select multiple thresholds across different regions within an image.

We determined a dynamic threshold for each VI_n based on the maximum VI_n value measured for water during the experiment following Cavanaugh et al. (2010). The depth where the mean VI_n value of submerged kelp dropped below the dynamic threshold value was considered the depth where kelp was spectrally indistinguishable from water. Since our experiment was conducted under ideal conditions (flat calm water, full sun, etc.) the dynamic thresholds were all negative values and the maximum depth of detection using these thresholds likely overstate the potential depths for kelp detection in actual remote sensing imagery. Therefore, we also used a second VI_n threshold of zero, based on the theoretical spectral properties of kelp within an individual pixel that contains 100% kelp. For example, within a pixel, if the R_{0+} value of band 2 (RE or NIR) equals the R_{0+} value as band 1 (the visible band), the numerator in the VI_n equation (Equation (2)), and therefore the overall VI_n value for that pixel, equals zero. This conservative threshold is closer to the values of 0.05 and 0.003 determined from remote sensing imagery by Nijland et al. (2019) and Mora-Soto et al. (2020), respectively.

Depth detection limits were reported to the nearest 10 cm depth on the shallow side of the threshold because the kelp was submerged in 10 cm intervals. To determine whether the detectable kelp (values above the threshold) and non-detectable kelp (values below the threshold) were statistically separable, the means for kelp measurements immediately above and below the threshold were compared for significant differences using Welch’s *t*-test [48].

3. Results

Here, we present the spectral characteristics of *Nereocystis* bulbs and blades as they are each submerged from the surface to 100 cm, as well as the changes seen in the hyperspectral data when they are simulated into multispectral sensor bandwidths. Next, we show VI_n comparisons for kelp, focusing on comparing the RE and NIR counterpart indices (e.g., NIR_R & RE_R, or NIR_B & RE_B) at each depth, and finally, we present the depth detection limits for each VI_n as determined by both dynamic and conservative thresholds.

3.1. Spectral Characteristics of Surface and Submerged Kelp

Overall, the R_{0+} of both *Nereocystis* bulbs and blades showed similar placement of spectral features, however, the magnitude of reflectance at these features was different (Figure 3a,b). For *Nereocystis*, spectral features in the visible wavelength ranges are largely due to absorption by a combination of chlorophyll-a, chlorophyll-c, and fucoxanthin pigments, which are characteristic pigments of bull kelp, as well as other kelp species [49,50]. Accordingly, here we saw a broad absorption feature in the 400–550 nm range and narrower absorption features around 633 and 675 nm for both bulbs and blades at the surface. These absorption features resulted in reflectance peaks at 575, 600, and 645 nm for both bulbs and blades (Figure 3a,b, insets). In the NIR region, broad reflectance peaks were detected from 690 nm (RE) to 900 nm (NIR) (Figure 3a,b, insets) and small, narrow peaks centered at 761 nm were observed (Figure 4a,b).

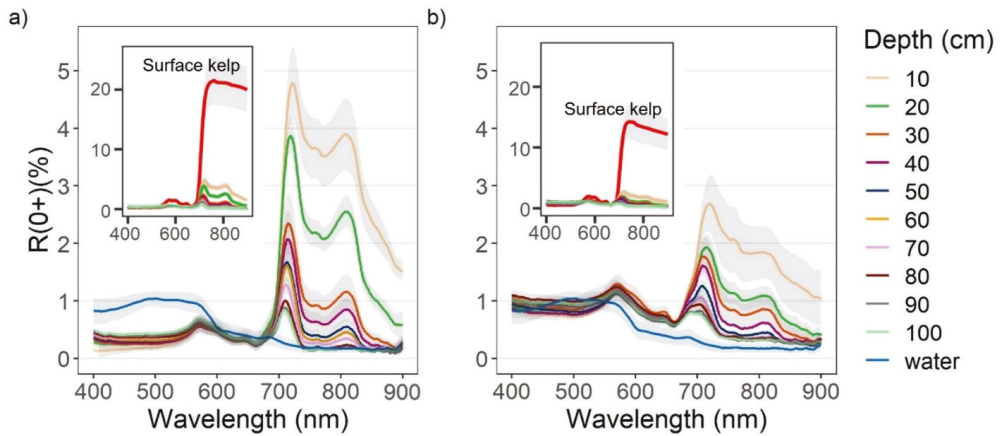


Figure 3. Reflectance values (R_{0+}) between 400–900 nm (mean \pm sd) of water with (a) *Nereocystis* bulbs, and (b) *Nereocystis* blades, at incremental depths below water surface. The inset plots contain spectra of bulbs and blades on the surface compared to the same spectra of submerged bulb and blades as in the main plots, for the purpose of showing the difference in magnitude.

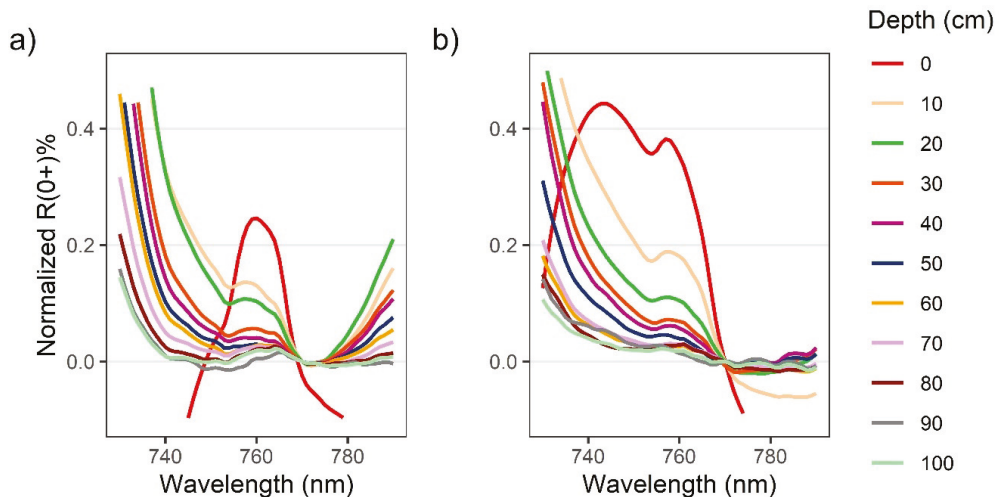


Figure 4. Zoomed in plot showing solar-induced chlorophyll fluorescence (SICF) peaks centered at 761 nm for above-water R_{0+} for *Nereocystis* bulbs (a) and blades (b) at incremental depths below the water surface. Spectra are normalized at 770 nm to show relative changes to the shape of the SICF peak with submergence.

When kelp structures were submerged, the influence of the water and its constituents on the R_{0+} signal increased with submersion for both bulb and blades. The decreases in R_{0+} in the RE and NIR region were far greater than decreases in R_{0+} observed across the visible region of the spectra (Figure 3a,b, insets). With initial submersion below the water's surface, the largest declines in the visible wavelength ranges were seen at 600 nm and 645 nm, although all peaks in the visible region continued to decrease with submersion (Figure 3a,b). While the R_{0+} at the absorption feature between 400–550 nm initially decreased with submersion, the reflectance then rose as the depth of submersion increased. In the NIR region of spectra for both structures, once kelp was submerged, the broad NIR peaks were

replaced by two peaks centered around 715 nm and 815 nm (Figure 3a,b), hereafter referred to as the RE peak and the NIR peak, respectively. At each depth, the R_{0+} at the RE peak was higher than the NIR peak. As submergence increased, the position of the RE peak shifted toward lower wavelengths within the RE wavelength ranges while the position of the NIR peaks remained relatively stable. The small peaks at 761 nm remained stable, but decreased in magnitude with submersion, becoming difficult to visibly distinguish around 50 cm depth (Figure 4a,b).

R_{0+WV} and R_{0+MSRE} showed the same general patterns as the hyperspectral data (Figure 5a–d). However, some spectral information was lost with the reduction of spectral resolution, such as the location and magnitude of different peaks. Overall, the differences in width and placement of bands resulted in only small differences in R_{0+WV3} and R_{0+MSRE} band values (Figure A1a,b). For both bulbs and blades at the surface, differences in the visible wavelength ranges between R_{0+WV} and R_{0+MSRE} were less than 0.8% for the red, blue, and green bands, and these differences became even smaller as kelp was submerged. In the RE and NIR bands, differences between R_{0+WV} and R_{0+MSRE} were less than 0.3% on the surface. Once submerged to 10 cm, differences between R_{0+WV} and R_{0+MSRE} increased to 1.8% in the NIR bands and 0.5% in the RE bands, although similar to the visible bands, the differences between R_{0+WV} and R_{0+MSRE} also became smaller as the kelp was submerged deeper.

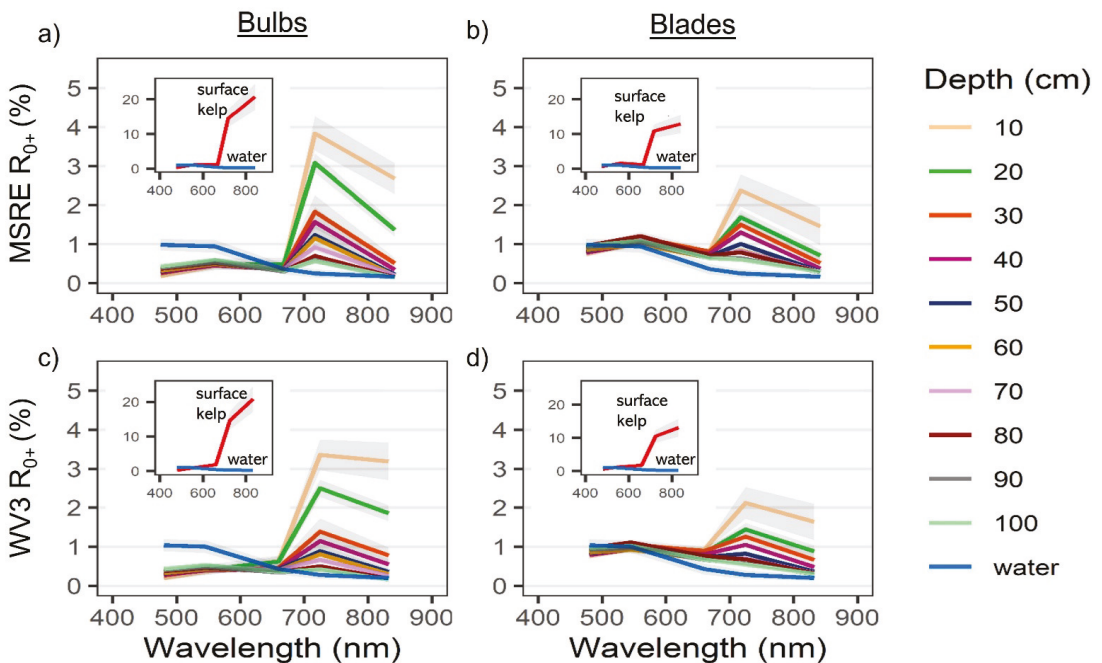


Figure 5. Reflectance values (R_{0+}) for bulbs (a,c) and blades (b,d) of simulated bands (mean \pm sd) shared by the Micasense RedEdge-MX (MSRE; a,b) and WorldView-3 (WV3; c,d), derived from the hyperspectral data (Figure 3) using Gaussian response functions (Figure 2).

3.2. Vegetation Indices: Signal Strength and Depth-Detection Limits of Submerged Kelp

Generally, RE VI_n values were higher than NIR VI_n values at a given depth as kelp was submerged (Figure 6). For bulbs, RE VI_n values decreased linearly from the surface to 100 cm, while NIR VI_n showed a steeper linear decrease over the first 50 cm, followed by an inflection point and a lesser decline towards 100 cm. For blades, trendlines of both NIR

and RE VI_n resemble exponential functions, with the NIR VI_n displaying a steeper decrease of values than the RE VI_n .

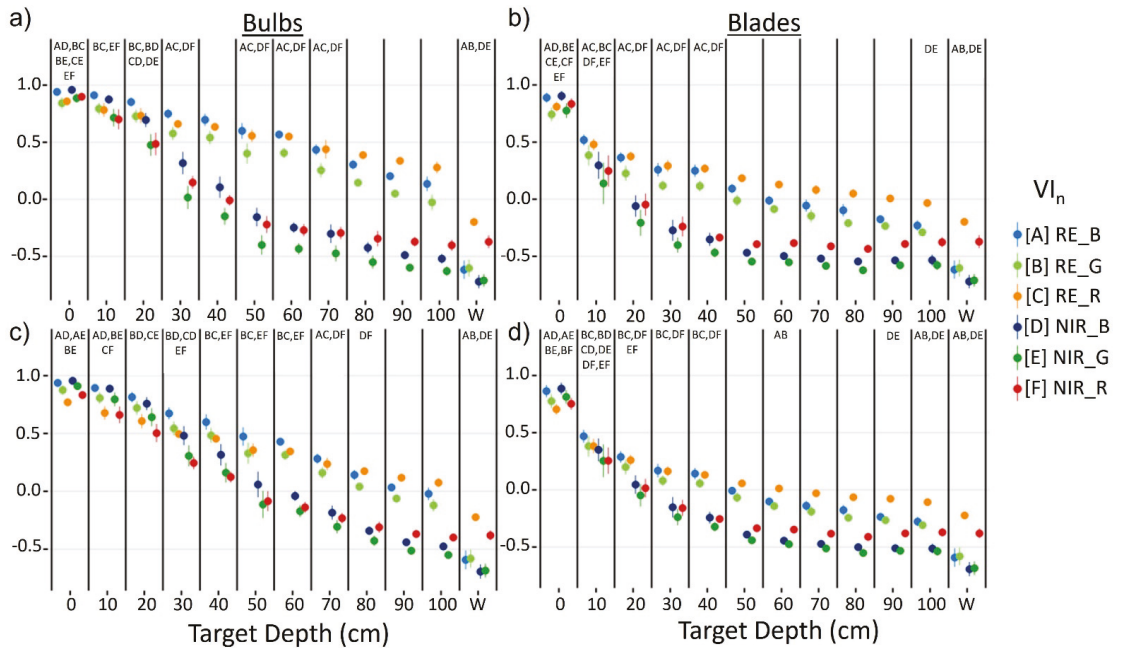


Figure 6. Mean \pm sd of vegetation index (VI_n) values for Nereocystis bulbs (a,c) and blades (b,d), submerged from the surface to 100 cm and water; derived from simulated Micasense RedEdge-MX (MSRE; a,b) and WorldView-3 (WV3; c,d) bandwidths. Paired letters above each column represent no significant differences ($p \geq 0.05$) between mean index values at that depth.

Specifically, the Games–Howell post hoc tests showed that for kelp at the surface, RE VI_n values were either smaller than or not significantly different from their counterpart NIR indices (Figure 6), depending on the visible band used. Once kelp was submerged, RE VI_n values were significantly greater than their NIR counterparts at each depth with the MSRE sensor. However, with the WV3 sensor, RE VI_n values were not significantly greater than their NIR counterparts until 10 cm and 20 cm depth for blades and bulbs, respectively. All VI_n values for water were negative, meaning that the R_{0+} at the visible band used in the VI_n was higher than the R_{0+} at the RE or NIR band used in the VI_n , regardless of sensor simulation or index combination. RE_R consistently showed the highest values for water, followed by NIR_R, and there were no significant differences between RE_B and RE_G water values, nor for NIR_B and NIR_G water values. Here, we focused on the statistical results comparing the RE and NIR counterpart indices only (e.g., NIR_R & RE_R, or NIR_B & RE_B) at each depth, however, Figure 6 displays paired letters to indicate all pairs of VI_n where no significant difference between VI_n pairs was detected.

The depth detection limits varied based on sensor type, kelp structure, and thresholding method (Table 5; Figure 7). Overall, when using the conservative (more realistic) threshold of zero, RE VI_n showed detection of kelp at least twice as deep as NIR VI_n , and bulbs were detectable at greater depths than blades. Detection limits for the same VI_n between sensors were generally within a range of 0–20 cm apart, although in a few cases (e.g., RE_R) these differences were larger. In addition, the choice of different visible bands for a VI_n only resulted in detection limit differences up to 20 cm, with RE_R once again proving the exception. No RE indices crossed below the dynamic thresholds at 100 cm

depth, meaning RE indices could detect kelp to at least 100 cm depth with these thresholds, while NIR indices could generally detect kelp to around 100 cm depth or less. In all cases, the RE indices at 100 cm depth were more separable from water than the NIR indices at the same depth. The use of different visible bands in the VI_n combination generally resulted in detection limit differences of 0–30 cm for bulbs. For all measured depth detection limits, the index values measured at the increments 10 cm above and below the threshold remained divergent ($p < 0.05$), suggesting that all the measured results for conservative and dynamic thresholds are accurate to at least 10 cm increments.

Table 5. Depth detection limits (cm) based on conservative threshold of 0.0 and the dynamic thresholds (maximum water value) for Nereocystis bulbs and blades, as simulated to Micasense RedEdge-MX (MSRE) and WorldView-3 (WV3) bandwidths.

| Index | | RE_B | RE_G | RE_R | NIR_B | NIR_G | NIR_R | |
|-------|-------|--------------------|------|------|-------|-------|-------|----|
| MSRE | Bulb | Conservative (0.0) | >100 | 90 | >100 | 40 | 30 | 30 |
| | | Dynamic (max.) | >100 | >100 | >100 | >100 | 90 | 50 |
| | Blade | Conservative (0.0) | 50 | 40 | 90 | 10 | 10 | 10 |
| | | Dynamic (max.) | >100 | >100 | >100 | >100 | >100 | 30 |
| WV3 | Bulb | Conservative (0.0) | 90 | 80 | 100 | 50 | 40 | 40 |
| | | Dynamic (max.) | >100 | >100 | >100 | >100 | >100 | 80 |
| | Blade | Conservative (0.0) | 40 | 40 | 60 | 20 | 10 | 20 |
| | | Dynamic (max.) | >100 | >100 | >100 | >100 | >100 | 40 |

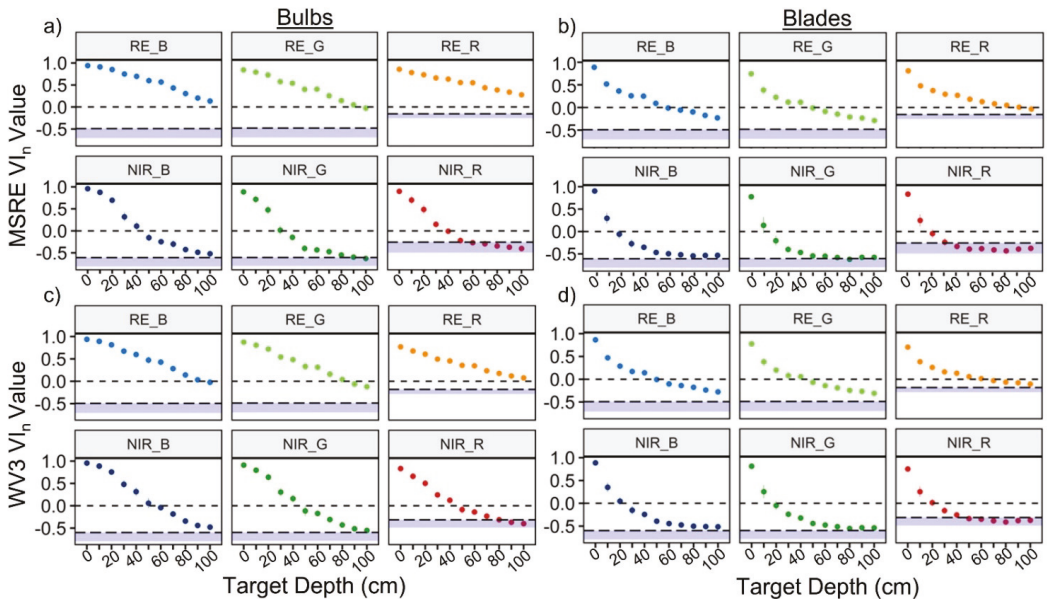


Figure 7. Mean \pm sd of vegetation index (VI_n) values for Nereocystis bulbs (a,c) and blades (b,d) submerged from the surface to 100 cm. derived from simulated Micasense RedEdge-MX (MSRE; a,b) and WorldView-3 (WV3; c,d) bandwidths. The black dashed lines at 0 represent the more conservative and realistic threshold, and the blue bars represent the full range of water values for each respective index, with the adjacent dashed lines representing the dynamic threshold.

4. Discussion

Overall, we found that submersion of kelp in water changes the shape and magnitude of R_{0+} in the RE and NIR region of kelp spectra (Figure 3), and *Nereocystis* bulbs had a higher magnitude R_{0+} in the RE and NIR region than blades (Figure 3). We also observed that RE VI_n values for submerged kelp had higher separability from water than their NIR counterparts (Figure 6), meaning that kelp can be positively classified at deeper depths when using an RE VI_n (Table 3; Figure 7). Our results also showed that VI_n that used a visible band with high R_{0+} (e.g., green or blue) had worse detectability for submerged kelp than a VI_n that used a visible band with low R_{0+} (e.g., red). Together, these findings have important implications for the application of kelp remote sensing to the applied monitoring of kelp forests.

4.1. Spectral Characteristics of Kelp as It Is Submerged

A broad R_{0+} peak across the NIR region was observed for surface measurements of *Nereocystis* as a result of the interaction of light with the cellular structure of the kelp [51]. Once submerged, our experiment showed two key changes in the NIR region of the kelp spectra (Figure 3), both due to characteristic absorption features of water: (1) the splitting of the single broad NIR peak into two narrower RE and NIR peaks due to prominent water absorption feature at 760 nm [52] and (2) higher R_{0+} at the RE peak versus the NIR peak, resulting from the continually increasing absorption of light by water above 600 nm [22]. Since *Macrocystis* and *Nereocystis* are spectrally similar to one another in the NIR region [15,18,27,50], and the changes seen in the spectra of submerged kelp are due to properties of water absorption, we expect that the spectral results of this experiment are generally applicable to both *Macrocystis* and *Nereocystis* canopies, making these findings relevant for surface-canopy forming kelp species globally.

The results of these experiments were generally in line with our expectations according to similar studies of submerged aquatic vegetation [24,25], although there were some interesting phenomena seen in the spectra that are worth noting. In the visible region of the spectra, R_{0+} in the red wavelength range decreased with depth, as expected. However, the R_{0+} at the absorption feature between 400 and 550 nm increased slightly with submersion. We hypothesize that this increase in R_{0+} is due to the scattering of light by the conditions of the water optical constituents, thus increasing the R_{0+} with depth. As such, we suspect that this increase in R_{0+} may be specific to the water conditions during the experiment and may not have occurred if the water had contained more optical constituents that absorb blue light, such as colored dissolved organic matter. Another interesting phenomenon noted in the floating kelp spectra was what appeared to be a sunlight-induced chlorophyll fluorescence (SICF) peak at 761 nm (Figure 4). Within the NIR region, photosynthetic organisms generally have a broad SICF peak centered at 740 nm [53]. However, due to the high magnitude of the NIR reflectance, the SICF is usually only visible as a small, narrow peak centered at 761 nm. Typically, the R_{0+} within the NIR wavelength range overwhelms the signal from SICF, however, atmospheric gasses highly absorb incoming irradiance at 761 nm, which can create a fill-in effect by the SICF in this region [53]. While this phenomenon has been correlated with photosynthetic output and general health of terrestrial vegetation and phytoplankton [53,54], we are not aware of any publications that report an SICF peak in kelp spectra, and this may present an opportunity for future hyperspectral research. Once kelp was submerged the SICF feature was dampened, and therefore future research should take note of the amount of kelp at the surface if attempting to derive information from an SICF peak.

4.2. NIR Differences between *Nereocystis* Bulbs and Blades

The magnitude of reflectance across the NIR region in vegetation is generally due to the cellular structure of the respective tissues [55]. Both *Nereocystis* bulb and blade tissues are composed of the same three cellular layers: the meristoderm, the medulla, and the cortex. The meristoderm is a thin chloroplast-packed epidermal layer that surrounds the entire

individual [56], and the medulla is a complex web of filaments that acts as a transportation system within the kelp, composing the innermost layer of kelp tissue [57,58]. Between these two layers is the cortex, which connects the meristoderm to the medulla, and generally provides structural support for the kelp [56,59]. Given this structural arrangement, we speculate that the NIR signal from bulbs is consistently higher compared to the blades' signal because (1) the bulb cortex is many times thicker than the blade cortex [57,59]; and (2) the gas cavity of the bulb is lined by the medulla [57], creating a high surface area with many large refractive differences—similar to the mesophyll layer of a terrestrial leaf [55,60]. In comparison, the blade medulla is housed in a gelatinous extracellular matrix between cells [57], and with no gas cavities, the refractive differences are much smaller, allowing for increased transmittance of NIR light through the blades [55]. For our experiment, spectral measurements for blades were taken using a single blade wrapped around the polyethylene frame with only slight overlap between the edges of the blade. However, *Nereocystis* individuals may have between 30–60 blades each. Overall, a thicker mass of blade tissues due to high overlap may result in higher R_{0+} in the RE and NIR wavelength ranges than seen in this experiment.

4.3. The Implications of VI_n Saturation for Detection of Floating and Submerged Kelp

When the density or biomass of the vegetation increases within a pixel of remote sensing imagery, the VI_n for that pixel will asymptotically approach a saturation (i.e., a high VI_n value) [39,61]. This happens because when vegetation is dense, the R_{0+} at band 2 (NIR or RE) is large relative to the R_{0+} at band 1 (the visible band). Our spectral measurements contained 100% kelp within the field of view, and accordingly, the VI_n values calculated from the multispectral simulations were saturated when kelp was at the surface. Therefore, it is critical to understand how saturation affected the VI_n values of floating kelp, as well as when kelp was submerged. For example, our WV3 simulations for bulbs at the surface showed that the R_{0+} at NIR and RE bands were large compared to the red band (21%, 14%, and 1%, respectively). As such, both NIR_R and RE_R indices for bulbs at the surface were approaching saturation (0.83 and 0.77 respectively) and either index would perform relatively well for detecting floating kelp if a VI_n of zero was used as a threshold to classify kelp and water. When the bulb was submerged, the R_{0+} in the NIR and RE bands decreased rapidly by 10 cm depth (3.2 and 3.4% respectively) but were still relatively high compared to the red band, which had also decreased (0.6%), and therefore the NIR_R and RE_R values (0.66 and 0.68 respectively) were still relatively saturated, despite the large decreases in R_{0+} at the RE and NIR bands (Figure 5). As the kelp continued to be submerged, the R_{0+} at the NIR, RE, and red bands all continued to decrease, however, the R_{0+} at the NIR band decreased at a faster rate and therefore the NIR_R value dropped below the threshold of zero by 50 cm while the RE_R value was still above the threshold by 100 cm. Ultimately, this example shows that due to VI_n saturation, the choice of RE or NIR will make little to no difference in classification of kelp at or near the surface. However, once submerged, the use of an RE VI_n will still detect kelp deeper than an NIR VI_n .

4.4. Depth Detection Limits and Separability between Kelp and Water

While it is important to understand how VI_n values change as kelp is submerged, ultimately the accuracy of submerged kelp classification depends on the spectral separability between the submerged kelp and water. Here, we defined the depth at which kelp and water were no longer separable as the depth at where VI_n values for submerged kelp decreased below the threshold value. RE VI_n values for kelp and water had higher separability at deeper depths than their NIR counterparts (Figure 6), meaning that deeper kelp can be accurately classified when using an RE VI_n . Higher separability between kelp and water classes when using RE VI_n has been documented using both high spatial-resolution multispectral UAV imagery [13] and with moderate spatial-resolution multispectral satellite imagery of *Macrocystis* [42], indicating that slight submergence of kelp surface-canopy may play a larger role in detection than previously thought.

While the choice between RE and NIR VI_n was an important factor in submerged kelp detection, the choice of the visible band can also shift the detection limits of submerged kelp. Our results show that both the water and submerged kelp spectra had higher R_{0+} in the green and blue wavelength ranges than in the red, and as such, submerged kelp became undetectable at shallower depths when using NIR_R compared to NIR_G or NIR_B. In the visible wavelength ranges, red is absorbed fastest by the water column, and in our experiment, the NIR signal is generally absorbed by around 50 cm depth, making it reasonable for this pairing to consistently have the shallowest detection limits for submerged kelp. At depths where the RE or NIR signal of kelp can no longer be detected, Figure 7 shows that subtle differences between kelp and water in the blue and green bands can still result in the kelp signal remaining above the dynamic threshold. However, these differences are small, and because conditions during the experiment were controlled, the added spectral noise from in situ environmental factors would likely complicate the detection of both surface and submerged kelp in more realistic situations. For example, the blue wavelength ranges can be highly compromised in remote sensing imagery [29,46], with local variation in atmospheric composition reducing the certainty of accuracy for blue band values. Additionally, the optical constituents of coastal water can be highly spatiotemporally variable—affecting all regions of the spectra [28,46]. At high concentrations phytoplankton in the water column may result in changes to reflectance in the visible wavelength ranges as well as high RE or NIR reflectance [62], while changes to optical constituents such as sediment or CDOM may also impede the detection of submerged kelp [47,63].

In this experiment, the optical water conditions (Secchi = 7.5) were typical of the coastal waters of British Columbia [18,28,64]. Considering the Secchi measurement, the local depth (12 m), and the R_{0+} from water with no kelp (Figure 3), the bottom substrate signal was not part of the measured R_{0+} in our experiment. Yet kelp on the coast of British Columbia is often found as fringing canopies near the shoreline [18], which can result in a strong contribution of benthic substrate to the R_{0+} measured by space and air-borne platforms. Reflectance from shallow benthic features can result in highly variable R_{0+} in both the visible and near-infrared wavelength ranges, resulting in misclassification of submerged vegetation as canopy kelp [47,64]. Therefore, it is important to understand site characteristics (e.g., bathymetry and water turbidity) to define better the use of NIR or RE for kelp classification. For instance, if enough understanding of the local conditions at the time of imagery acquisition is not available, it may be more appropriate to use NIR_R to reduce the addition of signal of the bottom substrate. Alternately, if imagery or associated ground truth data have a high enough spatial resolution (e.g., from UAV or other aerial platforms), visual interpretation of surface-canopy morphology from expert knowledge may be adequate for manual classification or ground truthing when using an RE VI_n .

4.5. Implications for Mixed Pixels

During the experiment, spectral data were collected using a small footprint to reduce uncertainties associated with having the reflectance signal of multiple targets within the field of view (i.e., mixed pixels). However, remote sensing imagery often contains mixed pixels [16,35]. This becomes especially problematic when sensors have a lower spatial resolution, where erroneous classification of a pixel as kelp may result in the overestimation of total kelp canopy. Multiple end-member spectral mixture analysis (MESMA) is an approach that has been applied to satellite imagery for both *Macrocystis* [11,35] and *Nereocystis* canopy [19,65] to determine what proportion of the pixel is kelp, and what proportion is water. When MESMA is applied to remote sensing imagery for kelp detection, it is assumed that all VI_n or band values within a pixel are a linear combination of kelp and water end-members [35]. However, if the kelp fraction within a pixel is low enough, the spectral contribution from water may overwhelm the kelp signal, lowering the overall pixel value and allowing the pixel to be erroneously classified as water [19,27]. Our results suggest that if submerged kelp is present when MESMA is performed, which is most often the case, the

reduced signal from the submerged kelp within the pixel may lead to an underestimation of the kelp fraction within the pixel. Using an RE VI_n when performing MESMA may allow the user to detect more submerged kelp, thus contributing to a higher overall pixel value and increasing the accuracy of the classification. This may be especially relevant if attempting to determine relationships between remote sensing imagery and biomass, since *Nereocystis* blades show a higher correlation to the mass of the individual than any other metric tested [10]. Further, *Nereocystis* canopy generally has less dense biomass at the surface than *Macrocystis* [65,66], and, therefore, is more likely to be misclassified in moderate or low spatial resolution imagery.

5. Conclusions

Our experiment contributes new, detailed information on the effects of kelp submersion on the above water reflectance, as well as a comparison of the depth detection limits of kelp when using red-edge and near-infrared indices. We determined that the near-infrared region of kelp spectra is strongly absorbed upon submersion, however, there is a narrow spectral peak in the red-edge region that can be used to enhance the remote sensor's ability to detect submerged kelp due to lower water absorption. Detection limits varied based on kelp tissue, the thresholding method, and the visible band used in the vegetation index calculation, but overall, red-edge vegetation indices detected deeper than their counterpart NIR indices, which may allow the remote sensor to improve accuracy when mapping sparse and partially submerged kelp canopy or attempting to derive biomass from canopy reflectance values. Kelp forests may be mapped using remote sensing for various reasons, ranging from estimation of biomass for kelp harvesting to multi-year temporal analyses to assess the impacts of environmental drivers on kelp ecosystems. Yet kelp systems can be highly variable in abundance between years, and our study shows that the spectral variables used to detect kelp canopy in remote sensing imagery play an important role in the amount of submerged kelp canopy detected. Therefore, it is critical for a remote sensing user to understand how the physical interaction between light and water may affect the depth at which kelp can be detected. For example, RE VI_n might be especially useful if resource managers are attempting to set quotas for harvestable biomass of *Nereocystis* and wish to detect as much blade biomass as possible for specific beds. However, if one wishes to reduce detection of subsurface kelp canopy or other shallow benthic vegetation, we recommend the use of the NIR_R (NDVI), which consistently had the shallowest detection limits of the indices tested.

Author Contributions: B.T., M.C. and L.Y.R. designed the study. B.T. and L.Y.R. carried out the experiment. B.T. conducted the analysis and wrote the manuscript with input and guidance from M.C., L.Y.R., F.J. and M.H.-L. All authors have read and agreed to the published version of the manuscript.

Funding: During this research BT was supported through a MITACS Accelerate internship with the Hakai Institute, as well as an NSERC CGS-M award and Costa's NSERC-DG.

Institutional Review Board Statement: Not applicable.

Informed Consent Statement: Not applicable.

Data Availability Statement: Data are available for research purposes upon request to the authors' institutions.

Acknowledgments: We thank the Hakai Institute and the Canada NSERC-DG for providing funding for this research as well as Robert Atwood for letting us use his slip at the Oak Bay marina to test this experiment. Also, thank you to Lianna Gendall for helping with the kelp in the graphical abstract.

Conflicts of Interest: The authors declare no conflict of interest.

Appendix A

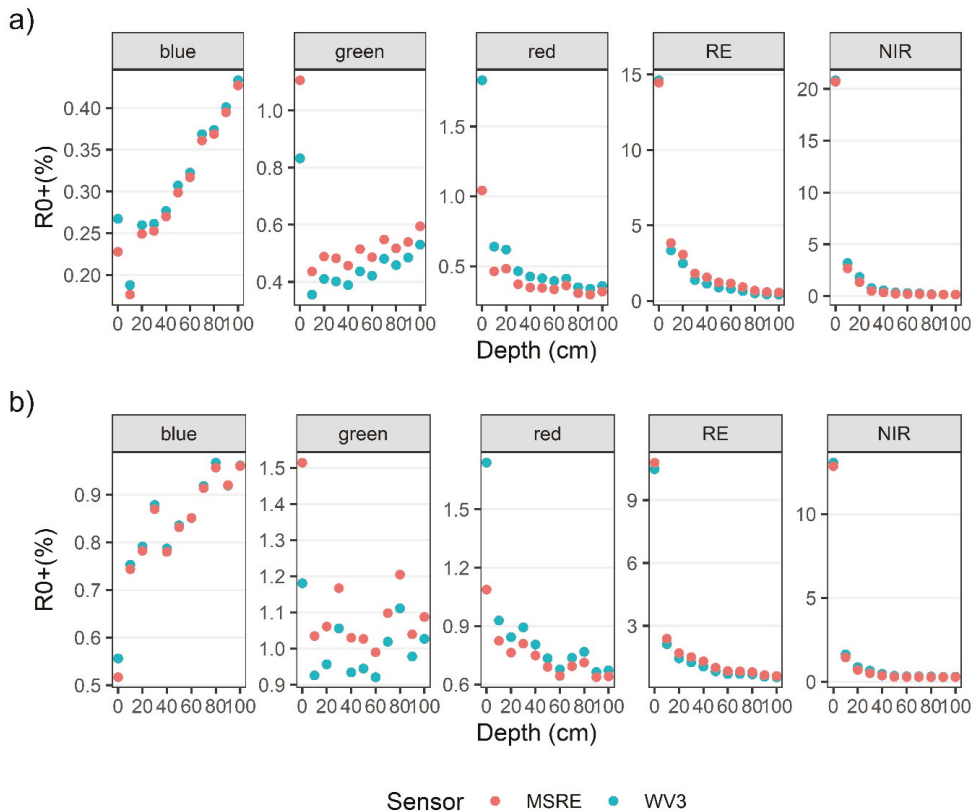


Figure A1. Differences between R_{0+} values of each shared band of the Micasense RedEdge-MX (MSRE) and WorldView-3 sensors, as simulated from the bulb (a) and blade (b) spectral measurements.

References

1. Druehl, L.D.; Wheeler, W.N. Population Biology of *Macrocystis Integrifolia* from British Columbia, Canada. *Mar. Biol.* **1986**, *90*, 173–179. [[CrossRef](#)]
2. Kain, J.M. Patterns of Relative Growth in *Nereocystis Luetkeana* (Phaeophyta). *J. Phycol.* **1987**, *23*, 181–187. [[CrossRef](#)]
3. Krumhansl, K.A.; Okamoto, D.K.; Rassweiler, A.; Novak, M.; Bolton, J.J.; Cavanaugh, K.C.; Connell, S.D.; Johnson, C.R.; Konar, B.; Ling, S.D.; et al. Global Patterns of Kelp Forest Change over the Past Half-Century. *Proc. Natl. Acad. Sci. USA* **2016**, *113*, 13785–13790. [[CrossRef](#)] [[PubMed](#)]
4. Druehl, L.D. The Pattern of Laminariales Distribution in the Northeast Pacific. *Phycologia* **1970**, *9*, 237–247. [[CrossRef](#)]
5. Jackson, G.A. Internal Wave Attenuation by Coastal Kelp Stands. *J. Phys. Oceanogr.* **1984**, *14*, 1300–1306. [[CrossRef](#)]
6. Mork, M. The Effect of Kelp in Wave Damping. *Sarsia* **1996**, *80*, 323–327. [[CrossRef](#)]
7. Krumhansl, K.A.; Scheibling, R. Production and Fate of Kelp Detritus. *Mar. Ecol. Prog. Ser.* **2012**, *467*, 281–302. [[CrossRef](#)]
8. Olson, A.M.; Hessing-Lewis, M.; Haggarty, D.; Juanes, F. Nearshore Seascape Connectivity Enhances Seagrass Meadow Nursery Function. *Ecol. Appl.* **2019**, *29*, e01897. [[CrossRef](#)]
9. Springer, Y.; Hays, C.; Carr, M.H.; Mackey, M. *Ecology and Management of the Bull Kelp, Nereocystis Luetkeana: A Synthesis with Recommendations for Future Research*; Lenfest Ocean Program: Washington, DC, USA, 2007; pp. 1–53.
10. Stekoll, M.S.; Deysher, L.E.; Hess, M. A Remote Sensing Approach to Estimating Harvestable Kelp Biomass. *J. Appl. Phycol.* **2006**, *18*, 323–334. [[CrossRef](#)]
11. Bell, T.W.; Allen, J.G.; Cavanaugh, K.C.; Siegel, D.A. Three Decades of Variability in California's Giant Kelp Forests from the Landsat Satellites. *Remote Sens. Environ.* **2020**, *238*, 110811. [[CrossRef](#)]

12. Pfister, C.A.; Berry, H.D.; Mumford, T. The Dynamics of Kelp Forests in the Northeast Pacific Ocean and the Relationship with Environmental Drivers. *J. Ecol.* **2017**, *106*, 1520–1533. [CrossRef]
13. Cavanaugh, K.C.; Bell, T.; Costa, M.; Eddy, N.E.; Gendall, L.; Gleason, M.G.; Hessing-Lewis, M.; Martone, R.; McPherson, M.; Pontier, O.; et al. A Review of the Opportunities and Challenges for Using Remote Sensing for Management of Surface-Canopy Forming Kelps. *Front. Mar. Sci.* **2021**, *8*, 1536. [CrossRef]
14. Jensen, J.R. Remote Sensing Techniques for Kelp Surveys. *Photogramm. Eng. Remote Sens.* **1980**, *46*, 743–755.
15. Cavanaugh, K.; Siegel, D.; Kinlan, B.; Reed, D. Scaling Giant Kelp Field Measurements to Regional Scales Using Satellite Observations. *Mar. Ecol. Prog. Ser.* **2010**, *403*, 13–27. [CrossRef]
16. Schroeder, S.B.; Dupont, C.; Boyer, L.; Juanes, F.; Costa, M. Passive Remote Sensing Technology for Mapping Bull Kelp (*Nereocystis Luetkeana*): A Review of Techniques and Regional Case Study. *Glob. Ecol. Conserv.* **2019**, *19*, e00683. [CrossRef]
17. Cavanaugh, K.C.; Cavanaugh, K.C.; Bell, T.W.; Hockridge, E.G. An Automated Method for Mapping Giant Kelp Canopy Dynamics from UAV. *Front. Environ. Sci.* **2021**, *8*, 587354. [CrossRef]
18. Schroeder, S.B.; Boyer, L.; Juanes, F.; Costa, M. Spatial and Temporal Persistence of Nearshore Kelp Beds on the West Coast of British Columbia, Canada Using Satellite Remote Sensing. *Remote Sens. Ecol. Conserv.* **2019**, *6*, 327–343. [CrossRef]
19. Hamilton, S.L.; Bell, T.W.; Watson, J.R.; Grorud-Colvert, K.A.; Menge, B.A. Remote Sensing: Generation of Long-Term Kelp Bed Data Sets for Evaluation of Impacts of Climatic Variation. *Ecology* **2020**, *101*, e03031. [CrossRef]
20. Britton-Simmons, K.; Eckman, J.E.; Duggins, D.O. Effect of Tidal Currents and Tidal Stage on Estimates of Bed Size in the Kelp *Nereocystis Luetkeana*. *Mar. Ecol. Prog. Ser.* **2008**, *355*, 95–105. [CrossRef]
21. Filella, I.; Penuelas, J. The Red Edge Position and Shape as Indicators of Plant Chlorophyll Content, Biomass and Hydric Status. *Int. J. Remote Sens.* **1994**, *15*, 1459–1470. [CrossRef]
22. Pegau, W.S.; Gray, D.; Zaneveld, J.R.V. Absorption and Attenuation of Visible and Near-Infrared Light in Water: Dependence on Temperature and Salinity. *Appl. Opt.* **1997**, *36*, 6035–6046. [CrossRef] [PubMed]
23. Han, L.; Rundquist, D.C. The Spectral Responses of *Ceratophyllum Demersum* at Varying Depths in an Experimental Tank. *Int. J. Remote Sens.* **2003**, *24*, 859–864. [CrossRef]
24. Kearney, M.S.; Stutzer, D.; Turpie, K.; Stevenson, J.C. The Effects of Tidal Inundation on the Reflectance Characteristics of Coastal Marsh Vegetation. *J. Coast. Res.* **2009**, *256*, 1177–1186. [CrossRef]
25. Turpie, K.R. Explaining the Spectral Red-Edge Features of Inundated Marsh Vegetation. *J. Coast. Res.* **2013**, *290*, 1111–1117. [CrossRef]
26. Song, B.; Park, K. Detection of Aquatic Plants Using Multispectral UAV Imagery and Vegetation Index. *Remote Sens.* **2020**, *12*, 387. [CrossRef]
27. Nijland, W.; Reshitnyk, L.; Rubidge, E. Satellite Remote Sensing of Canopy-Forming Kelp on a Complex Coastline: A Novel Procedure Using the Landsat Image Archive. *Remote Sens. Environ.* **2019**, *220*, 41–50. [CrossRef]
28. Phillips, S.R.; Costa, M. Spatial-Temporal Bio-Optical Classification of Dynamic Semi-Estuarine Waters in Western North America. *Estuar. Coast. Shelf Sci.* **2017**, *199*, 35–48. [CrossRef]
29. Mobley, C.D. *Light and Water: Radiative Transfer in Natural Waters*; Academic Press: San Diego, CA, USA, 1994; ISBN 978-0-12-502750-2.
30. Dierssen, H.M.; Chlus, A.; Russell, B. Hyperspectral Discrimination of Floating Mats of Seagrass Wrack and the Macroalgae Sargassum in Coastal Waters of Greater Florida Bay Using Airborne Remote Sensing. *Remote Sens. Environ.* **2015**, *167*, 247–258. [CrossRef]
31. Hu, L.; Hu, C.; Ming-Xia, H. Remote Estimation of Biomass of *Ulva Prolifera* Macroalgae in the Yellow Sea. *Remote Sens. Environ.* **2017**, *192*, 217–227. [CrossRef]
32. ASD Inc. *ASD Light Theory and Measurement Using the FieldSpec HandHeld 2 Portable Spectroradiometer*; ASD Inc.: Longmont, CO, USA, 2017.
33. Mobley, C.D. Estimation of the Remote-Sensing Reflectance from above-Surface Measurements. *Appl. Opt.* **1999**, *38*, 7442–7455. [CrossRef]
34. Mount, R. Acquisition of Through-Water Aerial Survey Images. Available online: <https://www.ingentaconnect.com/content/asprs/pers/2005/00000071/00000012/art00005> (accessed on 8 April 2020).
35. Cavanaugh, K.; Siegel, D.; Reed, D.; Dennison, P. Environmental Controls of Giant-Kelp Biomass in the Santa Barbara Channel, California. *Mar. Ecol. Prog. Ser.* **2011**, *429*, 1–17. [CrossRef]
36. Micasense RedEdge-MX—MicaSense. Available online: <https://micasense.com/rededge-mx/> (accessed on 17 January 2022).
37. Maxar WorldView-3. Available online: <https://resources.maxar.com/data-sheets/worldview-3> (accessed on 17 January 2022).
38. Rouse, W.; Haas, R.H.; Deering, W. *Monitoring the Vernal Advancement and Retrogradation (Green Wave Effect) of Natural Vegetation*; Goddard Space Flight Center: Greenbelt, MD, USA, 1974; p. 87.
39. Tucker, C.J. Red and Photographic Infrared Linear Combinations for Monitoring Vegetation. *Remote Sens. Environ.* **1979**, *8*, 127–150. [CrossRef]
40. Augenstein, E.W.; Stow, D.; Hope, A. Evaluation of SPOT HRV-XS Data for Kelp Resource Inventories. *Photogramm. Eng. Remote Sens.* **1991**, *57*, 501–509.
41. Gitelson, A.A.; Kaufman, Y.J.; Merzlyak, M.N. Use of a Green Channel in Remote Sensing of Global Vegetation from EOS-MODIS. *Remote Sens. Environ.* **1996**, *58*, 289–298. [CrossRef]

42. Mora-Soto, A.; Palacios, M.; Macaya, E.C.; Gómez, I.; Huovinen, P.; Pérez-Matus, A.; Young, M.; Golding, N.; Toro, M.; Yaqub, M.; et al. A High-Resolution Global Map of Giant Kelp (*Macrocystis Pyrifera*) Forests and Intertidal Green Algae (Ulvophyceae) with Sentinel-2 Imagery. *Remote Sens.* **2020**, *12*, 694. [[CrossRef](#)]
43. Schultz, B.B. Levene's Test for Relative Variation. *Syst. Biol.* **1985**, *34*, 449–456. [[CrossRef](#)]
44. Algina, J.; Oshima, T.C.; Lin, W.-Y. Type I Error Rates for Welch's Test and James's Second-Order Test Under Nonnormality and Inequality of Variance When There Are Two Groups. *J. Educ. Stat.* **1994**, *19*, 275–291. [[CrossRef](#)]
45. Shingala, M.C.; Rajyaguru, D.A. Comparison of Post Hoc Tests for Unequal Variance. *Int. J. New Technol. Sci. Eng.* **2015**, *2*, 12.
46. Morel, A.; Prieur, L. Analysis of Variations in Ocean Color. *Limnol. Oceanogr.* **1977**, *22*, 709–722. [[CrossRef](#)]
47. Vahtmäe, E.; Paavel, B.; Kutser, T. How Much Benthic Information Can Be Retrieved with Hyperspectral Sensor from the Optically Complex Coastal Waters? *J. Appl. Remote Sens.* **2020**, *14*, 016504. [[CrossRef](#)]
48. Welch, B.L. The Generalization of 'Student's' Problem When Several Different Population Variances Are Involved. *Biometrika* **1947**, *34*, 28–35. [[CrossRef](#)]
49. Wheeler, W.N.; Smith, R.G.; Srivastava, L.M. Seasonal Photosynthetic Performance of *Nereocystis Luetkeana*. *Can. J. Bot.* **1984**, *62*, 664–670. [[CrossRef](#)]
50. Olmedo-Masat, O.M.; Raffo, M.P.; Rodríguez-Pérez, D.; Arijón, M.; Sánchez-Carnero, N. How Far Can We Classify Macroalgae Remotely? An Example Using a New Spectral Library of Species from the South West Atlantic (Argentine Patagonia). *Remote Sens.* **2020**, *12*, 3870. [[CrossRef](#)]
51. Liew, O.W.; Chong, P.C.J.; Li, B.; Asundi, A.K. Signature Optical Cues: Emerging Technologies for Monitoring Plant Health. *Sensors* **2008**, *8*, 3205–3239. [[CrossRef](#)] [[PubMed](#)]
52. Ruru, D.; Yingqing, H.; Yan, Q.; Qidong, C.; Lei, C. Measuring Pure Water Absorption Coefficient in the Near-Infrared. *J. Remote Sens.* **2012**, *16*, 192–206.
53. Meroni, M.; Rossini, M.; Guanter, L.; Alonso, L.; Rascher, U.; Colombo, R.; Moreno, J. Remote Sensing of Solar-Induced Chlorophyll Fluorescence: Review of Methods and Applications. *Remote Sens. Environ.* **2009**, *113*, 2037–2051. [[CrossRef](#)]
54. Lu, Y.; Li, L.; Hu, C.; Li, L.; Zhang, M.; Sun, S.; Lv, C. Sunlight Induced Chlorophyll Fluorescence in the Near-Infrared Spectral Region in Natural Waters: Interpretation of the Narrow Reflectance Peak around 761 Nm. *J. Geophys. Res. Ocean.* **2016**, *121*, 5017–5029. [[CrossRef](#)]
55. Knipling, E.B. Physical and Physiological Basis for the Reflectance of Visible and Near-Infrared Radiation from Vegetation. *Remote Sens. Environ.* **1970**, *1*, 155–159. [[CrossRef](#)]
56. Nicholson, N.L. Field Studies on the Giant Kelp. *Nereocystis*. *J. Phycol.* **1970**, *6*, 177–182. [[CrossRef](#)]
57. Nicholson, N.L. Anatomy of the Medulla of *Nereocystis*. *Bot. Mar.* **1976**, *19*, 23–31. [[CrossRef](#)]
58. Schmitz, K.; Srivastava, L.M. The Fine Structure of Sieve Elements of *Nereocystis Lütkeana*. *Am. J. Bot.* **1976**, *63*, 679–693. [[CrossRef](#)]
59. Nicholson, N.L.; Briggs, W.R. Translocation of Photosynthate in the Brown Alga *Nereocystis*. *Am. J. Bot.* **1972**, *59*, 97–106. [[CrossRef](#)]
60. Slaton, M.R.; Hunt, E.R.; Smith, W.K. Estimating Near-Infrared Leaf Reflectance from Leaf Structural Characteristics. *Am. J. Bot.* **2001**, *88*, 278–284. [[CrossRef](#)] [[PubMed](#)]
61. Mutanga, O.; Skidmore, A.K. Hyperspectral Band Depth Analysis for a Better Estimation of Grass Biomass (*Cenchrus Ciliaris*) Measured under Controlled Laboratory Conditions. *Int. J. Appl. Earth Obs. Geoinf.* **2004**, *5*, 87–96. [[CrossRef](#)]
62. Gower, J.F.R.; Doerffer, R.; Borstad, G.A. Interpretation of the 685nm Peak in Water-Leaving Radiance Spectra in Terms of Fluorescence, Absorption and Scattering, and Its Observation by MERIS. *Int. J. Remote Sens.* **1999**, *20*, 1771–1786. [[CrossRef](#)]
63. O'Neill, J.D.; Costa, M.; Sharma, T. Remote Sensing of Shallow Coastal Benthic Substrates: In Situ Spectra and Mapping of Eelgrass (*Zostera Marina*) in the Gulf Islands National Park Reserve of Canada. *Remote Sens.* **2011**, *3*, 975–1005. [[CrossRef](#)]
64. O'Neill, J.D.; Costa, M. Mapping Eelgrass (*Zostera Marina*) in the Gulf Islands National Park Reserve of Canada Using High Spatial Resolution Satellite and Airborne Imagery. *Remote Sens. Environ.* **2013**, *133*, 152–167. [[CrossRef](#)]
65. Finger, D.J.I.; McPherson, M.L.; Houskeeper, H.F.; Kudela, R.M. Mapping Bull Kelp Canopy in Northern California Using Landsat to Enable Long-Term Monitoring. *Remote Sens. Environ.* **2021**, *254*, 112243. [[CrossRef](#)]
66. Sutherland, I.R. *Kelp Inventory, 1989 The Vancouver Island and Malcolm Island Shores of Queen Charlotte Strait Including a Summary of Historical Inventory Information for the Area*; Kelp Inventory; Ministry of Environment: Vancouver, BC, Canada, 1990; p. 46.



Article

Assessment of RTK Quadcopter and Structure-from-Motion Photogrammetry for Fine-Scale Monitoring of Coastal Topographic Complexity

Stéphane Bertin ^{1,2,*}, Pierre Stéphan ³ and Jérôme Ammann ¹

¹ UMR 6538 Geo-Ocean, University Brest-CNRS-Ifrermer, Institut Universitaire Européen de la Mer, Rue Dumont d'Urville, 29280 Plouzané, France; jerome.ammann@univ-brest.fr

² UAR 3113 Institut Universitaire Européen de la Mer (IUEM), University Brest-CNRS, Rue Dumont d'Urville, 29280 Plouzané, France

³ UMR 6554 Littoral, Environnement, Géomatique, Télédétection, University Brest-CNRS, Institut Universitaire Européen de la Mer, Rue Dumont d'Urville, 29280 Plouzané, France; pierre.stephan@univ-brest.fr

* Correspondence: stephane.bertin@univ-brest.fr

Abstract: Advances in image-based remote sensing using unmanned aerial vehicles (UAV) and structure-from-motion (SfM) photogrammetry continue to improve our ability to monitor complex landforms over representative spatial and temporal scales. As with other water-worked environments, coastal sediments respond to shaping processes through the formation of multi-scale topographic roughness. Although this topographic complexity can be an important marker of hydrodynamic forces and sediment transport, it is seldom characterized in typical beach surveys due to environmental and technical constraints. In this study, we explore the feasibility of using SfM photogrammetry augmented with an RTK quadcopter for monitoring the coastal topographic complexity at the beach-scale in a macrotidal environment. The method had to respond to resolution and time constraints for a realistic representation of the topo-morphological features from submeter dimensions and survey completion in two hours around low tide to fully cover the intertidal zone. Different tests were performed at two coastal field sites with varied dimensions and morphologies to assess the photogrammetric performance and eventual means for optimization. Our results show that, with precise image positioning, the addition of a single ground control point (GCP) enabled a global precision (RMSE) equivalent to that of traditional GCP-based photogrammetry using numerous and well-distributed GCPs. The optimal model quality that minimized vertical bias and random errors was achieved from 5 GCPs, with a two-fold reduction in RMSE. The image resolution for tie point detection was found to be an important control on the measurement quality, with the best results obtained using images at their original scale. Using these findings enabled designing an efficient and effective workflow for monitoring coastal topographic complexity at a large scale.

Keywords: topographic remote sensing; coastal monitoring; high-energy beaches; gravel spit; structure-from-motion photogrammetry; multicopter drone; RTK-GNSS; permanent GCPs; DEM error; workflow optimization

Citation: Bertin, S.; Stéphan, P.; Ammann, J. Assessment of RTK Quadcopter and Structure-from-Motion Photogrammetry for Fine-Scale Monitoring of Coastal Topographic Complexity. *Remote Sens.* **2022**, *14*, 1679. <https://doi.org/10.3390/rs14071679>

Academic Editors: Simona Niculescu, Junshi Xia and Dar Roberts

Received: 7 March 2022

Accepted: 29 March 2022

Published: 31 March 2022

Publisher's Note: MDPI stays neutral with regard to jurisdictional claims in published maps and institutional affiliations.



Copyright: © 2022 by the authors. Licensee MDPI, Basel, Switzerland. This article is an open access article distributed under the terms and conditions of the Creative Commons Attribution (CC BY) license (<https://creativecommons.org/licenses/by/4.0/>).

1. Introduction

The coast is a very dynamic and varied environment, constantly changing in response to complex interrelations between landforms and processes operating across a wide range of spatial and temporal scales. Understanding shoreline dynamics, for integration into process-based modelling, for example, and being able to predict future evolutions in the context of relative sea-level rise, requires an accurate characterization of the geomorphic processes acting at the sediment–water interface [1–5]. Sediment reworking on the beach and nearshore due to waves and currents traduces by the formation of topographic complexity (herewith generally called roughness), such as sedimentary bedforms. These

topo-morphological features are the imprint of the processes that shaped them, and, as such, measuring bedforms can provide meaningful information on hydrodynamic forces [6–10]. Besides, bedforms are roughness elements that modify the flow and dissipate energy [11,12]. They are, thus, interesting markers of the sediment bed propensity towards resistance to entrainment and dynamic equilibrium.

Different types of bedforms generally coexist in the coastal environment (e.g., Refs. [13–15]), whose dimensions and shapes depend on sediment availability, sediment type (e.g., size distribution and shape) and driving mechanisms (e.g., waves, currents, wind). Examples of small-scale bedforms are wave and current sand ripples, or gravel-bed clusters, with dimensions or length scales generally not exceeding a few tens of centimeters. Larger-scale bedforms include varied bar and trough morphologies (e.g., ridge and runnels) in the surf and swash zones [16], other rhythmic patterns most often found on the upper beach, such as beach cusps [17,18], as well as aeolian sand dunes. In between those, there are a wide range of topographic variations that take part in the continuum of roughness scales and contribute to the overall structural complexity of the seabed, backshore and dune system.

1.1. High-Resolution Topographic Surveying and Photogrammetric Remote Sensing of Coastal Morphology

In tidal environments, daily fluctuations in the water level mean that the water-worked seabed can be measured using topographic surveying, with the maximum coverage typically achieved during the lowest low tides. Previous work largely relied on RTK-GNSS, with a rover eventually mounted on a mobile platform, such as a quad, for monitoring the evolution of barred beaches and other coastal landforms [12,19]. The DEMs generated have resolutions ranging from a few meters cross-shore to tens of meters alongshore, in link with the topographic complexity and bedform orientation, while survey coverage can reach up to several kilometers alongshore, allowing to account for the rhythmic nature of the coastal morphology (e.g., rip-channel systems, cusps and megacusps). Common to point-based surveying techniques, enhancing the spatial resolution is generally counter-balanced by increased acquisition time or reduced spatial coverage [20–22], which means that using RTK-GNSS for the fine-scale monitoring of coastal topography remains problematic.

In contrast, remote sensing techniques, such as UAV photogrammetry, have greatly improved, rendering very-high-resolution (e.g., submeter) topographic surveying at a large scale (e.g., beach scale) feasible. Using off-the-shelf drones and cameras, ground sampling distances (GSD) as small as a few centimeters can be achieved during typical beach surveys [23–25]. Photogrammetric processing relies on the SfM method, which is based on the scale-invariant feature transform (SIFT) algorithm [26] for matching corresponding points in images, and uses external information, mostly taking the form of GCPs measured independently, for scaling and optimizing the photogrammetric model. Yet, previous work showed that the resulting DEM quality (e.g., horizontal and vertical precisions) is largely variable (e.g., Refs. [23,27,28]) and depends on a wide range of parameters, among which survey design (e.g., flying height, image overlap, camera orientation, GCP number and distribution) and processing strategies (e.g., direct georeferencing, camera calibration and point-matching methods) play a critical role.

Photogrammetry has been used previously in different domains of research to measure sedimentary bedforms of various dimensions, including particle clusters [29,30], bed undulations, such as sand [31–33] and gravel bars [34–36], and sand dunes [37–42], with measurements of small-scale bedforms generally performed in the laboratory. Hence, it is not yet known if fine-scale water-worked topographies can be efficiently and effectively measured using UAV photogrammetry in the field, such that there is currently a paucity of data for assessing coastal topographic roughness and shaping processes.

1.2. Photogrammetric Workflow Optimisation

A common limitation to achieving efficient surveys mentioned in previous work, and finding important echo in time-constrained (e.g., tidal) environments, is the need for a dense and well-measured network of GCPs for the accurate scaling and georeferencing of photogrammetric results (e.g., Ref. [43]). In the absence of other external controls, this requirement is particularly important, shown by observations of decreasing DEM quality with distance increases from the nearest GCP [44–46]. Relief can be procured through the installation of fixed (i.e., permanent) targets, although it is generally only partial and, in application to the coast, implies that fixed targets are limited to dry zones [37].

The uptake of high-precision RTK-GNSS technology for drone navigation can further improve survey efficiency. With RTK drones, image geolocations serve as airborne controls, which, despite a generally lower precision compared to GCPs and a repartition outside the measurement volume, can compensate for these caveats due to the comparatively very-large number of controls provided [47]. Previous research showed that results of a similar quality or even better can be achieved using a reduced number of GCPs when the camera positions are used as external controls [48]. Using the camera information as the only external control during photogrammetric processing forms the basis behind direct georeferencing (DG) approaches (e.g., Refs. [49–51]). The DG of photogrammetry is particularly advantageous when access to the field site and the measurement of GCPs are problematic. However, previous studies showed that DG generally comes at the cost of reduced measurement quality (e.g., lower accuracy and precision).

The commercialization of RTK drones at competitive prices (e.g., the Phantom 4 RTK quadcopter) has reinstated large interest in determining the capability of DG approaches across different settings, including building facades, urban and rural landscapes as well as river and coastal environments. Previous studies investigated the differences between drone positioning corrections provided either in real time (RTK) from a nearby base station managed by the field operators or through RTK networks, or post-processed (PPK) using observations at known base stations [52,53]. They also assessed the effect of the image viewing angle (nadir vs. oblique [54]), as well as changes in measurement quality with and without the provision of GCPs (e.g., Refs. [52–56]).

These studies concluded that, in the absence of GCPs, systematic error mainly through vertical bias can impact the measurement quality, which was related to the imprecise calibration of internal orientation parameters (IOP). Yet, contrasting results were obtained when it comes to the number of GCPs to introduce to correct this effect. Some studies reported that one GCP was enough, although the GCP position may be important, while other studies recommended using at least three GCPs. With the exception of the effort to survey 109 points with a theodolite on a building's facades by Taddia et al. [52], error evaluation is generally limited to a few check points (ChkPts), whose number and repartition may not be adequate for reliable error characterization. This, in turn, limits the generalization of the findings such that the measurement capabilities of RTK-assisted UAV photogrammetry over large and GCP-poor coastal tracts are not fully understood.

1.3. Paper Overview

In this study, we explored the feasibility of using an RTK quadcopter (Phantom 4 RTK) and SfM photogrammetry for fine-scale (e.g., submeter) monitoring of water-worked coastal topography. We carried out a variety of tests of interest for the application because of their influences on data collection time and measurement quality (e.g., resolution and precision). More specifically, we were interested in enhancing the survey efficiency to surpass tide-related constraints while ensuring the results' effectiveness through rigorous error characterization at two macrotidal coastal field sites with contrasting survey areas and morphologies. The DEM error evaluation at localized check points (ChkPts) was supplemented where possible by full DEM comparisons and the collection of over 2000 survey points with RTK-GNSS, whilst the availability of repeat surveys and invariant features enabled the assessment of the complete workflow replicability.

Our results show that at least five GCPs, in addition to camera information, were necessary to achieve the optimal model quality that minimized vertical bias and random errors. Under this configuration, the standard deviation of error representing measurement precision (~1 GSD) was approximately two times better than that when camera information was unused. First, the geomorphic analyses are presented, highlighting the potential of the method for submeter bedform characterization over entire beach systems.

2. Materials and Methods

2.1. Field Sites

The two coastal field sites presented in this study are located in Brittany in northwest France (Figure 1a,b). The field site at La Palue and Lostmarc’h beaches, hereafter generally referred to as “La Palue” for concision, is situated at the western end of Crozon Peninsula. Facing due west, La Palue and Lostmarc’h are adjacent beaches totaling ~2.5 km along-shore separated by a rocky promontory (Kerdra point) at high tide, backed by granitic cliffs (20–50 m high) at each end point and a mostly consolidated and vegetated dune elsewhere. It is a macrotidal environment with mean neap and spring tidal ranges of 2.25 and 5.60 m [57], respectively. Waves originate from Atlantic depressions generating SW through NW swells, but also shorter period seas from locally generated wind [58]. Based on samples collected on the intertidal beach and processed using traditional size-sieving, sediment belongs to fine to medium sand with a D_{50} (the median sediment size for which 50% of the sediment distribution is finer) of ~0.25 mm and a sorting coefficient ($\sqrt{D_{84}/D_{16}}$) of 1.35 (i.e., well-sorted). The upper beach abutting the dune is composed of cobbles, especially on the northern parts (Figure 2b). The morphodynamics are akin to intermediate beaches according to the Masselink and Short classification [59], covering a range of beach states depending on ongoing hydrodynamic conditions. Generally, a flatter profile is observed over winter, contrasting with marked bar and rip channel morphologies developing across calmer months. During spring tides, the intertidal beach is approximately 300–400 m wide (Figure 1c). Large patches of ripples and megaripples can often be observed. Bedrock may locally appear near the low-tide line, depending on sand levels. Outside a few of channelized access points and small blockhouses remnant of World War 2, human encroachments are limited. Man-made features, at the condition they are relatively flat, were useful for preparing fixed ground targets for photogrammetry. Depending on survey date, up to six red-painted crosses approximately 40 cm in size were used (Table 1).

Table 1. Overview of the field surveys and data collection for UAV-SfM photogrammetry. The tidal coefficient (20–120) represents the tide magnitude in relation to its mean.

| Field Site Date | Tidal Coefficient (-) | Flight Count/Image Count (-) | Flying Height (m) | Overlap Along/Cross (%) | Survey Area (m ²) | GSD (m/Pixel) | Target Count (Fixed Targets) (-) |
|--|-----------------------|------------------------------|-------------------|-------------------------|-------------------------------|---------------|----------------------------------|
| Sillon de Talbert 17 November 2020 | 103 | 2/734 | 58 | 80/70 | 125,000 | 0.014 | 21 (0) |
| La Palue 17 September 2020 | 101 | 5/1407 | 106 | 80/70 | 1,320,000 | 0.026 | 30 (5) |
| La Palue 17 December 2020 | 90 | 6/1548 | 105 | 80/70 | 1,280,000 | 0.026 | 22 (3) |
| La Palue 2 March 2021 | 103 | 5/1411 | 108 | 80/70 | 872,000 | 0.025 | 19 (1) |
| La Palue 29 April 2021 | 106 | 5/1386 | 107 | 80/70 | 1,080,000 | 0.026 | 28 (6) |

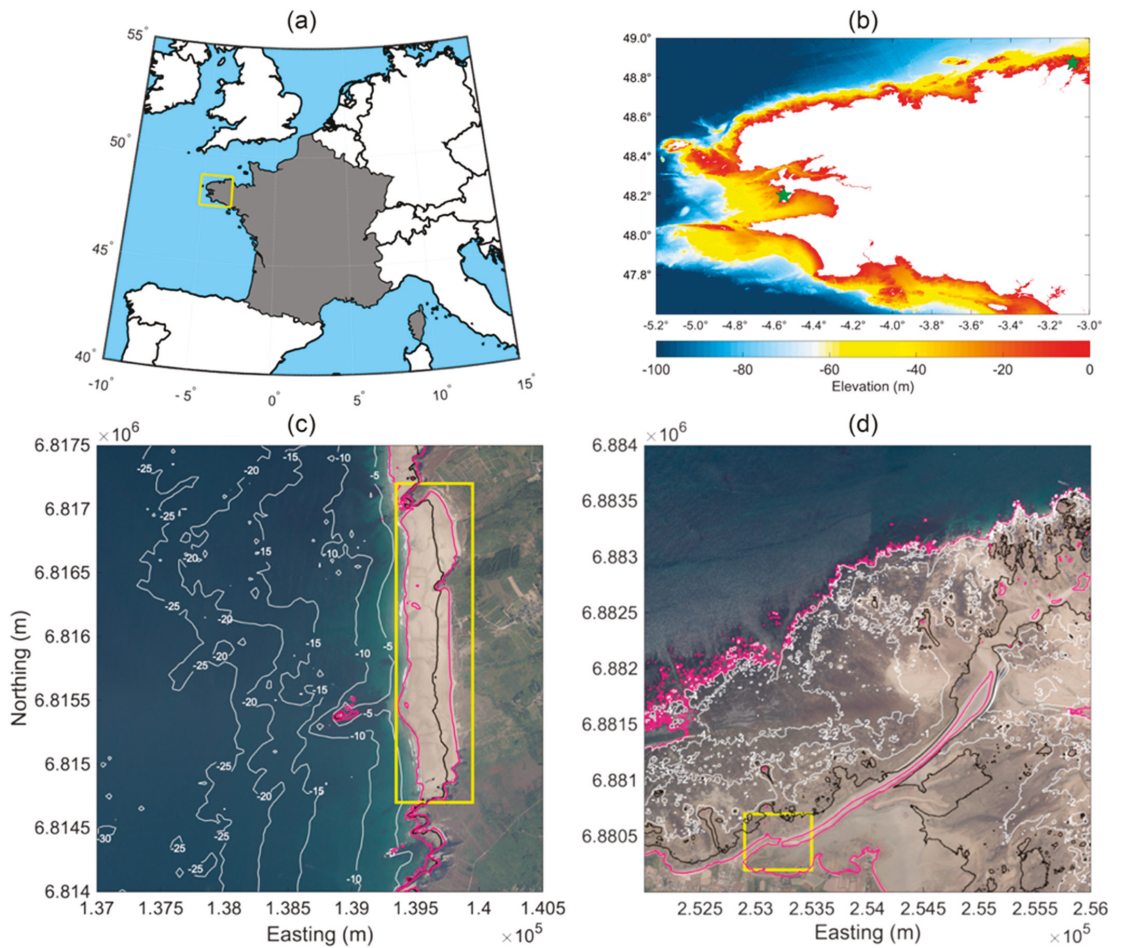


Figure 1. Survey sites. (a) Map of France; (b) bathymetric DEM of western Brittany with green stars representing field sites at La Palue (left) and Sillon de Talbert (top right); (c,d) orthophotographs (source: Ortho Littorale V2, Ministère en charge de l’environnement, 2013) of La Palue and Sillon de Talbert, respectively, showing the (yellow enclosed) survey area and depth contours (source: Litto3D Finistère 2014—Shom). Black and pink lines represent MSL and MLWS/MHWS, respectively.

The second field site corresponds to the proximal section of the Sillon de Talbert gravel spit. This 3.5-km-long swash-aligned barrier is located north of Brittany. The sediment volume is estimated at $1.23 \times 10^6 \text{ m}^3$ [60]. According to the barrier morphology and sedimentology, the gravel accumulation can be classed as a “composite gravel beach” [61,62]. The beach face shows a break slope point at the mean water level, which delimitates the gravel barrier from an otherwise flat rocky platform (slope = 0.01%) covered by thin and patchy periglacial deposits and/or recent sandy sheets. The upper part of the beach face is characterized by steeper slopes of between 5% and 15%. Back-barrier areas include a large sand-flat and salt-marshes. The site is located in a macrotidal to megatidal setting (maximum tidal range of 10.95 m) [57]. Dominant swell comes from the WNW, which means that waves break with a slight angle according to the shoreline orientation, generating a longshore drift oriented to the NE. Until the end of the 17th century, the barrier was connected to the islets of the Olone archipelago located to the NE. The disconnection of

the barrier occurred in the early 18th century [63]. In the 1970s and 1980s, several coastal defenses were installed to prevent the retreat of the barrier, especially in the proximal section where a groin was installed. Annual topographic surveys realized with RTK-GNSS since 2002 revealed a strong erosion of the beach face downdrift of the groin [64]. The loss of sediment was estimated to ca. 11,000 m³ between 2002 and 2017, which caused significant barrier lowering and narrowing locally. These morphological changes led to the opening of a breach at the beginning of March 2018, which has experienced a rapid enlargement (35 vs. 15 m) and deepening (3.4 vs. 1.25 m) over the following months [65]. For monitoring breach evolution, we have put in place trimestral UAV photogrammetry surveys.

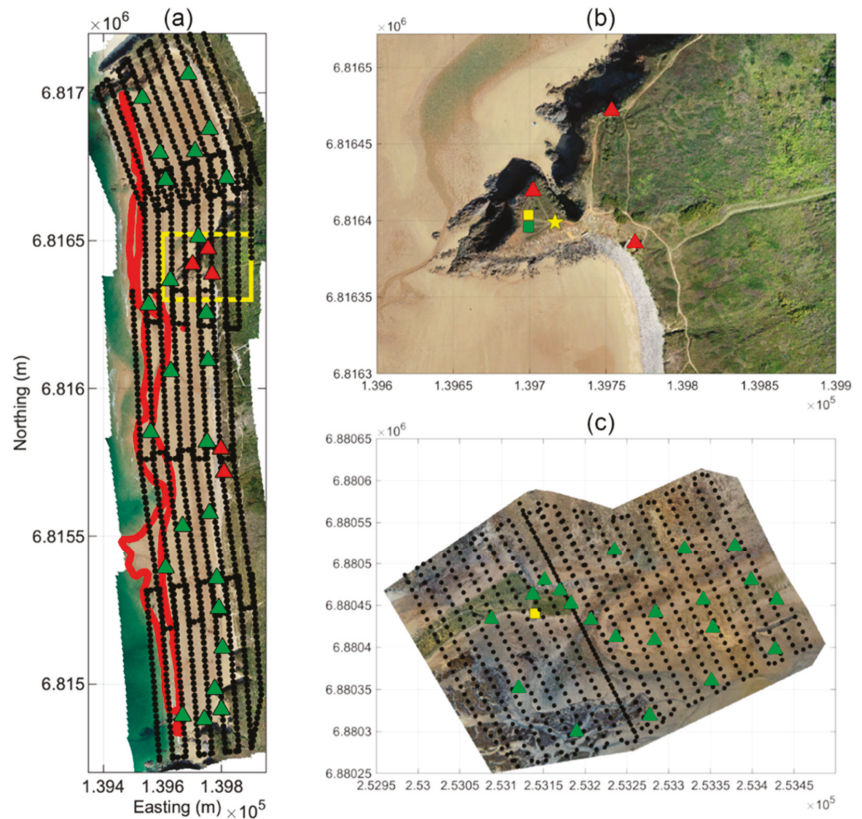


Figure 2. Field surveys. Orthophotos showing camera locations (black dots), DRTK-2 drone mobile station (green square), ground photogrammetric targets (triangles; the five fixed targets present at La Palue during the September survey are shown in red), GNSS base station (yellow square) and geodetic marks (yellow star) at (a,b) La Palue, and (c) Sillon de Talbert field sites, respectively. RTK-GNSS survey points used for the vertical evaluation of photogrammetry at La Palue are shown in red. At Sillon de Talbert, the GNSS base station and DRTK-2 drone mobile station were installed one after the other using the same geodetic mark.

2.2. Field Operation and Data Collection

Five surveys altogether covering a seven-month period are considered in this study: one at Sillon de Talbert and four at La Palue (Table 1). For the latter, only the first survey (17 September 2020) is described and analyzed in detail, the other three (repeat) surveys being used for assessing measurements' replicability (cf. Section 2.6).

Data collection starts with centimetric-accuracy RTK-GNSS (Topcon Hyper V) measurements of geodetic marks (cast metal disks installed on stable ground) and photogrammetric targets (red plastic plates 30 cm in diameter fixed to the ground using tent poles) for data georeferencing and validation (cf. Figure 2). Between 20 and 30 photogrammetric targets, including fixed targets, were deployed to be used either as GCPs or ChkPts (cf. Tables 1 and 2). Measurements are carried out in rapid-static mode (10 s average) using GNSS rovers mounted on a 2-m pole equipped with a bubble level. To provide RTK corrections, a GNSS base station was materialized at both sites using a geodetic mark. Fixed coordinates were obtained using long-static averaging with a tripod (~240 min), over several periods of time, and postprocessed in comparison with nearby IGN (Institut Géographique National) GNSS stations. Repeated measurements of other geodetic marks provide insights on georeferencing quality. For example, using between three and seven survey marks, the standard error (SE) was estimated to be 0.004 m horizontally and 0.002 m vertically on average at La Palue across four consecutive surveys. Geographic coordinates are referenced to the French legal systems for this region, i.e., RGF93-Lambert 93 for planimetry and NGF-IGN69 for altimetry. Elevation zero (m NGF) corresponds to approximately 0.5 m below mean sea level (MSL).

Table 2. Overview of the processing parameters and scenarios used for DEM reconstruction with Agisoft Metashape.

| Processing Step/Scenario | Image Alignment | Sparse Point Cloud Filtering | Model Optimization | Dense Matching and DEM |
|-------------------------------|--|--|--|--|
| Standard (High ₁) | <ul style="list-style-type: none"> • Key points: 60,000 • Tie points: 10,000 • Adaptive camera model fitting • Accuracy: “high” • Pair preselection: “source” | <ul style="list-style-type: none"> • Minimum image count: 3 • Maximum reprojection error: 0.4 pixel • Maximum reconstruction uncertainty: 5 | <ul style="list-style-type: none"> • Adaptive camera model fitting • Rolling shutter compensation • Camera accuracy: 1 m • Marker accuracy: error on marker coordinates (pixel) • Tie point accuracy: RMS reprojection error (pixel) on tie points • Camera positions and attitudes • 5 GCPs/N – 5 ChkPts | <ul style="list-style-type: none"> • Reconstruction quality: “high” • Depth filtering: “aggressive” • DEM resolution: 0.1 and 1 m |
| Low | Accuracy: “low” | - | - | DEM resolution: 1 m |
| Medium | Accuracy: “medium” | - | - | DEM resolution: 1 m |
| High ₂ | Pair preselection: “reference” | - | - | DEM resolution: 1 m |
| Highest | Accuracy: “highest” | - | - | DEM resolution: 1 m |
| S-GCP | - | - | <ul style="list-style-type: none"> • Camera positions and attitudes unused • N GCPs/0 ChkPts | DEM resolution: 1 m |
| S-RTK | - | - | 0 GCPs/N ChkPts | DEM resolution: 1 m |
| S-RTK-GCP | - | - | N GCPs/0 ChkPts | DEM resolution: 1 m |
| S-RTK-1GCP | - | - | 1 GCPs/N–1 ChkPts | DEM resolution: 1 m |
| S-RTK-3GCP | - | - | 3 GCPs/N–3 ChkPts | DEM resolution: 1 m |
| S-RTK-5GCP | - | - | 5 GCPs/N–5 ChkPts | DEM resolution: 1 m |
| S-RTK-9GCP | - | - | 9 GCPs/N–9 ChkPts | DEM resolution: 1 m |

N is the number of photogrammetric targets available, and - stands for standard parameters.

Aerial image acquisition for photogrammetry was carried out using DJI's Phantom 4 RTK quadcopter (P4 RTK) and D-RTK2 mobile station. The latter is used for drone RTK positioning. According to the manufacturer, this system allows image georeferencing precisions of 1 cm + 1 ppm (parts per million, i.e., 1 mm per 1000 m) and 1.5 cm + 1 ppm along the horizontal and vertical directions, respectively, traducing to absolute accuracies of around 0.05 m at a flying height of 100 m. During surveys, the D-RTK2 is positioned atop a geodetic mark with known coordinates (explanations above). The P4 RTK is equipped with a 20-megapixel (2.41 × 2.41-pixel size) complementary metal-oxide-semiconductor (CMOS) camera (FC6310R) with a mechanical global shutter and an 8.8 mm focal length. Besides precise positioning, the drone attitude (pitch, roll and yaw angles) is recorded automatically for each image using an onboard inertial measurement unit (IMU). For collecting images, we used a single photogrammetric block arrangement with a front and side overlap of 80% and 70%, respectively (Table 1, Figure 2) and a forward-looking camera angle of 6° off-nadir. The flying height, and, thus, the GSD, was adjusted depending on the field site in order to complete surveys within two hours around low tide. The flying height (relative to take-off elevation) was maintained at approximately 58 m and 106 m for the Sillon de Talbert and La Palue field sites, traducing to a GSD of 0.014 m and 0.026 m, respectively. To satisfy local drone regulations active at the sites, five flights, from five different take-off and landing spots, were necessary at La Palue, whereas two flights were enough to cover the breach at Sillon de Talbert. Flight pattern was designed to include an overlap between each image block (cf. Figure 2) while ensuring that flight duration remained below the 20-min mark. Before performing the flights, camera settings were tentatively adjusted to the environmental conditions.

Additional topographic measurements were carried out at La Palue using RTK-GNSS (Figure 2a) to serve as vertical ground truths for the evaluation of photogrammetry. To make for an efficient survey covering as much of the beach length as possible, a GNSS rover was securely mounted onto a bike, using a pannier rack above the rear wheel. The rover was mounted with the antenna pointing downwards (vertically) and aligned with the rear wheel axis. The approximate height of the antenna center above the ground was measured, using a tape ruler, to be ~0.60 m. Determination of the exact height was completed using a geodetic mark, with the bike positioned atop and loaded to replicate survey conditions. The height of the antenna center was used to reference the data into the same coordinate system as other surveys presented above. Point sampling along the beach using the "bike GNSS" was carried out in dynamic mode at 1 Hz. The survey was limited to the intertidal zone close to the low-tide water line with packed sand and where photogrammetric quality was expected to be lower due to the difficulty of deploying GCPs and more generally because of the presence of water, the latter making for more challenging tie point detection. Surveying was done by riding the bike alongshore (cf. Figure 2a) to limit as much as possible introducing a pitch angle between the GNSS antenna and the vertical. Roll minimization was made possible by a bubble level mounted onto the bike handlebar. Strategies to account for pitch and roll-related errors on point coordinates were implemented and will be presented in Section 2.5.

2.3. Photogrammetric Data Processing: Standard Workflow

Drone images were processed using the SfM method implemented in Agisoft Metashape (version 1.70). For producing the final data, the same "standard" workflow was implemented allowing results' comparison (Table 2). In the following, we present the standard workflow used before presenting variations to this workflow (Section 2.4), which was meant to assess controls on measurement quality and to validate our approach.

After importing images from all flights into a single chunk, image coordinates are converted from initially WGS84 ellipsoid to RGF93-Lambert 93 and NGF-IGN69. Automatic identification of low-quality images is performed using the "estimate image quality" tool, whereby each image is associated to a score between 0 and 1 representing sharpness (0 means totally blurred). Following recommendations, images with quality below 0.5 were

not processed in order not to negatively influence image alignment. Image alignment is carried out using the “High” accuracy setting, a reference pair preselection set to “source”, key point (tie point) limits set to 60,000 (10,000). After initial image alignment and the reconstruction of a sparse point cloud, photogrammetric targets’ coordinates are imported. Each target was manually tagged in at least eight images, progressively improving model georeferencing. To retain only the most reliable tie points, sparse point clouds were systematically cleaned using the “gradual selection” tool with the following parameters: minimum image count of 3, maximum reprojection error of 0.4 pixel and maximum reconstruction uncertainty of 5.

During photogrammetric model optimization, model georeferencing and 3D geometry are adjusted through self-calibrating bundle block adjustment (BBA) requiring external information. Using the standard workflow, BBA is carried out using all camera information available (i.e., position, attitude and associated precisions provided by the drone) and all targets as ChkPts but five (i.e., five targets used as GCPs). For all scenarios tested (explanations below), adaptive camera model fitting was used for camera self-calibration, allowing the complete set of calibration parameters (f , c_x , c_y , k_1 - k_4 , p_1 - p_2 and b_1 - b_2) to be automatically adjusted given user-decided weighting of the external information provided. Following recommendations in Ref. [43], the marker and tie point accuracy were adjusted to match the error in pixel on marker coordinates and the RMS reprojection error (pixel) on tie point coordinates, respectively.

For producing the final dense models, point cloud densification is carried out using a reconstruction quality set to “High” with “aggressive” depth filtering. Using “High” reconstruction quality setting, dense matching is applied to images resampled at half their resolution, speeding up the process and reducing data size. With this setting, the optimum DEM resolution (i.e., minimum grid spacing) is capped at 2 GSD, equaling 0.028 and 0.052 m at Sillon de Talbert and La Palue, respectively. It was considered sufficient for our application since DEMs analyzed have resolutions of 0.1 m and 1 m. Before producing the DEMs, dense point clouds were cleaned using the “Filter by confidence” tool, whereby each model point is graded (1–255) according to how many depth maps the point in question appears in. For this application, points with confidence between 0 and 3 were systematically filtered. Finally, DEMs and orthophotos with a minimum planimetric resolution of 0.1 m are created (interpolation enabled) and exported using same orthogonal grids with integer bounding values.

2.4. Alternative Photogrammetric Processing Scenarios

To validate our selection of the standard processing parameters, different tests were performed, which are shown in Table 2. The first test focused on image alignment accuracy setting, which was varied from “Low” to “Highest” and encompassing “Medium” and “High” accuracy settings, while other parameters were left unchanged. Using “High” accuracy, image alignment is performed using original images. Using “Highest”, the software upscales images by a factor two in each direction, while lower accuracy settings will see image resolution decreasing incrementally by a factor two. A compound test was performed in the case of “High” image alignment accuracy to assess the effect of disabling the reference pair preselection, which uses image coordinates to help finding matches.

Optimum strategies during photogrammetric model optimization were assessed through the declination of different scenarios (cf. Table 2). The Sillon de Talbert field site, with reduced superficies and a comparatively large number of well-distributed targets, was used as a testing ground. The first scenario (S-GCP) used all ground targets ($n = 21$) as GCPs with camera information disabled during processing. This scenario is equivalent to the classical approach relying solely on GCPs for camera calibration and model georeferencing. The second scenario (S-RTK-GCP) used all targets as GCPs, as well as camera information (location and attitude), for the optimization. Other scenarios using camera information were implemented by varying the number of GCPs used, hereafter referred to as S-RTK, S-RTK-1GCP, S-RTK-3GCP, S-RTK-5GCP and S-RTK-9GCP, corresponding to

using 0 (i.e., no GCPs), 1, 3, 5 and 9 GCPs, respectively. Scenarios using 1 and 3 GCPs were replicated (differentiation is done using subscripts ₁ and ₂) in that targets selected as GCPs were changed to test the effect of GCP location on model quality.

To facilitate results' comparison for the different scenarios tested and to expedite data processing, evaluations were performed on 1 m resolution DEMs created from the sparse point clouds. This decision was supported by the fact that dense matching has limited effect on the overall model georeferencing and geometry (e.g., 3D deformations that may be present in the sparse models following model optimization), improving mainly the representation of fine-scale features through a higher model resolution.

2.5. RTK-GNSS Data Processing

Mounting a GNSS rover onto a bicycle made for efficient topographic measurements, but, unlike a rover set atop a pole kept static and vertical during data acquisition, measured points' coordinates may well be affected by errors due to pitch and roll whereby the bike is subject to both the local relief in the direction of travel and its own instability. In order to minimize these effects, particularly pitch-related errors, which were easier to detect, survey points were cleaned according to (i) the confidence level with which they were obtained, and (ii) systematic errors due to the uneven terrain topography.

Where survey points were sufficiently close to each other, point confidence was estimated as the standard deviation of elevations within a circular window with 0.2 m radius, which was considered a proxy of the local bed complexity. For the points evaluated, only those with a confidence score below 0.035 m (the theoretical vertical precision of RTK-GNSS) were retained, hence filtering less reliable points due to a locally complex bed morphology and/or unnaturally large deviations among surrounding points.

Pitch-related errors due to the uneven terrain were estimated, assuming the bicycle followed a straight line between two consecutive survey points, that the antenna of the GNSS unit was vertically aligned with the real wheel center point when the bike is horizontal and that the system was well equilibrated at all times (i.e., no roll). Under these conditions, the bed slope in the travel direction, the pitch angle of the bicycle and that of the GNSS antenna are same. We calculated the horizontal (dx) and vertical (dz) point displacements due to a sloping bed using a distance between the two wheels of 1.2 m and a GNSS antenna height of 0.6 m. With the arrangement used, horizontal errors were predominant over vertical errors. As an indication, a 6° slope (equivalent to a beach gradient of 1 in 10) resulted in horizontal and vertical errors of approximately 0.062 m and 0.007 m, respectively. Similar to filtering by point confidence, points with pitch-related errors exceeding 0.035 m were systematically filtered to only retain data in permissible terrain (here, terrain with forward slopes below approximately 3°).

2.6. Measurement Quality Evaluation

Different strategies and error metrics (Table 3) were used to evaluate measurement quality achieved with photogrammetry. As much as possible, they were used simultaneously to assess results in terms of accuracy, precision and reliability [66]. While accuracy and precision were estimated in comparison with reference data (ground truth) supposed of higher quality, reliability represented the consistency between data obtained using different processing parameters determined through DEMs of differences (DoDs).

Results' accuracy, representing systematic deviations (bias) from the ground truth, and the precision with which they were obtained, were calculated, respectively, as the mean error (ME, Equation (1)) and the standard deviation of error (SDE, Equation (2)) between photogrammetric models and ground targets. RMSE (Equation (3)) is also provided, representing the global precision within results, combining both ME and SDE into a single statistical measure (Equation (4)). Error statistics were calculated along all three dimensions (x, y and z) and were eventually added in quadrature to produce a measure of the 3D error (Equation (5)). For ease of use and clarity of the text, error metrics without a direction

specifically mentioned refer to vertical error, which is of immediate interest for measuring morphological change with DEMs.

Table 3. Error metrics used for evaluation of measurement quality.

| Error Metric | Formula |
|-----------------------------------|---|
| Mean Error (ME) | $ME = \frac{1}{N} \sum_{i=1}^N (y_i - x_i) \quad (1)$ |
| Standard Deviation of Error (SDE) | $SDE = \sqrt{\frac{1}{N} \sum_{i=1}^N (y_i - \bar{x}_i)^2} \quad (2)$ |
| Root-Mean Square Error (RMSE) | $RMSE = \sqrt{\frac{1}{N} \sum_{i=1}^N (y_i - x_i)^2} \quad (3)$ |
| | $RMSE = \sqrt{ME^2 + SDE^2} \quad (4)$ |
| 3D Error ($_{3D}$) | $3D = \sqrt{X^2 + Y^2 + Z^2} \quad (5)$ |
| Mean Unsigned Error (MUE) | $MUE = \frac{1}{N} \sum_{i=1}^N y_i - x_i \quad (6)$ |

y is the measurement or observation, x the reference value and N the number of available comparisons. Horizontal and vertical bars represent the average (i.e., mean) and absolute (i.e., unsigned) values, respectively. X , Y and Z represent easting, northing and vertical (i.e., elevation) directions, respectively.

At La Palue field site only, DEM vertical accuracy and precision were also derived through comparisons with points surveyed with the bike GNSS. This allowed for independent error evaluation at a dense network of ground truth points. For assessing photogrammetric results, each GNSS survey point was compared with the closest DEM grid point, given a maximum distance for comparison of 0.2 m. The latter was decided considering comparisons with points further away would account more for the change in the local bed topography than measurement error itself.

Finally, the availability of four repeat DEMs obtained using the same workflow for collecting (Table 1) and processing (Section 2.3) the data enabled assessing photogrammetric replicability at La Palue. The temporal variability in bed elevations was estimated for each DEM cell using both the standard deviation of elevations and the maximum elevation range between repeat surveys. These metrics were used to assess whether a surface cell (and, hence, the underlying terrain) was stable over the survey period. We used a maximum range of 0.035 m to distinguish stable and unstable cells (cells with elevation range above threshold were considered unstable). To ensure a robust statistical characterization, only cells measured across all four repeat surveys were retained. A multitemporal ground truth DEM was formed by averaging repeat elevations over stable cells. Comparing individual surveys with the ground truth provided information on eventual deviations from the “average topography” of the stable zones.

3. Results

In the following, we present the results obtained at the two field sites, starting with the breach at Sillon de Talbert. With a reduced survey area compared to La Palue and dense ground controls, the breach at Sillon de Talbert represented an ideal testing ground for experimenting on the minimum number of GCPs for effective photogrammetric optimization using an RTK quadcopter. We then apply these findings to La Palue field site, and we validate the approach using larger-scale experiments and data validation methods. The implications of our findings and recommendations that arise from our results are discussed in Section 4.

3.1. The Breach at Sillon de Talbert

Figure 3 presents the results of photogrammetric quality evaluation for the different scenarios tested during model optimization. The reference DEM used for assessing the other DEMs was produced using scenario S-RTK-GCP. This decision was based on the consideration that using all the external information available during photogrammetric

optimization would produce the most reliable DEM. Besides, comparing the DEMs obtained using the other scenarios with this reference DEM enabled assessing the effect of using camera information or not, as well as the effect of GCP number and distribution.

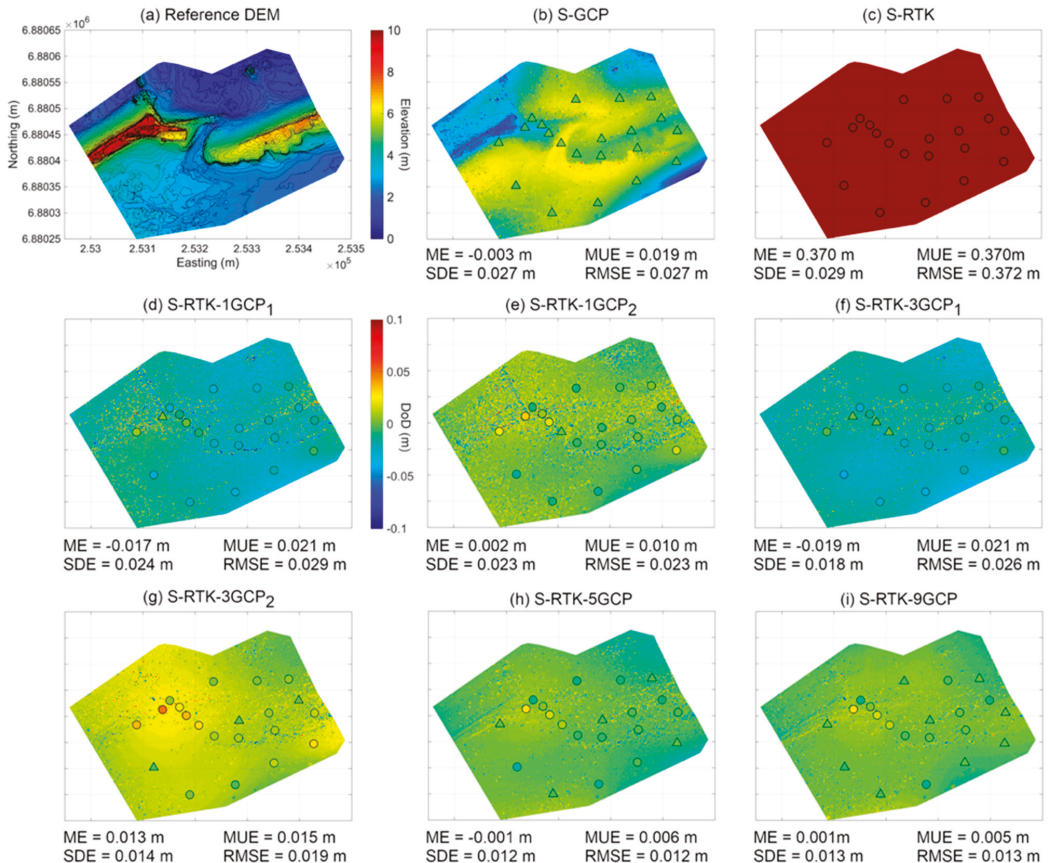


Figure 3. Assessment of model optimization at Sillon de Talbert showing (a) the reference DEM obtained with scenario S-RTK-GCP overlapped with depth contours every 0.2 m, as well as DoDs between the reference DEM and DEMs obtained using scenario (b) S-GCP, (c) S-RTK, (d) S-RTK-1GCP₁, (e) S-RTK-1GCP₂, (f) S-RTK-3GCP₁, (g) S-RTK-3GCP₂, (h) S-RTK-5GCP and (i) S-RTK-9GCP. Color coding for DoDs and error at photogrammetric targets is same for all. Photogrammetric targets used as GCPs and ChkPts are shown as triangles and circles, respectively. DEM comparisons were performed using 1 m resolution DEMs.

Figure 3 shows that the less reliable DEMs in terms of vertical precision (SDE) are those obtained using scenarios S-GCP and S-RTK, with respective precisions of 0.027 m and 0.029 m (~2 GSD). Not using camera information during photogrammetric optimization (Figure 3b), the DEM quality degraded noticeably where there was no GCP (e.g., peripheral parts of the DEM). Using only camera information (i.e., no GCPs) resulted in slightly poorer precision, but, most importantly, the S-RTK model was affected by a mean error of 0.37 m. This vertical bias was confirmed using ChkPts, showing ME = 0.36 m (Table 4). Progressively adding GCPs in addition to camera information during model optimization improved the DEM accuracy and precision (Figure 3d–i). A plateau was attained from five GCPs, whereby the bias was approximately zero and precision reached its minimum

at approximately 0.01 m (i.e., <1 GSD, Figure 3h,i). When one or three GCPs were used together with camera information, the GCP position had a noticeable effect on the DEM quality (Figure 3d–g), especially on residual bias, with variable results.

Table 4. Vertical error evaluation for the different scenarios presented in Figure 3 using ground targets (GCPs and ChkPts) measured with RTK-GNSS. The values between brackets correspond to GCP-based error.

| (a) Reference DEM: S-RTK-GCP | (b) S-GCP | (c) S-RTK |
|--|--|--|
| ME = N.A. (0.000 m) SDE = N.A. (0.002 m) | ME = N.A. (0.000 m) SDE = N.A. (0.007 m) | ME = 0.363 m (N.A.) SDE = 0.014 (N.A.) |
| (d) S-RTK-1GCP ₁ | (e) S-RTK-1GCP ₂ | (f) S-RTK-3GCP ₁ |
| ME = −0.019 m (0.003 m) SDE = 0.011 (0.000 m) | ME = 0.002 m (0.002 m) SDE = 0.012 (0.000 m) | ME = −0.022 m (0.001 m) SDE = 0.010 (0.001 m) |
| (g) S-RTK-3GCP ₂ | (h) S-RTK-5GCP | (i) S-RTK-9GCP |
| ME = 0.016 m (0.001 m) SDE = 0.014 (0.001 m) | ME = −0.001 m (0.000 m) SDE = 0.013 (0.002 m) | ME = 0.003 m (0.000 m) SDE = 0.012 (0.002 m) |

As shown in Table 4, using GCPs for error evaluation prevented detecting the vertical registration error in the DEMs and produced optimistic precision estimates. The SDE values estimated using GCPs were consistently lower by an order of magnitude than those estimated at ChkPts or those derived from model comparisons with the reference DEM (Figure 3). On the contrary, the MEs estimated using ChkPts and DEM comparisons were very consistent with each other. The SDE calculated using ChkPts remained slightly lower, suggesting better vertical precision.

The photogrammetric horizontal error estimated using GCPs and ChkPts is presented in Table 5 for the same DEMs. The results show larger horizontal error compared to vertical error for all the scenarios tested, with a ratio between horizontal and vertical error generally around 3:1. Similar to previous observations, adding GCPs in addition to camera information progressively improved the model quality mainly by reducing the horizontal bias to negligible levels (<0.01 m) from 5 GCPs, while the measurement precision remained relatively unaffected. Overall, the photogrammetric errors amounted to global precisions (RMSE_{3D}) of approximately 0.05 m under optimum configurations.

Table 5. Planimetric error (X easting and Y northing) evaluation for the different scenarios presented in Figure 3 using ground targets (GCPs and ChkPts) measured with RTK-GNSS. The values between brackets correspond to GCP-based error.

| (a) Reference DEM: S-RTK-GCP | (b) S-GCP | (c) S-RTK |
|---|---|---|
| MEX = N.A. (−0.001 m) SDEX = N.A. (0.027 m) MEY = N.A. (0.001 m) SDEY = N.A. (0.029 m) | MEX = N.A. (0.000 m) SDEX = N.A. (0.026 m) MEY = N.A. (0.000 m) SDEY = N.A. (0.027 m) | MEX = −0.022 m (N.A.) SDEX = 0.037 m (N.A.) MEY = 0.039 m (N.A.) SDEY = 0.053 m (N.A.) |
| (d) S-RTK-1GCP ₁ | (e) S-RTK-1GCP ₂ | (f) S-RTK-3GCP ₁ |
| MEX = −0.025 m (0.025 m) SDEX = 0.035 m (0.000 m) MEY = 0.036 m (0.019 m) SDEY = 0.053 m (0.000 m) | MEX = −0.019 m (−0.029 m) SDEX = 0.038 m (0.000 m) MEY = 0.037 m (−0.014 m) SDEY = 0.049 m (0.000 m) | MEX = −0.021 m (−0.013 m) SDEX = 0.037 m (0.036 m) MEY = 0.044 m (−0.007 m) SDEY = 0.048 m (0.028 m) |
| (g) S-RTK-3GCP ₂ | (h) S-RTK-5GCP | (i) S-RTK-9GCP |
| MEX = −0.019 m (0.003 m) SDEX = 0.037 m (0.022 m) MEY = 0.026 m (0.005 m) SDEY = 0.047 m (0.010 m) | MEX = −0.009 m (0.003 m) SDEX = 0.039 m (0.018 m) MEY = 0.004 m (0.009 m) SDEY = 0.047 m (0.016 m) | MEX = 0.003 m (−0.003 m) SDEX = 0.042 m (0.021 m) MEY = −0.009 m (0.004 m) SDEY = 0.050 m (0.014 m) |

3.2. La Palue Field Site

Figure 4 presents the results of the topographic measurements using RTK-GNSS mounted on a bike. The raw data counted 2036 survey points separated on average by approximately 2.5 m ($\sigma = 0.75$ m), showing that the data acquisition was carried out at an average speed of 9 km/h (2.5 m/s). Not shown in the figures, comparing the survey points with immediate neighbors (maximum distance of 0.2 m) enabled the point confidence to be evaluated at 39 locations, indicating a mean and maximum point confidence of 0.007 m and 0.015 m, respectively. As one may expect, the pitch-related errors due to the uneven terrain affecting the measurements were larger at the turning points (e.g., beach ends) since the bicycle was then moving up or down the beach (i.e., cross-shore), and where the local topography was suddenly changing (Figure 4b,c). The maximum forward slope recorded was just below 4° , traducing to maximum horizontal (dx) and vertical (dz) pitch-related errors of 0.04 m and 0.01 m, respectively. Filtering the data based on pitch-related errors (dx) resulted in the rejection of 158 points. The final number of survey points retained for comparison with photogrammetry thus amounted to 1878 (Figure 4c).

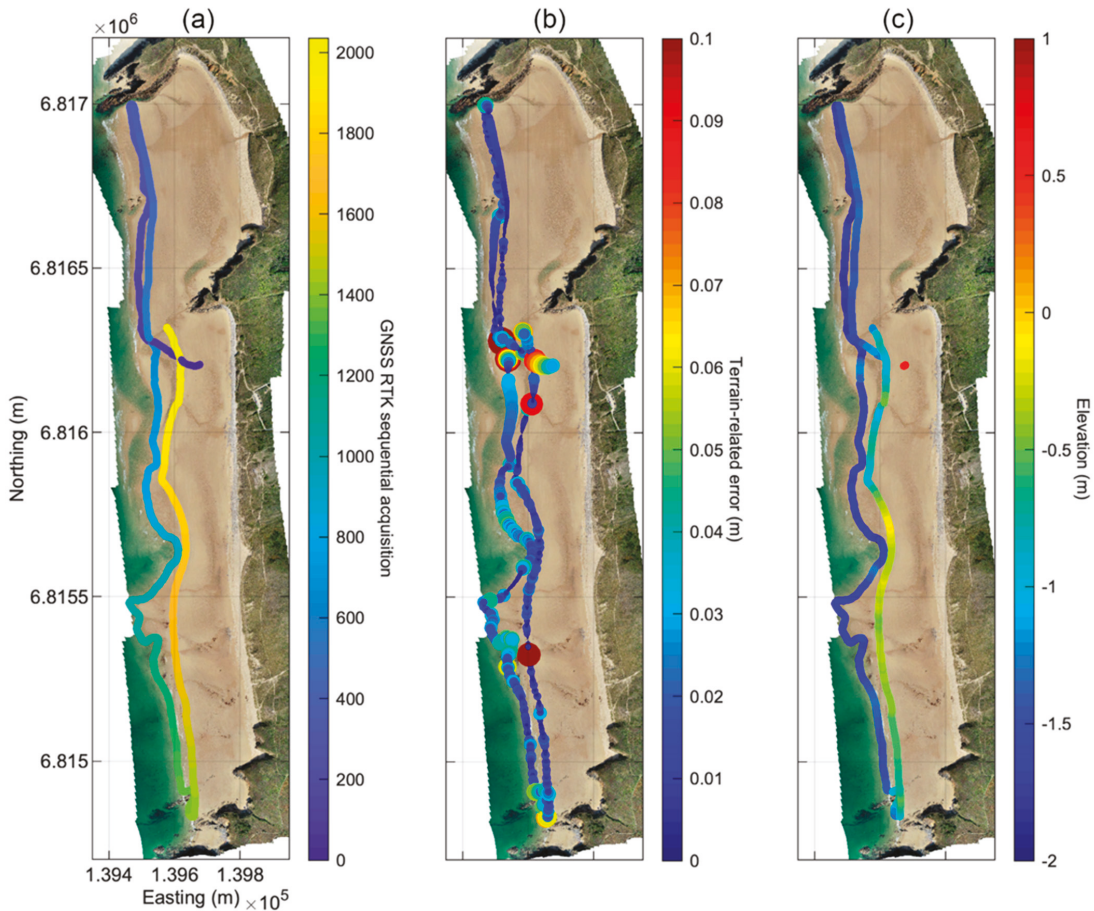


Figure 4. Verification of survey points obtained using a bike-mounted RTK-GNSS at La Palue, with (a) the chronology of point acquisition; (b) pitch-related horizontal error (dx), where marker size is proportional to error magnitude ($\times 1000$ magnification factor) and (c) the elevation of survey points retained serving as ground truths for photogrammetric evaluation.

Changing the accuracy setting during photogrammetric image alignment had major repercussions on the data processing time, as well as on the measurement density and quality (Table 6 and Figure 5). The image alignment time (1407 images) varied by two orders of magnitude, from 27 min (“Low”), through 43 min (“Medium”) and 105 min (“High₁” and “Highest”), to an outright maximum of 2721 min (~45 h, “High₂”) when “source” pair preselection was unused. The number of tie points after the alignment was the maximum using the “Highest” accuracy setting, followed by “High₁” and “High₂”, with ~1:5 variations overall (from 550,000 to 2,500,000 points). However, after the automatic filtering of less reliable tie points, the number of tie points decreased from a maximum of ~435,000 points with “High₁”, through “Medium”, “High₂”, “Highest” and, finally, “Low” accuracy settings with ~80,000 points (again, 1:5 variations overall). The comparison of the photogrammetric models obtained (DEMs at 1 m resolution) with the ground truths provided by RTK-GNSS shows a similar tendency, with DEM quality (Table 6) in decreasing order for “High₁” (SDE = 0.042 m or 1.6 GSD), “High₂”, “Medium”, “Highest” and, finally, “Low” (SDE = 0.125 m or 5 GSD) alignment accuracy with 1:3 variations overall. The photogrammetric deviations from the ground truth were essentially to be related to the measurement precision since no significant bias (i.e., ME ~0) was detected in the results. However, Figure 5 shows that the systematic errors, although of small magnitude, may still be present in the DEMs, taking the form of undulations. The color grading shows an error magnitude of ±0.04 m for the better-quality models (“High₁”, “High₂”, “Medium”), eventually exceeding 0.1 m at some locations when the “Highest” and “Low” accuracy settings were used. Using ground targets (GCPs and ChkPts) for error evaluation produced error statistics with no appreciable differences between the scenarios tested (differences were found to be non-significant at $p = 0.05$), and, for this reason, they are not presented.

Table 6. Effect of changing the image alignment accuracy setting during sparse DEM reconstruction at La Palue field site in terms of processing time, number of tie points (before and after filtering) and measurement error. Deviations between photogrammetric models (1 m resolution) and GNSS-RTK survey points, from which vertical error statistics are extracted, are presented in Figure 5.

| | (a) Low | (b) Medium | (c) High ₁ | (d) High ₂ | (e) Highest |
|--------------------|----------------|----------------|-----------------------|-----------------------|----------------|
| Alignment time | 27 min | 43 min | 105 min | 2721 min | 105 min |
| Initial tie points | 567,716 | 1,918,509 | 2,102,195 | 1,967,440 | 2,482,173 |
| Final tie points | 79,909 | 412,200 | 435,657 | 402,828 | 320,413 |
| Error statistics | ME = 0.000 m | ME = −0.001 m | ME = 0.000 m | ME = −0.002 m | ME = −0.004 m |
| | MUE = 0.096 m | MUE = 0.038 m | MUE = 0.031 m | MUE = 0.033 m | MUE = 0.045 m |
| | SDE = 0.125 m | SDE = 0.049 m | SDE = 0.042 m | SDE = 0.044 m | SDE = 0.062 m |
| | RMSE = 0.125 m | RMSE = 0.049 m | RMSE = 0.042 m | RMSE = 0.044 m | RMSE = 0.062 m |
| | Max = 0.368 m | Max = 0.145 m | Max = 0.117 m | Max = 0.144 m | Max = 0.213 m |

In comparison to previous tests, changing the depth filtering setting during dense model reconstruction had lesser effects on the DEM quality. Using RTK-GNSS for ground truthing produced nearly identical error statistics for all the settings, shown by SDE = 0.033 m for no filtering and “Mild” and SDE = 0.032 m for the “Moderate” and “Aggressive” settings, respectively. For this reason, Table 7 presents errors evaluated as DEM comparisons using the case of no filtering as a reference. Deviations from this reference DEM were essentially found at steep sections of the study site (e.g., cliff faces), resulting in potentially large elevation deviations over small spatial extents (indicated by the neat difference between MUE and SDE). Elevation deviations increased (in magnitude and occurrence) with increasing depth filtering, until a plateau was reached (“Moderate” and “Aggressive” have identical error statistics).

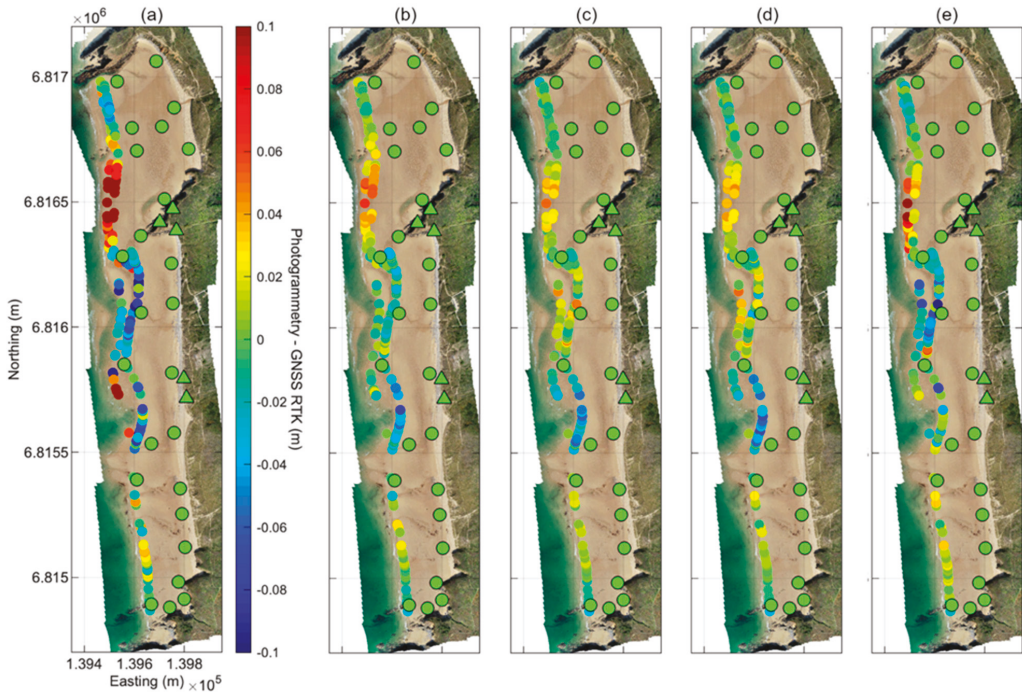


Figure 5. Evaluation of image alignment accuracy setting during sparse DEM reconstruction showing vertical errors at 177 RTK-GNSS survey points for (a) low, (b) medium, (c,d) high and (e) highest alignment accuracy setting. For all scenarios tested, “source” reference pair preselection was used, except for panel (d). Photogrammetric targets used as GCPs and ChkPs are shown as triangles and circles, respectively. Error evaluation was performed using 1 m resolution DEMs.

Table 7. Evaluation of depth filtering during dense DEM reconstruction at La Palue field site. Except for the reference DEM using no depth filtering, for which errors are estimated in comparison to 1381 RTK-GNSS survey points, vertical error statistics are the result of intercomparing DEMs with the reference DEM. All DEMs evaluated were reconstructed using “High” image alignment accuracy (Figure 5c) and “High” reconstruction quality for sparse and dense DEM reconstructions, respectively (cf. explanations in the text). Evaluations were performed using 0.1 m resolution DEMs.

| (a) Reference DEM | (b) Mild | (c) Moderate | (d) Aggressive |
|-------------------|-------------------|-------------------|-------------------|
| ME = 0.001 m | ME = 0.000 m | ME = −0.001 m | ME = −0.001 m |
| MUE = 0.027 m | MUE = 0.003 m | MUE = 0.005 m | MUE = 0.005 m |
| SDE = 0.033 m | SDE = 0.072 m | SDE = 0.084 m | SDE = 0.084 m |
| RMSE = 0.033 m | RMSE = 0.072 m | RMSE = 0.084 m | RMSE = 0.084 m |
| Maximum = 0.186 m | Maximum = 76.23 m | Maximum = 77.33 m | Maximum = 77.33 m |

Figure 6 presents the DEM obtained at La Palue using the standard workflow designed for this study (Table 2) and produced on a 0.1 m grid. The measured beach topography shows marked 3D morphologies, particularly on the northern side of Kerdra point and at the seaward DEM boundary, with numerous channels incised in the sand and humps and hollows representing sand accumulations and depressions (Figure 6a). The smaller-scale topography, which is apparent in the orthophoto and is suggested by uneven and rugged elevation contours, is somehow subdued by the general topography when viewed at this scale. The fine grid spacing was advantageous to allow comparisons at a large

number of RTK-GNSS survey points (1381 points). The photogrammetric errors (Figure 6b) show a similar spatial organization with the ones identified previously using 1 m DEMs reconstructed from sparse point clouds (Figure 5). DEM precision using the standard workflow was characterized by $SDE = 0.032$ m (i.e., 1.2 GSD, Figure 6c,d).

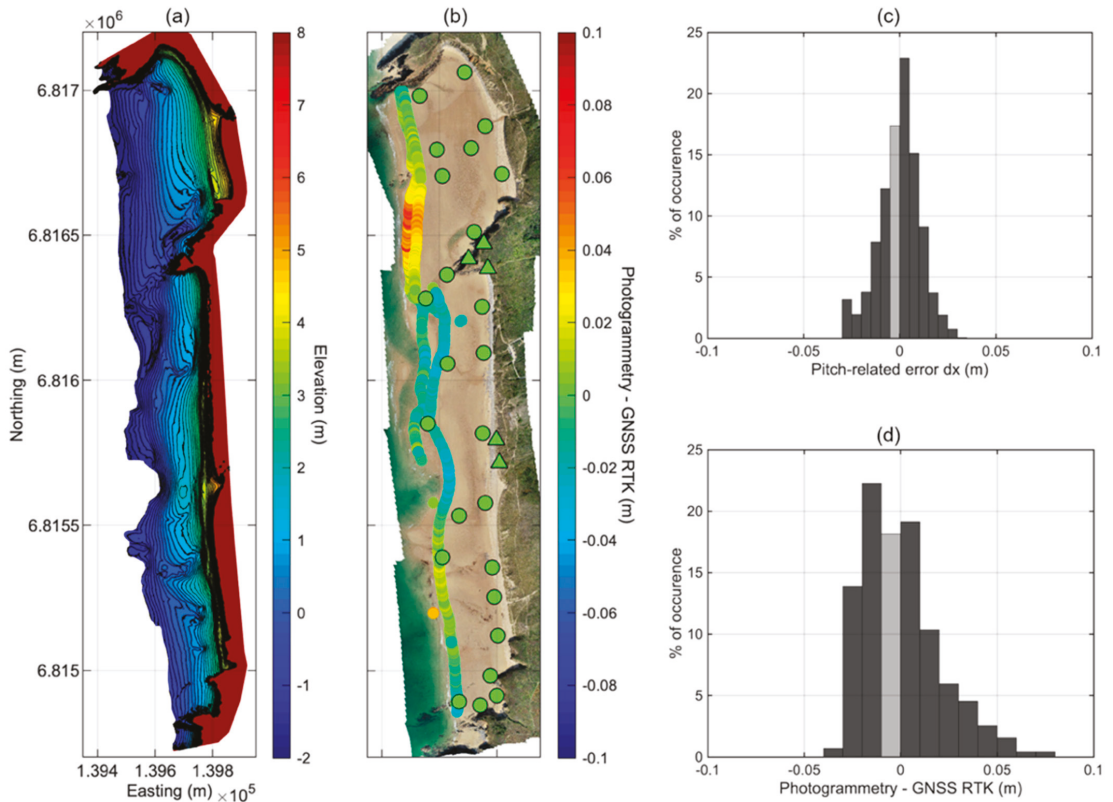


Figure 6. Quality assessment of the 0.1 m resolution photogrammetric DEM obtained using the standard workflow. (a) DEM overlapped with depth contours every 0.2 m; (b) vertical error at photogrammetric targets (GCPs and ChkPts) and 1381 RTK-GNSS survey points; (c) probability distribution function (PDF) of pitch-related error (dx) binned at 0.005 m and (d) PDF of photogrammetric vertical error in comparison to RTK-GNSS survey points binned at 0.01 m.

Four repeat photogrammetric surveys carried out between September 2020 and April 2021 are compared in Figure 7. Using the range and standard deviation of repeat bed elevations, representing the temporal variability in the elevation for each surface cell, shows that large portions of the back beach (i.e., dune and cliff tops), as well as rock deposits and outcrops, can be considered stable over the 7-month period during which the DEMs were obtained (here defined as cells with an elevation range between the four surveys below 0.035 m). Filtering the unstable surface cells left 587,105 invariant cells at a horizontal resolution of 0.1 m, and characterized by an overall (i.e., averaged over all the stable cells) range and standard deviation of repeat bed elevations of 0.025 m and 0.011 m, respectively. Averaging the repeat elevations over the stable cells of the DEM produced a multi-temporal ground truth backing the entire beach over all the sides except seaward, and with elevations spanning over 50 m (Figure 7d). The comparison of the 17 September 2020 survey with the ground truth (Figure 7e) suggests centimeter-scale deformations, which may echo deformations previously identified using RTK-GNSS survey

points (Figures 5 and 6). The quantitative comparison shows ME and SDE of $\sim 10^{-3}$ m and 0.01 m, respectively.

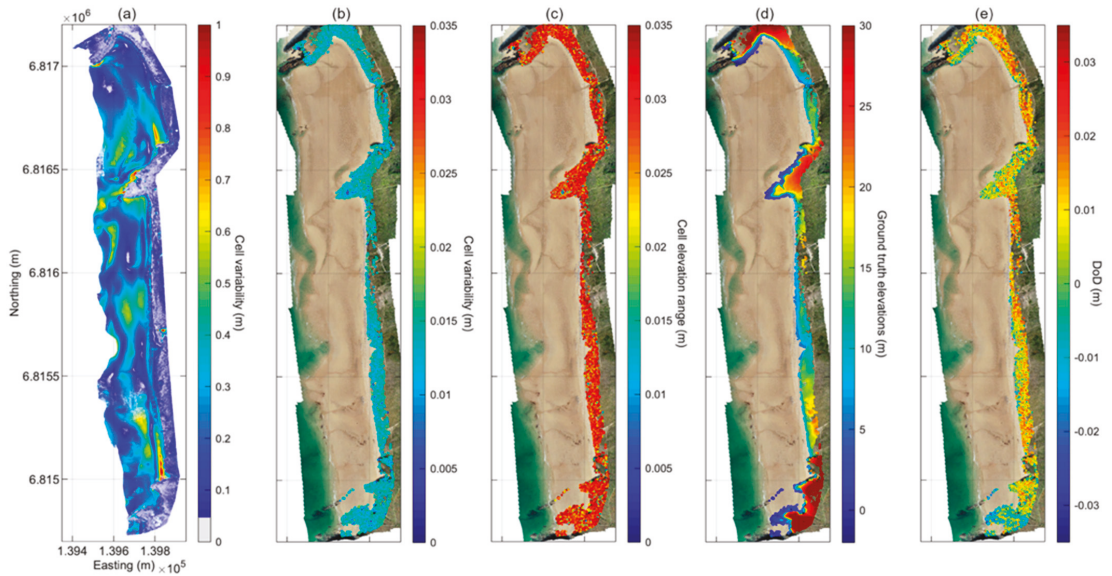


Figure 7. Assessment of photogrammetric workflow replicability at La Palue. (a) Cell variability using all repeat surveys ($n = 4$); (b) cell variability and (c) cell elevation range after thresholding to retain only supposedly stable cells ($n = 587,105$ cells); (d) resulting ground truth elevations over stable cells and (e) comparison of 17 September 2020 survey with the ground truth.

Figure 8 presents the first applications of very-high-resolution coastal monitoring at the La Palue field site, used here for beachface topographic complexity detection and mapping. Three zones are analyzed in more detail, corresponding to regions of return flows, creating narrow channels incising sand superimposed with complex small-scale topographies, such as (mega)ripples and hummocky patterns of different forms and dimensions. For detecting submeter bedforms, the 0.1 m resolution DEM was detrended from metric topography by subtracting the 1 m resolution DEM. Doing so left only the small-scale topographies not accounted for in the DEMs with resolutions of 1 m or above (Figure 8b).

The qualitative analysis of the orthophotos and DEMs suggests that the approach was suitable for characterizing sub-metric beach topography, creating realistic maps of the bedform arrangement at the beach scale (cf. Figure 8a,b). The submeter-scale topography is most evident at steep sections of the beach, such as seaward of the berm and where there is a sand-cobble transition, but is otherwise widely spread. It includes large patches of ripples and megaripples, channels of varied dimensions, and zones of water resurgence. Quantitatively, the net volume embodied in the sub-metric topography amounted to ~ 6000 m³, which is equivalent to a layer of sand of 0.011 m over the entire beach.

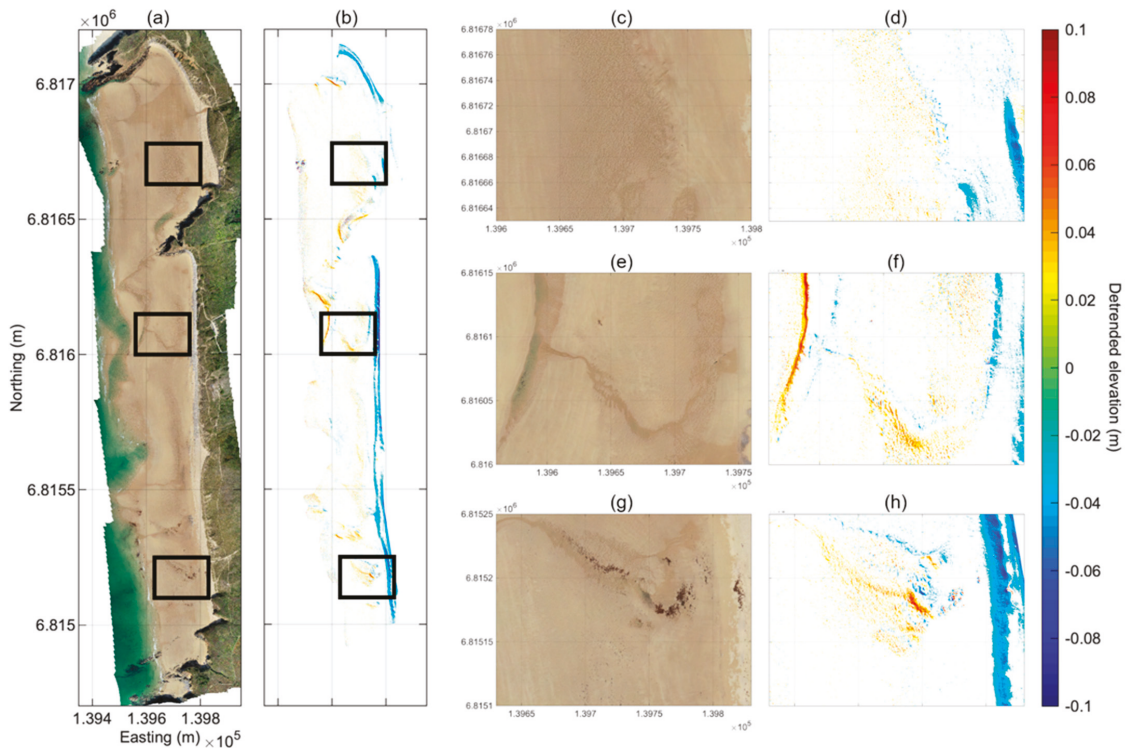


Figure 8. Application of RTK quadcopter and SfM photogrammetry for very-high-resolution measurement of topographic roughness and bedform mapping at the beach-scale at La Palue field site. (a) Orthophoto and the different zones investigated in panels (c–h); (b) 0.1 m resolution DEM detrended from metric topography (cf. explanation in the text); (c–h) 0.1 m resolution orthophotos and detrended DEMs cropped to the areas of interest. Detrended elevations below 0.02 m are not shown to help with figure comprehension. The colorbar is same for all DEMs.

4. Discussion and Conclusions

This study has tested the possibility of using SfM photogrammetry augmented with an RTK quadcopter for monitoring coastal topographic complexity at the beach-scale. The survey method had to respond to both resolution and time constraints, with final DEM resolutions of 0.1 m for a realistic representation of the topo-morphological features from submeter dimensions and a survey completed in two hours around low tide to cover the intertidal zone. The method implemented had to achieve effective measurements in a challenging environment characterized, for instance, by large topographic variations, differences in bed cover, such as rough surfaces alternating with textureless and reflective surfaces, such as sand, and the presence of water as thin patches or deeper puddles and channels, which can all represent important difficulties for photogrammetry.

To evaluate the effective measurement resolutions and precisions achieved by the survey method, and, hence, to be able to identify suitable protocols for collecting and processing the data that surpassed the above constraints, purpose-built SfM workflows were applied to aerial images collected at two coastal field sites (La Palue and the breach at Sillon de Talbert) and tested against different ground truths. Of interest for this application, because of their impact on the data collection time and DEM quality, we specifically assessed the effect of image resolution and using GCPs in addition to camera information during BBA. As much as possible, the error evaluations were diversified to enhance the spatial

coverage and the level of error detection afforded and, hence, to increase the chance of obtaining reliable error statistics.

Ideally, complete DEM comparisons should be undertaken to fully characterize the error magnitude and spatial distribution as it is now well-known that photogrammetric measurements can be affected by complex 3D deformations (e.g., the dome effect), which may remain undetected when using sparse ground controls [67,68]. In the absence of suitable ground truth at this scale, we analyzed the DoDs for different processing scenarios. This strategy proved effective for assessing the DEM reliability due to variations in the GCP number and distribution, showing that, in addition to aerial controls, at least five GCPs were necessary at Sillon de Talbert to achieve optimum quality that minimized measurement bias and random errors. Under this configuration, the global vertical precision (RMSE) improved two-fold in comparison to a processing workflow using all the targets as GCPs ($n = 21$) but no aerial controls. The benefit resulting from using RTK image positioning resided principally in an improved 3D geometry of the model, particularly at zones with limited to no ground controls. Using aerial controls only (akin to direct georeferencing), our results showed that the photogrammetric results were affected by vertical bias, explaining most of the error. The presence of vertical bias in models obtained using DG has been reported before and was explained by inaccurate IOP calibration (e.g., Refs. [49,52,56,69,70]). Likewise, our results showed that the addition of a single GCP was enough to reduce the vertical bias to the GSD level together with RMSE ~ 2 GSD, but the addition of other GCPs during BBA further improved the photogrammetric quality until a plateau was attained from 5 GCPs, with the RMSE mostly below 1 GSD.

Using ChkPts measured with RTK-GNSS enabled the assessment of both the horizontal and vertical error in RTK-assisted photogrammetry, showing a similar tendency to the DoD analysis, whereby 5 GCPs were necessary to achieve optimum accuracy and precision. Under this configuration, the global 3D precision (RMSE) remained below 0.05 m (3.6 GSD). We observed larger horizontal error over vertical error (ratios as large as 1:4), which is contrary to most previous research, where, generally, horizontal error is the lower bound (e.g., Refs. [46,56]). A reason may be the use of suboptimal photogrammetric targets for the present study. The targets we used had no marks at the center point where RTK-GNSS measurement is carried out, meaning that the target geolocation in the images can be prone to large horizontal uncertainties. The targets have been upgraded recently to include a chequerboard-like pattern, which has been recommended for pinpoint accuracy in RTK-GNSS measures and image positioning [71]. Nevertheless, we showed that error evaluation using ground targets can produce optimistic estimates, particularly when the error is evaluated at GCPs (used for photogrammetric processing). A difference in the error estimates between GCPs and ChkPts was also identified in Sanz-Ablanedo et al. [46], where it was suggested using a magnification coefficient to artificially inflate the error measures in the absence of independent ground controls (i.e., ChkPts). Although it may prove useful for guessing the precision within results (SDE), we showed, however, that using GCPs failed at detecting bias in the measurements, thus reinforcing that, ideally, numerous and well-distributed independent ChkPts should be used to characterize the DEM error.

Larger-scale experiments were conducted at La Palue field site to validate the workflow. Three operators were necessary to carry out the field operations, which included GNSS measurements of ~ 20 photogrammetric targets distributed over the whole beach ($\sim 2500 \times 400$ m²), using the bike-mounted GNSS to acquire ground truth data near the water line, performing all the flights, for finally removing the targets, all within a two-hour window around low tide. Five “permanent targets” were prepared before the September survey, consisting of red-painted crosses. They were created over flat and stable areas of the study site, all man-made and localized above the highest high tides so as not to introduce error in photogrammetry, which could otherwise arise due to imprecise identification in images or terrain changes. This means, however, that the spatial distribution of these permanent targets was limited to the landward side of the site.

Between 177 and 1381 RTK-GNSS survey points were used to assess the photogrammetric reconstruction for different processing scenarios (e.g., varying image resolution) both before and after model densification. In comparison to Sillon de Talbert, the best-case vertical precision achieved at La Palue was slightly worse, which may be related to an increased flying height and the different error evaluation methods used. Larger DEM error was measured at peripheral zones where the effective overlap index (i.e., apparition in images) is reduced, which is consistent with previous observations (e.g., Refs. [44,46,72]). Although of a small magnitude, the effect was increasing measurement noise and potentially centimeter-scale deformations of the photogrammetric model. Enlarging the survey area, especially on the seaward side (e.g., by adding an additional alongshore flight track), could strengthen the photogrammetric block and reduce the error at these distant locations. Regardless of the model densification, the DEM errors showed a similar pattern (Figure 5), reinforcing the fact that the DEM shape is essentially the result of image alignment and photogrammetric optimization taking place before dense point matching. The image resolution used for initial tie point detection and 3D reconstruction played a large role in mitigating or inflating the error, with a ratio of 1:3 depending on the setting. The best results were obtained using “High” alignment accuracy, followed by “Medium” and “Highest”, with the same order also observed in terms of the number of tie points retained. This suggests that the alignment accuracy setting is not fully representative of the tie point quality (e.g., density and precision). With our findings, we also suggest using RTK image positions (pair pre-selection) for speeding up image alignment, with two orders of magnitude improvement together with enhanced tie point quantity and quality. The final evaluation using four repeat surveys demonstrated a very good reproducibility of the complete workflow for DEM collection, shown by a large number of surface cells over hypothetical stable zones (~5870 m²) characterized by a range between repeat elevations below 3.5 cm and a standard deviation of 1.1 cm on average.

Using the measurement workflow enabled characterizing the submeter beach topographic roughness, creating realistic maps of bedform arrangement at the beach scale, whose interpretation is eased further through the provision of very-high-resolution orthophotos (0.1 m). This small-scale topographic complexity (e.g., patches of ripples and megaripples) was found to be widespread and represented a large volume of sediment not represented in the DEMs with metric resolutions and, hence, not accounted for in typical beach surveys. Through pursuing surveys, follow-up studies will be looking at bedform classification and interpreting the spatial patterns observed and their temporal evolution in relation to driving hydrodynamic processes. For dynamic environments such as beaches, this study further exemplified that photogrammetry has the potential to help characterizing morphological changes across a wide range of spatial and temporal scales.

Author Contributions: Conceptualization, S.B.; methodology, S.B. and J.A.; software, S.B. and P.S.; validation, S.B., P.S. and J.A.; formal analysis, S.B.; investigation, S.B.; data curation, S.B.; writing—original draft preparation, S.B.; writing—review and editing, S.B., P.S. and J.A.; visualization, S.B.; funding acquisition, S.B. All authors have read and agreed to the published version of the manuscript.

Funding: This research received funding from LTSER-France “Zone Atelier Brest-Iroise”.

Data Availability Statement: DEMs and orthophotos collected at La Palue can be accessed at <https://doi.org/10.35110/092918bf-dfb1-4d8e-805b-6bd420158160> (accessed on 6 March 2022).

Acknowledgments: The authors wish to thank LTSER-France “Zone Atelier Brest-Iroise” for financing data acquisition at La Palue field site, as well as Stevonn Lamarche and Valentin Gil for help with RTK-GNSS measurements. Sillon de Talbert is a monitoring site of the French coastal observatory SNO-DYNALIT (<https://www.dynalit.fr/>, accessed on 6 March 2022). Four reviewers provided comments on the initial manuscript, whose help is gratefully acknowledged.

Conflicts of Interest: The authors declare no conflict of interest. The funders had no role in the design of the study; in the collection, analyses, or interpretation of data; in the writing of the manuscript or in the decision to publish the results.

References

- Montaño, J.; Coco, G.; Antolínez, J.A.A.; Beuzen, T.; Bryan, K.R.; Cagigal, L.; Castelle, B.; Davidson, M.A.; Goldstein, E.B.; Ibaceta, R.; et al. Blind Testing of Shoreline Evolution Models. *Sci. Rep.* **2020**, *10*, 2137. [[CrossRef](#)] [[PubMed](#)]
- Robinet, A.; Castelle, B.; Idier, D.; Harley, M.D.; Splinter, K.D. Controls of Local Geology and Cross-Shore/Longshore Processes on Embayed Beach Shoreline Variability. *Mar. Geol.* **2020**, *422*, 106118. [[CrossRef](#)]
- D’Anna, M.; Castelle, B.; Idier, D.; Rohmer, J.; Le Cozannet, G.; Thieblemont, R.; Bricheno, L. Uncertainties in Shoreline Projections to 2100 at Truc Vert Beach (France): Role of Sea-Level Rise and Equilibrium Model Assumptions. *J. Geophys. Res. Earth Surf.* **2021**, *126*, e2021JF006160. [[CrossRef](#)]
- Adebisi, N.; Balogun, A.-L.; Mahdianpari, M.; Min, T.H. Assessing the Impacts of Rising Sea Level on Coastal Morpho-Dynamics with Automated High-Frequency Shoreline Mapping Using Multi-Sensor Optical Satellites. *Remote Sens.* **2021**, *13*, 3587. [[CrossRef](#)]
- Scardino, G.; Sabatier, F.; Scicchitano, G.; Piscitelli, A.; Milella, M.; Vecchio, A.; Anzidei, M.; Mastronuzzi, G. Sea-Level Rise and Shoreline Changes Along an Open Sandy Coast: Case Study of Gulf of Taranto, Italy. *Water* **2020**, *12*, 1414. [[CrossRef](#)]
- Michel, C.; Bot, S.L.; Druine, F.; Costa, S.; Levoy, F.; Dubrulle-Brunaud, C.; Lafite, R. Stages of Sedimentary Infilling in a Hypertidal Bay Using a Combination of Sedimentological, Morphological and Dynamic Criteria (Bay of Somme, France). *J. Maps* **2017**, *13*, 858–865. [[CrossRef](#)]
- Franzetti, M.; Le Roy, P.; Delacourt, C.; Garlan, T.; Cancouët, R.; Sukhovich, A.; Deschamps, A. Giant Dune Morphologies and Dynamics in a Deep Continental Shelf Environment: Example of the Banc Du Four (Western Brittany, France). *Mar. Geol.* **2013**, *346*, 17–30. [[CrossRef](#)]
- Bertin, S.; Groom, J.; Friedrich, H. Isolating Roughness Scales of Gravel-Bed Patches. *Water Resour. Res.* **2017**, *53*, 6841–6856. [[CrossRef](#)]
- Bertin, S.; Friedrich, H. Effects of Sand Addition and Bed Flushing on Gravel Bed Surface Microtopography and Roughness. *Water Resour. Res.* **2019**, *55*, 8076–8095. [[CrossRef](#)]
- Powell, D.M.; Ockelford, A.; Rice, S.P.; Hillier, J.K.; Nguyen, T.; Reid, I.; Tate, N.J.; Ackerley, D. Structural Properties of Mobile Armors Formed at Different Flow Strengths in Gravel-Bed Rivers. *J. Geophys. Res. Earth Surf.* **2016**, *121*, 1494–1515. [[CrossRef](#)]
- van Rijn, L.C. Unified View of Sediment Transport by Currents and Waves. I: Initiation of Motion, Bed Roughness, and Bed-Load Transport. *J. Hydraul. Eng.* **2007**, *133*, 649–667. [[CrossRef](#)]
- Castelle, B.; Bonneton, P.; Sénéchal, N.; Dupuis, H.; Butel, R.; Michel, D. Dynamics of Wave-Induced Currents over an Alongshore Non-Uniform Multiple-Barred Sandy Beach on the Aquitanian Coast, France. *Cont. Shelf Res.* **2006**, *26*, 113–131. [[CrossRef](#)]
- Turki, I.; Le Bot, S.; Lecoq, N.; Shafiei, H.; Michel, C.; Deloffre, J.; Héquette, A.; Sipka, V.; Lafite, R. Morphodynamics of Intertidal Dune Field in a Mixed Wave-Tide Environment: Case of Baie de Somme in Eastern English Channel. *Mar. Geol.* **2021**, *431*, 106381. [[CrossRef](#)]
- Hoekstra, P.; Bell, P.; van Santen, P.; Roode, N.; Levoy, F.; Whitehouse, R. Bedform Migration and Bedload Transport on an Intertidal Shoal. *Cont. Shelf Res.* **2004**, *24*, 1249–1269. [[CrossRef](#)]
- van Lancker, V.; Lanckneus, J.; Hearn, S.; Hoekstra, P.; Levoy, F.; Miles, J.; Moerkerke, G.; Monfort, O.; Whitehouse, R. Coastal and Nearshore Morphology, Bedforms and Sediment Transport Pathways at Teignmouth (UK). *Cont. Shelf Res.* **2004**, *24*, 1171–1202. [[CrossRef](#)]
- Biausque, M.; Grottoli, E.; Jackson, D.W.T.; Cooper, J.A.G. Multiple Intertidal Bars on Beaches: A Review. *Earth-Sci. Rev.* **2020**, *210*, 103358. [[CrossRef](#)]
- Matsumoto, H.; Young, A.P.; Guza, R.T. Cusp and Mega Cusp Observations on a Mixed Sediment Beach. *Earth Space Sci.* **2020**, *7*, e2020EA001366. [[CrossRef](#)]
- Dehouck, A.; Dupuis, H.; Sénéchal, N. Pocket Beach Hydrodynamics: The Example of Four Macrotidal Beaches, Brittany, France. *Mar. Geol.* **2009**, *266*, 1–17. [[CrossRef](#)]
- Castelle, B.; Bujan, S.; Marieu, V.; Ferreira, S. 16 Years of Topographic Surveys of Rip-Channelled High-Energy Meso-Macrotidal Sandy Beach. *Sci. Data* **2020**, *7*, 410. [[CrossRef](#)]
- Harley, M.D.; Turner, I.L.; Short, A.D.; Ranasinghe, R. Assessment and Integration of Conventional, RTK-GPS and Image-Derived Beach Survey Methods for Daily to Decadal Coastal Monitoring. *Coast. Eng.* **2011**, *58*, 194–205. [[CrossRef](#)]
- Baptista, P.; Cunha, T.; Bernardes, C.; Gama, C.; Ferreira, O.; Dias, A. A Precise and Efficient Methodology to Analyse the Shoreline Displacement Rate. *J. Coast. Res.* **2011**, *27*, 223–232. [[CrossRef](#)]
- Baptista, P.; Bastos, L.; Bernardes, C.; Cunha, T.; Dias, J. Monitoring Sandy Shores Morphologies by DGPS—A Practical Tool to Generate Digital Elevation Models. *J. Coast. Res.* **2008**, *24*, 1516–1528. [[CrossRef](#)]
- Jaud, M.; Delacourt, C.; Le Dantec, N.; Allemand, P.; Ammann, J.; Grandjean, P.; Nouaille, H.; Prunier, C.; Cuq, V.; Augereau, E.; et al. Diachronic UAV Photogrammetry of a Sandy Beach in Brittany (France) for a Long-Term Coastal Observatory. *IJGI* **2019**, *8*, 267. [[CrossRef](#)]
- Talavera, L.; Del Río, L.; Benavente, J.; Barbero, L.; López-Ramírez, J.A. UAS as Tools for Rapid Detection of Storm-Induced Morphodynamic Changes at Camposoto Beach, SW Spain. *Int. J. Remote Sens.* **2018**, *39*, 5550–5567. [[CrossRef](#)]
- Turner, I.L.; Harley, M.D.; Drummond, C.D. UAVs for Coastal Surveying. *Coast. Eng.* **2016**, *114*, 19–24. [[CrossRef](#)]
- Lowe, D.G. Distinctive Image Features from Scale-Invariant Keypoints. *Int. J. Comput. Vis.* **2004**, *60*, 91–110. [[CrossRef](#)]
- James, M.R.; Chandler, J.H.; Eltner, A.; Fraser, C.; Miller, P.E.; Mills, J.P.; Noble, T.; Robson, S.; Lane, S.N. Guidelines on the Use of Structure-from-Motion Photogrammetry in Geomorphic Research. *Earth Surf. Process. Landf.* **2019**, *44*, 2081–2084. [[CrossRef](#)]

28. Eltner, A.; Kaiser, A.; Castillo, C.; Rock, G.; Neugirg, F.; Abellán, A. Image-Based Surface Reconstruction in Geomorphometry: Merits, Limits and Developments. *Earth Surf. Dyn.* **2016**, *4*, 359–389. [\[CrossRef\]](#)
29. Heays, K.G.; Friedrich, H.; Melville, B.W. Laboratory Study of Gravel-Bed Cluster Formation and Disintegration. *Water Resour. Res.* **2014**, *50*, 2227–2241. [\[CrossRef\]](#)
30. Bertin, S.; Friedrich, H. Field Application of Close-Range Digital Photogrammetry (CRDP) for Grain-Scale Fluvial Morphology Studies: Fluvial Grain-Scale Morphology and Field Application of Photogrammetry. *Earth Surf. Process. Landf.* **2016**, *41*, 1358–1369. [\[CrossRef\]](#)
31. Brunier, G.; Fleury, J.; Anthony, E.J.; Gardel, A.; Dussouillez, P. Close-Range Airborne Structure-from-Motion Photogrammetry for High-Resolution Beach Morphometric Surveys: Examples from an Embayed Rotating Beach. *Geomorphology* **2016**, *261*, 76–88. [\[CrossRef\]](#)
32. Casella, E.; Rovere, A.; Pedroncini, A.; Mucerino, L.; Casella, M.; Cusati, L.A.; Vacchi, M.; Ferrari, M.; Firpo, M. Study of Wave Runup Using Numerical Models and Low-Altitude Aerial Photogrammetry: A Tool for Coastal Management. *Estuar. Coast. Shelf Sci.* **2014**, *149*, 160–167. [\[CrossRef\]](#)
33. Casella, E.; Rovere, A.; Pedroncini, A.; Stark, C.P.; Casella, M.; Ferrari, M.; Firpo, M. Drones as Tools for Monitoring Beach Topography Changes in the Ligurian Sea (NW Mediterranean). *Geo-Mar. Lett.* **2016**, *36*, 151–163. [\[CrossRef\]](#)
34. Groom, J.; Bertin, S.; Friedrich, H. Assessing Intra-Bar Variations in Grain Roughness Using Close-Range Photogrammetry. *J. Sediment. Res.* **2018**, *88*, 555–567. [\[CrossRef\]](#)
35. Li, W.; Bertin, S.; Friedrich, H. Combining Structure from Motion and Close-Range Stereo Photogrammetry to Obtain Scaled Gravel Bar DEMs. *Int. J. Remote Sens.* **2018**, *39*, 9269–9293. [\[CrossRef\]](#)
36. Bertin, S.; Friedrich, H.; Delmas, P.; Chan, E.; Gimel'farb, G. Digital Stereo Photogrammetry for Grain-Scale Monitoring of Fluvial Surfaces: Error Evaluation and Workflow Optimisation. *ISPRS J. Photogramm. Remote Sens.* **2015**, *101*, 193–208. [\[CrossRef\]](#)
37. Laporte-Fauret, Q.; Marieu, V.; Castelle, B.; Michalet, R.; Bujan, S.; Rosebery, D. Low-Cost UAV for High-Resolution and Large-Scale Coastal Dune Change Monitoring Using Photogrammetry. *J. Mar. Sci. Eng.* **2019**, *7*, 63. [\[CrossRef\]](#)
38. Seymour, A.C.; Ridge, J.T.; Rodriguez, A.B.; Newton, E.; Dale, J.; Johnston, D.W. Deploying Fixed Wing Unoccupied Aerial Systems (UAS) for Coastal Morphology Assessment and Management. *J. Coast. Res.* **2018**, *34*, 704–717. [\[CrossRef\]](#)
39. Gonçalves, J.A.; Henriques, R. UAV Photogrammetry for Topographic Monitoring of Coastal Areas. *ISPRS J. Photogramm. Remote Sens.* **2015**, *104*, 101–111. [\[CrossRef\]](#)
40. Guisado-Pintado, E.; Jackson, D.W.T.; Rogers, D. 3D Mapping Efficacy of a Drone and Terrestrial Laser Scanner over a Temperate Beach-Dune Zone. *Geomorphology* **2019**, *328*, 157–172. [\[CrossRef\]](#)
41. Nahon, A.; Molina, P.; Blázquez, M.; Simeon, J.; Capo, S.; Ferrero, C. Corridor Mapping of Sandy Coastal Foredunes with UAS Photogrammetry and Mobile Laser Scanning. *Remote Sens.* **2019**, *11*, 1352. [\[CrossRef\]](#)
42. Madurapperuma, B.; Lamping, J.; McDermott, M.; Murphy, B.; McFarland, J.; Deyoung, K.; Smith, C.; MacAdam, S.; Monroe, S.; Corro, L.; et al. Factors Influencing Movement of the Manila Dunes and Its Impact on Establishing Non-Native Species. *Remote Sens.* **2020**, *12*, 1536. [\[CrossRef\]](#)
43. James, M.R.; Robson, S.; d'Oleire-Oltmanns, S.; Niethammer, U. Optimising UAV Topographic Surveys Processed with Structure-from-Motion: Ground Control Quality, Quantity and Bundle Adjustment. *Geomorphology* **2017**, *280*, 51–66. [\[CrossRef\]](#)
44. Oniga, V.-E.; Breaban, A.-I.; Pfeifer, N.; Chirila, C. Determining the Suitable Number of Ground Control Points for UAS Images Georeferencing by Varying Number and Spatial Distribution. *Remote Sens.* **2020**, *12*, 876. [\[CrossRef\]](#)
45. Brunier, G.; Michaud, E.; Fleury, J.; Anthony, E.J.; Morvan, S.; Gardel, A. Assessing the Relationship between Macro-Faunal Burrowing Activity and Mudflat Geomorphology from UAV-Based Structure-from-Motion Photogrammetry. *Remote Sens. Environ.* **2020**, *241*, 111717. [\[CrossRef\]](#)
46. Sanz-Ablanedo, E.; Chandler, J.H.; Rodríguez-Pérez, J.R.; Ordóñez, C. Accuracy of Unmanned Aerial Vehicle (UAV) and SfM Photogrammetry Survey as a Function of the Number and Location of Ground Control Points Used. *Remote Sens.* **2018**, *10*, 1606. [\[CrossRef\]](#)
47. James, M.R.; Robson, S.; Smith, M.W. 3-D Uncertainty-Based Topographic Change Detection with Structure-from-Motion Photogrammetry: Precision Maps for Ground Control and Directly Georeferenced Surveys. *Earth Surf. Process. Landf.* **2017**, *42*, 1769–1788. [\[CrossRef\]](#)
48. Cledat, E.; Jospin, L.V.; Cucci, D.A.; Skaloud, J. Mapping Quality Prediction for RTK/PPK-Equipped Micro-Drones Operating in Complex Natural Environment. *ISPRS J. Photogramm. Remote Sens.* **2020**, *167*, 24–38. [\[CrossRef\]](#)
49. Bertin, S.; Levy, B.; Gee, T.; Delmas, P. Geomorphic Change Detection Using Cost-Effective Structure-from-Motion Photogrammetry: Evaluation of Direct Georeferencing from Consumer-Grade UAS at Orewa Beach (New Zealand). *Photogramm. Eng. Remote Sens.* **2020**, *86*, 289–298. [\[CrossRef\]](#)
50. Carbonneau, P.E.; Dietrich, J.T. Cost-Effective Non-Metric Photogrammetry from Consumer-Grade SUAS: Implications for Direct Georeferencing of Structure from Motion Photogrammetry. *Earth Surf. Process. Landf.* **2017**, *42*, 473–486. [\[CrossRef\]](#)
51. Turner, D.; Lucieer, A.; Wallace, L. Direct Georeferencing of Ultrahigh-Resolution UAV Imagery. *IEEE Trans. Geosci. Remote Sens.* **2014**, *52*, 2738–2745. [\[CrossRef\]](#)
52. Taddia, Y.; González-García, L.; Zambello, E.; Pellegrinelli, A. Quality Assessment of Photogrammetric Models for Façade and Building Reconstruction Using DJI Phantom 4 RTK. *Remote Sens.* **2020**, *12*, 3144. [\[CrossRef\]](#)

53. Forlani, G.; Dall'Asta, E.; Diotri, F.; di Cella, U.M.; Roncella, R.; Santise, M. Quality Assessment of DSMs Produced from UAV Flights Georeferenced with On-Board RTK Positioning. *Remote Sens.* **2018**, *10*, 311. [[CrossRef](#)]
54. Taddia, Y.; Stecchi, F.; Pellegrinelli, A. Using DJI Phantom 4 RTK Drone for Topographic Mapping of Coastal Areas. *Int. Arch. Photogramm. Remote Sens. Spat. Inf. Sci.* **2019**, *XLII-2/W13*, 625–630. [[CrossRef](#)]
55. Taddia, Y.; Stecchi, F.; Pellegrinelli, A. Coastal Mapping Using DJI Phantom 4 RTK in Post-Processing Kinematic Mode. *Drones* **2020**, *4*, 9. [[CrossRef](#)]
56. Benassi, F.; Dall'Asta, E.; Diotri, F.; Forlani, G.; Morra di Cella, U.; Roncella, R.; Santise, M. Testing Accuracy and Repeatability of UAV Blocks Oriented with GNSS-Supported Aerial Triangulation. *Remote Sens.* **2017**, *9*, 172. [[CrossRef](#)]
57. Shom. Références Altimétriques Maritimes (RAM). 2019. Available online: <https://data.europa.eu/data/datasets/5925720b88ee385b69385a47?locale=fr> (accessed on 6 March 2022).
58. Quilfen, V. Dynamique de Plages Sableuses Enclavées à la Pointe Bretagne. PhD Thesis, Université Paris-Est, Paris, France, 2016.
59. Masselink, G.; Short, A. The Effect of Tide Range on Beach Morphodynamics and Morphology: A Conceptual Beach Model. *J. Coast. Res.* **1993**, *9*, 785–800.
60. Stéphane, P. Quelques données nouvelles sur la mobilité récente (1930–2008) et le bilan sédimentaire des flèches de galets de Bretagne. *Géomorphologie Relief Process. Environ.* **2011**, *17*, 205–232. [[CrossRef](#)]
61. Carter, R.W.G.; Orford, J.D. Coarse Clastic Barrier Beaches: A Discussion of the Distinctive Dynamic and Morphosedimentary Characteristics. *Mar. Geol.* **1984**, *60*, 377–389. [[CrossRef](#)]
62. Jennings, R.; Shulmeister, J. A Field Based Classification Scheme for Gravel Beaches. *Mar. Geol.* **2002**, *186*, 211–228. [[CrossRef](#)]
63. Stéphane, P.; Suanez, S.; Fichaut, B. Long-Term Morphodynamic Evolution of the Sillon de Talbert Gravel Barrier Spit, Brittany, France. *Shore Beach* **2012**, *80*, 19–36.
64. Stéphane, P.; Suanez, S.; Fichaut, B.; Autret, R.; Blaise, E.; Houron, J.; Ammann, J.; Grandjean, P. Monitoring the Medium-Term Retreat of a Gravel Spit Barrier and Management Strategies, Sillon de Talbert (North Brittany, France). *Ocean. Coast. Manag.* **2018**, *158*, 64–82. [[CrossRef](#)]
65. Suanez, S.; Stéphane, P.; Floc'h, F.; Autret, R.; Fichaut, B.; Blaise, E.; Houron, J.; Ammann, J.; Grandjean, P.; Accensi, M.; et al. Fifteen Years of Hydrodynamic Forcing and Morphological Changes Leading to Breaching of a Gravel Spit, Sillon de Talbert (Brittany). *Géomorphologie Relief Process. Environ.* **2018**, *24*, 403–428. [[CrossRef](#)]
66. Cooper, M.A.R.; Cross, P.A. Statistical Concepts and Their Application in Photogrammetry and Surveying. *Photogramm. Rec.* **1988**, *12*, 637–663. [[CrossRef](#)]
67. Javernick, L.; Brasington, J.; Caruso, B. Modeling the Topography of Shallow Braided Rivers Using Structure-from-Motion Photogrammetry. *Geomorphology* **2014**, *213*, 166–182. [[CrossRef](#)]
68. James, M.R.; Antoniazza, G.; Robson, S.; Lane, S.N. Mitigating Systematic Error in Topographic Models for Geomorphic Change Detection: Accuracy, Precision and Considerations beyond Off-nadir Imagery. *Earth Surf. Process. Landf.* **2020**, *45*, 2251–2271. [[CrossRef](#)]
69. Štroner, M.; Urban, R.; Reindl, T.; Seidl, J.; Brouček, J. Evaluation of the Georeferencing Accuracy of a Photogrammetric Model Using a Quadcopter with Onboard GNSS RTK. *Sensors* **2020**, *20*, 2318. [[CrossRef](#)]
70. Grayson, B.; Penna, N.T.; Mills, J.P.; Grant, D.S. GPS Precise Point Positioning for UAV Photogrammetry. *Photogramm. Rec.* **2018**, *33*, 427–447. [[CrossRef](#)]
71. Cooper, H.; Wasklewicz, T.; Zhu, Z.; LeCompte, K.; Heffentrager, M.; Smaby, R.; Brady, J.; Howard, R. Evaluating the Ability of Multi-Sensor Techniques to Capture Topographic Complexity. *Sensors* **2021**, *21*, 2105. [[CrossRef](#)]
72. Dandois, J.P.; Olanò, M.; Ellis, E.C. Optimal Altitude, Overlap, and Weather Conditions for Computer Vision UAV Estimates of Forest Structure. *Remote Sens.* **2015**, *7*, 13895–13920. [[CrossRef](#)]



Article

Automatic and Accurate Extraction of Sea Ice in the Turbid Waters of the Yellow River Estuary Based on Image Spectral and Spatial Information

Huachang Qiu ^{1,2}, Zhaoning Gong ^{1,2,*}, Kuinan Mou ^{1,2}, Jianfang Hu ^{1,2}, Yinghai Ke ^{1,2} and Demin Zhou ^{1,2}

¹ College of Resource Environment and Tourism, Capital Normal University, Beijing 100048, China; 2190902141@cnu.edu.cn (H.Q.); 2190902184@cnu.edu.cn (K.M.); 2190902115@cnu.edu.cn (J.H.); yke@cnu.edu.cn (Y.K.); zhoudemin@cnu.edu.cn (D.Z.)

² MCA Key Laboratory of Disaster Assessment and Risk Prevention, Capital Normal University, Beijing 100048, China

* Correspondence: gongzhn@cnu.edu.cn

Abstract: Sea ice is an important part of the global cryosphere and an important variable in the global climate system. Sea ice also presents one of the major natural disasters in the world. The automatic and accurate extraction of sea ice extent is of great significance for the study of climate change and disaster prevention. The accuracy of sea ice extraction in the Yellow River Estuary is low due to the large dynamic changes in the suspended particulate matter (SPM). In this study, a set of sea ice automatic extraction method systems combining image spectral information and textural information is developed. First, a sea ice spectral information index that can adapt to sea areas with different turbidity levels is developed to mine the spectral information of different types of sea ice. In addition, the image's textural feature parameters and edge point density map are extracted to mine the spatial information concerning the sea ice. Then, multi-scale segmentation is performed on the image. Finally, the OTSU algorithm is used to determine the threshold to achieve automatic sea ice extraction. The method was successfully applied to Gaofen-1 (GF1), Sentinel-2, and Landsat 8 images, where the extraction accuracy of sea ice was over 93%, which was more than 5% higher than that of SVM and K-Means. At the same time, the method was applied to the Liaodong Bay area, and the extraction accuracy reached 99%. These findings reveal that the method exhibits good reliability and robustness.

Keywords: Yellow River Estuary; turbid area; spectral information; textural features; sea ice extension; automatic extraction

Citation: Qiu, H.; Gong, Z.; Mou, K.; Hu, J.; Ke, Y.; Zhou, D. Automatic and Accurate Extraction of Sea Ice in the Turbid Waters of the Yellow River Estuary Based on Image Spectral and Spatial Information. *Remote Sens.* **2022**, *14*, 927. <https://doi.org/10.3390/rs14040927>

Academic Editor: Simona Niculescu

Received: 29 December 2021

Accepted: 7 February 2022

Published: 14 February 2022

Publisher's Note: MDPI stays neutral with regard to jurisdictional claims in published maps and institutional affiliations.



Copyright: © 2022 by the authors. Licensee MDPI, Basel, Switzerland. This article is an open access article distributed under the terms and conditions of the Creative Commons Attribution (CC BY) license (<https://creativecommons.org/licenses/by/4.0/>).

1. Introduction

Sea ice refers to saltwater ice that is directly frozen from seawater, and also includes continental glaciers (icebergs and Iceland), river ice, and lake ice that enter the ocean. Sea ice greatly inhibits the heat and steam exchange between the ocean and atmosphere and alters the radiation budget and energy balance of the ocean's surface. These changes have an important impact on oceanic hydrological conditions, atmospheric circulation, and ocean climate [1]. In addition, the production and disappearance of sea ice greatly affects human marine activities. For example, sea ice significantly affects the development of marine resources and marine transportation [2]. Moreover, sea ice presents a potential freshwater resource [3]. Therefore, accurate real-time monitoring of sea ice bears an important application value and theoretical significance.

The bottom of the Yellow River Delta contains a small flat slope, shallow water low salinity, as a result of which seawater is easily frozen [4]. The development of conditions conducive to ice formation and persistence in this sea area is unstable; that is, the ice disappears as the temperature rises and reappears as the temperature drops [5]. Sea ice

is formed at a rapid rate and responds more closely to the local climate. Sea ice disasters frequently occur in the waters of the Yellow River Delta, and sea ice often has a major impact on fishing ports, wharves, shallow beach aquaculture, and offshore infrastructure [6]. For example, the operation area of the Shengli Oilfield, China's second-largest oilfield, is mainly concentrated in the Yellow River Delta, the Bohai Sea and its adjacent waters. Sea ice severely affects and threatens offshore oilfield production operations and various engineering facilities in the winter [7]. According to statistics, severe and relatively serious sea ice disasters occur roughly once every five years in China, and in some sea areas, sea ice disasters occur almost every year [8]. In the winter of 2009–2010, the Bohai Sea and the northern part of the Yellow Sea experienced the worst ice conditions in nearly 30 years. The severe ice conditions had a significant impact on the society and economy of the provinces (cities) along the Yellow Sea and the Bohai Sea. According to statistics, sea ice disasters caused economic losses totaling nearly USD 900 million [9]. Therefore, in the context of global warming, it is entirely possible that continuous low temperatures and severe sea ice disasters will occur in some areas. In particular, with the rapid economic development of the Bohai Rim region, the losses suffered by sea ice disasters are increasing year by year [10]. In the new era, the country should promote the understanding of the ocean, rationally develop and utilize marine resources, protect the rights and interests of the ocean, and insist on the harmonious coexistence of man and the ocean. Faced with the new requirements as China enters a new era and accelerates the building of its maritime power, the existing sea ice disaster prevention and mitigation capabilities can no longer fully meet the actual needs of the economic and social development in icy sea areas, and sea ice monitoring capabilities remain relatively weak [11]. It is the trend of future development to improve the three-dimensional marine disaster observation network that combines coastal observation, offshore platform and satellite remote sensing, so as to improve the ability of marine disaster observation [12]. Therefore, the precise extraction of sea ice provides the basis for strengthening the analysis of and research on sea ice conditions, and is necessary for improving early sea ice warning technology, as well as ice prevention and disaster reduction capabilities.

Traditional sea ice monitoring methods, such as shore-based observations and ice-breaker observations, cannot obtain large-scale sea ice information in a timely and accurate manner. Remote sensing monitoring technology has a high timeliness, can obtain repeated observations on a large scale, and is relatively inexpensive, providing long-term data support for dynamic and efficient sea ice monitoring [13–15].

Large-scale monitoring of sea ice in high latitudes can be carried out using remote sensing technologies such as microwave and optical remote sensing. Passive microwave and synthetic aperture radar (SAR) imagery enables all-weather observations and the ability to penetrate through clouds [16,17]. The automatic segmentation algorithm based on statistical distance realizes the classification of C-band fully polarized sea ice data [18]. A sea ice classification method is proposed for X-band, C-band and L-band fully polarized synthetic aperture radar images. By extracting the polarized features of sea ice classification, the feature vector provides input into the neural network classifier to realize the extraction of sea ice [19]. However, it is challenging to obtain due to the high cost and the long revisit period for most of them [20]. Optical remote sensing data, although limited by weather conditions, usually delivers better spatial resolution, lower cost, and shorter revisit times. For example, satellites such as Moderate Resolution Imaging Spectroradiometer (MODIS) [21], Advanced Very High-Resolution Radiometer (AVHRR), Geostationary Ocean Color Imager (GOCI) [22], and Feng Yun 3 (FY-3) [23] has a high time resolution and can be used for continuous monitoring of sea ice in a large-scale area and a long time sequence. The disadvantage is that the spatial resolution is low, and it is difficult to perform refined regional sea ice monitoring. High spatial resolution remote sensing data represented by GF1 [24], Landsat [25], and Sentinel-2 [26] can be used to achieve refined sea ice monitoring through data mining, and the effective combination of multi-source medium and high-

resolution satellite data compensates for the low time resolution of the data and further improves its sea ice monitoring capabilities.

Three main types of feature parameters are used for sea ice extraction: spectral features, spatial features, and temperature features. The spectrum processing methods commonly used for sea ice extraction include the band ratio, band difference, and various normalized indexes, which highlight the sea ice information [27]. In addition, the sample point selection and machine learning methods have also been used to extract spectral information about sea ice. The second concerns the spatial features. The spatial feature commonly used for sea ice extraction is the textural feature based on the gray-level co-occurrence matrix. Generally, the surface of sea ice is rough and has conspicuous irregular and unstable textural characteristics; while the surface of sea water is smooth and has constant textural characteristics [28]. The third refers to the temperature feature. This parameter is used to retrieve the surface temperature through the thermal infrared band of the remote sensing image. The temperature feature is simple and easy to use, but has fewer data sources and a low spatial resolution; the accuracy of the temperature retrieval algorithm is also not very high, limiting its application [29].

Current sea ice extraction methods can be divided into threshold segmentation methods, machine learning methods, and digital image processing methods. The threshold segmentation method mainly involves setting the threshold value of the sea ice's spectral, textural, temperature, and other parameters and determining the threshold values using an artificial or bimodal histogram, scatter plots, and other methods, such as using the red band and the ratio threshold of the near-infrared band to achieve rapid extraction of sea ice [27]. Su et al. used the red and near-infrared bands of Sentinel-3 images to establish a sea ice information index that highlights the spectral information of sea ice, and employed the Jenks method to determine the segmentation threshold of ice water [30]. Hayashi et al. used reflectance scatter plots of MODIS bands 1 and 2 to derive a formula suitable for extracting the area of thin ice [31]. Ice conditions in the Gulf of Riga in the Baltic Sea were counted by a bimodal histogram method, the statistical results were limited by the spatial resolution of MODIS [32]. The threshold segmentation method is simple and fast, but it is difficult to determine the threshold value using this method, and the threshold value of different images will be slightly different. Machine learning methods such as support vector machines and Classification and Regression Trees (CART) decision trees select certain sample points and then classify the sea ice and seawater areas [33]. The machine learning method is simple and easy to use, but the classification process is unclear, and the sample points need to be manually selected, making it difficult to achieve automation. In addition, the final accuracy depends entirely on the selected sample points. The digital image processing method is to highlight the sea ice information by processing and transforming the image. For example, Li et al. proposed a linear spectral decomposition method based on MODIS images with multiple constrained end members [34]. The pixels are decomposed to extract the range of the sea ice. Liu et al. used a wavelet transform to extract the textural information from a SAR image, converted a China–Brazil Earth Resources Satellite (CBERS-02B) optical image from Red–Green–Blue space to Hue–Saturation–Intensity space, and finally employed Principal Component Analysis (PCA) to fuse the HSI image and the texture images [35]. Digital image processing methods can highlight sea ice information more intuitively, but the process is more complicated and difficult to automate.

The seawater turbidity of the Yellow River Delta is high, and the changes are quite drastic, which intensifies the distinction between sea ice and seawater. Aiming at the problems of the low accuracy and efficiency of the current sea ice extraction methods used in the Yellow River Delta and based on multi-source remote sensing images, in this study, a set of sea ice automatic extraction method systems suitable for the Yellow River Delta was developed and the spatial and textural information about the sea ice was fully excavated. The automatic extraction method will be further extended to other areas such as Liaodong Bay in order to provide important technical support for the rational development of sea ice resources and to improve the early warning capabilities of sea ice disaster prevention and

mitigation systems. This method explores the spectral information and texture information of different ice types. The spectral information, texture information and edge information of sea ice are used to extract sea ice, and the completeness and accuracy of sea ice extraction results are improved through multi-scale segmentation of images. This method can provide a reliable method for extracting sea ice extent from high-resolution optical remote sensing data such as GF1.

2. Materials and Methods

2.1. Study Area and Data

The Yellow River Delta is located in the southeastern part of Bohai Bay and the northwestern part of Laizhou Bay (Figure 1). The sea area is located in a typical monsoon climate zone. The winter is controlled by the Eurasian continental high pressure system. The north and northwest winds are dominant, and the weather is dry and cold. When strong cold air invades, it is often accompanied by processes such as strong winds, snowfall, and sharp temperature drops. The coastline is more than 100 km long, and the sea water near the coast mostly contains suspended sediment from the mouth of the Yellow River. Therefore, the sea area has a wide intertidal bandwidth, a small and flat bottom slope, and shallow water depths. In winter, this area is greatly affected by the meteorological conditions and the continent. In addition, affected by the runoff from the Yellow River and other rivers entering the sea, the salt content of the seawater in this sea area is relatively low. The aforementioned special geographical environment and climatic conditions provide sufficient and necessary conditions for the freezing of seawater in this sea area. Sea ice often has a significant impact on fishing ports, wharves, shallow beach aquaculture, and marine infrastructure in this area. With the gradual expansion of the economic scale of the marine aquaculture industry in this area, the impact of sea ice on production activities has become more significant.

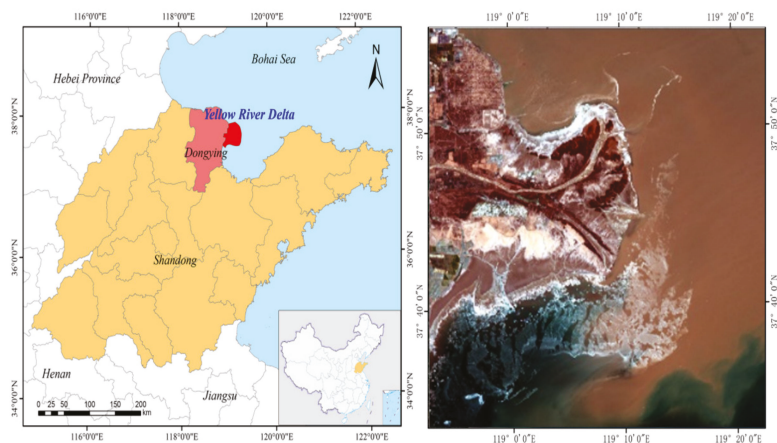


Figure 1. The study area.

According to the development stage of sea ice, the sea ice in the Yellow River Delta can be divided into new ice (NI), ice rind, nilas (NL), grey ice (GR), grey-white ice (GW), and white ice. New ice is formed by direct freezing of seawater or snow falling when the temperature is low, and the sea surface is not melted. It is mostly needle-like, flake-like, grease-like, or sponge-like. Ice rind is formed by the freezing of new ice or direct freezing of the calm sea surface. The surface of the ice crust is smooth, moist, and shiny. Its thickness is about 5 cm. It can fluctuate with the wind and is easily broken by wind and waves. Nilas ice is a thin, elastic ice crust with a thickness of less than 10 cm. It easily bends and breaks under external forces and can produce a finger-like overlapping phenomenon. Grey ice is

an ice cap layer with a thickness of 10–15 cm. It is developed from nilas. The surface is flat and moist. It is mostly grey. It is less elastic than nilas ice. It is easily broken by swells and overlaps when squeezed. Grey-white ice is an ice layer with a thickness of 15–30 cm, and is developed from grey ice. It has a rough surface, is greyish-white, and mostly forms when ice ridges are squeezed. White ice describes an ice layer with a thickness of greater than 30 cm. It develops from grey-white ice, has a rough surface, and is mostly white [36].

In this study, Sentinel-2 and Landsat8 images from 2017–2019 were selected to verify the applicability of the method. The time phase and image quality information obtained from the data is presented in Table 1.

Table 1. Image information table.

| Area | Date | Image | Band Number | Resolution | Cloud Cover |
|--------------------|------------------|------------|-------------|------------|-------------|
| Yellow River Delta | 21 January 2017 | GF1 | 4 | 16 m | 1% |
| Yellow River Delta | 12 January 2018 | GF1 | 4 | 16 m | 1% |
| Yellow River Delta | 12 January 2018 | Sentinel-2 | 10 | 10 m | 0% |
| Yellow River Delta | 23 January 2019 | Landsat8 | 7 | 30 m | 0% |
| Yellow River Delta | 21 January 2017 | Planet | 4 | 3 m | 1% |
| Yellow River Delta | 12 January 2018 | Planet | 4 | 3 m | 2% |
| Yellow River Delta | 23 January 2019 | Planet | 4 | 3 m | 1% |
| Liaodong Bay | 17 February 2019 | Landsat8 | 7 | 30 m | 0% |
| Liaodong Bay | 17 February 2019 | Planet | 4 | 30 m | 0% |

The GF1 data used in this article were obtained from the China Resources Satellite Application Center (<http://www.cresda.com/CN/>, accessed on 21 January 2017). The PIE-Basic software was used for geometric correction, atmospheric correction, orthorectification, image clipping, and other pre-processing work. The Sentinel-2 data were obtained from the European Space Agency's (ESA) data sharing website (<https://scihub.Coppe-rnicus.eu/>, accessed on 12 January 2018). The Sentinel-2 data released is a product of the Top-of-Atmosphere (TOA) reflectance that has been geometrically corrected and radiometrically corrected, so it was only necessary to perform atmospheric correction of this dataset. The SNAP software officially provided by the ESA was used to perform the atmospheric correction on the downloaded data. The Landsat data were obtained from <https://landlook.usgs.gov/> (accessed on 23 January 2019) and the ENVI software was used to perform the FLAASH atmospheric correction. In order to facilitate the subsequent statistical analysis, calculations, and other operations and to reduce the data storage space, all of the reflectance data were expanded by 10,000 times and rounded.

2.2. Sea–Land Separation

In order to avoid interference from land information, the sea and land need to be separated before the sea ice extraction. The Normalized Difference Vegetation Index (NDVI) and the Normalized Difference Water Index (NDWI) are the most commonly used indexes for water and land separation. They both use the normalized ratio of the reflectance between visible and near-infrared light. The difference is that the NDVI uses the green and near-infrared bands; while the NDWI uses the red and near-infrared bands. In the Yellow River Delta, the concentration of suspended sediment in some of the seawater is extremely high, which improves the reflectivity of the seawater in the near-infrared band. Figure 2 shows the spectral curve of the seawater and sea ice in the GF1 image. The reflectivity of the clean seawater is significantly higher in the visible light range than in the near-infrared band, while the reflectivity of the highly turbid seawater is higher in the near-infrared band than in the blue-green band. However, it is still lower than the reflectivity in the red band since the reflectivity in the blue and green bands will gradually become saturated as the concentration of suspended sediment increases, while the reflectivity in the red and near-infrared bands will continue to increase as the concentration of suspended sediment increases [37]. However, the near-infrared reflectivity is always lower than the red-band reflectivity. Sea ice 1 and sea ice 2 are defined as sea ice in clean water and turbid water, respectively, and the reflectivity in the near-infrared band is also lower than that in the

red band. Therefore, the effect of using the NDVI for sea–land separation is better. Pixels with NDVI values of less than 0 are classified as seawater, and pixels with NDVI values of greater than 0 are classified as land. In addition, after separation, it is necessary to filter out discrete areas such as rivers and lakes on the land and ultimately to only retain the ocean area. The results of the sea–land separation are shown in Figure 3.

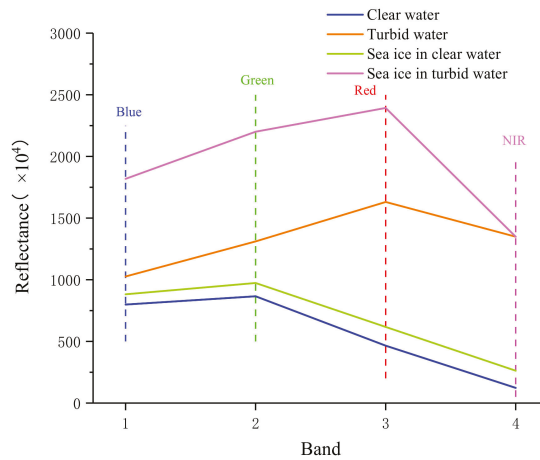


Figure 2. The reflectance of the ice and water in the GF1 image.

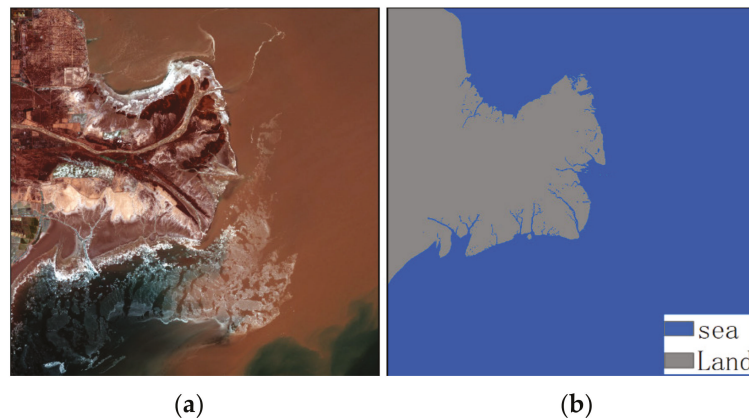


Figure 3. (a) True color GF1 image acquired on 12 January 2018; and (b) the results of the sea–land separation.

2.3. Sea Ice Spectral Information Extraction

Spectral information is the most commonly used feature for extraction. In this section, a sea ice spectral information index suitable for different suspended particulate matter concentrations based on the spectral characteristics of sea ice is developed. Generally, the reflectance of seawater in clear seas is higher than that of seawater. However, the suspended particulate matter (SPM) in the Yellow River Estuary increases the reflectance of the seawater. The reflectance of seawater with a high SPM content is even higher than that of sea ice with a lower SPM content (Figure 4). As can be seen from the box plot in Figure 4, as the wavelength increases, the reflectivity of the seawater fluctuates more widely, and the blue band is relatively less affected by the SPM content. This is due to the fact that as

the SPM content increases, the blue band reaches saturation first, followed by the green and red bands. From the perspective of the type of sea ice, in addition to grey ice and grey-white ice, a considerable part of the new ice and ice rind has the same reflectance as seawater. This is because grey ice and grey-white ice are thicker and have a much higher reflectivity than seawater, whereas new ice and ice rind are thin ice with a thickness of less than 10 cm and have a lower reflectivity. Therefore, a single waveband cannot distinguish all types of sea ice from seawater. The difficulty of sea ice extraction in the Yellow River Estuary is mainly the extraction of the new ice and ice rind from seawater with different SPM contents.

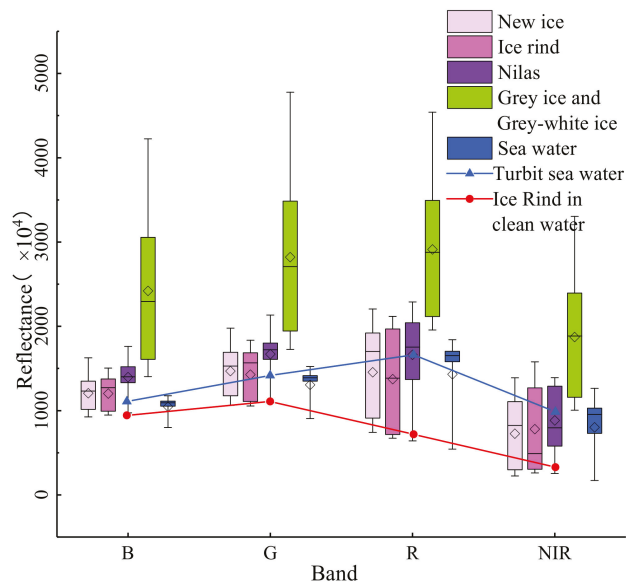


Figure 4. Sea ice and water reflectance box plot.

The commonly used spectral index such as the NDVI and NDSI, cannot eliminate the influence of SPM on sea ice extraction. Therefore, in this study, the spectral information concerning the sea ice was extracted by searching for an optimal band combination method. Since the visible light and near-infrared bands are the most important bands for extracting sea ice, these four bands were selected as the best band combination from the data source. The scatter plot can intuitively reflect the separation of the different samples. As shown in Figures 3 and 4, each point in the scatter plot formed by any two bands represents the position of the sea ice or seawater in this two-dimensional space. If the points of sea ice and seawater are scattered together (Figure 5a), then the separation of the sea ice and seawater in the two-dimensional space formed by these two wavebands is poor; and if the sea ice and seawater each gather in one location, it indicates that the sea ice and seawater can be separated well using this waveband combination (Figure 5b). In this way, a straight line separating the sea ice and seawater can be drawn in this two-dimensional space.

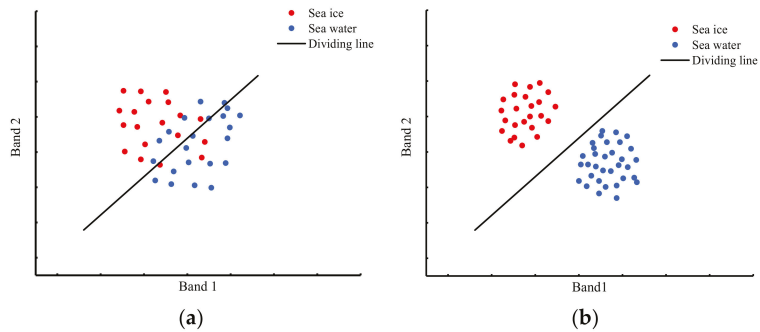


Figure 5. (a) Band 1 and Band 2 exhibit good separation in this scatter plot; (b) Band 1 and Band 2 display poor separation in this scatter plot.

In order to test all of the band combinations as much as possible, in this study, combinations of the four red, green, blue, and near-infrared bands were tested first. The results of these combinations are presented in Table 2. There are 28 results in total. Two of these 28 bands were chosen to construct a two-dimensional scatter plot, with a total of 378 combinations. For example, if the NDVI can better distinguish between sea ice and seawater, then the scatter plots constructed with the NIR – R and NIR + R bands will exhibit better separation. Finally, the reflectivity of grey ice and grey-white ice is much higher than that of primary ice and ice skins, and the extraction is relatively simple. In order to make the scatter plot show the separation of new ice, ice rind, and seawater better, first only the sample points of new ice, ice rind, and seawater were selected to construct the scatter plot. The optimal band combination was selected by averaging the Euclidean distance and inter-class variance combined with visual interpretation.

Table 2. First band combination list.

| | | | | | | |
|---------|-------|-------|---------|---------|---------|---------|
| R | G | R + G | R + B | R + NIR | G + B | G + NIR |
| B | NIR | R * G | R * B | R * NIR | G * B | G * NIR |
| B + NIR | R – G | R – B | R – NIR | G – B | G – NIR | B – NIR |
| B * NIR | R/G | R/B | R/NIR | G/B | G/NIR | B/NIR |

The average Euclidean distance is

$$x = \frac{1}{n} \sum_{i=1}^n x_i, \tag{1}$$

where $x_{(y)}$ is the average Euclidean distance of the sea ice or seawater on the x -axis or y -axis, n is the number of sea ice or seawater sample points, and x_i is the reflectivity of sea ice or seawater.

$$U = \sqrt{(x_{ice} - y_{ice})^2 + (x_{sea} - y_{sea})^2}, \tag{2}$$

where U is the average Euclidean distance between the sea ice and seawater in two-dimensional space, x and y are the average Euclidean distances of the sea ice sample points on the x -axis and y -axis, respectively, and x and y are the sea ice sample points on the x -axis and y -axis, respectively.

The variance between classes is

$$\sigma = \sum_{i=1}^n (x_i - \bar{x})^2, \tag{3}$$

where σ is the between-class variance of sea ice or seawater, and x_i is the number of sample points of sea ice or seawater. The larger the average Euclidean distance and the smaller the variance between classes, the higher the degree of separation is.

According to the principle of a larger average Euclidean distance and a smaller variance between classes, the top 12 band combinations were selected and their scatter plots were examined. As shown in Figure 6, the abscissas and ordinates of the scatter plots are the reflectance of the band after a band combination, for example, B is the reflectance of the green band, and R/B is the ratio of the reflectance of the red band to the green band. It was found that in the scatter plots of B and R/B, sea ice and seawater can basically be separated by a straight line. The mixing of seawater is more serious. Therefore, the band combination with the best reflectivity ratio between the green band and the red band was finally selected.

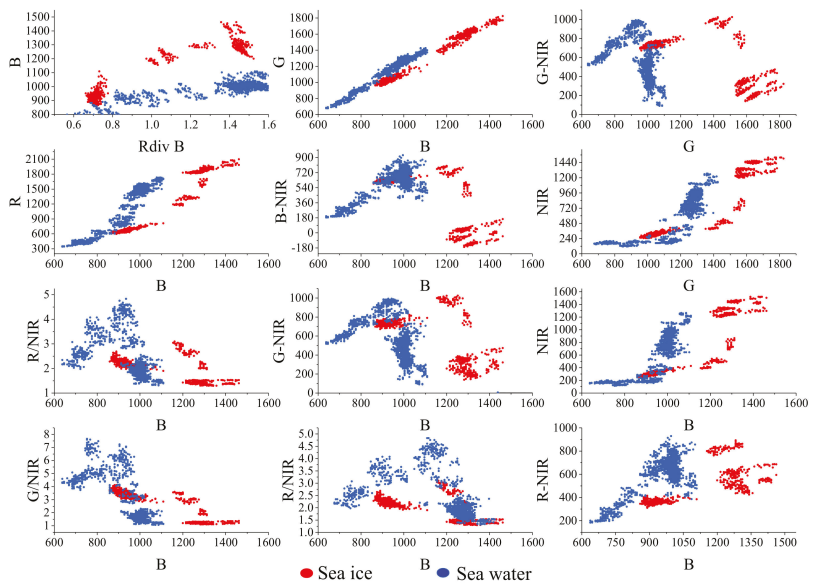


Figure 6. Scatter plots of band combinations for seawater and sea ice.

R/B and B were used as the x -axis and y -axis, respectively, to draw the scatter plots of the seawater and different ice types (Figure 7). The seawater reflectance samples exhibit good linearity in the scatter plots. The different types of sea ice are located above the straight line. Therefore, the linear equation of seawater was obtained through linear fitting as the dividing line.

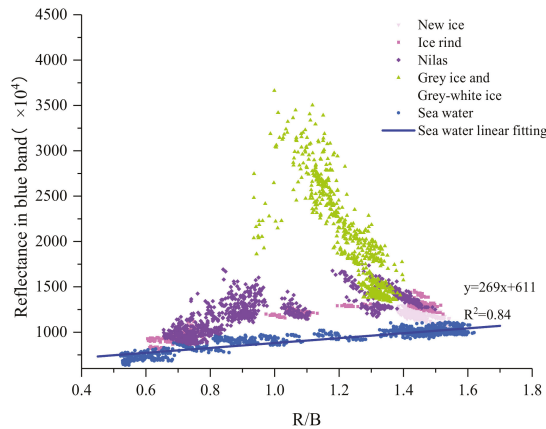


Figure 7. Scatter plot of the reflectivity of the different types of sea ice and seawater.

The dividing line equation is

$$y = 269x + 611, \quad (4)$$

where x is the reflectance ratio of the red band to the green band, and y is the reflectance of the green band.

In order to make the value of the sea ice a positive number to facilitate subsequent statistical analysis and the determination of the threshold, only the slope of the seawater linear fitting line was used, and finally the sea ice spectral information index was constructed:

$$y = B - 269 \times (R/B), \quad (5)$$

where y is the calculated reflectance value of each pixel in the image (sea ice has a larger value and seawater has a relatively small value); B is the reflectance value of the green band; and R/B is the ratio of the reflectance in the red band to that in the green band.

2.4. Sea Ice Spatial Information Extraction

As shown in Figure 8, in optical images, such as GF1, Landsat, and Sentinel-2 images, some thin ice such as new ice and ice rind exhibits spectra very similar to that of seawater containing suspended particles. Sea ice in seawater with a higher concentration of suspended particulate matter cannot be extracted using spectral information alone. Therefore, it is necessary to distinguish this part of the sea ice from the seawater based on the spatial information concerning the sea ice. Compared with the smooth spatial characteristics of the seawater surface, the surface of sea ice is generally rough, with conspicuous irregular and unstable textural characteristics. In this section, three different spatial information extraction schemes are designed to explore the applicability of the textural features and edge features of the gray-level co-occurrence matrix to the extraction of various types of ice; and through comparison of these schemes, the best method for extracting sea ice spatial information is determined.

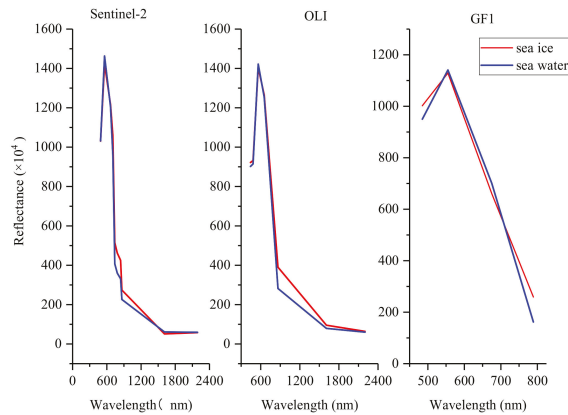


Figure 8. The similarity of the sea ice and seawater spectral curves for the different sensors.

The textural features represent the surface conditions of the object, such as smooth or rough, which helps to distinguish homogeneous and heterogeneous regions. Since sea ice has irregular and unstable textural characteristics, the textural characteristics of the image were added when the sea ice was extracted in order to solve the problem of sea ice and seawater bearing similar spectra. At present, the commonly used method of extracting sea ice textural features is the gray-level co-occurrence matrix method. The gray-level co-occurrence matrix is a matrix that counts the gray-level relationship between pixels within a certain interval in a local area of an image. The factors affecting the gray level co-occurrence matrix are the image quantization level, the size of the moving window, the movement direction, and the movement step length. The gray-level co-occurrence matrix provides information about the image's gray direction, interval, and change range. Based on the gray-level co-occurrence matrix, the statistical attributes that quantitatively describe the textural features are extracted. Haralick et al. (1973) defined 14 textural features [38]. The feature statistics commonly used to extract textural information from remote sensing images mainly include the mean, variance, homogeneity, contrast, dissimilarity, entropy, angular second moment, and correlation. Recently, many related studies have been conducted on the extraction of sea ice information based on the textural features of the gray level co-occurrence matrix, but there remains a lack of research on the applicability of textural features to various types of ice. Therefore, the applicability and advantages of the different textural features in extracting sea ice types were explored.

Sea ice has conspicuous edge characteristics under different SPM contents. The Sobel edge detection operator has the advantage of easy calculations and a strong anti-noise ability. The edge detection image value of the Sobel operator represents the gradient value of the pixels in the region, and the edge of the sea ice has a higher gradient value. Therefore, the edge points of the sea ice were extracted using the Sobel operator, and the edge point density map is generated with the number of sea ice edge points in a certain range. The edge point density map represents the density of the sea ice edges in a local area. The higher the sea ice density, the greater the number of sea ice edge points. The edge point density map was used to explore the edge characteristics of the sea ice.

In order to further explore the best scheme for extracting the spatial information about the sea ice and to delve deeper into the sea ice spatial information, Scheme 3 combines the edge point density map and the statistics of each textural feature through multiplication, and further explores the ability to combine the edge and textural features to extract the sea ice.

2.5. Object-Oriented Extraction of Sea Ice Extent

Object-oriented classification refers to the segmentation of images to form objects with adjacent homogeneous pixels, which overcomes the limitations of traditional remote sensing image classification methods that use pixels as the basic classification and processing unit to contain more semantic information [39]. The object is the processing unit, which can achieve a higher level of remote sensing image classification. The object-oriented remote sensing image classification method is not only based on the spectral features but also uses the textural features of the image to segment and classify the image. The classification results avoid speckle noise and have good integrity. Image segmentation is the most basic and critical step in the object-oriented classification method, which directly determines the accuracy of the classification results and the workload of the classification process. In order to improve the accuracy and efficiency of the segmentation, in this paper study, the edge detection segmentation algorithm and the full lambda schedule merge algorithm in ENVI were used.

The blue band is less affected by a high SPM content, and the texture and edge information about the sea ice is clearer. Therefore, the blue band of the image was selected as the reference image to segment the sea ice spectral information and the spatial information in the image. The mean attribute of the segmented object was used to extract the sea ice. Figure 9 shows that the object-oriented method can not only reduce the speckle noise in the classification results, but also limit the influence of the spatial feature window factor when using the spatial features to extract the sea ice and can improve the accuracy of the classification results.

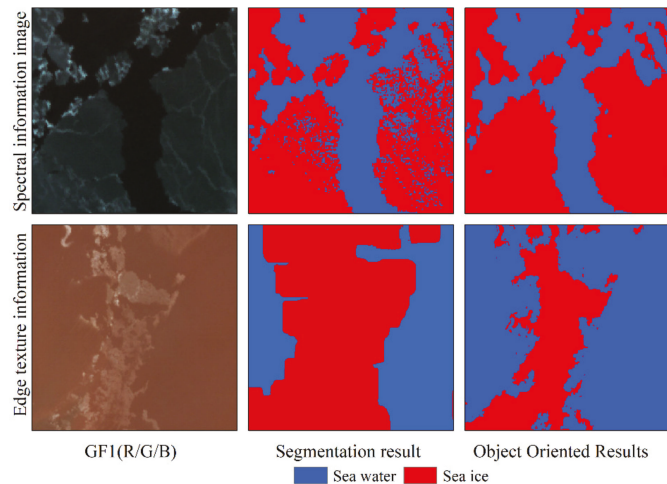


Figure 9. Object-oriented segmentation results.

2.6. Determination of Segmentation Threshold Based on OTSU

The automatic determination of the object-oriented segmentation threshold affects the final classification result and the automatic process of sea ice range extraction. In this study, the OTSU method was used to automatically determine the threshold. The principle of the OTSU method is to continuously iteratively determine an optimal threshold to maximize the variance between the target and the background. Before conducting the OTSU threshold segmentation, the terrestrial mask pixels need to be removed. This is because the OTSU determines the segmentation threshold based on histogram statistics. Land pixels will affect the structure of the histogram and cause the predicted threshold to deviate. After removing the land pixels, the double peaks in the histogram are clearer. This improves the accuracy of the threshold.

2.7. Accuracy Verification

In order to better evaluate the robustness and applicability of the method developed in this study, the proposed method was compared with the extraction results of the Support Vector machine (SVM) and K-Means methods, and the three methods were applied to GF1, Landsat-8, and Sentinel-2 images. In order to quantitatively evaluate the accuracy of the sea ice extraction, ArcGIS was used to randomly generate 800 test points in the sea area, and the type was marked based on a planet satellite image with a resolution of 3 m. To ensure that the test points were evenly distributed in the study area and that all types of sea ice and seawater were present, their total accuracy and kappa coefficient (κ) were calculated.

3. Results

3.1. Analysis of Sea Ice Spectral Information Index

Based on a GF1 image acquired on 12 January 2018, 800 sea ice and seawater sample points were selected, and the sea ice spectral information index was used to plot the distribution ranges of the different types of sea ice and seawater reflectance values (Figure 10). The results revealed that after the sea ice spectral information index was constructed, the reflectance values of the different types of sea ice were larger, while the reflectance values of the seawater were concentrated within a small interval, indicating that the sea ice spectral information index can effectively extract the sea ice spectral information.

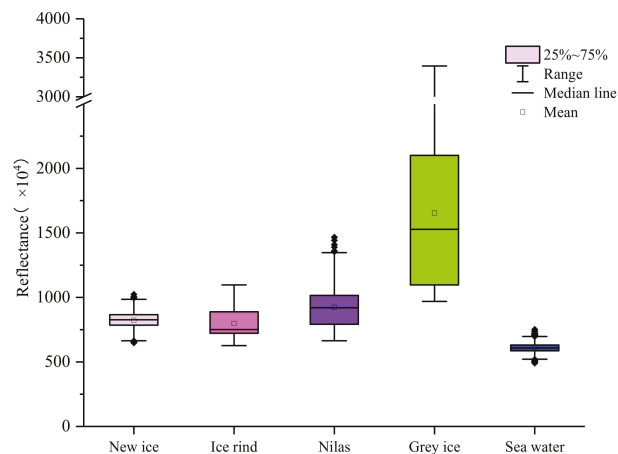


Figure 10. The range of sea ice spectral information index of sea ice and sea water.

The sea ice can be initially extracted by selecting a suitable threshold. Figure 11 shows the sea ice extraction results. It can be seen that the sea ice spectral information index can effectively extract the sea ice in seawater with different suspended sediment concentrations. The new ice and ice rind in the high suspended sediment area can also be extracted more accurately. However, there are still some problems in the classification results. First, there is the salt and pepper phenomenon, which is a common problem in pixel-based classification methods. This will be solved by object segmentation and extraction. Second, there is still a small amount of confusion between seawater and sea ice in area c, which is mainly concentrated in the areas where the concentration of suspended particles changes drastically. This is because the seawater in these areas display spectral curves that are extremely similar to those of some of the types of sea ice such as new ice and ice rind, and this phenomenon is present in the GF1, Landsat, and Sentinel-2 images (Figure 8). Therefore, it is not possible to completely distinguish between sea ice and seawater using only the spectral characteristics of the image, thus necessitating the addition of the spatial characteristics of the image.

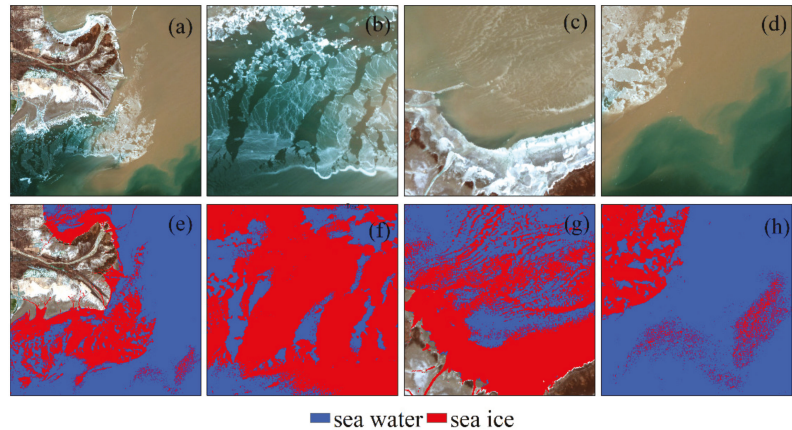


Figure 11. Sea ice extraction results using spectral information. (a) GF1 image (R/G/B); (b–d) The three sub-areas of the study area; (e–h) The extraction results using spectral information, respectively.

3.2. Optimization of Spatial Feature Extraction Scheme

Scheme 1: The textural feature parameters based on the gray-level co-occurrence matrix mainly include the quantization level, the size of the moving window, and the movement direction and step length. Since the directional characteristics of sea ice are not evident, default values (0,1) were used for the movement directions of the x-axis and y-axis. Moreover, the movement step length was set to a default value of 1. The following section only discusses the quantization level of the gray-level co-occurrence matrix and the moving window size in detail.

Without compressing the gray level of the original image, the size of the gray level co-occurrence matrix is the square of the gray level of the original image, which will greatly increase the calculation load of the gray level co-occurrence matrix. Therefore, in practical applications, in order to improve the efficiency of the calculation of the textural features, the gray level of the original image is usually compressed, and quantization levels of 64, 32, and 16 are generally used.

Figure 12 shows the characteristics of the sea ice and seawater in the GF1 images under different quantitative levels. It can be observed that the images with 64 quantization levels maintain the textural characteristics of the original images better; the images with 32 quantization levels display a reduced ability to maintain details; and the images with 16 quantization levels have lost a significant amount of textural information. Therefore, the higher the quantization level, the better the textural details of the original image are preserved. However, images with high quantization levels are not suitable for the extraction of sea ice textural information. Figure 13 shows the four textural feature indexes of the homogeneity, dissimilarity, entropy, and second moment under different quantization levels. Due to the drastic changes in the concentration of the suspended sediment in the Yellow River Delta, the images with 64 quantization levels exhibit a large amount of speckle noise in the seawater area. In the 32 quantization level images, this speckle noise is greatly suppressed. In addition, since the calculation load increases with increasing quantization level, the calculation efficiency is lower. Therefore, the quantization level of the gray-level co-occurrence matrix was finally set to 32.

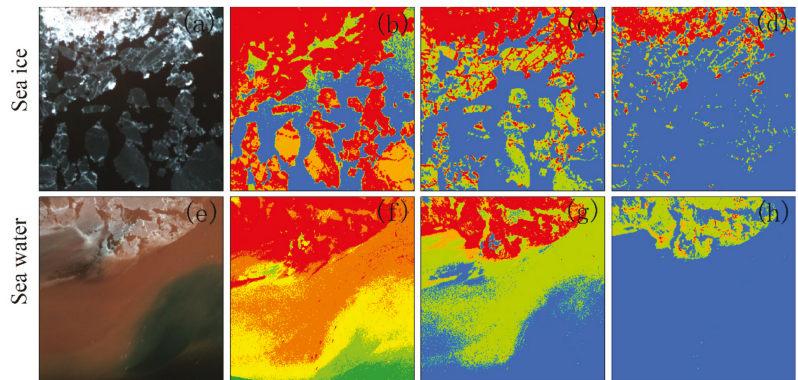


Figure 12. Image features at different quantization levels. (a) Sea ice areas in GF1 images; (b–d) sea ice images at 64, 32, and 16 quantization levels, respectively; (e) Sea water areas in GF1 images; (f–h) sea water images at 64, 32, and 16 quantization levels, respectively.

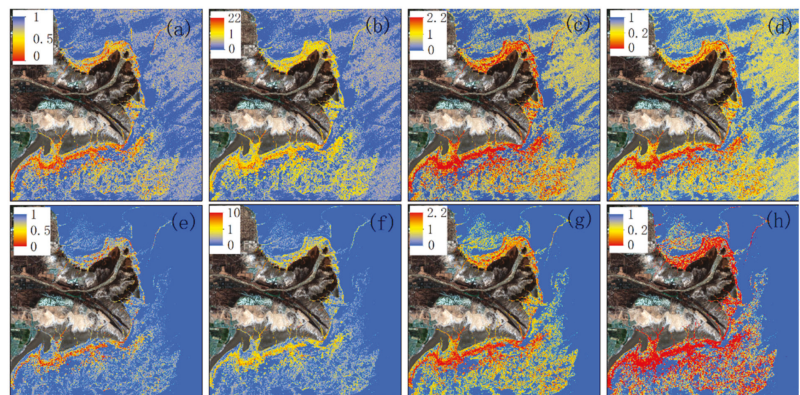


Figure 13. Images with different textural feature parameters under different quantization levels. (a–d) Texture image of homogeneity, dissimilarity, entropy, second moment at 64 quantization levels; (e–h) Texture image of homogeneity, dissimilarity, entropy, second moment at 32 quantization levels.

The moving window is an important factor that affects the textural feature extraction of the gray-level co-occurrence matrix. Figure 14 shows the distribution range of the textural feature values of various types of sea ice and seawater for different window sizes. It can be seen that the size of the window has little effect on the textural characteristics of the sea ice and seawater, but as the texture window increases, the calculation load increases greatly, thus the window size selected in this study was 3. Based on the statistical results of the textural feature index values of the various types of sea ice and seawater, grey ice and grey-white ice have a higher degree of discrimination from seawater in terms of each textural feature value. The types of thin ice such as new ice, ice rind, and nilas cannot be completely distinguished from the textural characteristics of seawater. This is because the surfaces of the ice rind and nilas are relatively smooth, which is similar to the textural characteristic value of seawater. The surfaces of grey ice and grey-white ice are rough, and the textural characteristic value of seawater is quite different.

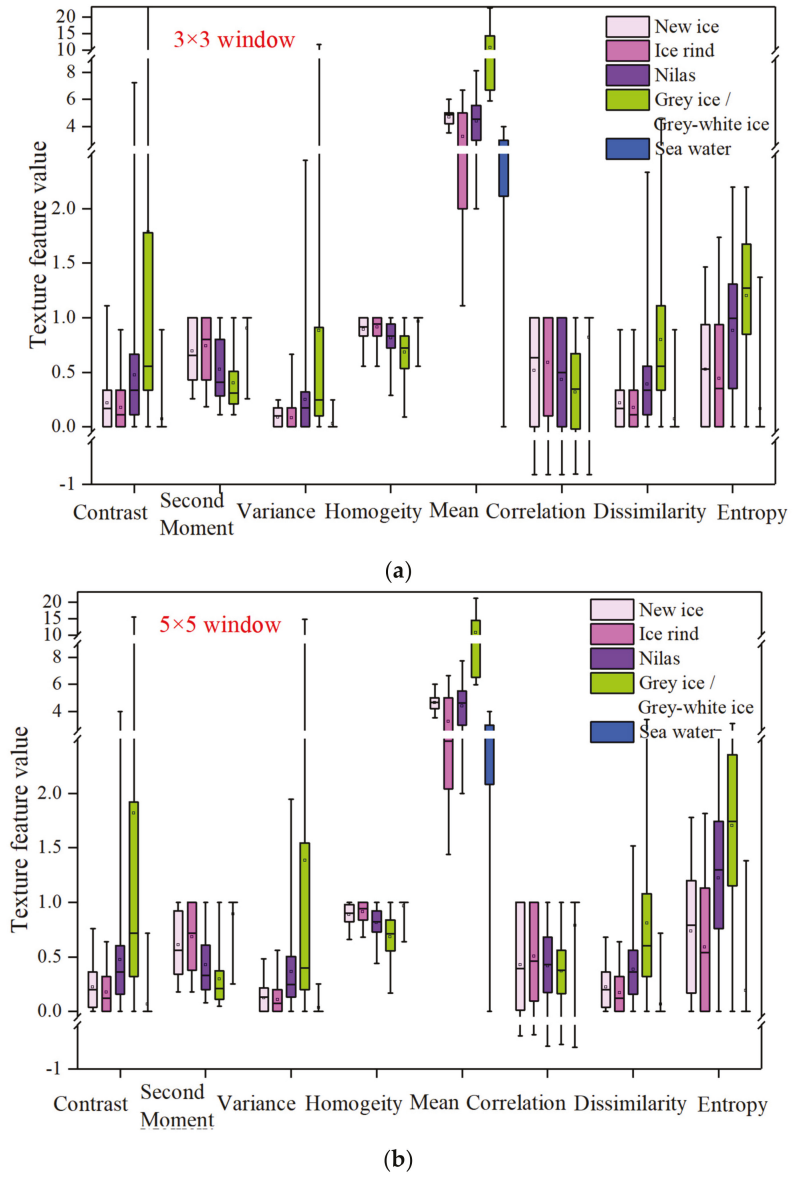
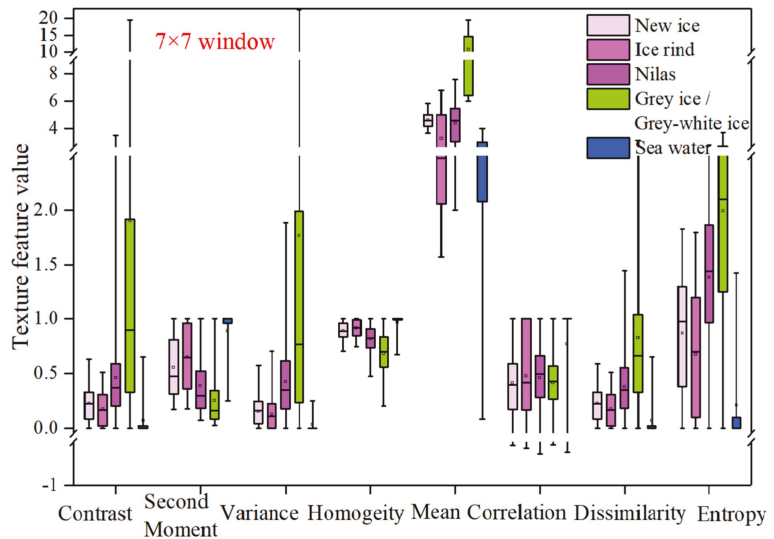
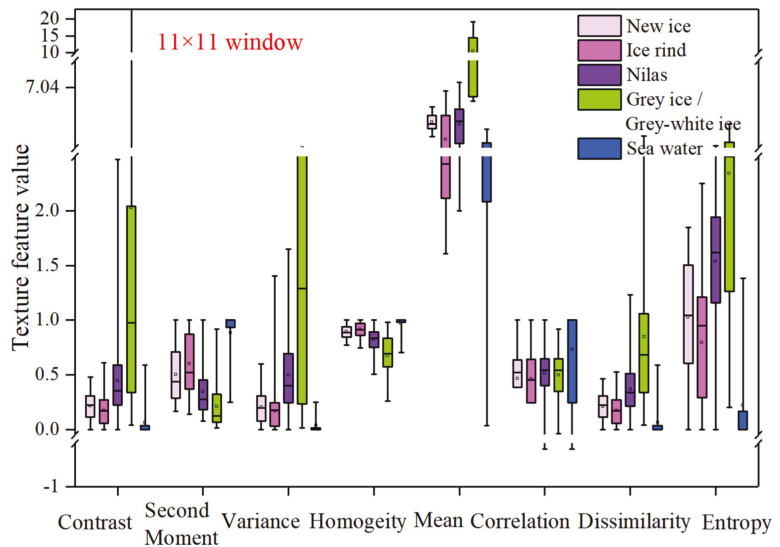


Figure 14. Cont.



(c)



(d)

Figure 14. Plots of the ice water textural characteristic indicators for different window sizes. (a) Ice and water texture value distribution in 3 window sizes; (b) Ice and water texture value distribution in 5 window sizes; (c) Ice and water texture value distribution in 7 window sizes; (d) Ice and water texture value distribution in 11 window sizes.

Scheme 2 uses the Sobel operator to generate an edge point density map to highlight the edge features of the sea ice. The distribution ranges of the edge density values of the different types of sea ice and the seawater for different window sizes were calculated (Figure 15), and the optimal calculation window size for the sea ice edge points was compared and analyzed.

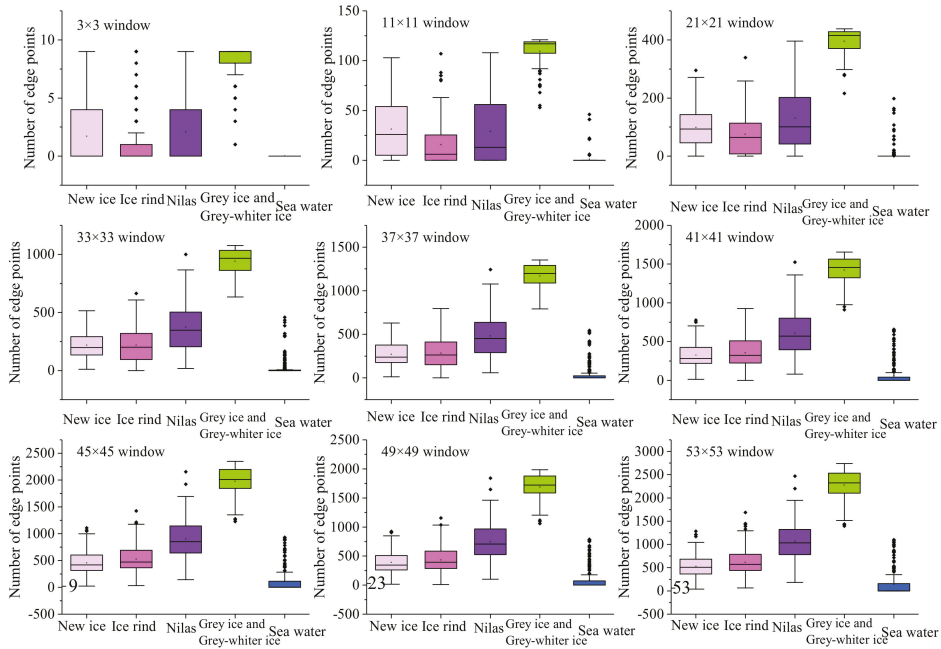


Figure 15. The effect of the window size on sea ice extraction using an edge point density map.

When the window was small, the edge density value of the seawater basically approached 0, and the edge density values of the grey ice, grey-white ice, and seawater were significantly different. The edge density values of the new ice, ice rind, nilas, and seawater partially overlapped. The overlapping area mainly contained the inner smooth sea ice. As the window size increased, the number of edge points that were detected inside the thin ice region such as new ice, ice rind, and nilas increased, and the edge point density value gradually increased. When the window size reached 45, the edge point density values of the various types of sea ice were significantly different from those of the seawater. As the window continued to grow, it greatly increased the amount of calculation load, thus 45 was selected as the best window size.

In Scheme 3, the texture feature window size was set to 3×3 , and the quantization level was set to 32. After the edge point density map was combined with the various textural feature indicators, the distribution ranges of the various types of sea ice and the seawater were determined (Figure 16). It can be seen from Figure 16 that the combination of textural feature indicators such as the variance, homogeneity, and contrast with the edge point density map failed to produce a better extraction effect. After the mean textural feature was combined with the edge point density map, the range of the seawater decreased further and became more concentrated, and the distinction between the various types of sea ice and the seawater increased further. Therefore, the edge point density map combined with the mean textural feature index was selected as the final solution for extracting the sea ice spatial information.

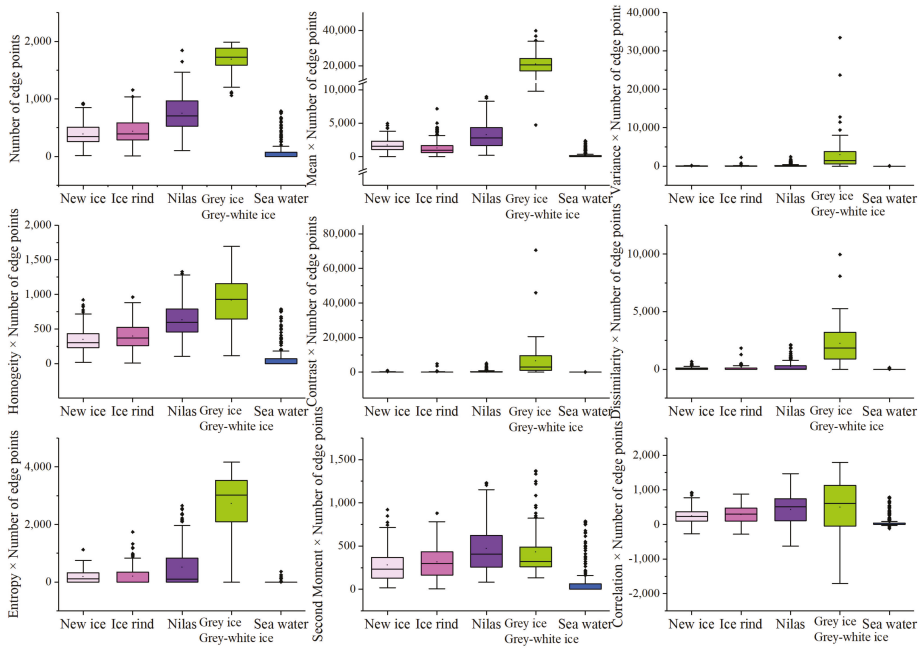


Figure 16. Box plots for the combinations of the edge density map and textural feature.

Figure 17 shows the comparison between the edge texture information extraction results and the spectral information extraction results. The edge texture image can extract the extent of the sea ice as a whole and can extract the types of ice such as new ice, nilas, grey ice, and grey-white ice. The most important factor is that the texture images at the edges can compensate for the similarity between the spectra of the sea ice and the seawater. As shown in Figure 17j,o, the extraction accuracy of the spectral information is lower in areas where the concentration of the suspended particulate matter changes drastically. The edge texture images solve this problem. Although the seawater in the crevices between portions of ice can also be identified as sea ice, it can be combined with the spectral information to achieve a more accurate sea ice extraction.

3.3. Accuracy Verification

Figure 18 shows the sea ice extraction results obtained using the different methods for a GF1 image acquired on 12 January 2018. Four scenes including new ice, ice rind, nilas, grey ice, and grey-white ice were selected to illustrate the results of the sea ice extraction. In addition, the results were compared with the sea ice extraction results obtained using the K-Means and SVM methods. Taking into account the complexity of the changes between the various types of sea ice in the seawater with different suspended particulate matter concentrations in the Yellow River Delta, in order to improve the accuracy of the K-Means and SVM methods as much as possible, the K-Means method categories were set to 2–10 categories, and then, the classification post-processing was performed. The image was finally divided into two categories, namely, sea ice and seawater. When the SVM method was employed to select the sample points, the sample points were selected according to the types of ice in the Yellow River delta, turbid seawater, and clear seawater in order to improve the accuracy of the sea ice extraction.

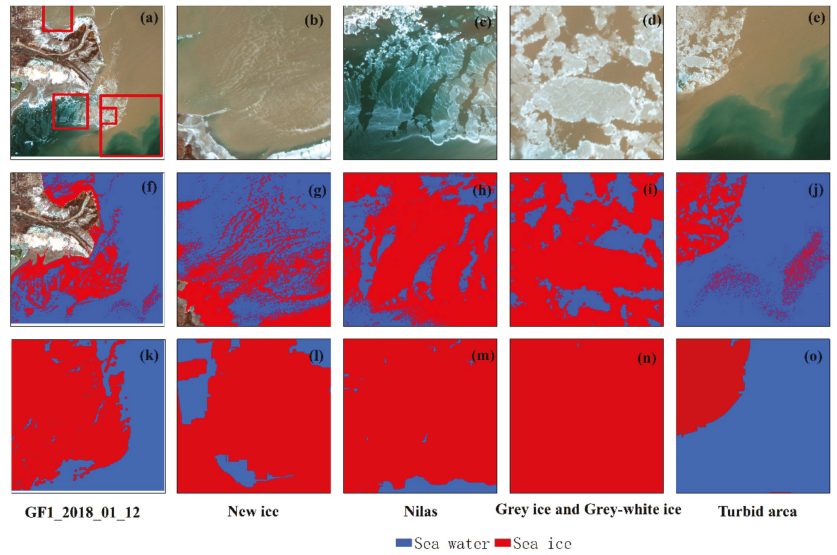


Figure 17. Comparison of edge texture results and spectral results. (a–e) GF1 true color images; (f–j) results of sea ice extraction from spectral information; and (k–o) results of the sea ice extraction from edge texture information.

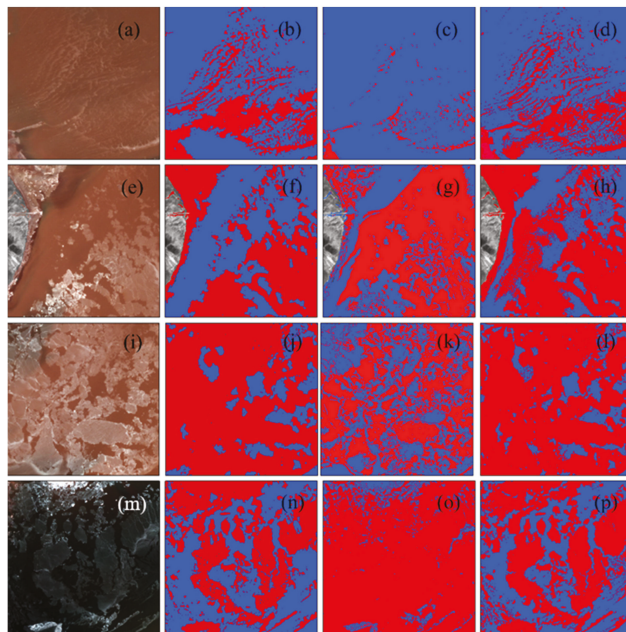


Figure 18. Comparison of the sea ice extraction results obtained using different methods. (a,e,i,m) True color images of the GF1 image acquired on 12 January 2018; (b,f,j,n) Classification results for the method proposed in this paper; (c,g,k,o) K-Means classification results; (d,h,l,p) SVM classification results.

It can be observed from Figure 18c,h that the K-Means method cannot completely extract the sea ice when extracting thin ice such as new ice and ice rind in seawater with a high suspended particulate matter concentration. As Figure 18g,o shows, most of the seawater was classified as sea ice in the areas with high suspended particulate matter concentrations near the shore and in the clear water areas. This demonstrates that the K-Means method is greatly affected by suspended sediment. The results of the SVM method of extracting sea ice were generally better than those of the K-Means method, but most of the seawater remained classified as sea ice in the areas with high suspended particulate matter concentrations. In addition, there is a significant salt and pepper phenomenon present in the extraction results. The method proposed in this paper can accurately extract the various types of sea ice in both turbid seas and clean seas. It also greatly reduces the salt and pepper phenomenon and improves the integrity of the sea ice extraction.

In order to quantitatively evaluate the accuracy of the sea ice extraction, the overall accuracies and kappa coefficients of the classification results for the GF1, Landsat 8, and Sentinel-2 images were compared and analyzed and additionally compared with those of the K-Means and SVM methods. In addition, the method was applied to the Yellow River Delta and Liaodong Bay. The results are presented in Table 3. The overall accuracy of the method proposed in this paper is basically >95%, the kappa coefficient is > 80%, and the accuracy is 5% higher than those of the SVM and K-Means methods. On 21 January 2017, there were mixed pixels of clouds and water in some areas, which affected the accuracy of the final sea ice extraction. In Liaodong Bay, the accuracy of the SVM was close to that of the method proposed in this paper. This is because the sea ice in Liaodong Bay is predominantly thick ice such as grey ice and grey-white ice, and is less affected by suspended sediment. Therefore, both the proposed method and the SVM method achieved better accuracies.

Table 3. Accuracy evaluation table.

| Area | Date | Image | Method | OA | k |
|--------------------|------------------|-------------|-------------|------|------|
| Yellow River Delta | 12 January 2018 | GF1 | This method | 0.98 | 0.96 |
| | | GF1 | SVM | 0.93 | 0.86 |
| | | GF1 | K-Means | 0.78 | 0.55 |
| | 21 January 2017 | GF1 | This method | 0.93 | 0.81 |
| | | GF1 | SVM | 0.84 | 0.59 |
| | | GF1 | K-Means | 0.77 | 0.45 |
| | 12 January 2018 | Sentinel-2 | This method | 0.99 | 0.98 |
| | | Sentinel-2 | SVM | 0.9 | 0.95 |
| | | Sentinel-2 | K-Means | 0.81 | 0.60 |
| 23 January 2019 | Landsat-8 | This method | 0.94 | 0.88 | |
| | Landsat-8 | SVM | 0.89 | 0.77 | |
| | Landsat-8 | K-Means | 0.76 | 0.46 | |
| Liaodong Bay | 17 February 2019 | Landsat-8 | This method | 0.99 | 0.98 |
| | | Landsat-8 | SVM | 0.96 | 0.95 |
| | | Landsat-8 | K-Means | 0.91 | 0.82 |

The final results show that the accuracy of the K-Means method was the lowest among the three methods. This is due to the similarity between the spectra of the highly turbid seawater and thin ice sheets in the Yellow River Delta and the complexity of the various types of sea ice in the different turbid seawater regions. This led to the relatively low classification accuracy of the K-Means method. The SVM method exhibited a better classification accuracy than the K-Means method overall, but it only used the spectral information, thus the classification accuracy of the ice types, such as in the high suspended sediment areas and for ice rind, was lower. In addition, the SVM method is reliant on prior knowledge. It is a time-consuming process to manually select sample points, and the quality of the sample points directly affects the accuracy of the final classification. The method proposed in this paper attained good accuracy in both the turbid water and clear

water areas, and achieved automation of the sea ice extraction. All processing methods were carried out in ENVI. The ENVI functions are called using IDL and can be easily automated.

4. Discussion

In recent years, extreme weather such as high temperatures, droughts and floods have occurred frequently, and climate anomalies have become the norm, which has led to people's cognitive thinking on global climate change and human living environment [40,41]. As an indicator of global climate change, sea ice change is related to global warming, rises in sea levels and other issues [42,43]. The development of ice conditions in the Yellow River Delta waters in China is unstable, and the formation of sea ice is rapid, which responds more closely to local regional climates. Accurate monitoring of sea ice extent is therefore crucial. Suspended sediment in the mouth of the Yellow River significantly affects the accuracy of sea ice extent extraction. This paper proposes an automatic extraction method of sea ice that combines texture, edge and spectral information, which improves the accuracy of sea ice extraction under highly dynamic suspended sediment changes. Compared with SVM and K-Means, the accuracy is improved by more than 5%. This method provides a basis for accurate sea ice identification using GF1 images, and also offers a method for other optical remote sensing data. High-resolution satellite data based on multiple sources can compensate for the lack of data time resolution and further improve its sea ice monitoring capabilities. Therefore, sea ice monitoring based on multi-source remote sensing data will be the key direction of future development. Moreover, this method provides an approach for other optical remote sensing data, which is of great significance for making full use of multi-source remote sensing data to study the law of sea ice change. Accurate identification of sea ice extent is of great significance to sea ice monitoring, sea ice prediction, disaster prevention and mitigation, and climate research in the Yellow River Delta region. Although this paper discusses the characteristics of various sea ices in detail and enables higher-precision sea ice extraction, it does not distinguish between various sea ice types. Accurate identification of sea ice types is of great significance to the study of sea ice production, ablation and migration. Most of the sea ice in the Yellow River Delta is less than 30 cm thick, and it remains difficult to classify them with greater precision. In addition, the spectrum, texture, and edge information of coastal ice and floes such as grey and white ice are relatively close, and it is difficult to distinguish between coastal ice and floating ice. Therefore, in the future, we will study the distinction of various sea ice types and realize the identification methods of different types of sea ice.

5. Conclusions

The automatic and accurate extraction of sea ice is essential for studying the laws of sea ice generation and migration, improving sea ice disaster prevention and mitigation, and monitoring climate change. Accurate real-time observations of sea ice bear an important application value and is of theoretical significance.

In order to solve the problem of the low sea ice extraction accuracy caused by the influence of the suspended sediment in the Yellow River Delta, in this study, an automatic sea ice extraction method combining sea ice spectral, texture and edge information is proposed, where the sea ice extraction accuracy can reach over 93%, which is more than 5% higher than SVM and K-means. Compared with previous studies, the sea ice spectral information index suitable for different suspended sediment concentrations is constructed by a two-dimensional scatter diagram of characteristic bands, which improves the applicability of sea ice spectral information index. In changing from discussing the texture characteristics of sea ice as a whole in the past, this study discusses the texture characteristics and edge characteristics of various sea ice types in the Yellow River Delta in detail, laying a foundation for the classification of sea ice types. In addition, the automatic determination of threshold based on OTSU can realize the automatic extraction of sea ice. The method in this paper uses only four bands of visible light and near-infrared to extract sea ice, thus providing a method to be extended to other high-resolution optical remote

sensing data and is of great significance to maximally utilize multi-source remote sensing data for real-time monitoring of sea ice.

In future research, we may expand the research area to the Bohai Sea in China, and realize real-time observation of sea ice through Landsat, Sentinel-2, GF1 and other optical remote sensing data. In terms of data sources, in order to improve the frequency of sea ice monitoring, SAR data may also be applied. We hope to conduct high-precision and high-frequency sea ice monitoring, so as to make a certain contribution to preventing disasters and studying climate change around the Bohai Sea.

Author Contributions: Conceptualization, H.Q. and Z.G.; methodology, H.Q.; software, K.M.; validation, H.Q., J.H. and Y.K.; formal analysis, D.Z.; investigation, Z.G. and Y.K.; resources, H.Q.; data curation, H.Q.; writing—original draft preparation, H.Q.; writing—review and editing, H.Q.; visualization, H.Q.; supervision, H.Q.; project administration, H.Q.; funding acquisition, Z.G. All authors have read and agreed to the published version of the manuscript.

Funding: This research was funded by National Natural Science Foundation of China grant numbers 41971381 and 42071396. This research was funded by National Key R&D Program of China grant number 2017YFC0505903.

Institutional Review Board Statement: Not applicable.

Informed Consent Statement: Not applicable.

Data Availability Statement: Not applicable.

Conflicts of Interest: The authors declare no conflict of interest.

References

- Ouyang, L.; Hui, F.; Zhu, L.; Cheng, X.; Cheng, B.; Shokr, M.; Zhao, J.; Ding, M.; Zeng, T. The spatiotemporal patterns of sea ice in the Bohai Sea during the winter seasons of 2000–2016. *Int. J. Digit. Earth* **2017**, *12*, 893–909. [\[CrossRef\]](#)
- Zherui, L.; Huiwen, C. Sea Ice Automatic Extraction in the Liaodong Bay from Sentinel-2 Imagery Using Convolutional Neural Networks. *E3S Web Conf.* **2020**, *143*, 2015. [\[CrossRef\]](#)
- Gu, W.; Gu, S. Research on the Temporal Variation Characteristics of Sea Ice Thickness and the Regeneration Period of Sea Ice. *Resource Sci.* **2003**, *24*–32.
- Zhang, X.-L.; Zhang, Z.-H.; Xu, Z.-J.; Li, G.; Sun, Q.; Hou, X.-J. Sea ice disasters and their impacts since 2000 in Laizhou Bay of Bohai Sea, China. *Nat. Hazards* **2012**, *65*, 27–40. [\[CrossRef\]](#)
- Liu, C.; Gu, W.; Chao, J.; Li, L.; Yuan, S.; Xu, Y. Spatio-temporal characteristics of the sea-ice volume of the Bohai Sea, China, in winter 2009/10. *Ann. Glaciol.* **2013**, *54*, 97–104. [\[CrossRef\]](#)
- Zhang, D.-Y.; Yu, S.-S.; Wang, Y.; Yue, Q.-J. Sea Ice Management for Oil and Gas Platforms in the Bohai Sea. *Pol. Marit. Res.* **2017**, *24*, 195–204. [\[CrossRef\]](#)
- Sun, M.; Yuan, B. The characteristics of ice conditions in the operation sea area of Shengli Oilfield and countermeasures for disaster mitigation. *Ocean. Dev. Manag.* **2017**, *34*, 98–102.
- Yuan, B.; Guo, J. Research on my country's Sea Ice Disaster Prevention and Mitigation Countermeasures in the New Era. In Proceedings of the 3rd Annual Ocean Development and Management Academic Conference, China, 20 September 2019.
- Sun, S.; Su, J. Features of sea ice disaster in the Bohai Sea in 2010. *J. Nat. Disasters* **2011**, *20*, 87–93. [\[CrossRef\]](#)
- Yuan, B.; Guo, J. Ideas and measures for improving my country's sea ice disaster prevention and mitigation capabilities in the new era. In Proceedings of the 9th Maritime Power Strategic Forum, China, 20 November 2018.
- Shutler, J.D.; Quartly, G.D.; Donlon, C.J.; Sathyendranath, S.; Platt, T.; Chapron, B.; Johannessen, J.A.; Girard-Ardhuin, F.; Nightingale, P.D.; Woolf, D.K.; et al. Progress in satellite remote sensing for studying physical processes at the ocean surface and its borders with the atmosphere and sea ice. *Prog. Phys. Geogr. Earth Environ.* **2016**, *40*, 215–246. [\[CrossRef\]](#)
- Yuan, S.; Liu, C.; Liu, X.; Chen, Y.; Zhang, Y. Research advances in remote sensing monitoring of sea ice in the Bohai sea. *Earth Sci. Inf.* **2021**, *14*, 1729–1743. [\[CrossRef\]](#)
- Han, Y.; Wei, C.; Zhou, R.; Hong, Z.; Zhang, Y.; Yang, S. Combining 3D-CNN and Squeeze-and-Excitation Networks for Remote Sensing Sea Ice Image Classification. *Math. Probl. Eng.* **2020**, *2020*, 1–15. [\[CrossRef\]](#)
- Quincey, D.; Luckman, A. Progress in satellite remote sensing of ice sheets. *Prog. Phys. Geogr. Earth Environ.* **2009**, *33*, 547–567. [\[CrossRef\]](#)
- Yan, Q.; Huang, W. Sea Ice Remote Sensing Using GNSS-R: A Review. *Remote Sens.* **2019**, *11*, 2565. [\[CrossRef\]](#)
- Wong, A.; Yu, P.; Wen, Z.; Clausi, D.A. IceSynth II: Synthesis of SAR Sea-Ice Imagery Using Region-Based Posterior Sampling. *IEEE Geosci. Remote Sens. Lett.* **2010**, *7*, 348–351. [\[CrossRef\]](#)
- Dabboor, M.; Montpetit, B.; Howell, S.; Haas, C. Improving Sea Ice Characterization in Dry Ice Winter Conditions Using Polarimetric Parameters from C- and L-Band SAR Data. *Remote Sens.* **2017**, *9*, 1270. [\[CrossRef\]](#)

18. Moen, M.-A.N.; Doulgeris, A.P.; Anfinsen, S.N.; Renner, A.H.H.; Hughes, N.; Gerland, S.; Eltoft, T. Comparison of feature based segmentation of full polarimetric SAR satellite sea ice images with manually drawn ice charts. *Cryosphere* **2013**, *7*, 1693–1705. [[CrossRef](#)]
19. Singha, S.; Johansson, M.; Hughes, N.; Hvidegaard, S.M.; Skourup, H. Arctic Sea Ice Characterization Using Spaceborne Fully Polarimetric L-, C-, and X-Band SAR With Validation by Airborne Measurements. *IEEE Trans. Geosci. Remote Sens.* **2018**, *56*, 3715–3734. [[CrossRef](#)]
20. Hollands, T.; Linow, S.; Dierking, W. Reliability Measures for Sea Ice Motion Retrieval from Synthetic Aperture Radar Images. *IEEE J. Sel. Top. Appl. Earth Obs. Remote Sens.* **2014**, *8*, 67–75. [[CrossRef](#)]
21. Huck, P.; Light, B.; Eicken, H.; Haller, M. Mapping sediment-laden sea ice in the Arctic using AVHRR remote-sensing data: Atmospheric correction and determination of reflectances as a function of ice type and sediment load. *Remote Sens. Environ.* **2007**, *107*, 484–495. [[CrossRef](#)]
22. Yan, Y.; Huang, K.; Shao, D.; Xu, Y.; Gu, W. Monitoring the Characteristics of the Bohai Sea Ice Using High-Resolution Geostationary Ocean Color Imager (GOCI) Data. *Sustainability* **2019**, *11*, 777. [[CrossRef](#)]
23. Wang, X.-D.; Wu, Z.-K.; Wang, C.; Li, X.-W.; Qiu, Y.-B.; Wand, X.-D. Reducing the Impact of Thin Clouds on Arctic Ocean Sea Ice Concentration from FengYun-3 MERSI Data Single Cavity. *IEEE Access* **2017**, *5*, 16341–16348. [[CrossRef](#)]
24. Wu, J.; Sun, L.; Zhang, Y.; Ji, R.; Yu, W.; Feng, R.; Guo, L. Study on Sea Ice Extraction and Area Correction Model Based on MODIS and GF Data. *IOP Conf. Ser. Mater. Sci. Eng.* **2018**, *392*, 62105. [[CrossRef](#)]
25. Markus, T.; Cavalieri, D.J.; Tschudi, M.A.; Ivanoff, A. Comparison of aerial video and Landsat 7 data over ponded sea ice. *Remote Sens. Environ.* **2003**, *86*, 458–469. [[CrossRef](#)]
26. König, M.; Hieronymi, M.; Oppelt, N. Application of Sentinel-2 MSI in Arctic Research: Evaluating the Performance of Atmospheric Correction Approaches Over Arctic Sea Ice. *Front. Earth Sci.* **2019**, *7*, 1–33. [[CrossRef](#)]
27. Su, H.; Wang, Y.; Yang, J. Monitoring the Spatiotemporal Evolution of Sea Ice in the Bohai Sea in the 2009–2010 Winter Combining MODIS and Meteorological Data. *Estuaries Coasts* **2011**, *35*, 281–291. [[CrossRef](#)]
28. Guo, H.; Fan, Q.; Zhang, X. Multifeature fusion for polarimetric synthetic aperture radar image classification of sea ice. *J. Appl. Remote Sens.* **2014**, *3*, 610–621. [[CrossRef](#)]
29. Su, H.; Wang, Y.; Xiao, Y.; Yan, X.-H. Classification of MODIS images combining surface temperature and texture features using the Support Vector Machine method for estimation of the extent of sea ice in the frozen Bohai Bay, China. *Int. J. Remote Sens.* **2015**, *36*, 2734–2750. [[CrossRef](#)]
30. Su, H.; Ji, B.; Wang, Y. Sea Ice Extent Detection in the Bohai Sea Using Sentinel-3 OLCI Data. *Remote Sens.* **2019**, *11*, 2436. [[CrossRef](#)]
31. Hayashi, K.; Naoki, K.; Cho, K. Thin ice area extraction in the seasonal sea ice zones of the northern hemisphere using modis data. *ISPRS Int. Arch. Photogramm. Remote Sens. Spat. Inf. Sci.* **2018**, XLII-3, 485–490. [[CrossRef](#)]
32. Siitam, L.; Sipelgas, L.; Pärn, O.; Uiboupin, R. Statistical characterization of the sea ice extent during different winter scenarios in the Gulf of Riga (Baltic Sea) using optical remote-sensing imagery. *Int. J. Remote Sens.* **2016**, *38*, 617–638. [[CrossRef](#)]
33. Zhang, N.; Wu, Y.; Zhang, Q. Detection of sea ice in sediment laden water using MODIS in the Bohai Sea: A CART decision tree method. *Int. J. Remote Sens.* **2015**, *36*, 1661–1674. [[CrossRef](#)]
34. Li, Y.; Yang, D. Extraction of Bohai Sea ice from MODIS data based on multi-constraint endmembers and linear spectral unmixing. *Int. J. Remote Sens.* **2020**, *41*, 5525–5548. [[CrossRef](#)]
35. Liu, M.; Dai, Y.; Zhang, J.; Zhang, X.; Meng, J.; Xie, Q. PCA-based sea-ice image fusion of optical data by HIS transform and SAR data by wavelet transform. *Acta Oceanol. Sin.* **2015**, *34*, 59–67. [[CrossRef](#)]
36. Zhou, Y.; Zhang, Y.; Zhang, Y. Research on application of environment-1 satellite data in monitoring of beach and sea ice conditions in oilfields. In Proceedings of the 16th China Environmental Remote Sensing Application Technology Forum, Nanning, China, 29 March 2012.
37. Li, P.; Ke, Y.; Bai, J.; Zhang, S.; Chen, M.; Zhou, D. Spatiotemporal dynamics of suspended particulate matter in the Yellow River Estuary, China during the past two decades based on time-series Landsat and Sentinel-2 data. *Mar. Pollut. Bull.* **2019**, *149*, 110518. [[CrossRef](#)]
38. Haralick, R.M.; Shanmugam, K.; Dinstein, I.H. Textural Features for Image Classification. *IEEE Trans. Syst. Man Cybern.* **1973**, *SMC-3*, 610–621. [[CrossRef](#)]
39. Miao, X.; Xie, H.; Ackley, S.F.; Zheng, S. Object-Based Arctic Sea Ice Ridge Detection from High-Spatial-Resolution Imagery. *IEEE Geosci. Remote Sens. Lett.* **2016**, *13*, 787–791. [[CrossRef](#)]
40. Caldeira, K.; Cvijanovic, I. Estimating the Contribution of Sea Ice Response to Climate Sensitivity in a Climate Model. *JCLI* **2014**, *27*, 8597–8607. [[CrossRef](#)]
41. An, D.; Du, Y.; Berndtsson, R.; Niu, Z.; Zhang, L.; Yuan, F. Evidence of climate shift for temperature and precipitation extremes across Gansu Province in China. *Arch. Meteorol. Geophys. Bioclimatol. Ser. B* **2019**, *139*, 1137–1149. [[CrossRef](#)]
42. Cvijanovic, I.; Caldeira, K. Atmospheric impacts of sea ice decline in CO₂ induced global warming. *Clim. Dynam. CIDY* **2015**, *44*, 1173–1186. [[CrossRef](#)]
43. Noerdlinger, P.D.; Brower, K.R. The melting of floating ice raises the ocean level. *Geophys. J. Int.* **2007**, *170*, 145–150. [[CrossRef](#)]



Article

Classification of Land-Water Continuum Habitats Using Exclusively Airborne Topobathymetric Lidar Green Waveforms and Infrared Intensity Point Clouds

Mathilde Letard ^{1,*}, Antoine Collin ¹, Thomas Corpetti ², Dimitri Lague ³, Yves Pastol ⁴ and Anders Ekelund ⁵

¹ Coastal GeoEcology Lab, Ecole Pratique des Hautes Etudes—PSL Université, 35800 Dinard, France; antoine.collin@ephe.psl.eu

² UMR 6554 LETG, Université Rennes 2, CNRS, 35000 Rennes, France; thomas.corpetti@univ-rennes2.fr

³ Géosciences Rennes—UMR 6118, Univ Rennes, CNRS, 35000 Rennes, France; dimitri.lague@univ-rennes1.fr

⁴ Service Hydrographique et Océanographique de la Marine, 29200 Brest, France; yves.pastol@shom.fr

⁵ Airborne Hydrography AB, 553 03 Jonkoping, Sweden; anders.ekelund@hexagon.com

* Correspondence: mathilde.letard@ephe.psl.eu

Abstract: Coastal areas host highly valuable ecosystems that are increasingly exposed to the threats of global and local changes. Monitoring their evolution at a high temporal and spatial scale is therefore crucial and mostly possible through remote sensing. This article demonstrates the relevance of topobathymetric lidar data for coastal and estuarine habitat mapping by classifying bispectral data to produce 3D maps of 21 land and sea covers at very high resolution. Green lidar full waveforms are processed to retrieve tailored features corresponding to the signature of those habitats. These features, along with infrared intensities and elevations, are used as predictors for random forest classifications, and their respective contribution to the accuracy of the results is assessed. We find that green waveform features, infrared intensities, and elevations are complimentary and yield the best classification results when used in combination. With this configuration, a classification accuracy of 90.5% is achieved for the segmentation of our dual-wavelength lidar dataset. Eventually, we produce an original mapping of a coastal site under the form of a point cloud, paving the way for 3D classification and management of land and sea covers.

Keywords: topobathymetric lidar; full-waveform lidar; classification; coastal habitats; habitat mapping

Citation: Letard, M.; Collin, A.; Corpetti, T.; Lague, D.; Pastol, Y.; Ekelund, A. Classification of Land-Water Continuum Habitats Using Exclusively Airborne Topobathymetric Lidar Green Waveforms and Infrared Intensity Point Clouds. *Remote Sens.* **2022**, *14*, 341. <https://doi.org/10.3390/rs14020341>

Academic Editor: Junshi Xia

Received: 15 November 2021

Accepted: 7 January 2022

Published: 12 January 2022

Publisher's Note: MDPI stays neutral with regard to jurisdictional claims in published maps and institutional affiliations.



Copyright: © 2022 by the authors. Licensee MDPI, Basel, Switzerland. This article is an open access article distributed under the terms and conditions of the Creative Commons Attribution (CC BY) license (<https://creativecommons.org/licenses/by/4.0/>).

1. Introduction

Monitoring coastal areas is essential to the preservation of the land-water continuum's habitats and the services they provide, particularly in a context of local and global changes [1]. Seagrasses, salt marshes, mangroves, macroalgae, sandy dunes, or beaches are examples of such habitats that continually interact with the tide levels. They can be found along the temperate shorelines and play key roles in the ecological equilibrium of these ecotones. Seagrasses ensure water quality and are a significant carbon sink, along with salt marshes and mangroves [1,2]. Coastal habitats also provide protection from marine hazards to coastal communities and infrastructures and supply many recreational activities such as snorkeling, fishing, swimming, and land sailing [1–3]. Finally, they support a wide range of endemic species by offering them nurseries, food, and oxygen [1,2]. However, coastal (including estuarine) habitats are exposed to a plethora of natural and anthropic threats that may be amplified by global changes. Thorough observation of coastal processes is necessary to identify the trends of evolution of these fragile environments. It requires regular data acquisition along the shoreline with spatial resolution and time spacing both adapted to the task. However, the surveying complexities inherent to land-water continuum areas hinder their monitoring at a time scale relevant to their fast evolution, and over large, representative extents. Remote sensing can adequately address this issue.

Due to the presence of water, coastal surveys are conventionally split between topographic and bathymetric campaigns, both constrained to the tide and the field accessibility. Subtidal areas can be surveyed with waterborne acoustic techniques, while supratidal domains are documented with passive or active imagery using satellite, airborne, or unmanned aerial vehicles (UAV) [4–6]. Boats being unable to reach very shallow areas and imagery being limited by the water surface, intertidal, and shallow water areas are harder to accurately monitor [7]. Distinct terrestrial and marine surveying campaigns can also be difficult to merge, considering they might rely on different reference systems, and their thin overlapping area can be challenging to sample thoroughly with ground control points. Existing seamless surveying techniques over land-water interface areas are summarized in the following section.

Multispectral or superspectral imagery can be used for coastal habitat mapping. In clear and shallow water, traditional image classification techniques can be applied [7]. A more accurate approach consists in suppressing the effects of water on light refraction and diffusion by using inversion models on superspectral imagery. Using such models, it is possible to obtain satellite-derived bathymetry [8] or satellite-derived topobathymetry [9,10], which are proven to improve the classification of coastal covers obtained [11]. Bathymetry can also be extracted using multispectral imagery, as demonstrated in [12]. Multispectral imagery has the advantage of being accessible with different platforms: UAVs, planes, or satellites nowadays all benefit from multiband sensors. The cost of acquisition can therefore be lowered depending on the chosen source, and the revisit time can allow high temporal resolution monitoring.

Hyperspectral imagery is the last passive imagery-based method to map the land-water continuum [13,14]. The key principle of methods using hyperspectral imagery to study submerged areas is to model the interactions of light with the water column and correct them to obtain imagery unaffected by these processes. By inverting a radiative transfer model of the water column, it is possible to derive the seafloor reflectance and estimate the bathymetry [15]. These products are adapted to the characterization of sea bottom types and can be used for benthic classification tasks.

Although satellite passive imagery overcomes the issue of accessibility and temporal resolution, its spatial resolution is sometimes too coarse to spot specific changes (depending on the sensor and the quality of pan-sharpening), and it only penetrates water in shallow, clear areas [16]. The main issue with passive imagery remains the depth range in which it is usable. Due to optical phenomena, past a certain depth threshold that varies with water clarity, passive imagery can no longer give information on what lies beneath the water surface. Bathymetry extraction via active imaging then becomes the only way to gather information on these areas. Furthermore, even in shallow waters, bathymetry derived from active sensors gives access to the seabed covers' elevation but also to the seabed's elevation itself, providing 3D information on these covers, which enables biomass estimation or other structural assessments [17–20]. The bathymetry measurements obtained with active sensors (airborne bathymetric lidar or waterborne acoustic soundings) also leverage a higher vertical precision, useful for ecological structural assessments [12].

Airborne topobathymetric lidar is a reliable alternative: it ensures information continuity between land and water, covers vast areas quickly, penetrates a depth of up to dozens of meters and has a higher spatial resolution than satellite imagery [21,22]. Current approaches to map coastal interfaces using airborne lidar mostly make use of the digital terrain models or digital surface models derived from the lidar point clouds (PCs), including those obtained for the water bottoms after removing points corresponding to the water bodies [17]. Fewer studies rely on the 3D PCs of the lidar surveys to generate coastal or riverside habitats maps. Directly processing the PCs and avoiding rasterization has the advantage of preserving the dense spatial sampling provided by lidar sensors. It also opens possibilities for 3D rendering of the results, and structural analysis thanks to the rich spatial information contained in PCs. Indeed, the vertical repartition of the points offers useful information on scene architecture, providing relevant features to determine their origin,

namely for vegetation or building identification. Analysis of this geometrical context is the most frequently used method to produce maps of land and water covers [23–25]. Research works conducted on PCs processing mostly rely on the computation of geometrical features using spherical neighborhoods [23] and, more recently, on deep neural networks [26].

Another possibility with airborne lidar is to exploit the spectral details contained in the backscattered signals. These can be recorded under the form of time series of intensities received by the sensor: lidar waveforms. Each object of the surveyed environment illuminated by the sensor's laser reflects light in a specific way, generating a characteristic signature in the signal. Waveforms consequently provide additional information on the structure and physical attributes of the targets. The shape, width, and amplitude of their spectral signature—a peak—are information that can be used for land and water covers mapping [27–29]. Waveforms are therefore a useful indicator of the diversity of coastal areas. Though many methods have been proposed to process airborne topographic lidar full-waveforms, airborne bathymetric lidar full-waveforms are, to the best of our knowledge, much less explored. They are even less employed for classification tasks, and often only analyzed to retrieve bathymetry. There are currently three main approaches to waveform processing. The first consists in decomposing the waveforms to isolate each element of the train of echoes in the signal [30,31]. The second consists in reconstructing the signal by fitting statistical models to the waveforms [32]. Knowing how to approximate the sensed response allows to extract the position and the attributes of each component. The last approach is to analyze waveforms straightforwardly as any 1D signal to detect their peaks [27], using first derivative thresholding for example. Identifying waveform components is useful in order to localize the objects populating the scene, but also to extract features to describe them and prepare their automatic classification [27,33,34].

Classification of land or water covers using lidar data has been well explored recently. Even when using waveform data, most of the published research is based on 2D data classification [17,25,27,29,33] while fewer articles exploit PCs [24,34,35]. Many studies researching ways to classify lidar data used machine learning algorithms such as support vector machine (SVM), maximum likelihood (ML), or random forests. The maximum likelihood is mostly used for 2D lidar data, while SVM and random forests have been proofed on PCs. SVM and random forest seem to have similar classification performances on 3D lidar data [36]. However, with these algorithms, the spatial context around each point is not considered and does not impact the prediction [36]. Research papers show that conditional random field (CRF) and Markov random field (MRF) classifications produce better results in that way [36,37]. However, these require heavier computation and are more difficult to apply to large datasets. Currently, there is a consensus on the efficiency of random forest on that aspect [36]. Contrary to SVM, CRF, or MRF, it is easy to apply to large datasets. Random forest is, furthermore, robust to overfitting issues and offers the possibility to retrieve predictors contribution easily. In this article, we therefore wish to implement a hand-crafted features' random forest classification to map coastal habitats. Although machine learning classification of lidar waveform features has been explored previously, we have found no point-based studies dedicated to mapping a large number of habitats both marine and terrestrial. Previously cited studies such as [24,34,35] classified either only marine or only terrestrial habitats from PCs and [27] processed 2D data to produce their map of coastal habitats.

The present study aims at mapping an array of 21 habitats of the 3D land-water continuum seamlessly using exclusively airborne topobathymetric bispectral lidar. Our objective is to bridge the gap between marine and terrestrial surveys, demonstrate that efficient methods can be developed to automatically map the land-water interface, and show that an integrated vision of coastal zones is feasible and advised. Our contributions consist in (1) developing a point-based approach to exploit full-waveform data acquired during topobathymetric surveys for subtidal, intertidal, and supratidal habitats mapping, (2) quantifying the contribution of green waveform features, infrared (IR) intensities, and relief information to the classification accuracy based on a random forest machine learner.

We improve an experimental method presented in a previous work [29] and test it on a wider area including both emerged and submerged domains to determine the suitability of full-waveform lidar data for coastal zone mapping. UAV data, inexpensive to implement, is used to estimate the accuracy of the resulting very high spatial resolution maps, which are produced under the form of PCs, paving the way for 3D classification of land and sea covers using solely topobathymetric lidar data.

2. Materials

2.1. Study Area

The study location was chosen along the northern coasts of Brittany, France, for its ecological diversity and due to the availability of full-waveform lidar data acquired by the French Hydrographic Office (Shom) as part of the Litto3D[®] project [38]. The study area, presented in Figure 1, features typical coastal habitats such as fine sand or pebble beaches, a sandy dune, rocky areas provided with macroalgae, seagrass meadows, and salt marshes at the estuary of a local river. It also hosts a small resort town, Sables d'Or les Pins (48°38'27"N; 2°24'24"W). Buildings, tar or concrete-covered paths, boats in mooring, vehicles in parking lots, wooded areas populated with evergreen pine trees or deciduous species, and crop fields are also present in the selected zone. All these habitats are home to a rich variety of species: shellfish; dune plant vegetation; green, red, and brown seaweed; eelgrasses; evergreen and deciduous trees; crops; and salt marsh plants such as glasswort, common soda, sea purslane, or sea lavender.

2.2. Full-Waveform Airborne Topobathymetric Lidar

Airborne lidar is an active remote sensing technique that uses the backscatter of laser light in the environment to compute ranges to the ground cover and produce 3D maps of the environment, knowing the absolute position of the sensor. Topobathymetric lidar relies on two different lasers with distinct wavelengths: a green laser is added to the usual IR laser to detect the seabed or riverbed [21,22,39]. It exploits the physical properties of the green spectrum that penetrates the water surface, whereas the IR light does not. Lidar waveform is the recording of the full backscattered signal on the surveyed environment. A waveform consists in samples of recorded backscattered intensities over time. Since laser light is reflected by objects standing on its path, each element illuminated by the lidar laser backscatters a fraction of the emitted beam, which results in a peak in the waveform. Peaks are theoretically more or less intense depending on the object's albedo, its geometry and the laser incidence angle [40]. Due to the different layers of coverage in the environment (tree canopy, tree branches, bushes, soils, for example), there can be several peaks in the same waveform, all corresponding to a different layer in the reality. A typical topographic waveform (i.e., resulting from a laser beam hitting the land) has as many peaks as there are objects of different elevation in its way [28,39]. A bathymetric waveform usually has three main components: the first is the water surface return, the second is the water column return (originating from the backscatter of photons on particles suspended in the water such as sediments or nutrients), and the third is the return originating from the reflection on the seabed or riverbed [21,22,39]. Since all objects present in the cone illuminated by the laser reflect some light towards the sensor, they all contribute to the recorded waveform's shape [28]. Each element of the landscape/seascape is therefore characterized by the shape of its component in the waveform, which can be used for land or sea cover detection and classification [27,29,34,41]. In this work, backscattered intensities are converted into pseudo-reflectances by dividing them with the emitted pulse's intensity. Examples of a typical bathymetric waveform and a typical topographic waveform are presented in Figure 2.



Figure 1. Study area (datum: WGS 84; projection: UTM 30N).

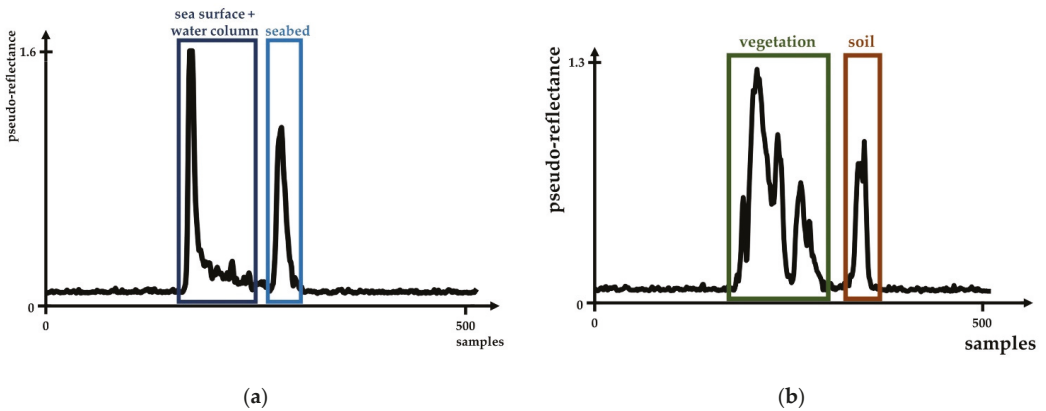


Figure 2. Examples of typical lidar waveforms (for a green laser with a wavelength of 515 nm). (a) Bathymetric waveform acquired in a coastal area; (b) topographic waveform acquired in a vegetated area. A sample corresponds to 556 picoseconds.

2.3. Datasets

The lidar data [42] used for this research were acquired over the coast of Sables d'Or les Pins in September 2019 by the Shom as part of the Litto3D[®] project [38], using a Leica HawkEye 4X sensor. The HawkEye 4X produces laser pulses at wavelengths of 515 nm and 1064 nm on three different channels. Depths under 10 m have a dedicated shallow green laser, while a more powerful laser, the deep channel, is used to detect deeper seabed. These two channels provide PCs with a density of at least five points per m² and one point per m² and they have a laser spot size diameter of 1.8 m and 3.4 m, respectively. The IR laser has a laser spot size of 0.2 m and a point density of at least 10 points per m². For green channels only, backscattered intensities are recorded with a time frequency of 1.8 GHz, providing waveforms with a sample every 556 picoseconds. This information is not available for the IR laser.

The survey was conducted with a constant laser amplification. Due to the power needed to penetrate through several meters of water, the shallow laser's backscattered intensities tend to be saturated over highly reflective land surfaces, but they are still usable. The deep channel's returned intensities, however, are systematically saturated and do not provide usable information for land cover classification. In this study, only shallow full waveforms were used, considering the selected area's range of depths. The green waveforms used were available for every shallow green laser shot. Over the studied area, their average density was 3.75 waveforms per m². Reanalyzed echo PCs for both shallow green and IR wavelengths were also used: the IR PC brought additional spectral information, while the green PC was used to accurately position the raw waveforms, since this PC underwent refraction correction before delivery. The effects of refraction were not corrected in the raw waveform files.

To provide knowledge on the environment on site, ground truth data (presented in Figure 3) were acquired in the form of photoquadrats and UAV imagery. They helped label the lidar data to perform habitat classification. UAV imagery was acquired over five smaller areas of interest, each representing typical coastal habitats, in March and April 2021 using an RGB DJI Phantom 4 Pro V2, and a Parrot Sequoia+ including a near IR nadir sensor (770 nm to 810 nm) with a zenithal irradiance sensor. These flights were calibrated with a total of 55 ground control points. An array of 150 photoquadrats were captured with RGB cameras and georeferenced, to seize the ecological diversity of the study area. Over marine parts of the study site, a PowerVision unmanned surface vehicle (USV) was used to gather knowledge of the seabed covers. The underwater images were acquired in September 2021. An RGB orthoimage acquired in 2014 over the whole area was also used to give extra information on the habitats present on site four years prior to the data acquisition.

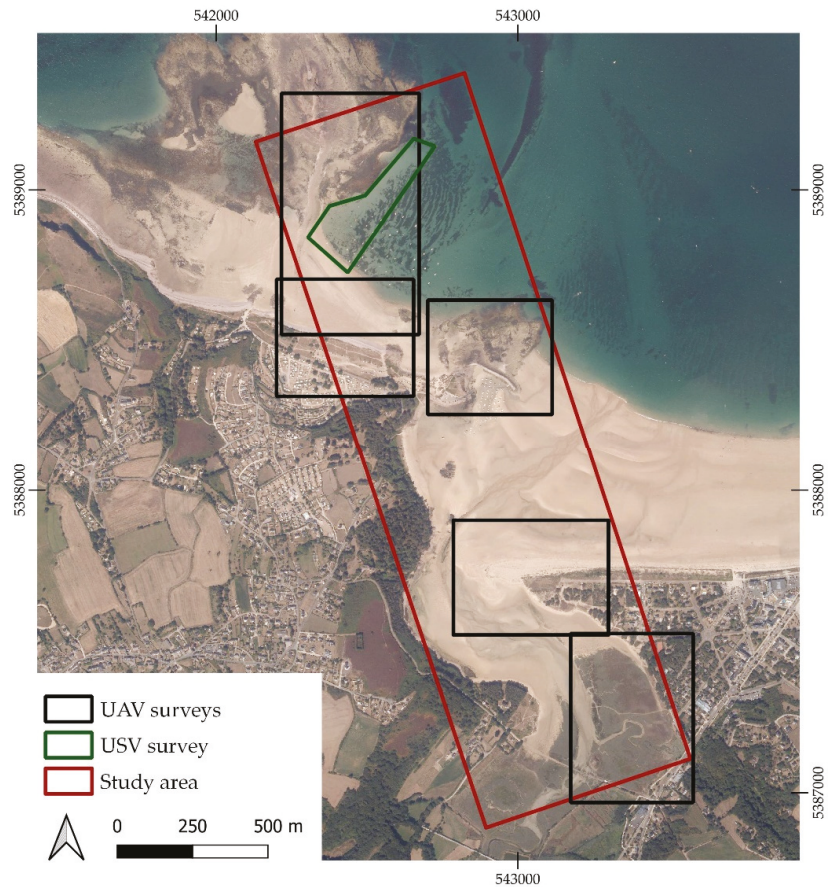


Figure 3. Ground truth data spatial coverage (datum: WGS 84; projection: UTM 30N).

3. Methodology

The algorithm developed in this study was first introduced in [29] to identify marine habitats using green full-waveform spectral features. In [29], only seagrasses and sediments (two classes) at few meters' depths were classified. We significantly improved this algorithm and adapted it to the classification of 21 habitats across the land-water interface, to test its abilities in supratidal and intertidal environments.

The enhanced version presented here was tailored to the identification of land and sea covers: the seabed or riverbed type was considered in the presence of water while we focused on the surface cover over terrestrial areas (i.e., if there were two layers of surface covers, such as a trees and grass beneath it, the land cover was labelled as tree). It used a supervised point-based classification algorithm trained on various sets of input features and evaluated on a test dataset. Classified PCs of the whole area were also produced to observe the ability of each predictor sets to produce a map of the habitats in the study area using this approach.

3.1. Classes of Land and Sea Covers Investigated

A total of 21 classes of land and sea covers has been designed based on on-site observations and photo-interpretation. These classes are illustrated in Table 1.

Table 1. Classes of land and sea covers identified in the study area.

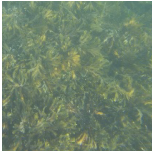
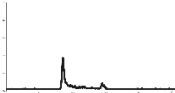

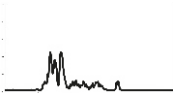
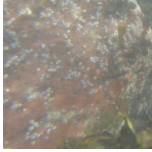
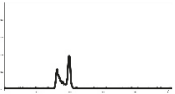
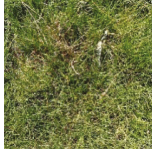
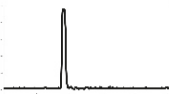

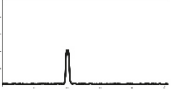

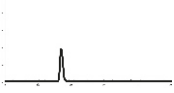

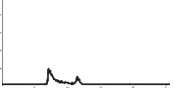

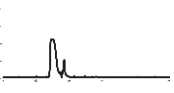
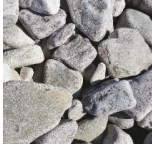
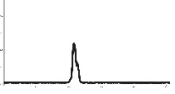

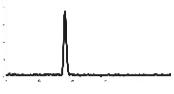

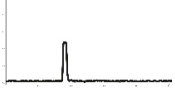
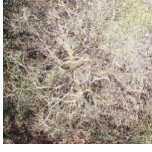
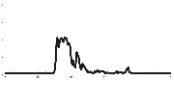
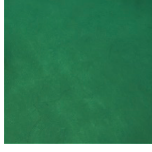
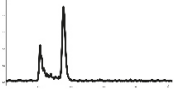
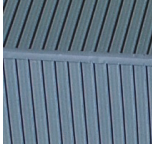
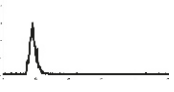
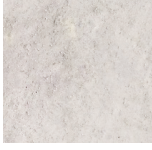
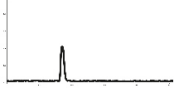
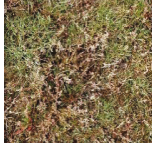
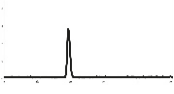

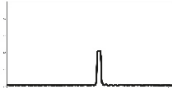

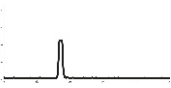
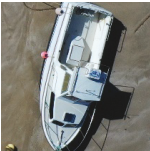
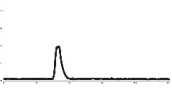

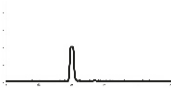


| Class Name | Illustration | Waveform | Class Name | Illustration | Waveform |
|-----------------------|---|---|-----------------------|---|---|
| Fleshy macroalgae |  |  | Evergreen tree |  |  |
| Submerged rock |  |  | Lawn/grass/crop field |  |  |
| Emerged rock |  |  | Wet sand |  |  |
| Seagrasses |  |  | Shrub |  |  |
| Pebble/cobble/boulder |  |  | Dry sand |  |  |
| Concrete |  |  | Deciduous tree |  |  |
| Submerged sand |  |  | Roof |  |  |
| Soil |  |  | Low salt marsh |  |  |

Table 1. Cont.

| Class Name | Illustration | Waveform | Class Name | Illustration | Waveform |
|------------|---|---|-----------------|---|---|
| Tar |  |  | Mid salt marsh |  |  |
| Boat |  |  | High salt marsh |  |  |
| Car |  |  | | | |

3.2. Data Pre-Processing

The classification algorithm developed for this research aimed at processing bispectral lidar data. Two PCs were therefore used, but full-waveforms were available only for the green wavelength. IR data were thus incorporated as reflected intensities only. Due to the sensor's configuration, IR and green lasers of the topobathymetric lidar used are not co-focal. They also do not have the same swath, density, and precision. The two resulting PCs are consequently different, and the points acquired do not have identical locations. A preprocessing step was therefore required to obtain the IR backscattered intensity at each green waveform's location. Intensities of the IR PC were matched with each point of the green waveforms PC, which was kept as the reference PC, using the median IR intensity of the 10 nearest neighbors of each green waveform's location in the IR PC, which was computed and assigned to the waveform as an attribute. To this end, we used the PC processing software "CloudCompare" [43], in which the neighborhood search is performed by computing the 3D Euclidean distance between each point of the reference PC and the points of the compared PC. The coordinates of the waveforms' cover component were used to locate each waveform and obtain a green waveform PC. Consequently, each waveform was synthesized as a point, and we obtained a green waveforms PC. The IR PC was cleaned manually beforehand, to ensure all noise points, significantly above the surface, were removed from the data.

The median intensity of the 10 closest neighbors in the IR PC was chosen for two reasons. First, the number of 10 neighbors was relevant considering the difference of the two lasers' spot sizes and the resulting density of the PCs. Second, the use of the median intensity was more suited to the task than the mean intensity to avoid outliers' artefacts in spheres located at the interface of two habitats.

3.3. Training and Testing Datasets

Two main datasets were designed to perform the data classifications and assess their quality, called the training dataset and test dataset. We collected 1000 training and 500 testing samples of each class. To do so, we first drew polygons over representative areas of the 21 land and water covers, based on the ground-truth data, and made sure none of the polygons intersected. We used these to segment the PC and extract points located within representative areas of each class. For each class, we then randomly selected 1000 of them

for the training datasets and 500 others for testing, which resulted in training and test datasets of 21,000 and 10,500 items, respectively. This draw without replacement ensured that no training and testing points were the same and that they were all independent. We chose to use the same areas for random drawing of training and testing points in order to account for the widest diversity possible in the training and testing samples. The resulting training and test points have a mean distance of 1.6 m; their repartition is presented in Figure 4.

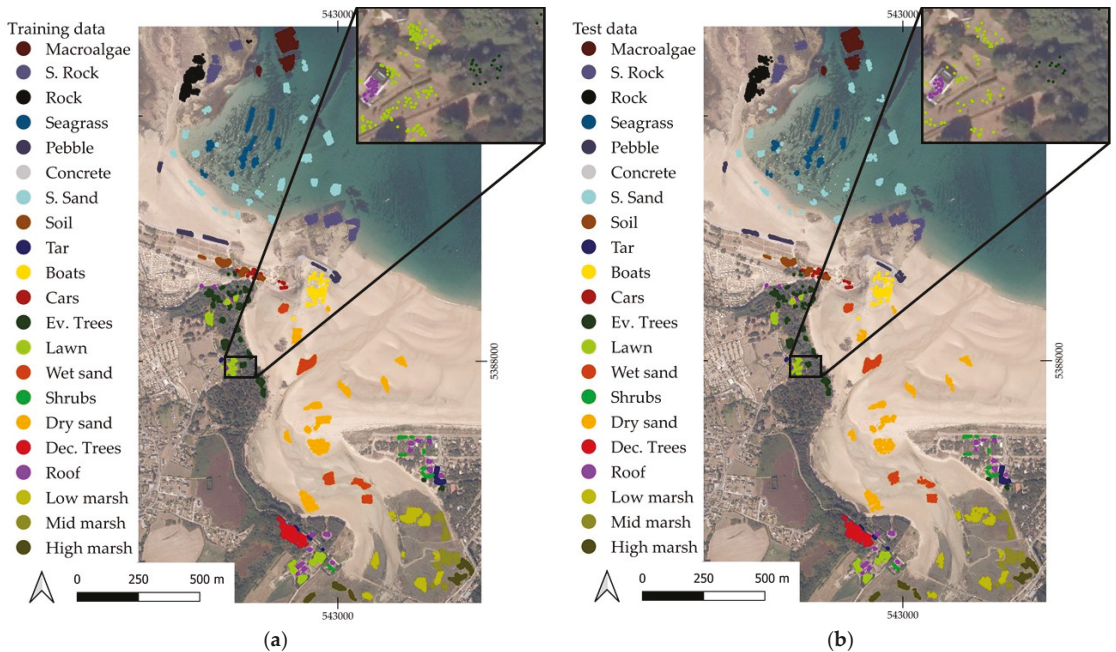


Figure 4. Repartition of the training and test data over the study area (datum: WGS 84; projection: UTM 30N). (a) Training data distribution; (b) test data distribution. S. = submerged, Ev. = evergreen, Dec. = deciduous. The size of the points in the illustration may give a false impression of overlapping, but all points have distinct locations.

Each array of coordinates, IR intensities, and waveform features was associated to one integer label between 1 and 21, forming a dataset with the structure illustrated in Figure 5.

$$\begin{array}{cccccccccccccccccccc}
 X^1, & Y^1, & Z^1, & \text{Feature}^1_1, & \dots & \dots & \dots & \dots & \dots & \dots & \dots & \dots & \dots & \dots & \dots & \dots & \dots & \text{Feature}^1_{16}, & \text{IR}^1, & \text{label}^1 \\
 \vdots & \vdots & \vdots & \vdots & & & & & & & & & & & & & & & \vdots & \vdots & \vdots \\
 \vdots & \vdots & \vdots & \vdots & & & & & & & & & & & & & & \vdots & \vdots & \vdots \\
 \vdots & \vdots & \vdots & \vdots & & & & & & & & & & & & & & \vdots & \vdots & \vdots \\
 X^n, & Y^n, & Z^n, & \text{Feature}^n_1, & \dots & \dots & \dots & \dots & \dots & \dots & \dots & \dots & \dots & \dots & \dots & \dots & \dots & \text{Feature}^n_{16}, & \text{IR}^n, & \text{label}^n
 \end{array}$$

Figure 5. Structure of the dataset obtained after waveform and infrared intensities processing.

The point-based classification method is described in the following paragraphs. It relied on the interpolated IR intensities and on spectral features extracted from the green waveforms.

3.4. Waveform Processing Method

The waveform processing steps are presented in Figure 6 and detailed in the following paragraphs. All these steps were performed using tailored scripts developed with Python 3.8.8.

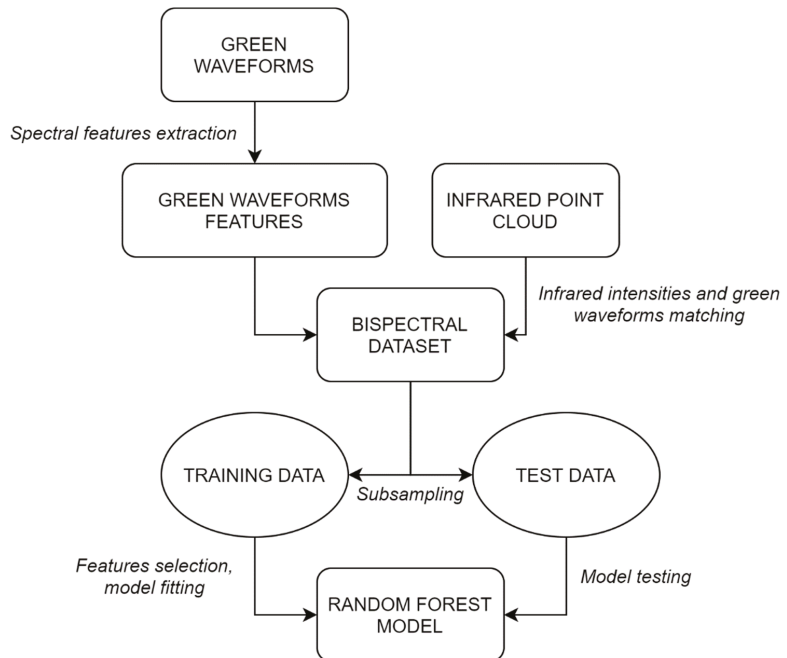


Figure 6. Flowchart of the overall methodology.

The base concept consists in extracting tailored features from the relevant part of the waveforms. Here, we considered this part to be any return detected after the water surface component in submerged domains, and the part of the waveform encompassing the backscattered signal in terrestrial zones. In these zones, the sole processing was to isolate the useful part of the green waveform by identifying where the backscatter begins and the noise ends. This was made by evaluating the mean level of noise observable at the beginning and at the end of the waveform and extracting the part of the wave where the intensity was above this noise level.

To distinguish marine and terrestrial waveforms, we relied on a flag attributed by the Leica survey software Leica LIDAR Survey Studio (LSS) to points in the PC that correspond to an interpolated water surface under which refraction correction is made. Since waveform files integrate this information, it was possible to use it to differentiate submerged and emerged areas. This step is a pre-classification made by LSS before the data was delivered to us.

In submerged areas, further processing was required to detect the different peaks and isolate the parts of the signal that correspond to the water surface and the water column components. All green waveforms were first filtered using the Savitzky–Golay piecewise polynomial functions estimation method to remove the noise. As explained in [29], a threshold was then applied to the first derivative of the smoothed waveforms to bring out the peaks. This step was well suited to the detection of the most significant peaks; however, depending on local conditions affecting the reflection of light, some bottom returns may be less intense and hard to expose. We therefore included a second thresholding: when only one peak was identified with the first threshold, another derivative thresholding step was

introduced to try to detect peaks after the water surface (i.e., the peak already detected). This second threshold had a lower value, which would exacerbate noise if it were used on the whole waveform, but it was adapted to the detection of more attenuated returns when used on the underwater part of the waveform. If no additional return was identified with this first derivative thresholding, we concluded that no seabed was retrieved and discarded the waveform since there was no return to compute features on.

The same correction of the signal’s attenuation in water as the one in [29] was applied to bathymetric waveforms; it relied on the fitting of an exponential function on the water column component to compensate for the effects of water absorption and diffusion in water on the bottom return. This was based on the estimation of the diffuse attenuation coefficient [21,22] through the evaluation of the intensity gradient at the end of the surface return. However, since there were mathematical limitations to this approach in very shallow water areas, no correction was applied in depths under 0.125 m since the optimization was impossible on a water column component containing less than two waveform samples (one sample corresponds to 0.063 m in that scenario). In places where depths were smaller than 0.125 m and over land, the attenuation was fixed at 0.

The waveform processing is summarized and illustrated in Figure 7.

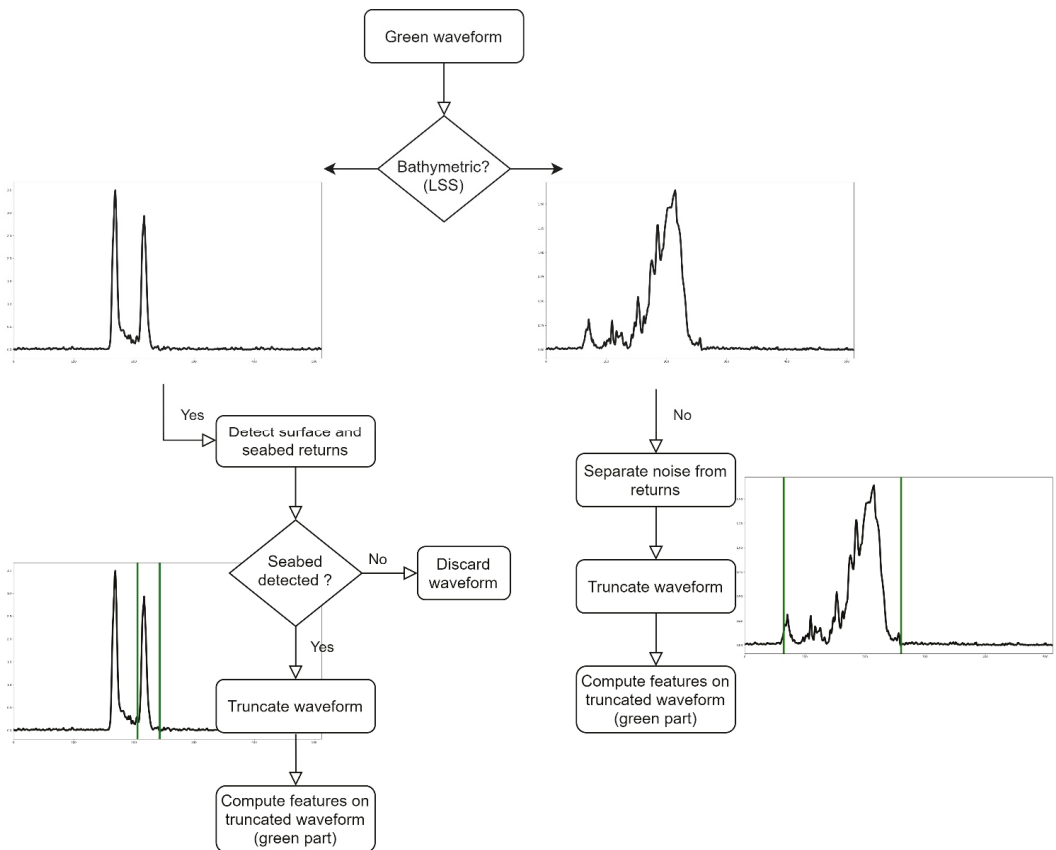


Figure 7. Waveform processing method flowchart and illustration on two different waveforms: one acquired over the sea, the other over land.

3.5. Waveform Features' Extraction

Once all waveform components corresponding to ground or seabed covers were isolated, these intensities time series were converted into pseudo-reflectance series by dividing them with the emitted laser pulse intensity. This allowed us to remove potential bias induced by slightly varying emitted laser intensity. Statistical parameters were then computed on these truncated and normalized waveforms. They were selected based on [27,29,44] and are described in Table 2.

Table 2. Name and definition of the features extracted from the green waveforms during processing and used as input variables to the random forest model.

| Name | Definition |
|---|---|
| Z | Elevation of the ground (beneath any surface cover) |
| Diffuse attenuation coefficient estimated value | Value of the coefficient of attenuation of light in water (=0 for depths < 0.125 m and on land) |
| Complexity of the peak | Number of sign changes of the peak's first derivative |
| Mean | Mean pseudo-reflectance of the peak (after attenuation correction) |
| Median | Median pseudo-reflectance of the peak (after attenuation correction) |
| Maximum | Maximum pseudo-reflectance of the peak (after attenuation correction) |
| Standard deviation | Standard deviation of the pseudo-reflectance of the peak (after attenuation correction) |
| Variance | Variance of the pseudo-reflectance of the peak (after attenuation correction) |
| Skewness | Skewness of the peak (after attenuation correction) |
| Kurtosis | Kurtosis of the peak (after attenuation correction) |
| Area under curve | Area under the curve formed by the peak (after attenuation correction) |
| Amplitude | Amplitude of the pseudo-reflectance of the peak (after attenuation correction) |
| Time range | Time duration of the peak (in number of samples) |
| Total | Sum of pseudo-reflectance values forming the peak (after attenuation correction) |
| Height | Difference of altitude between the peak of the first layer of cover and the last peak. |
| Maximum before correction | Maximum pseudo-reflectance of the peak (without attenuation correction) |
| Position of the maximum in the peak | Position of the maximum in the peak (in sample indices) |

The terrain's elevation value was also extracted: for topographic waveforms, it corresponds to the last return's altitude (computed using traditional time of flight range measurement, extracted from the PC). For bathymetric waveforms, it was computed using the depth of the last return identified by our algorithm and withdrew to the altitude of our detected surface return, positioned with the PC. The vertical reference was the IGN 1969 system.

The spectral features computed on the truncated green waveforms, the IR intensities associated with the points and the elevations were then used as predictors for random

forest classifications of ground covers over the study area. The 21,000 items of the dedicated dataset were used for the algorithm's training, and the 10,500 items of the testing dataset were used to assess the quality of the predictions.

3.6. Random Forest Classification

Contrary to [29], the data were not rasterized but features were directly classified to produce a 3D habitat map so as to avoid information loss. We also relied on a different classifier to predict data labels. A random forest model with 150 trees was used for the classification step. Considering that we wished to apply it to a dataset containing 24.5 million items after fitting, we chose a high number of trees to populate the forest, knowing that more trees theoretically equal to better classification accuracy and that the number of trees needs to be adapted to the complexity of the dataset. We also based our choice on the observation made in [45] on several different datasets that state that past 128 trees in the forest, classification accuracy gains become negligible for each additional tree, compared to computational demands. The maximum tree depth was not fixed so that nodes expanded until the leaves were pure. We relied on impurity to determine whether a leaf has to be split or not using the Gini impurity criterion, which was calculated using the following formula:

$$\text{GiniIndex} = 1 - \sum_j p_j^2, \quad (1)$$

where p_j is the probability of class j . This criterion is close to 0 when the split is optimal.

We controlled the generalizability and over-fitting of the model by monitoring the generalization score obtained on random out-of-bag samples at each fitting step. The random forest implementation of the Python library *scikit-learn* was used.

3.7. Comparative Study

Random forest classifications were launched on several sets of predictors that were clustered based on their conceptual similarity. The performance metrics of each group of features were then retrieved. This allowed us to evaluate the contribution of each family of feature to the classification accuracy. The feature sets were the following:

- Statistical features: mean, median, maximum, standard deviation, variance, amplitude, and total;
- Peak shape features: complexity, skewness, kurtosis, area under curve, time range, and height;
- Lidar return features: diffuse attenuation coefficient estimated value, maximum, maximum before attenuation correction, position of the maximum in the peak, and associated IR intensity;
- Green spectral features: all features extracted from the green waveforms, except elevation (which is later referred to as Z).

We also performed importance variable contribution analysis by dropping green waveform features one by one and computing the classification accuracy difference between the reduced set of 15 predictors and the full 16 attributes.

3.8. Results' Quality Assessment

Classification performances were assessed by considering the values obtained on the test dataset by the random forest classifier for the following metrics: overall accuracy (OA, ratio of correct predictions, best when its value is 1), precision (fraction of correct predictions among each ground truth classes, best when its value is 1), recall (fraction of correct estimation for each predicted classes, best when its value is 1), and F-score (combination of precision and recall, best when its value is 1). The precision, recall, and F-score were computed for each label, and their unweighted mean was used to compare the results obtained. Confusion matrixes presenting the producer's accuracies (PA) were also created to analyze the performances of classification on each of the 21 classes.

3.9. Spatialization of the Random Forest Predictions

Although coordinates were not used during classification, the arrays of features were geolocated with the position of the waveform's last echo, as illustrated by Figure 5. To visualize our classification results as PCs, we associated the predictions' vector to these coordinates. This allowed us to obtain the result under the form of a classified PC. The fact that we did not rasterize our data had the advantage of preserving the spatial density and therefore the spatial resolution, while also avoiding the critical issue of mixed pixels [46].

Each waveform was localized with the planar coordinates of its last return using the PC coordinates. For bathymetric waveforms, this ensured that the effects of refraction of the laser beam on the air/water interface were considered, since the green PC was corrected before data delivery.

4. Results

4.1. Random Forest Classifications' Performances on the Test Dataset

Ten random forest models were trained on the training dataset—one for each configuration of predictors defined in Section 3.7. Their performances were evaluated using four metrics computed on the predictions made on the test dataset. Four of them were then used to predict labels for the complete study area and produce habitat maps under the form of PCs.

Fitting the models to the 21,000 items training dataset took on average 0.4 s. Predictions on the test dataset (which contains 10,500 items) required a mean computing time of 0.2 s. The complete area, representing a total of more than 24.5 million items, was covered in 17 to 18 min. All computations were made on a machine equipped with an AMD Ryzen 9 5900X 12-Core CPU and an NVIDIA GeForce RTX 3080 GPU.

The classification metrics obtained on each set of features defined in Section 3.7. are presented in Table 3. The very close values observed between the four criteria for each feature set are due to the averaging of each metric's value obtained for each classification label. They are also explained by the fact that all classes are balanced. The scores obtained show that our method does not have a systematic tendency to over- or under-estimate some classes.

When using only subsets of green waveform features, the random forest predictions were more often false than they were correct. However, grouping the waveform variable families improved the accuracy by at least 4%. The best configuration—composed of peak shape features and lidar return features—provided a classification accuracy of 69%. Globally, coupling statistical features with peak shapes features tended to result in accuracy loss while using combinations where they were not mixed resulted in classification performance gains. Indeed, the complete set of features obtained through green waveform processing predicted the habitat type with an OA of 56%, while the output of the classification of statistical and lidar return features was correct in 67% of cases (see Table 3).

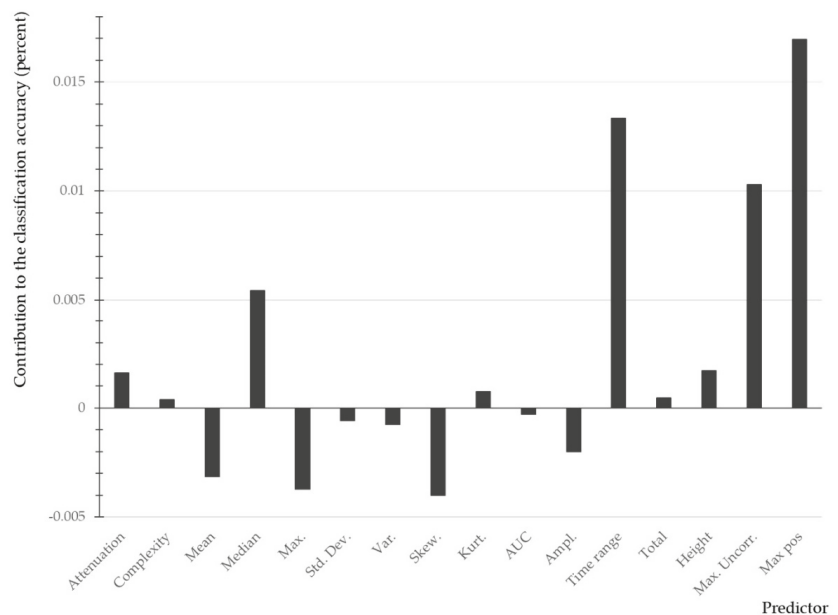
The addition of IR intensity values to the full set of green waveform parameters improved the OA of 13%, which is 5% above the best OA obtained on a subset of green waveform attributes. The contribution of the elevation to the classification accuracy was even higher: there was a 31.5% gain in OA between the green spectral features' classification and the classification of green spectral features and elevations. Gathering the three sources of information produced the most accurate result, with an OA of 90.5% (Table 3).

Table 3. Performance metrics obtained by each random forest experiment.

| Features Set | Overall Accuracy | Recall | Precision | F-Score |
|--|------------------|--------|-----------|---------|
| Statistical features | 0.45 | 0.45 | 0.444 | 0.444 |
| Peak shape features | 0.463 | 0.463 | 0.452 | 0.455 |
| Lidar return features | 0.479 | 0.479 | 0.471 | 0.474 |
| Statistical features + Peak shape features | 0.519 | 0.519 | 0.512 | 0.513 |
| Peak shape features + Lidar return features | 0.686 | 0.686 | 0.681 | 0.681 |
| Statistical features + Lidar return features | 0.662 | 0.662 | 0.657 | 0.657 |
| Green spectral features | 0.559 | 0.559 | 0.552 | 0.552 |
| Z | 0.551 | 0.551 | 0.549 | 0.549 |
| IR intensity | 0.241 | 0.241 | 0.238 | 0.238 |
| Green spectral features and IR intensity | 0.691 | 0.691 | 0.687 | 0.687 |
| IR intensity + Z | 0.75 | 0.75 | 0.745 | 0.746 |
| Green spectral features + Z | 0.874 | 0.874 | 0.875 | 0.873 |
| Green spectral features + IR intensity + Z | 0.905 | 0.905 | 0.905 | 0.905 |

4.2. Green Waveform Features' Contribution to the Classification Accuracy

Figure 8 illustrates the contribution of each predictor to the accuracy of the classification of green waveform features. It sheds light on the value-added of each attribute computed on the truncated waveforms. This assessment reveals that 9 of the 16 features extracted on each waveform contributed positively to the classification performance. The seven others had a negative impact on the quality of the random forest predictions. They were mostly parameters of the “statistical features” set, although each type of waveform parameter—statistical, peak shape-related, or lidar return-related—was represented in the nine positively contributing attributes.

**Figure 8.** Predictors' contribution to the green waveform features' classification accuracy (in fraction of accuracy).

An in-depth analysis of the four last random forest experiments is provided in the following sections.

4.3. Land-Water Continuum Habitat 3D Modelling

By running the waveform processing algorithm and the classifiers on the whole study area, we obtained a 21-class semantic segmentation of our complete bathymetric lidar dataset.

As expected, when dealing with PCs and not rasters, the results were noisy, but some areas had lower speckle than others. The observable ratio between information and noise gradually improved with the addition of IR intensity and elevations. The best output was obtained by combining green waveform features, IR intensities, and elevations; it is presented in Figure 9. The other results are presented in Appendix A (Figures A1–A3).



Figure 9. Projected 3D map of the habitats obtained with the predictions of a random forest classifier on green spectral features, infrared intensities, and elevation values; orthoimage of the study area. The orthoimage was captured in 2014, while lidar data are not contemporaneous as they date from 2019. S. = submerged, Ev. = evergreen, Dec. = deciduous.

The main strength of this result was the distinction between submerged and emerged domains: except for boat false-positives on the water surface, marine classes were rarely detected over land, and vice versa. Globally, this map showed better definition of the considered habitats than the others (see Figures A1–A3), and fewer classification errors, although improvements on some classes coexisted with poorer performance on other classes. Figures 10–13 gave a more detailed insight into the classification in specific areas.

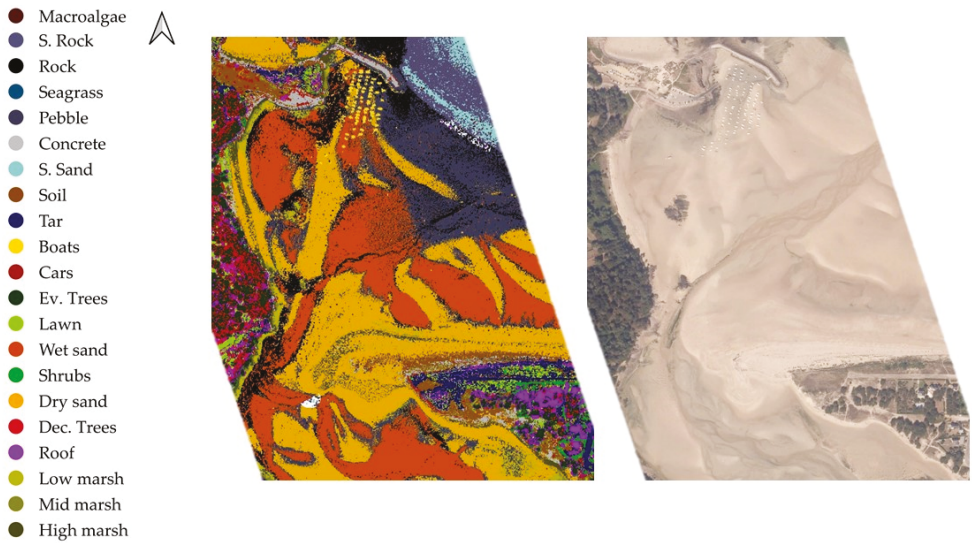


Figure 10. Urban area and sand beach classification: Extract of the projected 3D map of the habitats obtained with the predictions of a random forest classifier on green spectral features, infrared intensities, and elevation values, and extract of an orthoimage of the same area. The orthoimage was captured in 2014, while lidar data are not contemporaneous as they date from 2019. S. = submerged, Ev. = evergreen, Dec. = deciduous.

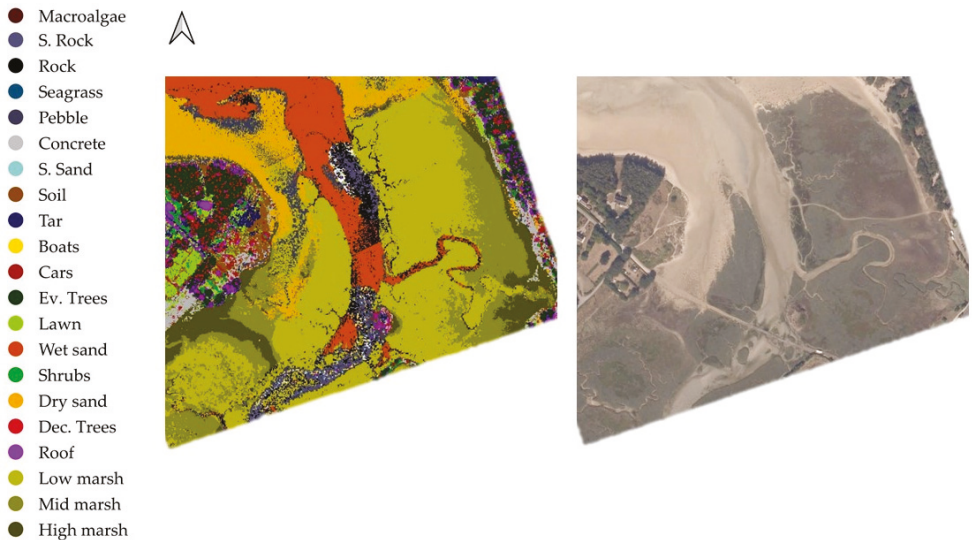


Figure 11. Salt marsh classification: Extract of the projected 3D map of the habitats obtained with the predictions of a random forest classifier on green spectral features, infrared intensities, and elevation values, and extract of an orthoimage of the same area. The orthoimage was captured in 2014, while lidar data are not contemporaneous as they date from 2019. S. = submerged, Ev. = evergreen, Dec. = deciduous.

- Macroalgae
- S. Rock
- Rock
- Seagrass
- Pebble
- Concrete
- S. Sand
- Soil
- Tar
- Boats
- Cars
- Ev. Trees
- Lawn
- Wet sand
- Shrubs
- Dry sand
- Dec. Trees
- Roof
- Low marsh
- Mid marsh
- High marsh

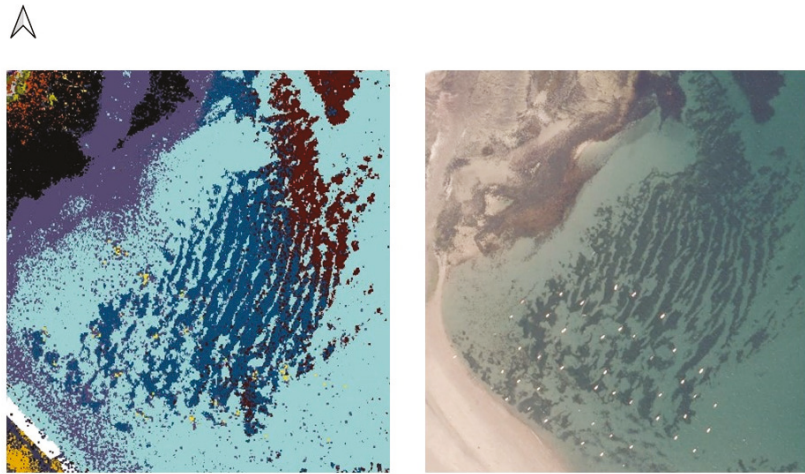


Figure 12. Seagrass meadow classification: Extract of the projected 3D map of the habitats obtained with the predictions of a random forest classifier on green spectral features, infrared intensities, and elevation values, and extract of an orthoimage of the same area. The orthoimage was captured in 2014, while lidar data are not contemporaneous as they date from 2019. S. = submerged, Ev. = evergreen, Dec. = deciduous.

| | | Predicted | | | | | | | | | | | | | | | | | | | | | | |
|----------|------------|------------|---------|------|----------|--------|----------|---------|------|------|-------|------|-----------|------|---------|--------|---------|------------|------|----------|----------|----------|------|------|
| Class | | Macroalgae | S. Rock | Rock | Seagrass | Pebble | Concrete | S. Sand | Soil | Tar | Boats | Cars | Ev. trees | Lawn | W. sand | Shrubs | D. sand | Dec. trees | Roof | L. marsh | M. marsh | H. marsh | | |
| True | Macroalgae | 0.84 | 0.00 | 0.00 | 0.16 | 0.00 | 0.00 | 0.01 | 0.00 | 0.00 | 0.00 | 0.00 | 0.00 | 0.00 | 0.00 | 0.00 | 0.00 | 0.00 | 0.00 | 0.00 | 0.00 | 0.00 | 0.00 | |
| | S. Rock | 0.01 | 0.90 | 0.00 | 0.04 | 0.00 | 0.00 | 0.05 | 0.00 | 0.00 | 0.00 | 0.00 | 0.00 | 0.00 | 0.00 | 0.00 | 0.00 | 0.00 | 0.00 | 0.00 | 0.00 | 0.00 | 0.00 | |
| | Rock | 0.00 | 0.00 | 0.94 | 0.00 | 0.03 | 0.00 | 0.00 | 0.00 | 0.00 | 0.00 | 0.00 | 0.00 | 0.00 | 0.00 | 0.01 | 0.00 | 0.00 | 0.00 | 0.00 | 0.00 | 0.00 | 0.00 | 0.00 |
| | Seagrass | 0.10 | 0.04 | 0.00 | 0.86 | 0.00 | 0.00 | 0.00 | 0.00 | 0.00 | 0.00 | 0.00 | 0.00 | 0.00 | 0.00 | 0.00 | 0.00 | 0.00 | 0.00 | 0.00 | 0.00 | 0.00 | 0.00 | 0.00 |
| | Pebble | 0.00 | 0.00 | 0.08 | 0.00 | 0.77 | 0.04 | 0.00 | 0.00 | 0.00 | 0.00 | 0.03 | 0.00 | 0.00 | 0.00 | 0.00 | 0.00 | 0.00 | 0.00 | 0.00 | 0.02 | 0.02 | 0.02 | 0.04 |
| | Concrete | 0.00 | 0.00 | 0.00 | 0.00 | 0.00 | 0.95 | 0.00 | 0.02 | 0.00 | 0.00 | 0.00 | 0.00 | 0.01 | 0.00 | 0.00 | 0.00 | 0.00 | 0.00 | 0.00 | 0.00 | 0.00 | 0.00 | 0.01 |
| | S. Sand | 0.01 | 0.07 | 0.00 | 0.00 | 0.00 | 0.00 | 0.93 | 0.00 | 0.00 | 0.00 | 0.00 | 0.00 | 0.00 | 0.00 | 0.00 | 0.00 | 0.00 | 0.00 | 0.00 | 0.00 | 0.00 | 0.00 | 0.00 |
| | Soil | 0.00 | 0.00 | 0.00 | 0.00 | 0.00 | 0.03 | 0.00 | 0.83 | 0.00 | 0.00 | 0.00 | 0.00 | 0.12 | 0.00 | 0.00 | 0.01 | 0.00 | 0.00 | 0.00 | 0.00 | 0.00 | 0.00 | 0.00 |
| | Tar | 0.00 | 0.00 | 0.00 | 0.00 | 0.00 | 0.00 | 0.00 | 0.01 | 0.97 | 0.00 | 0.00 | 0.00 | 0.00 | 0.01 | 0.00 | 0.00 | 0.00 | 0.00 | 0.01 | 0.00 | 0.00 | 0.00 | 0.00 |
| | Boats | 0.00 | 0.00 | 0.00 | 0.00 | 0.01 | 0.00 | 0.00 | 0.00 | 0.00 | 0.99 | 0.00 | 0.00 | 0.00 | 0.00 | 0.00 | 0.00 | 0.00 | 0.00 | 0.00 | 0.00 | 0.00 | 0.00 | 0.00 |
| | Cars | 0.00 | 0.00 | 0.00 | 0.00 | 0.00 | 0.00 | 0.00 | 0.01 | 0.00 | 0.00 | 0.96 | 0.00 | 0.01 | 0.00 | 0.01 | 0.00 | 0.00 | 0.00 | 0.00 | 0.00 | 0.00 | 0.00 | 0.00 |
| | Ev. trees | 0.00 | 0.00 | 0.00 | 0.00 | 0.00 | 0.00 | 0.00 | 0.00 | 0.00 | 0.00 | 0.00 | 0.73 | 0.00 | 0.00 | 0.01 | 0.00 | 0.24 | 0.02 | 0.00 | 0.00 | 0.00 | 0.00 | 0.00 |
| | Lawn | 0.00 | 0.00 | 0.00 | 0.00 | 0.00 | 0.03 | 0.00 | 0.05 | 0.01 | 0.00 | 0.00 | 0.00 | 0.90 | 0.00 | 0.00 | 0.00 | 0.00 | 0.01 | 0.00 | 0.00 | 0.00 | 0.00 | 0.00 |
| | W. sand | 0.00 | 0.00 | 0.01 | 0.00 | 0.00 | 0.00 | 0.00 | 0.00 | 0.00 | 0.00 | 0.00 | 0.00 | 0.00 | 0.99 | 0.00 | 0.00 | 0.00 | 0.00 | 0.00 | 0.00 | 0.00 | 0.00 | 0.00 |
| | Shrubs | 0.00 | 0.00 | 0.00 | 0.00 | 0.00 | 0.00 | 0.00 | 0.01 | 0.00 | 0.00 | 0.00 | 0.00 | 0.00 | 0.00 | 0.96 | 0.00 | 0.00 | 0.01 | 0.00 | 0.00 | 0.00 | 0.00 | 0.00 |
| | D. sand | 0.00 | 0.00 | 0.00 | 0.00 | 0.01 | 0.01 | 0.00 | 0.01 | 0.00 | 0.00 | 0.00 | 0.00 | 0.00 | 0.00 | 0.00 | 0.95 | 0.00 | 0.00 | 0.00 | 0.00 | 0.00 | 0.01 | 0.01 |
| | Dec. trees | 0.00 | 0.00 | 0.00 | 0.00 | 0.00 | 0.00 | 0.00 | 0.00 | 0.00 | 0.00 | 0.00 | 0.20 | 0.00 | 0.00 | 0.00 | 0.00 | 0.00 | 0.77 | 0.03 | 0.00 | 0.00 | 0.00 | 0.00 |
| | Roof | 0.00 | 0.00 | 0.00 | 0.00 | 0.00 | 0.00 | 0.00 | 0.00 | 0.02 | 0.00 | 0.01 | 0.02 | 0.01 | 0.00 | 0.03 | 0.00 | 0.02 | 0.89 | 0.03 | 0.00 | 0.00 | 0.00 | 0.00 |
| | L. marsh | 0.00 | 0.00 | 0.00 | 0.00 | 0.02 | 0.00 | 0.00 | 0.00 | 0.00 | 0.00 | 0.00 | 0.00 | 0.00 | 0.00 | 0.00 | 0.01 | 0.00 | 0.00 | 0.96 | 0.00 | 0.00 | 0.00 | 0.00 |
| | M. marsh | 0.00 | 0.00 | 0.00 | 0.00 | 0.01 | 0.00 | 0.00 | 0.00 | 0.00 | 0.00 | 0.00 | 0.00 | 0.00 | 0.00 | 0.00 | 0.00 | 0.00 | 0.00 | 0.00 | 0.01 | 0.97 | 0.00 | 0.00 |
| H. marsh | 0.00 | 0.00 | 0.00 | 0.00 | 0.02 | 0.03 | 0.00 | 0.00 | 0.00 | 0.00 | 0.00 | 0.00 | 0.00 | 0.00 | 0.00 | 0.02 | 0.00 | 0.00 | 0.00 | 0.00 | 0.00 | 0.00 | 0.92 | |

Figure 13. Confusion matrix obtained by the random forest classification of the green waveforms' features, infrared intensities, and elevations. The three highest and three lowest class accuracy values are highlighted in green and orange, respectively. S. = submerged, Ev. = evergreen, Dec. = deciduous.

4.3.1. Urban Area and Sand Beach Classification

As Figure 10 shows, the detection of planar, highly reflective surfaces such as tar and concrete was accurate, but their specific type was sometimes misidentified. Although the pier located north of Figure 10 was correctly mapped as concrete, there was confusion between soil and tar on the sandy dune (southeast of the same figure).

The classification of roof was satisfactory both west and east of the area presented in Figure 10 but showed cases of overdetection. In the urban area developed on the sandy dune (southeast of Figure 10), tar, rooves, trees, and shrubs were distinguished precisely, but sandy dune vegetation, shrubs, and trees were sometimes confused for rooves or tar.

A weaker aspect of this result was the classification of the sand beaches: patches of wet sand were well defined, but the borders between wet and dry sand featured many false detections of pebble. Confusion between pebble and sand was high, as shown in the wide area of sand beach that is classified as pebble in the northeast in Figure 10.

4.3.2. Salt Marsh Classification

Figure 11 presented a closer look at the classification obtained in the salt marsh area. The three types of salt marsh distinguished—low, mid, and high marsh—appeared to be well identified.

The classification of the salt marsh channels was less correct: instead of wet sand and submerged sand, the classifier predicted rock and submerged rock in various areas.

4.3.3. Seagrass Meadow Classification

In Figure 12, the focus was set on the seagrass meadow located in the north of the study site. Emerged and submerged parts of the rocky island were well mapped, even though submerged rock was detected in places where the seabed is sandy. The two types of underwater vegetation we attempted to map were very precisely defined: the patches of seagrass meadow and macroalgae were mapped with very low confusion with submerged sand or rock. However, the type of underwater vegetation (macroalgae or seagrass) was not correct in all places. There were classification errors in the seagrass meadow, where macroalgae was detected. Seagrasses were also found in macroalgae-covered areas.

Figure 12 also showed the precision of the classification of boats: boats mooring in the seagrass meadow were correctly labelled even though no training or test data were collected in that area for the boats class.

4.4. Confusion Matrix Obtained with Green Waveform Features, Infrared Intensities and Elevations on the Test Dataset

The confusion matrix obtained using green waveform features, IR intensities, and elevations on the test dataset is presented in Figure 13. It confirmed the observations made on the visual results. All classes were predicted with at least 70% of correctness. The most frequent confusions were between seagrasses and macroalgae, deciduous and evergreen trees, and submerged rock and submerged sand, which corroborated the observations made on the application of the model to the broader dataset.

The other confusion matrixes can be found in Appendix B (Figures A4–A6).

5. Discussion

We improved an approach initially designed to distinguish two seabed covers—fine sediment and seagrass—to map all land and sea covers present in our study scene in 3D. The findings showed lidar waveforms can be used to classify and map habitats of the coastal fringe and bridge the gap between marine and terrestrial surveys. All 21 selected classes were classified with at least 70% of accuracy in the best configuration obtained, which had an OA of 90%. Here, we discuss the results obtained regarding the classification predictors and the methodology employed. We also provide potential explanations for the performances of the algorithm.

5.1. Green Waveform Features

Our research partially aimed at exploring whether green lidar waveforms can be relevant for coastal habitat mapping. We defined 16 features to extract from the portions of the waveforms that correspond to layers of ground or seabed covers. These were efficiently retrieved both on land and underwater. However, our approach did not handle extremely shallow waters, where the surface component and the bottom return overlap in the waveforms. In these cases, the peak detection employed did not distinguish the seabed from the water surface and no features were retrieved. There was consequently a 24 m wide band without data in the surf zone on the sand beaches in our processed lidar dataset.

We also noticed cases of confusion between seabed return and noise in the water column component of the waveform, which resulted in a mis-located detected seabed. These issues could be handled by improving the way the different waveform components are isolated: using waveform decomposition [31] or deconvolution [47,48] could produce better results on that aspect.

The features defined to describe the spectral signatures of coastal habitats seemed to be equally relevant for land and sea covers mapping. However, they did not provide a highly accurate classification (56% of OA). This can be explained by analyzing the green waveforms obtained with the HawkEye III on land. Since this sensor was particularly designed for bathymetry extraction, its green lasers are set to be powerful enough to reach the seabed up to several dozens of meters in coastal waters. Over land, the laser power is so high that most of the waveforms originating from highly reflective surfaces are saturated. The green wavelength alone might consequently not encompass a fine enough range of intensities over land to allow separation of similar environments such as plane habitats, different types of herbaceous vegetation, etc. The shapes of the saturated waveform returns are also affected: there is lacking information on the shape of the peak around its maximum. This can explain why there was a lot of confusion between topographic habitats when using green waveforms only.

Though green information alone may not be enough to distinguish the 21 habitats accurately, our findings suggested that a finer selection of the waveform attributes used for classification could enhance the green waveform feature predictions. The results presented in Table 3 and Figure 8 revealed negative interactions between some of the features chosen. Combining the full sets of statistical and peak shape features (defined in Section 3.7) resulted in lower accuracy than using them separately. Furthermore, the predictors' contribution assessment (Figure 8) showed that out of the 16 predictors, only nine contributed positively to the classification accuracy. This might be due to information redundancy between features relying on similar concepts such as mean and median intensity, for example. It could be due to the correction of attenuation performed on bathymetric waveforms. This exponential correction produced extremely high values of backscattered intensities under water, which made little sense physically. On the other hand, topographic waveforms were not corrected: their typical intensity order of magnitude was several times smaller, which might have disrupted the classifier. Fixing the issue of attenuation correction and using only a selected set of waveform predictors based on an assessment of their contribution would certainly result in better results when using the green wavelength alone.

The three different types of waveform features appeared to be complimentary: the nine predictors with a positive influence on the OA (Figure 8) represented each feature family defined in Section 3.7. This was consistent: the shape of the waveform return is characteristic of its nature, and the complexity, length, shape, maximum, and position of its maximum sum up the essential information differentiating one waveform from another.

5.2. Infrared Data

The addition of the IR wavelength increased the OA by 13%. The classification results certainly benefited from IR light's interaction with water and chlorophyll pigments, which provided essential information for the labelling of vegetation and other topographic classes such as wet sand. Considering that the green wavelength was less adapted to land cover classification, the performance increase obtained by using both lasers was expected.

Our research showed the added value of topobathymetric lidar: on top of providing quasi-continuity between land and water, both wavelengths provided complementary information for land covers' classification. The IR PC alone could not provide a coastal habitat map since it did not reach the seabed and riverbed; the OA obtained using only this wavelength (24%, presented in Table 3) confirmed that. They also showed that green lidar features alone do not provide a sufficient basis for classification either, reaching an OA of only 56%. Coupling both wavelengths improved the overall result significantly, bringing together the strengths of IR data on land covers, and the ability of green lidar to penetrate

the water surface. The matrixes presented in Figures A4 and A5 show that the addition of IR intensities to green waveform features resulted in an accuracy increase for all but two of the 21 classes. The gain ranged between 0% (submerged sand) and 39% (tar). The minimum accuracy observed over the 21 labels rose from 21% to 29%. Water covers classes such as seagrass and submerged rock also benefited from the addition of IR intensities, as their accuracy showed an improvement of 1% and 6%, respectively. As HawkEye III is tailored for bathymetry, its green laser's power was set to be high, which resulted in saturated intensities over land. The IR channel provided complimentary information in places when the green channel was weaker, which partially explains the algorithm's performances we observe. The classification accuracies obtained for land covers confirm that; for example, the classification of soil, wet sand, and lawn was significantly enhanced: +28%, +34%, and +23% of OA, respectively. Our future work will focus on exploiting both IR and green waveforms for habitat classification, to maximize the accuracy attainable with full-waveform topobathymetric lidar.

5.3. Ground and Seabed Elevation

Similarly to the IR data, elevations contributed greatly to the improvement of the OA of the habitat classification, but could not be separated from spectral predictors and used alone to provide accurate detection of land and sea covers. Indeed, Table 3 revealed that elevations produced a classification with an OA of 55%, which is less than what can be achieved with spectral predictors. This was expected since many different habitats coexist at similar altitudes and are mainly differentiated by their reflectance. However, for some others, mainly salt marsh types, elevation is an intrinsic quality and the base of their definition. This explains why those are the type of classes that benefited the most from the addition of elevation to a set of spectral predictors in terms of classification accuracy. Respectively, the classification accuracy of low salt marsh, mid salt marsh, and high salt marsh rose from 71%, 76%, and 21% by adding elevations to the green waveform features in the set of predictors (see Figures A4 and A6).

Even though elevation combined with spectral information already provided high classification accuracy (90%, see Table 3), the values extracted with our approach were not always consistent with those provided by the original PCs in marine areas, as explained above. To remove artifacts due to water quality, a post-processing step could be implemented, and the neighboring elevations could be used to regularize the processed PC obtained.

5.4. Classification Approach

Our results showed that topobathymetric lidar is fitted to the classification of coastal habitats. Although elevations, IR intensities, and green waveform features did not produce high accuracy classifications of the land-water continuum, they were complimentary and achieved high-precision results when combined. To the best of our knowledge, no similar papers proposing point-based land and water covers mapping from bispectral lidar data were published, so no direct comparisons of results are possible. However, our observations corroborate those made in [35], which successfully used random forest algorithms to classify full-waveform lidar data over urban areas and obtained an overall accuracy of over 94% when identifying four types of land covers. This paper only focuses on terrestrial areas but confirms the high accuracy we observe when using waveform features without rasterization for mapping purposes. Class-wise, our results seem more homogeneous for the land covers we have in common, although this means that our approach performs less accurately than theirs on some urban classes. Indeed, ref. [35] presents a PA of 94.8% for buildings, which is higher than we observe on our roof class (89%), but our vegetation classes (trees and shrubs) have an average PA of 82.6%, while theirs is 68.9%, and our natural ground classes (soil, lawn, salt marsh) reach an average PA of 91.6%, higher than the 32.7% presented in [35]. Our approach and the method introduced in [35] perform similarly on artificial ground (for us, tar and concrete), with PAs of 96% and 96.4%, respectively.

Although we found no other research performing point-based classification of subtidal, intertidal, and supra-tidal habitats, we can compare our findings to those in [34], where the authors also observed that the use of waveform data improves seabed maps and obtained an OA of 86% for their classification of seabed substrates and aquatic macrovegetation. Their approach provides a better mapping of low underwater vegetation on soft substrate (100% versus 85% of PA in our case) but a less accurate detection of hard seabed substrate (68% versus 90% of PA in our study). Again, although we have less accurate results for some classes, our method seems to provide more balanced and homogeneous performances among different classes.

Our results also confirm those from [27], where 19 land-water continuum habitats were classified with an OA of 90%, and in which the authors concluded that the best classification results were obtained when combining spectral information and elevation. However, in [27], the authors used digital models of waveform features that they obtained by rasterizing their data, and they relied on an ML classifier. Although our metrics are similar, our classification has the advantage of preserving the spatial density and repartition of the data.

Other studies such as [49–51] used 2D lidar-derived data and imagery along with machine learning classifiers to map similar coastal habitats as the ones we attempted to map. They obtained performance scores in the same range as ours, with OA between 84% and 92%. The authors did not use waveform data in these studies and observed low accuracy when classifying only digital elevation models obtained with lidar surveys, therefore requiring the additional processing of imagery. Our approach has the advantage of requiring only one source of data out of the two sources often used in existing literature, which facilitates both acquisition procedures and processing.

Globally, our results are in line with [27,35,52], which all state that bathymetric lidar waveforms are well suited for benthic habitats mapping and observe the same complementarity between spectral and elevation information for habitat mapping. Our method offers an OA similar to existing research in lidar data classification for habitat mapping, while extending the application to a wider range of habitats—both marine and terrestrial—and avoiding information loss through rasterization. Although the PAs obtained for some classes are lower than results previously presented in other studies [34,35], this method also has the advantage of offering homogeneous performances and low inter classes PA differences, contrary to other existing research results [34,35].

The random forest models trained showed low overfitting, as the extended application results illustrated. The classification of boats located outside of the training and test data collection area, for example, illustrated that the classifiers obtained could be applied to other datasets accurately. Natural, semi-natural and anthropic habitats were well distinguished, and vegetation was precisely isolated, which opened perspectives for ecological assessments of those coastal areas. The remaining errors often involved classes that were close semantically. For example, there was confusion between salt marsh and high natural grasses but low confusion between lawns and low marsh. A potential improvement could be to review the classes defined initially and distinguish vegetation by layers (herbaceous, arbustive, arborescent) and by their natural, semi-natural, or anthropic nature.

Besides the quality of the training and test datasets established, a source of explanation for remaining classification errors could be found in the technical specifications of the sensor. The diameter of the HawkEye III's green laser's footprint is 1.80 m, which means that the returned waveform condensates information in a 2.5 m² area. This parameter may have had an influence on the ability of a given array of features to describe pebble or sand, mostly at interfaces between habitats. This could partially explain the confusion between deciduous and evergreen trees: in a mixed-species forest, two different trees can coexist in a 2.5 m² patch.

Although the main issues identified visually reflected in the metrics computed on the test dataset, there was a gap between the estimated quality of the map and the statistics computed. For example, the classification of portions of sandy beaches as pebble was

not as obvious in the confusion matrix as it is in the map. This showed the influence of the way the test dataset is built. Further work should try to incorporate validation maps in addition to test datasets to qualify the output on the complete study site. A finer tree species inventory could also be integrated to better assess the results obtained.

Nonetheless, our results highlighted a strong classification approach, leveraging the strengths of 3D bispectral data. Working at the PC scale and not in 2D opens perspectives for 3D classifications, identifying all layers of land and sea cover, mostly in vegetated areas, by using waveform segmentation instead of waveform PC segmentation, as experimented in [53]. It also shows possibilities for post-processing and neighbor-based result regularization, as well as the exploitation of spatial information through the addition of geometrical features such as roughness or local density. Lastly, the accurate classification of habitats through 3D data offers opportunities for structural ecology assessments and communication of these results to environmental managers through virtual reality or more relatable 3D visualizations, for the implementation of sustainable integrated management of coastal areas. Figure 14 provides a 3D view of the 3D habitat mapping achieved in the present study.



Figure 14. 3D map of the habitats obtained over the complete study area by the random forest classifier trained on green waveform features, infrared intensities, and elevations. S. = submerged, Ev. = evergreen, Dec. = deciduous.

6. Conclusions

In this article, we proposed an approach to map coastal habitats exclusively using topobathymetric lidar, including both full waveforms and reanalyzed echoes. We produced results under the form of PCs and extended the application of our best classifier—which obtained 90% of OA on the test dataset—to a dataset of 24.5 million points covering a very diverse coastal area. A total of 21 classes of land and sea covers were defined and mapped in 3D. We found that green waveforms and IR intensities complement each other: while green data provided strong results in submerged areas, the IR wavelength improved the distinction of land covers. Elevations further increased the classification accuracy by perfecting the classification of plane classes and classes, such as low, mid, and high salt marsh, which were principally differentiated by their elevation. It is of special interest to note that green waveforms alone produced better results than IR intensities or elevations alone. However, the combination of the three sources of information yielded the best result, highlighting that they each bring a specific contribution to the result. Our research showed

how fit topobathymetric lidar is to the classification of such numerous land-water interface habitats. We enhanced a waveform processing method to apply it to topo-bathymetric environments. The use of PCs instead of rasters and the addition of a second wavelength provided an original 3D map of 21 coastal habitats at very high spatial resolution. This provides encouraging perspectives for 3D mapping and ecological assessment of the land-water interface and paves the way to integrated management of coastal areas, bridging the gap between marine and terrestrial domains.

Author Contributions: Conceptualization, M.L., A.C., T.C. and D.L.; methodology, M.L.; software, M.L.; validation, M.L.; formal analysis, M.L.; investigation, M.L.; resources, Y.P., A.E., A.C. and M.L.; data curation, M.L. and Y.P.; writing—original draft preparation, M.L.; writing—review and editing, M.L., A.C., T.C., D.L., Y.P. and A.E.; visualization, M.L.; supervision, A.C., T.C. and D.L.; project administration, A.C., T.C. and D.L.; funding acquisition, M.L., A.C., T.C. and D.L. All authors have read and agreed to the published version of the manuscript.

Funding: This research was funded by a Ph.D. grant from Région Bretagne, and by the Saur Group's patronage. The APC was funded by the Nantes-Rennes topobathymetric lidar platform of the University of Rennes 1.

Data Availability Statement: Data sharing is not applicable to this article.

Acknowledgments: The authors are grateful to Airborne Hydrography AB (AHAB), an affiliate company of Leica Geosystems, for their technical support, their assistance with software and development issues, and their help in understanding the specificities of the sensor and its data. M.L. would like to thank the lab members who contributed to ground truth data acquisition—Hélène Gloria, Dorothée James, Alyson Le Quilleuc, Antoine Mury, and Léna Véle—and external volunteers. M.L. is also grateful to the Rennes 2 University for the field work equipment support. The authors deeply acknowledge the input of the anonymous reviewers, which improved the quality of the manuscript.

Conflicts of Interest: The authors declare no conflict of interest. The funders had no role in the design of the study; in the collection, analyses, or interpretation of data; in the writing of the manuscript, or in the decision to publish the results.

Appendix A

Appendix A contains the projected 3D maps of the habitats obtained for 3 random forest experiments: the classification of green waveform features only, the classification of green waveform features and IR intensities, and the classification of green waveform features and elevations.



Figure A1. Projected 3D map of the habitats obtained with the predictions of a random forest classifier on green spectral features; orthoimage of the study area. The orthoimage was captured in 2014, while lidar data are not contemporaneous as they date from 2019. S. = submerged, Ev. = evergreen, Dec. = deciduous.



Figure A2. Projected 3D map of the habitats obtained with the predictions of a random forest classifier on green spectral features and infrared intensities; orthoimage of the study area. The orthoimage was captured in 2014, while lidar data are not contemporaneous as they date from 2019. S. = submerged, Ev. = evergreen, Dec. = deciduous.



Figure A3. Projected 3D map of the habitats obtained with the predictions of a random forest classifier on green spectral features and elevation values; orthoimage of the study area. The orthoimage was captured in 2014, while lidar data are not contemporaneous as they date from 2019. S. = submerged, Ev. = evergreen, Dec. = deciduous.

Appendix B

Appendix B contains the confusion matrix or difference matrixes obtained for 3 random forest experiments: the classification of green waveform features only, the classification of green waveform features and IR intensities, and the classification of green waveform features and elevations.

| Class | Predicted | | | | | | | | | | | | | | | | | | | | | | | |
|------------|------------|---------|------|----------|--------|----------|---------|------|------|-------|------|-----------|------|---------|--------|---------|------------|------|----------|----------|----------|------|------|------|
| | Macroalgae | S. Rock | Rock | Seagrass | Pebble | Concrete | S. Sand | Soil | Tar | Boats | Cars | Ev. trees | Lawn | W. sand | Shrubs | D. sand | Dec. trees | Roof | L. marsh | M. marsh | H. marsh | | | |
| Macroalgae | 0.84 | 0.00 | 0.00 | 0.14 | 0.00 | 0.00 | 0.01 | 0.00 | 0.00 | 0.00 | 0.00 | 0.00 | 0.00 | 0.00 | 0.00 | 0.00 | 0.00 | 0.00 | 0.00 | 0.00 | 0.00 | 0.00 | 0.00 | |
| S. Rock | 0.01 | 0.83 | 0.00 | 0.04 | 0.00 | 0.00 | 0.04 | 0.00 | 0.00 | 0.01 | 0.03 | 0.00 | 0.00 | 0.00 | 0.02 | 0.00 | 0.00 | 0.00 | 0.00 | 0.00 | 0.00 | 0.00 | 0.00 | 0.00 |
| Rock | 0.00 | 0.02 | 0.28 | 0.00 | 0.03 | 0.07 | 0.00 | 0.10 | 0.11 | 0.00 | 0.02 | 0.00 | 0.06 | 0.02 | 0.00 | 0.00 | 0.00 | 0.00 | 0.01 | 0.06 | 0.08 | 0.14 | 0.00 | 0.00 |
| Seagrass | 0.13 | 0.04 | 0.00 | 0.82 | 0.00 | 0.00 | 0.00 | 0.00 | 0.00 | 0.00 | 0.00 | 0.00 | 0.00 | 0.00 | 0.00 | 0.00 | 0.00 | 0.00 | 0.00 | 0.00 | 0.00 | 0.00 | 0.00 | 0.00 |
| Pebble | 0.00 | 0.01 | 0.02 | 0.00 | 0.51 | 0.06 | 0.00 | 0.04 | 0.01 | 0.05 | 0.03 | 0.00 | 0.00 | 0.09 | 0.00 | 0.09 | 0.00 | 0.05 | 0.00 | 0.02 | 0.03 | 0.00 | 0.00 | |
| Concrete | 0.00 | 0.00 | 0.04 | 0.00 | 0.04 | 0.49 | 0.00 | 0.11 | 0.05 | 0.00 | 0.00 | 0.00 | 0.07 | 0.04 | 0.00 | 0.01 | 0.00 | 0.03 | 0.04 | 0.03 | 0.05 | 0.00 | 0.00 | |
| S. Sand | 0.01 | 0.06 | 0.00 | 0.00 | 0.00 | 0.00 | 0.92 | 0.00 | 0.00 | 0.01 | 0.00 | 0.00 | 0.00 | 0.00 | 0.00 | 0.00 | 0.00 | 0.00 | 0.00 | 0.00 | 0.00 | 0.00 | 0.00 | |
| Soil | 0.00 | 0.00 | 0.12 | 0.00 | 0.02 | 0.08 | 0.00 | 0.30 | 0.11 | 0.00 | 0.00 | 0.00 | 0.06 | 0.11 | 0.00 | 0.03 | 0.00 | 0.00 | 0.07 | 0.04 | 0.06 | 0.00 | 0.00 | |
| Tar | 0.00 | 0.00 | 0.07 | 0.00 | 0.00 | 0.06 | 0.00 | 0.10 | 0.29 | 0.00 | 0.00 | 0.00 | 0.16 | 0.01 | 0.00 | 0.00 | 0.00 | 0.02 | 0.12 | 0.06 | 0.10 | 0.00 | 0.00 | |
| Boats | 0.00 | 0.03 | 0.00 | 0.00 | 0.04 | 0.00 | 0.00 | 0.00 | 0.00 | 0.61 | 0.19 | 0.00 | 0.00 | 0.00 | 0.03 | 0.00 | 0.02 | 0.07 | 0.00 | 0.00 | 0.00 | 0.00 | 0.00 | |
| Cars | 0.00 | 0.01 | 0.00 | 0.00 | 0.02 | 0.00 | 0.00 | 0.00 | 0.00 | 0.18 | 0.69 | 0.00 | 0.00 | 0.00 | 0.07 | 0.00 | 0.00 | 0.02 | 0.00 | 0.00 | 0.00 | 0.00 | 0.00 | |
| Ev. trees | 0.01 | 0.00 | 0.00 | 0.00 | 0.00 | 0.00 | 0.00 | 0.00 | 0.00 | 0.01 | 0.00 | 0.64 | 0.00 | 0.00 | 0.00 | 0.00 | 0.32 | 0.01 | 0.00 | 0.00 | 0.00 | 0.00 | 0.00 | |
| Lawn | 0.00 | 0.00 | 0.05 | 0.00 | 0.01 | 0.04 | 0.00 | 0.02 | 0.12 | 0.00 | 0.00 | 0.00 | 0.54 | 0.00 | 0.00 | 0.00 | 0.00 | 0.02 | 0.12 | 0.04 | 0.03 | 0.00 | 0.00 | |
| W. sand | 0.00 | 0.00 | 0.02 | 0.00 | 0.03 | 0.01 | 0.00 | 0.09 | 0.00 | 0.00 | 0.00 | 0.00 | 0.00 | 0.59 | 0.00 | 0.12 | 0.00 | 0.00 | 0.02 | 0.09 | 0.03 | 0.00 | 0.00 | |
| Shrubs | 0.00 | 0.01 | 0.00 | 0.00 | 0.00 | 0.01 | 0.00 | 0.00 | 0.00 | 0.04 | 0.04 | 0.00 | 0.00 | 0.00 | 0.86 | 0.00 | 0.01 | 0.02 | 0.00 | 0.00 | 0.00 | 0.00 | 0.00 | |
| D. sand | 0.00 | 0.00 | 0.00 | 0.00 | 0.06 | 0.00 | 0.00 | 0.01 | 0.00 | 0.00 | 0.00 | 0.00 | 0.08 | 0.00 | 0.78 | 0.00 | 0.00 | 0.00 | 0.01 | 0.01 | 0.04 | 0.00 | 0.00 | |
| Dec. trees | 0.00 | 0.00 | 0.00 | 0.00 | 0.00 | 0.00 | 0.00 | 0.00 | 0.00 | 0.02 | 0.28 | 0.00 | 0.28 | 0.00 | 0.01 | 0.00 | 0.65 | 0.02 | 0.00 | 0.00 | 0.00 | 0.00 | 0.00 | |
| Roof | 0.01 | 0.02 | 0.02 | 0.00 | 0.10 | 0.06 | 0.01 | 0.02 | 0.02 | 0.12 | 0.05 | 0.02 | 0.09 | 0.01 | 0.07 | 0.00 | 0.04 | 0.32 | 0.03 | 0.01 | 0.02 | 0.00 | 0.00 | |
| L. marsh | 0.00 | 0.00 | 0.09 | 0.00 | 0.01 | 0.03 | 0.00 | 0.03 | 0.14 | 0.00 | 0.00 | 0.00 | 0.15 | 0.11 | 0.00 | 0.04 | 0.00 | 0.00 | 0.24 | 0.09 | 0.06 | 0.00 | 0.00 | |
| M. marsh | 0.00 | 0.00 | 0.07 | 0.00 | 0.01 | 0.02 | 0.00 | 0.06 | 0.05 | 0.00 | 0.00 | 0.00 | 0.04 | 0.25 | 0.00 | 0.04 | 0.00 | 0.00 | 0.09 | 0.21 | 0.15 | 0.00 | 0.00 | |
| H. marsh | 0.00 | 0.00 | 0.06 | 0.00 | 0.04 | 0.05 | 0.00 | 0.06 | 0.07 | 0.00 | 0.00 | 0.00 | 0.02 | 0.12 | 0.00 | 0.11 | 0.00 | 0.01 | 0.05 | 0.08 | 0.34 | 0.00 | 0.00 | |

Figure A4. Confusion matrix obtained by the random forest classification of the green waveforms' features. The three highest and three lowest class accuracy values are highlighted in green and orange, respectively. S. = submerged, Ev. = evergreen, Dec. = deciduous.

| | | Predicted | | | | | | | | | | | | | | | | | | | | | |
|----------|------------|------------|---------|-------|----------|--------|----------|---------|-------|-------|-------|-------|-----------|-------|---------|--------|---------|------------|-------|----------|----------|----------|-------|
| | | Macroalgae | S. Rock | Rock | Seagrass | Pebble | Concrete | S. Sand | Soil | Tar | Boats | Cars | Ev. trees | Lawn | W. sand | Shrubs | D. sand | Dec. trees | Roof | L. marsh | M. marsh | H. marsh | |
| True | Macroalgae | -0.01 | 0.00 | 0.00 | 0.02 | 0.00 | 0.00 | 0.00 | 0.00 | 0.00 | 0.00 | 0.00 | 0.00 | 0.00 | 0.00 | 0.00 | 0.00 | 0.00 | 0.00 | 0.00 | 0.00 | 0.00 | 0.00 |
| | S. Rock | 0.00 | 0.06 | 0.00 | 0.00 | 0.00 | 0.00 | 0.01 | 0.00 | 0.00 | -0.01 | -0.03 | 0.00 | 0.00 | 0.00 | -0.02 | 0.00 | 0.00 | 0.00 | 0.00 | 0.00 | 0.00 | 0.00 |
| | Rock | 0.00 | -0.02 | 0.23 | 0.00 | 0.02 | -0.02 | 0.00 | -0.04 | -0.03 | 0.01 | -0.02 | 0.00 | -0.05 | -0.02 | 0.00 | 0.00 | 0.00 | 0.00 | 0.00 | 0.01 | 0.01 | -0.07 |
| | Seagrass | -0.01 | 0.00 | 0.00 | 0.01 | 0.00 | 0.00 | 0.00 | 0.00 | 0.00 | 0.00 | 0.00 | 0.00 | 0.00 | 0.00 | 0.00 | 0.00 | 0.00 | 0.00 | 0.00 | 0.00 | 0.00 | 0.00 |
| | Pebble | 0.00 | -0.01 | 0.05 | 0.00 | 0.13 | -0.02 | 0.00 | -0.03 | -0.01 | 0.00 | -0.01 | 0.00 | 0.00 | -0.03 | 0.00 | -0.07 | 0.00 | 0.00 | -0.03 | 0.01 | 0.00 | -0.02 |
| | Concrete | 0.00 | 0.00 | 0.01 | 0.00 | 0.00 | 0.08 | 0.00 | 0.00 | -0.04 | 0.00 | 0.00 | 0.00 | -0.01 | -0.04 | 0.00 | 0.00 | 0.00 | 0.00 | -0.02 | 0.03 | 0.00 | -0.01 |
| | S. Sand | 0.00 | 0.00 | 0.00 | 0.00 | 0.00 | 0.00 | 0.00 | 0.00 | 0.00 | -0.01 | 0.00 | 0.00 | 0.00 | 0.00 | 0.00 | 0.00 | 0.00 | 0.00 | 0.00 | 0.00 | 0.00 | 0.00 |
| | Soil | 0.00 | 0.00 | -0.09 | 0.00 | -0.01 | 0.01 | 0.00 | 0.28 | -0.11 | 0.00 | 0.00 | 0.00 | 0.04 | -0.11 | 0.00 | 0.02 | 0.00 | 0.00 | -0.01 | -0.03 | 0.00 | 0.02 |
| | Tar | 0.00 | 0.00 | -0.02 | 0.00 | 0.00 | -0.02 | 0.00 | -0.06 | 0.39 | 0.00 | 0.00 | 0.00 | -0.15 | -0.11 | 0.00 | 0.00 | 0.00 | 0.00 | -0.01 | -0.07 | -0.03 | -0.03 |
| | Boats | 0.00 | -0.03 | 0.00 | 0.00 | -0.01 | 0.00 | 0.00 | 0.00 | 0.00 | 0.20 | -0.13 | 0.00 | 0.00 | 0.00 | 0.00 | 0.00 | 0.00 | -0.01 | -0.03 | 0.00 | 0.00 | 0.00 |
| | Cars | 0.00 | -0.01 | 0.00 | 0.00 | -0.01 | 0.00 | 0.00 | 0.00 | 0.00 | -0.04 | 0.05 | 0.00 | 0.00 | 0.00 | 0.00 | 0.00 | 0.00 | 0.00 | 0.00 | 0.00 | 0.00 | 0.00 |
| | Ev. trees | 0.00 | 0.00 | 0.00 | 0.00 | 0.00 | 0.00 | 0.00 | 0.00 | 0.00 | -0.01 | 0.00 | 0.02 | 0.00 | 0.00 | 0.00 | 0.00 | 0.00 | -0.02 | 0.00 | 0.00 | 0.00 | 0.00 |
| | Lawn | 0.00 | 0.00 | -0.05 | 0.00 | 0.00 | -0.01 | 0.00 | 0.05 | -0.10 | 0.00 | 0.00 | 0.00 | 0.23 | 0.00 | 0.00 | 0.00 | 0.00 | 0.00 | -0.08 | -0.04 | 0.00 | 0.00 |
| | W. sand | 0.00 | 0.00 | -0.01 | 0.00 | -0.03 | -0.01 | 0.00 | -0.09 | 0.02 | 0.00 | 0.00 | 0.00 | 0.00 | 0.34 | 0.00 | -0.12 | 0.00 | 0.00 | -0.01 | -0.06 | -0.03 | |
| | Shrubs | 0.00 | -0.01 | 0.00 | 0.00 | 0.00 | -0.01 | 0.00 | 0.00 | 0.00 | 0.00 | 0.00 | 0.00 | 0.00 | 0.00 | 0.01 | 0.00 | 0.00 | 0.00 | 0.00 | 0.00 | 0.00 | 0.00 |
| | D. sand | 0.00 | 0.00 | 0.00 | 0.00 | -0.04 | 0.01 | 0.00 | 0.01 | 0.00 | 0.00 | 0.00 | 0.00 | 0.00 | -0.08 | 0.00 | 0.12 | 0.00 | 0.00 | 0.00 | 0.00 | 0.00 | -0.01 |
| | Dec. trees | 0.00 | 0.00 | 0.00 | 0.00 | 0.00 | 0.00 | 0.00 | 0.00 | -0.01 | 0.00 | 0.05 | 0.00 | 0.00 | 0.00 | -0.01 | 0.00 | -0.05 | 0.00 | 0.00 | 0.00 | 0.00 | 0.00 |
| | Roof | 0.00 | 0.00 | 0.00 | 0.00 | -0.09 | -0.04 | 0.00 | -0.01 | 0.00 | -0.06 | -0.02 | 0.00 | -0.05 | 0.00 | 0.00 | 0.00 | -0.01 | 0.31 | 0.01 | -0.01 | -0.02 | |
| | L. marsh | 0.00 | 0.00 | 0.04 | 0.00 | 0.02 | 0.02 | 0.00 | -0.03 | -0.13 | 0.00 | 0.00 | 0.00 | -0.11 | -0.08 | 0.00 | 0.00 | 0.00 | 0.00 | 0.25 | 0.05 | -0.03 | |
| | M. marsh | 0.00 | 0.00 | 0.02 | 0.00 | 0.06 | 0.00 | 0.00 | -0.04 | -0.04 | 0.00 | 0.00 | 0.00 | -0.02 | -0.16 | 0.00 | -0.03 | 0.00 | 0.00 | 0.10 | 0.17 | -0.07 | |
| H. marsh | 0.00 | 0.00 | 0.01 | 0.00 | 0.00 | 0.01 | 0.00 | 0.11 | -0.06 | 0.00 | 0.00 | 0.00 | 0.03 | -0.10 | 0.00 | 0.03 | 0.00 | -0.01 | 0.00 | 0.01 | -0.05 | | |

Figure A5. Difference of the confusion matrixes obtained for the classification of green waveforms' features plus infrared intensities, and green waveforms' features only. The three highest and three lowest class accuracy values are highlighted in green and orange, respectively. S. = submerged, Ev. = evergreen, Dec. = deciduous.

| | | Predicted | | | | | | | | | | | | | | | | | | | | | |
|----------|------------|------------|---------|-------|----------|--------|----------|---------|-------|-------|-------|-------|-----------|-------|---------|--------|---------|------------|-------|----------|----------|----------|-------|
| | | Macroalgae | S. Rock | Rock | Seagrass | Pebble | Concrete | S. Sand | Soil | Tar | Boats | Cars | Ev. trees | Lawn | W. sand | Shrubs | D. sand | Dec. trees | Roof | L. marsh | M. marsh | H. marsh | |
| True | Macroalgae | -0.01 | 0.00 | 0.00 | 0.02 | 0.00 | 0.00 | 0.00 | 0.00 | 0.00 | 0.00 | 0.00 | 0.00 | 0.00 | 0.00 | 0.00 | 0.00 | 0.00 | 0.00 | 0.00 | 0.00 | 0.00 | |
| | S. Rock | 0.01 | 0.08 | 0.00 | -0.01 | 0.00 | 0.00 | 0.00 | 0.00 | 0.00 | -0.01 | -0.03 | 0.00 | 0.00 | 0.00 | -0.02 | 0.00 | 0.00 | 0.00 | 0.00 | 0.00 | 0.00 | |
| | Rock | 0.00 | -0.02 | 0.65 | 0.00 | 0.02 | -0.07 | 0.00 | -0.10 | -0.11 | 0.00 | -0.02 | 0.00 | -0.06 | -0.01 | 0.00 | 0.00 | 0.00 | 0.00 | -0.01 | -0.06 | -0.08 | -0.14 |
| | Seagrass | -0.02 | -0.01 | 0.00 | 0.03 | 0.00 | 0.00 | 0.00 | 0.00 | 0.00 | 0.00 | 0.00 | 0.00 | 0.00 | 0.00 | 0.00 | 0.00 | 0.00 | 0.00 | 0.00 | 0.00 | 0.00 | |
| | Pebble | 0.00 | -0.01 | 0.06 | 0.00 | 0.21 | -0.02 | 0.00 | -0.04 | -0.01 | -0.01 | -0.03 | 0.00 | 0.00 | -0.08 | 0.00 | -0.06 | 0.00 | -0.05 | 0.03 | 0.01 | 0.01 | |
| | Concrete | 0.00 | 0.00 | -0.04 | 0.00 | 0.04 | 0.46 | 0.00 | -0.10 | -0.05 | 0.00 | 0.00 | 0.00 | -0.06 | -0.04 | 0.00 | -0.01 | 0.00 | -0.03 | -0.04 | -0.03 | -0.03 | |
| | S. Sand | 0.00 | 0.01 | 0.00 | 0.00 | 0.00 | 0.00 | 0.00 | 0.00 | 0.00 | 0.01 | 0.00 | 0.00 | 0.00 | 0.00 | 0.00 | 0.00 | 0.00 | 0.00 | 0.00 | 0.00 | 0.00 | |
| | Soil | 0.00 | 0.00 | -0.12 | 0.00 | -0.02 | -0.01 | 0.00 | 0.48 | -0.10 | 0.00 | 0.00 | 0.00 | 0.06 | -0.11 | 0.00 | -0.02 | 0.00 | 0.00 | -0.07 | -0.04 | -0.06 | |
| | Tar | 0.00 | 0.00 | -0.07 | 0.00 | 0.00 | -0.06 | 0.00 | -0.10 | 0.61 | 0.00 | 0.00 | 0.00 | -0.08 | -0.01 | 0.00 | 0.00 | 0.00 | -0.01 | -0.12 | -0.06 | -0.10 | |
| | Boats | 0.00 | -0.03 | 0.00 | 0.00 | -0.03 | 0.00 | 0.00 | 0.00 | 0.00 | 0.37 | -0.19 | 0.00 | 0.00 | 0.00 | -0.03 | 0.00 | -0.02 | -0.07 | 0.00 | 0.00 | 0.00 | |
| | Cars | 0.00 | -0.01 | 0.00 | 0.00 | -0.02 | 0.00 | 0.00 | 0.01 | 0.00 | -0.18 | 0.28 | 0.00 | 0.00 | 0.00 | -0.06 | 0.00 | 0.00 | -0.01 | 0.00 | 0.00 | 0.00 | |
| | Ev. trees | -0.01 | 0.00 | 0.00 | 0.00 | 0.00 | 0.00 | 0.00 | 0.00 | 0.00 | -0.01 | 0.00 | 0.06 | 0.00 | 0.01 | 0.00 | -0.06 | 0.02 | 0.00 | 0.00 | 0.00 | | |
| | Lawn | 0.00 | 0.00 | -0.05 | 0.00 | -0.01 | -0.01 | 0.00 | 0.04 | -0.05 | 0.00 | 0.00 | 0.00 | 0.26 | 0.00 | 0.00 | 0.00 | 0.00 | 0.01 | -0.12 | -0.04 | -0.03 | |
| | W. sand | 0.00 | 0.00 | 0.00 | 0.00 | -0.03 | -0.01 | 0.00 | -0.09 | 0.00 | 0.00 | 0.00 | 0.00 | 0.00 | 0.36 | 0.00 | -0.09 | 0.00 | 0.00 | -0.02 | -0.09 | -0.03 | |
| | Shrubs | 0.00 | -0.01 | 0.00 | 0.00 | 0.00 | -0.01 | 0.00 | 0.01 | 0.00 | -0.04 | -0.04 | 0.00 | 0.00 | 0.00 | 0.11 | 0.00 | -0.01 | 0.00 | 0.00 | 0.00 | 0.00 | |
| | D. sand | 0.00 | 0.00 | 0.00 | 0.00 | -0.03 | 0.02 | 0.00 | 0.00 | 0.00 | 0.00 | 0.00 | 0.00 | 0.00 | -0.01 | 0.00 | 0.04 | 0.00 | 0.00 | 0.02 | 0.00 | -0.04 | |
| | Dec. trees | 0.00 | 0.00 | 0.00 | 0.00 | 0.00 | 0.00 | 0.00 | 0.00 | 0.00 | -0.02 | 0.00 | -0.07 | 0.00 | 0.00 | -0.01 | 0.00 | 0.10 | 0.01 | 0.00 | 0.00 | 0.00 | |
| | Roof | -0.01 | -0.02 | -0.02 | 0.00 | -0.10 | -0.06 | 0.00 | 0.01 | -0.01 | -0.12 | -0.04 | 0.01 | -0.01 | -0.01 | -0.03 | 0.00 | -0.02 | 0.47 | -0.03 | -0.01 | -0.02 | |
| | L. marsh | 0.00 | 0.00 | -0.09 | 0.00 | 0.01 | -0.03 | 0.00 | -0.03 | -0.14 | 0.00 | 0.00 | 0.00 | -0.15 | -0.11 | 0.00 | -0.01 | 0.00 | 0.00 | 0.71 | -0.09 | -0.06 | |
| | M. marsh | 0.00 | 0.00 | -0.07 | 0.00 | 0.00 | -0.02 | 0.00 | -0.06 | -0.05 | 0.00 | 0.00 | 0.00 | -0.04 | -0.25 | 0.00 | -0.03 | 0.00 | 0.00 | -0.08 | 0.77 | -0.15 | |
| H. marsh | 0.00 | 0.00 | -0.06 | 0.00 | -0.01 | 0.00 | 0.00 | -0.06 | -0.07 | 0.00 | 0.00 | 0.00 | -0.02 | -0.12 | 0.00 | -0.09 | 0.00 | -0.01 | -0.05 | -0.08 | 0.57 | | |

Figure A6. Difference of the confusion matrixes obtained for the classification of green waveforms' features plus elevations, and green waveforms' features only. The three highest and three lowest values are highlighted in green and orange, respectively. S. = submerged, Ev. = evergreen, Dec. = deciduous.

References

- Barbier, E.B.; Hacker, S.D.; Kennedy, C.; Koch, E.W.; Stier, A.C.; Silliman, B.R. The Value of Estuarine and Coastal Ecosystem Services. *Ecol. Monogr.* **2011**, *81*, 169–193. [CrossRef]
- Turner, R.K.; Schaafsma, M.; Mee, L.; Elliott, M.; Burdon, D.; Atkins, J.P.; Jickells, T. Conceptual Framework. In *Coastal Zones Ecosystem Services: From Science to Values and Decision Making*; Turner, R.K., Schaafsma, M., Eds.; Studies in Ecological Economics; Springer International Publishing: Cham, Switzerland, 2015; pp. 11–40, ISBN 978-3-319-17214-9.
- Mury, A.; Collin, A.; Etienne, S.; Jeanson, M. Wave Attenuation Service by Intertidal Coastal Ecogeosystems in the Bay of Mont-Saint-Michel, France: Review and Meta-Analysis. In Proceedings of the 20th EGU General Assembly EGU2018, Vienna, Austria, 4–13 April 2018; pp. 555–572.
- Collin, A.; Dubois, S.; James, D.; Houet, T. Improving Intertidal Reef Mapping Using UAV Surface, Red Edge, and Near-Infrared Data. *Drones* **2019**, *3*, 67. [CrossRef]
- Collin, A.; Dubois, S.; Ramambason, C.; Etienne, S. Very High-Resolution Mapping of Emerging Biogenic Reefs Using Airborne Optical Imagery and Neural Network: The Honeycomb Worm (*Sabellaria Alveolata*) Case Study. *Int. J. Remote Sens.* **2018**, *39*, 5660–5675. [CrossRef]

6. Collin, A.; Lambert, N.; Etienne, S. Satellite-Based Salt Marsh Elevation, Vegetation Height, and Species Composition Mapping Using the Superspectral WorldView-3 Imagery. *Int. J. Remote Sens.* **2018**, *39*, 5619–5637. [CrossRef]
7. Kutser, T.; Hedley, J.; Giardino, C.; Roelfsema, C.; Brando, V.E. Remote Sensing of Shallow Waters—A 50 Year Retrospective and Future Directions. *Remote Sens. Environ.* **2020**, *240*, 111619. [CrossRef]
8. Collin, A.; Etienne, S.; Feunteun, E. VHR Coastal Bathymetry Using WorldView-3: Colour versus Learner. *Remote Sens. Lett.* **2017**, *8*, 1072–1081. [CrossRef]
9. Collin, A.; Hench, J.L.; Pastol, Y.; Planes, S.; Thiault, L.; Schmitt, R.J.; Holbrook, S.J.; Davies, N.; Troyer, M. High Resolution Topobathymetry Using a Pleiades-1 Triplet: Moorea Island in 3D. *Remote Sens. Environ.* **2018**, *208*, 109–119. [CrossRef]
10. Adler-Golden, S.M.; Acharya, P.K.; Berk, A.; Matthew, M.W.; Gorodetzky, D. Remote Bathymetry of the Littoral Zone from AVIRIS, LASH, and QuickBird Imagery. *IEEE Trans. Geosci. Remote Sens.* **2005**, *43*, 337–347. [CrossRef]
11. Collin, A.; Anel, M.; Lecchini, D.; Claudet, J. Mapping Sub-Metre 3D Land-Sea Coral Reefs Using Superspectral WorldView-3 Satellite Stereoimagery. *Oceans* **2021**, *2*, 315–329. [CrossRef]
12. Stumpf, R.P.; Holderied, K.; Sinclair, M. Determination of Water Depth with High-Resolution Satellite Imagery over Variable Bottom Types. *Limnol. Oceanogr.* **2003**, *48*, 547–556. [CrossRef]
13. Lesser, M.; Mobley, C. Bathymetry, Water Optical Properties, and Benthic Classification of Coral Reefs Using Hyperspectral Remote Sensing Imagery. *Coral Reefs* **2007**, *26*, 819–829. [CrossRef]
14. Klonowski, W.M.; Fearn, P.R.C.S.; Lynch, M.J. Retrieving Key Benthic Cover Types and Bathymetry from Hyperspectral Imagery. *J. Appl. Remote Sens.* **2007**, *1*, 011505. [CrossRef]
15. Sandidge, J.C.; Holyer, R.J. Coastal Bathymetry from Hyperspectral Observations of Water Radiance. *Remote Sens. Environ.* **1998**, *65*, 341–352. [CrossRef]
16. Kutser, T.; Vahtmäe, E.; Martin, G. Assessing Suitability of Multispectral Satellites for Mapping Benthic Macroalgal Cover in Turbid Coastal Waters by Means of Model Simulations. *Estuar. Coast. Shelf Sci.* **2006**, *67*, 521–529. [CrossRef]
17. Wedding, L.M.; Friedlander, A.M.; McGranaghan, M.; Yost, R.S.; Monaco, M.E. Using Bathymetric Lidar to Define Nearshore Benthic Habitat Complexity: Implications for Management of Reef Fish Assemblages in Hawaii. *Remote Sens. Environ.* **2008**, *112*, 4159–4165. [CrossRef]
18. Nie, S.; Wang, C.; Zeng, H.; Xi, X.; Li, G. Above-Ground Biomass Estimation Using Airborne Discrete-Return and Full-Waveform LiDAR Data in a Coniferous Forest. *Ecol. Indic.* **2017**, *78*, 221–228. [CrossRef]
19. Ene, L.T.; Næsset, E.; Gobakken, T.; Gregoire, T.G.; Ståhl, G.; Nelson, R. Assessing the Accuracy of Regional LiDAR-Based Biomass Estimation Using a Simulation Approach. *Remote Sens. Environ.* **2012**, *123*, 579–592. [CrossRef]
20. Lindberg, E.; Olofsson, K.; Holmgren, J.; Olsson, H. Estimation of 3D Vegetation Structure from Waveform and Discrete Return Airborne Laser Scanning Data. *Remote Sens. Environ.* **2012**, *118*, 151–161. [CrossRef]
21. Guenther, G.C. *Airborne Laser Hydrography: System Design and Performance Factors*; National Oceanic and Atmospheric Administration: Rockville, MD, USA, 1985; pp. 23–40.
22. Philpot, W. Airborne Laser Hydrography II. Available online: <https://ecommons.cornell.edu/handle/1813/66666> (accessed on 30 October 2021).
23. Brodu, N.; Lague, D. 3D Terrestrial Lidar Data Classification of Complex Natural Scenes Using a Multi-Scale Dimensionality Criterion: Applications in Geomorphology. *ISPRS J. Photogramm. Remote Sens.* **2012**, *68*, 121–134. [CrossRef]
24. Hansen, S.S.; Ernsten, V.B.; Andersen, M.S.; Al-Hamdani, Z.; Baran, R.; Niederwieser, M.; Steinbacher, F.; Kroon, A. Classification of Boulders in Coastal Environments Using Random Forest Machine Learning on Topo-Bathymetric LiDAR Data. *Remote Sens.* **2021**, *13*, 4101. [CrossRef]
25. Teo, T.-A.; Wu, H.-M. Analysis of Land Cover Classification Using Multi-Wavelength LiDAR System. *Appl. Sci.* **2017**, *7*, 663. [CrossRef]
26. Guo, Y.; Wang, H.; Hu, Q.; Liu, H.; Liu, L.; Bennamoun, M. Deep Learning for 3D Point Clouds: A Survey. *IEEE Trans. Pattern Anal. Mach. Intell.* **2021**, *43*, 4338–4364. [CrossRef]
27. Collin, A.; Long, B.; Archambault, P. Merging Land-Marine Realms: Spatial Patterns of Seamless Coastal Habitats Using a Multispectral LiDAR. *Remote Sens. Environ.* **2012**, *123*, 390–399. [CrossRef]
28. Mallet, C.; Bretar, F. Full-waveform topographic lidar: State-of-the-art. *ISPRS J. Photogramm. Remote Sens.* **2009**, *64*, 1–16. [CrossRef]
29. Letard, M.; Collin, A.; Lague, D.; Corpetti, T.; Pastol, Y.; Ekelund, A.; Pergent, G.; Costa, S. Towards 3D Mapping of Seagrass Meadows with Topo-Bathymetric Lidar Full Waveform Processing. In Proceedings of the 2021 IEEE International Geoscience and Remote Sensing Symposium IGARSS, Brussels, Belgium, 11–16 July 2021; pp. 8069–8072.
30. Song, S.; Wang, B.; Gong, W.; Chen, Z.; Xin, L.; Sun, J.; Shi, S. A New Waveform Decomposition Method for Multispectral LiDAR. *ISPRS J. Photogramm. Remote Sens.* **2019**, *149*, 40–49. [CrossRef]
31. Shen, X.; Li, Q.-Q.; Wu, G.; Zhu, J. Decomposition of LiDAR Waveforms by B-Spline-Based Modeling. *ISPRS J. Photogramm. Remote Sens.* **2017**, *128*, 182–191. [CrossRef]
32. Chauve, A.; Mallet, C.; Bretar, F.; Durrieu, S.; Deseilligny, M.P.; Puech, W. Processing full-waveform lidar data: Modelling raw signals. In Proceedings of the ISPRS Workshop on Laser Scanning 2007, Espoo, Finland, 12 September 2007; Volume 36, pp. 102–107.

33. Eren, F.; Pe'eri, S.; Rzhanov, Y.; Ward, L. Bottom Characterization by Using Airborne Lidar Bathymetry (ALB) Waveform Features Obtained from Bottom Return Residual Analysis. *Remote Sens. Environ.* **2018**, *206*, 260–274. [CrossRef]
34. Tulldahl, H.M.; Wikström, S.A. Classification of Aquatic Macrovegetation and Substrates with Airborne Lidar. *Remote Sens. Environ.* **2012**, *121*, 347–357. [CrossRef]
35. Chehata, N.; Guo, L.; Mallet, C. Airborne lidar feature selection for urban classification using random forests. In Proceedings of the Laserscanning, Paris, France, 1–2 September 2009.
36. Yan, W.Y.; Shaker, A.; El-Ashmawy, N. Urban Land Cover Classification Using Airborne LiDAR Data: A Review. *Remote Sens. Environ.* **2015**, *158*, 295–310. [CrossRef]
37. Niemeyer, J.; Wegner, J.D.; Mallet, C.; Rottensteiner, F.; Soergel, U. Conditional Random Fields for Urban Scene Classification with Full Waveform LiDAR Data. In *Proceedings of the Photogrammetric Image Analysis*; Stilla, U., Rottensteiner, F., Mayer, H., Jutzi, B., Butenuth, M., Eds.; Springer: Berlin/Heidelberg, Germany, 2011; pp. 233–244.
38. Pastol, Y. Use of Airborne LIDAR Bathymetry for Coastal Hydrographic Surveying: The French Experience. *J. Coast. Res.* **2011**, *62*, 6–18. [CrossRef]
39. Lague, D.; Feldmann, B. Chapter 2—Topo-bathymetric airborne LiDAR for fluvial-geomorphology analysis. In *Developments in Earth Surface Processes*; Tarolli, P., Mudd, S.M., Eds.; Remote Sensing of Geomorphology; Elsevier: Amsterdam, The Netherlands, 2020; Volume 23, pp. 25–54.
40. Kashani, A.G.; Olsen, M.J.; Parrish, C.E.; Wilson, N. A Review of LIDAR Radiometric Processing: From Ad Hoc Intensity Correction to Rigorous Radiometric Calibration. *Sensors* **2015**, *15*, 28099–28128. [CrossRef]
41. Wilson, N.; Parrish, C.E.; Battista, T.; Wright, C.W.; Costa, B.; Slocum, R.K.; Dijkstra, J.A.; Tyler, M.T. Mapping Seafloor Relative Reflectance and Assessing Coral Reef Morphology with EAARL-B Topobathymetric Lidar Waveforms. *Estuaries Coasts* **2019**. [CrossRef]
42. Shom, IGN, Etat Français, Région Bretagne, DREAL Bretagne, FEDER. Litto3D® Bretagne. 2021. Available online: <https://diffusion.shom.fr/pro/risques/altimetrie-littorale.html> (accessed on 30 October 2021).
43. Girardeau-Montaut, D. CloudCompare. 2016. Available online: <https://www.danielgm.net/cc/> (accessed on 30 October 2021).
44. Collin, A.; Long, B. Mapping the Shallow Water Seabed Habitat with the Shoals. *IEEE Trans. Geosci. Remote Sens.* **2008**, *46*, 2947–2955. [CrossRef]
45. Oshiro, T.M.; Perez, P.S.; Baranauskas, J.A. How Many Trees in a Random Forest? In *Proceedings of the Machine Learning and Data Mining in Pattern Recognition*; Perner, P., Ed.; Springer: Berlin/Heidelberg, Germany, 2012; pp. 154–168.
46. Hsieh, P.-F.; Lee, L.C.; Chen, N.-Y. Effect of Spatial Resolution on Classification Errors of Pure and Mixed Pixels in Remote Sensing. *IEEE Trans. Geosci. Remote Sens.* **2001**, *39*, 2657–2663. [CrossRef]
47. Zhou, T.; Popescu, S.C.; Krause, K.; Sheridan, R.D.; Putman, E. Gold—A Novel Deconvolution Algorithm with Optimization for Waveform LiDAR Processing. *ISPRS J. Photogramm. Remote Sens.* **2017**, *129*, 131–150. [CrossRef]
48. Wu, J.; van Aardt, J.A.N.; Asner, G.P. A Comparison of Signal Deconvolution Algorithms Based on Small-Footprint LiDAR Waveform Simulation. *IEEE Trans. Geosci. Remote Sens.* **2011**, *49*, 2402–2414. [CrossRef]
49. Butler, J.D.; Purkis, S.J.; Yousif, R.; Al-Shaikh, I.; Warren, C. A High-Resolution Remotely Sensed Benthic Habitat Map of the Qatari Coastal Zone. *Mar. Pollut. Bull.* **2020**, *160*, 111634. [CrossRef]
50. Grande, M.; Chust, G.; Fernandes, J.; Galparsoro Iza, I. Assessment of the Discrimination Potential of Bathymetric LIDAR and Multispectral Imagery for Intertidal and Subtidal Habitats. In Proceedings of the 33th International Symposium on Remote Sensing of Environment (ISRSE), Stresa, Italy, 12 February 2009.
51. Chust, G.; Grande, M.; Galparsoro, I.; Uriarte, A.; Borja, Á. Capabilities of the Bathymetric Hawk Eye LiDAR for Coastal Habitat Mapping: A Case Study within a Basque Estuary. *Estuar. Coast. Shelf Sci.* **2010**, *89*, 200–213. [CrossRef]
52. Neuschwander, A.L.; Magruder, L.A.; Tyler, M. Landcover Classification of Small-Footprint, Full-Waveform Lidar Data. *J. Appl. Remote Sens.* **2009**, *3*, 033544. [CrossRef]
53. Letard, M.; Collin, A.; Corpetti, T.; Lague, D.; Pastol, Y.; Gloria, H.; James, D.; Mury, A. Classification of coastal and estuarine ecosystems using full waveform topobathymetric lidar data and artificial intelligence. In Proceedings of the 2021 IEEE Oceans Conference, San Diego, CA, USA, 20–23 September 2021.



Article

Satellite-Derived Topography and Morphometry for VHR Coastal Habitat Mapping: The Pleiades-1 Tri-Stereo Enhancement

Dorothee James ^{1,*}, Antoine Collin ^{1,2}, Antoine Mury ¹ and Rongjun Qin ^{3,4,5,6}

¹ Ecole Pratique des Hautes Etudes, Université PSL, CNRS UMR 6554 LETG, 35800 Dinard, France; antoine.collin@ephe.psl.eu (A.C.); antoine.mury@etu.ephe.psl.eu (A.M.)

² LabEx CORAIL, 66860 Perpignan, France

³ Geospatial Data Analytics Lab, The Ohio State University, Columbus, OH 43210, USA; qin.324@osu.edu

⁴ Department of Civil, Environmental and Geodetic Engineering, The Ohio State University, Columbus, OH 43210, USA

⁵ Department of Electrical and Computer Engineering, The Ohio State University, Columbus, OH 43210, USA

⁶ Translational Data Analytics Institute, The Ohio State University, Columbus, OH 43210, USA

* Correspondence: dorothee.james@ephe.psl.eu

Abstract: The evolution of the coastal fringe is closely linked to the impact of climate change, specifically increases in sea level and storm intensity. The anthropic pressure that is inflicted on these fragile environments strengthens the risk. Therefore, numerous research projects look into the possibility of monitoring and understanding the coastal environment in order to better identify its dynamics and adaptation to the major changes that are currently taking place in the landscape. This new study aims to improve the habitat mapping/classification at Very High Resolution (VHR) using Pleiades-1-derived topography, its morphometric by-products, and Pleiades-1-derived imageries. A tri-stereo dataset was acquired and processed by image pairing to obtain nine digital surface models (DSM) that were 0.50 m pixel size using the free software RSP (RPC Stereo Processor) and that were calibrated and validated with the 2018-LiDAR dataset that was available for the study area: the Emerald Coast in Brittany (France). Four morphometric predictors that were derived from the best of the nine generated DSMs were calculated via a freely available software (SAGA GIS): slope, aspect, topographic position index (TPI), and TPI-based landform classification (TPILC). A maximum likelihood classification of the area was calculated using nine classes: the salt marsh, dune, rock, urban, field, forest, beach, road, and seawater classes. With an RMSE of 4 m, the DSM#2-3_1 (from images #2 and #3 with one ground control point) outperformed the other DSMs. The classification results that were computed from the DSM#2-3_1 demonstrate the importance of the contribution of the morphometric predictors that were added to the reference Red-Green-Blue (RGB, 76.37% in overall accuracy, OA). The best combination of TPILC that was added to the RGB + DSM provided a gain of 13% in the OA, reaching 89.37%. These findings will help scientists and managers who are tasked with coastal risks at VHR.

Keywords: Pleiades-1; photogrammetry; RSP; topography; classification; maximum likelihood; landscape

Citation: James, D.; Collin, A.; Mury, A.; Qin, R. Satellite-Derived Topography and Morphometry for VHR Coastal Habitat Mapping: The Pleiades-1 Tri-Stereo Enhancement. *Remote Sens.* **2022**, *14*, 219. <https://doi.org/10.3390/rs14010219>

Academic Editors: Dar Roberts, Junshi Xia and Simona Niculescu

Received: 31 October 2021

Accepted: 23 December 2021

Published: 4 January 2022

Publisher's Note: MDPI stays neutral with regard to jurisdictional claims in published maps and institutional affiliations.



Copyright: © 2022 by the authors. Licensee MDPI, Basel, Switzerland. This article is an open access article distributed under the terms and conditions of the Creative Commons Attribution (CC BY) license (<https://creativecommons.org/licenses/by/4.0/>).

1. Introduction

1.1. Global Change

Coastal landscapes have faced significant changes over billions of years, and their evolution is concomitant with major climatic upheavals. In its sixth and most recent report, the Intergovernmental Panel on Climate Change (IPCC) indicates that climate change is occurring more rapidly than originally predicted, with unprecedented increases in sea levels, heat waves, and the faster melting of polar ice caps [1]. Currently, mankind is trying

to cope with and adapt to rapid climate changes that influence ocean currents, winds, precipitations, temperatures, and strongly re-shaped landscapes [2].

1.2. Landuse/Landcover Observation Techniques

Observation techniques for tracking landscape changes are many and varied. At local-scale and very-high (VH) spatial resolution, unmanned aerial vehicles (UAV) are useful for the VH temporal resolution monitoring of coastal socio-ecosystems [3]. UAVs are cost-efficient and easily deployable for shoreline detection [4] and for the identification of seasonal variations in saltmarsh meadows [5]. They are, however, not well suited for monitoring areas at the landscape scale (several km²) due to not only the restrictions that are imposed by legislation but also the technical limitations that are enforced by the number of flight times that are permitted by the battery capacity. In addition, in coastal areas, the meteorological and marine conditions require a maximum time of presence on the site due to the tides (\pm one hour after low water slack).

Manned aerial vehicles (MAV) serve as a robust alternative that leverages passive sensors with a basic red-green-blue (RGB) spectrum and sometimes the infrared spectrum [6] or an active light detection and ranging (LiDAR) sensor [7]. The complete solution makes it difficult to plan missions, and sensors such as LiDAR are rather expensive.

1.3. Spaceborne Acquisition and Stereoscopy

Yet, the analysis of the environment at the landscape scale is made possible by satellites which have a VH spatial, a multispectral, and even a hyperspectral resolution for the best-equipped satellites [8].

A spaceborne solution exists to obtain multispectral VH resolution images that are 0.50 m and 0.30 m pixels in size, which are provided by Pleiades-1 or WorldView-3 and 4, respectively. Satellite-based multispectral VH resolution mapping of the coastal fringe has been successfully performed in studies focusing on tropical [9] or temperate environments [10].

Since 2000, some remote sensing satellites that are specialized in stereo acquisition have been launched into orbit around the Earth, such as the Worldview-1, -2, -3, -4 constellations, GeoEye-1 and -2, the Pleiades-1 and, -1B constellations, and the 2021-launched Pleiades Neo, whose images are not yet available for research at the time of this submission [11]. The operating principle of stereoscopy is to photograph an object or a landscape from two different angles in the same way as human vision is able to, with a specific overlap for determining the 3D information of the obtained images. Sometimes a third angle (nadir) of view can be available as a redundant observation to increase the accuracy when producing a digital elevation or surface model.

Satellite-based stereo topography has the capability of improving coastal mapping by improving the spectral discrimination of eco-geo-morphological objects [12]. However, when a tri-stereo product is used, do they augment/boost this coastal mapping? Do the morphometric parameters that are derived from the topography contribute to a better classification of coastal ecosystems than basic spectral information? This paper along with the experimental results that are presented in it will seek to answer these two questions.

2. Materials and Methods

2.1. The Study Site

The entire study site (76 km² terrestrial part) is located on the Emerald Coast in Brittany (France) along the Channel Sea (48.60° N, 2.00° W; Figure 1). It is characterized by a diversity of ecosystems that are shaped by the proximity of a megatidal sea and is one of the six areas with the highest tidal ranges in the world (up to 14 m) [13]. The Rance, a coastal river, ends its course in the bay of Saint Malo, dividing the area in two sub-sites. In terms of land cover, this study area is composed of temperate zone coastal vegetation, salt marshes, rocks, dunes, and fine sand beaches. The coastline is strongly indented, leaving multiple sandy beaches surrounded by rocky points and islets a little further offshore.

Bays are also common on this coastal fringe and are featured by the presence of salt marsh meadows. In terms of urbanism, this Brittany coastal fringe is subject to strong anthropic pressures. The small fishing villages of the past have evolved into resort urban areas that now attract tourists in search of iodized air and marine landscapes.

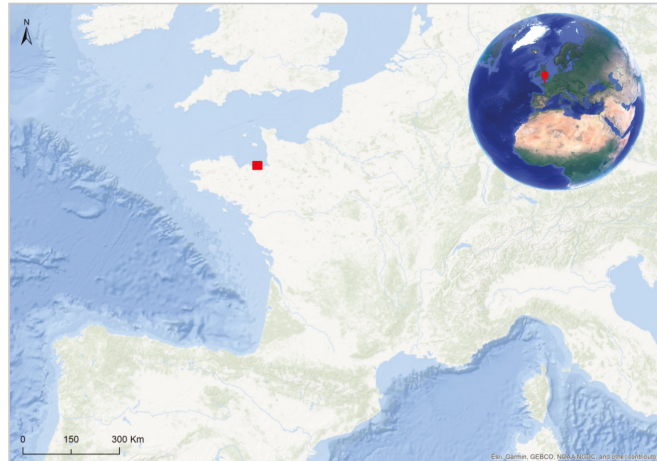


Figure 1. Location of the study on the Emerald Coast (France).

As with all coastal areas in the world, the Emerald Coast is not exempted from coastal risks. Its highly populated coastline increases the vulnerability of lowland populations.

2.2. Pleiades-1 Satellite Imageries

The Pleiades-1A and 1B constellation multispectral satellites were launched on 16 December 2011 and 2 December 2012, respectively [14]. The Pleiades-1 constellation acquires images of the Earth daily and can cover up to 1,000,000 km² per day. The radiometric spectrum of the sensor extends from 430 nm to 940 nm (B: 430–550 nm; G: 500–620 nm; R: 590–710 nm; and NIR: 740–940 nm).

Data collection is based on tri-stereo images from the Pleiades-1 satellite sensor (Table 1; Figure 2a). The satellite orbited over the study area on 28 November 2020 to collect three images at 11 h 26 min 14 s (UTC), then at 11 h 26 min 24 s (UTC), and finally at 11 h 26 min 32 s (UTC; Table 1). Each dataset of images contains panchromatic and multi-spectral images (R, G, B, NIR) that are 0.5 m and 2 m pixels in size, respectively (Table 1, Figure 2b,c). The images were delivered without initial geometric processing (primary level) and without radiometric processing.

Table 1. Pleiades-1 specificities of the tri-stereo acquisitions over the study site.

| Parameters | Image #1 | Image #2 | Image #3 |
|-------------------------------------|------------------|------------------|------------------|
| Acquisition date | 28 November 2020 | 28 November 2020 | 28 November 2020 |
| Time | 11 h 26 min 14 s | 11 h 26 min 24 s | 11 h 26 min 32 s |
| Image orientation angle (in degree) | 180.01 | 180.03 | 180.01 |
| Incidence angle (in degrees) | 16.41 | 15.35 | 16.05 |
| Sun azimuth (in degree) | 172.60 | 172.60 | 172.60 |
| Sun elevation (in degree) | 19.77 | 19.77 | 19.77 |

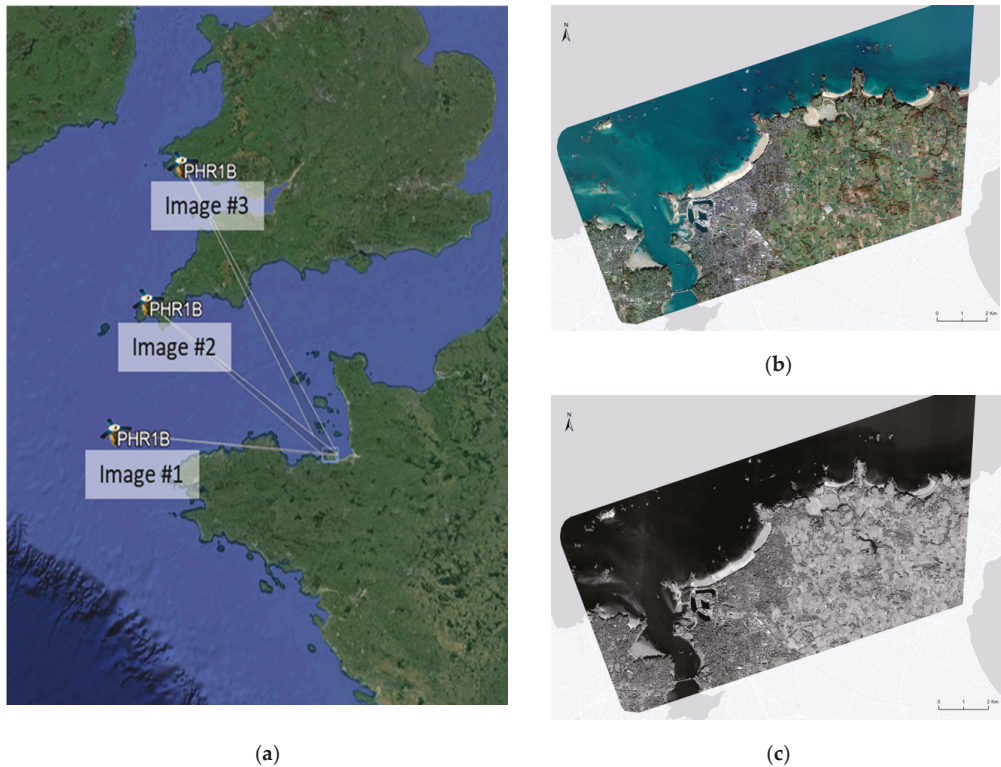


Figure 2. Viewing directions with respect to the target area of the tri-stereo Pleiades-1 images (a); natural-coloured nadir imagery at 2 m pixel size (b), and panchromatic nadir imagery at 0.5 m pixel size (c) of the study site.

2.3. LiDAR Airborne Dataset

Thanks to multiple LiDAR data acquisition campaigns on the French territory by the French Navy's Hydrographic and Oceanographic Department (SHOM), a LiDAR point cloud was available for the study site. The land/sea continuum is guaranteed by the precision of the topo-bathymetric dataset (horizontal and vertical topographic accuracy of 0.20 m), which was acquired with a Leica HawkEye-3 sensor (Chiroptera + Deep channel).

The 2018 LiDAR point cloud was used to calibrate and validate the digital elevation model (DEM) using 36 validation points that were evenly distributed over the study area. The coordinates in XY (WGS84 UTM 30N) and Z (ellipsoidal height) were extracted for each point (Figure 3).

2.4. Coastal Landscape Classes

Nine classes that are representative of the coastal landscape were identified (Table 2, Figure 4): dune (white dune vegetation *Ammophila arenaria*), salt marsh (salt marsh vegetation composed mainly of *Spartina*, *Salicornia*, *Suaeda*, and *Halimione portulacoides*), rock, urban (building roof), forest (mix of deciduous and coniferous), field (cultivated and uncultivated), beach (wet and dry sand of grain of 0.06 to 2 mm), road (mainly asphalt), and seawater (shallow to deep salt water). A sub-study site was extracted for the classification tests (red rectangle in Figure 3).

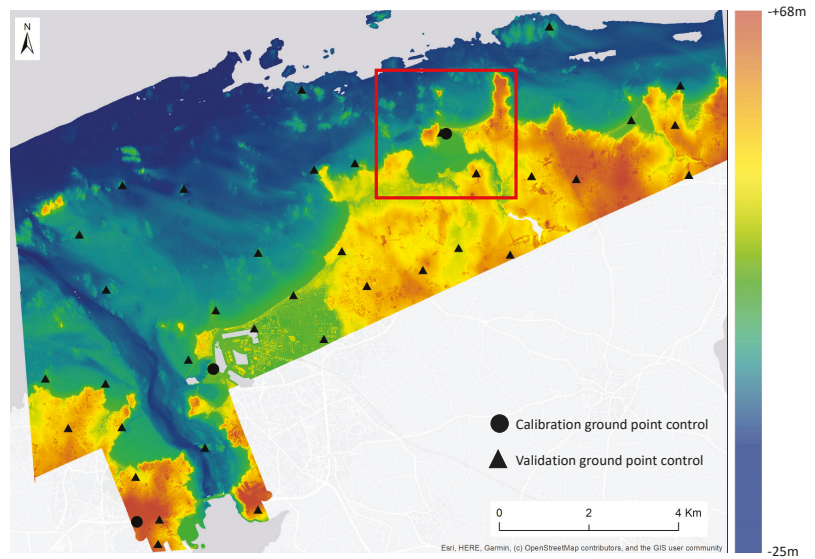


Figure 3. 2018 LiDAR of Emerald Coast with evenly distributed calibration points (black circle) and validation points (black triangle); the red rectangle corresponds to the sub-study site.

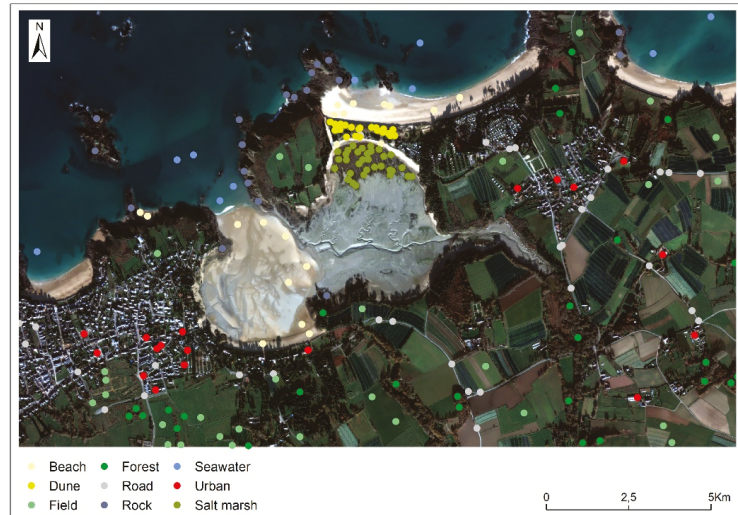









Figure 4. Natural-coloured nadir Pleiades-1 imagery with the calibration/validation class locations.

2.5. Satellite-Derived Topography: Photogrammetry Reconstruction

Three couples of panchromatic images, which were characterized by three intersection angles, were processed using the opensource software RSP (RPC stereo processor, [15], Figure 5) from the tri-stereo images from Pleiades-1. RSP was used to process stereo satellite images so as to create point dense clouds and then to create a Digital Surface Model (DSM) using the photogrammetry technique. For each pair of images, RSP used the Rational Polynomial Coefficients (RPC) files, which were delivered with the Pleiades-1 images, which contain the geometric parameters for the same images to build the projection

relationship between the 3D and 2D space. The additional Ground Control Points (GCP) increased the accuracy of the reconstruction horizontally and vertically.

Table 2. Pleiades-1 natural-coloured thumbnail of the nine coastal landscape classes.

| Class Name | Thumbnail |
|------------|--|
| Dune |  |
| Salt marsh |  |
| Rock |  |
| Urban |  |
| Forest |  |
| Field |  |
| Beach |  |
| Road |  |
| Seawater |  |

Three image pairs (1) without, (2) with 1, or (3) with 3 GCP (DSM#2-3_0, DSM#2-3_1, DSM#2-3_3, DSM#1-2_0, DSM#1-2_1, DSM#1-2_3, DSM#1-3_0, DSM#1-3_1, DSM#1-3_3) were computed using RSP, and nine DSM were evaluated using the root mean square error (RMSE). The lowest RMSE was the factor that identified what the best photogrammetry-based DSM was.

$$RMSE = \sqrt{\frac{\sum_{i=1}^n (P_i - O_i)^2}{n}}, \quad (1)$$

where P is the value of the calculated DSM ellipsoidal height; O is the value of the LiDAR ellipsoidal height; and n is the number of observations.

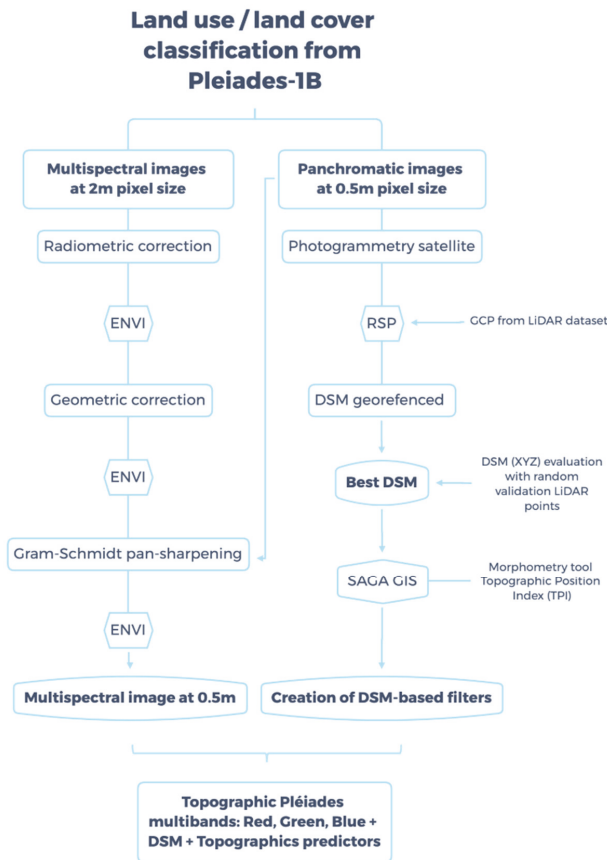


Figure 5. Flowchart describing methodology for coastal landscape classification from Pleiades-derived topography and morphometry.

In addition, the DSMs were also evaluated at the ecosystem scale by referring to the nine identified classes. A mean of the ellipsoidal heights per class was calculated, and a dispersion parameter such as standard deviation was determined to show the homogeneity or heterogeneity of the statistical series.

The MS images underwent three pre-processing stages before they were integrated into the analyses:

ENVI's FLAASH tool was used to correct the influence of the atmosphere (top of atmosphere, TOA) for each pixel in the images. The radiometric correction of the MS images consisted of converting the numerical radiance values into TOA reflectance values. The reflectance was calculated according to the radiance/irradiance (solar) ratio.

The MS images were also geometrically corrected using both the RPC files and the DSMs, which had been created previously from the panchromatic stereo images. This pre-processing stage corrected the distortions in the images that were related to the positioning of the satellite or the structure of the landform.

The MS images were pan-sharpened using the Gram-Schmidt algorithm. It resampled the 2 m pixel size of the MS image to be of the 0.5 m pixel size of the panchromatic images (see James et al., 2021).

2.6. Satellite-Derived Morphometry

The morphometric features such as slope, aspect, topographic position index (TPI), and TPI-based landform classification (TPILC) were calculated from the best DSMs using the SAGA GIS opensource software (Figure 5) [16]. These indicators that were related to the topography of the study site were coupled with the basic RGB spectral information to reveal the contributions of each predictor. The near-infrared band of the image was also compared to the morphometric predictors.

The slope highlights the inclination of a pixel, and this aspect defines the orientation of the slope from a compass direction. The slope and aspect predictors generate raster images that are computed from the DSM. The percentage of slope is the ratio between the difference in altitude and the horizontal distance. A 3×3 pixel moving window compares the values of a pixel around its neighbors to define the slope percentage.

TPI computes the elevation or altitude of each pixel and subtracts it from the mean elevation or altitude of a neighborhood of that pixel of a grid raster [17]. Values that are lower than 0 correspond to valleys. Values higher than 0 are ridges, and those that are around 0 are flat areas. TPI-based landform classification was founded on the same principle as the basic TPI. Two different scales were combined to allow for the better identification of the topographic differences [18].

2.7. Classification Algorithm

A supervised machine learning classifier algorithm was tested: maximum likelihood (ML) with ENVI[®] software (Figure 5) [19]. ML is a probabilistic method that calculates the variance and covariance of each class by assuming that the statistics of each class in each band are normally distributed. A pixel is then assigned to the class with the most likely probability of membership.

An array of 500 calibration pixels and 500 validation pixels per class were extracted from the satellite-derived products (Table 2). Overall accuracy (OA) is determined as the sum of the correctly classified pixels divided by the number of pixels. The producer accuracy (PA) corresponds to the accuracy of the map from the producer's point of view, i.e., from the algorithm. The result expressed in % indicates the fraction of correctly classified pixels of those that are known to belong to the class [20]. The OA of each by-product combination was evaluated through the calibration/validation pixels that were calculated with the confusion matrix.

3. Results

After the DSMs were derived and evaluated, the best one was further investigated to build topographic by-products. A ML algorithm was applied to this DSM using nine representative landscape classes from the study site. The contribution of each derived topographic band was evaluated at the landscape (OA) and class (PA) level.

3.1. Pleiades-1 Digital Surface Model

3.1.1. Global Evaluation

The results of the overall DSM evaluation showed a slight increase in the overall accuracy of the DSMs with the addition of GCPs (Figure 6). Thus, without GCP, with 1 GCP, and with 3 GCPs, the results were 4.03 m, 4 m, and 4.01 m for DSM#2-3 (Figures 6 and 7a). DSM#1-2 and DSM#1-3 increased their accuracy by 0.04 m and 0.02 m, respectively, as soon as a GCP was added (Figures 6 and 7b,c). However, image pairs #1-#2 and #1-#3 gave unsatisfactory results compared to image pair #2-#3.

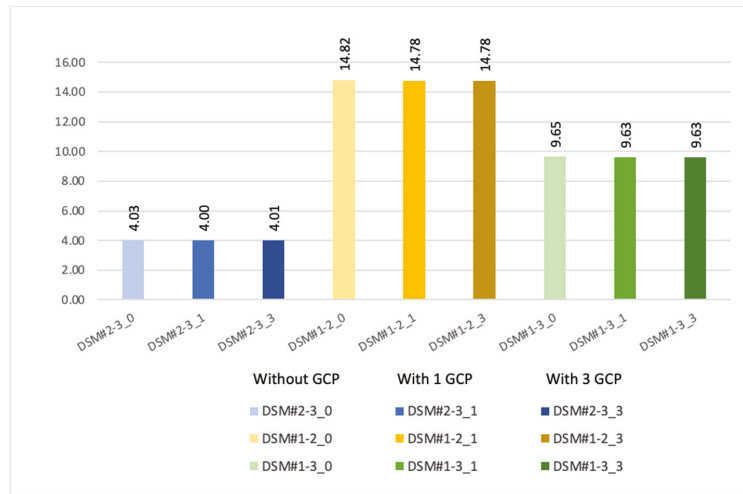
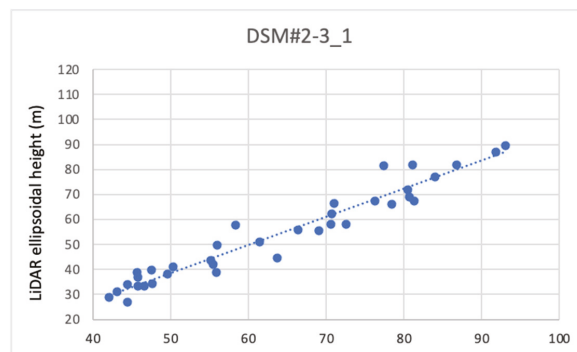


Figure 6. Bar plot of the root mean square error from Pleiades-1 DSM computed by pairs without, with 1, or with 3 ground control points.

At the global scale, the analysis of the three best DSMs (DSM#2-3_1, DSM#1-2_3, and DSM#1-3_3) can be compared to the validation points that were extracted from the LiDAR-2018 (Figure 7a-c). The distribution of the DSM#2-3_1 points shows a low dispersion and therefore a positive correlation between the LiDAR-2018 dataset and DSM#2-3_1 (Figure 7a). The DSM#1-3_3 appeared to be sparsely correlated to the LiDAR-2018 dataset.

3.1.2. Class Level DSM Evaluation

The analysis of the DSM results from the Pleiades-1 images can also be examined at the class level (Figure 8) on the sub-study site. Based on the validation polygons from the classes, each DSM was evaluated.



(a)

Figure 7. Cont.

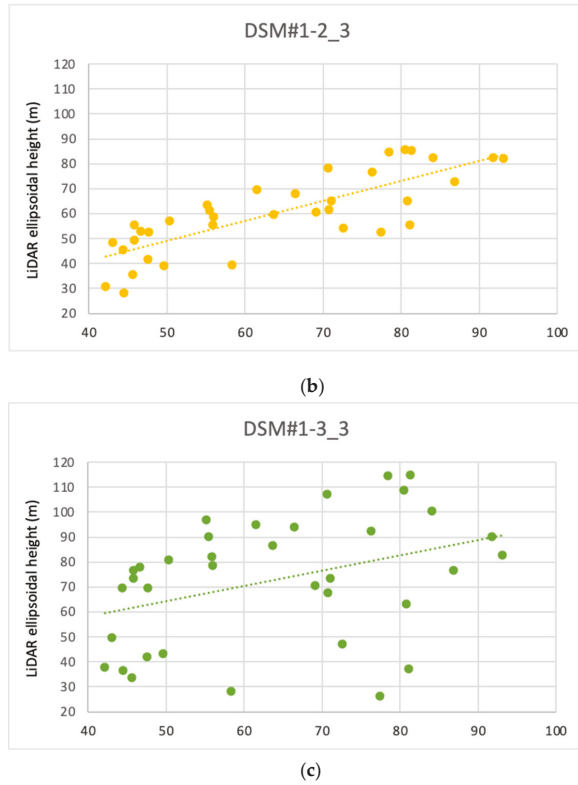


Figure 7. Comparison of ellipsoidal height of the LiDAR dataset and the three best digital surface models: DSM#2-3_1 (a), DSM#1-2_3 (b) and DSM#1-3_3 (c).

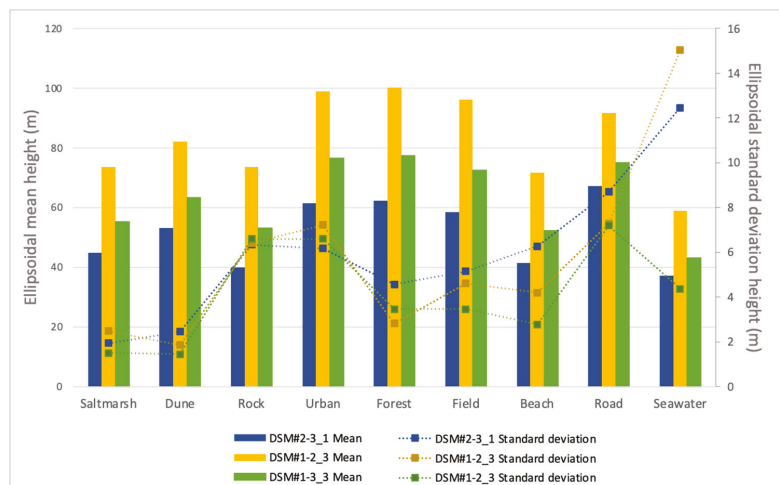


Figure 8. Ellipsoidal mean and standard deviation height at the class level on the sub-study site from the three best digital surface models.

Depending on the ecosystem, the mean heights between the DSMs within the same class can vary. This is the case for almost all of the classes if the three DSMs are compared to each other.

However, when DSM#2–3_1 and DSM#1–3_3 are compared to each other (due to their performance at the landscape scale), the mean differences in heights were: +10.35 m, +10.22 m, +13.16 m, +15.24 m, +15.11 m, +13.95 m, +10.83 m, +7.71, and +6.15 m for the salt marsh, dune, rock, urban, forest, beach, road, and seawater classes, respectively.

3.2. Morphometric Derivatives

Four main morphometric by-products were calculated:

- The slope values ranged from 0 to 89°, with 0° corresponding to a flat surface such as the seawater or flatland (in green) and 89° corresponding to a steep cliff (in red in Figure 9a).
- The aspect is categorized in 10 classes from 0 to 360°, according to the main cardinal points (north, south, east, west; Figure 9b). A value of −1 corresponds to flat areas such as those for seawater.
- TPI is the third morphometric contributor (Figure 9c).
- Finally, TPILC (Figure 9d) groups the landscapes into 10 classes (1 to 10).

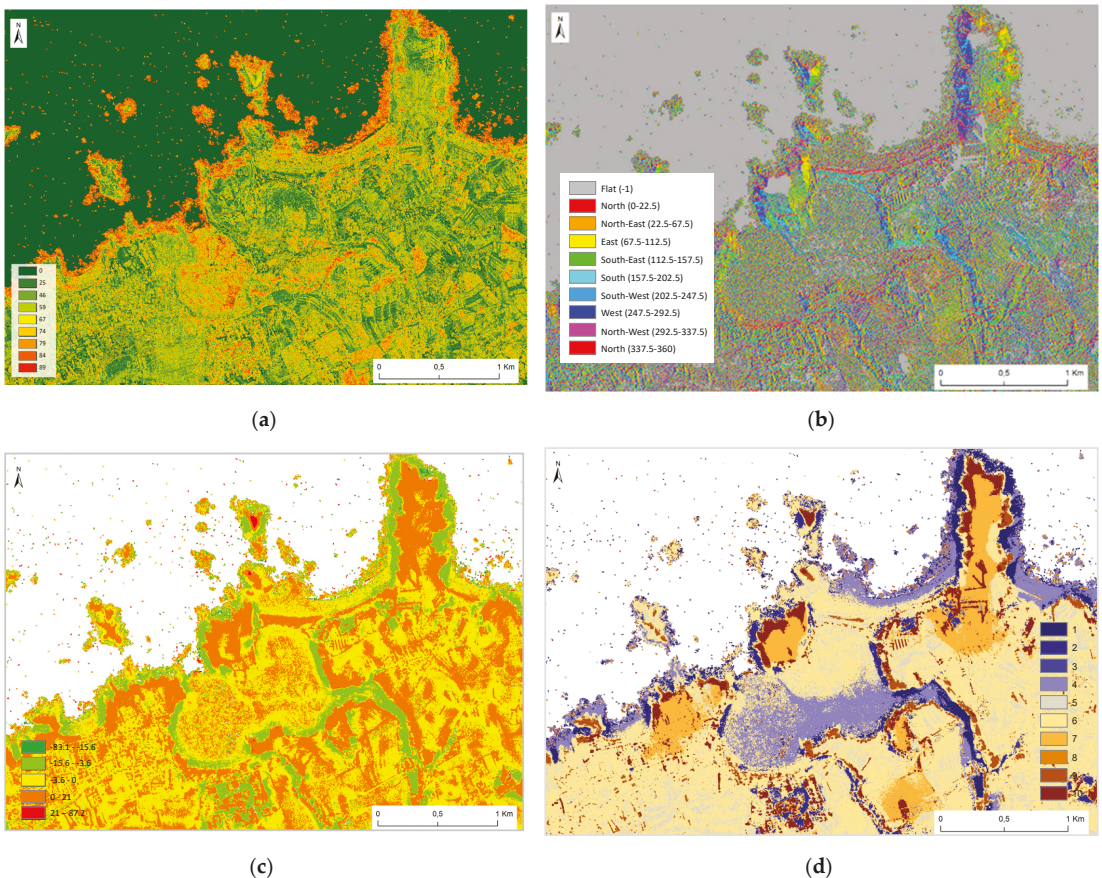


Figure 9. Morphometric variables derived from the best Pleiades-1 DSM#2–3_1: slope in degrees (a); aspect (b); topographic position index, (TPI) (c); TPI-based landform classification (d).

3.3. Pixel-Based Classification

3.3.1. Overall Accuracy at the Landscape Scale

At the landscape scale, each band combination was assessed. To test individual contribution, the RGB spectral composite was used as a basis, achieving an OA of 76.37% (Figure 10).

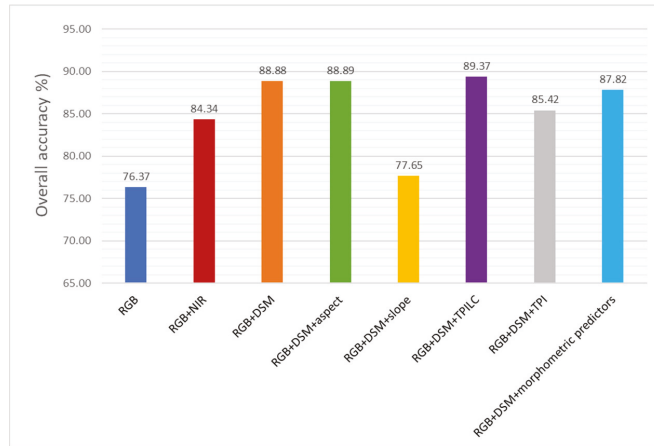


Figure 10. Overall accuracy of the eight classifications performed with the maximum likelihood classifier.

The NIR band was also tested and obtained a score of 84.34% combined with the RGB.

Thus, in addition to the RGB, the DSM significantly enhanced the OA by +12.51%, but RGB + DSM + slope decreased the score (−11.23%) compared to the RGB + DSM combination (Figure 10).

The morphometric predictor combinations provided a strong contribution to the classification, with +9.05%, +11.45%, and +12.52% for the RGB + DSM + TPI and RGB + DSM + morphometric predictors and for RGB + DSM + aspect, respectively.

Finally, the best combination was the TPILC predictor combined with RGB + DSM, with a classification score of 89.37%, namely an augmentation of +13%.

3.3.2. Evaluation at the Class Level

The analysis of the confusion matrix of each morphometric predictor added to the basic RGB highlights a heterogeneity between the classes (Table 3, Figures 11 and 12).

Table 3. Producer accuracy (in %) from confusion matrix using the maximum likelihood classifier for the salt marsh, dune, rock, urban, field, forest, beach, road, and seawater classes.

| | Salt Marsh | Dune | Rock | Urban | Field | Forest | Beach | Road | Seawater |
|-------------------------------------|------------|-------|-------|-------|-------|--------|-------|-------|----------|
| RGB | 84.47 | 58.67 | 64.8 | 62.27 | 87.67 | 57 | 80.27 | 92.27 | 100 |
| RGB + NIR | 89.13 | 68.93 | 75.07 | 71 | 90.27 | 73.67 | 99.4 | 91.67 | 100 |
| RGB + DSM | 95.2 | 94.67 | 70.8 | 73 | 88.6 | 89.27 | 97.67 | 92.33 | 98.47 |
| RGB + DSM + slope | 82 | 61.47 | 65.8 | 64.73 | 87.47 | 59.47 | 86.13 | 92.47 | 99.4 |
| RGB + DSM + aspect | 95.2 | 95.13 | 70.8 | 72.93 | 88.4 | 89.53 | 97.33 | 92.33 | 98.4 |
| RGB + DSM + TPI | 98.6 | 99.07 | 13.27 | 80.4 | 93.6 | 94.6 | 98.07 | 91.47 | 99.73 |
| RGB + DSM + TPILC | 96.67 | 96.27 | 75.27 | 70.13 | 89.67 | 87.93 | 97.6 | 92.4 | 98.47 |
| RGB + DSM + morphometric predictors | 98.33 | 98.67 | 26.33 | 84.13 | 92.93 | 97.2 | 99.13 | 94.2 | 99.53 |

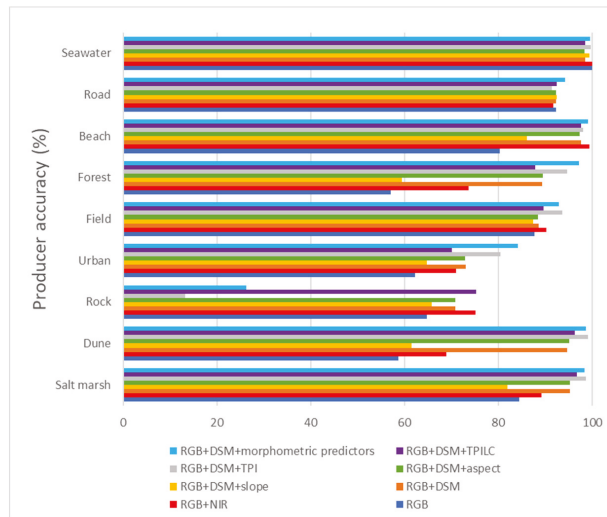


Figure 11. Bar plot of the producer accuracy of the morphometric predictor on the basis RGB at the class level (salt marsh, dune, rock, field, forest, beach, road, and seawater).

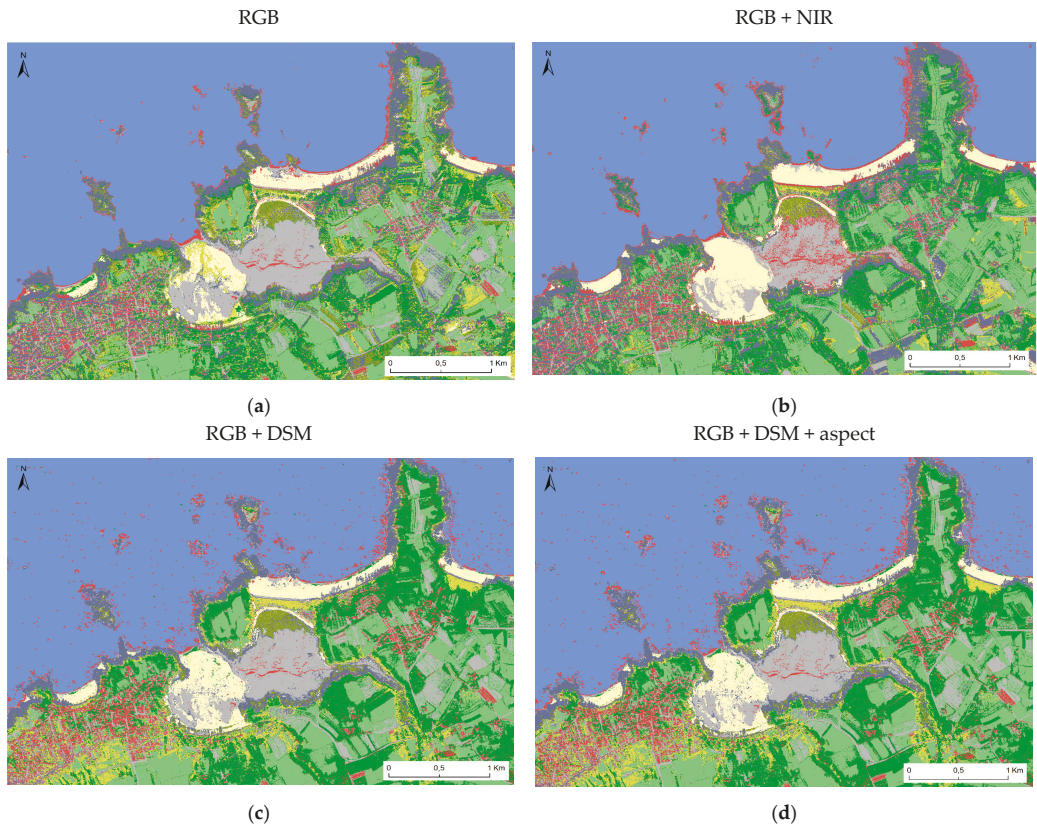


Figure 12. Cont.

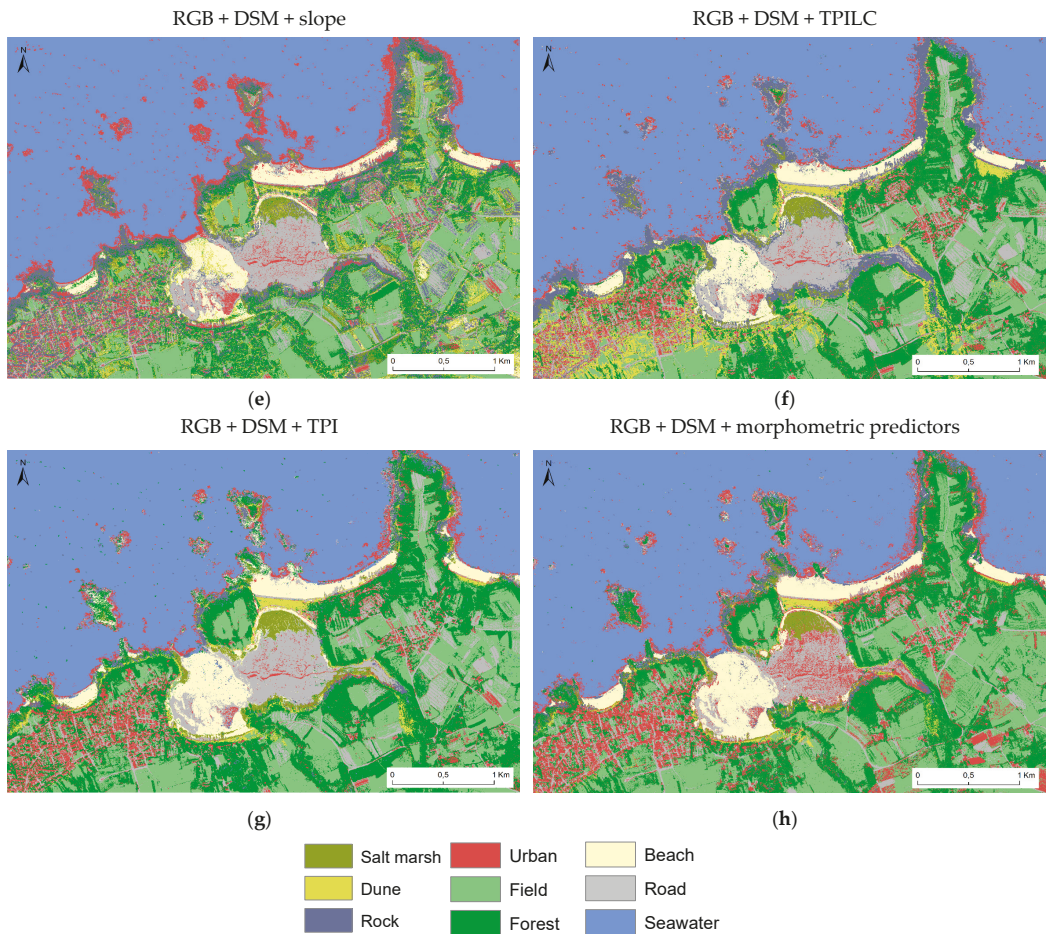


Figure 12. Coastal mapping classification at the class level computed with the maximum likelihood classifier: Basis RGB (a); RGB + NIR (b); RGB + DSM (c); RGB + DSM + slope (d); RGB + DSM + aspect (e); RGB + DSM + TPI (f); RGB + DSM + TPILC (g); RGB + DSM + morphometric predictors (h).

Thus, the urban class obtained the worst results with the RGB and increased in terms of classification performance when another predictor was added. The slope predictor increased by 2.46. The addition of a morphometric predictor allowed the 70.13% of classification performance to increase until the threshold of 84.13% as reached with the combination RGB + DSM + morphometric predictor. The NIR predictor holds up reasonably, achieving a score of with 71% (Table 3, Figures 11 and 12).

The trend for the forest class seems to be the same as the trend observed for the urban class. The slope provides a modest contribution of 2.47%, followed by the NIR predictor with a contribution of 16.67%, and then by the DSM contribution with a contribution of 32.27%. When added to the RGB + DSM, morphometric predictors aspect, TPILC, TPI, and the entire combination obtain values of +30.93%, +30.97%, +37.6%, and +40.2%, respectively.

The salt marsh, beach, and dune classes increased in classification accuracy when a morphometric variable was added to the reference RGB: +10.73%, +17.4%, and +36%, respectively with the RGB + DSM combination until the addition of TPI variable at 98.6% and 99.07% for the salt marsh and dune classes. The beach class obtained the best result

with RGB + NIR, achieving results of 99.4%. In contrast to the salt marsh and beach classes, the rock class performed worst, with 13.27% and 26.33% with the RGB + TPI combinations and the complete combination of morphometric variables added to the RGB, respectively.

The road class obtained linear classification scores between 91.47% for RGB + DSM + TPI and 94.2% for the RGB + DSM + morphometric predictors.

The field class follows a slightly different pattern than the other classes since the worst result, which was still very acceptable, is achieved by the combination RGB + DSM + slope, with a score of 86.47%. The RGB combination increased the classification performance by only +0.2% and +0.93% for the RGB + DSM + aspect and +1.13% for the RGB + DSM combination. The RGB + DSM + TPILC, RGB + NIR, and RGB + DSM + morphometric predictors increased the classification performance by +2.2%, 2.8%, and +5.46%. The best combination for the field class was obtained by RGB + DSM + TPI, with a score of 93.6%.

The seawater class achieved high scores of almost 100% PA, regardless of the predictor (Table 3, Figures 11 and 12).

4. Discussion

4.1. Pleiades-1 Digital Surface Model

4.1.1. The Intersection Angle as a Key Determinant

At the global scale, nine DSM were computed via RSP from three Pleiades-1 satellite images captured at three different angles of incidence: 16.41° for image #1, 15.35° for image #2, and 16.05° for image #3 (Figure 2a and Table 1). DSM#2-3_1, which was derived from the stereo reconstruction of images #2 and #3 outperformed, the other DSMs. According to the results of the satellite photogrammetry, reconstructions with the closest intersection angles (5.13°) produced better point-measurement accuracy compared to the the 2018-LiDAR altimetric reference. Another answer can also be provided by focusing on the solar angle [21]. Moreover, close or near-similar intersection angles increase the risk of “hidden sides” because of their proximity [22,23].

However, many studies have shown interest in using tri-stereo satellite images to benefit, when possible, from a nadir view [24]. The benefit of such a tri-stereo enables a reduction in the shadows that are created by trees or buildings. This approach is highly valued by urban planners, as it limits the risk of shadows and hidden areas [25].

As for photogrammetric reconstructions from UAV images, a deficient RMSE could be explained by reconstruction artifacts related to the algorithm or to the images themselves [26].

4.1.2. Ground Control Point Effect

At a more local scale, three scenarios can explain the results that were obtained. The first is the number of GCP that were extracted from the 2018-LiDAR as calibration points for our topographic models. The tests that were performed without GCP, with one, or with three GCP, showed that when we added GCP points, the model is more accurate [27]. However, The RPC files that were delivered with the Pleiades-1 images could be more powerful. The RPC files integrate all of the parameters that are related to the photographs in order to correct for the satellite images. This approach could be investigated in a future study.

4.1.3. Information Reflected by the LiDAR Wavelengths

Two laser sensors were used for the whole LiDAR dataset: a mixed topo-bathymetric laser in the NIR and green spectra, and a stronger bathymetric laser in the green spectrum, which was specifically used for deeper areas. Depending on the nature (albedo) of the coastal habitat, the wavelength that is used by the LiDAR does not return the same information, being more or less reflected. Thus, the reflectance in the NIR is strong for eco-geo-systems with high chlorophyll dominance, and conversely, it is fully absorbed by habitats with a high water content, such as seawater, for example [28].

The density of the LiDAR points may also play a crucial role. The intertidal and coastal land area is denser in a number of points per square meter than marine area (deep water area) is. The detection of features such as trees is easy when the density of measured points is high [29].

4.2. Topographic Contribution to Habitat Classification

At the landscape scale, the contribution of the morphometric predictors surpassed the classification performance. Although the basic RGB performs well, as soon as morphometric predictors are added, the OA increases (from +1.28% to +13%). The positive effect of the slope raster and its by-products on the landscape classification were evidenced in several studies based on satellite sensors [30] as well as in UAV studies [31]. The classification test with the addition of the NIR band showed the relevance of a classification with morphometric variables. Indeed, when these variables were added to the RGB, the classification performance on the coastal fringe increased considerably contrary to the multispectral RGB + NIR combination without any other predictors.

At the ecosystem class level, the morphometric predictors produced different results depending on the coastal habitat type. For example, the topographic variables provided successful results for salt marshes. This particular ecosystem is located in a geographical area that is sheltered from strong prevailing marine currents. Coastal erosion has minimal or no impact on the meadows, allowing the different plant species to grow.

5. Conclusions

This research study on satellite photogrammetry with Pleiades-1 tri-stereo images is meaningful for the classification of coastal landscapes at VHR, especially in the context of climate change and increasing anthropic pressure on the coastal fringe.

Three pairs of Pleiades-1 panchromatic images at the 0.5 m pixel size were tested for DSM generation, and nine DSM were evaluated from 36 2018 LiDAR validation points.

The best DSM was derived from images #2 and #3 (DSM#2-3_1), which featured, respectively, with incidence angles of 15.35° and 16.05° and an intersection angle of 5.13°. From this new DSM, four morphometric by-products were calculated: slope, aspect, topographic position index (TPI), and TPI-based landform classification (TPILC).

A pixel-based classifier, the probabilistic maximum likelihood, was applied to the 0.5 m pansharpened RGB images, which initially had a pixel side of 2 m. Nine classes (dune, salt marsh, rock, urban, field, forest, beach, road, and seawater) were examined to map the study site (Figure 13). The best combination of morphometric predictors provided a gain of 13% in the OA, reaching 89.37%, when added to the RGB + DSM. These findings will help scientists and managers who tasked with the coastal risks at VHR.

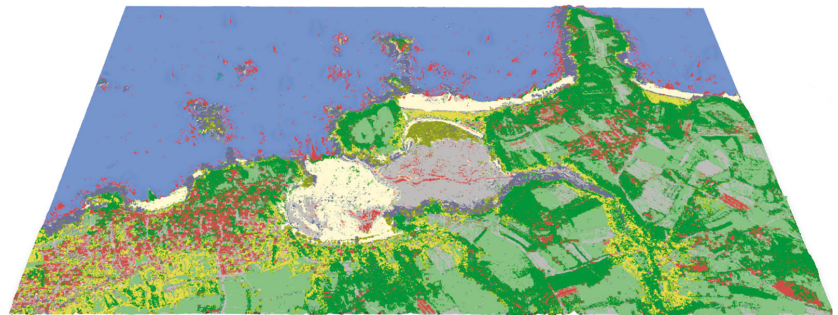


Figure 13. Best map classification draped over the best digital surface model.

In a study that will be published in the near future, photogrammetric reconstruction from a Pleiades-Neo panchromatic triplet at the 0.30 m spatial resolution will be evaluated, given that this new sensor benefits from six bands (purple, blue, green, red, red edge, NIR),

meaning that it has two additional bands compared to Pleiades-1. Moreover, the purple band will be interesting to investigate for the sake of bathymetry extraction.

Author Contributions: Conceptualization, D.J. and A.C.; methodology, D.J.; software, R.Q. and D.J.; validation, A.C., A.M. and R.Q.; formal analysis, A.C., A.M. and D.J.; investigation, D.J.; resources, D.J.; data curation, A.C. and D.J.; writing—original draft preparation, D.J.; writing—review and editing, D.J., A.C., A.M. and R.Q.; visualization, D.J.; supervision, A.C.; project administration, A.C. and D.J.; funding acquisition, A.C. and D.J. All authors have read and agreed to the published version of the manuscript.

Funding: This research received no external funding. The APC was internally funded by the coastal geoeological laboratory.

Institutional Review Board Statement: Not applicable.

Informed Consent Statement: Not applicable.

Data Availability Statement: Not applicable.

Acknowledgments: The authors would like to thank the dinamis platform for access to the Pleiades images and the CNES “Pléiades © CNES 2020, Distribution Airbus DS” and the SHOM for the provision of the LiDAR dataset (SHOM, 2020. MNT topo-bathymétrie côtier d’une partie du golfe normand-breton (PAPI Saint-Malo)). The authors gratefully acknowledge the three anonymous reviewers whose comments helped to improve the manuscript.

Conflicts of Interest: The authors declare no conflict of interest.

References

- Zhu, Z.; Lu, L.; Zhang, W.; Liu, W. *AR6 Climate Change 2021: The Physical Science Basis*; IPCC: Geneva, Switzerland, 2021.
- Mousavi, M.E.; Irish, J.L.; Frey, A.E.; Olivera, F.; Edge, B.L. Global warming and hurricanes: The potential impact of hurricane intensification and sea level rise on coastal flooding. *Clim. Chang.* **2010**, *104*, 575–597. [\[CrossRef\]](#)
- Collin, A.; James, D.; Jeanson, M. Mapping Tropical Coastal Social–Ecological Systems Using Unmanned Airborne Vehicle (UAV). In *Marine Geological and Biological Habitat Mapping Geohab*; 2019. Available online: <https://hal.archives-ouvertes.fr/hal-02134739/document> (accessed on 23 October 2021).
- Zanutta, A.; Lambertini, A.; Vittuari, L. UAV Photogrammetry and Ground Surveys as a Mapping Tool for Quickly Monitoring Shoreline and Beach Changes. *J. Mar. Sci. Eng.* **2020**, *8*, 52. [\[CrossRef\]](#)
- James, D.; Collin, A.; Mury, A.; Letard, M.; Guillot, B. UAV Multispectral Optical Contribution to Coastal 3D Modelling. In Proceedings of the 2021 IEEE International Geoscience and Remote Sensing Symposium IGARSS, Brussels, Belgium, 11–16 July 2021; pp. 7951–7954.
- Collin, A.; Dubois, S.; Ramambason, C.; Etienne, S. Very high-resolution mapping of emerging biogenic reefs using airborne optical imagery and neural network: The honeycomb worm (*Sabellaria alveolata*) case study. *Int. J. Remote Sens.* **2018**, *39*, 5660–5675. [\[CrossRef\]](#)
- Ishiguro, S.; Yamada, K.; Yamakita, T.; Yamano, H.; Oguma, H.; Matsunaga, T. Classification of Seagrass Beds by Coupling Airborne LiDAR Bathymetry Data and Digital Aerial Photographs. *Landsc. Ecol. Asian Cult.* **2016**, 59–70. [\[CrossRef\]](#)
- Collin, A.M.; Andel, M.; James, D.; Claudet, J. The superspectral/hyperspatial worldview-3 as the link between spaceborne hyperspectral and airborne hyperspatial sensors: The case study of the complex tropical coast. *ISPRS Int. Arch. Photogramm. Remote Sens. Spat. Inf. Sci.* **2019**, *XLII-2/W13*, 1849–1854. [\[CrossRef\]](#)
- Collin, A.; Archambault, P.; Planes, S. Bridging Ridge-to-Reef Patches: Seamless Classification of the Coast Using Very High Resolution Satellite. *Remote Sens.* **2013**, *5*, 3583–3610. [\[CrossRef\]](#)
- Airbus Imaging Corporation. Available online: <https://www.satimagingcorp.com/satellite-sensors/> (accessed on 30 October 2021).
- James, D.; Collin, A.; Mury, A.; Costa, S. Very high resolution land use and land cover mapping using pleiades-1 stereo im-agery and machine learning. *Int. Arch. Photogramm. Remote Sens. Spat. Inf. Sci.* **2020**, *43*, 675–682. [\[CrossRef\]](#)
- James, D.; Collin, A.; Mury, A.; Letard, M. Enhancing uav coastal mapping using infrared pansharpening. *ISPRS Int. Arch. Photogramm. Remote Sens. Spat. Inf. Sci.* **2021**, *XLIII-B3-2*, 257–264. [\[CrossRef\]](#)
- Archer, A.W. World’s highest tides: Hypertidal coastal systems in North America, South America and Europe. *Sediment. Geol.* **2013**, *284*, 1–25. [\[CrossRef\]](#)
- Airbus. Available online: <https://www.intelligence-airbusds.com/imagery/constellation/pleiades/> (accessed on 30 October 2021).
- Qin, R. Rpc stereo processor (rsp)—A software package for digital surface model and orthophoto generation from satellite stereo imagery. *ISPRS Ann. Photogramm. Remote Sens. Spat. Inf. Sci.* **2016**, *3*, 77. [\[CrossRef\]](#)

16. Saga Gis. Available online: <http://www.saga--gis.org/> (accessed on 17 October 2021).
17. Weiss, A.D. Topographic position and landforms analysis. In Proceedings of the Poster Presentation, ESRI Users Conference, San Diego, CA, USA, 9–13 July 2001.
18. Guisan, A.; Weiss, S.B.; Weiss, A.D. GLM versus CCA spatial modeling of plant species distribution. *Plant Ecol.* **1999**, *143*, 107–122. [[CrossRef](#)]
19. Harris Geospatial. Available online: <https://www.l3harrisgeospatial.com/Software--Technology/ENVI> (accessed on 21 July 2021).
20. Story, M.; Congalton, R.G. Accuracy assessment: A user’s perspective. *Photogramm. Eng. Remote Sens.* **1986**, *52*, 397–399.
21. Qui, R. A Critical Analysis of Satellite Stereo Pairs for Digital Surface Model Generation and A Matching Quality Prediction Model. *ISPRS J. Photogramm. Remote Sens.* **2019**, *154*, 139–150.
22. Poli, D.; Remondino, F.; Angiuli, E.; Agugiaro, G. Evaluation of pleiades–1a triplet on trento testfield. *ISPRS Int. Arch. Photogramm. Remote Sens. Spat. Inf. Sci.* **2013**, *XL–1/W1*, 287–292. [[CrossRef](#)]
23. Collin, A.; Hench, J.L.; Pastol, Y.; Planes, S.; Thiault, L.; Schmitt, R.J.; Holbrook, S.J.; Davies, N.; Troyer, M. High resolution topobathymetry using a Pleiades–1 triplet: Moorea Island in 3D. *Remote Sens. Environ.* **2018**, *208*, 109–119. [[CrossRef](#)]
24. Bernard, M.; Decluseau, D.; Gabet, L.; Nonin, P. 3D capabilities of pleiades satellite. *ISPRS Int. Arch. Photogramm. Remote Sens. Spat. Inf. Sci.* **2012**, *XXXIX–B3*, 553–557. [[CrossRef](#)]
25. Panagiotakis, E.; Chrysoulakis, N.; Charalampopoulou, V.; Poursanidis, D. Validation of Pleiades Tri–Stereo DSM in Urban Areas. *ISPRS Int. J. Geo Inf.* **2018**, *7*, 118. [[CrossRef](#)]
26. Pichon, L.; Ducanhez, A.; Fonta, H.; Tisseyre, B. Quality of digital elevation models obtained from unmanned aerial vehicles for precision viticulture. *OENO One* **2016**, *50*, 3. [[CrossRef](#)]
27. Rupnik, E.; Deseilligny, M.P.; Delorme, A.; Klinger, Y. Refined satellite image orientation in the free open–source photogram–metric tools Apero/Micmac. *ISPRS Ann. Photogramm. Remote Sens. Spat. Inf. Sci.* **2016**, *3*, 83. [[CrossRef](#)]
28. Letard, M.; Collin, A.; Lague, D.; Corpetti, T.; Pastol, Y.; Ekelund, A.; Pergent, G.; Costa, S. Towards 3D Mapping of Seagrass Meadows with Topo–Bathymetric Lidar Full Waveform Processing. In Proceedings of the 2021 IEEE International Geoscience and Remote Sensing Symposium IGARSS, Brussels, Belgium, 11–16 July 2021; pp. 8069–8072. [[CrossRef](#)]
29. Farid, A.; Rautenkranz, D.; Goodrich, D.C.; Marsh, S.E.; Sorooshian, S. Riparian vegetation classification from airborne laser scanning data with an emphasis on cottonwood trees. *Can. J. Remote Sens.* **2006**, *32*, 15–18. [[CrossRef](#)]
30. Lee, D.G.; Shin, Y.H.; Lee, D.C. Land Cover Classification Using SegNet with Slope, Aspect, and Multidirectional Shaded Relief Images Derived from Digital Surface Model. *J. Sens.* **2020**, *2020*, 8825509. [[CrossRef](#)]
31. James, D.; Collin, A.; Houet, T.; Mury, A.; Gloria, H.; Le Poulain, N. Towards Better Mapping of Seagrass Meadows using UAV Multispectral and Topographic Data. *J. Coast. Res.* **2020**, *95*, 1117–1121. [[CrossRef](#)]



Article

Very High-Resolution Satellite-Derived Bathymetry and Habitat Mapping Using Pleiades-1 and ICESat-2

Alyson Le Quilleuc ^{1,*}, Antoine Collin ^{2,3}, Michael F. Jasinski ⁴ and Rodolphe Devillers ⁵

¹ ENSTA Bretagne Engineering School, 29200 Brest, France

² Section des Sciences de la Vie et de la Terre, EPHE-PSL University, CNRS LETG, 35800 Dinard, France; antoine.collin@ephe.psl.eu

³ LabEx CORAIL, BP 1013, 98729 Papetoai, French Polynesia

⁴ NASA, Goddard Space Flight Center, Greenbelt, MD 20771, USA; michael.f.jasinski@nasa.gov

⁵ Espace-Dev (IRD-UM-UG-UR-UA-UNC), 34934 Montpellier, France; rodolphe.devillers@ird.fr

* Correspondence: alyson.le_quilleuc@ensta-bretagne.org

Abstract: Accurate and reliable bathymetric data are needed for a wide diversity of marine research and management applications. Satellite-derived bathymetry represents a time saving method to map large shallow waters of remote regions compared to the current costly in situ measurement techniques. This study aims to create very high-resolution (VHR) bathymetry and habitat mapping in Mayotte island waters (Indian Ocean) by fusing 0.5 m Pleiades-1 passive multispectral imagery and active ICESat-2 LiDAR bathymetry. ICESat-2 georeferenced photons were filtered to remove noise and corrected for water column refraction. The bathymetric point clouds were validated using the French naval hydrographic and oceanographic service Litto3D[®] dataset and then used to calibrate the multispectral image to produce a digital depth model (DDM). The latter enabled the creation of a digital albedo model used to classify benthic habitats. ICESat-2 provided bathymetry down to 15 m depth with a vertical accuracy of bathymetry estimates reaching 0.89 m. The benthic habitats map produced using the maximum likelihood supervised classification provided an overall accuracy of 96.62%. This study successfully produced a VHR DDM solely from satellite data. Digital models of higher accuracy were further discussed in the light of the recent and near-future launch of higher spectral and spatial resolution satellites.

Keywords: bathymetry; Mayotte; marine habitat; coral reefs; ICESat-2; Pleiades-1; LiDAR; VHR multispectral imagery

Citation: Le Quilleuc, A.; Collin, A.; Jasinski, M.F.; Devillers, R. Very High-Resolution Satellite-Derived Bathymetry and Habitat Mapping Using Pleiades-1 and ICESat-2.

Remote Sens. **2022**, *14*, 133. <https://doi.org/10.3390/rs14010133>

Academic Editors: Simona Niculescu, Junshi Xia and Dar Roberts

Received: 1 November 2021

Accepted: 22 December 2021

Published: 29 December 2021

Publisher's Note: MDPI stays neutral with regard to jurisdictional claims in published maps and institutional affiliations.



Copyright: © 2021 by the authors. Licensee MDPI, Basel, Switzerland. This article is an open access article distributed under the terms and conditions of the Creative Commons Attribution (CC BY) license (<https://creativecommons.org/licenses/by/4.0/>).

1. Introduction

Mapping coastal areas is essential to tackle a broad range of environmental and social issues [1–3]. Therefore, a wide variety of scientific research disciplines could benefit from a better knowledge of this interface, especially regarding the monitoring and protection of coral reefs in archipelagos or the production of navigational charts [4].

Numerous reliable and accurate techniques exist to acquire bathymetric soundings. Data are often obtained through marine surveys equipped with multibeam or single-beam echosounders [5]. However, these approaches are usually impracticable in remote and shallow areas as well as time consuming and limited in terms of spatial coverage, and therefore remain costly. As an alternative, remote sensing is increasingly used to retrieve coastal bathymetry. Airborne data acquired with bathymetric LiDAR are useful to map larger areas but remain costly and limited spatially [6,7].

Over the past few years, satellite-derived bathymetry (SDB) has been increasingly used as it offers a more affordable and time saving alternative. Scientific studies have demonstrated the possibility of obtaining reliable bathymetric data through hyperspectral and multispectral (MS) imagery at various spatial resolutions, due to a correlation between water depth and reflectance data [8–11]. Nevertheless, SDB mostly relies on passive imagery,

which strongly constrains its use to clear and shallow water areas [12,13]. Depth can be retrieved from satellite MS imagery using physics-based or empirical models. Physics-based models rely on the physics or the radiative transfer of light in the water column and the physical properties of the water constituents that can be estimated with or without field measurements of depth for calibration. Some physics-based models are entirely based on the inversion of the radiative transfer model, such as WASI and BOMBER, but they can be complex to implement [14–16]. On the other hand, empirical models are limited by the need to calibrate the MS imagery with in situ measurements [17,18].

There is a real need for producing bathymetric data solely from satellite images. In this context, the launch of the NASA Ice, Cloud, and Land Elevation Satellite-2 (ICESat-2) in September 2018 offered new prospects [19]. This satellite aims to monitor the cryosphere and terrestrial biosphere using the green 532 nm LiDAR with photon-counting capability. Pre-launch studies highlighted its potential to penetrate the upper part of the water column and reach the bottom [20]. A pioneer study has recently validated accurate ICESat-2 bathymetry retrieval at 38 m depth in very clear waters [21]. A second relevant study used ICESat-2 bathymetric measurements, down to 18 m depth, to calibrate and validate Sentinel-2 imagery at 10 m pixel size [17]. This spatial resolution nonetheless remains limiting for some applications (e.g., marine ecology, navigation).

Our paper aims to create a higher resolution digital depth model (DDM) by fusing active ICESat-2 bathymetric soundings and 0.5 m Pleiades-1 passive MS imagery in order to provide very high-resolution (VHR) satellite-based bathymetry and habitat maps of the coral reefs in Mayotte. First, a density-based algorithm was implemented on ICESat-2 ATL03 L2 dataset to remove the noise in photon data and detect the water surface. The noise arises from several sources, including the laser pulse being scattered by the atmosphere, the solar background noise effects, and the detector dark noise. In our study, the main noise source is associated with photons that are scattered by particles in the water column [22]. Based on this first clustering, photons from the seabed were identified and corrected for the refraction effect occurring at the air-water interface. Producing bathymetric maps requires finding a function that describes the relationship between bathymetry measurements and the remotely sensed spectral values of the satellite image [8]. In this study, we used the band ratio model developed by [23]. First, we derived the above water surface reflectance log ratio of two spectral bands. Then, we characterized the relationship between the ratio and ICESat-2 water depth measurements [17]. Therefore, this study innovatively produces a VHR DDM and VHR benthic habitats map of the area from satellite data without a need for in situ measurements. Bathymetric data were used to remove the effect of the water column and generate a digital albedo model (DAM) to classify benthic habitats [24–27]. Finally, the vertical accuracy of the predicted depths was assessed by comparing the bathymetric data to the French naval hydrographic and oceanographic service SHOM bathymetric LiDAR and multibeam echosounder reference dataset (Litto3D[®]). Classification performances were evaluated using a confusion matrix.

2. Materials and Methods

2.1. Study Site and Data

2.1.1. Study Site

The study site is located in the northwest of the island of Mayotte (latitude: 12.63°–12.68°S, longitude: 45.10°–45.15°E), a French overseas territory located in the southwest Indian Ocean (Figure 1). This site is partially sheltered from wind and wave influence, factors known to affect the quality of SDB estimates. Mayotte coasts offer a wide variety of marine fauna and flora strongly affected by global climate and local anthropogenic changes, requiring environmental monitoring [1,3]. This region was also selected due to the availability of high-resolution airborne bathymetric LiDAR and multibeam echosounder data necessary for validation.

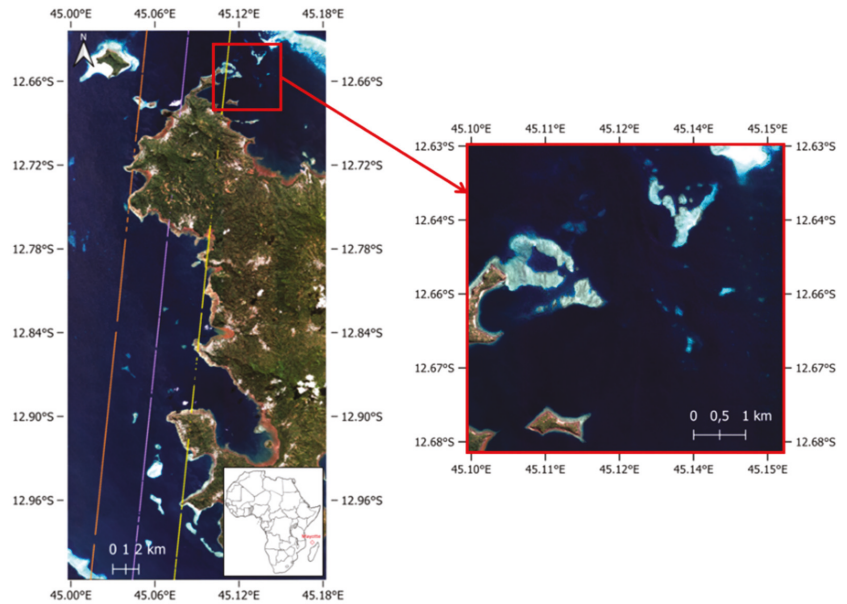


Figure 1. Map of the ground tracks of ICESat-2 over Mayotte collected on 14 May 2020. The satellite multispectral imagery was acquired by Pleiades-1A on 25 May 2020. The red square identifies the study area.

Water clarity is a key parameter in SDB estimation. Clarity is related to light ray penetration in the water column, thus impacting the quality and quantity of the available bathymetric soundings [27–31]. This variable can be estimated using a diffuse attenuation coefficient of 490 nm measured at 4 km resolution by the moderate-resolution imaging spectroradiometer (MODIS-Aqua, publicly accessible from <https://oceancolor.gsfc.nasa.gov/13/>, last accessed: 28 December 2021) [32]. A diffuse attenuation coefficient value of 0.0615 m^{-1} was obtained for the month of May 2020 for the study site, indicating a very clear water type. Previous studies using ICESat-2 for bathymetric estimations had a diffuse attenuation coefficient ranging from 0.032 m^{-1} for the Virgin Island to 0.123 m^{-1} for the Bahamas, both known to be areas with very clear water [21,33].

2.1.2. Litto3D[®] Reference Dataset

The French Oceanographic and Hydrographic Marine Service (SHOM) and the French National Institute for Geographical and Forest Information (IGN) conducted a joint altimetric and hydrographic survey of Mayotte from 2003 to 2010. Most of the island was mapped using the airborne topographic and bathymetric LiDAR and multibeam echosounder. The resulting Litto3D[®] product provides soundings located in a three-dimensional geometric reference system with high spatial resolution and a land-sea continuum (data are available for free from <https://diffusion.shom.fr/>, last accessed: 28 December 2021). Data extracted from this dataset, corresponding to the ICESat-2 ground track, and used for comparison, include bathymetric points acquired using the bathymetric LiDAR and multibeam echosounder.

Litto3D[®] soundings are provided in a cartesian coordinate system in the horizontal plane and with orthometric heights. The point cloud density is constrained by the acquisition method over a specific area and the gridded model is provided with a spatial spacing of either 1 m or 5 m. Specification regarding the positioning and the geodesy of the Litto3D[®] dataset are presented in Table 1 [34]. A local geoid, RGM04, was used as a reference for this dataset.

Table 1. Specifications of the Litto3D[®] dataset acquired over Mayotte.

| | |
|-----------------|------------------------------|
| Geodetic system | RGM04 |
| Ellipsoid | IAG GRS80 |
| Projection | UTM 38 S |
| Vertical frame | Orthometric heights (MAYO53) |

This dataset was used during the validation phase to measure the accuracy of the SDB, but Litto3D[®] data were not used as calibration points for the models.

2.1.3. Pleiades-1A Multispectral Satellite Imagery

A MS Pleiades-1A imagery acquired on 25 May 2020, at 07 h 24 min UTC, was provided by the French space agency CNES through the data platform DINAMIS (<https://dinamis.data-terra.org/>, last accessed: 28 December 2021). Pleiades-1A imagery is delivered with four MS bands at 2 m pixel size, with an 11-bit dynamic range: Blue (430–550 nm), green (500–620 nm), red (590–710 nm), and near infrared (740–940 nm). Moreover, a panchromatic band at 0.5 m pixel size (470–830 nm) is included, with the same radiometric resolution [35]. The four-band imagery is geometrically projected with the WGS84/UTM38S coordinate system and radiometrically corrected to units of top of atmosphere (TOA) reflectance.

2.1.4. ICESat-2 LiDAR Satellite Soundings

ICESat-2 is in a near-polar orbit at an altitude of 496 km and operates with a revisit period of 91 days over oceans [19,36]. ICESat-2 was mainly designed to measure icesheet topography, sea ice, and various inherent properties of the atmosphere and terrestrial vegetation, although ocean and inland surface waters are also observed. The Advanced Topographic Laser Altimeter (ATLAS), a photon-counting LiDAR, is the only sensor onboard the satellite, emitting a green laser beam at a wavelength of 532 nm. ATLAS enhances spatial sampling by splitting the laser beam into three pairs of beams separated by 3.3 km. Each pair, separated by 90 m, consists of a “weak” energy beam and a “strong” beam with a four-fold higher pulse energy [19,36]. ICESat-2 data can be downloaded with different degrees of processing, depending on the users’ needs. This study uses the 3rd version of the L2 ATL03 georeferenced photons (data publicly available at <https://search.earthdata.nasa.gov/search>, last accessed: 28 December 2021) [37]. Data about each photon are provided with the latitude, the longitude, and the height relative to the WGS84 ellipsoid as well as other ancillary information. Considering that ICESat-2 was not designed to study the sub-surface water or the bottom topography, it is necessary to include in the analyses a correction for refraction bias induced by the water column.

We selected the ICESat-2 track acquired on the date closest to the acquisition date of the MS imagery. The two datasets were acquired 10 days, 10 h and 33 min apart. Then, the specific study area in Mayotte was selected based on the range of depths for which calibration data were available. ICESat-2 passed over Mayotte on 14 May 2020, at 20 h 51 min UTC, and collected bathymetric data down to a depth of 15 m.

2.2. Data Processing

Most of the ICESat-2 photons that reach the oceans penetrate into the water. However, compared to the water surface returns, only a small fraction is returned from the water column backscatter and bottom reflectance. Therefore, ICESat-2 signal photons correspond primarily to the water surface reflectance, water column backscatter, seabed reflectance, and noise.

ICESat-2 ATL03 data are provided with a preliminary classification of every photon regarding how likely it is to be signal or noise (confidence levels are: Noise, Low, Medium, High, and Buffer). Photons classified as “Buffer” are identified after all the signal photons are clustered. These are the photons for which doubt remains, which are at the limit to be identified as part of the signal. Therefore, this category has been created to ensure that all of

the photons identified as signal are present in the corrected product [37]. Figure 2 presents the transect used in this study, indicating the original classification of the georeferenced photons. In this figure, photon positions (latitude and longitude) were projected onto a local geographic plane. Therefore, the horizontal axis corresponds to the along track distance. The origin point corresponds to the northernmost location of the trajectory. However, this clustering is not suited to underwater environments as it considers a considerable amount of the seafloor as noise. Therefore, all of the photons were considered and a modified density-based spatial clustering of application with noise (DBSCAN) algorithm was used to separate the photons characterizing the noise and the sea surface from those related to the seabed [17,38–40].

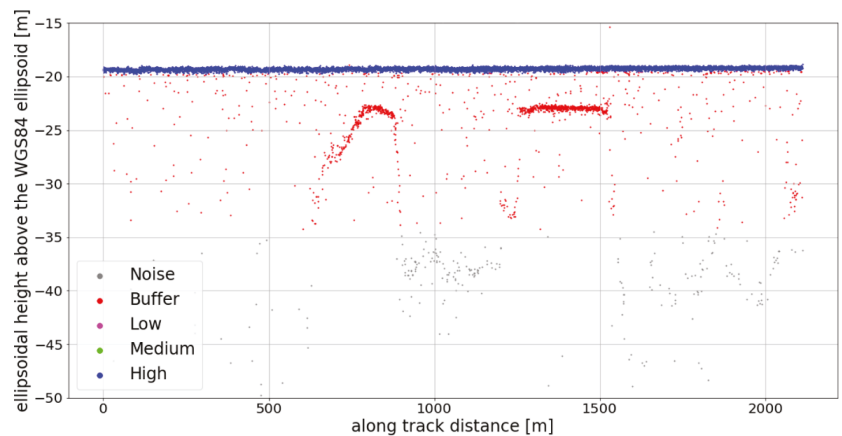


Figure 2. Photon point clouds of the transect along ICESat-2 gt11 (strong beam), acquired on 14 May 2020. The confidence levels provided by ATL03 are displayed.

2.2.1. Noise Removal and Detection of the Sea Surface

In the dataset, noise corresponds to sparse points with a low spatial density compared to the sea surface and seabed clusters. Georeferenced photons likely to be noise were removed, and photons associated with the sea surface were identified.

Here, a density-based spatial clustering method was used, which is an unsupervised learning method used to identify clusters in a dataset. The method is based on the premise that each cluster is defined as a region of points with a given density and spatially isolated from other groups by areas of lower density. The DBSCAN algorithm used scanned the entire dataset and established a search radius on each point successively. The point considered during a given step is a “core point”. DBSCAN allows the users to specify a search radius size according to two criteria: The search circle radius ϵ and the minimum number of points $MinPts$. Once a criterion is no longer satisfied, the algorithm begins a new classification group [41].

Previous studies successfully implemented DBSCAN on the ICESat-2 dataset of islands located in the south of China and in the Bahamas. One particular study provides formulas to configure the $MinPts$ and the ϵ radius parameters of the DBSCAN algorithm [17]. In the present research, the search radius was manually chosen by the user to guide the clustering process and optimize the results. In addition, the $MinPts$ parameter is defined by Equation (1) [17] (this formula is suited for a study of a water column whose depth is not expected to exceed 60 m).

$$MinPts = \frac{2SN_1 - SN_2}{\ln\left(\frac{2SN_1}{SN_2}\right)}, \quad (1)$$

where SN_1 is the number of expected photons corresponding to signal and noise and defined by Equation (2):

$$SN_1 = \frac{\pi\epsilon^2 N_1}{hl}, \quad (2)$$

where N_1 is the total number of photons (both signal and noise), h is the vertical range and l is the along track range. SN_2 is the expected noise photons number and is defined by Equation (3):

$$SN_2 = \frac{\pi\epsilon^2 N_2}{h_2 l}, \quad (3)$$

where N_2 corresponds to the number of photons in the layer with the fewer bathymetric photons, while h_2 is the height of the corresponding layer [17].

The variable *MinPts* is constrained to a value no lower than 3. If the previous formula provides a value lower than this threshold, then *MinPts* was set to 3 [17]. This algorithm might not be optimal in the present situation, since the dataset contains isolated photons from the seabed which could be identified as noise. Considering the small number of photons from the seabed, it was decided not to optimize the noise cleaning process, even if it meant that some manual cleaning had to be done. Therefore, the remaining noise points were removed manually using GlobalMapper software 22.1.0 (Blue Marble Geographics, Hallowell, ME, USA).

2.2.2. Detection of the Seabed

The sea surface is the cluster with the highest number of photons. It is a high-density group of photons spread over a continuous line, depending on the state of the sea. The sea surface cluster is clearly visible in blue in Figure 2.

According to [17], after removing the noise, the seabed is defined as every signal photon below a threshold value underneath the water surface. Therefore, every photon whose elevation is lower than LMS-3SV (where LMS is the Local Mean Sea level and SV the Surface Variance), was identified as a return signal from the seabed [17].

2.2.3. Correction for the Refraction Bias

Geolocated signal photons located below the water surface are not corrected for the refraction effect that redirects the light, and thus the LiDAR beams. It induces a positioning bias for photons in the water layer that would impact the bathymetry estimate.

A relevant coordinate system is important to compute simple correction formulas. In this paper, the results presented were obtained using the coordinate system defined by [21] and the correction formulas were recomputed from this point. Corrections were applied in a satellite-centered coordinate system, where Z is the vertical direction (opposite to the direction of local gravity), and Y is orthogonal to Z (in the horizontal plane) and oriented along the azimuth of the pointing vector [21]. The resulting geometry is presented in Figure 3.

2.2.4. Validation of ICESat-2 Seabed Ellipsoidal Heights

The Litto3D[®] dataset was used to validate the seabed photon ellipsoidal heights corrected from the refraction bias. While the ICESat-2 photons' geographic coordinates are projected onto a local tangent plane (ENU) during the refraction bias correction, the vertical references are different. Soundings measured by the SHOM bathymetric LiDAR are provided with orthometric heights. The latter were converted into ellipsoidal heights (relative to the IAG GRS 80 ellipsoid) using Circe 5.2.1 (IGN free software). Data visualization and extraction were conducted in GlobalMapper software, and the points were processed using Spyder 4.15 python interpreter (an open-source MIT environment) to qualify the accuracy. The point density from Litto3D[®] is considerably higher compared to the ICESat-2 dataset, it was interpolated to allow a comparison with the ICESat-2 dataset.

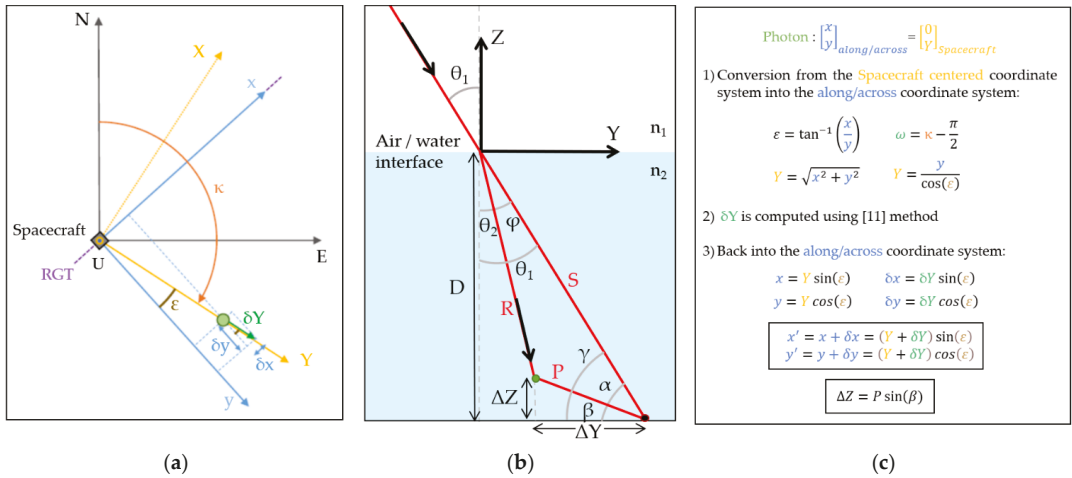


Figure 3. (a) Schematic diagram for the change of coordinate systems and the computation of the refraction bias in the horizontal plane; (b) in the vertical plane (figure adapted from [21]); and (c) correction formulas.

2.3. Satellite-Derived Bathymetry

2.3.1. Ratio Transform Method

The SDB ratio transform algorithm provided by ENVI 5.3 (L3Harris Geospatial Solutions, Broomfield, CO, USA) was used to retrieve the relative DDM of the study area. The DDM is based on the relationship between reflectance and bathymetry, which is described by [23]. The semi-empirical model provides values of relative bathymetry by computing the logarithmic ratio of the reflectance of two spectral bands from a MS imagery. First, the 2 m pixel size imagery was converted into TOA reflectance values and was geometrically projected to the WGS84/UTM38S. At this point, the spatial resolution was enhanced using the Gram-Schmidt pan-sharpening method [42,43]. Second, the MS image was cropped with a spatial subset tool to isolate the geographical area of interest. Finally, the ratio transform was implemented with the algorithm developed by [23]. A map of the relative water depth (i.e., log ratio of the spectral bands) was derived from the log ratio between the green and blue spectral bands [44–49].

This method is one of the most commonly used methods in SDB studies, as it proved to provide accurate results and does not require many points for the calibration phase [18,23]. The advantages are that only two parameters need to be set and it works on all types of albedos. This method is also mainly suited for clear case 1 water, which is the case in this study [18,23].

Working with spectral band ratios is a way to compensate for the variability of ocean bottom type, since changes in the albedo values will affect approximately equally both spectral bands. On the contrary, a variation of depth has a higher impact on the spectral band, which is the most intensely absorbed in the water column. Therefore, depth is expected to be retrieved by this method independently of bottom albedo and can be obtained by inverting the radiative transfer equation as follows [23]:

$$z = m_1 \frac{\ln(nR_w(\lambda_j))}{\ln(nR_w(\lambda_i))} - m_0, \quad (4)$$

where z is the depth, n is a constant needed for the ratio to stay positive, R_w is the reflectance of the water, m_0 is the offset for a depth of 0 m, and m_1 is the gain coefficient.

Each pixel of the MS imagery was assigned a value between 0 and 1. The final DDM was obtained by calibrating the relative bathymetry product with field-based depth measurements.

The final DDM was produced by finding the equation that best fits (i.e., lowest RMSE and higher R^2 with a simple equation formula) the relationship between the relative bathymetric values and the ground truth depth measurements. If bathymetric soundings measured by ICESat-2 are reliable and accurate enough, they could be used as a calibration/validation dataset to produce bathymetry solely from satellite observations.

2.3.2. Calibration with ICESat-2 Soundings

During the calibration phase, pixels from the relative DDM were matched to bathymetric points measured by ICESat-2.

To produce a DDM, i.e., a map of the water height at the acquisition date of the satellite MS imagery, ICESat-2 vertical heights were converted into the appropriate datum. First, the ellipsoidal heights measured by the ICESat-2 satellite were referenced to the IAG GRS 80 ellipsoid and had to be referenced to the chart datum. The SHOM (<https://data.shom.fr/>, last accessed: 28 December 2021) provides accurate altimetric information over Mayotte island, including the distance between the ellipsoid and the chart datum in Dzaoudzi locality (distance of -21.74 m). Second, the water height above the chart datum, at the acquisition time of the MS satellite imagery, was added. The closest tide gauge from the study site was also located at Dzaoudzi and the measurements were available from the SHOM website. The tide gauge recorded a water height of 1.02 m above the chart datum on 25 May 2020, at 07 h 24 min UTC. Figure 4 illustrates the different variables involved to compute the bathymetry from ICESat-2 ellipsoidal heights.

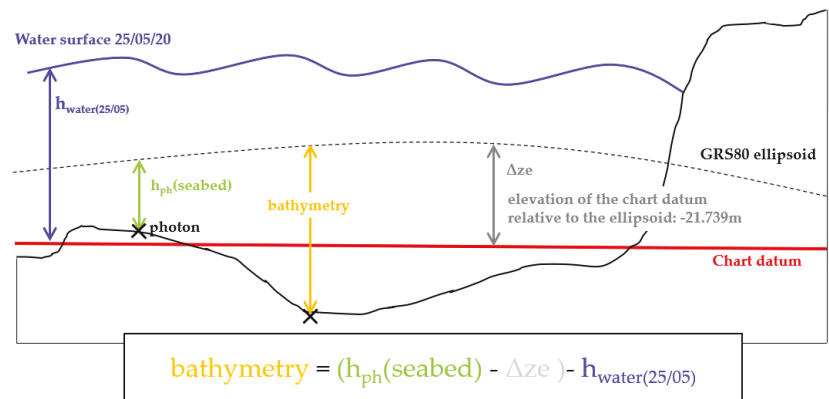


Figure 4. Variables involved in the process of retrieving ICESat-2 bathymetry at the acquisition time of Pleiades-1A.

Relative bathymetry points from the MS imagery were collected at the exact same location as the measurement points of ICESat-2 and an equation linking the two datasets was determined. Finally, the equation was applied to the relative DDM using the ENVI band math tool to generate the final DDM.

2.3.3. Digital Depth Model Validation

We compared different regression models. The aim was to find the model that best matches the bathymetry measurements of ICESat-2 with the remotely sensed spectral values of Pleiades-1A. The best regression was chosen based on the RMSE and based on the coefficient of determination, R^2 . The final DDM was validated in comparison to the Litto3D[®] reference dataset by computing the root mean square error (RMSE) and the maximum absolute error (MAE) statistical indicators.

2.4. Benthic Habitats Mapping

2.4.1. Processing of the Multispectral Imagery

This paper further intends to classify the seabed into five general types: Sand, sand with coral rubble, rock with coral rubble, corals and algae, and deep water. The classification is based upon a DAM obtained from the MS imagery and the DDM.

In theory, it would be feasible to train the classification algorithm directly on the MS imagery, without any preliminary corrections. It would also be conceivable to add a fifth spectral band, corresponding to the bathymetry, to add extra information for the algorithm to get better results. However, this method was not optimal as classifying MS imagery without correcting the image for the decay of light rays in the water column might induce confusion between the spectral signatures of benthic habitats [50]. A better solution was to generate a DAM. Bathymetric data are necessary to quantify the loss of light in the water column, to compensate for this loss, and finally to obtain a DAM [25,50]. Benthic albedo values were obtained with Equation (5) [25]:

$$A_b = (R_w - R_\infty)e^{2K_d z} + R_\infty \quad (5)$$

where A_b is the bottom albedo, R_w is the water column reflectance, R_∞ is the reflectance in deep water, and K_d is the diffuse attenuation coefficient.

The TOA reflectance value for each spectral band was obtained after processing. First, the 2 m pixel size MS imagery was cropped to the area of interest and then orthorectified. Second, the image was converted into bottom of atmosphere (BOA) reflectance values using the FLAASH algorithm (see [50] for further details). At this point, it was possible to enhance the spatial resolution using pan-sharpening. These reflectance values were applied in Equation (5) to remove the water column contribution and obtain a bottom of hydrosphere (BOH) reflectance imagery from the BOA reflectance imagery.

The diffuse attenuation coefficient K_d was estimated for every spectral band of the visible range using values from a previous study on case 1 waters [51]. Values were given for a wide range of wavelength and were weighed with the appropriate factor found according to the wavelength sensitivities of Pleiades-1A sensor. Finally, an average value of K_d was computed for the three spectral bands in the visible range (Table 2).

Table 2. Diffuse attenuation coefficient (K_d) for every spectral band of Pleiades-1A sensor in the visible range.

| Spectral Band | λ [nm] | K_d [m^{-1}] |
|---------------|----------------|---------------------------|
| Blue | (430–550) | 0.0211 |
| Green | (500–620) | 0.0659 |
| Red | (590–710) | 0.2635 |

2.4.2. Supervised Classification Process

Similar to most coastal areas worldwide, the study area is lacking high-resolution benthic habitat data. Therefore, the supervised classification process was based on a visual identification of marine habitats assisted by two local marine scientists familiar with the area. The visual mapping by these experts was performed using the 0.5 m MS BOH reflectance imagery and the 0.5 m MS TOA reflectance imagery in parallel. Five benthic habitats were identified on several areas of the MS imagery (see Figure 5).

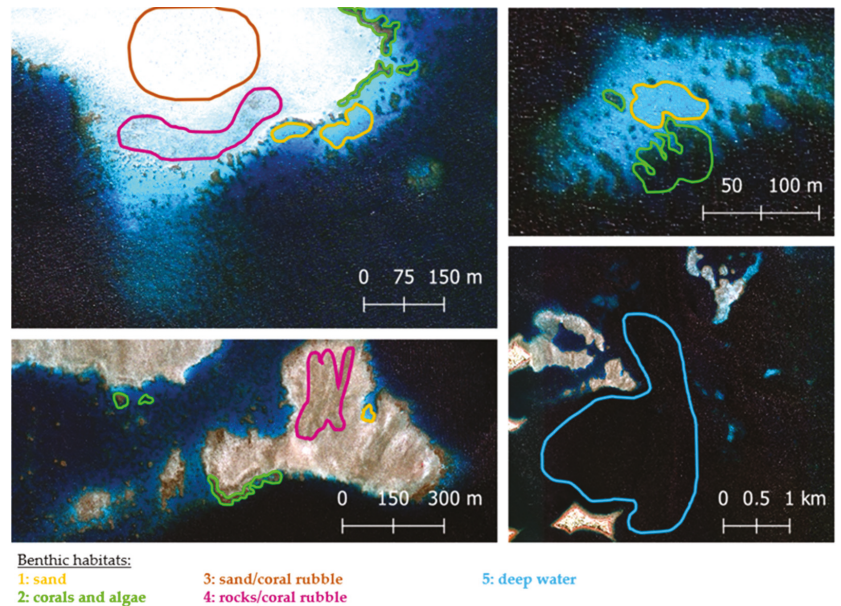


Figure 5. Maps of the five benthic habitats identified on the 0.5 m Pleiades-1A TOA reflectance imagery.

Corals are often visible on the edges of patch reefs. They appear in the form of brown and dark slender spots on the MS imagery and they are often colonized by algae. Sand areas are very bright areas often found on the border of the patch reefs, alongside corals. Two other main categories of benthic habitats can be distinguished. The first one corresponds to a mix of sand and coral rubbles. It appears as bright areas with dark brown spots. The other group contains mainly rocks and coral rubbles and appears as dark areas. While coral colonies are found on the edges, these two areas are often located towards the inner parts of the patch reefs. Coral rubbles are often transported towards the inner part of patch reefs by waves. Finally, both deep water areas, where the bottom was not visible, and land areas were masked.

In an attempt to enhance the classification accuracy, the albedo imagery was separated according to depth ranges. A first mask was created to suppress the depth values higher than the highest depth value measured by ICESat-2 over the area (i.e., 15 m). Then, the extinction depth of every spectral band was computed based on [50,51] (see Table 3 for results).

Table 3. Extinction depths for every spectral band of Pleiades-1A in the visible range.

| Spectral Band [nm] | Average for K_d [m^{-1}] | Extinction Depth ($1/K_d$) [m] |
|--------------------|--------------------------------|----------------------------------|
| Blue (430–550) | 0.211 | 47.4 |
| Green (500–620) | 0.0659 | 15.2 |
| Red (590–710) | 0.263 | 3.8 |

A first DAM was created for depths in the range of 0–3.8 m using three spectral bands (Red, Green, and Blue). A second DAM was created for depths in the range of 3.8–15 m using two spectral bands (Green and Blue), as the extinction depth of the red band was exceeded. Due to the fact that some habitats are not present in the studied depth range, two sets of regions of interest (ROI) were created for each DAM. The DAM with the lower depth range was classified using four ROIs, namely: Sand, coral and algae, sand and coral

rubble, and rocks and coral rubble. The DAM with the higher depth range was classified using three ROIs, namely: Sand, coral and algae, and deep water.

Moreover, a choice of three morphological predictors was made to complement the MS bands of the DAM in order to enhance the classification results. The first predictor added was the slope before adding the aspect and the profile convexity all together. Classifications were computed using a 3×3 pixel kernel size.

Three classification algorithms were compared in this study: Neural network (NN), maximum likelihood (ML), and support vector machine (SVM).

2.4.3. Validation of the Supervised Classification

A validation dataset based on the MS imagery was produced with the same knowledge as for the calibration phase. A post-classification accuracy assessment using a confusion matrix provided information on overall accuracy (OA) and the kappa coefficient (κ) [52,53].

The ML and the SVM classifiers were set with the default parameters. A neural network classification was implemented with one and three hidden neurons in one hidden layer, in order to test the depth of the neuronal architecture.

3. Results

3.1. DDM

3.1.1. Correction of ICESat-2 Dataset

The ICESat-2 gt1l transect from the 2020 dataset corresponds to the strong beam and presents some variability in the depth range. The results obtained in this study, after removing the noise photons and correcting the signal for refraction bias, are presented in Figure 6. For comparison, the official signal detection and classification provided with the downloaded L2 ATL03 dataset were presented in Figure 2.

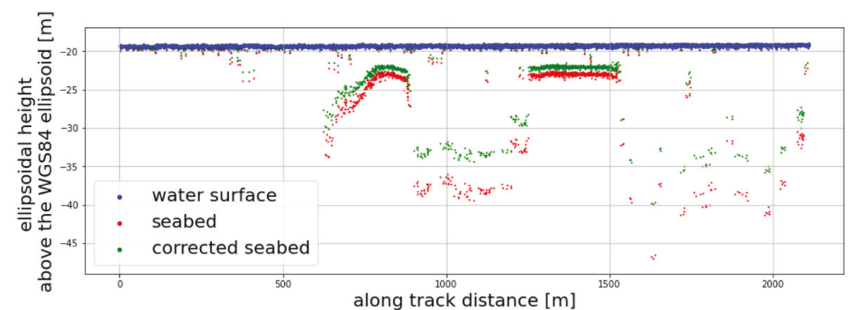


Figure 6. Point clouds of the ICESat-2 signal acquired on 14 May 2020. The signal was processed to remove the noise, correct for refraction, and identify the seafloor. Uncorrected seafloor photons appear in red, while corrected photons are in green.

In Figure 6, photon positions (latitude and longitude) were projected onto a local geographic plane. Therefore, the horizontal axis corresponds to the along track distance. The origin point corresponds to the northernmost location of the trajectory. For the current study, the analysis indicates that (1) points from the seabed detected in this study are following the bottom topography, distinguishable on the satellite imagery; (2) while the ATL03 data classified with a high and medium confidence level (corresponding to the blue and green points in Figure 2) are located at or close to the surface, our bathymetry algorithm correctly identifies the bottom topography from low and buffer confidence points, a much smaller portion of the returned signal; and finally (3) the ATL03 dataset removed only a small fraction of the noise photons in comparison to the results generated with the DBSCAN.

The DBSCAN algorithm was configured based on an empirical approach with the value $\epsilon = 0.65$ m. This value, valid for our study area, allowed us to retrieve a majority of

the seabed signal while eliminating most of the noise photons. The remaining noise points can be manually removed during the validation phase.

3.1.2. Validation of ICESat-2 Data

The comparison between ICESat-2 ellipsoidal heights and the Litto3D[®] ellipsoidal heights is presented in Figure 7.

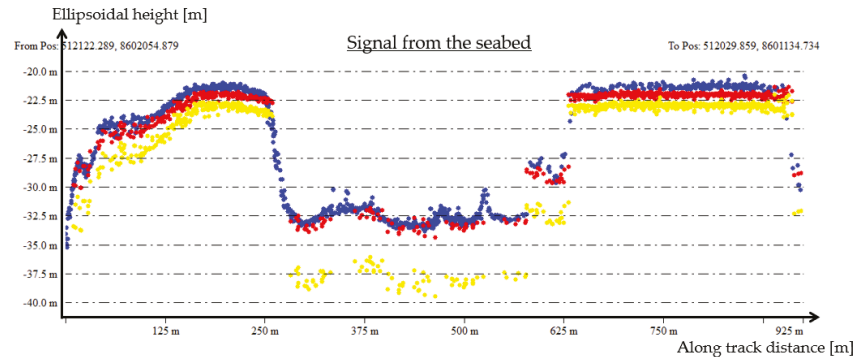


Figure 7. Point clouds of Litto3D[®] dataset (blue), and ICESat-2 raw (yellow) and corrected (red) seabed photons.

Figure 7 highlights the importance of correcting for the refraction bias, as a vertical bias is clearly visible between the corrected (red) and non-corrected (yellow) data. The error generated by refraction alone can reach up to 2 m in shallower waters and 5 m for deeper waters with a RMSE of 0.89 m and a MAE of 0.73 m. A vertical bias of about 1 m is visible on Figure 7 between the reference dataset and the corrected ICESat-2 data close to the surface.

3.1.3. Digital Depth Model

ICESat-2 corrected and validated data were used to calibrate the relative DDM. The calibration required the identification of a good model to bound the ICESat-2 dataset to the relative water depth values from the 0.5 m MS imagery.

Scaled pixel values were extracted from the relative water depth map derived from the 0.5 m MS imagery at the same location than ICESat-2 bathymetric points using QGIS 3.18.3 (open-source geographic information system). Several regression models were tested, and the corresponding equations and their performance (in terms of the RMSE) are presented in Figure A1 (Appendix A). The regression chosen is a 2nd degree polynomial (Equation (6)). The expression of the latter is simple and performs well, with a RMSE of 0.895 m (see Figure 8).

$$y = -45.87x^2 + 74.567x - 31.581 \quad (6)$$

Figure 9 shows the final DDM obtained using ENVI through the application of the model to the relative DDM. The hatched areas correspond to depths greater than the maximum calibration depth.

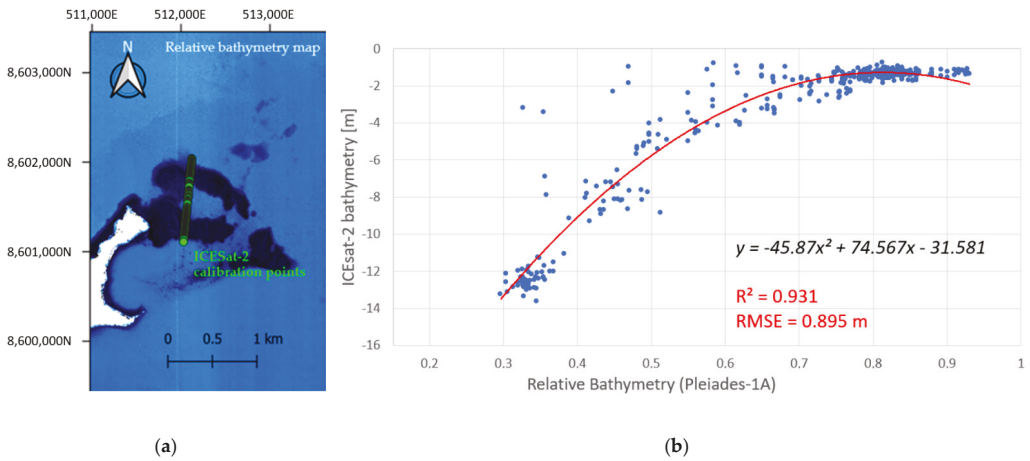


Figure 8. (a) Relative DDM with superposition of ICESat-2 bathymetric points; (b) 2nd degree polynomial regression.

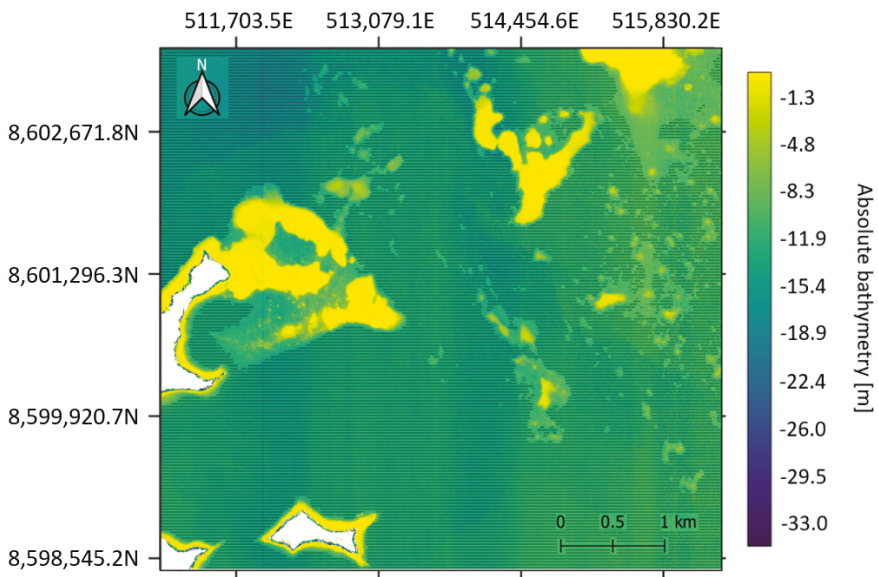


Figure 9. Digital depth model at the acquisition time of Pleiades-1A, calibrated with the ICESat-2 dataset.

3.1.4. Digital Depth Model Validation

The reliability of the DDM was quantified by comparing the estimated bathymetry to the Litto3D[®] reference dataset. Points from the bathymetric LiDAR point clouds were extracted, along the path of ICESat-2, from the DDM. The predicted RMSE was 0.895 m and the observed RMSE was 0.874 m along the ICESat-2 path. The predicted R² coefficient was 0.931 and the observed R² coefficient was 0.97. In addition, we report a MAE of 0.701 m.

3.2. Benthic Habitat Classification

Results from the four classifiers tested using different combinations of predictors are summarized in Figure 10, presenting both the overall accuracy and the kappa coefficient values.

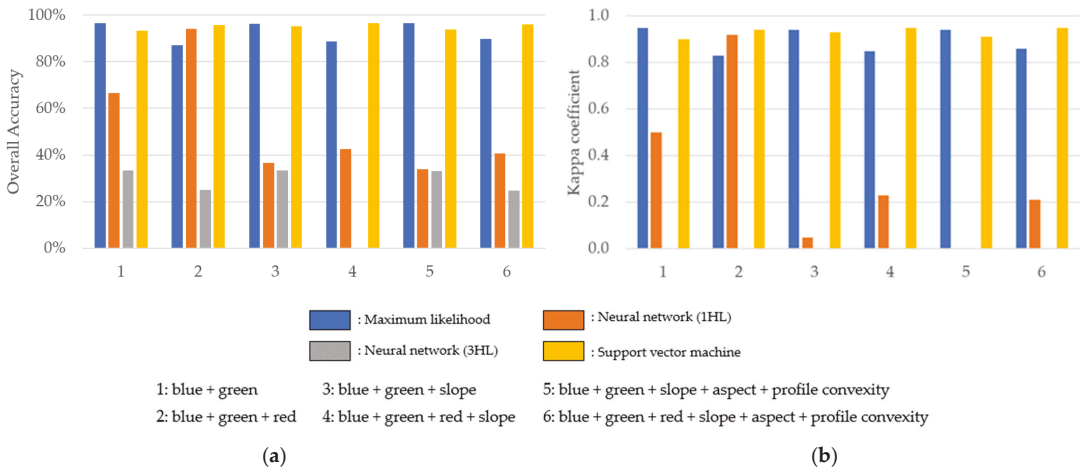


Figure 10. Performances of the different classifiers using different geomorphological predictors. (a) Overall accuracy; (b) Kappa coefficient.

The NN algorithm configured with three hidden neurons for one layer systematically provided the lowest accuracy and the lowest kappa score with an overall accuracy which does not exceed 33.33% and kappa coefficient values that are all null. The neural network using only one hidden neuron produced better, yet inconclusive results, except for the combination of predictors "2".

The ML and the SVM algorithms generally produced the best classification results. The ML algorithm allows for a global accuracy of 96.62% and a kappa coefficient of 0.94 when using two spectral bands (Green and Blue) and with the addition of the three geomorphic predictors.

The SVM results were not as affected by the absence of the red spectral band. The results are constant and reached an overall accuracy of 96.50% and a kappa coefficient of 0.95 when using a DAM with three spectral bands and the slope as the only geomorphic predictor.

Maps of the benthic habitats with the best classification results for each depth range, are presented in Figure 11.

These results, compared to the 0.5 m MS imagery and the DAM, are consistent with the classification presented in Figure 5, except for a bias in the classification of corals and algae, appearing in Figure 11a. The green band on the right of the image is an error in the classification process.

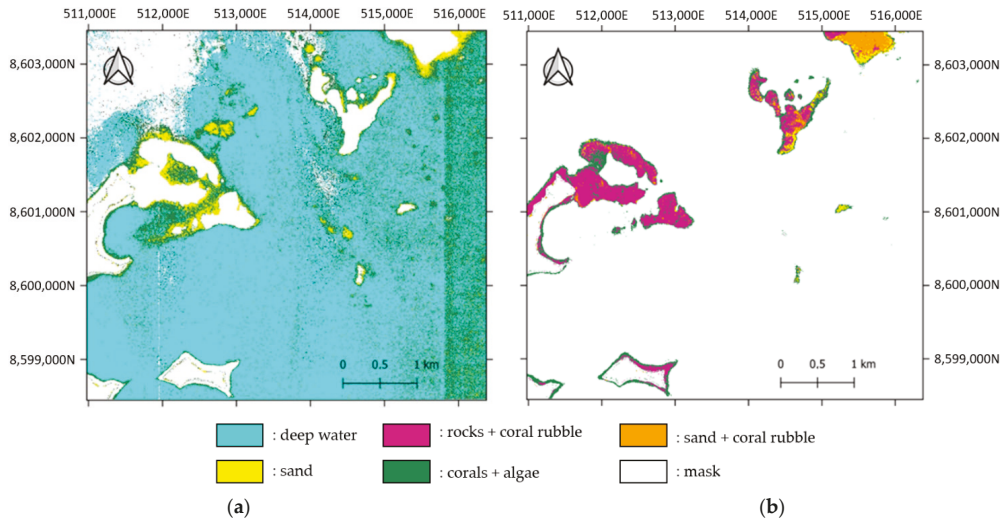


Figure 11. Maps of benthic habitats in the study area. (a) Classification map generated using the SVM with the slope geomorphic predictor. This map corresponds to depths shallower than 3.8 m and is based on all three spectral bands (R, G, and B); (b) classification map generated with the ML classifier and the three geomorphic predictors. This map corresponds to depths in the range of 3.8–15 m and is based on two spectral bands (G and B).

4. Discussion

4.1. Bathymetric Errors

RMSE values comparing the DDM to the Litto3D[®] dataset were obtained along the ICESat-2 ground track, thus at the same place used for the calibration. Here, we discuss the impact of both the depth values and the location of the validation transect on the results.

Figure 12 shows the DDM from the Litto3D[®] dataset. While the DDM produced in our study reaches 33 m depth, the Litto3D[®] survey of this area indicated depths reaching at least 82 m.

The map of the differences between the Litto3D[®] and the DDM calibrated with ICESat-2 dataset is shown in Figure 13. The extrapolation works very well over the range of depths used in the calibration. However, the error increases at deeper depths. Once again, in this figure, the hatched areas correspond to depths greater than the maximum calibration depth of the model.

Large error values seem to appear in deeper waters (over 15 m depth), probably due to the fact that the bathymetry was calibrated with a limited depth range (the ICESat-2 dataset does not exceed a depth of 15 m). On the other hand, the fact data sampling was restricted to the ICESat-2 track is not ideal for the calibration. Most of the soundings represent a depth lower than 5 m (this concerns nearly 85% of the total amount of points for the 2020 dataset). The dataset only has a few points representing higher depth values. This was confirmed by the study of three other transects, taken at different places over the area (a transect along the ICESat-2 swath, a transect perpendicular to the swath, and a transect extracted far from the swath). The results of those tests are visible in Figures A2–A4 (Appendix B), showing that depth strongly affects the quality of the bathymetry. Consequently, errors increase for depth exceeding around 15 m. However, for shallower depth values, the results are similar, regardless of the transect location.

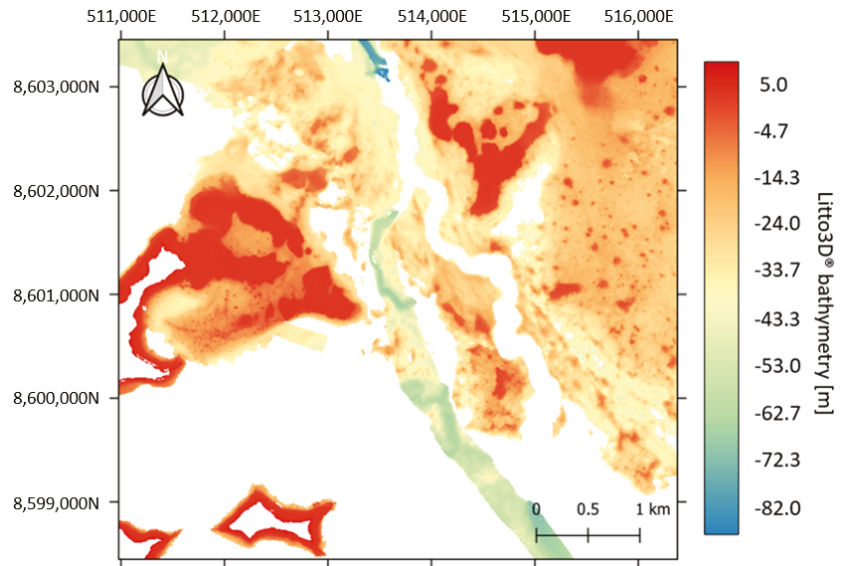


Figure 12. Digital depth model generated from the Litto3D[®] dataset acquired over Mayotte and centered on the study site. The land area is masked.

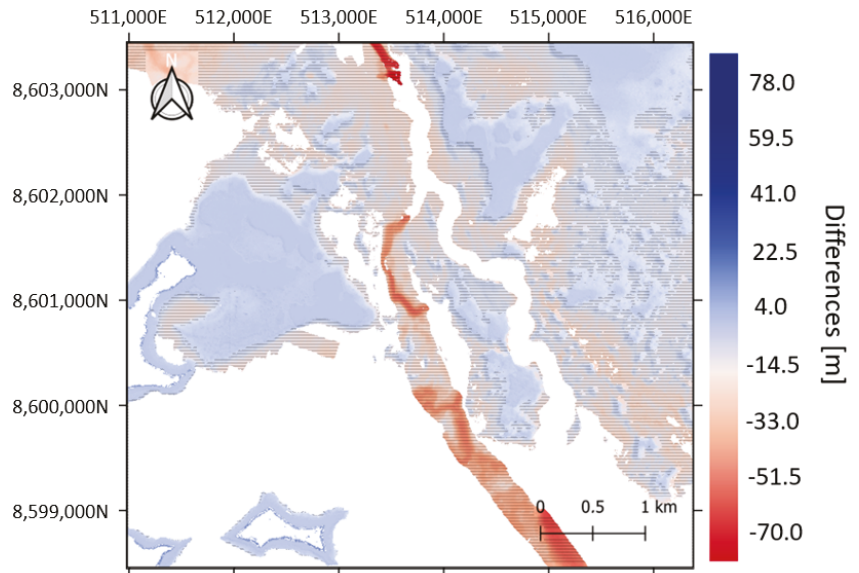


Figure 13. Map of the differences between the DDM derived from the Litto3D[®] and the ICESat-2/Pleiades-1 fusion.

The 10-year difference in the time of acquisition between Litto3D[®] and ICESat-2 could also induce a systematic error, due to a change in the bottom topography caused, for instance, by erosion or a change in the mean sea level (MSL), although those changes are likely to be well beyond the vertical accuracy provided by the method.

Mayotte has been prone to a succession of earthquakes since May 2018. The origin of these earthquakes is located to the east of the island. There are four permanent GPS stations

in Mayotte and their rigorous monitoring has allowed experts to observe a displacement of all the stations by several centimeters towards the East and a subsidence of several centimeters since the beginning of the events [54–56].

In addition, the conversion of datums, using CIRCE software, could be a source of error. The grid used for the calculation is the GGM04V1 and the resulting vertical accuracy is estimated by the software at 10/20 cm.

On the other hand, during the correction of the refraction effect, n_1 and n_2 refractive indices were assumed and could therefore contribute to a small bias.

The method used to retrieve the map of the relative water depth could be improved to obtain more accurate DDM by implementing more recent and innovative approaches, such as IMBR, OBRA, MODPA or SMART-SDB [11,24,57–59].

4.2. Impact of the Spatial Resolution of the Multispectral Imagery

In this study, the DDM was generated at the VHR of 0.5 m. However, other studies used sensors providing a spatial resolution of 10 m (Sentinel-2) or 30 m (Landsat-8) [17,39,60]. The spatial resolution drawn from the Pleiades-1A sensor was degraded in order to compare the RMSE. This process was done in ENVI with the “Resize Data” tool. The pixel size of the output was set according to the desired spatial resolution. The results are presented in Figure 14 and Table 4.

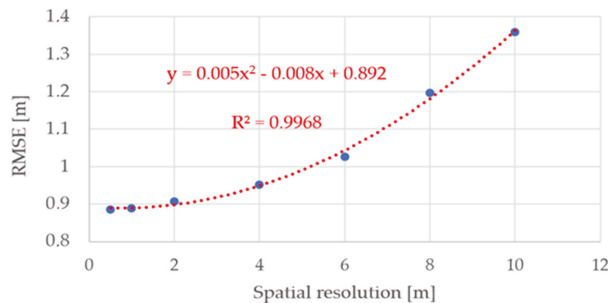


Figure 14. Performances of the DDMs obtained from different spatial resolutions of Pleiades-1A and calibrated with ICESat-2.

Table 4. Accuracy using the original image resolution and lower spatial resolution.

| Spatial Resolution [m] | RMSE [m] |
|------------------------|----------|
| 0.5 | 0.89 |
| 1 | 0.89 |
| 2 | 0.91 |
| 4 | 0.95 |
| 6 | 1.03 |
| 8 | 1.20 |
| 10 | 1.36 |

Figure 14 highlights the importance of the imagery spatial resolution on the accuracy of the bathymetry. RMSE remained under 1 m when the spatial resolution remained below 5 m, but increased rapidly after.

In other studies, the RMSE reached between 1.5 and 2 m for the Yongle atoll, located in South China [17]. It was 1.2 m on average in the Acklins islands in the Bahamas based on the Sentinel-2 MS satellite with a 10 m spatial resolution [17]. The RMSE was 0.96 m with the MS satellite Sentinel-2B (10 m spatial resolution) and 1.54 m using the Landsat-8 satellite (30 m spatial resolution) in the Virgin Islands [33]. Moreover, these study areas had a diffuse attenuation coefficient (K_d) similar to the Mayotte study area.

One of these studies obtained different results using Sentinel-2 observations and ICESat-2 observations from multiple swaths [60]. The DDM was produced with an extrapolation process conducted over the entire area with a RMSE of 3.36 m. However, when the study area was constrained between the two ICESat-2 swaths, the RMSE decreased to 0.35 m. This study area had a higher turbidity of $K_d = 1.68 \text{ m}^{-1}$ [60].

During the acquisition time of some of these studies, meteorological events such as hurricanes occurred and could have impacted the topography of the bottom and affected the results. However, the evaluation of possible episodic events was not reported for this study or investigated.

4.3. Benthic Classification

Classification algorithms performed very differently. It is difficult to assess the impact of the geomorphic predictors on the results. It seems that adding extra information did not impact the SVM and ML classifications, but could have degraded the NN (+1HL) classification. A large amount of information could have undermined the results due to a redundancy in the information. The major change seems to be related to the use of the red spectral band. The results were sometimes better without the red spectral band, probably due to the fact that the corresponding maps were in the depth range of 3.7–15 m, for which benthic classes, such as sand and coral rubble and rocks and coral rubble, are not present. A reduced number of groups tends to enhance the algorithm performance.

The benthic classification is based on a visual recognition of general benthic classes based on experts' knowledge. Although, commonly done, identifying benthic classes on MS imagery is not as reliable as direct underwater observations. Living corals could have been confused for dead corals colonized by algae. As a matter of fact, the classification presented in Figure 11a presented very good results, while having a major bias in the classification of coral and algae in areas of deep water. Some regions selected both to train the algorithm and for further validation presented corals which were distinguishable but very dark, due to the depth. Those were confused with deep and dark water areas.

Moreover, Mayotte is a complex area. The tidal range reaches 4 m. Therefore, when the tide is the lowest, corals can be above the water surface and bleached. Dead corals are theoretically recognizable by their bright color, but they can get darker as they are often colonized by algae. The winds and the waves have the effect to break coral colonies and to create coral rubble areas which are difficult to identify, as they get mixed with sand and rocks and can be mixed up with areas of isolated corals.

5. Conclusions

This study aimed to evaluate the quality of VHR DDM and DAM generated from satellite data. A DDM calibrated with data from the satellite ICESat-2 presented a RMSE of 0.89 m along ICESat-2 ground track, i.e., around 6% of the maximum depth retrieved by ICESat-2. Bathymetric results were generally satisfying down to a depth of around 15 m, which is close to the maximum depth of the calibration data used. Marine habitat classification results were very heterogeneous, depending on the number of predictors used, the type of predictors, and the algorithm used. However, some combinations of parameters provided satisfactory results. The classification with the ML classification using Blue and Green spectral bands with the three geomorphic predictors provided an overall accuracy of 96.62% and a κ coefficient of 0.94. In addition, the SVM classification using Blue, Green, and Red spectral bands with the addition of the slope geomorphic predictor presented an overall accuracy of 96.50% and a κ coefficient of 0.95. This approach can be of strong interest to map coastal areas lacking bathymetry and marine habitat maps and for which field observations are difficult.

While the quality of the results obtained in this study can support coastal management and conservation, the accuracy of bathymetry predictions remains limited for applications, such as navigation, that require higher spatial accuracy. It would be interesting to pursue this research to get more accurate DDMs.

Further work, implementing this method on diverse study sites, would confirm the robustness of the method implemented. In the prospect of future studies, it would be relevant to consider several ICESat-2 ground tracks from the area of interest and even to add the points from other times that ICESat-2 surveyed the area. This would provide a better variability of depths and a better spatial distribution of the data for the calibration process. Moreover, this increase in the number of points opens prospects for the use of deep learning methods to generate DDMs.

Developing an algorithm dedicated to the processing of seafloor data generated from ICESat-2 datasets would be important. The correction for the refraction effect has proven necessary and reliable, but could be further enhanced. The water column properties are changing with depth and the refraction correction should also adapt according to the water column properties.

It would be relevant to also improve the seabed signal correction by considering the state of the sea (for instance, presence of waves on the water surface), in helping to develop a method that could be used in less sheltered areas [17].

In this study, the results presented were obtained using a MS imagery acquired by the Pleiades-1A sensor with four spectral bands and a VHR of 0.5 m using the panchromatic band. The correlation between spatial resolution and the quality of the resulting bathymetry has been demonstrated in this paper. Therefore, future studies could consider generating better quality DDMs using the WV3 sensor (eight spectral bands at 0.30 m using the panchromatic band) or even the sensor of the new Pleiades Neo constellation launched in early 2021 (six spectral bands at 0.3 m with the panchromatic band).

The ICESat-2 products produced by NASA are constantly enhanced and one can be very optimistic regarding the future quality of DDMs and by-products obtained using ICESat-2 measurements.

Author Contributions: Conceptualization, A.L.Q., A.C. and R.D.; methodology, A.L.Q., A.C. and M.F.J.; software, A.L.Q. and A.C.; validation, A.L.Q., A.C., M.F.J. and R.D.; formal analysis, A.L.Q., A.C., M.F.J. and R.D.; investigation, A.L.Q., A.C., M.F.J. and R.D.; resources, A.L.Q., A.C., M.F.J. and R.D.; data curation, A.C.; writing—original draft preparation, A.L.Q.; writing—review and editing, A.C., M.F.J. and R.D.; supervision, A.C. and R.D.; project administration, A.C. and R.D.; funding acquisition, R.D. All authors have read and agreed to the published version of the manuscript.

Funding: With the support of Montpellier Université d'Excellence (MUSE) KIM Sea and Coast program for funding the PhotonExplorer project.

Institutional Review Board Statement: Not applicable.

Informed Consent Statement: Not applicable.

Data Availability Statement: The Pleiades-1A imagery provided by CNES-AIRBUS through the DINAMIS platform is not publicly available. The ICESat-2 L2 ATL03 geolocated photons analyzed during this study are publicly available at <https://search.earthdata.nasa.gov/search>, last accessed: 28 December 2021. The Litto3D[®] dataset used for validation is publicly available from <https://diffusion.shom.fr/>, last accessed: 28 December 2021. The diffuse attenuation coefficient of 490 nm measured at 4 km resolution by MODIS is available publicly from <https://oceancolor.gsfc.nasa.gov/13/>, last accessed: 28 December 2021. Altimetric information over Mayotte island are available from the SHOM website, <https://data.shom.fr/>, last accessed: 25 October 2021.

Acknowledgments: The authors gratefully thank the NASA for distributing the ICESat-2 data and for the support of the ICESat-2 Applied Users group, and the SHOM for providing us with the airborne LiDAR survey data. The authors would like to thank the DINAMIS platform for access to the Pleiades images and, the CNES "Pleiades © CNES 2020, Distribution Airbus DS". Pleiades-1 imagery is a courtesy from CNES-AIRBUS. Thank you to Thomas Claverie (UMR Marbec) and Aline Aubry (UMR Espace-Dev) from CUFM Mayotte for providing expert knowledge used for habitat mapping. The authors would also like to thank the reviewers for improving the manuscript with their comments and corrections.

Conflicts of Interest: The author declares no conflict of interest. The funders had no role in the design of the study; in the collection, analyses, or interpretation of data; in the writing of the manuscript, or in the decision to publish the results.

Appendix A

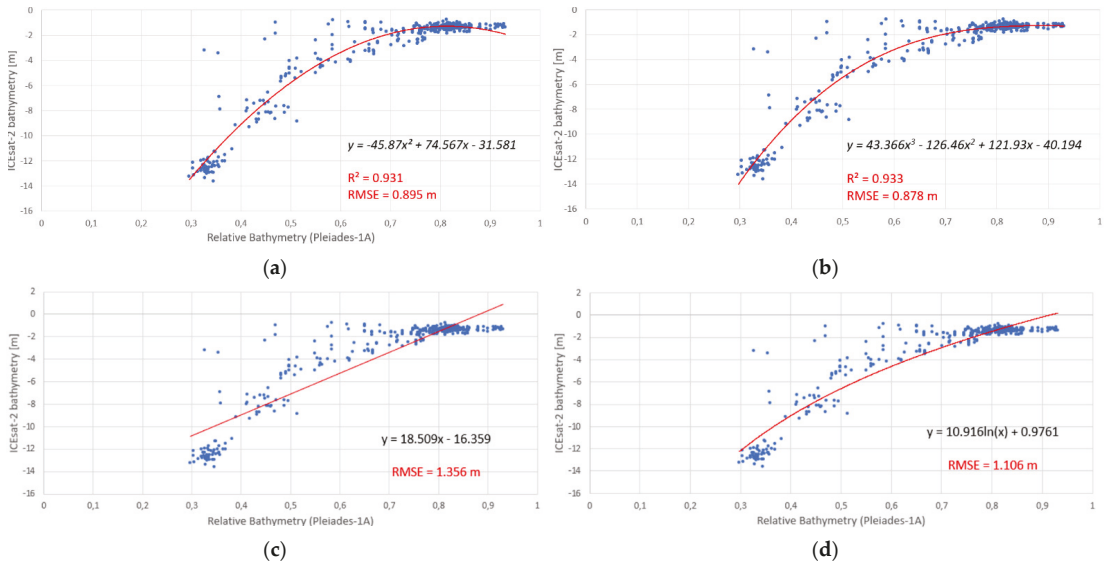


Figure A1. Different regression models tested to link the relative bathymetry points to ICESat-2 bathymetric measurements. (a) Second degree polynomial regression; (b) third degree polynomial regression; (c) linear regression; (d) logarithmic regression.

Appendix B

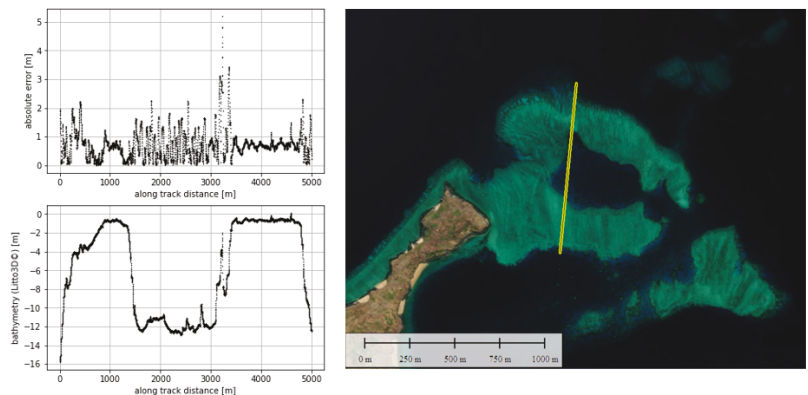


Figure A2. Evolution of the absolute error with depth on a transect along the ICESat-2 ground track.

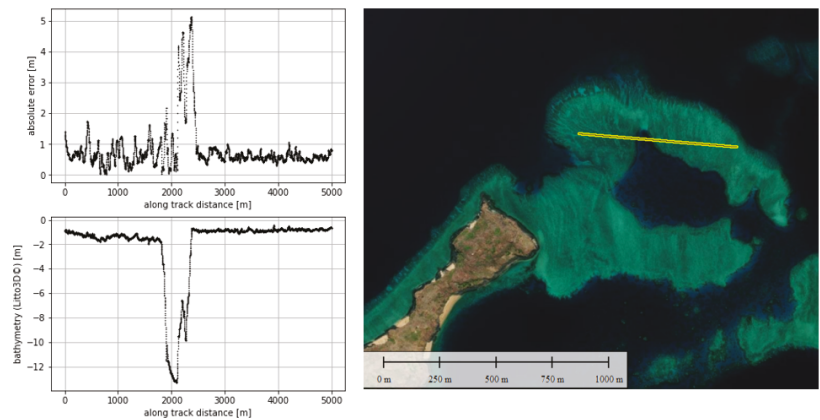


Figure A3. Evolution of the absolute error with depth on a transect across the ICESat-2 ground track.

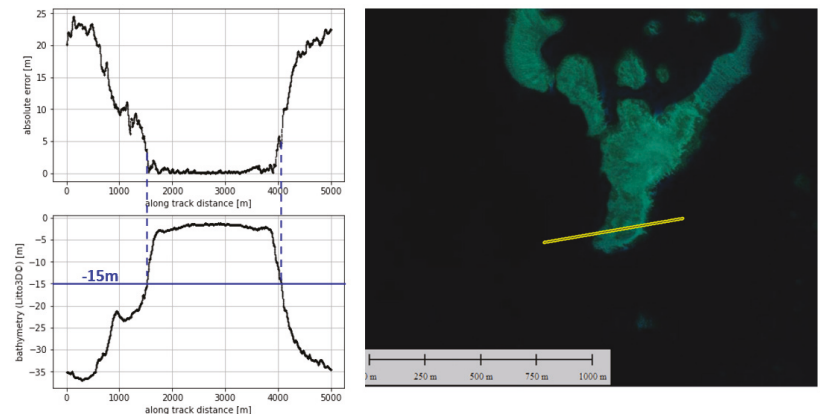


Figure A4. Evolution of the absolute error with depth on a transect far from the ICESat-2 ground track.

References

1. Lionel, G.; Salvat, B. Coral reefs in French overseas territories: A retrospective study of changes in health conditions of these diversified and vulnerable ecosystems recorded by monitoring networks. *Rev. Ecol.* **2008**, *63*, 13–22.
2. Baker, E.; Harris, P. Habitat mapping and marine management. In *GeoHab Atlas of Seafloor Geomorphic Features and Benthic Habitats*, 2nd ed.; Baker, E., Harris, P., Eds.; Elsevier: Amsterdam, The Netherlands, 2020; pp. 17–33.
3. Quod, J.-P.; Dahalani, Y.; Bigot, L.; Nicet, J.B. Status of coral reefs at Réunion, Mayotte, Madagascar. In *Coral Reef Degradation in the Indian Ocean*; Wilhelmsson, D., Obura Olof Linden, D., Souter, D., Eds.; CORDIO SAREC Marine Science Program: Kalmar, Sweden, 2002; pp. 185–189.
4. Collin, A.; Andel, M.; Lecchini, D.; Claudet, J. Mapping Sub-Metre 3D Land-Sea Coral Reefscapes Using Superspectral WorldView-3 Satellite Stereoimagery. *Oceans* **2021**, *2*, 315–329. [[CrossRef](#)]
5. Dierssen, H.; Theberge, A. Bathymetry: Assessing Methods. In *Encyclopedia of Natural Resources*; Wang, Y., Ed.; Taylor & Francis Group: Abingdon-on-Thames, UK, 2014; Volume 2, pp. 1–8.
6. Collin, A.; Ramambason, C.; Pastol, Y.; Casella, E.; Rovere, A.; Thiault, L.; Espiau, B.; Siu, G.; Lerouvreux, F.; Nakamura, N.; et al. Very high-resolution mapping of coral reef state using airborne bathymetric LiDAR surface-intensity and drone imagery. *Int. J. Remote Sens.* **2018**, *39*, 5676–5688. [[CrossRef](#)]
7. Chen, Y.; Zhu, Z.; Le, Y.; Qiu, Z.; Chen, G.; Wang, L. Refraction correction and coordinate displacement compensation in nearshore bathymetry using ICESat-2 lidar data and remote-sensing images. *Opt. Express* **2021**, *29*, 2411–2430. [[CrossRef](#)]
8. Collin, A.; Etienne, S.; Feunteun, E. VHR Coastal bathymetry using WorldView-3: Colour versus learner. *Remote Sens. Lett.* **2017**, *8*, 1072–1081. [[CrossRef](#)]
9. Misra, A.; Vojinovic, Z.; Ramakrishnan, B.; Luijendijk, A.; Ranasinghe, R. Shallow water bathymetry mapping using Support Vector Machine (SVM) technique and multispectral imagery. *Int. J. Remote Sens.* **2018**, *38*, 1–20. [[CrossRef](#)]

10. Alevizos, E. A Combined Machine Learning and Residual Analysis Approach for Improved Retrieval of Shallow Bathymetry from Hyperspectral Imagery and Sparse Ground Truth Data. *Remote Sens.* **2020**, *12*, 3489. [CrossRef]
11. Muzirafuti, A.; Barreca, G.; Crupi, A.; Faina, G.; Paltrinieri, D.; Lanza, S.; Randazzo, G. The Contribution of Multispectral Satellite Image to Shallow Water Bathymetry Mapping on the Coast of Misano Adriatico, Italy. *J. Mar. Sci. Eng.* **2020**, *8*, 126. [CrossRef]
12. Eugenio, F.; Marcello, J.; Martin, J. High-resolution maps of bathymetry and benthic habitats in shallow-water environments using multispectral remote sensing imagery. *IEEE Trans. Geosci. Remote Sens.* **2015**, *53*, 3539–3549. [CrossRef]
13. Dekker, A.G.; Phinn, S.R.; Anstee, J.; Bissett, P.; Brande, V.E.; Casey, B.; Fearn, P.; Hedley, J.D.; Klonowski, W.; Lee, Z.P.; et al. Intercomparison of shallow water bathymetry, hydro-optics and benthos mapping techniques in Australian and Caribbean coastal environment. *Limnol. Oceanogr. Methods* **2011**, *9*, 396–425. [CrossRef]
14. Niroumand-Jadidi, M.; Bruzzone, L.; Bovolo, F. Physics-based Bathymetry and Water Quality Retrieval Using PlanetScope Imagery: Impacts of 2020 COVID-19 Lockdown and 2019 Extreme Flood in the Venice Lagoon. *Remote Sens.* **2020**, *12*, 2381. [CrossRef]
15. Gege, P. WASI-2D: A software tool for regionally optimized analysis of imaging spectrometer data from deep and shallow waters. In *Computers & Geosciences*; Collon, P., Grana, D., Mueller, U., Eds.; Elsevier: Amsterdam, The Netherlands, 2014; Volume 62, pp. 208–215.
16. Giardino, C.; Candiani, G.; Bresciani, M.; Lee, Z.; Gagliano, S.; Pepe, M. BOMBER: A tool for estimating water quality and bottom properties from remote sensing images. In *Computers & Geosciences*; Collon, P., Grana, D., Mueller, U., Eds.; Elsevier: Amsterdam, The Netherlands, 2012; Volume 45, pp. 313–318.
17. Ma, Y.; Xu, N.; Liu, Z.; Yang, B.; Yang, F.; Wang, X.; Li, S. Satellite-derived bathymetry using the ICESat-2 lidar and Sentinel-2 imagery datasets. *Remote Sens. Environ.* **2020**, *250*, 112047. [CrossRef]
18. Ashphaq, M.; Srivastava, P.K.; Mitra, D. Review of near-shore satellite-derived bathymetry: Classification and account of five decades of coastal bathymetry research. *J. Ocean Eng. Sci.* **2021**, *6*, 340–359. [CrossRef]
19. Neumann, T.A.; Martino, A.J.; Markus, T.; Bae, S.; Bock, M.R.; Brenner, A.C.; Brunt, K.M.; Cavanaugh, J.; Fernandes, S.T.; Hancock, D.W.; et al. The Ice, cloud and land elevation satellite-2 mission: A global geolocated photon product derived from the advanced topographic laser altimeter system. *Remote Sens. Environ.* **2019**, *233*, 111325. [CrossRef] [PubMed]
20. Jasinski, M.; Stoll, J.; Cook, W.; Ondrusek, M.; Stengel, E.; Brunt, K. Inland and Near-Shore Water Profiles Derived from the High-Altitude Multiple Altimeter Beam Experimental Lidar (MABEL). *J. Coast. Res.* **2016**, *76*, 44–55. [CrossRef] [PubMed]
21. Parrish, C.; Magruder, L.; Neuenschwander, A.; Forfinski-Sarkozi, N.; Alonzo, M.; Jasinski, M. Validation of ICESat-2 ATLAS Bathymetry and Analysis of ATLAS's Bathymetric Mapping Performance. *Remote Sens.* **2019**, *11*, 1634. [CrossRef]
22. Zhang, Z.; Liu, X.; Ma, Y.; Xu, N.; Zhang, W.; Li, S. Signal Photon Extraction Method for Weak Beam Data of ICESat-2 Using Information Provided by Strong Beam Data in Mountainous Areas. *Remote Sens.* **2021**, *13*, 863. [CrossRef]
23. Stumpf, R.; Holderied, K.; Sinclair, M. Determination of water depth with high-resolution satellite imagery over variable bottom types. *Limnol. Oceanogr.* **2003**, *48*, 547–556. [CrossRef]
24. Minghelli, A.; Vadakke-Chanath, S.; Chami, M.; Guillaume, M.; Migne, E.; Grillas, P.; Boutron, O. Estimation of Bathymetry and Benthic Habitat Composition from Hyperspectral Remote Sensing Data (BIODIVERSITY) Using a Semi-Analytical Approach. *Remote Sens.* **2021**, *13*, 1999. [CrossRef]
25. Maritorena, S.; Morel, A.; Gentili, B. Diffuse reflectance of oceanic shallow waters: Influence of water depth and bottom albedo. *Limnol. Oceanogr.* **1994**, *39*, 1689–1703. [CrossRef]
26. Mishra, D.; Narumalani, S.; Rundquist, D.; Lawson, M. Benthic habitat mapping in tropical marine environments using Quickbird multispectral data. *Photogramm. Eng. Remote Sens.* **2006**, *72*, 1037–1048. [CrossRef]
27. Liew, S.; Chen, P.; Daengtuksin, B.; Chang, C. Estimating water optical properties, water depth and bottom albedo using high resolution satellite imagery for coastal habitat mapping. In Proceedings of the 2011 IEEE International Geoscience and Remote Sensing Symposium, Vancouver, BC, Canada, 24–29 July 2011; pp. 2338–2340.
28. NOAA. Available online: <https://www.ngs.noaa.gov/RSD/topobathy/> (accessed on 28 December 2021).
29. Saylam, K.; Brown, R.; Hupp, J. Assessment of depth and turbidity with airborne Lidar bathymetry and multiband satellite imagery in shallow water bodies of the Alaskan North Slope. In *International Journal of Applied Earth Observation and Geoinformation*; Li, J., Ed.; Elsevier: Amsterdam, The Netherlands, 2017; Volume 58, pp. 191–200.
30. Caballero, I.; Stumpf, R.P.; Meredith, A. Preliminary Assessment of Turbidity and Chlorophyll II Impact on Bathymetry Derived from Sentinel-2A and Sentinel-3A Satellites in South Florida. *Remote Sens.* **2019**, *11*, 645. [CrossRef]
31. Peeri, S.; Azuiki, C.; Parrish, C. Satellite-derived bathymetry a reconnaissance tool for hydrography. *Hydro Int.* **2013**, *17*, 16–19.
32. NASA Goddard Space Flight Center, Ocean Ecology Laboratory, Ocean Biology Processing Group; 2014: MODIS-Aqua Ocean Color Data; NASA Goddard Space Flight Center, Ocean Ecology Laboratory, Ocean Biology Processing Group. Available online: <https://oceancolor.gsfc.nasa.gov/13/> (accessed on 28 December 2021).
33. Babel, B.; Parrish, C.; Magruder, L. ICESat-2 Elevation Retrievals in Support of Satellite-Derived Bathymetry for Global Science Applications. *Geophys. Res. Lett.* **2021**, *48*, e2020GL090629. [CrossRef]
34. IGN. Available online: <https://geodesie.ign.fr/contenu/fichiers/documentation/SRCfrance.pdf> (accessed on 28 December 2021).
35. Global Scan Technologies. Available online: <http://www.gstdubai.com/satelliteimagery/pleiades-1a.html> (accessed on 28 December 2021).

36. ESA. Available online: <https://earth.esa.int/web/eoportal/satellite-missions/i/icesat-2> (accessed on 28 December 2021).
37. Neumann, T.A.; Brenner, A.; Hancock, D.; Robbins, J.; Saba, J.; Harbeck, K.; Gibbons, A.; Lee, J.; Luthcke, S.B.; Rebold, T.; et al. *ATLAS/ICESat-2 L2A Global Geolocated Photon Data, Version 3. [ATL03]*; NASA National Snow and Ice Data Center Distributed Active Archive Center: Boulder, CO, USA, 2020.
38. Ester, M.; Kriegel, H.-P.; Sander, J.; Xu, X. A density-based algorithm for discovering clusters in large spatial databases with noise. In Proceedings of the Second International Conference on Knowledge Discovery and Data Mining (KDD'96), Portland, OR, USA, 2–4 August 1996; AAAI Press: Palo Alto, CA, USA, 1996; pp. 226–231.
39. Xie, C.; Chen, P.; Pan, D.; Zhong, C.; Zhang, Z. Improved Filtering of ICESat-2 Lidar Data for Nearshore Bathymetry Estimation Using Sentinel-2 Imagery. *Remote Sens.* **2021**, *13*, 4303. [[CrossRef](#)]
40. Xun, N.; Ma, X.; Ma, Y.; Zhao, P.; Yang, J.; Wang, H. Deriving Highly Accurate Shallow Water Bathymetry From Sentinel-2 and ICESat-2 Datasets by a Multitemporal Stacking Method. *IEEE J. Sel. Top. Appl. Earth Obs. Remote Sens.* **2021**, *14*, 6677–6685.
41. Khater, I.; Nabi, I.R.; Hamarneh, G. A Review of Super-Resolution Single-Molecule Localization Microscopy Cluster Analysis and Quantification Methods. *Patterns* **2020**, *1*, 100038. [[CrossRef](#)] [[PubMed](#)]
42. Randazzo, G.; Barreca, G.; Cascio, M.; Crupi, A.; Fontana, M.; Gregorio, F.; Lanza, S.; Muzirafuti, A. Analysis of Very High Spatial Resolution Images for Automatic Shoreline Extraction and Satellite-Derived Bathymetry Mapping. *Geosciences* **2020**, *10*, 172. [[CrossRef](#)]
43. Gabr, B.; Ahmed, M.; Marmoush, Y. PlanetScope and Landsat 8 Imageries for Bathymetry Mapping. *J. Mar. Sci. Eng.* **2020**, *8*, 143. [[CrossRef](#)]
44. Pe'eri, S.; Parrish, C.; Azuike, C.; Alexander, L.; Armstrong, A. Satellite Remote Sensing as a Reconnaissance Tool for Assessing Nautical Chart Adequacy and Completeness. *Mar. Geodesy* **2014**, *37*, 293–314. [[CrossRef](#)]
45. Poppenga, S.; Palaseanu-Lovejoy, M.; Gesch, D.; Danielson, J.; Tyler, D. *Evaluating the Potential for Near-Shore Bathymetry on the Majuro Atoll, Republic of the Marshall Islands, Using Landsat 8 and WorldView-3 Imagery*; Scientific Investigations Report 2018-5024; U.S. Geological Survey: Reston, VA, USA, 2018.
46. Favoretto, F.; Morel, Y.; Waddington, A.; Lopez-Calderon, J.; Cadena-Roa, M.; Blanco-Jarvio, A. Testing of the 4SM Method in the Gulf of California Suggests Field Data Are not Needed to Derive Satellite Bathymetry. *Sensors* **2017**, *17*, 2248. [[CrossRef](#)] [[PubMed](#)]
47. Nur, H.; Othman, Y.; Wiwin, W.; Saiful, S. Integration of Satellite-Derived Bathymetry and Sounding Data in Providing Continuous and Detailed Bathymetric Information. In *IOP Conference Series: Earth and Environmental Science, Proceedings of the 2nd Maritime Science and Advanced Technology, Marine Science and Technology in Framework of The Sustainable Development Goals, Makassar, Indonesia, 7–8 August 2019*; IOP Publishing Ltd.: Bristol, UK, 2020; Volume 618, p. 012018.
48. Yakup, D.; Zeliha, S.; Bulent, S.; Mehmet, A.; Dagdeviren, M. Determination of sediment deposition of Hasanlar Dam using bathymetric and remote sensing studies. *Nat. Hazards* **2019**, *97*, 211–227.
49. Monteys, X.; Harris, P.; Caloca, S.; Cahalane, C. Spatial Prediction of Coastal Bathymetry Based on Multispectral Satellite Imagery and Multibeam Data. *Remote Sens.* **2015**, *7*, 13782–13806. [[CrossRef](#)]
50. Collin, A.; Planes, S. Enhancing Coral Health Detection Using Spectral Diversity Indices from WorldView-2 Imagery and Machine Learners. *Remote Sens.* **2012**, *4*, 3244–3264. [[CrossRef](#)]
51. Morel, A.; Maritorena, S. Bio-optical properties of oceanic waters: A reappraisal. *J. Geophys. Res.* **2001**, *106*, 7163–7180. [[CrossRef](#)]
52. Mogstad, A.; Johnsen, G.; Ludvigsen, M. Shallow-Water Habitat Mapping using Underwater Hyperspectral Imaging from an Unmanned Surface Vehicle: A Pilot Study. *Remote Sens.* **2019**, *11*, 685. [[CrossRef](#)]
53. Story, M.; Congalton, R.G. Accuracy assessment: A user's perspective. *Photogramm. Eng. Remote Sens.* **1986**, *52*, 397–399.
54. Lemoine, A.; Briole, P.; Bertil, D.; Roullé, A.; Fournel, M.; Thion, I.; Raucoules, D.; de Michele, M.; Valt, P.; Hoste Colomer, R. The 2018–2019 seismo-volcanic crisis east of Mayotte, Comoros islands: Seismicity and ground deformation markers of an exceptional submarine eruption. *Geophys. J. Int.* **2020**, *223*, 22–44. [[CrossRef](#)]
55. Cesca, S.; Letort, J.; Razafindrakoto, H.N.T.; Heimann, S.; Rivalta, E.; Isken, M.P.; Nikkhoo, M.; Passarelli, L.; Petersen, G.L.; Cotton, F.; et al. Drainage of a deep magma reservoir near Mayotte inferred from seismicity and deformation. *Nat. Geosci.* **2020**, *13*, 87–93. [[CrossRef](#)]
56. Feuillet, N.; Jorry, S.; Crawford, W.; Deplus, C.; Thion, I.; Jacques, E.; Van der Woerd, J. Birth of a large volcanic edifice through lithosphere-scale dyking offshore Mayotte (Indian Ocean). *Nat. Geosci.* **2021**. under review. [[CrossRef](#)]
57. Amrari, S.; Bourassin, E.; Andréfouët, S.; Soulard, B.; Lemonnier, H.; Le Gendre, R. Shallow Water Bathymetry Retrieval Using a Band-Optimization Iterative Approach: Application to New Caledonia Coral Reef Lagoons Using Sentinel-2 Data. *Remote Sens.* **2021**, *13*, 4108. [[CrossRef](#)]
58. Niroumand-Jadidi, M.; Vitti, A.; Lyzenga, D.R. Multiple Optimal Depth Predictors Analysis (MODPA) for river bathymetry: Findings from spectroradiometry, simulations, and satellite imagery. *Remote Sens. Environ.* **2018**, *218*, 132–147. [[CrossRef](#)]
59. Niroumand-Jadidi, M.; Bovolo, F.; Bruzzone, L. SMART-SDB: Sample-specific multiple band ratio technique for satellite-derived bathymetry. *Remote Sens. Environ.* **2020**, *251*, 112091. [[CrossRef](#)]
60. Albright, A.; Glennie, C. Nearshore Bathymetry From Fusion of Sentinel-2 and ICESat-2 Observations. *IEEE Geosci. Remote Sens. Lett.* **2021**, *18*, 900–904. [[CrossRef](#)]



Article

Easily Implemented Methods of Radiometric Corrections for Hyperspectral–UAV—Application to Guianese Equatorial Mudbanks Colonized by Pioneer Mangroves

Marion Jaud ^{1,2,*}, Guillaume Sicot ³, Guillaume Brunier ⁴, Emma Michaud ⁴, Nicolas Le Dantec ^{1,2}, Jérôme Ammann ², Philippe Grandjean ⁵, Patrick Launeau ⁶, Gérard Thouzeau ⁴, Jules Fleury ⁷ and Christophe Delacourt ²

- ¹ IUEM-UMS 3113, CNRS, University Brest, IRD, Rue Dumont D’Urville, F-29280 Plouzané, France; nicolas.ledantec@univ-brest.fr
 - ² Laboratoire Géosciences Océans—UMR 6538, CNRS, University Brest, Rue Dumont D’Urville, F-29280 Plouzané, France; jerome.ammann@univ-brest.fr (J.A.); christophe.delacourt@univ-brest.fr (C.D.)
 - ³ ENSTA Bretagne, M3 Team-Lab-STICC—UMR CNRS 6285, 2 rue François Verny, F-29200 Brest, France; guillaume.sicot@ensta-bretagne.fr
 - ⁴ CNRS, University Brest, IRD, Ifremer, LEMAR, F-29280 Plouzané, France; guillaume_brunier@hotmail.fr (G.B.); emma.michaud@univ-brest.fr (E.M.); gerard.thouzeau@univ-brest.fr (G.T.)
 - ⁵ Laboratoire de Géologie de Lyon: Terre, Planètes, Environnement-UMR 5276, University Lyon, Université Claude Bernard Lyon 1, ENS Lyon, CNRS, F-69622 Villeurbanne, France; philippe.grandjean@univ-lyon1.fr
 - ⁶ Laboratoire de Planétologie et Géodynamique—UMR 6112, University Nantes, 2 Chemin de la Houssinière, F-44300 Nantes, France; patrick.launeau@univ-nantes.fr
 - ⁷ CEREGE—UMR 7330, University Aix Marseille, CNRS, IRD, INRA, Collège de France, F-13545 Aix-en-Provence, France; fleury@cerge.fr
- * Correspondence: marion.jaud@univ-brest.fr; Tel.: +33-298498891

Citation: Jaud, M.; Sicot, G.; Brunier, G.; Michaud, E.; Le Dantec, N.; Ammann, J.; Grandjean, P.; Launeau, P.; Thouzeau, G.; Fleury, J.; et al.

Easily Implemented Methods of Radiometric Corrections for Hyperspectral–UAV—Application to Guianese Equatorial Mudbanks Colonized by Pioneer Mangroves.

Remote Sens. **2021**, *13*, 4792. <https://doi.org/10.3390/rs13234792>

Academic Editor: Junshi Xia

Received: 8 September 2021

Accepted: 24 November 2021

Published: 26 November 2021

Publisher’s Note: MDPI stays neutral with regard to jurisdictional claims in published maps and institutional affiliations.



Copyright: © 2021 by the authors. Licensee MDPI, Basel, Switzerland. This article is an open access article distributed under the terms and conditions of the Creative Commons Attribution (CC BY) license (<https://creativecommons.org/licenses/by/4.0/>).

Abstract: Hyper-DRELIO (Hyperspectral DRone for Environmental and Littoral Observations) is a custom, mini-UAV (unmanned aerial vehicle) platform (<20 kg), equipped with a light push broom hyperspectral sensor combined with a navigation module measuring position and orientation. Because of the particularities of UAV surveys (low flight altitude, small spatial scale, and high resolution), dedicated pre-processing methods have to be developed when reconstructing hyperspectral imagery. This article presents light, easy-implementation, in situ methods, using only two Spectralon[®] and a field spectrometer, allowing performance of an initial calibration of the sensor in order to correct “vignetting effects” and a field standardization to convert digital numbers (DN) collected by the hyperspectral camera to reflectance, taking into account the time-varying illumination conditions. Radiometric corrections are applied to a subset of a dataset collected above mudflats colonized by pioneer mangroves in French Guiana. The efficiency of the radiometric corrections is assessed by comparing spectra from Hyper-DRELIO imagery to in situ spectrometer measurements above the intertidal benthic biofilm and mangroves. The shapes of the spectra were consistent, and the spectral angle mapper (SAM) distance was 0.039 above the benthic biofilm and 0.159 above the mangroves. These preliminary results provide new perspectives for quantifying and mapping the benthic biofilm and mangroves at the scale of the Guianese intertidal mudbanks system, given their importance in the coastal food webs, biogeochemical cycles, and the sediment stabilization.

Keywords: drone; hyperspectral imaging; radiometric calibration; reflectance; pioneer mangroves; intertidal sediments

1. Introduction

Mangroves are highly productive ecosystems, which dominate the intertidal zone of tropical and subtropical coasts. Mangroves fulfil numerous ecological functions (habitats,

breeding grounds, nursery, carbon sink, water filtration, sediment retention) [1]. Mangroves grow on fine sand to silty sediments in areas protected from high-energy wave action, mainly found in depositional coastal environments, such as the deltaic, lagoon, or mudflat systems. However, these ecosystems are more and more threatened by global changes, which include anthropogenic pressures (i.e., pollution, urbanization, fisheries, aquaculture . . .) as well as climate change (i.e., increase of temperatures and sea level, high-intensity cyclones . . .) [2,3]. This is even truer on the coasts of countries with rapidly increasing human demography. Management and restoration of these ecosystems has become highly necessary. An initial step toward adequate management is monitoring, which can be done using different techniques. Remote sensing appears to be a valuable approach for field observations given the practical difficulties to access and carry out in situ measurements in those complex and dynamical systems (for reviews, see, for example, [4–6]). Indeed, remote sensing offers synoptic information, allowing the detection, classification, or mapping of mangroves and the monitoring of their spatial organization and temporal evolution. In Amazon-influenced coastal areas, as in large tropical deltaic coasts, mangroves grow over vast intertidal mudflats. Thus, mangroves ecosystems cannot be characterized only through the spatial coverage of mangrove trees. Indeed, they also include a variety of geomorphological forms, such as the creeks, ridges, runnels, sediment platforms, and depressions—that can be observed from aerial view—and, depending on pixel resolution of the imaging sensors, the spatial coverage and density of the trees and the age of the forests. This spatial heterogeneity of habitats increases the complexity in signal processing of remote sensing data, concerning the identification and quantification of the trees and intertidal benthic constituents.

Over the last decades, remote sensing has undergone major developments resulting from a combination of technological progress in platforms, sensors, data processing, and data availability. Among all the possible remote sensing issues (e.g., meteorology, military applications, cartography, topography, oceanography, geology, natural hazards, etc.), several applications make use of the radiometric properties of the scene, such as computation of classification indices, spectral unmixing, or radiative transfer modelling [7]. Indeed, each substrate has a specific spectral signature (i.e., the reflectance as a function of wavelength), which can be used for material identification or classification. This requires a high spectral fidelity and the measurement of a wide spectrum at high resolution, which are only offered by hyperspectral sensors [8]. Until then, hyperspectral data were mainly collected from airborne or satellite platforms, as the Hyperion satellite imaging spectrometer, with a spatial resolution from about 50 cm for low altitude (<1500 m) airborne surveys [9] to dozens of meters for high altitude surveys [10]. VNIR (visible and near infrared) hyperspectral sensors provide hundreds of continuous spectral bands between 400 nm and 1100 nm. Such a spectral richness allows accurate mapping and classification of complex environments, such as vegetation and ground features. The development of airborne sensors and high spatial resolution hyperspectral images meets a large audience in environmental research and particularly in forestry. Numerous studies over a significant range of forest types, using various classification algorithms, have emerged during this decade [11–14]. That underlines the applicability and potential of hyperspectral images for mapping vegetation over various spatial footprints and spatial resolutions. Hyperspectral monitoring of mangrove forests has mostly been developed since the early 2000s from aircraft vessels along the southeastern coast of the USA [15], the Indian coast [16–18], the Australian coast [12], and the southeastern coast of Asia [19–21].

Considering their ability to provide quick and cost-effective observations with great flexibility in survey planning, the use of unmanned aerial vehicles (UAVs) or drones has boomed over the last decade. Because of limited payload, small UAVs are mostly equipped with RGB or VNIR multispectral cameras. Nevertheless, drone-based hyperspectral sensing solutions also arose in the last few years [22]. These hyperspectral–UAV systems can now complement airborne and satellite approaches for hyperspectral imaging and bridge the gap in resolution and spatial coverage between remote data and ground-based measurements.

In flying at low altitude (below 150 m), UAVs offer the opportunity to collect very high spatial resolution data, capturing a larger number of details. Furthermore, hyperspectral-UAV systems also allow a great flexibility regarding devices configuration and flight plan adjustments or times at which surveys are carried out. Surveys of mangrove forests by drones equipped with a hyperspectral camera mark a recent turning point in terms of image resolution and survey repeatability. The studies involving hyperspectral-UAV surveys of mangrove forests mostly took place on the southeastern coast of China [19,23,24]. To our knowledge, there has been no previous study, involving a hyperspectral-UAV camera, conducted over mangrove forests in South America and French Guiana.

These drone platforms offer interesting capabilities, provided one has adequate algorithms for georeferencing and radiometric corrections. Several studies refer mainly to helicopters or fixed-wing UAVs, designed to support large and heavy (>5 kg) payloads [25–28]. However, helicopters generate high frequency vibrations and require specially trained operators. Fixed-wing platforms provide long and smooth flights but are wide UAVs, which require a large area, suitable for take-off and landing. On the contrary, multi-rotor UAVs have a shorter autonomy and generate high-frequency vibrations; however, being able to take-off and land vertically and fly at a steady altitude, they are more suited to field areas of few hectares [22]. Usually considered as “mini-UAVs” (<20 kg), they support lighter payloads (<5 kg) [29–31]. Stuart et al. [22] propose a review of relatively low-cost, field-deployable hyperspectral devices, particularly UAV-based devices, for environmental monitoring. These drone-based technologies include point-based spectrometers, push broom sensors, and, more recently, hyperspectral frame cameras. These systems differ in their spatial coverage, in the tradeoff between spatial and spectral resolutions, and in how easy image reconstruction and georeferencing are with their use. Dedicated pre-processing methods usually have to be developed for data georeferencing and radiometric corrections. Specific algorithms for radiometric corrections also need to be elaborated, given that classical models for geometric, atmospheric, and radiometric corrections are not suited to UAV data, considering the flight height and temporal and spatial scales of UAV surveys [8,29,32–34].

The electromagnetic radiation received by the sensor is referred to as the spectral radiance. In reality, the sensor records raw digital numbers (DN). In many studies, the parameter of interest is the ratio of upwelling radiation in a given direction toward the sensor (radiance) to downwelling radiation (irradiance), known as remote sensing reflectance. The latter is a key parameter, sometimes denoted as the spectral signature, which theoretically allows a description of the nature of the studied surface, independently of the sensor, viewing geometry, sun azimuth, elevation, or the weather conditions. Thus, radiometric corrections, consisting in converting the DN recorded by the sensor into ground reflectance values, can rely on different approaches, often requiring the acquisition of complementary field data. This process is necessary for data interpretation or diachronic comparisons. The geometric, radiometric, and spectral properties of the instruments can be partly characterized and calibrated through laboratory tests, but this requires having a dedicated test bed [34]. Regarding radiometric corrections, Saari et al. [32] proposed a drone equipped with downwelling and upwelling irradiance sensors to record illumination conditions during the flight. However, adding embedded sensors increases the payload, which is generally the main limit of UAV systems [29,34]. Another approach consists of using additional systems on the ground, especially white reference panels, to convert the sensor’s digital number (DN) to reflectance [8,33–35].

Drone monitoring has proven particularly useful as a non-destructive data acquisition technic in dynamic and complex coastal and estuarine systems where ground-based field surveys are very difficult, especially for monitoring purposes in unconsolidated temperate mudflats [36] and along the French Guiana (FG) littoral zone, for sandy beaches and mangrove-colonized mudbanks [37,38]. Belonging to the largest mudflat in the world, the French Guianese coastline, dominated by mangroves, is indeed experiencing extremely rapid morphological changes in response to the large amounts of Amazonian sedimentary

inputs [39]. Mangrove ecosystems development or disappearance accompanies the alternation of Amazonian mudbanks accretion and erosion phases along the north coast of South America between the Amazon and Orinoco Rivers [40,41]. At a regional scale, geomorphology changes rapidly and becomes favorable to the development of different mangrove stand ages [40,41] and specific benthic biodiversity, which in turn modify the geomorphological evolution of the mudbanks. Indeed, as the mud consolidates, the substrate elevation increases and the flooding time during each tidal cycle decreases. As results of such dynamics, biological processes within sediments are intense, enhanced by both benthic biofilm development and bioturbation by crabs [37,42]. In these geographical areas, the benthic biofilm is as important as the mangrove trees in terms of carbon biomass and as a source of organic matter for the coastal food webs and regional biogeochemical cycles [43–46].

In this natural and complex context, it is necessary to explore the spatial and spectral richness of hyperspectral-UAV data. A reliable analysis of these data requires a first step of radiometric pre-processing. The present study describes and implements a radiometric correction method on UAV in situ data, collected along a gradient of pioneer mangroves in French Guiana, using the Hyper-DRELIO drone. Radiometric corrections here encompass calibration and in situ standardization. The method we propose is easy to implement, without adding embedded sensors and with limited additional equipment.

2. Study Area and Survey Setup

The field campaign took place in the northwestern part of French Guiana (Awala-Yalimapo; Figure 1a,b), during the dry season in September 2018. Besides the natural dynamics of mudbanks, this region is submitted to additional anthropogenic pressure following polder erosion, making the area unstable [47]. Preliminary results showed that mangroves colonized the consolidated part of the mudbank in 2015 and the oldest trees were about 3 years old at the time of our field measurements campaign. The northwestern part of the mudbank was characterized by unconsolidated bare mud.

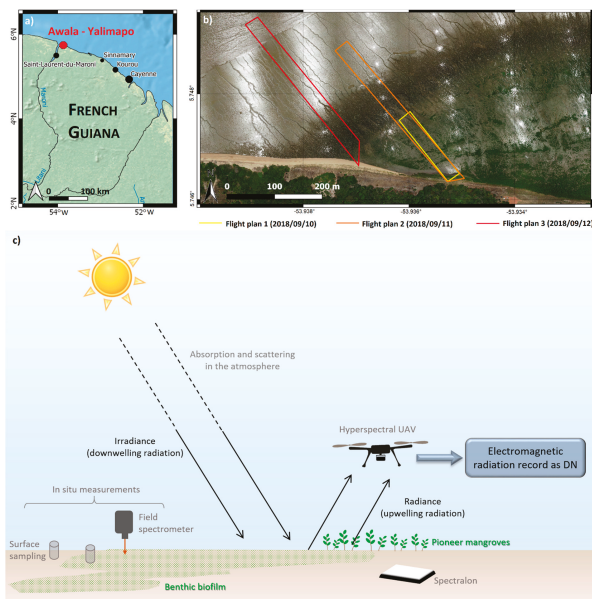


Figure 1. (a) Localization of the study area in Awala-Yalimapo in the western part of French Guiana. (b) UAV flight plans above the study area, designed to capture the various mud facies (from bare mud to mangrove stages). (c) Diagram of a survey setup and the physical variables to be measured.

Tides at this location are semidiurnal in the study area with high spring tide ranges up to 3.5 m and a mean tidal range of 1.68 m (<https://maree.shom.fr> for “Les Hattes” site—access on 1 April 2020).

Taking advantage of the flexibility of drone-based systems, we tailored the survey to examine benthic biofilm development in relation to the tidal cycle, carrying out the flights at low tide during spring tide. As depicted in Figure 1c, hyperspectral drone surveys were synchronized with in situ measurements for radiometric correction and validation purposes.

3. Materials and Methods

3.1. Hyperspectral UAV

The integration of the light push broom hyperspectral sensor onboard the multirotor UAV, called Hyper-DRELIO (Hyperspectral DRone for Environmental and Littoral Observations), is described in Jaud et al. (2018). The system is composed of an electric octocopter platform (Figure 2a,b), an imaging module, and a navigation module, synchronized via CPU (central processing unit) timestamps. To complement this system, a ground segment allows sensor parametrization, data quality control during the flight, and flight parameter control.

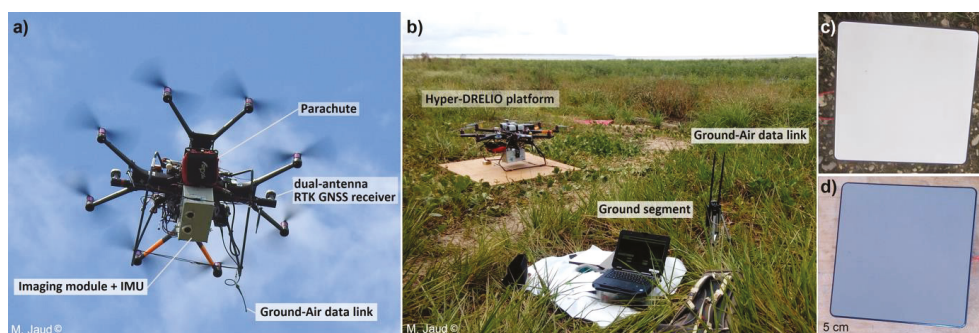


Figure 2. (a,b) Hyper-DRELIO (Hyperspectral DRone for Environmental and Littoral Observations) platform, unmanned aerial vehicle (UAV) for hyperspectral imagery. IMU: inertial motion unit; RTK GNSS: real time kinematic global navigation satellite system. (c) White Spectralon panel (reflectivity: 99%). (d) Grey Spectralon panel (reflectivity: 20%).

The drone has a diameter of 1.2 m, weighs 13.4 kg, and can handle a payload of 5 kg (including batteries, cables, navigation modules, and imagery modules). Considering the duration of ascent and descent phases and a safety cushion, the programmed flight plan duration must not exceed 7–8 min [30]. The onboard flight control system of the drone is composed of a global navigation satellite system (GNSS) and an autopilot, run by DJI® iOSD® software. The navigation module, which measures position and orientation during the flight, is composed of a dual-antenna RTK (real time kinematics) GNSS receiver with a baseline of 85 cm and an Ekinox-D® (SBG System®) inertial motion unit (IMU). The hyperspectral camera, a Micro-Hyperspec® VNIR (Headwall®), is a push broom (or line-scanning) system, collecting reflected light through an image slit. The principle of operation of this camera relies on holographic diffraction, using gratings and mirrors to split monochromatic light into 250 spectral bands, ranging between 400 nm and 1000 nm, with 1.85 nm of spectral resolution. The manufacturer carried out a wavelength calibration beforehand, in order to determine the correspondence relationship between imaging spectrometer probe elements and the central wavelength. On the CCD sensor matrix, rows collect spatial, across-track information and columns record the spectral content of the signal. Values for each element of the matrix are expressed as 12-bit DN (i.e., values between 0 and 4096). The camera is equipped with a fixed focus lens, focused to infinity. Aperture and sensor gain G were adjusted before the flight, depending on the illumination

conditions, in order to avoid saturation of the CCD cells. The integration time remained fixed during the flight, which required that there is no major variation of the illumination conditions during the flight (around 12 min duration).

The acquisition frame rate was parametrized to 50 Hz, which is compatible with a UAV speed of around 3–4 m/s (close to the lower boundary for drone stability). At 50 m above ground level, the configuration chosen for this study, the swath was 45 m wide and the across-track ground resolution was 4.5 cm. With a speed of 3 m/s, the along-track ground sampling was about 6 cm.

A line-by-line geo-registration procedure was proposed in [30] for geometrical pre-processing of hyperspectral data. The accuracy of this direct georeferencing method is on the order of 1 m for a flight at 50 m of altitude. The quality of the georeferencing process is limited by several factors: mechanical stability of the platform, the timing accuracy, and more particularly, the resolution and accuracy of the proprioceptive sensors (GNSS receivers and IMU). This geo-registration to realign and geo-reference the push broom data is non-intrusive and preserves fragile substrates, such as mud. Ground control points would have allowed a more accurate estimation of the geo-registration error, but their installation would have been very destructive to the substrate.

With such characteristics, the Hyper-DRELIO system is adequate to cover areas of approximately 10,000 m² and to study objects ranging from 10 centimeters to several meters. The main advantage of the drone is that it can perform repeated overflights over an area that changes over time (such as the mudflat during a tidal cycle). However, push broom technology is not suitable for imaging moving objects, such as waves or animals. In addition, the drone platform is dependent on weather conditions and flights cannot be performed in rain or strong winds. Cloudy skies are the preferred conditions to avoid sun glint effects; however, all flights during the mission took place in sunny conditions.

3.2. Ground-Based Measurements

Ground positioning measurements were performed using RTK-differential GNSS, achieving centimetric accuracy after post-processing of the base station. The device used for this study was a Topcon[®] HiPer V GNSS receiver. The same base receiver was used both for ground measurements and for the navigation module of Hyper-DRELIO.

The in situ data for radiometric standardization and validation were measured with a GER 1500 field spectrometer (developed by Spectra Vista Corporation[®]), providing fast, at-target radiance measurements from 350 nm to 1050 nm. Each measurement was triplicated and averaged. A white Spectralon[™] panel with a reflectivity of 99% allowed an indirect measurement of the irradiance. This Spectralon (Figure 2c) was a 40 × 40 cm white reference panel made of a fluoropolymer, which is highly reflective (the highest diffuse reflectance of any known material) and has Lambertian behavior [48]. This Spectralon[™] panel is placed on flat ground near the take-off area. For the initial calibration, a grey Spectralon[™] (Figure 2d), with a reflectivity of 20%, was also used. As 20% reflectivity is close to the reflectance of bare mud, this grey Spectralon[™] was also used to adjust the parametrization of the hyperspectral camera (aperture and sensor gain G) before the flight.

The spectrometer measurements were carried out in a flight-synchronous manner on different types of substrates. In order to limit the movements of the operators, which were very slow, difficult, and very destructive for the mudflat, these measurements were carried out around a fixed platform placed on the mud.

3.3. Radiometric Correction Method

Radiometric corrections aim to convert the raw digital numbers (DN) recorded by the sensor into remote sensing reflectance. Once the reflectance is computed, hyperspectral images can be exploited in different ways, such as computation of spectral indices for classification (e.g., [49,50]), study of the red edge position (e.g., [51]), or spectral unmixing [52].

For hyperspectral measurements acquired with drones, radiometric corrections were realized using complementary in situ data. Given the practical challenges in carrying out

surveys in mangrove or mudflat areas, the proposed method must be easy to implement, without adding embedded sensors and with as little equipment as possible. Computational routines to apply corrections were implemented in Matlab®, including several steps, which are summarized in Figure 3. During the acquisition, the signal was impacted by noise, called the dark current (DC) [53], which is partly function of sensor temperature and partly integration time. In our case, this DC is assumed steady. Furthermore, as the survey was focused on mudflats, the topographic effects could be neglected. Finally, as the flight altitude remained low (<150 m), we hypothesized that the at-target radiance was equal to the at-sensor radiance at 50 m height [54]. To validate this hypothesis, raw spectra (in DN) were measured by the hyperspectral camera above the white Spectralon™ panel, both from the ground and in flight. The mean difference between the “on ground” spectra and “on flight” spectra was about 7.5% with a standard deviation of 5.3% and a preserved shape of spectra.

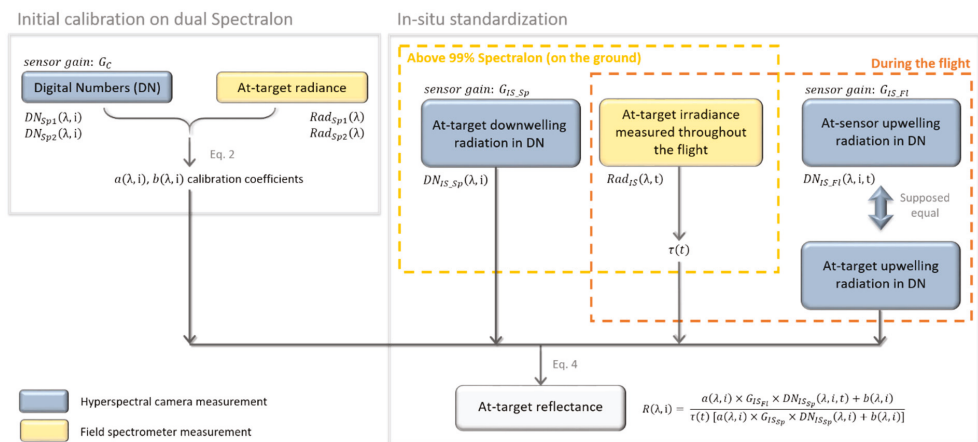


Figure 3. Processing steps performed for radiometric corrections (“i” is the index of the pixel along the sensor array, in the across-track spatial dimension).

3.3.1. Initial Calibration

Hyperspectral images suffer from variations or distortions of the spectrogram along the CCD array (possibly caused by the quality of the dispersive element or misalignments of the light from the slit). This results in vertical “stripes” in our push broom images. This spatial dependence of DN, and particularly its decrease towards the image edges, is called the “vignetting effect” for frame sensors [53] and corresponds rather to the “lining effect” for push broom sensors.

The calibration parameters aim to compensate for this effect and to convert DN to physical units of radiance. We chose an image-based calibration method, and we assumed a linear relationship between the DN and the at-sensor radiance [54,55], according to the following empirical transfer function (Equation (1)):

$$Rad_C(\lambda, i) = a(\lambda, i) \times DN_C(\lambda, i)/G_C + b(\lambda, i) \tag{1}$$

With the following:

- λ : wavelength (nm);
- i: index of the pixel in the sensor array;
- Rad_C : at-sensor radiance ($W \cdot m^{-2} \cdot sr^{-1}$) during calibration step;
- G_C : sensor gain during calibration step;
- DN_C : digital number collected during calibration step;
- a, b: calibration coefficients.

To calculate a and b coefficients, we considered the radiance measured by the field spectrometer above both white and grey Spectralon panels, and the DN measured simultaneously by the hyperspectral camera. Each Spectralon was thus targeted simultaneously by the GER1500 field spectrometer and by the hyperspectral camera, while the drone was on the ground, in such a way that the field spectrometer and the hyperspectral camera were at the same distance from the Spectralon panel and the measurements were synchronized. The a and b coefficients were calculated per pixel and per spectral band, according to the following equations (Equation (2)):

$$\begin{cases} a(\lambda, i) = G_C \times \frac{Rad_{Sp1}(\lambda, i) - Rad_{Sp2}(\lambda, i)}{[DN_{Sp1}(\lambda, i) - DN_{Sp2}(\lambda, i)]} \\ b(\lambda, i) = Rad_{Sp1}(\lambda, i) - \frac{a}{G_C} DN_{Sp1}(\lambda, i) \end{cases} \quad (2)$$

With the following:

$Sp1, Sp2$: ID of each Spectralon used for the calibration;

$Rad_{Sp1, Sp2}$: radiance ($W \cdot m^{-2} \cdot sr^{-1}$) measured by the field spectrometer above the $Sp1$ (respectively, $Sp2$) Spectralon;

$DN_{Sp1, Sp2}$: digital number collected by the hyperspectral camera above the $Sp1$ (respectively, $Sp2$) Spectralon.

To avoid local effects due to possible wear marks on the Spectralon surface, several hyperspectral lines were recorded by the hyperspectral camera (500 lines were selected and averaged) and 8 spectra were measured by the field spectrometer from various directions and averaged. To visually confirm the efficiency of this calibration, a and b coefficients were applied to DN_{Sp1} (respectively, DN_{Sp2}), measured above the white Spectralon (respectively, the grey Spectralon). The results above the white Spectralon, before and after calibration, are depicted in Figure 4, representing, in natural colors, the hyperspectral lines collected by the camera.

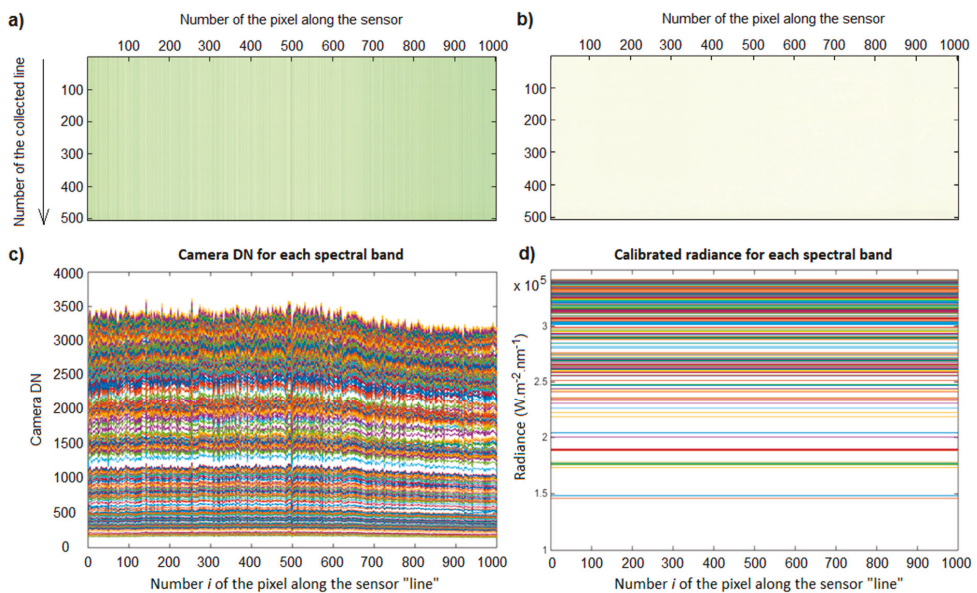


Figure 4. Hyperspectral lines collected above the white Spectralon by the hyperspectral camera before (a,c) and after (b,d) calibration. (a,b) represent, in natural colors, the hyperspectral lines collected by the camera; (c,d) represent the values of digital number (DN) (c) and radiance (d) along the sensor line for each spectral band (in colors).

This calibration step was carried out once (at least for the entire field campaign) and the coefficients were then applied to all the different following surveys. The a and b coefficients are exported to a “calibration file”, which will be reused in the in situ standardization step.

3.3.2. In Situ Standardization

For each in situ survey, the collected data DN_{IS} are calibrated using the a and b coefficients (Equation (1)). Applying Equation (1) enables compensation for the lining effects and provides a result with physical units of radiance; however, this is not the real in situ at-target radiance. Indeed, considering Equation (2), the a and b coefficients are related to the illumination conditions at the moment of the dual Spectralon measurements with both hyperspectral sensors during the calibration step. Therefore, Equation (1) needs to be standardized to the in situ atmospheric conditions at the time of the survey.

For each survey, before the flight, the irradiance was indirectly measured on the white 99% Spectralon panel, by the hyperspectral camera, held about 30 cm above the Spectralon. During this step, the operators had to be careful not to create shade on the Spectralon, which can be complicated when placing the drone-borne camera above it. As for the calibration step, to avoid local effects due to possible wear marks on the Spectralon surface, several hyperspectral lines recorded by the camera were selected and averaged. The irradiance before the flight was also measured with the field spectrometer, which was targeted to the white 99% Spectralon almost simultaneously with the hyperspectral camera, and from the same distance of about 30 cm, to serve as a reference for temporal variations of irradiance.

The sensor gain (G_{IS}) at the time of the survey also needed to be taken into account. The in situ sensor gain (G_{IS}) is adjusted before the flight, according to the illumination conditions, to avoid signal saturation. Therefore, it can be different from the gain G_C used during the calibration step. Besides, if the flown-over area is expected to have a low reflectivity, the in situ gain in flight (G_{IS_Fl}) can also be parametrized differently from the in situ gain used, above the 99% Spectralon G_{IS_Sp} .

The in situ reflectance was calculated by forming the ratio of the upwelling radiation to the downwelling radiation. This is given by Equation (3):

$$R(\lambda, i) = \frac{a(\lambda, i) \times \frac{DN_{IS_Fl}(\lambda, i, t)}{G_{IS_Fl}} + b(\lambda, i)}{a(\lambda, i) \times \frac{DN_{IS_Sp}(\lambda, i)}{G_{IS_Sp}} + b(\lambda, i)} \quad (3)$$

With the following:

G_{IS_Sp} : sensor gain used during in situ measurements of the 99% Spectralon;

G_{IS_Fl} : sensor gain used during the in situ flight;

DN_{IS_Sp} : digital number collected in situ by the hyperspectral camera of the 99% Spectralon;

DN_{IS_Fl} : digital number collected in situ by the hyperspectral camera during the flight;

R : resulting remote-sensing reflectance.

3.3.3. Taking Temporal Variations of Irradiance into Account

The illumination changes during data acquisition are generally pointed as a source of difficulties in hyperspectral surveys [22,56]. Our approach to addressing this issue is almost comparable to the “dual-spectrometer” method, proposed for a ground-based system in Bachmann et al. [48], and consists of monitoring illumination change using a reference panel, simultaneously with data acquisition [22].

To mitigate the variations of ambient light, the field spectrometer regularly recorded the irradiance above the white Spectralon (with a time-step from 10 s to 20 s) (Figure 5a). The internal clock of the field spectrometer was synchronized with the GPS time (used in the header file of the hyperspectral camera). We hypothesized that the shape of the irradiance spectra would vary linearly over time, mainly according to a single, time-dependent multiplying coefficient called τ (Figure 5b). The τ coefficients, calculated for

each field spectrometer record, were then interpolated over time to obtain a coefficient for irradiance evolution ($\tau(t)$) throughout the survey (Figure 5c). This dimensionless coefficient represents the percentage of irradiance variation in comparison to the irradiance measured just when the in situ standardization was performed (t_0). Therefore, τ is equal to 1 when the illumination does not change, greater than 1 if the illumination increases, and lower than 1 if it decreases. To take into account the variations of irradiance, Equation (3) is changed into Equation (4):

$$R(\lambda, i) = \frac{a(\lambda, i) \times \frac{DN_{IS_{Fl}}(\lambda, i, t)}{G_{IS_{Fl}}} + b(\lambda, i)}{\tau(t) \times a(\lambda, i) \times \frac{DN_{IS_{Sp}}(\lambda, i)}{G_{IS_{Sp}}} + b(\lambda, i)} \quad (4)$$

where the τ coefficient represents the percentage of irradiance variation during the flight.

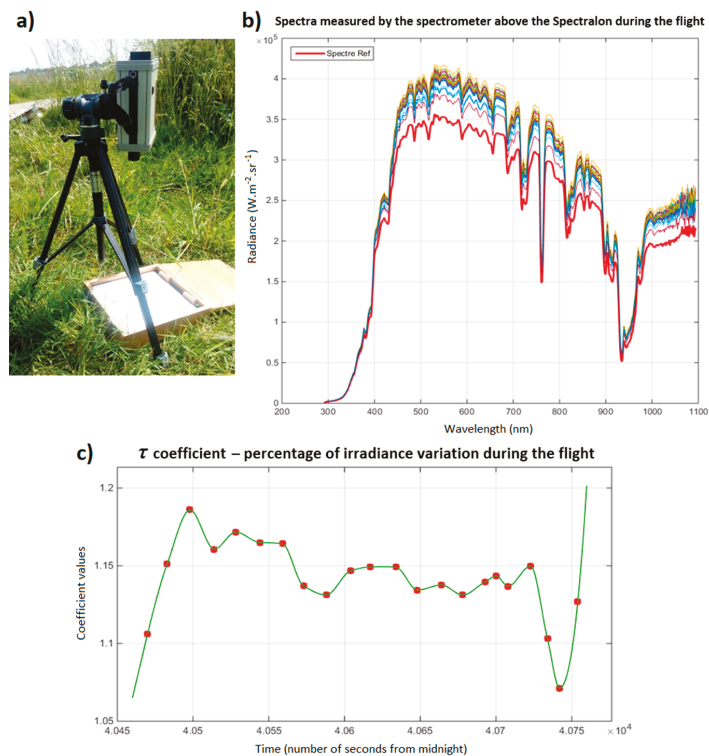


Figure 5. (a) Field spectrometer (GER 1500) measuring the irradiance variability above the white Spectralon. (b) Example of variability of the spectra measured by the field spectrometer during a flight. (c) Example of the τ coefficient interpolated (green line) from the percentage of irradiance variations measured (red dots) during the flight.

To complete this procedure of radiometric corrections, a signal enhancement was performed, using a minimum noise fraction (MNF) transform, as implemented in *ENVI*[®] software (modified from [57]). A forward transform is performed to manually identify the bands containing the coherent images and those containing noise-dominated images. Noise is removed from the data by performing an inverse transform using a spectral subset which only includes the bands with a high signal-to-noise ratio.

4. Results

With the configuration used, a flight of about 10 minutes can collect usable hyperspectral images (i.e., excluding take-off, landing, and turning phases) over an area of about $2.6 \times 104 \text{ m}^2$ (2.6 ha), with a resolution of $4.5 \text{ cm} \times 6 \text{ cm}$. The reflectance spectra obtained at each pixel are inherent signatures of the targeted surfaces, resulting from the presence, the shape, and the position/orientation of specific absorption features, such as pigments, which compose the surface. For identification and classification purposes, the spectrum of each class of targets has to be uniquely characterized by its general shape, combined with local absorption or reflectance peaks.

The quality of the results is assessed in two ways:

(i) Firstly, by comparing the spectra obtained from Hyper-DRELIO imagery with spectra, measured by the field spectrometer on the same types of substrates or sediment coverage.

(ii) Secondly, by comparing spectra from Hyper-DRELIO imagery acquired at two different times on a surface assumed to be stable over time—in this case, sand.

4.1. Comparison to Field Spectrometer

Hyper-DRELIO imagery and field spectrometer control measurements are not exactly synchronous (separated by a few minutes to an hour). In addition, since the field spectrometer measurements are performed from the fixed platform, they can be separated from the Hyper-DRELIO images by several tens of meters. Differences between the spectra may appear, depending on the type/concentration of the benthic biofilm, which is related to the tidal time or on local variations of the targeted materials (concentration, structure, spectral mixing, or surface orientation).

Figures 6 and 7 show the spectra obtained over the sediment surface covered by benthic biofilm and over the pioneer mangroves, respectively. For a given class of targets, the characteristics of the spectra are globally similar between the field spectrometer and Hyper-DRELIO imagery, with local minima and maxima being clearly identifiable, both for the benthic biofilm and the pioneer mangroves. Thus, Hyper-DRELIO imagery succeeds in spatially capturing the spectral specificities of each target class. However, Hyper-DRELIO data are noisier for wavelengths higher than 800 nm. To evaluate the degree of similarity between the Hyper-DRELIO reflectance spectra and the field spectrometer reflectance spectra, we used a correlation coefficient to compare the reflectance levels and the spectral angle mapper (SAM) method [58]. The SAM “distance” assesses the similarity between the shape of two spectra by calculating the angle between these spectra and is, therefore, less sensitive to multiplicative noise. The smaller the SAM distance, the higher the similarity (two exactly similar spectra would have a zero SAM distance). We compare the mean value of three spectra measured by the field spectrometer (Figures 6b and 7c) and the mean value of eight spectra extracted from Hyper-DRELIO images (Figures 6c and 7d) for the two biota. Above the benthic biofilm, a SAM distance of 0.039 and a correlation coefficient of 0.96 were found. Above the pioneer mangrove, the SAM distance was 0.159 and the correlation coefficient was 0.97.

With a small pixel size, the probability of capturing different class of targets in a pixel is limited. Nevertheless, a very high spatial resolution also captures some complexities that are not visible at lower resolutions, such as the structure of the foliage. Figures 6c and 7d show a disparity between the spectra extracted from Hyper-DRELIO imagery (mean standard deviation of 0.004 for the biofilm, and 0.061 for the mangrove, respectively). In the visible spectrum, the spectral signature is mainly influenced by pigment composition. In NIR (near infrared), the spectrum is rather influenced by the structure and water content of the target. That explains the higher disparity (particularly in NIR) obtained among mangrove spectra, extracted from Hyper-DRELIO imagery.

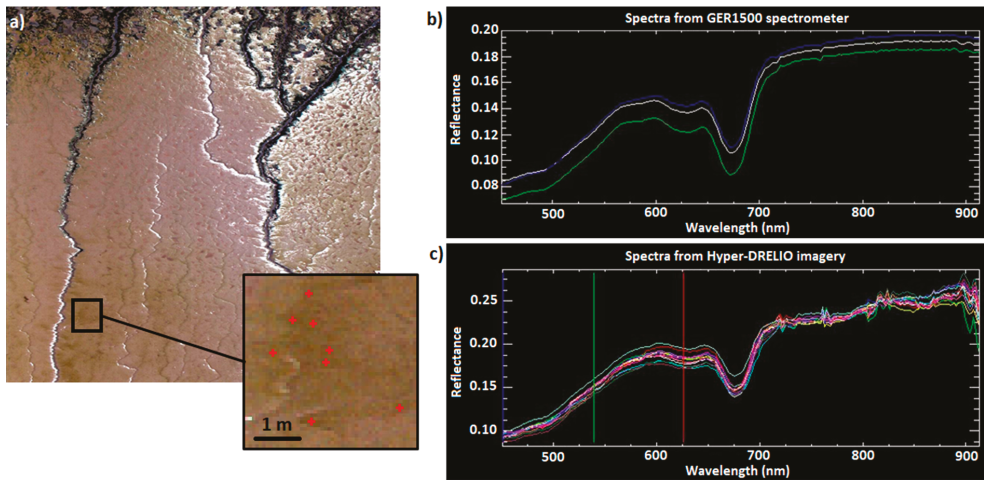


Figure 6. Spectra comparison above the benthic biofilm. (a) Biofilm patch on the Hyper-DRELIO image (in natural colours) where the spectra are pointed (red crosses). The image was acquired on 2018-09-12 at 13:15. (b) Biofilm spectra measured by GER1500 spectrometer. (c) Biofilm spectra extracted from Hyper-DRELIO imagery (mean standard deviation between the reflectance spectra: 0.004).

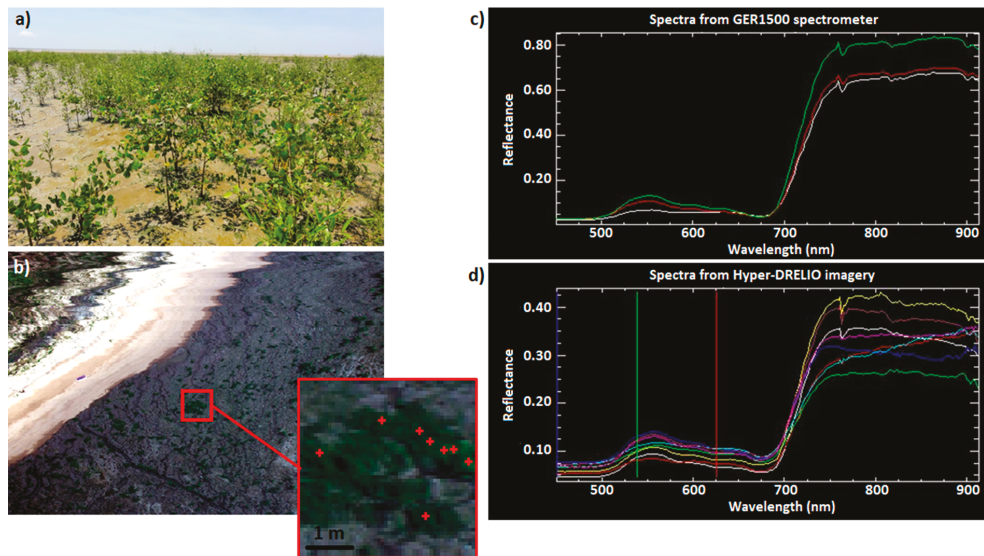


Figure 7. Spectra comparison above the pioneer mangroves. (a) Aerial oblique photograph of the pioneer mangroves. (b) Mangrove patch on the Hyper-DRELIO image (in natural colours) where the spectra are pointed (red crosses). The image was acquired on 12 September 2018 at 11:08. (c) Mangrove spectra measured by GER1500 spectrometer. (d) Mangrove spectra extracted from Hyper-DRELIO imagery (mean standard deviation between the reflectance spectra: 0.061).

4.2. Relative Comparison over the Sandy Beach

As the flights were conducted at different times of the day, one way of checking the effectiveness of the radiometric corrections is to compare the spectra acquired several hours apart over the same substrate. Since the surface texture of the mudflat may change during the tidal cycle because of biofilm development, desiccation, and/or bioturbation

processes, the part of the study area assumed to change the least over time was the upper sandy beach.

Two sets of five spectra were extracted on the supra-tidal part of the beach for the flight on 12 September 2018 at 11:30 (Flight 1) and for the flight on 12 September 2018 at 13:30 (Flight 2). From these spectra (Figure 8), the intra-set variability (for the same flight) was evaluated from the standard deviation (averaged over all wavelengths). For the spectra of Flight 1 (respectively, Flight 2), the standard deviation was 0.024 (or 5.48%), respectively, 0.037 (or 8.81%) for Flight 2. The quality of the radiometric corrections was assessed by comparing the average spectra from the two data sets (Vol 1 and Vol 2). The average difference between these average spectra was 0.026 (or 5.64%). This deviation was considered satisfactory as it was of the same order of magnitude as the intra-set variability.

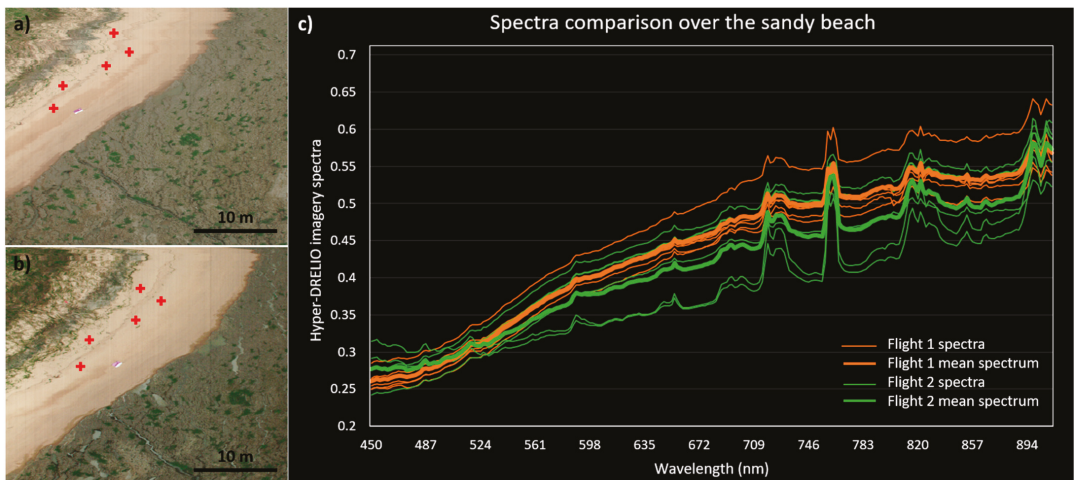


Figure 8. Spectra comparison above the supra-tidal sandy beach. (a,b) Sandy beach on the Hyper-DRELI0 images (in natural colours) where the spectra are pointed (red crosses). The images were acquired on 12 September 2018 at 11:08 (Flight 1) (a) and on 12 September 2018 at 13:14 (Flight 2) (b). (c) Sand spectra extracted from Hyper-DRELI0 imagery for Flight 1 (orange colour) and Flight 2 (green colour). The mean spectrum for each data set is depicted in bold.

5. Discussion

As previously mentioned, the goal of this study was to propose an efficient and easily implemented method to perform radiometric corrections of UAV-borne hyperspectral imagery—without adding embedded sensors and with minimum equipment (i.e., only two Spectralon panels and a field spectrometer)—which is adequate for “hard-to-access” ecosystems, such as the huge intertidal mudbanks along the Amazon-influenced, northeast coast of South America. Smith and Milton [55] reported that the empirical line method allows the calibration of remotely sensed data to reflectance with errors of only a few percent. This efficiency was confirmed for our UAV data by the obtained SAM distances and correlation scores. Here, we calculated a higher SAM distance for the pioneer mangrove forest than for the benthic biofilm. This result is coherent with the higher diversity observed among the mangroves spectra (both with the field spectrometer and with the UAV-borne camera—Figure 7c,d). Indeed, point-wise measurement (with the field spectrometer) and very high spatial resolution hyperspectral images (with UAV-borne camera) reflect the complex morphology induced by the mangroves canopy. On the contrary, a slightly lower correlation coefficient was obtained for the benthic biofilm. This could be due to the higher disparity, both spatially and temporally, of the biofilm concentration at the sediment surface, alongside local changes in sediment elevation and bioturbation activities [37].

This method of radiometric corrections, especially the initial calibration step, can also be used to monitor the drift of the manufacturer's calibration. As previously mentioned, Hyper-DRELIO data are noisier for wavelengths higher than 800 nm. Proctor and He [8] explained that this effect is common and is due to the combination of a sharp decrease of quantum efficiency in the NIR, the lower solar output in the NIR, and reduced sensitivity of the imager resulting in lower signal and greater noise. The proposed radiometric correction process relies on simplifying assumptions, which are likely to cause some errors. For instance, remaining noise can be due to DC, which has been considered steady here. Besides, as the "sun–target–sensor" geometry varies for all the pixels recorded by the camera, bidirectional reflectance effects can also influence the signal [33]. As mentioned by Garzonio et al. [34], light intensity could be optimized by placing neutral filters to avoid saturation for very high light intensities. Lastly, the proposed approach to take into account temporal variations of irradiance suits for the variations of ambient light but fails to take into account local effects, which are not captured by the field spectrometer above the 99% Spectralon panel. Therefore, some parts of the images can be affected by spatial changes in the illumination fields, due to isolated clouds or shadows originating from the geometrical configuration of the scene (e.g., presence of trees).

Moreover, as the Spectralon panels are of great importance in this method for radiometric corrections, the results would be sensitive to defects in Spectralon surfaces. For that matter, Bachmann et al. [48] mention that white Spectralon panels are subject to repeated handling and exposed to various environmental factors. Therefore, their calibration coefficients drift over time.

The methodology proposed can be extended to other types of areas, provided that topography-induced illumination differences are taken into account [59].

For now, we have not assessed the impact of platform vibrations on the radiometric and spectral stability of the hyperspectral camera (shift, band broadening, etc.). According to Garzonio et al. [34], however, the impact of platform mechanical vibrations would be almost insignificant in terms of band centre, width, and radiometric response.

Field access in the mangroves developing under Amazonian influence is particularly difficult. Thus, in this particular rapidly evolving ecosystem, future work should aim to assess the extent to which the very high spatial and spectral resolution provided by hyperspectral UAV can capture the biological complexity of the substrate. The good correlations found in this study between drone imagery after radiometric corrections and the in situ spectrometer measurements for the benthic biofilm and pioneer mangroves should allow simultaneous mapping of mangrove forests and benthic biofilm distribution at the mudbank scale, integrating small-scale heterogeneity, caused by the combined effects of geomorphology, tides, and biology (e.g., bioturbation). This method, tested in mangroves under limited human impacts, shows new possibilities for monitoring mangrove ecosystems facing different levels of pressure and subsequent alteration along the nearby coastline (Guyana and Surinam), as well as in other biogeographic regions with other mangrove species and dynamics.

6. Conclusions

Hyper-DRELIO allowed hyperspectral data to be collected above few hectares of mangrove forests and mudbanks in French Guiana, with both high spatial resolution and high spectral resolution in the VNIR domain. One of the main advantages of drones being their flexibility, the associated imagery calibration procedures have to be as simple as possible to keep the latter. This study proposes an easy, in situ radiometric calibration method, dedicated to drone-based hyperspectral surveys, without adding embedded sensors and with minimum equipment, using only two Spectralon (white and grey) and a ground spectrometer. The proposed procedure enables to calibrate the sensor, by correcting lining effects and transforming the raw relative DN generated by the hyperspectral camera into reflectance values standardized to in situ illumination conditions.

The radiometric corrections were applied to a small subset of a dataset collected above mudbanks colonised by benthic biofilm and a pioneer mangrove forest. Besides the fact that the shapes of spectra are globally consistent between the radiometrically corrected Hyper-DRELIO spectra and the in situ typical spectra, their degree of similarity was assessed using the SAM distance and correlation coefficient. SAM distance values of 0.039 above biofilm and 0.159 above pioneer mangrove forest, together with associated correlation coefficients (of 0.96 and 0.97, respectively), are greatly satisfying for substrate classification. Future work will consist of applying this method to the entire study area, in order to spatialize the results, and comparing hyperspectral and in situ data in order to obtain the finest possible classification of the various detectable elements.

Author Contributions: Conceptualization, M.J. and G.S.; data curation, M.J.; formal analysis, M.J., G.B. and P.L.; funding acquisition, E.M., N.L.D. and C.D.; investigation, M.J., G.B., E.M., J.A., P.G., G.T. and J.F.; methodology, M.J. and G.S.; project administration, E.M.; resources, E.M., G.T. and C.D.; software, M.J.; supervision, E.M., N.L.D., P.L., G.T. and C.D.; validation, M.J. and G.B.; visualization, M.J.; writing—original draft preparation, M.J., G.B. and E.M.; writing—review and editing, M.J., G.S., G.B., E.M., N.L.D., G.T. and C.D. All authors have read and agreed to the published version of the manuscript.

Funding: This research was funded by the French National Agency under the programs “Investissements d’Avenir” (LabexMER: ANR-10-LABX-19; EQUIPEX CRITEX: ANR-11-EQPX-0011) and by the CNRS MITI program (“Pépière Interdisciplinaire de Guyane” through the BIOGEMORPHO project). This work was supported by ISblue project, Interdisciplinary graduate school for the blue planet (ANR-17-EURE-0015) and co-funded by a grant from the French government under the program “Investissements d’Avenir”.

Institutional Review Board Statement: Not applicable.

Informed Consent Statement: Not applicable.

Data Availability Statement: Data available on request due to privacy restrictions.

Acknowledgments: The authors are grateful to the Reserve Naturelle de l’Amana, Parc Naturel Régional de Guyane, DEAL Guyane for the use of their facilities and to I. Bihannic, A. Gardel, M. Jolivet, and S. Morvan for their help on the field. This paper is a GDR Liga’s contribution.

Conflicts of Interest: The authors declare no conflict of interest.

References

- Sandilyan, S.; Kathiresan, K. Mangrove Conservation: A Global Perspective. *Biodivers. Conserv.* **2012**, *21*, 3523–3542. [[CrossRef](#)]
- Alongi, D.M. Mangrove Forests: Resilience, Protection from Tsunamis; and Responses to Global Climate Change. *Estuar. Coast. Shelf Sci.* **2008**, *76*, 1–13. [[CrossRef](#)]
- Thomas, N.; Lucas, R.; Bunting, P.; Hardy, A.; Rosenqvist, A.; Simard, M. Distribution and Drivers of Global Mangrove Forest Change, 1996–2010. *PLoS ONE* **2017**, *12*, e0179302. [[CrossRef](#)] [[PubMed](#)]
- Green, E.P.; Clark, C.D.; Mumby, P.J.; Edwards, A.J.; Ellis, A.C. Remote Sensing Techniques for Mangrove Mapping. *Int. J. Remote Sens.* **1998**, *19*, 935–956. [[CrossRef](#)]
- Kuenzer, C.; Bluemel, A.; Gebhardt, S.; Quoc, T.V.; Dech, S. Remote Sensing of Mangrove Ecosystems: A Review. *Remote Sens.* **2011**, *3*, 878–928. [[CrossRef](#)]
- Wang, L.; Jia, M.; Yin, D.; Tian, J. A Review of Remote Sensing for Mangrove Forests: 1956–2018. *Remote Sens. Environ.* **2019**, *231*, 111223. [[CrossRef](#)]
- Schaepman, M.E.; Ustin, S.L.; Plaza, A.J.; Painter, T.H.; Verrelst, J.; Liang, S. Earth System Science Related Imaging Spectroscopy—An Assessment. *Remote Sens. Environ.* **2009**, *113*, 123–137. [[CrossRef](#)]
- Proctor, C.; He, Y. Workflow for Building a Hyperspectral UAV: Challenges and Opportunities. *ISPRS Ann. Photogramm. Remote Sens. Spat. Inf. Sci.* **2009**, *XL-1/W4*, 415–419. [[CrossRef](#)]
- Launeau, P.; Kassouk, Z.; Debaine, F.; Roy, R.; Mestayer, P.G.; Boulet, C.; Rouaud, J.-M.; Giraud, M. Airborne Hyperspectral Mapping of Trees in an Urban Area. *Int. J. Remote Sens.* **2017**, *38*, 1277–1311. [[CrossRef](#)]
- Kruse, F.A.; Boardman, J.W.; Huntington, J.F. Comparison of Airborne Hyperspectral Data and Eo-1 Hyperion for Mineral Mapping. *IEEE Trans. Geosci. Remote Sens.* **2003**, *41*, 1388–1400. [[CrossRef](#)]
- Burai, P.; Deák, B.; Valkó, O.; Tomor, T. Classification of Herbaceous Vegetation Using Airborne Hyperspectral Imagery. *Remote Sens.* **2015**, *7*, 2046–2066. [[CrossRef](#)]

12. Kamal, M.; Phinn, S. Hyperspectral data for mangrove species mapping: A comparison of pixel-based and object-based approach. *Remote Sens.* **2011**, *3*, 2222–2242. [[CrossRef](#)]
13. Peerbhaya, K.Y.; Mutanga, O.; Ismail, R. Commercial tree species discrimination using airborne AISA Eagle hyperspectral imagery and partial least squares discriminant analysis (PLS-DA) in KwaZulu–Natal, South Africa. *ISPRS J. Photogramm. Remote Sens.* **2013**, *79*, 19–28. [[CrossRef](#)]
14. Richter, R.; Reu, B.; Wirth, C.; Doktor, D.; Vohland, M. The use of airborne hyperspectral data for tree species classification in a species-rich Central European forest area. *Int. J. Appl. Earth Obs. Geoinf.* **2016**, *52*, 464–474. [[CrossRef](#)]
15. Yang, C.; Everitt, J.H.; Fletcher, R.S.; Jensen, R.R.; Mausell, P.W. Evaluating AISA + Hyperspectral Imagery for Mapping Black Mangrove along the South Texas Gulf Coast. *Photogramm. Eng. Remote Sens.* **2009**, *4*, 425–435. [[CrossRef](#)]
16. Chaube, N.R.; Lele, N.; Misra, A.; Murthy, T.; Manna, S.; Hazra, S.; Panda, M.; Samal, R.N. Mangrove species discrimination and health assessment using AVIRIS-NG hyperspectral data. *Curr. Sci.* **2019**, *116*, 1136. [[CrossRef](#)]
17. Hati, J.P.; Goswami, S.; Samanta, S.; Pramanick, N.; Majumdar, S.D.; Chaube, N.R.; Misra, A.; Hazra, S. Estimation of vegetation stress in the mangrove forest using AVIRIS-NG airborne hyperspectral data. *Model. Earth Syst. Environ.* **2021**, *7*, 1877–1889. [[CrossRef](#)]
18. Hati, J.P.; Samanta, S.; Chaube, N.R.; Misra, A.; Giri, S.; Pramanick, N.; Gupta, K.; Majumdar, S.D.; Chanda, A.; Mukhopadhyay, A.; et al. Mangrove classification using airborne hyperspectral AVIRIS-NG and comparing with other spaceborne hyperspectral and multispectral data. *Egypt. J. Remote Sens. Space Sci.* **2021**, *24*, 273–281. [[CrossRef](#)]
19. Jiang, Y.; Zhang, L.; Yan, M.; Qi, J.; Fu, T.; Fan, S.; Chen, B. High-Resolution Mangrove Forests Classification with Machine Learning Using Worldview and UAV Hyperspectral Data. *Remote Sens.* **2021**, *13*, 1529. [[CrossRef](#)]
20. Liu, L.; Coops, N.C.; Aven, N.W.; Pang, Y. Mapping urban tree species using integrated airborne hyperspectral and LiDAR remote sensing data. *Remote Sens. Environ.* **2017**, *200*, 170–182. [[CrossRef](#)]
21. Li, Q.; Wong, F.K.K.; Fung, T. Mapping multi-layered mangroves from multispectral, hyperspectral, and LiDAR data. *Remote Sens. Environ.* **2021**, *258*, 112403. [[CrossRef](#)]
22. Stuart, M.B.; McGonigle, A.J.S.; Willmott, J.R. Hyperspectral Imaging in Environmental Monitoring: A Review of Recent Developments and Technological Advances in Compact Field Deployable Systems. *Sensors* **2019**, *19*, 3071. [[CrossRef](#)] [[PubMed](#)]
23. Cao, J.; Leng, W.; Liu, K.; Liu, L.; He, Z.; Zhu, Y. Object-based mangrove species classification using unmanned aerial vehicle hyperspectral images and digital surface models. *Remote Sens.* **2018**, *10*, 89. [[CrossRef](#)]
24. Liu, X.; Wang, L. Feasibility of using consumer-grade unmanned aerial vehicles to estimate leaf area index in Mangrove forest. *Remote Sens. Lett.* **2018**, *9*, 1040–1049. [[CrossRef](#)]
25. Jaakkola, A.; Hyypä, J.; Kukko, A.; Yu, X.; Kaartinen, H.; Lehtomäki, M.; Lin, Y. A low-cost multi-sensoral mobile mapping system and its feasibility for tree measurements. *ISPRS J. Photogramm. Remote Sens.* **2010**, *65*, 514–522. [[CrossRef](#)]
26. Kosugi, Y.; Mukoyama, S.; Takabayashi, Y.; Uto, K.; Oda, K.; Saito, G. Low-altitude hyperspectral observation of paddy using radio-controlled helicopter. In Proceedings of the IEEE International Geoscience and Remote Sensing Symposium (IGARSS), Vancouver, BC, Canada, 24–29 July 2011; pp. 1748–1751.
27. Hruska, R.; Mitchell, J.; Anderson, M.; Glenn, N.F. Radiometric and Geometric Analysis of Hyperspectral Imagery Acquired from an Unmanned Aerial Vehicle. *Remote Sens.* **2012**, *4*, 2736–2752. [[CrossRef](#)]
28. Gallay, M.; Eck, C.; Zraggen, C.; Kaňuk, J.; Dvorný, E. High Resolution Airborne Laser Scanning and Hyperspectral Imaging with a small UAV platform. *ISPRS Ann. Photogramm. Remote Sens. Spat. Inf. Sci.* **2016**, *XLI-B1*, 823–827. [[CrossRef](#)]
29. Lucieer, A.; Malenovsky, Z.; Veness, T.; Wallace, L. HyperUAS—Imaging Spectroscopy from a Multirotor Unmanned Aircraft System. *J. Field Rob.* **2014**, *31*, 571–590. [[CrossRef](#)]
30. Jaud, M.; Le Dantec, N.; Ammann, J.; Grandjean, P.; Constantin, D.; Akhtman, Y.; Barbioux, K.; Allemand, P.; Delacourt, C.; Merminod, B. Direct Georeferencing of a Pushbroom, Lightweight Hyperspectral System for Mini-UAV Applications. *Remote Sens.* **2018**, *10*, 204. [[CrossRef](#)]
31. Oliveira, R.A.; Tommaselli, A.M.G.; Honkavaara, E. Generating a Hyperspectral Digital Surface Model Using a Hyperspectral 2D Frame Camera. *ISPRS J. Photogramm. Remote Sens.* **2019**, *147*, 345–360. [[CrossRef](#)]
32. Saari, H.; Pölonen, I.; Salo, H.; Honkavaara, E.; Hakala, T.; Holmlund, C.; Mäkynen, J.; Mannila, R.; Antila, T.; Akujärvi, A. Miniaturized hyperspectral imager calibration and uav flight campaigns. In Proceedings of the SPIE, Sensors, Systems, and Next-Generation Satellites XVII, Dresden, Germany, 24 October 2013; Volume 8889. [[CrossRef](#)]
33. Aasen, H.; Burkart, A.; Bolten, A.; Bareth, G. Generating 3D Hyperspectral Information with Lightweight UAV Snapshot Cameras for Vegetation Monitoring: From Camera Calibration to Quality Assurance. *ISPRS J. Photogramm. Remote Sens.* **2015**, *108*, 245–259. [[CrossRef](#)]
34. Garzonio, R.; Di Mauro, B.; Colombo, R.; Cogliati, S. Surface Reflectance and Sun-Induced Fluorescence Spectroscopy Measurements Using a Small Hyperspectral UAS. *Remote Sens.* **2017**, *9*, 472. [[CrossRef](#)]
35. Burkart, A.; Cogliati, S.; Schickling, A.; Rascher, U. A Novel UAV-Based Ultra-Light Weight Spectrometer for Field Spectroscopy. *IEEE Sens. J.* **2014**, *14*, 62–67. [[CrossRef](#)]
36. Jaud, M.; Grasso, F.; Le Dantec, N.; Verney, R.; Delacourt, C.; Ammann, J.; Deloffre, J.; Grandjean, P. Potential of UAVs for Monitoring Mudflat Morphodynamics (Application to the Seine Estuary, France). *ISPRS Int. J. Geoinf.* **2016**, *5*, 50. [[CrossRef](#)]

37. Brunier, G.; Michaud, E.; Fleury, J.; Anthony, E.J.; Morvan, S.; Gardel, A. Assessing the relationships between macro-faunal burrowing activity and mudflat geomorphology from UAV-based Structure-from-Motion photogrammetry. *Remote Sens. Environ.* **2020**, *241*, 111717. [[CrossRef](#)]
38. Jolivet, M.; Anthony, E.J.; Gardel, A.; Brunier, G. Multi-Decadal to Short-Term Beach and Shoreline Mobility in a Complex River-Mouth Environment Affected by Mud From the Amazon. *Front. Earth Sci.* **2019**, *7*, 187. [[CrossRef](#)]
39. Anthony, E.J.; Gratiot, N. Coastal Engineering and Large-Scale Mangrove Destruction in Guyana; South America: Averting an Environmental Catastrophe in the Making. *Ecol. Eng.* **2012**, *47*, 268–273. [[CrossRef](#)]
40. Fromard, F.; Puig, H.; Mougou, E.; Marty, G.; Betoulle, J.L.; Cadamuro, L. Structure, above-ground biomass and dynamics of mangrove ecosystems: New data from French Guiana. *Oecologia* **1998**, *115*, 39–53. [[CrossRef](#)]
41. Gardel, A.; Gensac, E.; Anthony, E.; Lesourd, S.; Loisel, H.; Marin, D. Wave-formed mud bars: Their morphodynamics and role in opportunistic mangrove colonization. *J. Coast. Res.* **2011**, *Special Issue 64*, 384–387.
42. Aschenbroich, A.; Michaud, E.; Stieglitz, T.; Fromard, F.; Gardel, A.; Tavares, M.; Thouzeau, G. Brachyuran crab community structure and associated sediment reworking activities in pioneer and young mangroves of French Guiana, South America. *Estuar. Coast. Shelf Sci.* **2016**, *182*, 60–71. [[CrossRef](#)]
43. Aller, R.C.; Blair, N.E. Carbon Remineralization in the Amazon–Guianas Tropical Mobile Mudbelt: A Sedimentary Incinerator. *Cont. Shelf Res.* **2006**, *26*, 2241–2259. [[CrossRef](#)]
44. Gontharet, S.; Mathieu, O.; Lévêque, J.; Milloux, M.-J.; Lesourd, S.; Philippe, S.; Caillaud, J.; Gardel, A.; Sarrazin, M.; Proisy, C. Distribution and Sources of Bulk Organic Matter (OM) on a Tropical Intertidal Mud Bank in French Guiana from Elemental and Isotopic Proxies. *Chem. Geol.* **2014**, *376*, 1–10. [[CrossRef](#)]
45. Ray, R.; Michaud, E.; Aller, R.; Vantrepotte, V.; Gleixner, G.; Walcker, R.; Devesa, J.; Le Goff, M.; Morvan, S.; Thouzeau, G. The sources and distribution of carbon (DOC, POC, DIC) in a mangrove dominated estuary (French Guiana, South America). *Biogeochemistry* **2018**, *138*, 297–321. [[CrossRef](#)]
46. Ray, R.; Thouzeau, G.; Walcker, R.; Vantrepotte, V.; Gleixner, G.; Morvan, S.; Devesa, J.; Michaud, E. Mangrove-Derived Organic and Inorganic Carbon Exchanges Between the Sinnamary Estuarine System (French Guiana, South America) and Atlantic Ocean. *J. Geophys. Res. Biogeosci.* **2020**, *125*, e2020JG005739. [[CrossRef](#)]
47. Brunier, G.; Anthony, E.J.; Gratiot, N.; Gardel, A. Exceptional Rates and Mechanisms of Muddy Shoreline Retreat Following Mangrove Removal. *Earth Surf. Process. Landf.* **2019**, *44*, 1559–1571. [[CrossRef](#)]
48. Bachmann, C.M.; Montes, M.J.; Parrish, C.E.; Fusina, R.A.; Nichols, C.R.; Li, R.-R.; Hallenborg, E.; Jones, C.A.; Lee, K.; Sellars, J.; et al. A Dual-Spectrometer Approach to Reflectance Measurements under Sub-Optimal Sky Conditions. *Opt. Express* **2012**, *20*, 8959. [[CrossRef](#)]
49. Kazempour, F.; Méléder, V.; Launeau, P. Optical Properties of Microphytobenthic Biofilms (MPBOM): Biomass Retrieval Implication. *J. Quant. Spectrosc. Radiat. Transf.* **2011**, *112*, 131–142. [[CrossRef](#)]
50. Launeau, P.; Méléder, V.; Verpoorter, C.; Barillé, L.; Kazempour-Ricci, F.; Giraud, M.; Jesus, B.; Le Menn, E. Microphytobenthos Biomass and Diversity Mapping at Different Spatial Scales with a Hyperspectral Optical Model. *Remote Sens.* **2018**, *10*, 716. [[CrossRef](#)]
51. Cho, M.A.; Skidmore, A.K. A New Technique for Extracting the Red Edge Position from Hyperspectral Data: The Linear Extrapolation Method. *Remote Sens. Environ.* **2006**, *101*, 181–193. [[CrossRef](#)]
52. Alvarez-Vanhard, E.; Houet, T.; Mony, C.; Lecoq, L.; Corpetti, T. Can UAVs Fill the Gap between in Situ Surveys and Satellites for Habitat Mapping? *Remote Sens. Environ.* **2020**, *243*, 111780. [[CrossRef](#)]
53. Aasen, H.; Bendig, J.; Bolten, A.; Bennertz, S.; Willkomm, M.; Bareth, G. Introduction and Preliminary Results of a Calibration for Full-Frame Hyperspectral Cameras to Monitor Agricultural Crops with UAVs. *ISPRS Ann. Photogramm. Remote Sens. Spat. Inf. Sci.* **2014**, *XL-7*, 1–8. [[CrossRef](#)]
54. Honkavaara, E.; Khoramshahi, E. Radiometric Correction of Close-Range Spectral Image Blocks Captured Using an Unmanned Aerial Vehicle with a Radiometric Block Adjustment. *Remote Sens.* **2018**, *10*, 256. [[CrossRef](#)]
55. Smith, G.M.; Milton, E.J. The Use of the Empirical Line Method to Calibrate Remotely Sensed Data to Reflectance. *Int. J. Remote Sens.* **1999**, *20*, 2653–2662. [[CrossRef](#)]
56. Näsi, R.; Honkavaara, E.; Blomqvist, M.; Lyytikäinen-Saarenmaa, P.; Hakala, T.; Viljanen, N.; Kantola, T.; Holopainen, M. Remote Sensing of Bark Beetle Damage in Urban Forests at Individual Tree Level Using a Novel Hyperspectral Camera from UAV and Aircraft. *Urban. For. Urban. Green.* **2018**, *30*, 72–83. [[CrossRef](#)]
57. Green, A.; Berman, M.; Switzer, P.; Craig, M.D. A transformation for ordering multispectral data in terms of image quality with implications for noise removal. *IEEE Trans. Geosci. Remote Sens.* **1988**, *26*, 65–74. [[CrossRef](#)]
58. Kruse, F.A.; Lefkoff, A.B.; Boardman, J.B.; Heidbrecht, K.B.; Shapiro, A.T.; Barloon, P.J.; Goetz, A.F.H. The Spectral Image Processing System (SIPS)—Interactive Visualization and Analysis of Imaging spectrometer data. *Remote Sens. Environ.* **1993**, *44*, 145–163. [[CrossRef](#)]
59. Lorenz, S.; Salehi, S.; Kirsch, M.; Zimmermann, R.; Unger, G.; Vest Sørensen, E.; Gloaguen, R. Radiometric Correction and 3D Integration of Long-Range Ground-Based Hyperspectral Imagery for Mineral Exploration of Vertical Outcrops. *Remote Sens.* **2018**, *10*, 176. [[CrossRef](#)]



Article

Spatiotemporal Trends of Bora Bora's Shoreline Classification and Movement Using High-Resolution Imagery from 1955 to 2019

Emma Gairin ^{1,2,3,*}, Antoine Collin ^{1,4}, Dorothée James ¹, Tehani Maueau ⁵, Yoann Roncin ⁶, Lucas Lefort ⁶, Franck Dolique ⁷, Matthieu Jeanson ^{8,9} and David Lecchini ^{4,10}

¹ Section des Sciences de la Vie et de la Terre, EPHE-PSL University, CNRS LETG, 35800 Dinard, France; antoine.collin@ephe.psl.eu (A.C.); dorothee.james@ephe.psl.eu (D.J.)

² Département de Biologie, École Normale Supérieure, PSL University, 75005 Paris, France

³ Okinawa Institute of Science and Technology, 1919-1 Tancha, Onna-Son, Kunigami District, Okinawa 904-0495, Japan

⁴ LabEx CORAIL, 98729 Papetoai, French Polynesia, France; david.lecchini@ephe.psl.eu

⁵ Association Ia Vai Ma Noa Bora-Bora, 98730 Bora-Bora, French Polynesia, France; tehanimaueau@netcourrier.com

⁶ Section Cadastre-Topographie de la Direction des Affaires Foncières (DAF), 98713 Papeete, French Polynesia, France; yoann.roncin@foncier.gov.pf (Y.R.); lucas.lefort@foncier.gov.pf (L.L.)

⁷ Laboratoire de Biologie des Organismes et Écosystèmes Aquatiques (BOREA), Université des Antilles-MNHN-CNRS 8067-SU-IRD 207-UCN, 97275 Schoelcher, Martinique, France; franck.dolique@univ-antilles.fr

⁸ ESPACE-DEV, Univ Montpellier, IRD, Univ Antilles, Univ Guyane, Univ Réunion, 34000 Montpellier, France; matthieu.jeanson@univ-mayotte.fr

⁹ Département Lettres et Sciences Humaines, University Center of Mayotte CUFR, BP53 Dombeni, Mayotte, France

¹⁰ EPHE-PSL University, CRIOBE, BP 1013 Papetoai, French Polynesia, France

* Correspondence: emma.gairin@oist.jp

Citation: Gairin, E.; Collin, A.; James, D.; Maueau, T.; Roncin, Y.; Lefort, L.; Dolique, F.; Jeanson, M.; Lecchini, D. Spatiotemporal Trends of Bora Bora's Shoreline Classification and Movement Using High-Resolution Imagery from 1955 to 2019. *Remote Sens.* **2021**, *13*, 4692. <https://doi.org/10.3390/rs13224692>

Academic Editors: Dar Roberts, Junshi Xia and Simona Niculescu

Received: 31 October 2021

Accepted: 17 November 2021

Published: 20 November 2021

Publisher's Note: MDPI stays neutral with regard to jurisdictional claims in published maps and institutional affiliations.



Copyright: © 2021 by the authors. Licensee MDPI, Basel, Switzerland. This article is an open access article distributed under the terms and conditions of the Creative Commons Attribution (CC BY) license (<https://creativecommons.org/licenses/by/4.0/>).

Abstract: Coastal urbanisation is a widespread phenomenon throughout the world and is often linked to increased erosion. Small Pacific islands are not spared from this issue, which is of great importance in the context of climate change. The French Polynesian island of Bora Bora was used as a case study to investigate the historical evolution of its coastline classification and position from 1955 to 2019. A time series of very high-resolution aerial imagery was processed to highlight the changes of the island's coastline. The overall length of natural shores, including beaches, decreased by 46% from 1955 to 2019 while human-made shores such as seawalls increased by 476%, and as of 2019 represented 61% of the coastline. This evolution alters sedimentary processes: the time series of aerial images highlights increased erosion in the vicinity of seawalls and embankments, leading to the incremental need to construct additional walls. In addition, the gradual removal of natural shoreline types modifies landscapes and may negatively impact marine biodiversity. Through documenting coastal changes to Bora Bora over time, this study highlights the impacts of human-made structures on erosional processes and underscores the need for sustainable coastal management plans in French Polynesia.

Keywords: coast; erosion; urbanisation; airborne imagery; spaceborne imagery; French Polynesia

1. Introduction

Since the end of the 19th century, coastal areas have become increasingly sought-after worldwide, and are now largely urbanised [1]. Human populations have grown, with numerous urban centres and cities located along the shore. Infrastructures such as harbours, marinas, and seaside roads have been developed to support local development as well as global maritime trade and transport. This phenomenon is particularly widespread

in Europe, Asia, Australia, and the USA, where up to 50% of coastlines are modified by engineering works [2]. However, the tropical Pacific Ocean, and the French Polynesian island of Bora Bora in particular, have not been spared. In French Polynesia, coastlines have been strongly modified for a range of reasons, mostly since the mid-1900s, from acquiring more land through infilling shallow reef areas to building walls to protect constructions from waves [3–6]. These modifications alter sediment transport processes. Along with the dredging of fringing reefs to open navigation channels, sea level rise, and background sediment transport, these modifications lead to changes in shoreline position [7].

These changes, beyond altering coastal landscapes, have impacts on local livelihoods as well as on economic activities. Many urban centres and residential areas are located along the coastline in French Polynesia, notably due to the lack of inland space, either due to steep topographies (e.g., for the volcanic Society islands such as Bora Bora) or simply to the limited size of the islands (e.g., in the case of the Tuamotu atolls). Furthermore, increased urbanisation and erosion pose a threat to beaches, which are a major resource for tourism activities. On Bora Bora, coastal erosion was already noted as a serious issue at the southern beach of Matira, a major tourism spot, in the 1990s [8]. Characterising coastal urbanisation and erosion in the coral reef islands of the tropical Pacific Ocean at a very high spatial resolution (VHR) can shed light on human impacts on sedimentary processes and provide key knowledge to better manage coastlines in the future, in the context of local urbanisation, global climate change-induced sea level rise, and more frequent and intense storm surges.

On Bora Bora, the availability of imagery from 1955 to 2019 enables long-term monitoring of changes through manual photointerpretation of VHR aerial and satellite imagery [9]. This article aims at addressing the issue of coastal modification and its impacts on the shoreline classification and position on Bora Bora from 1955 to 2019 through an original long-term and very high-resolution approach. This study adds to the growing awareness of the vulnerability of shorelines due to urbanisation and its effects in French Polynesia (e.g., [3]).

2. Materials and Methods

2.1. Study Site

2.1.1. Physical Setting

Bora Bora ($16^{\circ}29' S$, $151^{\circ}44' W$, highest summit: 727 m) is a ~ 20 km² tropical volcanic island circled by a 70 km² barrier reef, in the Society archipelago of French Polynesia in the South Pacific (Figure 1). It has an approximately 40 km complex coastline forming numerous bays and peninsulas that are bordered by 50 to 150 m-wide fringing reefs [8]. There are multiple motu (sandy islands) on the reef margin around the island which hinder water circulation in and out of the lagoon as well as constrain sediment transport from the barrier reef crest and from lagoonal sand accumulations to the island [10]. There are a few shallow channels (hoa) through which oceanic water enters the lagoon. A 48 m deep pass connects the lagoon to the ocean to the west of the island [10]. The general water circulation in the lagoon is south to north [8] but depends on tides (spring tidal range: 0.4 m [11]), wind conditions, and temperature-related water column stratification [12]. The only available wave height data for Bora Bora is based on a record from a sensor located outside the lagoon near Bora Bora's only pass on the western side of the island [13]. The main island is sheltered from the waves by the barrier reef and it is, hence, difficult to estimate its wave climate as well as the variability around the island; outside of the lagoon, the main wave direction is East to West, parallel to the trade wind direction [13].

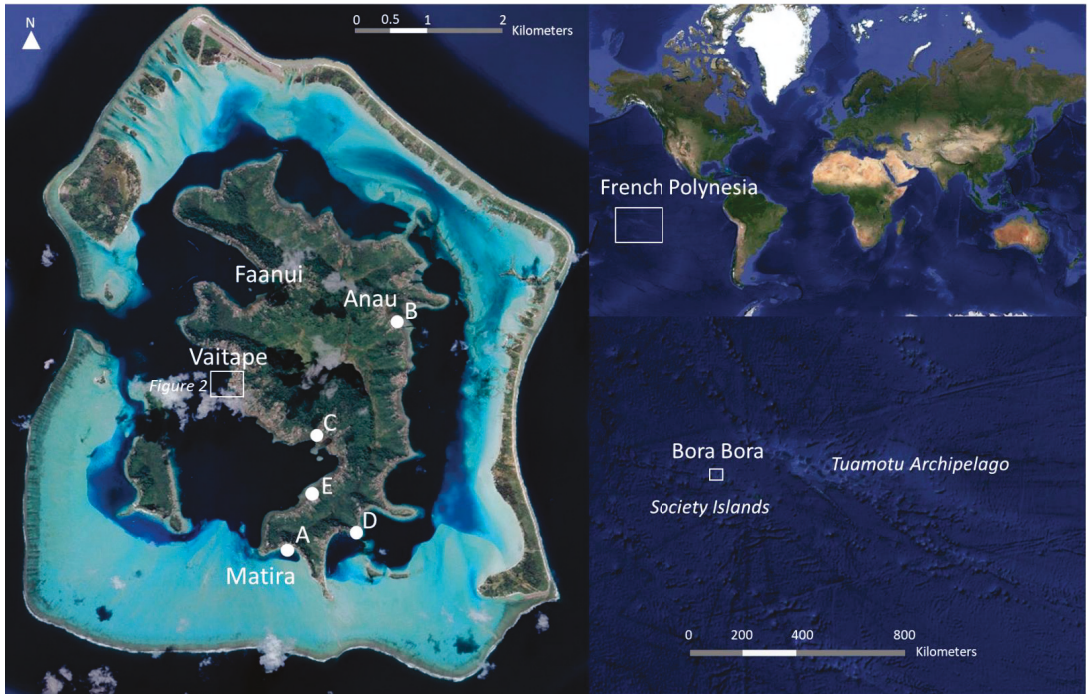


Figure 1. Geographical location of Bora Bora in French Polynesia and satellite imagery of Bora Bora (image from 20 July 2019) highlighting the main topological locations discussed in the article. The white rectangle on the image of Bora Bora above Vaitape corresponds to the location of the images of Figure 2. Letters A–E indicate the location of the coastal habitats featured in Figure 3. Imagery from CNES/Airbus 2019 and Google Earth 2021.

Bora Bora's lagoon is characterised by a majority of medium to coarse sediments in the shallow areas near the barrier reef (over 98% of the total fraction is $>125 \mu\text{m}$) and fringing reefs (30% of the total fraction $>125 \mu\text{m}$), and a larger fraction of fine sediments at depth, below 22 m ($>95\%$ of fine grains of sizes $<125 \mu\text{m}$). Most sediments are derived from the breakdown of skeletal fragments from reef organisms [10]; a fraction of sediments are modern cemented non-skeletal grains such as ooids that arise from the precipitation of calcium carbonate on the shallow areas between the motu and the lagoon where currents are weak and allow for carbonate super-saturation [10].

The absence of sustained riverine input of sediments (no permanent rivers on Bora Bora apart from a stream in the north-western Faanui bay) leads to a mostly carbonate sedimentology with few siliciclastic components (mostly clay) derived from the volcanic island [10].

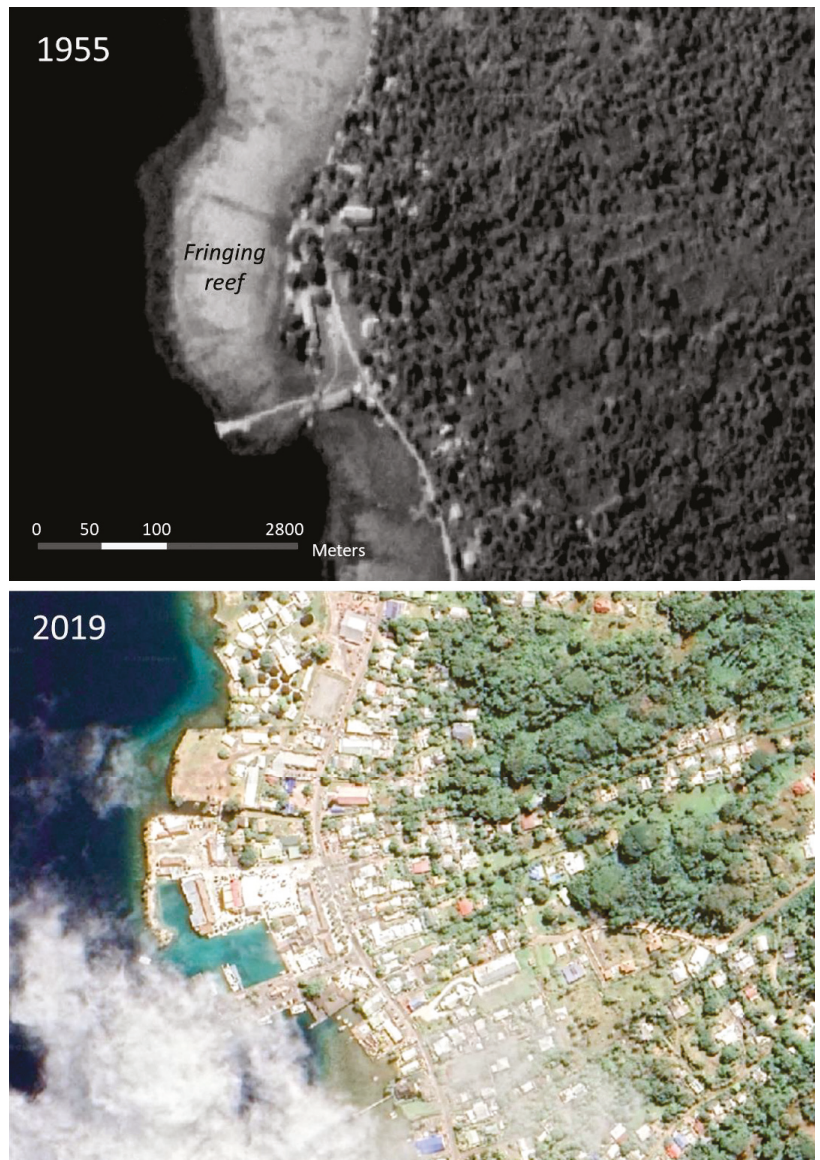


Figure 2. Very high-resolution imagery of the same location at the centre of Vaitape in 1955 (aerial photograph) and 2019 (CNES/Airbus imagery), highlighting the infilling of fringing reefs for constructions and urban development of the area.

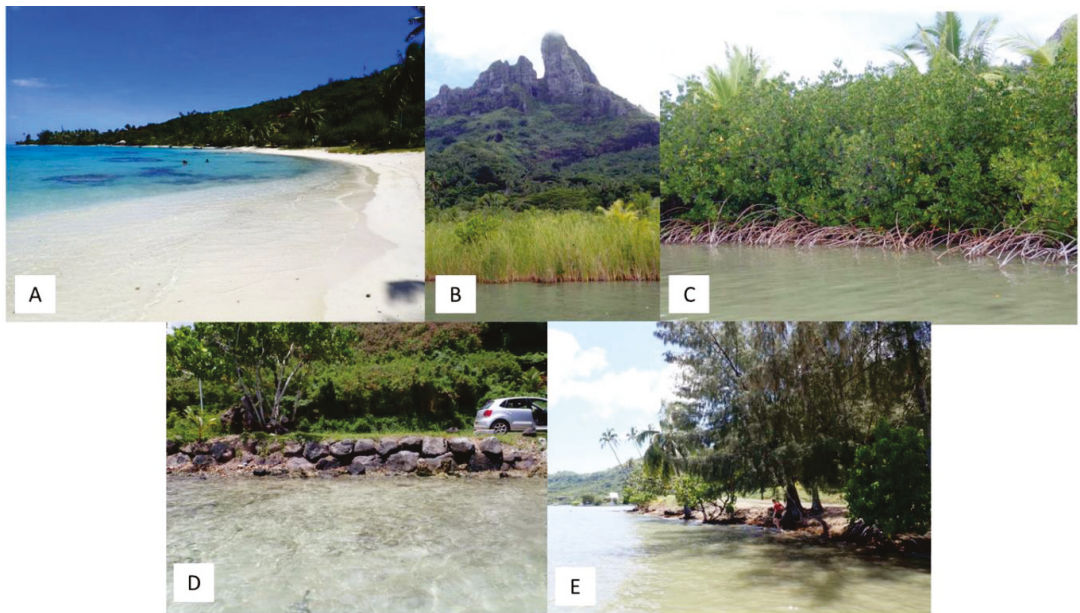


Figure 3. Examples of ground view of coastal classes. (A) sandy beach, (B) grass, (C) mangrove, (D) road embankment, (E) trees.

2.1.2. Human Presence

Bora Bora's first infrastructures were constructed during the 1940s, with an airport, roads, quays, embankments. Since then, Bora Bora has been the stage of an important demographic boom (2215 inhabitants in 1971, 10,549 in 2017 [14]; average population density in 2017: 350/km²) and economic development, most notably through tourism and recreational activities (over 80% of international tourists coming to French Polynesia visit the island [15]).

This demographic and economic development is associated with the rapid urbanisation of the coastline, as most of the inner island is constituted of steep cliffs and dense forest. Faanui and Vaitape (Figure 2), on the western side, house more than two thirds of the island's population while Anau in the east has a population of around 2000. This urbanisation is accompanied by coastal modifications (dredging and removal of sand to build roads, authorised and unauthorised land fillings to extend gardens and houses over the fringing reef) and structures (roads, quays, embankments, seawalls).

2.2. Data Acquisition

The study is based on a time series of images of Bora Bora obtained through vertical aerial photographs taken from a plane, provided by the Urbanism service of French Polynesia (1955, 1977, 1987, and 1999) and satellite imagery extracted from Google Earth (2006, 2010, 2019), as detailed in Table 1. These dates were selected for their negligible or absent cloud cover. The satellite imagery was extracted at very high spatial resolution (<0.5 m) from Google Earth following the method from [16]; by adjusting the eye altitude to match the satellite spatial resolution, putting the nadir at 90°, and positioning the view northward, over 60 images of the island were saved at maximum resolution for each date, with an overlap of around 30% between each subsequent image; these images were then assembled into orthomosaics similarly to the aerial images taken from a plane (see Section 2.3.1. Image preparation). Furthermore, a ground-based survey of the coastal

typology was performed in 2019 using a GPS, by walking and sailing around the island and recording the location of different coastal types (similar methodology to [3]).

Table 1. Year, type of image, and spatial resolution of the time series of images of Bora Bora.

| Year | Acquisition Method | Source | Image Type | Spatial Resolution (m) |
|------|--------------------|--------------------|------------------|------------------------|
| 1955 | Plane | Aerial photographs | Singleband grey | 1.58 |
| 1977 | Plane | Aerial photographs | Singleband grey | 0.64 |
| 1987 | Plane | Aerial photographs | Singleband grey | 0.52 |
| 1999 | Plane | Aerial photographs | Multiband colour | 0.41 |
| 2006 | Satellite | Maxar Technologies | Multiband colour | 0.48 |
| 2010 | Satellite | Maxar Technologies | Multiband colour | 0.50 |
| 2019 | Satellite | CNES/Airbus | Multiband colour | 0.48 |

2.3. Data Processing

2.3.1. Image Preparation

The images were assembled using Agisoft Metashape to obtain orthomosaics for each acquisition year. These were georeferenced with ArcGIS 10.8.1 using ground control points (geospatial reference: tefenua.gov.pf (accessed on 15 January 2021)) with either adjust or 2nd polynomial transformations. Fixed geomorphological features such as lagoon pinnacles were used along with anthropogenic features as ground control points (similarly to [17]).

2.3.2. Shoreline Tracing

The shoreline was manually traced based on the sea-side edge of vegetation (including the sea-side edge of mangroves and grass/reed areas), as per previous publications (similarly to the stability line used in [17]), with the Editor tool on ArcGIS. When sparse coastal vegetation (i.e., spaced-out trees) had dense canopies, the middle of the canopy, in the alignment of non-vegetated areas with a clear shoreline position, was used to position the shoreline. For sandy beaches, the line of first vegetation was used and not the sea-sand boundary for two reasons:

1. The time of acquisition and, hence, tidal stage of the images is unknown; although the tidal range in the Society Islands is typically below 0.4 m [13], beaches tend to have shallow slopes and, hence, the sea-sand boundary may change by over 1 m throughout a daily tidal cycle.
2. The images are separated by multiple years—the position and extent of sand accumulations may be variable on daily to monthly timescales, which cannot be resolved with the dataset used in this article due to the lack of regular aerial imaging in the years before the start of satellite imagery.

Clouds were present over a few tens of meters of the coastline in 2019 in the urban area of Vaitape, in a zone with embankments and no natural shoreline. A ground survey confirmed the lack of further constructions or changes compared to the previous image of 2016. The shoreline was, hence, traced in the same position as for 2016. No other clouds were present over the coastline at any date.

The total error (E_{tot}) of the shoreline positioning is taken as the square root of the sum of the squares (cf. [18]) of the three sources of error identified for this study: the spatial resolution (E_{res}), the georeferencing error (provided by the forward error of the ground control points on ArcGIS, E_{geo}) and the shoreline tracing inaccuracies (E_{tra}) (Equation (1)).

$$E_{tot} \text{ (in m)} = \sqrt{E_{res}^2 + E_{geo}^2 + E_{tra}^2} \quad (1)$$

The shoreline error (total and yearly) is provided in Table 1 for each date.

2.3.3. Shoreline Classification

The coastline was classified into the eight categories that were discernible on aerial images: sandy beaches, mangroves, trees (tall vegetation on a muddy substrate), grass (or reeds), natural rocky shores, road embankments (and seawalls, necessary for urbanisation purposes), private embankments (to consolidate lands), and quays (cf. Figures 3 and 4; “method similar to [3]). The coastal classification for 2019 was performed first using the ground-based survey of the different coastal typologies to identify the bird-eye aspect of each category (Figure 3) and obtain a baseline from which to work backward in time and classify previous images through photointerpretation. The classification was performed by splitting the shoreline (Editor tool on ArcGIS). The length of each segment was calculated, and the percentage of the shoreline belonging to each category was extracted (cf. Figure 3 for examples of each category on aerial images).



Figure 4. Examples of aerial view of coastal classes. (A) road embankment (red) and private embankment (pink); (B) quay; (C) sandy beach; (D) mangrove (dark green), grass (clear green), private embankment (pink); (E) trees.

2.3.4. Shoreline Position

The Digital Shoreline Analysis System (DSAS [19]) plug-in on ArcGIS was used to study erosion and accretion phenomena along the shoreline. The baseline was placed 25 m inland with respect to the innermost shoreline at any given position. Transects were cast every 5 m, with a maximum search distance from the baseline of 250 m and a smoothing distance of 200 m. The shorelines were set to have a default data uncertainty of 5 m (linked to the uncertainty of the determination of dark reef flat features vs. coastal bushes). Two parameters were calculated between each date and over the whole period (1955 to 2019)

with the DSAS plug-in on ArcGIS, with a confidence interval of 95.5 (2σ): the Net Shoreline Movement (NSM)—total distance between the earliest and most recent shorelines for each transect, in meters—and the End Point Rate (EPR)—NSM divided by the number of years between the earliest and the most recent shorelines, in meters per year.

These statistics were studied in relation to the categories obtained beforehand to identify which categories were responsible for the most change in shoreline position around the island since the mid-1950s. For selected parts of the island, the average EPR was calculated for each 10° change in azimuth (i.e., average from 0 to 10° , 10 to 20°) and time interval. To identify temporal changes in sedimentary dynamics, linear correlation coefficients were calculated by comparing the average EPR at each 10° azimuth change between each pair of year intervals. For instance, a hypothetical net erosion of -1 m between 0 and 10° and accretion of 1 m between 10° and 20° for a given time interval, and net erosion of -0.5 m at $0-10^\circ$ and accretion of 0.5 m at $10-20^\circ$ for another time interval would yield a linear correlation coefficient r of 1 between those two time intervals.

3. Results

3.1. Evolution of the Shoreline Classification from 1955 to 2019

Using aerial images of Bora Bora, the maps below (Figure 5) were produced to display the evolution in coastal categories (sandy beaches, rocks, trees, grass, road embankments, private embankments, quays, cf. Figures 3 and 4) from 1955 to 2019. Sandy beaches have remained constrained to the southern part of the island, but the southernmost tip was altered from a sandy beach to a private embankment in the 2000s. Along the rest of the island, the dominant coastal category has switched from trees to private embankments. Most changes occurred between the 1970s and 1990s, and the coastline classification has remained relatively similar since 2006.

In detail, the natural (sandy beaches, rocks, trees, grass areas, and mangroves) shoreline length has decreased by over 46% from 1955 to 2019, from 32.2 km to 17.2 km out of over 40 km of shoreline (varying length depending on the year and human-made changes; Figure 6). At the same time, the human-made shoreline length (quay, road embankment, and private embankment) has increased by 476%. The percentage of the shoreline transformed into embankments to stabilise public roads has remained relatively constant on Bora Bora, at 8–10% (total length: 2979 m in 1955, 4273 m in 2019), while the percentage of the shoreline as quays has increased slightly (1% to 5%). The extent of mangroves and grass areas have remained limited (<0.5 to 1% throughout). Overall, Bora Bora's coastline has undergone strong changes, transitioning from natural to mostly human-made categories from 1955 to 2019.

3.2. Evolution of the Shoreline Position from 1955 to 2019

3.2.1. Shoreline Positioning Error

To investigate the relationship between shoreline classification and positioning in Bora Bora over time, the position of the shoreline was estimated manually using the available VHR imagery. The error of the shoreline position determined for each year is detailed by Table 2. The tracing error was estimated to be two meters for each date, notably due to uncertainties in the determination of the position of the shoreline in vegetated areas due to treetops, but also in the case of low spatial resolution leading to difficulties in distinguishing the land from the sea. The georeferencing error ranges from 0 (2019 is used as the reference) to 4.02 m (for 1955). The total error (Equation (1)) is maximum for 1955 (4.76 m) and minimum for 2019 (2.06 m), and is between 3.20 and 3.95 m for the other dates.

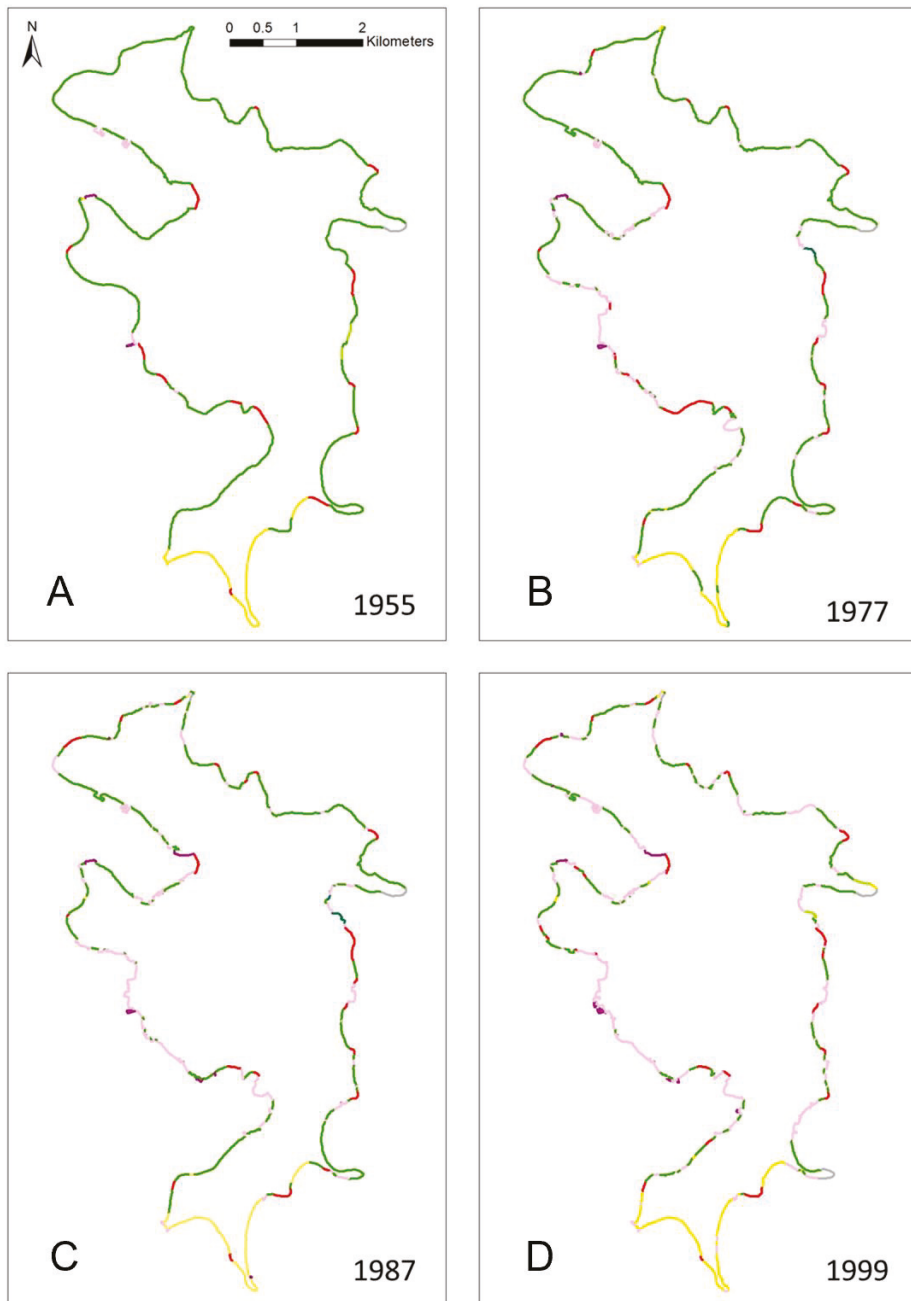


Figure 5. Cont.

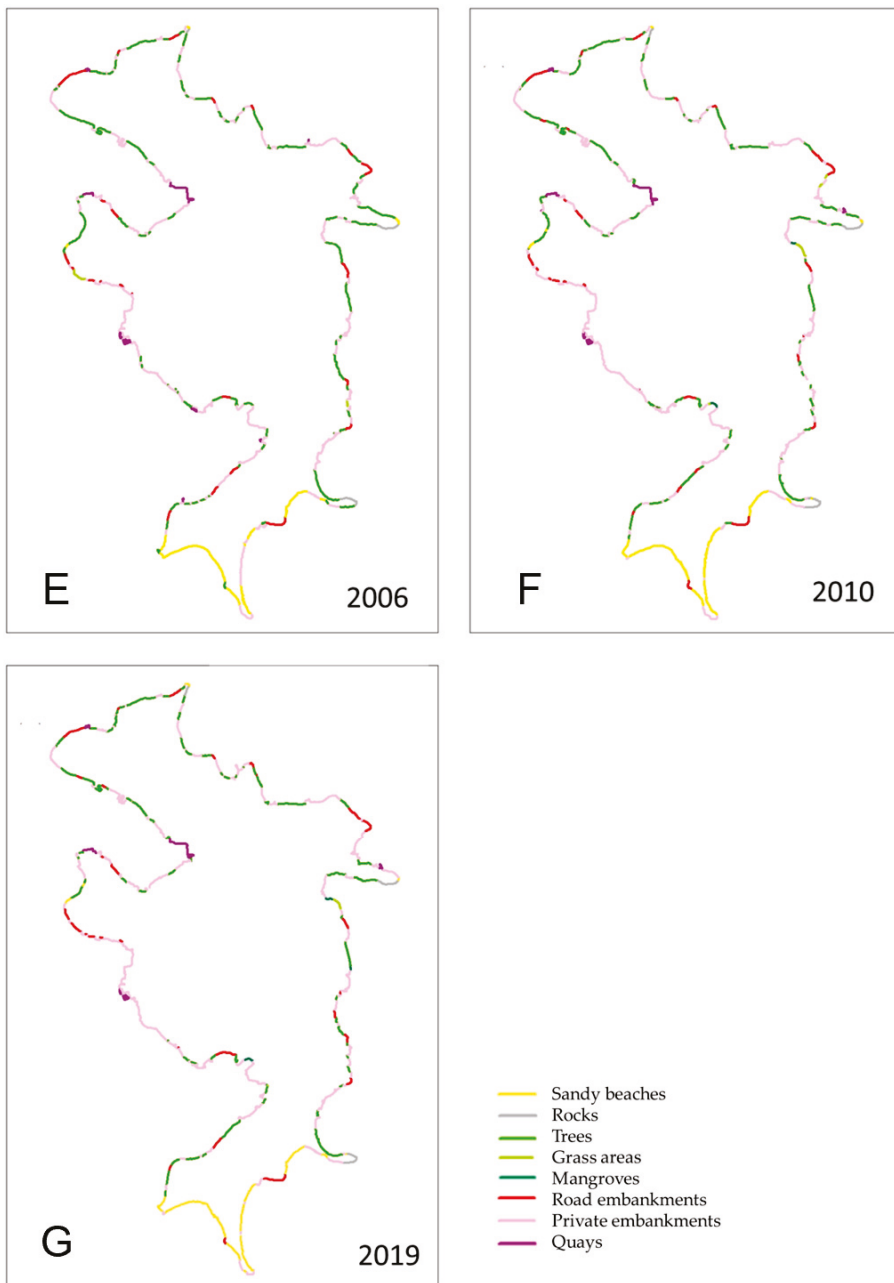


Figure 5. Map of the coastline classification (sandy beaches, rocks, trees, grass areas, mangroves, road embankments, private embankments, quays) of the main island of Bora Bora for (A) 1955, (B) 1977, (C) 1987, (D) 1999, (E) 2006, (F) 2010, and (G) 019.

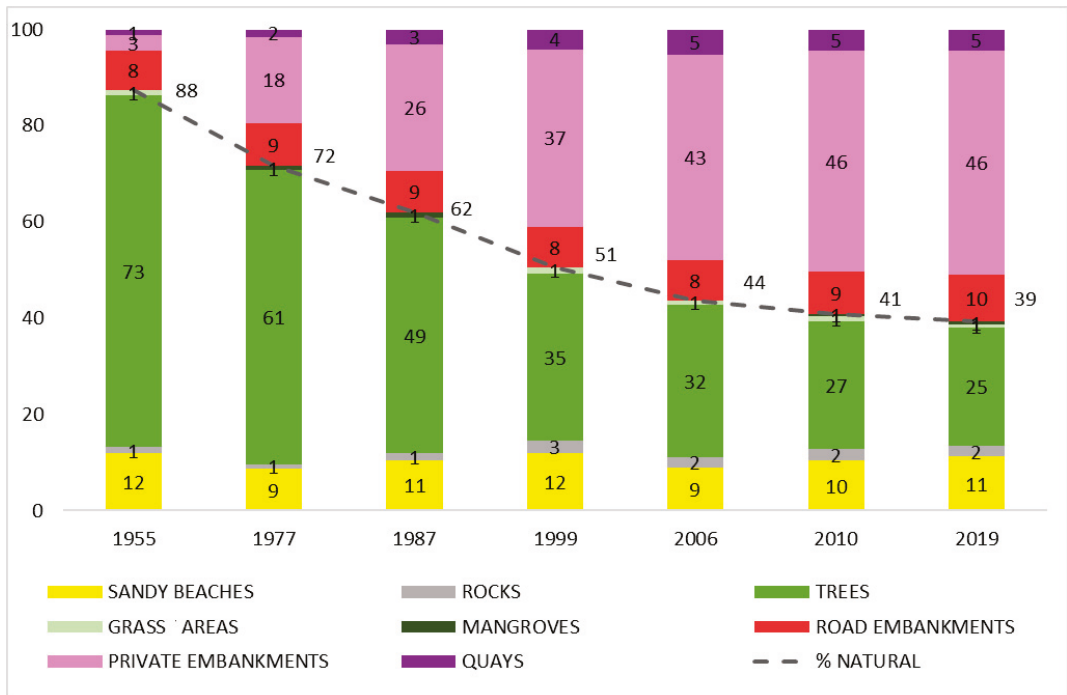


Figure 6. Percentage of the coastline as sandy beaches, rocks, trees, grass areas, mangroves, road embankments, private embankments, and quays, as well as overall percentage of natural (sandy beach, rocks, grass areas, and mangrove) for 1955, 1977, 1987, 1999, 2006, 2010, and 2019 on the main island of Bora Bora. A conservative error on these percentages, caused by coastline tracing subjectivity and classification uncertainty for older images, may be estimated as approximately 10% of their value (i.e., $46 \pm 5\%$ of the coastline is a private embankment and $1 \pm 0.1\%$ is a mangrove on Bora Bora in 2019).

Table 2. Spatial resolution, georeferencing error, tracing error, and total error (based on Equation (1)) of the shoreline position for each date.

| Year | Spatial Resolution (m) | Georeferencing Error (m) | Tracing Error (m) | Total Error (m) |
|------|------------------------|--------------------------|-------------------|-----------------|
| 1955 | 1.58 | 4.02 | 2 | 4.76 |
| 1977 | 0.64 | 3.26 | 2 | 3.88 |
| 1987 | 0.52 | 3.37 | 2 | 3.95 |
| 1999 | 0.41 | 2.46 | 2 | 3.20 |
| 2006 | 0.48 | 2.58 | 2 | 3.30 |
| 2010 | 0.50 | 2.85 | 2 | 3.52 |
| 2019 | 0.48 | 0 | 2 | 2.06 |

3.2.2. Overall Changes in Shoreline Position

The changes in shoreline position on Bora Bora between 1955 and 2019 (for transects every 5 m) have a median of 5.6 m (positive values correspond to net accretion) and an interquartile range of $[-0.09, 19.5]$: approximately 25% of the shoreline has undergone erosion, and 50% have experienced accretion of up to 19.5 m, while the remaining 25% have gained more than 19.5 m over the sea. In detail, the construction of embankments and quays has led to strong ‘artificial’ accretion in the most densely populated parts of the

island (Vaitape, Faanui, and Anau; often over 15 m, and up to 220 m gained over the sea; Figure 7). Neighbouring natural sections (most often corresponding to the tree category, which is the most common natural category) have undergone erosion, most commonly of 2 to 5 m, from 1955 to 2019 (cf. the red erosion zones interspersed by green ‘artificial’ accretion zones on Figure 7A). On the southern beaches, the East-exposed portions have undergone erosion (over 2 m of landward net sea movement from 1955 to 2019) while the other portions have undergone accretion (Figure 7B), either naturally or due to the construction of embankments at the southernmost tip (Figure 5).

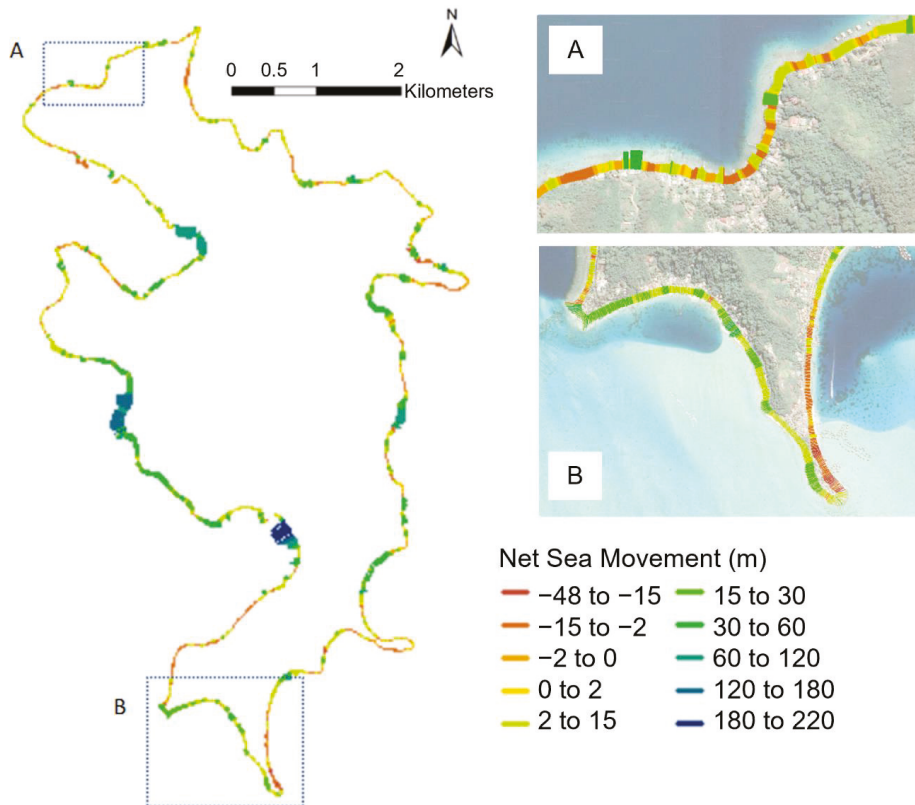


Figure 7. Map of the Net Sea Movement between 1955 and 2019 extracted from the DSAS module on ArcGIS 10.8.1. (A) mostly urbanised section in Faanui, with alternating accretion (linked to the construction of seawalls) and erosion (in the nearby natural areas); (B) sandy beach zone of Matira.

Overall, Bora Bora has, hence, increased in size due to the construction of embankments and quays; natural shoreline areas that persisted from 1955 to 2019 have mostly undergone erosion (e.g., natural zones with trees near embankments).

3.2.3. Changes in Shoreline Position on the Southern Beaches

Placing a focus on the southern beaches, End Point Rate values (change in shoreline position in meters per year) were averaged over 10° intervals. In detail, between 1955 and 1999, accretion mostly occurred on the south-west facing beaches (azimuths between 0° and 90° ; Figure 8) and erosion on the east- and north-east facing beaches (azimuths between 220° and 0°). Between 1999 and 2006, there was limited erosion on the north-facing beaches and accretion was predominant on all other azimuths. In 2006–2010, erosion occurred on the

south-west facing beaches with relatively important rates (up to $1.27 \pm 0.10 \text{ m y}^{-1}$ between 10 and 20°, the maximum rate across all azimuths and time periods) while accretion was limited (with one outlier at $1.02 \pm 0.40 \text{ m y}^{-1}$ corresponding to an additional seawall). Lastly, from 2010 to 2019, only one averaged azimuth experienced erosion (-0.53 ± 0.22 between 220 and 230°), while accretion was limited elsewhere (mostly below 0.5 m y^{-1}).

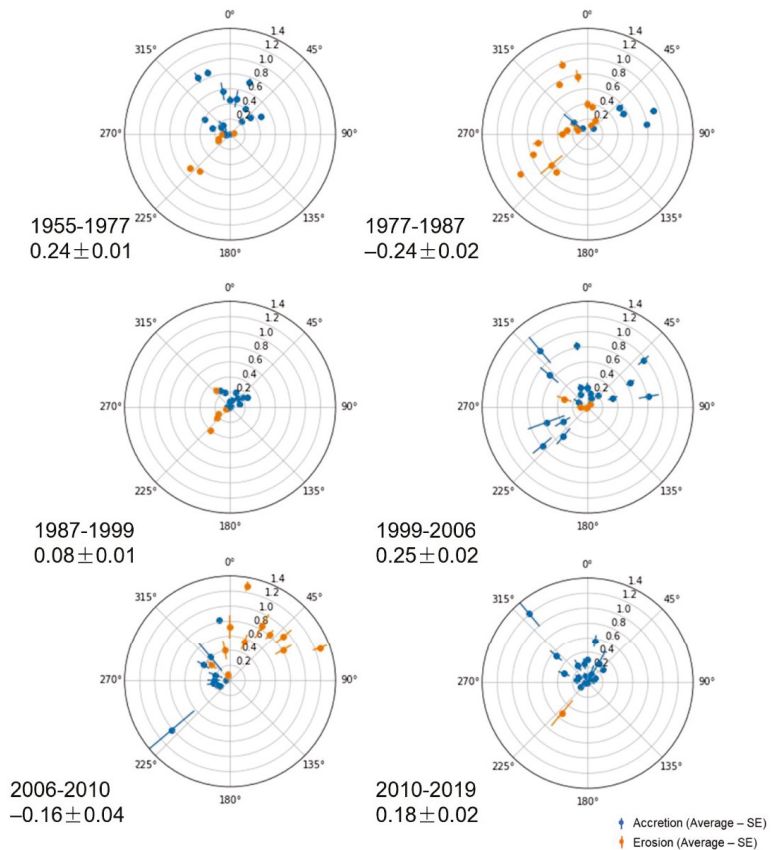


Figure 8. Radar plot of the average (dot) and standard error (whiskers) of the End Point Rate (in meters per year, from 0 to 1.4 m y^{-1} on the plot) for 10°-averaged azimuths on the southern beaches of Bora Bora. Blue colours indicate accretion (positive EPR) and orange colours indicate erosion (negative EPR). An azimuth of 0° corresponds to a south-facing beach (land on the north side, sea on the south side of the shoreline). The values below the date intervals correspond to the overall average and standard error of the End Point Rate across the beaches.

There were significant contrasts between some years (Table 3). There notably are significant negative linear correlations between 2006–2010 (after the construction of the large-scale embankment) and each time range before 1999 (1955–1977, 1977–1987, 1987–1999). There is also a strong positive linear correlation (0.78) between 1955–1977 and 1987–1999, which may indicate a lack of sedimentary regime change between those dates. There are no significant differences between the other dates.

Table 3. Linear correlation coefficients r for the 10° average End Point Rate values calculated for Bora Bora’s southern beaches of Matira.

| Year Interval | 1977–1987 | 1987–1999 | 1999–2006 | 2006–2010 | 2010–2019 |
|---------------|-----------|-----------|-----------|-----------|-----------|
| 1955–1977 | 0.06 | 0.78 | −0.19 | −0.45 | 0.36 |
| 1977–1987 | | 0.27 | 0.19 | −0.52 | 0.27 |
| 1987–1999 | | | −0.24 | −0.64 | 0.03 |
| 1999–2006 | | | | 0.00 | 0.24 |
| 2006–2010 | | | | | −0.04 |

Threshold for 5% significance: $r = \pm 0.43$.

4. Discussion

4.1. Drivers of the Evolution of the Shoreline Classification and Potential Impacts on Sedimentary Processes on Bora Bora from 1955 to 2019

Throughout the second part of the 20th century, infillings to build public and private properties onto the fringing reef (notably on the densely populated western side of the island; Figures 2 and 5) have been the prominent factor of shoreline category and position changes on Bora Bora. Trees and vegetation were removed and replaced by private embankments to consolidate infillings (from 3% or 1.2 km in 1955 to 46% or 20.3 km in 2019). Similar evolutions have been noted on other French Polynesian islands, notably an increase from 12% in 1977 to 57% in 2018 of embankments on the island of Moorea, which has similar geological, geomorphological, and socio-economical characteristics [3]. Through interviews with long-term Bora Bora residents performed in March 2021, it emerged that these embankments were initially linked to a drive to extend the island’s land surface outwards and construct houses on the highly sought-after seaside, notably until the 1990s. For instance, a large fraction of the houses as well as public infrastructure on the west side of Bora Bora, most notably in Vaitape, is constructed on infilled fringing reefs (Figures 2 and 5). However, since the 2000s, the main reason for embankment construction (with or without building licences) has been the reinforcement of private land boundaries. This reinforcement is perceived as necessary in the face of continuous coastal erosion, linked to background swell, storms and cyclones (notably in reaction to the passage of cyclone Oli in 2010), and to anticipate future sea level changes (which are forecasted to be up to 0.76 m higher in 2080–2100 with respect to 1986–2005 for an intermediate global warming scenario [20]).

Modifying Bora Bora’s coastline may have had strong impacts on the island’s sedimentary regimes and, along with drainage canals and other land features altering sediment transport from the island to the sea, it may be a factor leading to heightened erosional effects [3]. Infillings and walls may reroute and strengthen currents and waves, leading neighbouring zones to experience stronger erosion [17] (Figure 7A). As visible on the aerial images and confirmed by interviews with residents, landowners in the vicinity of newly constructed coastal structures eventually have to build embankments as well to protect their gardens from erosion, leading to a ripple effect and a progressive artificialisation of the shoreline (Figure 5).

On a larger scale, a stark example of the impact of urbanisation on coastal sedimentation is the effect of a large protective embankment in Matira (southern tip of Bora Bora) on the neighbouring sandy beaches. This protective embankment to stabilise the shoreline position at the tip of the peninsula was first built on a small scale before 1999 and then extended to most of the peninsula between 2005 and 2006. It may have modified currents and sedimentary processes and altered the erosional regime in the area (Figure 8, Table 2), leading to enhanced erosion on previously stable sections of the beaches. Before the construction, the sandy beaches underwent net erosion on the northeast-facing side and accretion on the southwest-facing side. This movement corresponded to the average wind-driven surface currents (the main wind regime is West to East in Bora Bora [13]) and,

hence, may have been mostly of natural causes. During the construction, the signal was blurred (1999 to 2006), and was then inverted after 2006. However, the development of hotels, seaside gardens, and planting of coconut trees has artificially led to a net accretion between 2010 and 2019 on the beaches due to the definition of the shoreline position used in this study (sea-side edge of vegetation). Overall, these erosional processes remain limited (generally under 1 m y^{-1}) and may partly be noise due to the shoreline positioning error of this study (2.06 to 4.76 m).

The time series used here enables the assessment of overall long-term changes in coastal typology and position, which can be linked to human activities, as sea level rise was small ($\sim 2 \text{ cm}$) between 1955 and 2019 in Bora Bora. However, the temporal resolution of the time series used here (4 to 22-year gaps between each image) is too broad to assess changes due to most intense short-term events. An exception is the passage of Cyclone Oli in February 2010, two months before Bora Bora was imaged by satellite (Table 1). Although the island of Bora Bora is protected from strong swells by a barrier reef and circled by a wide lagoon, extreme weather events can have damaging impacts along the shoreline of the main island. The passage of this storm may notably have led to the strong erosion of the sandy beaches of Matira (Figure 8) and additional erosion in other natural sections of the coastline, although this cannot be certain in the absence of other images between 2006 and 2010.

The recent availability of data from satellites with daily and high spatial resolution imaging capacity (e.g., [21]) as well as the LiDAR campaign conducted on Bora Bora in 2015 [22] could be combined for future high-resolution 2D or 2.5D monitoring (see review by [9]) of the evolution of the coastline of the island and help to disentangle the individual effects of various factors (background waves, storms, constructions) on sedimentary processes.

4.2. Further Consequences of Coastal Urbanisation and Perspectives for Management

Beyond impacting coastal erosion, infillings and embankments are costly and can lead to economic and biological issues. Firstly, infillings and embankments are built over shallow fringing reef ecosystems, which typically house numerous juvenile fish and invertebrate organisms [23]. These constructions and the associated modified currents and sedimentology are, hence, accompanied with a removal and degradation of ecosystems. This could have wide-reaching impacts on marine communities throughout Bora Bora's lagoon and, hence, impact local fisheries and livelihoods. Furthermore, requesting building permits is a lengthy administrative process, which nowadays most often results in a refusal. In addition, using adequate building materials, such as volcanic rocks, leads to additional expenses. As a result, many private infillings and embankments are built illegally [24] using tyres, construction rubble, or rusty metal spikes. Beyond altering seascapes on an island that is famous worldwide for its scenery, these may spread pollutants into the nearby marine ecosystems [25].

In addition to the numerous private embankments, public infrastructure, most notably roads and quays, are associated with seawalls. In particular, the main road of Bora Bora is a belt road which, in many areas, is located only a few meters away from the shoreline. This road is protected from the sea by embankments that represent approximately 10% of the island's shoreline (Figures 5 and 6). This road, hence, plays a non-negligible role in the artificialisation of the coastline, damage to coastal ecosystems, and changes in sedimentary regimes. In some areas, no wall has yet been constructed to protect the belt road, but there are projects to implement some (e.g., along the high school of Bora Bora located between Vaitape and Matira), notably because the road can be flooded during strong swell events. Instead of seeking to protect a belt road located close to the sea, building a new road further inland wherever possible, and restoring natural shoreline types by removing the walls, could be efficient solutions to mitigate the impact of urbanisation on Bora Bora's shoreline.

Indeed, in opposition to human-made constructions enhancing erosion, natural shoreline types such as mangroves and grass have widely acknowledged ecological functions [26]

and act as sediment accumulation zones on Bora Bora (Figures 5 and 7). This is partially due to the geographical position of these areas: mangroves and grass areas are located within bays on Bora Bora and directly receive sediment-rich runoff from the surrounding land following rainfall. Net accretion is enabled by the presence of plant roots slowing down currents and leading to sediment deposition [27]. Coastal management and restoration projects on Bora Bora could aim at removing erosion-inducing walls and revegetating the shoreline to consolidate it. There are numerous plants that can stabilise the shoreline: low-lying vegetation (grass, bushes), strong-rooted trees (local varieties such as aito—*Casuarina equisetifolia*, purau—*Hibiscus tiliaceus*, miki miki—*Penzance acidula*, or even coconut trees—*Cocos nucifera*, although they are less efficient at trapping sediments). In addition, promoting coral growth on the fringing reefs—leading to hard structures that attenuate wave energy—could also be a positive management solution [28]. Expanding mangroves (*Rhizophora stylosa*) due to their efficient sediment-trapping roots, however, is debatable in the context of French Polynesian islands. Indeed, mangroves were absent from French Polynesia until the 1930s and were only introduced in the 1930s to promote oyster and crab production [29]. They are often viewed negatively, as invasive species (notably taking over adjacent grass areas, cf. Figure 4), and are actively removed by local inhabitants. Nevertheless, there are numerous alternative nature-based solutions available to replace walls without compromising shoreline stability. However, although most residents that were interviewed were aware of and suggested natural methods to prevent coastal erosion, a strong majority was opposed to removing walls and planting trees on their private lands. This opposition was mostly due to the costs involved and uncertainty in the resulting shoreline stability. Performing experiments in various parts of the island by removing walls and monitoring shoreline stability, communicating with the public about the results, and financially contributing to coastal restoration could provide incentives to remove private embankments around the island.

The important impact of embankments and seawalls on shoreline stability throughout Bora Bora underscores the sensitivity of the island's sedimentary regime to human-made structures. This type of human-induced shoreline destabilisation is common in French Polynesia (e.g., in the atolls of the Tuamotu Archipelago [17]; in Moorea, of similar geomorphology to Bora Bora [3]). The urbanisation of coastlines has profound impacts on physical processes around the islands, from modifying sedimentary processes to increasing vulnerability to coastal erosion, storm surges, and sea level rise [17]. Geologically younger volcanic islands such as Bora Bora [10] may be assessed as less vulnerable to coastal erosion than low-lying atolls such as in the Tuamotu Archipelago or even the motu dotted along the barrier reef of Bora Bora (Figure 1). However, shorelines with hard volcanic lithology, which are spared from erosion and accretion on decadal time scales, are rare on Bora Bora (rock category, under 3%, Figure 6). In addition, most seawalls and embankments on Bora Bora have a height of less than one meter. If the island's coastal lifestyle continues in the future, in the absence of sustainable coastal management solutions, there will be a need to keep infilling land and elevate seawalls to cope with rising sea levels. As demonstrated by the imagery timeline used in this study, increasing the artificialisation of the coastline may lead to even more coastal erosion in a positive feedback loop, and is not a sustainable solution. Lastly, beyond the economic importance of preserving white sandy beaches on the tourist island of Bora Bora, the strong human density and rarity of inhabitable areas in the steep inner parts of the island make coastal erosion a major challenge on Bora Bora, especially in the context of increasing human populations on the island [14]. There is a need to adapt lifestyles and public infrastructures to the changing climate, sea level rise, and more frequent and intense storm surges and swell [20]. There must be incentives to encourage islanders to move further inland when possible and revegetate the shorelines rather than fight a losing fight against erosion and aggravate the problem. Communicating with the public, developing management plans, and stabilising the coastline with nature-based solutions are required to tackle the issue head-on in Bora Bora and in similar contexts worldwide.

5. Conclusions

High-resolution aerial images of Bora Bora obtained from 1955 to 2019 highlighted the extensive coastal urbanisation undergone by the island since the mid-20th century. While quays and embankments were scarce in the 1950s, they represent 61% of the shoreline nowadays. This transition away from natural shorelines is accompanied by modified sedimentary regimes, and results in enhanced coastal erosion. In the context of climate change and increasing demographic pressure, preserving shoreline stability on small Pacific islands, where most constructions are located within meters of the sea, is crucial for livelihoods. The long-term impact of coastal modifications on erosional processes on Bora Bora indicated by the aerial imagery series highlight the need for proactive local management, with the removal of embankments and restoration of natural shoreline types, notably of vegetation possessing robust root systems capable of stabilising sediments.

Author Contributions: Conceptualization, E.G., A.C., D.J. and D.L.; formal analysis, E.G.; funding acquisition, D.L.; investigation, E.G.; methodology, E.G., A.C., D.J. and F.D.; resources, T.M., Y.R. and L.L.; software, A.C. and D.J.; supervision, A.C., D.J. and D.L.; validation, A.C., D.J., T.M., Y.R., L.L. and D.L.; writing—original draft, E.G.; writing—review and editing, E.G., A.C., F.D., M.J. and D.L. All authors have read and agreed to the published version of the manuscript.

Funding: This work has received several grants: Fondation de France (2019-08602), Ministère de l’Economie verte et du domaine-Délégation à la recherche de Polynésie française (contrat N3622 MED-EPHE), Office Français de la Biodiversité (AFB/2019/385-OFB.20.0888), Polynésienne des Eaux, ANR-19-CE34-0006-Manini, ANR-19-CE14-0010-SENSO, the Rāhui Forum and Ressource Center supported by Bloomberg’s Philanthropy.

Institutional Review Board Statement: Not applicable.

Informed Consent Statement: Not applicable.

Data Availability Statement: The data presented in this study are openly available in FigShare at doi.org/10.6084/m9.figshare.17048672.

Acknowledgments: We would like to thank the staff of Section Cadastre-Topographie de la direction des affaires foncières (DAF) de Polynésie-Française for providing the satellite images, as well as the staff of ‘Polynésienne des Eaux’ and of the Mairie of Bora Bora for their help in the field. We also thank the Earth and Biodiversity Science Graduate Program of PSL Université Paris (PG EABIS).

Conflicts of Interest: The authors declare no conflict of interest.

References

- Cooper, J.A.G.; Jackson, D.W.T. Coasts in Peril? A Shoreline Health Perspective. *Front. Earth Sci.* **2019**, *7*, 260. [[CrossRef](#)]
- Dafforn, K.A.; Mayer-Pinto, M.; Morris, R.L.; Waltham, N.J. Application of management tools to integrate ecological principles with the design of marine infrastructure. *J. Environ. Manag.* **2015**, *158*, 61–73. [[CrossRef](#)] [[PubMed](#)]
- Madi Moussa, R.; Fogg, L.; Bertucci, F.; Calandra, M.; Collin, A.; Aubanel, A.; Polti, S.; Benet, A.; Salvat, B.; Galzin, R.; et al. Long-term coastline monitoring on a coral reef island (Moorea, French Polynesia). *Ocean Coast. Manag.* **2019**, *180*, 104928. [[CrossRef](#)]
- Collin, A.; Duvat, V.; Pillet, V.; Salvat, B.; James, D. Understanding Interactions between Shoreline Changes and Reef Outer Slope Morphometry on Takapoto Atoll (French Polynesia). *J. Coast. Res.* **2018**, *85*, 496–500. [[CrossRef](#)]
- Collin, A.; Calle, C.; James, D.; Costa, S.; Maquaire, O.; Davidson, R.; Trigo-Teixeira, A. Modelling 2D Coastal Flooding at Fine-scale Over Vulnerable Lowlands using Satellite-derived Topobathymetry, Hydrodynamic and Overflow Simulations. *J. Coast. Res.* **2020**, *95*, 1052–1056. [[CrossRef](#)]
- Aubanel, A.; Marquet, N.; Colombani, J.-M.; Salvat, B. Modifications of the shore line in the Society islands (French Polynesia). *Ocean Coast. Manag.* **1999**, *42*, 419–438. [[CrossRef](#)]
- Gallop, S.L.; Kennedy, D.M.; Loureiro, C.; Naylor, L.A.; Muñoz-Pérez, J.J.; Jackson, D.W.T.; Fellowes, T.E. Geologically controlled sandy beaches: Their geomorphology, morphodynamics and classification. *Sci. Total Environ.* **2020**, *731*, 139123. [[CrossRef](#)] [[PubMed](#)]
- Gabriel, C.; Planes, S.; Baldwin, J.; Bonvallot, J.; Chauvet, C.; Vernaudon, Y.; Payri, C.; Galzin, R. Study of the coral reefs of Bora-Bora (society archipelago, French Polynesia) for the development of a conservation and management plan. *Ocean Coast. Manag.* **1994**, *25*, 189–216. [[CrossRef](#)]

9. Mury, A.; Collin, A.; James, D. Morpho–Sedimentary Monitoring in a Coastal Area, from 1D to 2.5D, Using Airborne Drone Imagery. *Drones* **2019**, *3*, 62. [[CrossRef](#)]
10. Gischler, E. Sedimentary Facies of Bora Bora, Darwin’s Type Barrier Reef (Society Islands, South Pacific): The Unexpected Occurrence of Non-Skeletal Grains. *J. Sediment. Res.* **2011**, *81*, 1–17. [[CrossRef](#)]
11. Pirazzoli, P.; Brousse, R.; Delibrias, G.; Montaggioni, L.; Faure, G.; Salvat, B. Leeward islands, Maupiti, Tupai, Bora Bora, Huahine, Society archipelago. In Proceedings of the 5th International Coral Reef Congress, Tahiti, France, 27 May–1 June 1985; Volume 1.
12. Lecchini, D.; Bertucci, F.; Brooker, R.M.; Berthe, C.; Gasc, J.; Jossinet, F.; Ellacott, S.; Zipper, E.; Blay, G.; Schneider, D.; et al. Rapid localized decline of a French Polynesian coral reef following a climatic irregularity. *Estuar. Coast. Shelf Sci.* **2020**, *246*, 107049. [[CrossRef](#)]
13. Bosserelle, C.; Reddy, S.; Lal, D. WACOP Wave Climate Reports. French Polynesia. Bora Bora; Pacific Community Science Division: Nabua, Fiji 2015.
14. INSEE/ISPF. *Le Recensement de la Population en Polynésie Française en 2017*; Institut de la statistique de la Polynésie française: Papeete, French Polynesia, France, 2017.
15. Polynesia Tourism Department Polynesia Tourism Department. 2020. Available online: <https://tahititourisme.fr/fr-fr/fr> (accessed on 11 August 2021).
16. Collin, A.; Nadaoka, K.; Nakamura, T. Mapping VHR water depth, seabed and land cover using google earth data. *ISPRS Int. J. Geo-Inf.* **2014**, *3*, 1157–1179. [[CrossRef](#)]
17. Duvat, V.K.E.; Pillet, V. Shoreline changes in reef islands of the Central Pacific: Takapoto Atoll, Northern Tuamotu, French Polynesia. *Geomorphology* **2017**, *282*, 96–118. [[CrossRef](#)]
18. Hapke, C.J.; Himmelstoss, E.A.; Kratzmann, M.G.; List, J.H.; Thieler, E. *Historical Shoreline Change along the New England and Mid-Atlantic Coasts*; United States Geological Survey: Woods Hole, MA, USA, 2011; Volume 1118.
19. Oyedotun, T.D.T. Shoreline Geometry: DSAS as a Tool for Historical Trend Analysis. *Geomorphol. Tech. Online Ed.* **2014**, *2*, 1–12.
20. IPCC Summary for Policymakers. *Climate Change 2021: The Physical Science Basis. Contribution of Working Group I to the Sixth Assessment Report of the Intergovernmental Panel on Climate Change*; Masson-Delmotte, V., Zhai, P., Pirani, A., Connors, S.L., Péan, C., Berger, S., Caud, N., Chen, Y., Goldfarb, L., Gomis, M.I., et al., Eds.; Cambridge University Press: Cambridge, UK, 2021.
21. Planet Team. Planet Application Program Interface: In Space for Life on Earth. 2017. Available online: <https://www.planet.com/> (accessed on 8 September 2021).
22. Shom-SAU LiDAR Polynésie française 2015. Available online: <https://diffusion.shom.fr/pro/risques/lidar-polynesie-francaise-borabora-2015.html> (accessed on 15 February 2021).
23. Adams, A.J.; Dahlgren, C.P.; Kellison, G.T.; Kendall, M.S.; Layman, C.A.; Ley, J.A.; Nagelkerken, I.; Serafy, J.E. Nursery function of tropical back-reef systems. *Mar. Ecol. Prog. Ser.* **2006**, *318*, 287–301. [[CrossRef](#)]
24. Calandra, M.; Wencélius, J.; Moussa, R.M.; Gache, C.; Berthe, C.; Waqalevu, V.; Ung, P.; Lerouvreur, F.; Bambridge, T.; Galzin, R.; et al. Local perceptions of socio-ecological drivers and effects of coastal armoring: The case of Moorea, French Polynesia. *Popul. Environ.* **2021**, 1–21. [[CrossRef](#)]
25. Mohajerani, A.; Burnett, L.; Smith, J.V.; Markovski, S.; Rodwell, G.; Rahman, M.T.; Kurmus, H.; Mirzababaei, M.; Arulrajah, A.; Horpibulsuk, S.; et al. Recycling waste rubber tyres in construction materials and associated environmental considerations: A review. *Resour. Conserv. Recycl.* **2020**, *155*, 104679. [[CrossRef](#)]
26. Harborne, A.R.; Mumby, P.J.; Micheli, F.; Perry, C.T.; Dahlgren, C.P.; Holmes, K.E.; Brumbaugh, D.R. The Functional Value of Caribbean Coral Reef, Seagrass and Mangrove Habitats to Ecosystem Processes. *Adv. Mar. Biol.* **2006**, *50*, 57–189. [[CrossRef](#)] [[PubMed](#)]
27. Reed, D.; van Wesenbeeck, B.; Herman, P.M.J.; Meselhe, E. Tidal flat-wetland systems as flood defenses: Understanding biogeomorphic controls. *Estuar. Coast. Shelf Sci.* **2018**, *213*, 269–282. [[CrossRef](#)]
28. Gracia, A.; Rangel-Buitrago, N.; Oakley, J.A.; Williams, A.T. Use of ecosystems in coastal erosion management. *Ocean Coast. Manag.* **2018**, *156*, 277–289. [[CrossRef](#)]
29. Cavaloc, E. *Palétuviers Moorea: Colonisation des Rhizophora Récemment Introduits à Moorea (Société, Polynésie française). Bilan de Répartition et Conséquences Écologiques*; Rapport 111; EPHE-CRIOBE-Naturalia et Biologia: Moorea, Polynésie Française, France, 1988; 44p.



Article

A Multi-Satellite Mapping Framework for Floating Kelp Forests

Lianna Gendall ^{1,*}, Sarah B. Schroeder ¹, Peter Wills ², Margot Hessing-Lewis ^{2,3} and Maycira Costa ¹

¹ SPECTRAL Remote Sensing Laboratory, University of Victoria, 3800 Finnerty Road, Victoria, BC V8P 5C2, Canada

² Canadian Hydrographic Service, Institute of Ocean Sciences, 9860 West Saanich Rd, Sidney, BC V8L 4B2, Canada

³ Hakai Institute, Campbell River, BC V0P 1H0, Canada

* Correspondence: gendall@ualberta.ca

Abstract: Kelp forests provide key habitat on the Pacific Coast of Canada; however, the long-term changes in their distribution and abundance remain poorly understood. With advances in satellite technology, floating kelp forests can now be monitored across large-scale areas. We present a methodological framework using an object-based image analysis approach that enables the combination of imagery from multiple satellites at different spatial resolutions and temporal coverage, to map kelp forests with floating canopy through time. The framework comprises four steps: (1) compilation and quality assessment; (2) preprocessing; (3) an object-oriented classification; and (4) an accuracy assessment. Additionally, the impact of spatial resolution on the detectability of floating kelp forests is described. Overall, this workflow was successful in producing accurate maps of floating kelp forests, with global accuracy scores of between 88% and 94%. When comparing the impact of resolution on detectability, lower resolutions were less reliable at detecting small kelp forests in high slope areas. Based on the analysis, we suggest removing high slope areas (11.4%) from time series analyses using high- to medium-resolution satellite imagery and that error, in this case up to 7%, be considered when comparing imagery at different resolutions in low–mid slope areas through time.

Keywords: kelp forests; multispectral; satellite; time series; spatial resolution; object-based image analysis; remote sensing

Citation: Gendall, L.; Schroeder, S.B.; Wills, P.; Hessing-Lewis, M.; Costa, M. A Multi-Satellite Mapping Framework for Floating Kelp Forests. *Remote Sens.* **2023**, *15*, 1276. <https://doi.org/10.3390/rs15051276>

Academic Editors: Junshi Xia, Dar Roberts and Simona Niculescu

Received: 1 December 2022

Revised: 11 February 2023

Accepted: 12 February 2023

Published: 25 February 2023



Copyright: © 2023 by the authors. Licensee MDPI, Basel, Switzerland. This article is an open access article distributed under the terms and conditions of the Creative Commons Attribution (CC BY) license (<https://creativecommons.org/licenses/by/4.0/>).

1. Introduction

Kelp, brown algae in the order Laminariales, are dominant habitat-forming organisms found in cool waters across approximately one-third of the Earth's coastlines [1–3]. Kelp create extensive aquatic forests that provide shelter and food for ecologically and economically important species [1,4,5]. Additionally, kelp provide myriad ecosystem goods and services, such as fisheries production, nutrient cycling and carbon removal, estimated at USD 684 billion per year worldwide [6,7]. However, climate change, overfishing, pollution and increasing harvest threaten the health and persistence of kelp forests globally [1,5,8]. Recent work highlights the negative impacts of heatwaves on kelp forests [9–14] and the loss of key predators, such as sea otters and sea stars, leading to overgrazing-induced regime shifts from kelp forests to urchin barrens [6,15–17].

Kelp forests are dynamic by nature and show high interannual variability [18–20]. Considering that kelp forests are threatened globally, but are highly variable through time, it is important to establish long-term time series to understand how kelp forests are responding to environmental conditions in a time of global change [5,10,20]. Historically, kelp forest research is based on physical field data collection, such as surveys by boats, snorkeling, or SCUBA (self-contained underwater breathing apparatus) diving [5,8,18,21–23]. These survey techniques generally cover small areas and are difficult to maintain long-term because of intensive labor requirements and high operating costs.

Furthermore, these techniques remain logistically difficult due to the seasonality and inter-annual variability of kelp forests and their extensive distribution along complex remote coastlines with highly variable and sometimes extreme conditions, such as the Pacific Coast of Canada [8,14,24,25].

Specifically on the Pacific Coast of Canada (British Columbia, BC), floating canopy-forming kelp, *Nereocystis luetkeana* and *Macrocystis pyrifera*, support a variety of commercially, recreationally and culturally important species [26,27]. Kelp forests with floating canopies are produced by kelp that grow from the bottom of the ocean up to the surface, which then aggregate in beds, henceforth referred to as floating kelp forests [28]. Only a few local areas of floating kelp forests on the BC coast have been mapped at singular time points by aerial surveys [23,29–31,31–36]. Some local-scale studies have measured kelp forests through time, but show variable patterns of change [17,23,37–40]. This highlights the need for large-scale, long-term monitoring initiatives to understand threats and assess floating kelp forest dynamics. In other areas of the Pacific Coast, some successful aerial surveys have quantified floating kelp forest trends [41–43], but these aerial surveys remain operationally cost prohibitive at the scale of the BC coast.

With the enhancement of satellite imagery technology, the ability to monitor floating kelp forests has dramatically improved, specifically with the increasing availability of high-resolution (≤ 10.0 m) satellite imagery in the 21st century. Differences in the spectral properties of floating kelp and water allow multispectral satellite sensors to distinguish kelp canopies at or near the surface of the ocean, due mainly to kelp's high reflectance in the near-infrared range of the electromagnetic spectrum [25,44]. Many different methods of classification have been applied for mapping floating kelp forests, including manual, pixel-based (supervised, unsupervised, thresholds, spectral unmixing) and object-oriented approaches (see summary by [24]). However, no standardized practices for mapping have been developed and broadly accepted in the literature, making the monitoring of floating kelp forests at large-scales difficult for non-remote sensing experts [8].

Multiple factors influence accuracy when using satellite imagery to map floating kelp forests, such as glint, clouds, tide, bathymetry, coastline morphology, shadow, currents, waves, phytoplankton blooms and adjacency impacts [25,45–47]. In particular, many of these challenges increase in severity from south to north along the West Coast of North America, such as increasing cloud cover, tidal amplitude and coastal complexity [47]. Considering these challenges, the mapping of floating kelp forests using satellite imagery has been largely developed in California, where extensive offshore *Macrocystis* kelp forests are mapped using medium spatial resolution satellites, including Landsat and SPOT imagery from the 1980s onwards (e.g., [13,19,20,48–50]). Several studies have adopted the methods developed in California to map floating kelp forests in other areas of the world, e.g., South Africa [51], Oregon [52], the Falkland Islands [53] and Canada [46]. However, using medium-resolution satellites to map floating kelp forests in BC remains challenging, due to the presence of small fringing kelp forests and the high topographical complexity of the BC shoreline [25,46].

Over the last 50 years, the spatial resolution of Earth observation satellite imagery has rapidly evolved from 80 m to submeter resolutions. Even though satellite data (archived and new) at different spatial resolutions are available globally, no large-scale, long-term study has taken advantage of data from multiple sensors to reconstruct floating kelp forest trends. Here, we present a methodological framework for mapping floating kelp forests from archived medium- to high-resolution satellite imagery, using an object-oriented analysis approach. We discuss the advantages and limitations of combining these data to reconstruct trends. Specifically, the impact of using satellite imagery acquired at different spatial resolutions to detect floating kelp forests are explored, and suggestions for drawing appropriate conclusions when using multiple sensors, are described. Here, we use a test site that supports both small fringing and large kelp forests located on the East Coast of Haida Gwaii, BC, Canada, as a case study to develop a multi-satellite mapping framework for detecting floating canopy of kelp forests. We focus on the methodological framework for

creating this time series, not the time series analysis [54]. This framework will contribute to advancements in the remote sensing of floating kelp forests, not only in BC, Canada, but will allow for trends to be understood in remote regions and ultimately help inform effective management strategies for the protection and longevity of floating kelp forest ecosystems globally.

2. Materials and Methods

2.1. Study Area

The test site for defining the multi-satellite mapping framework is located in Haida Gwaii on the West Coast of Canada, in the unceded territory of the Haida Nation; whose relationship to the land and sea long predates colonial settlement and still exists to this day [27,55]. Haida Gwaii is a large archipelago with a complex coastline of approximately 4660 km, situated in the Northeast Pacific Ocean (Figure 1A,B [56,57]). Specifically, the study site spans roughly 800 km² on the Northeast Coast of Moresby Island, just west of Hecate Strait (Figure 1C). Both dominant floating canopy-forming kelp species, *Macrocystis* and *Nereocystis*, are found in this region. *Macrocystis* grows year round and *Nereocystis* is a perennial species; however, peak biomass occurs in the summer to early fall for both species [22,58,59]. Haida highlight this region's importance for the harvest of *Macrocystis* kelp for the spawn on kelp herring roe fishery, but remark on the significant decline of kelp forests in recent history [60]. In this region, the complex bathymetry supports dense kelp forests of various sizes, from small fringing forests to large offshore forests that span kilometers. Large areas are characterized by very gradual sloping ocean floors, supporting some of the most extensive kelp forests found in BC, which are easily detectable with Landsat imagery of 60.0 m (resampled from 80.0 m) spatial resolution, or better (Figure 1E,F). In contrast, this region also includes smaller, less detectable kelp forests that grow in narrow fringing beds along the steep sloping coastline (Figure 1F). These fringing kelp forests are generally characteristic of kelp forests found across the remainder of the BC coast [38,46,47,61]. This range in kelp forest size makes this region an ideal area to define a framework for using different resolution satellites to map floating canopy area through time.

2.2. Methodological Framework

The framework is a workflow that allows researchers to compile robust temporal datasets of floating kelp canopy area through the evolution of medium- to high-resolution satellites. The workflow consists of four main steps, including: (1) imagery compilation and quality assessment; (2) preprocessing and enhancements; (3) object-oriented image classification; and (4) an accuracy assessment (Figure 2). To compare floating canopy area derived from multiple satellites, we analyzed kelp's detectability at different spatial resolutions.

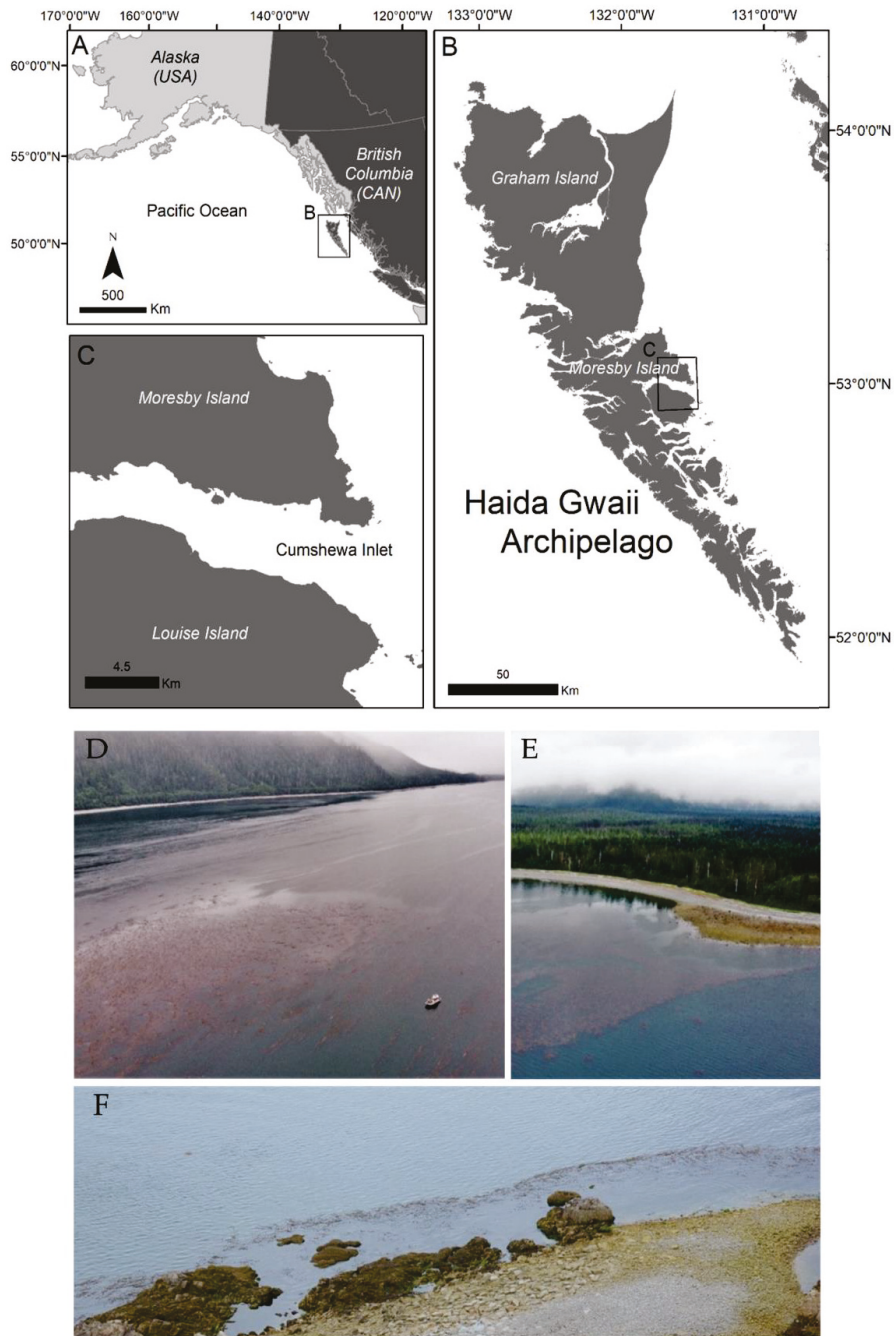


Figure 1. An overview of: (A) the Northwest Coast of North America; (B) the location of Haida Gwaii in reference to the British Columbia coast; and (C) the Cumshewa Inlet study area. The study site includes: (D) large offshore; (E) large nearshore; and (F) small fringing nearshore kelp forests. Image source: (D,E) Lianna Gendall; (F) Environment and Climate Change Canada.

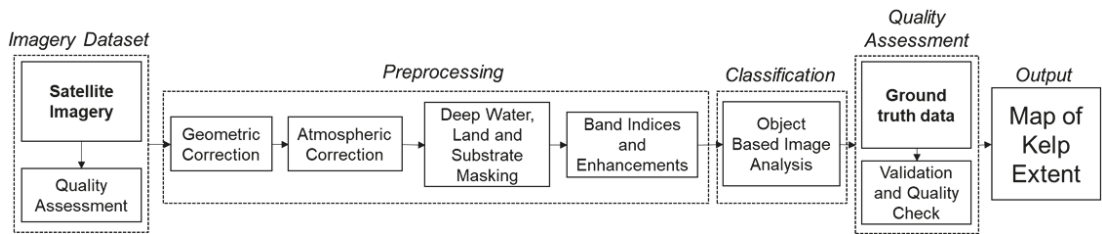


Figure 2. The workflow of the methodological framework.

2.2.1. Step 1: Imagery Dataset

Archived high- to medium-resolution (0.5–60.0 m) multispectral satellite imagery was compiled from 20 satellite sensors spanning from 1973 to 2021 through diverse sources, including open data, private data sharing agreements, and commercial acquisition (Table 1). Archived imagery is not necessarily collected during optimal conditions for mapping, and therefore special consideration should be given to any factors that may lead to inaccurate maps of floating kelp forests, such as clouds, tidal height, glint, shadow, haze, water turbidity, waves, algal blooms and time of imagery acquisition [19,25,43,45,47]. To minimize possible inaccuracies, a set of criteria were developed, and images were visually assessed considering: glint, waves, shadows, clouds, the month and tidal height of acquisition. Each category was scored from 0 to 3, where the lower the score, the better the quality. For instance, the criteria for ideal conditions (score of 0) consisted of an acquisition time between June and October, a low tidal height (<3 m above lower low-water large tide chart datum) and the minimal presence (<5%) of glint, waves, shadow and cloud within the nearshore areas where floating kelp forests are found within the imagery [25,38]. Once combined, images showing suboptimal conditions for detection (overall criteria score ≥ 7) were removed from the dataset. Importantly, the quality score results should be framed within the context that more recent imagery is intrinsically more reliable for mapping floating kelp forests due to their higher spatial resolutions.

Table 1. Medium- to high-resolution satellite imagery used to develop the methodological framework (NDVI: the normalized difference vegetation index. G-NDVI: NDVI with green instead of red. RE/G: band ratio between red and green. R/Y: band ratio between red and yellow. R/G: band ratio between red and green. NIR/G: band ratio between near-infrared and green).

| Sensor | Dates | Ground Resolution | Swath | Revisit | Bands and Wavelengths (NM) | Atmospheric Correction | Band Inputs | Source of Imagery | Sources for Indices |
|----------------|------------------------|--|--------|---------|--|--|---------------------------------------|--|------------------------|
| Landsat Series | LS-8 2013–present | 30 m multispectral 15 m panchromatic | 170 km | 16 days | Blue 450–520 Green 540–600 Red 630–690 NIR 770–900 SWIR 1550–1750 SWIR II 2110–2290 Pan 520–680 | Surface reflectance ready product | NDVI Green, Red, NIR | Freely Available from United States Geological Survey (USGS) | [13,19,20,46,53,62–64] |
| | LS-4-7 1984–present | 30 m multispectral 15 m panchromatic | 170 km | 16 days | Blue 450–520 Green 520–600 Red 630–690 NIR 770–900 NIR 1550–1750 MIR 2080–23500 Pan 520–900 | | | | |
| | LS-1-3 1972–1983 | 60 m multispectral (Resampled from 80 m) | 170 km | 18 days | Green 500–600 Red 600–700 NIR 700–800 NIR 800–1100 | Rayleigh correction | NDVI Green, Red, NIR | | |
| Sentinel-2 | 2015–present | 60 m–10 m multispectral | 290 km | 5 days | Coastal 443–463 Blue 490–555 Green 560–595 Red 665–695 Red Edge I 705–720 Red Edge II 740–755 Red Edge 1 783–803 NIR1 842–957 NIR2 865–885 SWIR I 1380–1410 SWIR I 1910–2000 SWIR II 2190–2370 | Surface reflectance ready product from SNAP Sen2Cor processor | NDVI Green, Red, NIR | Freely Available from United States Geological Survey (USGS) | [65] |

Table 1. Cont.

| Sensor | Dates | Ground Resolution | Swath | Revisit | Bands and Wavelengths (NM) | Atmospheric Correction | Band Inputs | Source of Imagery | Sources for Indices |
|--------------------------|---|---|---------------|----------|--|-----------------------------------|--|---|------------------------------|
| Spot Series | SPOT 4 1989–2013 | 20 m multispectral 10 m panchromatic | 60–80 km | 5 days | Green: 500–590 | Rayleigh correction | NDVI | Data sharing available to researchers through the Centre National d'Études Spatiales (CNES) | [50,65,66] |
| | | | | | Red: 610–680 | | Green, | | |
| | Near IR: 790–890 SWIR 1530–1750 Pan 610–680 | Red, NIR | | | | | | | |
| SPOT 5 2002–present | 10 m multispectral 5 m panchromatic | | | 2–3 days | Green: 500–590 | | | | |
| | | | | | Red: 610–680 | | | | |
| SPOT 6–7 2012–present | 6 m multispectral 1.5 m Panchromatic | | | 1–3 days | Near IR: 780–890 SWIR 1580–1750 Pan 480–710 | | | Purchased through Apollo Mapping with academic discount | |
| Geoeye-1 | 2008–present | 1.84 m multispectral 0.46 m panchromatic | 15.2 km | 2.6 days | Blue 450–510 | Rayleigh correction | G–NDVI | Private data Sharing agreement | Determined using m–statistic |
| | | | | | Green 510–580 | | Green, | | |
| | | | | | Red 630–690 NIR 780–920 Pan 450–800 | | Red, NIR | | |
| Quick-Bird-2 | 2001–2015 | 2.62 m multispectral 0.65 panchromatic | 15.2 km | 2–3 days | Blue 450–520 | Rayleigh correction | G–NDVI | Private data sharing agreement | Determined using m–statistic |
| | | | | | Green 520–600 | | Green, | | |
| | | | | | Red 630–690 NIR 760–900 Pan 450–800 | | Red, NIR | | |
| Rapid-Eye Series | 2009–present | 5 m multispectral | 77 km | 1–6 days | Blue 440–510 Green 520–590 Red 630–685 Red edge 690–730 NIR 760–850 | Surface reflectance ready product | RE/G Green, Red, RedEdge NIR | Available to researchers through Planet Labs Inc. | Determined using m–statistic |
| World-view Series | WV-3–4 2014–present | 1.24 m multispectral 0.31 m panchromatic | 13.1 km | 1–3 days | Coastal 400–450 | Rayleigh correction | RE/Y | Private data sharing agreement | Determined using m–statistic |
| | WV-2 2009–present | 1.84 m multispectral 0.46 m panchromatic | 16.4 km | | Blue 450–510 Green 510–580 Yellow 585–625 Red 630–690 | | Green, Red, NIR | | |
| Planetscope Series | 2018–present | 3.7 m multispectral | 24 km–32.5 km | Daily | Red Edge 705–745 NIR1 770–895 NIR2 860–1040 Pan 450–800 | Surface reflectance ready product | Pansharpened without NIR R/G Green Blue | Available to researchers through Planet Labs Inc. | [25,38,46] |
| | | | | | Blue: 455–515 Green: 500–590 Red: 590–670 NIR: 780–860 Blue: 464–517 Green: 547–585 Red: 650–682 NIR: 846–888 | | NIR/G Green, Red, NIR | | |

2.2.2. Step 2: Preprocessing

After selecting the optimal images for mapping, the following techniques were applied to reduce geometric and radiometric uncertainties and enhance the spectral signal of floating kelp to improve classification accuracies [25]. Geometric distortions occur in imagery due to errors during acquisition, such as variations in altitude, attitude, the velocity of the satellite, earth curvature, atmospheric refraction, and nonlinearities in the satellite path [44,67]. All selected images were checked for geometric distortions against the ESRI satellite base map in the WGS 1984 coordinate system, and those with distortions were georectified in ArcGIS using ground control points and a nearest neighbor interpolation [44,68]. However, where overlaps between imagery occurred, the overlapping images were georectified to the previous images to ensure the best match. The root mean squared error (RMSE) was calculated to evaluate the quality of the georectification, and a threshold of less than two pixels was deemed acceptable, except for the Landsat imagery, which was given an allowance of one pixel due to the coarser spatial resolution.

Following the georectification, images were evaluated for radiometric/atmospheric issues, which may impact the band indices used and, consequently, the imagery classification outputs [69,70]. When possible, we obtained atmospherically corrected images from suppliers (Table 1). For the other imagery, a simple approach considering a histogram shift determined by the Rayleigh scattering factor was applied [71], hereafter referred to as the Rayleigh correction. This approach considers that the scattering intensity is inversely proportional to the fourth power of the wavelength (λ^{-4}), and assumes that the darkest pixels in an image, corresponding to shadowed or offshore deep-water areas, should have null reflectance; however, because of Rayleigh scattering, nonzero values are recorded [71]. To account for the Rayleigh scattering, these nonzero values are subtracted from the spectral signal of each specific satellite band, considering the spectral relationship between bands according to the Rayleigh factor (λ^{-4}) [71]. The initial step is to define the lowest reflectance value in the blue band acquired from the darkest (lowest reflectance) pixels within the image (B_c), which is consequently subtracted from each pixel in the blue band. If no blue band was available (i.e., SPOT 4 and 5, Landsat-1 to 3), the value from the darkest pixels in the green band was divided in half to account for the lower proportion of Rayleigh scattering occurring and used in place of the blue B_c . Then, for each remaining visible band, the following equation is used to calculate the Rayleigh correction value (R_c):

$$R_c = \left(\left(\frac{1}{\lambda_b^4} \right) / \left(\frac{1}{\lambda_{vis}^4} \right) \right) \times B_c,$$

where λ_b represents the mean wavelength (nm) of the blue band, and λ_{vis} represents the mean wavelength (nm) of whichever visible band the equation is being used to calculate the correction for (e.g., 560 nm when correcting the green band of Geoeye-1). To ensure images were properly corrected, we evaluated the corrected reflectance of water and floating kelp for a subset of imagery from each sensor and compared them to the known reflectance for floating kelp and water from the literature [25,44,62].

Following the required corrections, images were subjected to: (i) a lowest tide land mask; (ii) a deep-water mask; and (iii) a soft substrate mask to eliminate areas where floating kelp forests are not found, and to minimize processing time and false positives. Vegetation and intertidal seaweed on land have a high near-infrared (NIR) reflectance compared to kelp [72,73], and therefore removing these features enhances the ability to digitally differentiate floating kelp from water through contrast enhancement [25]. We created the land mask using an object-based segmentation (Trimble eCognition Developer V8.64) on the imagery with the lowest tide. For each resolution of imagery used in this study, we added a buffer of one pixel to minimize land reflectance adjacency impacts from the shoreline. To eliminate any areas where floating kelp forests were unable to grow [74,75], a 20-m deep-water mask was created using a bathymetry dataset from the Canadian Hydrographic Service [38,46,76]. Lastly, we masked shallow-soft sediment bottom, which is uninhabitable to kelp [77], using overlapping areas defined as soft sediment in the BC

Marine Conservation Analysis (BCMCA) benthic classes dataset [78] and the DFO bottom patch model [77].

The final task in the preprocessing workflow was to select the combination of bands, and band indices and/or band ratios, that perform best in the classification step. The normalized difference vegetation index (NDVI, i.e., the normalized difference between the reflectance of the near-infrared and red bands [79]) was used since it is commonly used to enhance floating kelp canopies in imagery from the Sentinel-2, Landsat and SPOT satellites [19,25,46,48,50,62–66] (Table 1). Additionally, for any imagery acquired by a sensor that had not been readily used for floating kelp forest detection in the literature, the M-statistic, a measure of class separability [80], was calculated for defining other possible band indices and ratios. A high M-statistic represents high separability between two classes with significant separation when M is larger than 1.0 [80,81]. For each sensor, we combined the two to three highest scoring band indices, or ratios, with the visible bands and visually assessed the combinations to choose which provided the best overall classification results (Table 1). The selected bands, band indices and ratios, were then linearly enhanced to maximize the spectral signal of floating kelp for the final input into the classification.

2.2.3. Step 3: Classification

An object-based image analysis (OBIA) was used based on the recommendation for classifying dense floating kelp forests [25]. The OBIA approach combined a multiresolution segmentation followed by a supervised nearest neighbor classification using the Trimble eCognition Developer (V8.64) software to classify floating kelp forests within the imagery. The OBIA classification offers several advantages over pixel-based classification methods. OBIA has shown better accuracy than pixel-based methods when compared across a range of spatial resolutions and ecosystems [82–86] and allows for the size of objects to be scaled, so that object size remains relatively constant across different resolutions [84]. As part of the eCognition software, OBIA allows for the definition of features beyond the pixel values of the input data, including the mean and standard deviation of object radiometry, object size and shape, and the spatial relationships of objects. This is not considered in pixel-based classification, thus increasing separability among classes and reducing the contribution of noise to the classification comparatively to pixel-based methods [87]. In the OBIA, the final enhanced bands, band indices and/or band ratios for each image were subjected to a multiresolution segmentation (Scale: Table 2; Shape: 0.3; Compactness: 0.5) to group similar pixels into objects. From those objects, training classes corresponding to floating kelp, submerged kelp/understory seaweed, water, glint/waves, cloud, shadow and shallow water, were defined using expert knowledge. Figure 3 shows examples of the most common classes used in the OBIA. Of note, not all classes were present in all imagery. In particular, some classes, such as glint/waves and submerged kelp/understory seaweed were indistinguishable in the medium-resolution satellite imagery. Because classes varied by image, the feature space optimization tool in the eCognition software was used to mathematically calculate the best number and combination of object features, such as the spatial, spectral and contextual information (e.g., the mean of bands/band indices, the standard deviation of bands/band indices, the maximum difference across all values of all bands/band indices), to separate classes based on training samples [88]. This tool compares features of different sample classes to find the optimal combination that produces the largest average minimum distance between samples, to be used when categorizing the remaining image objects into those given classes [88]. The ability of the feature space optimization tool chosen features to separate classes was evaluated based on the analysis of boxplots and three-axis scatter plots of the top three selected features for a subset of images. Following this evaluation, we performed a nearest neighbor classification, using the optimal features defined by the feature space optimization tool, to categorize the remaining image objects into their respective classes. Before validation, the outputs were visually subjected to a quality assessment using a knowledge-based approach where erroneous classifications were manually reclassified in ArcGIS. Lastly, for the validation step, the outputs of the

classification were turned into two binary classes: floating kelp forests (1) and all other classes (0).

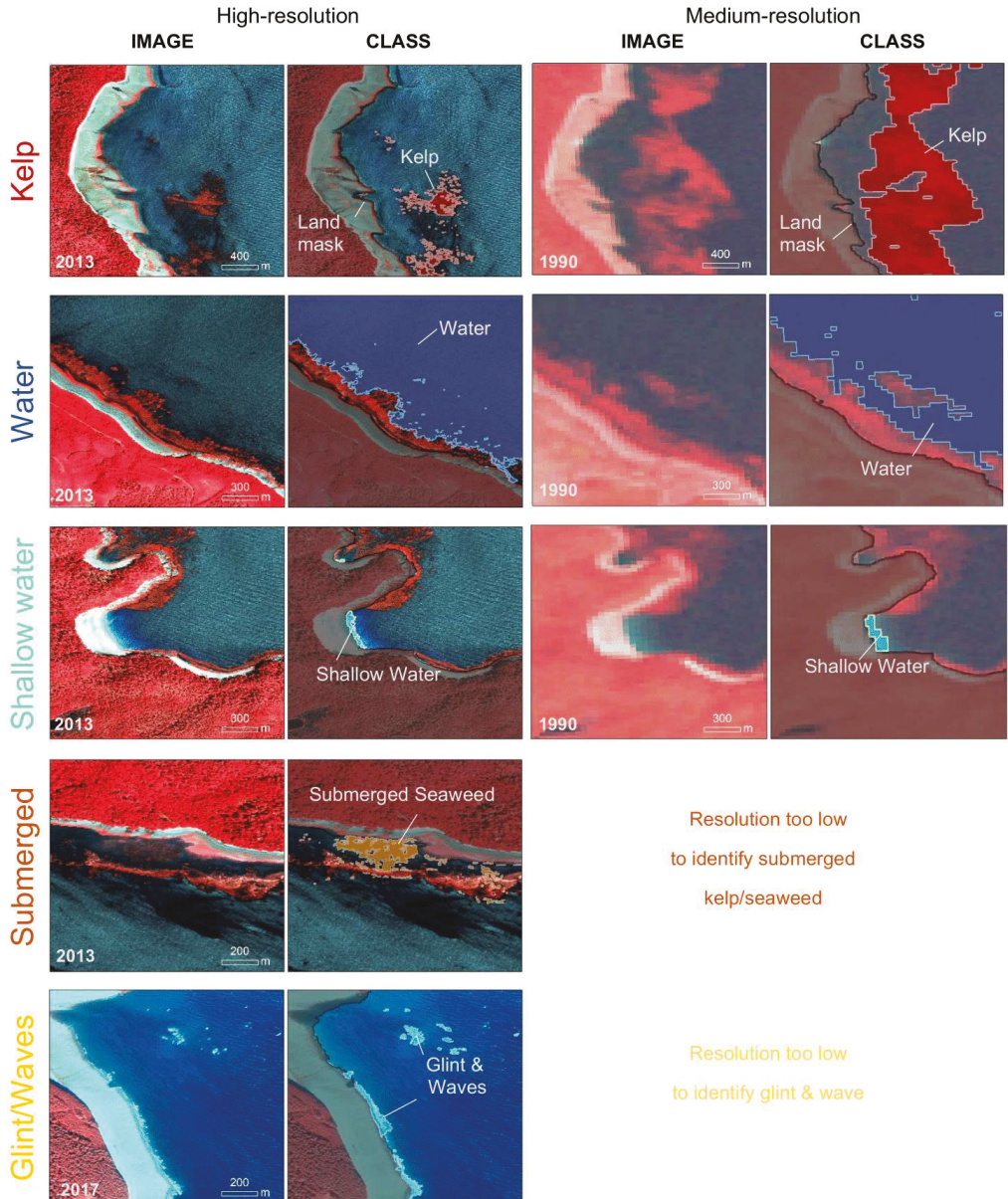


Figure 3. The most common class types used in the object-based image classification for high-resolution (QuickBird-2 images from 2013 and 2017 at 2.6 m resolution) and medium-resolution (Landsat image from 1990 at 30.0 m resolution) satellite imagery.

Table 2. The different scale factors used to determine object size in the segmentation step of the classification.

| Resolution | Sensor | Scale |
|------------|---|-------|
| 0.5 | Aerial Imagery, Pansharpened Worldview | 40 |
| 2–3 | QuickBird, Worldview | 30 |
| 4 | PlanetScope | 28 |
| 5 | Rapid Eye | 25 |
| 6 | Spot | 20 |
| 10 | Spot | 10 |
| 20 | Sentinel-2 | 7 |
| 30 | Landsat-4-8 | 5 |
| 60 | Landsat-1-3 | 5 |

2.2.4. Step 4: Quality Assessment

For the classification validation, in situ kelp data and historical survey data for the region were compiled. Ideally, ground-truth data should be collected at the time of satellite imagery acquisition [25]. However, if no ground-truth data are available, other forms of data can be used, such as past surveys showing the location of floating kelp forests [38,50,89], or expert knowledge based on reflectance values [35]. For our dataset, we compiled two forms of validation data: (i) in situ and (ii) archived data (Figure 4). The in situ data, including drone images, photoquadrats (camera mounted above a 1 m quadrat lowered to the seafloor), above water oblique photos from a boat, and remotely operated underwater vehicle footage, were acquired in August 2021, a day after PlanetScope imagery acquisition. Archived surveys were obtained, comprised of oblique photos from an aerial survey performed by Environment and Climate Change Canada (ECCC) in 2015, multiple years of SCUBA surveys (1990, 1994, 2007, 2012, 2017) from the Department of Fisheries and Oceans Canada (DFO) [90] and kelp shoreline classifications from an aerial survey conducted in 1997 by ShoreZone. All validation data were combined into a dataset of spatial points and classified as either floating kelp present or absent. Specifically, the DFO Scuba surveys and ShoreZone data were simplified from species specific data (*Macrocystis* and *Nereocystis*) to presence and absence. For the archived aerial images from ECCC, a random subset of images was visually assessed for presence or absence. All validation data were compared to the classification produced from imagery in the matching year to produce measurements of accuracy corresponding to users', producers' and global accuracy, meaning errors of commission (false-positives), omission (false-negatives) and overall accuracy [91]. No archived validation data were available during the years of acquisition for the three highest resolution satellites, so in order to validate products from the QuickBird-2, Geoeye-1 and Worldview-2 satellites, the ECCC oblique photos were used with the assumption that some errors would be associated with yearly variability.

2.2.5. Resolution Analysis

Here, we evaluate the impact of spatial resolution on the detectability of floating kelp forests in satellite imagery at different scales. This analysis allowed us to define an independent variable (ocean floor slope) to be used as an indicator of kelp forest size, highlighting areas of uncertainty. The following steps were adopted in this analysis:

Step 1: Images from QuickBird (2.6 m), RapidEye (5.0 m) and Sentinel-2 (10.0 m), with their original spatial resolutions, were resampled using bilinear interpolation to the different resolutions matching the satellite database (6.0 m, 10.0 m, 20.0 m, 30.0 m, 60.0 m; Table 1) following [92,93]. Sentinel-2 was included in the analysis to address possible interpolation errors [94] associated with resampling high-resolution imagery from QuickBird-2 and RapidEye to 20.0 m, 30.0 m and 60.0 m resolutions. The original and resampled images were classified using the OBIA method described in Sections 2.2.2 and 2.2.3. To ensure that images from the same sensor remained comparable, we used the same areas to train the

classifier for each set of down-sampled images. After the classification of the resampled images, the overall detectability across the study region was measured as the total amount of floating canopy area (m²) detected in the downgraded resolution, divided by the total floating canopy area (m²) detected in the original image, and presented as the percentage of floating canopy area.

Step 2: A 1 km segment-based approach was used as the areal unit to evaluate the impact of resolution (see Figure 5 for the delineation of segments). Due to the complex bathymetry and presence of large offshore and nearshore floating kelp forests in our study area, ocean floor slope was used to delineate these segments, as adapted from [95]. To achieve segments that could extend kilometers offshore, segments were created in two categories, along the shoreline (ocean floor slope greater than 3%) and out across the low slope areas extending offshore (ocean floor slope of less than or equal to 3%), using 20 m bathymetry data from CHS [76]. These ocean floor slope categories were only used to construct the segments and were not used in further analyses.

Step 3: Ocean floor bathymetry often limits the size of kelp forests by reducing the available area to grow [46,96]; therefore, we assume it can be used as a proxy for kelp forest size. For example, in high slope areas, the bottom quickly becomes too deep, limiting the availability of light needed for kelp to establish and grow. In these conditions kelp only grows in narrow fringing forests, which are more difficult to detect in satellite imagery. Consequently, ocean floor slope was used to define areas where we would expect larger inaccuracies of the classification at different resolutions. However, first we tested the assumption that high slope areas support small fringing kelp forests [46].

For this, the relationship between ocean floor slope and kelp forest size was explored (classified from the original QuickBird-2, RapidEye and Sentinel-2 images and measured in m²). For each segment, we defined the mean ocean floor slope based on the 20 m bathymetry data from CHS [70], where a single kelp 'forest' was defined as a continuous patch of attached floating kelp where kelp objects in the classification were connected. Based on the relationship of floating kelp forest size and ocean floor slope, we divided the segments into two broad categories: low-mid slope areas (0–11.3%), which support large and small kelp forests, and high slope areas (11.4–37.0%), which support only small kelp forests. Next, floating canopy area percentage was compared between the two slope categories.

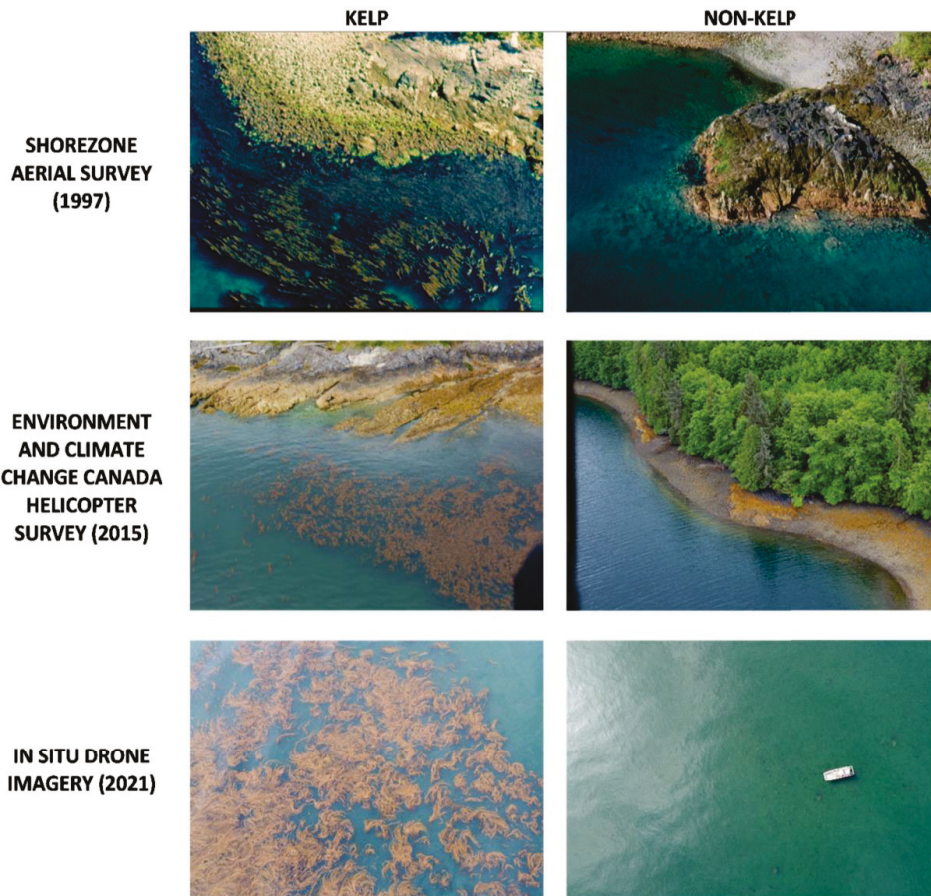


Figure 4. Examples of in situ and archived data for the accuracy assessment of the classification. The DFO SCUBA surveys are not shown.

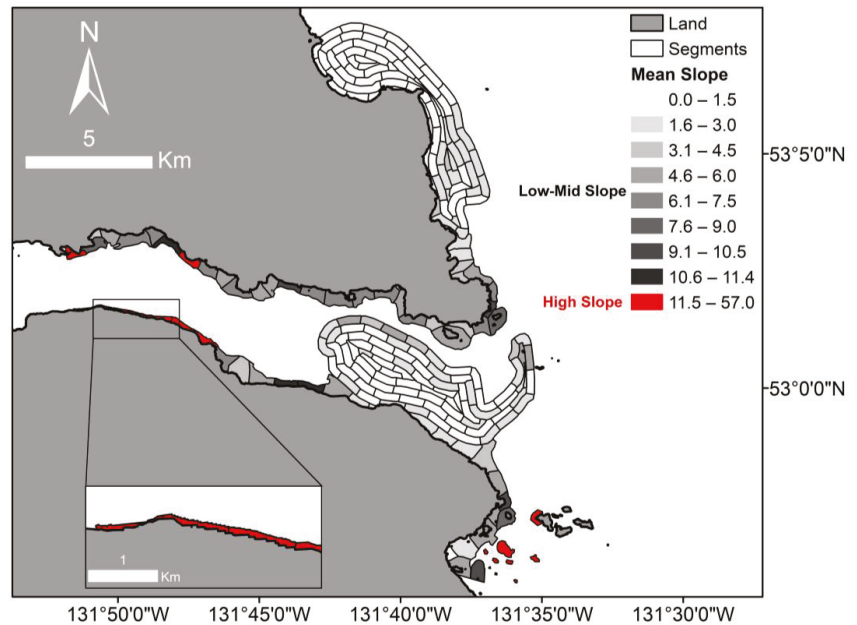


Figure 5. A map of approximately 1 km segments categorized into two main groups based on segment mean slope: low–mid (0–11.3%) shown in greyscale and high (11.4–37.0%) shown in red.

3. Results

3.1. Imagery Quality Assessment

Out of hundreds of archived images examined across many different sources (Table 1), a total of 52 images (from 1973 to 2021) were selected after the quality assessment step. No good-quality images were found for a total of 12 years, including 1975, 1978–1981, 1983, 1987, 1993, 1995, 1996, 2003 and 2004. Landsat was the only freely available satellite imagery provider before 2004 and thus the preferred choice for imagery; in particular, Landsat-7's scan line corrector failure in 2003 [97] led to no available images for 2003 and 2004. For years following 2005, the preferential choice was for high-resolution imagery (2.0–20.0 m). Imagery from a single Spot 4 image (20.0 m) to numerous images from Sentinel-2 (10.0 m), QuickBird-2 (2.6 m), Geoeye-1 (1.8 m), Worldview (1.2 m and 1.8 m), PlanetScope (3.0 m resampled from 3.7 m) and RapidEye (5.0 m) satellites were compiled. In addition to the high-resolution satellite imagery, we included a single nadir RGB aerial image (0.5 m spatial resolution) from the Canadian Hydrographic Service in the dataset because of the lack of good-quality high-resolution satellite imagery in 2007.

The 52 archived images selected through the criteria were acquired in various conditions, leading to a range in quality scores (Table 3). The largest proportion of imagery (46%) were acquired during 'optimal' conditions for floating kelp forest mapping, followed by the second largest proportion (37%) acquired during 'good' conditions. Together, the 'good' and 'optimal' imagery account for 83% of the total imagery. Among the defined criterion, more often, high tides or the presence of glint and cloud in imagery led to lower scores than waves and haze (Table 3). Notably, in some years, no optimal low tide (<3 m above chart datum) imagery was available because of the high tidal exchange that occurs in Haida Gwaii (up to 7.8 m above chart datum) [98], leading to 33% of images ranked in the lowest category for tides (5.0 to 6.0 m). These images were still included in the time series dataset because floating kelp forests were readily visible upon inspection.

Table 3. A summary of image quality criteria where percent (%) is the proportion of the 52 images that fall into each category.

| Quality | Cloud (%) | Tide (%) | Glint (%) | Waves (%) | Timing (%) | Haze (%) | Quality | Score | Percent (%) |
|---------|-----------|----------|-----------|-----------|------------|----------|------------|--------|-------------|
| 0 | 79 | 31 | 52 | 96 | 92 | 77 | Optimal | <1 | 46 |
| 1 | 10 | 17 | 42 | 4 | 8 | 12 | Good | 2 to 3 | 37 |
| 2 | 10 | 19 | 4 | 0 | 0 | 6 | Medium | 4 to 5 | 15 |
| 3 | 2 | 33 | 2 | 0 | 0 | 6 | Acceptable | 6 | 2 |

3.2. Preprocessing

Considering the selected imagery used for further analysis, a total of six images needed geometric correction: one from Landsat-1, and all imagery from QuickBird-2 and Geoeye-1, resulting in a RMSE within the two pixel threshold (average RMSE: QuickBird-2: 4.49 m, Geoeye-1:3.61 m, Landsat-1: 16.48 m). For the next step, Rayleigh correction was applied to imagery from Landsat-1–3, QuickBird-2, SPOT 5–7 and Geoeye-1; images acquired by the other sensors (Sentinel-2, RapidEye, PlanetScope and Landsat-5) were provided in atmospherically corrected products. After Rayleigh correction, our results showed that compared to the original values, floating kelp and dark water pixels in the blue band were reduced to zero or just slightly above, in the green band, pixels values decreased by approximately half, and by approximately a third in the red band (Figure 6). This conforms with the shape of kelp spectra and water spectra from in situ hyperspectral measurements of floating kelp and water, in literature [25,44,62].

After geometric and Rayleigh corrections, the different spectral indices were evaluated based on the M-statistics. Among the available spectral indices, the M-statistic results showed different optimal indices for the different satellites (Table 4). For Geoeye-1 and QuickBird-2, a normalized vegetation index with the green band (G-NDVI) instead of the red band had the highest separability (>1.44). Meanwhile, for PlanetScope imagery, a simple ratio combination of the near-infrared and green bands showed the highest separability (>11.34). Lastly, for satellites that included a red-edge band, RapidEye and Worldview, a simple band ratio of red-edge over green (>1.69), and red-edge over yellow (>2.72), was best at separating kelp from water, respectively. The statistically selected indices and bands were used as the input data for the object-oriented classification.

Table 4. A summary of the M-statistic of different band indices and ratios for kelp and non-kelp classes observed in the imagery during band selection (R: red, Y: yellow, G: green, B: blue, RE: red-edge, NIR: near-infrared, G-NDVI: NDVI with green instead of red, RE-NDVI: NDVI with red-edge instead of NIR, B-NDVI: NDVI with blue instead of red, B-RE-NDVI: NDVI with blue instead of red and red-edge instead of NIR, G-RE-NDVI: NDVI with green instead of red and red-edge instead of NIR). Indices selected for input into classification are bolded.

| Satellite | Kelp-Water | Kelp-Shallow Water | Kelp-Shadow | Kelp-Glint/Waves | | | | |
|-------------|---------------|--------------------|---------------|------------------|---------------|------|---------------|-------|
| Worldview-2 | RE/Y | 3.19 | NIR1/B | 4.91 | RE/Y | 2.72 | - | - |
| | RE-NDVI | 2.96 | NDVI | 4.63 | RE-NDVI | 2.32 | - | - |
| | NIR2/Y | 2.51 | G-NDVI | 4.43 | RE/R | 1.99 | - | - |
| Geoeye-1 | G-NDVI | 6.58 | B-NDVI | 6.58 | - | - | B-NDVI | 28.59 |
| | NIR/G | 6.52 | NDVI | 6.52 | - | - | NDVI | 13.66 |
| | B-NDVI | 1.44 | G-NDVI | 1.44 | - | - | G-NDVI | 4.74 |
| Quickbird-2 | G-NDVI | 9.81 | NIR/R | 15.80 | G-NDVI | 7.46 | - | - |
| | NIR/R | 7.34 | G-NDVI | 9.85 | NIR/G | 6.95 | - | - |
| | NIR/G | 7.24 | NIR/G | 7.08 | NDVI | 5.02 | - | - |
| Planetscope | NIR/G | 14.02 | NIR/G | 11.34 | - | - | NIR/G | 19.63 |
| | NIR/R | 8.55 | NIR/R | 7.53 | - | - | NIR/R | 8.81 |
| | NDVI | 7.55 | NDVI | 7.32 | - | - | NDVI | 7.39 |
| Rapideye | RE/G | 1.69 | NIR/R | 31.74 | - | - | NIR/R | 12.00 |
| | B-RE-NDVI | 1.46 | NIR/G | 11.23 | - | - | NIR/G | 10.81 |
| | G-RE-NDVI | 1.42 | RE/R | 9.11 | - | - | RE/R | 10.17 |

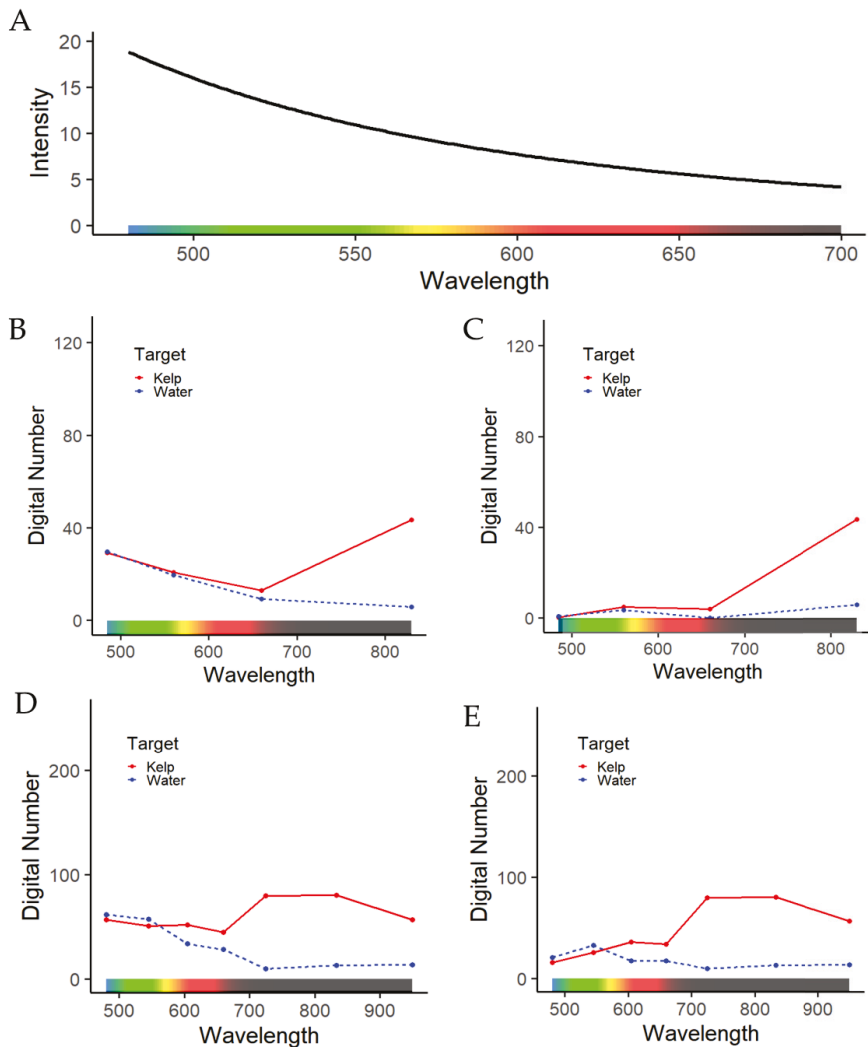


Figure 6. Examples of spectra before and after performing the Rayleigh correction using the (A) Rayleigh scattering curve to atmospherically correct imagery. (B,C) show a QuickBird-2 image before and after correction and (D,E) show a Worldview-3 image before and after correction. Of note, the magnitude of the digital number and wavelengths varies between sensors.

3.3. Classification & Accuracy Assessment

Here, the results are presented according to the order of the various decision processes for the classification and validation. In an object-oriented classification approach, after the initial segmentation step (see Methodological Framework Step 3: Classification), the feature space optimization tool of eCognition defined the combination of object features that best differentiate classes. Specifically, the feature space optimization function defines the best combination of object features that gives the highest possible separability between classes, as illustrated by the example of features chosen to classify a QuickBird-2 image (Figure 7). In this particular case, the feature space optimization tool chose the standard deviation of G-NDVI, the mean G-NDVI, and the maximum difference between

all bands and band indices to differentiate floating kelp canopy from submerged sea-weed/kelp, glint/waves and water sample classes. Mean G-NDVI alone can differentiate kelp from all other classes present in the image. However, the feature space optimization chose both the standard deviation of G-NDVI and the maximum difference between all bands and band indices because, when combined, they can differentiate among all classes (Figure 7). For the majority of the dataset, the feature space optimization tool selected between three and 10 features depending on the image, with, generally, the mean of the red-edge band (when available), the mean of the near-infrared band and/or the mean of the band indices selected.

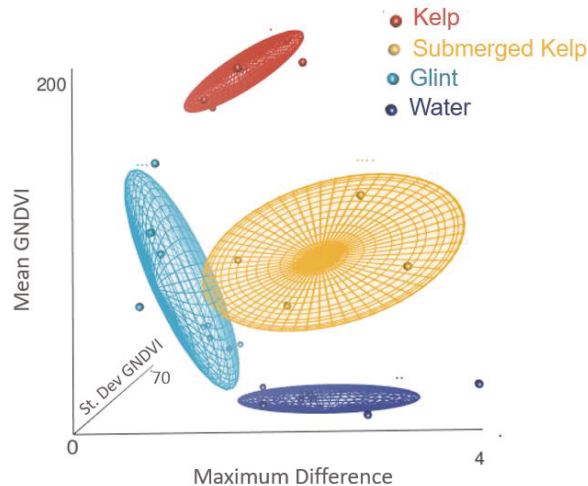


Figure 7. A three-axis scatter plot of the top three features chosen by the Feature Space Optimization tool showing the separability of classes: the standard deviation (St. Dev) of G-NDVI; mean G-NDVI; and the maximum difference between all (G, R, NIR and G-NDVI) input bands. The example was done with a QuickBird-2 image.

After selecting the optimal features, we ran the classification according to the nearest neighbor algorithm, followed by an evaluation of the classification results, considering user, producer, and global accuracies (Table 5). The overall global accuracy for all sensors ranged from 88% to 94% (Table 5). Generally, producers' and users' accuracy for kelp was high (from 83% to 96% and from 90% to 100%, respectively; Figure 8C,D). Producers' accuracy for non-kelp classes were also high (from 89% to 100%). The lowest scores occurred within the non-kelp users' accuracy (from 64% to 100%) with errors occurring where floating kelp was misclassified as water (see example in Figure 8A,B). Lastly, we found no apparent differences when comparing the accuracy assessments that used concurrent and non-concurrent validation data for QuickBird-2, GeosEye-1 and Worldview-2 (Table 5).

We used, on average, 124 validation points (85 kelp points and 39 non-kelp points), except for with the classification of RapidEye and the aerial imagery. For these, only nine validation data points were available for each, and thus even though high accuracy was achieved, caution about the results is recommended. The lowest resolution satellite, Landsat-5 (30.0 m), included in the validation, had similar accuracy to the higher-resolution satellites (Table 5); however, it produced the lowest measure of users' accuracy for non-kelp targets (64%). Upon inspection, smaller thin fringing forests in steep nearshore areas were misclassified as water or omitted due to the lowest tide land mask's coarse resolution.

Table 5. A summary of the accuracy assessment where users' accuracy (%) refers to how often classes (non-kelp and kelp) on the map are present in situ, and producers' accuracy (%) refers to how often real features (non-kelp and kelp) on the ground are correctly classified on the maps.

| Timing | Satellite | Kelp Users' Accuracy | Kelp Producers' Accuracy | n= | Non-Kelp Users' Accuracy | Non-Kelp Producers' Accuracy | n= | Global Accuracy | n= |
|----------------|-------------|----------------------|--------------------------|-----|--------------------------|------------------------------|----|-----------------|-----|
| Concurrent | PlanetScope | 100 | 92 | 171 | 70 | 100 | 30 | 94 | 201 |
| | Spot 7 | 100 | 88 | 64 | 86 | 100 | 48 | 93 | 112 |
| | Landsat-5 | 97 | 82 | 113 | 64 | 92 | 39 | 89 | 152 |
| | Aerial | 100 | 83 | 6 | 75 | 100 | 3 | 88 | 9 |
| | Rapid Eye | 100 | 88 | 7 | 100 | 100 | 1 | 88 | 9 |
| Non-concurrent | QuickBird-2 | 90 | 96 | 47 | 95 | 89 | 45 | 92 | 92 |
| | Geoeye-1 | 95 | 89 | 64 | 77 | 89 | 27 | 89 | 91 |
| | Worldview-2 | 98 | 84 | 50 | 85 | 98 | 46 | 91 | 96 |

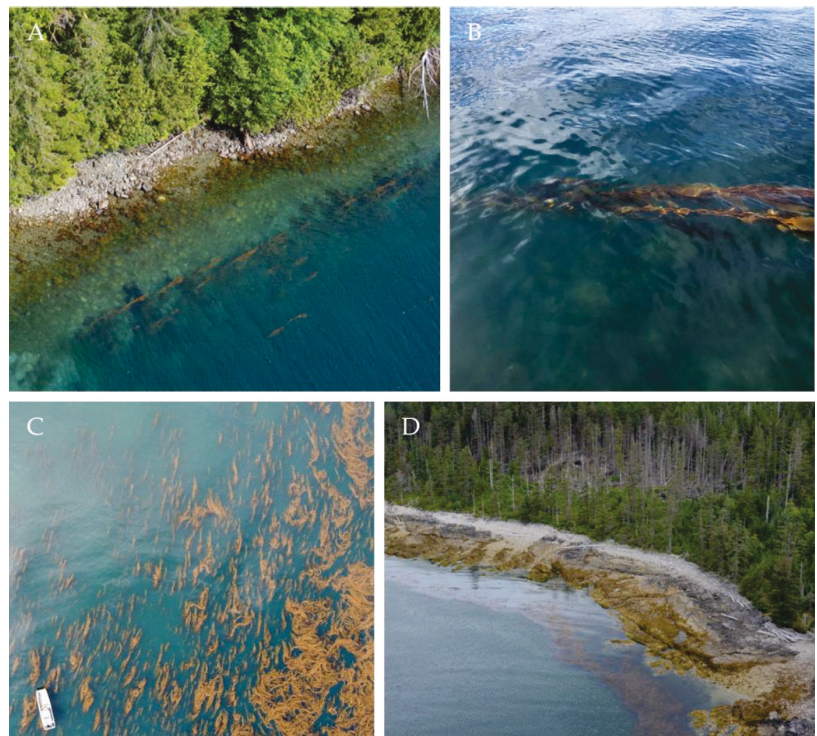


Figure 8. Examples of (A,B) kelp that was misclassified as water, and examples of (C,D) kelp that was correctly classified during the accuracy assessment. Image sources: (A,D) Environment and Climate Change Canada; (B,C) Gendall, L.

3.4. Resolution Analysis

Figure 9 illustrates the relationship between pixel size and the mixing of the spectral signature of different features within a pixel. Specifically, within a pixel resolution (for instance, 30.0 by 30.0 m for Landsat-5), the kelp spectral signature is averaged with the spectral signature of other classes in close proximity (e.g., water), decreasing the ability to accurately map floating kelp forests as pixel size increases. In particular, as resolution

decreases, floating kelp and water spectrum are mixed, and the reflectance in the near-infrared wavelengths decrease (Figure 9G). At the sample location shown in Figure 9, the object-based classification can no longer differentiate the floating kelp signal from water at 60.0 m (Figure 9G).

Pixel mixing decreases the ability to correctly classify floating kelp when using medium-resolution imagery. We show that at downgraded resolution, images generally produced a floating canopy area within 9% of their image's original kelp forest area (Figure 10). For instance, at 6.0 m resolution, the mapped floating kelp canopy area is 93%, i.e., 7% lower than the mapped area at the original 2.6 m resolution. This can be assumed up to a certain downgraded resolution because the further an image is downgraded away from its original resolution, the more likely artifacts or errors from the interpolation methods may occur, such as blurring and edge halos [94]. This possible issue is minimized by avoiding data analysis of downgraded high- to medium-resolution, and instead, considering a downgraded Sentinel-2 image from 10.0 m (SE10) to 20.0 m, 30.0 m and 60.0 m (SE20, SE30 and SE60, respectively). In this case, the results show that the floating kelp canopy area remained almost unchanged when downgrading the medium-resolution Sentinel-2 image from 10.0 m to 20.0 m, 30.0 m and 60.0 m (Figure 10C).

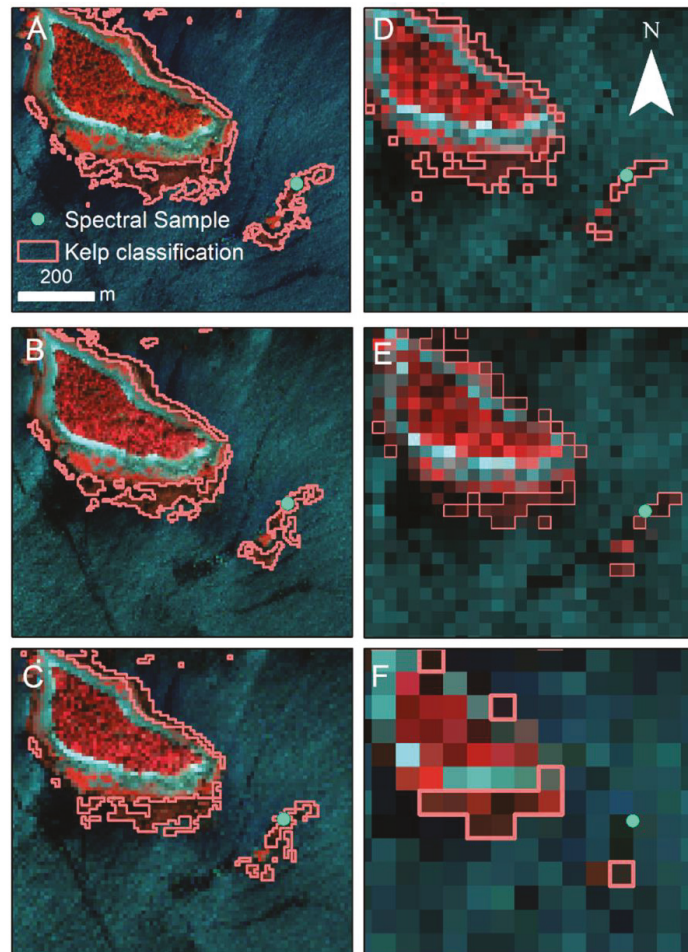


Figure 9. Cont.

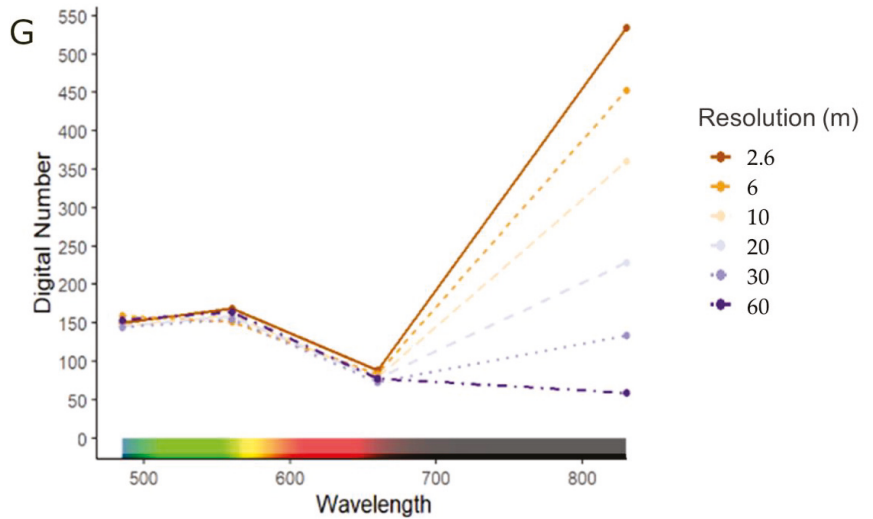


Figure 9. Clips of the same location of (A) the QuickBird-2 image (2.6 m) down sampled to (B) 6.0 m, (C) 10.0 m, (D) 20.0 m, (E) 30.0 m and (F) 60.0 m, with (G) showing the spectra measured at the sample location. Floating kelp forest classification is shown as a pink outline. Images are false color infrared showing land vegetation and seaweeds (including kelp) as red, rock/sand as light blue and water as dark blue to black.

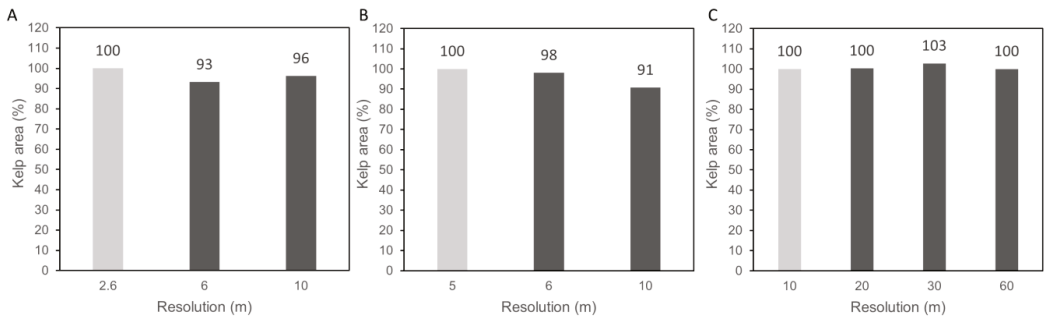


Figure 10. The change in kelp area as a percentage of the kelp area (dark grey bars) derived from the original image’s resolution (light grey bar) plotted by resolution for (A) QuickBird-2 (original resolution: 2.6 m), (B) RapidEye (original resolution: 5.0 m) and (C) Sentinel-2 (original resolution: 10.0 m).

Figure 11 shows the relationship between floating kelp forest size (produced from the three original images) and ocean floor slope. Generally, areas of low–mid slope (0–11.3%) were associated with both small (<17,000 m²) and large kelp forests (≥17,000 m²), whereas high slope (>11.4%) areas were only associated with small fringing kelp forests (<17,000 m²). The low–mid slope areas exhibited a lower percent difference (within 7%) of floating kelp forest area between the various imagery resolutions than the high slope areas (up to 50%) overall (Figure 12). In particular, the differences in floating canopy area in high slope regions were much more pronounced in the downgraded medium-resolution imagery (SE20, SE30 and SE60) than the high-resolution imagery (QB6, QB10, RE6 and RE10). These results allowed us to restrict the use of medium-resolution imagery to map floating kelp forests only in areas of mid–low slope, i.e., imagery resolution between

20.0 and 60.0 m is not recommended for high slope areas where fringing small kelp forests dominantly occur.

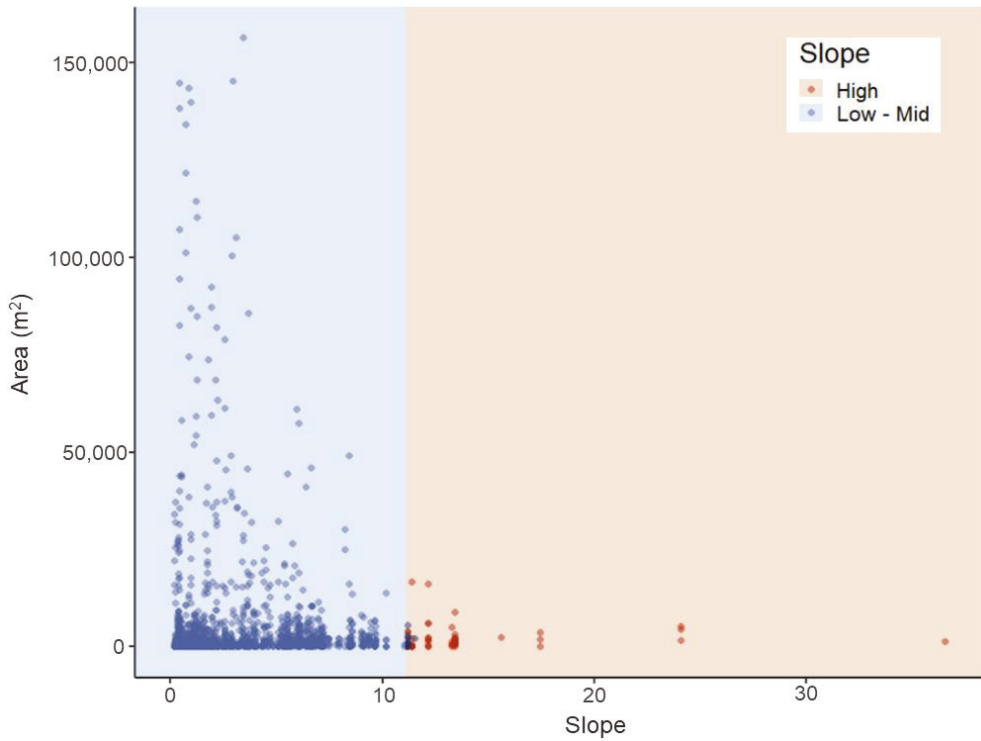


Figure 11. Kelp forest size (m²) by segment slope where blue represents all kelp forests found within the low–mid slope category (0–11.3%) and orange represents high slope area (11.4–37.0%).

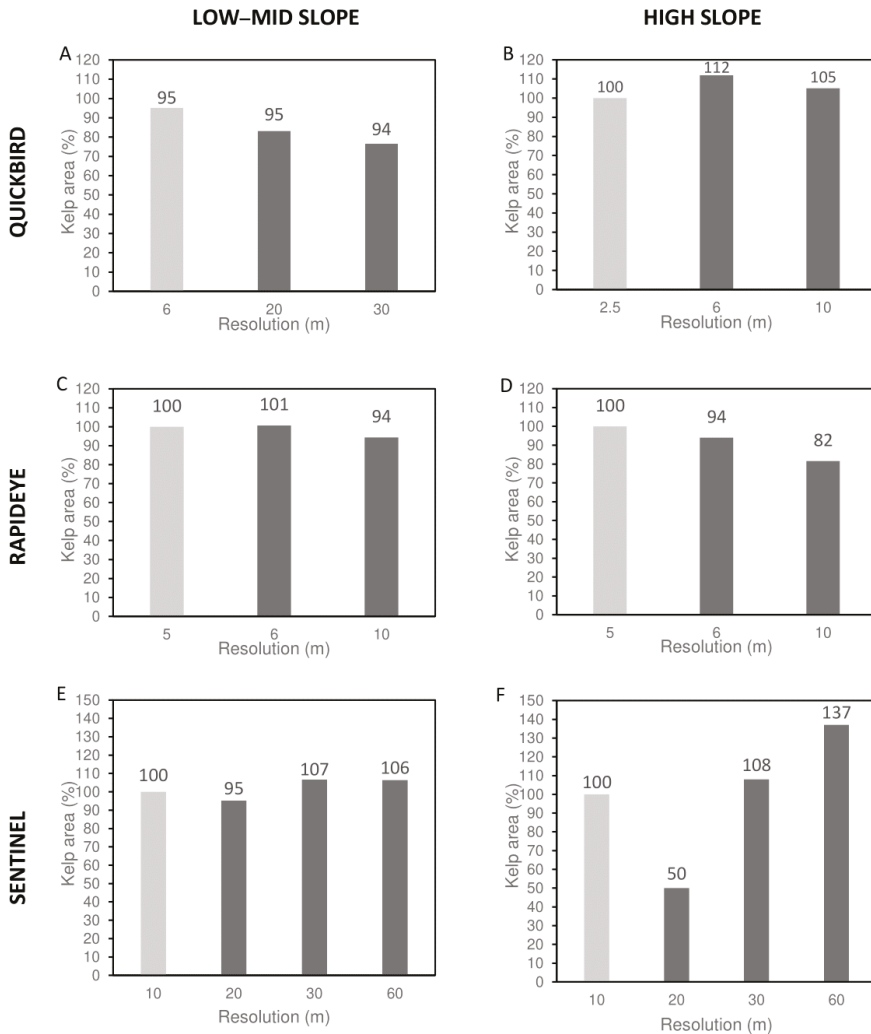


Figure 12. The change in floating canopy area as a percentage of that derived from the original image plotted by resolution separated into (A,C,D) low-mid and (B,D,F) high slope categories for (A,B) QuickBird-2 (original resolution: 2.6 m), (C,D) RapidEye (original resolution: 5.0 m) and (E,F) Sentinel-2 (original resolution: 10.0 m).

4. Discussion

With advances in remote sensing technology, opportunities to map and monitor important ecosystems across large scales through time are increasing. The Landsat series offers the best tool to map floating kelp forests at a single resolution (30.0 m) back through time [13,19,46,62,63,99]. However, the ability to use medium-resolution imagery to accurately map changes in floating kelp canopy area through time remains difficult in regions with small fringing kelp forests, such as the Pacific Coast of Canada and Oregon [46,52]. Here, we developed a framework combining standardized practices and adaptable methods to produce a long time series of accurate maps of floating kelp forests from satellite imagery acquired at various spatial resolutions. We show that the ability to map floating kelp forests at different imagery resolutions can vary spatially based on ocean floor slope,

and thus this metric can be used to highlight areas of uncertainty. Herein, we make a case for the workflow, discuss the impact of spatial resolution on kelp detection, summarize recommendations for researchers when using the multi-satellite mapping framework (Table 6) and more broadly consider the limitations and applications of the research.

Table 6. A summary of the recommendations outlined in the discussion for researchers applying the multi-satellite floating kelp mapping framework to create a long-term time series of kelp forest canopy area.

| The Multi-Satellite Kelp Mapping Framework Recommendations | |
|---|--|
| Quality Criteria | <p>Have a set of quality criteria adapted for the specific area of interest when choosing what images to use to minimize the time and cost associated with building an archived imagery time series.</p> <p>Things to consider in the development of criteria for a given area:</p> <ul style="list-style-type: none"> Peak biomass for acquisition timing; Aim for low tidal heights; Minimize cloud cover and haze; Minimize glint and waves; Minimize low sun angles and shadows; Minimize adjacency effects. |
| Geometric and Atmospheric Corrections | <p>When possible, attain imagery as atmospherically and geometrically corrected products and when not possible use simple approaches such as a first-order polynomial shift for geometric correction and the Rayleigh correction method to adjust atmospheric scattering and attenuation.</p> |
| Band Indices/Ratios | <p>Use a measure of class separability such as the M-statistic to determine the best combination of band indices and ratios to use for each sensor. The most common band index used in floating kelp forest remote sensing is NDVI. However, we found G-NDVI, as well as band indices using the RedEdge band, often produced higher M-statistic scores.</p> |
| Classification | <p>To classify floating kelp area within different imagery from different satellites, use an adaptable OBIA classification with the help of the feature space optimization tool to minimize errors and attain high-accuracy scores. In this case, the feature space optimization tool often selected between three and 10 features depending on the image, with, generally, the mean of the red-edge band, the mean of the near-infrared band and/or the mean of the band indices selected. Of note, expert knowledge is required to choose samples to train the classifier and a visual quality assessment of the classification should be performed to minimize erroneous classifications prior to the accuracy assessment.</p> |
| Accuracy Assessment | <p>When possible, collect in situ validation data. However, if no ground-truth data are available, other forms of data can be used to validate the classification, such as past surveys that show the location of kelp forests, or expert knowledge based on reflectance values.</p> |
| Resolution | <p>The ability to map floating kelp forests at different imagery resolutions can vary spatially based on ocean floor slope, and thus this metric can be used to highlight areas of uncertainty.</p> <p>Based on the Haida Gwaii test area:</p> <p>We suggest that regions with slopes higher than 11.4% should either be mapped only with the high-resolution imagery or excluded from comparisons between high- and medium-resolution imagery. We suggest that changes up to 7% be taken into consideration when comparing kelp distributions from imagery at different resolutions in low–mid slope areas.</p> <p>Special attention should be given to the detection limits at different resolutions when applying the framework in new areas, thus we suggest performing similar resolution analyses and adjusting the ocean floor slope threshold accordingly, especially if segment size and kelp forest density and species vary significantly from those presented in this study.</p> |

4.1. Methodological Framework: Standardization and Adaptability

In remote sensing, Earth observation satellite data has become readily available, and users often face confusion when trying to determine which satellites to use to produce the best results for their given application [100]. In this paper, we highlighted some of the most well-known sensors for mapping floating kelp forests, such as the Landsat, SPOT and Sentinel-2 satellites (e.g., [19,46,62,65]), while also presenting some new cost-effective high-resolution options such as imagery from RapidEye, Worldview and PlanetScope satellites, which add valuable data into the kelp mapping field with their coverage since 2008, 2009 and 2018, respectively. In addition to the choice of satellites, having a specific set

of criteria when choosing what images to use is crucial in minimizing the time and cost associated with building a time series (Table 6) [38,100,101]. We demonstrated one possible set of criteria that can be used to minimize errors associated with environmental conditions and the timing of satellite imagery acquisition. Of note, the criterion should always be selected based on the specific areas of interest. In particular, other factors that could lead to the erroneous classification of floating kelp forests in satellite imagery are land adjacency effects, high currents independent from tides, water turbidity and the presence of algal blooms [47]. Our analysis did not consider these because they were largely absent in our study region. However, in our case, clouds and higher amplitude tides often limited the availability of good quality images. As such, some mid- to high-tide images (3.0–5.0 m above chart datum) were included, based on a visual assessment of the imagery. A loss of floating canopy area up to 42% when comparing a 2.0 m tidal height difference was found on the Central Coast of BC [46]. In California, where *Macrocystis* kelp forms large offshore forests similar to those found within the study area, increases in tidal height of 1 m in UAV imagery reduced the floating canopy area from 15% to 30%, but was site dependent [102]. However, little to no difference was detected in Landsat satellite-derived kelp biomass measurements across a 2.0 m tidal difference, likely related to the coarse resolution [19,50]. Consequentially, researchers should be aware of the impact that tides can have on detection when determining their tide criterion and using this framework for time series analyses. The impact of tides can be site, species, density and kelp forest size dependent [102,103]. Upon visual comparison we found no major difference between tidal heights used in this study; however, more analyses are needed to understand and quantify the impact of tides in this region.

Once a good quality imagery database is created, users are faced with many inconsistent and complex approaches to correct systematic errors, such as atmospheric attenuation and geometric distortions in imagery [25,104]. In order to keep the workflow streamlined and easy to use, we propose a simple geometric and atmospheric correction method that can be applied to imagery from various sensors (Table 6). For georectification, we found that a simple first-order polynomial shift, which considers systematic and random distortions in images [44,67,105], properly addressed any geometric distortions present. There are numerous atmospheric correction methods that range from simple techniques like the Rayleigh correction method [63] to the more complex algorithms that need supplemental data, including atmospheric models and, ideally, in situ measurements [106,107]. Other researchers, for instance, have effectively used models such as the Fast line-of-sight Atmospheric Analysis of Hypercubes (FLAASH) [35] and the Atmospheric and Topographic Correction (ATCOR) [46]. Nonetheless, these methods can often under- or overcorrect values when parameters are not adequately chosen, making it challenging for non-remote sensing experts to use, and problematic when applied over large bodies of water [108–110]. When possible, imagery should be downloaded as already corrected products, such as in [52,53,62,65]. For example, the United States Geological Survey (USGS) provides Landsat Analysis Ready Data (ARD) products [111] and the Planet provides Surface Reflectance (SR) products [112]. However, when these products are not available, adhering to a simple method that only requires within-image information is recommended to prevent errors related to inconsistent methods or data input. We found that the adopted Rayleigh correction method resulted in similar floating kelp and water spectra as those from the literature [25,44,62]. More importantly, the shape of the floating kelp and water spectra from the corrected images were akin to those of the atmospherically corrected products.

Numerous band ratios and vegetative indices have been used to enhance floating kelp forests in satellite imagery [25]. Most notably, NDVI, which was initially used to detect healthy land vegetation [113], has been co-opted for floating kelp forests [19,25,46,48,50,52,53,63,114]. Based on the literature, NDVI has been effectively applied to Sentinel-2, Landsat and SPOT satellite imagery to differentiate kelp from other classes. Alternatively, based on M-statistic analysis, and similar to [25], we found that the NDVI with the green band (G-NDVI)

instead of the red band performed better, most likely because less noise was visible in the green band than in the red band. Additionally, indices that included the red-edge band outperformed other indices, likely associated with the ability to detect slightly deeper kelp better than the near-infrared band [115]. Considering these factors, within an image pixel, there is likely a spectral signal mixture of submerged and floating kelp canopy with water; consequently, users should consider that the red-edge indices may produce a higher reflectance signal or slightly more kelp area than nonred-edge indices, depending on the properties of the kelp forest (percentage submerged, depth, size, density, species, object size). Although different band indices were chosen in our analysis, the overall accuracy of the kelp maps produced remained high across all satellites regardless of chosen index, indicating the viability of using different band indices to enhance the detection of floating kelp forests.

Among the many different forms of classification, a commonly used method, the Multiple Endmember Spectral Mixture Analysis (MESMA), has been effectively used for mapping kelp forests in Landsat imagery. The MESMA is a pixel-based approach, which linearly models the amount of kelp and seawater in each pixel using one kelp pixel endmember and multiple water pixel endmembers [19,19,50,62,99,116,117]. In comparison, the OBIA approach presented herein and first used by [25,38] to map kelp forests, is based on clustering pixels into objects before the classification. The advantages of using the OBIA approach proposed in this framework are related to less computational power, less consideration of imagery noise commonly found in pixel-based classifications, the ability to mimic the visual interpretation of features in an image, and the ability to scale object sizes to remain similar across different resolution imagery [25,83,84,84,85,118,119]. Most importantly, the feature space optimization tool allows for the classification to be optimized on a per image basis. With an OBIA approach, single kelp plants are not being detected, but the aggregates of plants floating at the surface, with the inclusion or some submerged kelp and water gaps between patches, depending on the size of objects selected by the user. This gives users the ability to define the best object size based on forests in their region and the resolution of imagery used. Additionally, when users are trying to detect very small and sparse fringing forests in high-resolution imagery, that result in single pixels needing to be classified as kelp, a pixel-based classification has shown to outperform OBIA [25]. In this case, users should be cognizant of the limitations of OBIA and should test the performance of pixel-based methods described in [25].

Across all sensors, the multi-satellite mapping framework resulted in high overall global accuracy (from 88% to 94%) when compared to the range (from 59% to 94%) documented in the literature [25,38,46,52,66]. It is important to note that different sources of validation data were used to evaluate the classification results, including field observations concurrent with imagery acquisition, data acquired from airplane and SCUBA surveys, matched for the same year, and some not matching the same year. However, for using all the different data sources, expert knowledge was always embedded prior to the accuracy assessment to minimize the use of erroneous classification outputs when comparing with validation data. Generally, the errors of omission and commission showed that most errors occurred at medium-resolutions where sparse, and narrow fringing forests along steep shorelines were misclassified as water or omitted due to the coarse resolution low water mask, similar to [46]. This indicates that the relationship between imagery spatial resolution and floating canopy area has to be considered to highlight mapped areas with high uncertainties.

4.2. The Impact of Resolution and Drawing Appropriate Conclusions

The framework presented here incorporated the analysis of a large range of satellite imagery with spatial resolutions ranging from 2.5 to 60.0 m (except for the one aerial image with a resolution of 0.5 m). Generally, although the imagery resolutions differed by one order of magnitude, the mapped floating canopy area at the regional level did not largely differ among resolutions. However, at a finer spatial scale, we found that the floating

canopy area mapped in high slope areas (associated with fringing kelp forests) were more impacted at coarser resolutions, indicating that these areas are prone to higher classification errors. As such, we propose the addition of a new parameter, ocean floor slope, to define the limitations of mapping floating kelp forests from different resolution imagery. Particularly, the comparison between floating kelp forest size and slope showed that high slope areas support small kelp forests, leading to more uncertainty when mapping with medium-resolution imagery (up to 50%). Based on these factors, we suggest that regions with slopes higher than 11.4% should either be mapped only with the high-resolution imagery or excluded from comparisons between high-resolution and medium-resolution imagery (Table 6). Additionally, for the time series of floating kelp forest change, we recommend that users consider that a certain percentage of differences among years can be attributed to errors due to resolution, and not be attributed to true changes in floating canopy area. Within our region, we suggest that changes up to 7% (with high slope areas removed from the analysis) be taken into consideration when comparing area from imagery at different resolutions (Table 6).

4.3. The Challenges and Broad Applications of the Methodological Framework

A few challenges and limitations remain when using this proposed framework. Unfortunately, the remote sensing of kelp canopies in this framework are currently limited to those floating on or close to the surface, due to water's high-absorption of the near-infrared signal [115]. The detection of subsurface kelp forest canopy from aerial and satellite imagery remains difficult, is limited to shallow depths, generally necessitates clear waters and often requires the use of high-resolution imagery or hyperspectral data [66,120–122]. More work would be needed to expand these methods to subsurface kelp forests. Additionally, environmental impacts (e.g., tides and currents) are challenging to isolate because they largely differ based on location, species type, density and the time of imagery acquisition. We were able to minimize the impact that different environmental conditions have on imagery through criteria; however, we were unable to quantify or create correction factors for the impact of tides or currents. Of note, given our goal to produce highly accurate floating kelp forest maps, the approach suggested here is a supervised classification method and needs some expert knowledge to determine good training samples for the classifier in any given area. Moreover, when using the multi-satellite mapping framework, researchers should consider the species and density of kelp forests present within their region. In our case, floating kelp forests were generally dense, regardless of the forest size and species, thus conforming with the presented framework. For other regions where sparse kelp forests dominate or areas containing solely *Nereocystis* kelp forests, special attention should be given to the detection limits at different resolutions, the use of OBIA versus pixel-based classifications for very small sparse forests [25] and the ocean floor slope threshold.

The spatial resolution analysis and subsequent recommendations were conducted with rigorous methodological criteria; however, the analysis was limited to samples of imagery from three satellites. We acknowledge that the sample size is limited, and other satellite-associated variables beyond spatial resolution, including spectral resolution, signal-to-noise ratio, and satellite vicarious calibration, also play a role in detectability [25,123,124]. However, the resolution analysis allows for a conservative approach when drawing conclusions from the time series of floating kelp forests. Additional research in the future may include defining correction factors, similar to the tidal correction factor applied by [62], to minimize the effects of the different spatial resolutions. For this, we recommend multiple replicates of comparisons between satellite images collected at different spatial resolutions in similar conditions over the same location, within a short time frame. Furthermore, it is important to note that our unit of analysis was ~1 km segments. In the literature, the size of segments for kelp time series analyses vary substantially (e.g., 100 m in [38], 8 km in [43] and 1 km in [125]), and as such, special consideration should be given to the scale of future analyses. We advise that further explorations of the resolutions'

impact on kelp detectability be made if the unit of analysis (segments length) significantly differs from the 1 km segment size presented in this study.

Many methods exist to detect floating kelp forests from satellite imagery; however, most focus on compiling a time series using a single type of sensor, which can limit either the spatial resolution of imagery available (i.e., 30.0 m Landsat imagery from 1984 onwards), or with the use of high-resolution satellite imagery the length of the time. The MESMA approach, used with Landsat imagery from 1984 onwards to detect large offshore forests of kelp in California [19,50,62,117], has been used to map *Macrocystis* in the southernmost part of Argentina [108] and *Nereocystis* off the coast of Northern California [91] and Oregon [52]. However, when this approach was used to map kelp forests on the Central Coast of BC, between 28% and 75% of kelp that was present in the shoreline areas was missed due to the medium-resolution of the Landsat imagery [43]. Recently, a similar method using 10.0 m Sentinel-2 data was created [65], and although this method uses higher-resolution imagery, the Sentinel-2 data repository only dates back to 2015. In contrast, the methodology presented here enables trends to be understood with high-resolution data back to the early 2000s, and medium-resolution data back to the 1970s. The methods proposed by [25,46,50,65], and the one shown here, when integrated with the growing availability of higher-resolution imagery such as the Planetscope satellite series (available since 2018), will streamline the monitoring of floating kelp forests into the future. It will also continue to allow scientists to better understand large-scale trends in floating kelp forests in a time of unprecedented kelp forest loss, such as those documented in California [117,126], Baja California [12], Japan [127,128], Australia [9,10,129–132], Oman [133], Norway [134], Spain [135,136], Chile [137] and the Atlantic Coast of Canada [11].

5. Conclusions

Globally, threats to kelp forests are on the rise; however, locally, kelp forests show highly variable patterns of change [1,3]. This study highlights that with the advancement in Earth observation satellite technology, archived satellite imagery can be leveraged for the monitoring of crucial floating kelp forest ecosystems using medium-resolution imagery from the 1970s onwards, and more recently, using high-resolution imagery from the early 2000s onwards. The multi-satellite mapping framework allows for the creation of a floating kelp canopy area time series using medium- to high-resolution satellite imagery through standardized practices (i.e., the image quality criteria, geometric and Rayleigh correction) and adaptable image-to-image methods (i.e., band index/ratio selection and OBIA). We acknowledge that differing resolutions have an impact on kelp detection, and that when using this framework we suggest using ocean floor slope (removing areas of slope > 11.4%) as a metric to highlight areas of uncertainty in kelp detectability. Creating these long time series of floating kelp forests using the framework can facilitate the monitoring and protection of these important nearshore habitats from emerging threats. Additionally, when coupled with environmental driver data and/or climate prediction modelling, it can highlight the regions of risk and resilience of floating kelp forests globally.

Author Contributions: L.G., M.C. and M.H.-L. designed the methodological framework; L.G. carried out the compilation, the processing of data and the writing of the manuscript with guidance from S.B.S., M.C. and M.H.-L.; P.W. facilitated the provision of some of the high-resolution satellite imagery and provided revisions on the manuscript. All authors have read and agreed to the published version of the manuscript.

Funding: During this research L.G. was supported through a MITACS Accelerate internship with the Hakai Institute, as well as M.C.'s NSERC-DG.

Data Availability Statement: Data are available for research purposes upon request to the authors' institutions.

Acknowledgments: We thank the Hakai Institute for partially funding this work, as well as the Canadian Hydrographic Service, Transport Canada, the Department of Fisheries and Oceans Canada (in particular Joanne Lessard), Environment and Climate Change Canada, and ShoreZone, for

providing satellite data and ground-truth data. A special thanks to Lynn Lee with Parks Canada and Stuart Crawford with the Council of the Haida Nation for assistance with field equipment in Haida Gwaii.

Conflicts of Interest: The authors declare no conflict of interest.

References

- Wernberg, T.; Krumhansl, K.; Filbee-Dexter, K.; Pedersen, M.F. Chapter 3—Status and Trends for the World’s Kelp Forests. In *World Seas: An Environmental Evaluation*, 2nd ed.; Sheppard, C., Ed.; Academic Press: Cambridge, MA, USA, 2019; pp. 27–78. ISBN 978-0-12-805052-1.
- Jayathilake, D.R.M.; Costello, M.J. Version 2 of the World Map of Laminarian Kelp Benefits from More Arctic Data and Makes It the Largest Marine Biome. *Biol. Conserv.* **2021**, *257*, 109099. [[CrossRef](#)]
- Bolton, J.J. The Biogeography of Kelps (Laminariales, Phaeophyceae): A Global Analysis with New Insights from Recent Advances in Molecular Phylogenetics. *Helgol. Mar. Res.* **2010**, *64*, 263–279. [[CrossRef](#)]
- Johnson, S.W.; Murphy, M.L.; Csepp, D.J.; Harris, P.M.; Thedinga, J.F. *A Survey of Fish Assemblages in Eelgrass and Kelp Habitats of Southeastern Alaska*; U.S Department of Commerce: Washington, DC, USA, 2003; p. 48.
- Krumhansl, K.A.; Okamoto, D.K.; Rassweiler, A.; Novak, M.; Bolton, J.J.; Cavanaugh, K.C.; Connell, S.D.; Johnson, C.R.; Konar, B.; Ling, S.D.; et al. Global Patterns of Kelp Forest Change over the Past Half-Century. *Proc. Natl. Acad. Sci. USA* **2016**, *113*, 13785–13790. [[CrossRef](#)] [[PubMed](#)]
- Filbee-Dexter, K.; Wernberg, T. Rise of Turfs: A New Battlefield for Globally Declining Kelp Forests. *BioScience* **2018**, *68*, 64–76. [[CrossRef](#)]
- Eger, A.; Marzinelli, E.; Baes, R.; Blain, C.; Blamey, L.; Carnell, P.; Choi, C.G.; Hessing-Lewis, M.; Kim, K.Y.; Lorda, J.; et al. The Economic Value of Fisheries, Blue Carbon, and Nutrient Cycling in Global Marine Forests. *EcoEvoRxiv* **2021**. [[CrossRef](#)]
- Bennion, M.; Fisher, J.; Yesson, C.; Brodie, J. Remote Sensing of Kelp (Laminariales, Ochrophyta): Monitoring Tools and Implications for Wild Harvesting. *Rev. Fish. Sci. Aquac.* **2019**, *27*, 127–141. [[CrossRef](#)]
- Wernberg, T.; Smale, D.A.; Tuya, F.; Thomsen, M.S.; Langlois, T.J.; de Bettignies, T.; Bennett, S.; Rousseaux, C.S. An Extreme Climatic Event Alters Marine Ecosystem Structure in a Global Biodiversity Hotspot. *Nat. Clim. Change* **2013**, *3*, 78–82. [[CrossRef](#)]
- Wernberg, T.; Bennett, S.; Babcock, R.C.; de Bettignies, T.; Cure, K.; Depczynski, M.; Dufois, F.; Fromont, J.; Fulton, C.J.; Hovey, R.K.; et al. Climate-Driven Regime Shift of a Temperate Marine Ecosystem. *Science* **2016**, *353*, 169–172. [[CrossRef](#)]
- Filbee-Dexter, K.; Feehan, C.; Scheibling, R. Large-Scale Degradation of a Kelp Ecosystem in an Ocean Warming Hotspot. *Mar. Ecol. Prog. Ser.* **2016**, *543*, 141–152. [[CrossRef](#)]
- Arafeh-Dalmau, N.; Montaña-Moctezuma, G.; Martínez, J.A.; Beas-Luna, R.; Schoeman, D.S.; Torres-Moye, G. Extreme Marine Heatwaves Alter Kelp Forest Community Near Its Equatorward Distribution Limit. *Front. Mar. Sci.* **2019**, *6*, 499. [[CrossRef](#)]
- Cavanaugh, K.C.; Reed, D.C.; Bell, T.W.; Castorani, M.C.N.; Beas-Luna, R. Spatial Variability in the Resistance and Resilience of Giant Kelp in Southern and Baja California to a Multiyear Heatwave. *Front. Mar. Sci.* **2019**, *6*, 413. [[CrossRef](#)]
- Smale, D.A. Impacts of Ocean Warming on Kelp Forest Ecosystems. *New Phytol.* **2020**, *225*, 1447–1454. [[CrossRef](#)] [[PubMed](#)]
- Dean, T.A.; Schroeter, S.C.; Dixon, J.D. Effects of Grazing by Two Species of Sea Urchins (*Strongylocentrotus Franciscanus* and *Lytechinus Anamesus*) on Recruitment and Survival of Two Species of Kelp (*Macrocystis Pyrifera* and *Pterygophora Californica*). *Mar. Biol.* **1984**, *78*, 301–313. [[CrossRef](#)]
- Estes, J.A.; Duggins, D.O. Sea Otters and Kelp Forests in Alaska: Generality and Variation in a Community Ecological Paradigm. *Ecol. Monogr.* **1995**, *65*, 75–100. [[CrossRef](#)]
- Burt, J.M.; Tinker, M.T.; Okamoto, D.K.; Demes, K.W.; Holmes, K.; Salomon, A.K. Sudden Collapse of a Mesopredator Reveals Its Complementary Role in Mediating Rocky Reef Regime Shifts. *Proc. R. Soc. B* **2018**, *285*, 20180553. [[CrossRef](#)] [[PubMed](#)]
- Dayton, P.K.; Tegner, M.J.; Edwards, P.B.; Riser, K.L. Temporal and Spatial Scales of Kelp Demography: The Role of Oceanographic Climate. *Ecol. Monogr.* **1999**, *69*, 219–250. [[CrossRef](#)]
- Cavanaugh, K.; Siegel, D.; Reed, D.; Dennison, P. Environmental Controls of Giant-Kelp Biomass in the Santa Barbara Channel, California. *Mar. Ecol. Prog. Ser.* **2011**, *429*, 1–17. [[CrossRef](#)]
- Bell, T.W.; Allen, J.G.; Cavanaugh, K.C.; Siegel, D.A. Three Decades of Variability in California’s Giant Kelp Forests from the Landsat Satellites. *Remote Sens. Environ.* **2020**, *238*, 110811. [[CrossRef](#)]
- Cameron, F.K. *Potash from Kelp*; U.S. Government Printing Office: Washington, DC, USA, 1915.
- Druehl, L.D. The Pattern of Laminariales Distribution in the Northeast Pacific. *Phycologia* **1970**, *9*, 237–247. [[CrossRef](#)]
- Sutherland, I.R.; Karpouzi, V.; Mamoser, M.; Carswell, B. *Kelp Inventory, 2007: Areas of the British Columbia Central Coast from Hakai Passage to the Bardswell Group*; Oceans and Marine Fisheries Branch, Ministry of Environment, Fisheries and Oceans Canada, Ministry of Agriculture and Lands and Heiltsuk Tribal Council: Victoria, BC, Canada, 2008.
- Yesson, C.; Bush, L.E.; Davies, A.J.; Maggs, C.A.; Brodie, J. The Distribution and Environmental Requirements of Large Brown Seaweeds in the British Isles. *J. Mar. Biol. Assoc. UK* **2015**, *95*, 669–680. [[CrossRef](#)]
- Schroeder, S.B.; Dupont, C.; Boyer, L.; Juanes, F.; Costa, M. Passive Remote Sensing Technology for Mapping Bull Kelp (*Nereocystis luetkeana*): A Review of Techniques and Regional Case Study. *Glob. Ecol. Conserv.* **2019**, *19*, e00683. [[CrossRef](#)]

26. DFO. *Report on the Progress of Recovery Strategy Implementation for Northern Abalone (Haliotis kamtschatkana) in Pacific Canadian Waters for the Period 2007–2012*; Species at Risk Act Recovery Strategy Report Series; Fisheries and Oceans Canada: Ottawa, ON, Canada, 2015; p. 28.
27. Marine Planning Partnership Initiative. *Haida Gwaii Marine Plan*; Marine Planning Partnership Initiative: Haida Gwaii, BC, Canada, 2015; ISBN 978-0-7726-6885-1.
28. Reed, D.C.; Kinlan, B.P.; Raimondi, P.T.; Washburn, L.; Gaylord, B.; Drake, P.T. CHAPTER 10-A Metapopulation Perspective on the Patch Dynamics of Giant Kelp in Southern California. In *Marine Metapopulations*; Kritzer, J.P., Sale, P.F., Eds.; Academic Press: Burlington, NJ, USA, 2006; pp. 353–386, ISBN 978-0-12-088781-1.
29. Blakley, B.B.; Chalmers, W.T. *Masset Kelp Inventory*; Department of Environment, Fisheries Operations, Province of British Columbia: Vancouver, BC, Canada, 1973.
30. Field, E.J.; Coon, L.M.; Clayton, W.E.L.; Clark, E.A.C. *Kelp Inventory, 1976, Part 1. The Estevan Group and Campania Island*; Marine Resources Branch, Ministry of Environment, Province of British Columbia: Victoria, BC, Canada, 1977.
31. Coon, L.M.; Roland, W.; Sutherland, I.R.; Hall, R. *Kelp Inventory 1978 NorthWest Coast of Vancouver Island*; Marine Resources Branch, Ministry of Environment, Province of British Columbia: Victoria, BC, Canada, 1978.
32. Coon, L.M.; Roland, W.; Field, E.J.; Clayton, W.E.L. *Kelp Inventory 1976. Part 3. North & West Coasts Graham Island (Q.C.I)*; Marine Resources Branch, Ministry of Environment, Province of British Columbia: Victoria, BC, Canada, 1979.
33. Field, E.J.; Clark, E.A.C. *Kelp Inventory, 1976, Part 2. The Dundas Group*; Marine Resources Branch, Ministry of Environment, Province of British Columbia: Victoria, BC, Canada, 1978.
34. Sutherland, I.R. *Kelp Inventory, 1989, The Vancouver Island and Malcolm Island Shores of Queen Charlotte Strait*; Fisheries Development Report; Aquaculture and Commercial Fisheries Branch, Ministry of Agriculture and Fisheries Province of British Columbia: Victoria, BC, Canada, 1990.
35. Sutherland, I.R. *Kelp Inventory, 1996 Porcher Island, Groschen Island, Banks Island, and the Estevan Group*; Fisheries Development Report; Aquaculture and Commercial Fisheries Branch, Ministry of Agriculture, Fisheries and Food, Province of British Columbia: Victoria, BC, Canada, 1998.
36. Sutherland, I.R. *Kelp Inventory, 1995 Nootka Sound*; Fisheries Management Report; Sustainable Economic Development Branch, Ministry of Fisheries, Province of British Columbia: Victoria, BC, Canada, 1999.
37. Watson, J.; Estes, J.A. Stability, Resilience, and Phase Shifts in Rocky Subtidal Communities along the West Coast of Vancouver Island, Canada. *Ecol. Monogr.* **2011**, *81*, 215–239. [[CrossRef](#)]
38. Schroeder, S.B.; Boyer, L.; Juanes, F.; Costa, M. Spatial and Temporal Persistence of Nearshore Kelp Beds on the West Coast of British Columbia, Canada Using Satellite Remote Sensing. *Remote Sens. Ecol. Conserv.* **2019**, *32*, e2673. [[CrossRef](#)]
39. Starko, S.; Bailey, L.A.; Creviston, E.; James, K.A.; Warren, A.; Brophy, M.K.; Danasel, A.; Fass, M.; Townsend, J.A.; Neufeld, C. Environmental Heterogeneity Mediates Scale-Dependent Declines in Kelp Diversity on Intertidal Rocky Shores. *PLoS ONE* **2019**, *14*, e0213191. [[CrossRef](#)]
40. Starko, S.; Neufeld, C.J.; Gendall, L.; Timmer, B.; Campbell, L.; Yakimishyn, J.; Druehl, L.; Baum, J.K. Microclimate Predicts Kelp Forest Extinction in the Face of Direct and Indirect Marine Heatwave Effects. *Ecol. Appl.* **2022**, *32*, e2673. [[CrossRef](#)]
41. North, W.J.; James, D.E.; Jones, L.G. History of Kelp Beds (*Macrocystis*) in Orange and San Diego Counties, California. *Hydrobiologia* **1993**, *260*, 277–283. [[CrossRef](#)]
42. Parnell, P.E.; Miller, E.F.; Cody, C.E.L.; Dayton, P.K.; Carter, M.L.; Stebbins, T.D. The Response of Giant Kelp (*Macrocystis pyrifera*) in Southern California to Low-Frequency Climate Forcing. *Limnol. Oceanogr.* **2010**, *55*, 2686–2702. [[CrossRef](#)]
43. Pfister, C.A.; Berry, H.D.; Mumford, T. The Dynamics of Kelp Forests in the Northeast Pacific Ocean and the Relationship with Environmental Drivers. *J. Ecol.* **2018**, *106*, 1520–1533. [[CrossRef](#)]
44. Jensen, J.R. Remote Sensing Techniques for Kelp Surveys. *Photogramm. Eng.* **1980**, *13*, 743–755.
45. Britton-Simmons, K.; Eckman, J.; Duggins, D. Effect of Tidal Currents and Tidal Stage on Estimates of Bed Size in the Kelp *Nereocystis luetkeana*. *Mar. Ecol. Prog. Ser.* **2008**, *355*, 95–105. [[CrossRef](#)]
46. Nijland, W.; Reshitnyk, L.; Rubidge, E. Satellite Remote Sensing of Canopy-Forming Kelp on a Complex Coastline: A Novel Procedure Using the Landsat Image Archive. *Remote Sens. Environ.* **2019**, *220*, 41–50. [[CrossRef](#)]
47. Cavanaugh, K.C.; Bell, T.; Costa, M.; Eddy, N.E.; Gendall, L.; Gleason, M.G.; Hessing-Lewis, M.; Martone, R.; McPherson, M.; Pontier, O.; et al. A Review of the Opportunities and Challenges for Using Remote Sensing for Management of Surface-Canopy Forming Kelps. *Front. Mar. Sci.* **2021**, *8*, 1536. [[CrossRef](#)]
48. Augenstein, E.; Stow, D.; Hope, A. Evaluation of Spot Hrv-Xs Data for Kelp Resource Inventories. *Photogramm. Eng. Remote Sens.* **1991**, *57*, 501–509.
49. Deysher, L.E. Evaluation of Remote Sensing Techniques for Monitoring Giant Kelp Populations. *Hydrobiologia* **1993**, *260*, 307–312. [[CrossRef](#)]
50. Cavanaugh, K.; Siegel, D.; Kinlan, B.; Reed, D. Scaling Giant Kelp Field Measurements to Regional Scales Using Satellite Observations. *Mar. Ecol. Prog. Ser.* **2010**, *403*, 13–27. [[CrossRef](#)]
51. Anderson, R.; Rand, A.; Rothman, M.; Share, A.; Bolton, J. Mapping and Quantifying the South African Kelp Resource. *Afr. J. Mar. Sci.* **2007**, *29*, 369–378. [[CrossRef](#)]
52. Hamilton, S.L.; Bell, T.W.; Watson, J.R.; Grorud-Colvert, K.A.; Menge, B.A. Remote Sensing: Generation of Long-Term Kelp Bed Data Sets for Evaluation of Impacts of Climatic Variation. *Ecology* **2020**, *101*, e03031. [[CrossRef](#)]

53. Houskeeper, H.F.; Rosenthal, I.S.; Cavanaugh, K.C.; Pawlak, C.; Trouille, L.; Byrnes, J.E.K.; Bell, T.W.; Cavanaugh, K.C. Automated Satellite Remote Sensing of Giant Kelp at the Falkland Islands (Islas Malvinas). *PLoS ONE* **2022**, *17*, e0257933. [CrossRef]
54. Gendall, L. Drivers of Change in Haida Gwaii Kelp Forests: Combining Satellite Imagery with Historical Data to Understand Spatial and Temporal Variability. Master's Dissertation, University of Victoria, Victoria, BC, Canada, 2022.
55. *Haida Nation v. British Columbia (Minister of Forests)*; 2004; Report 3 S.C.R. 511. Available online: <https://scc-csc.lexum.com/scc-csc/scc-csc/en/item/2189/index.do> (accessed on 1 November 2022).
56. Sloan, N.A.; Bartier, P.M. *Living Marine Legacy of Gwaii Haanas. I: Marine Plant Baseline to 1999 and Plant-Related Management Issues*; Parks Canada: Gatineau, QC, Canada, 2000; p. 114.
57. Sloan, N.A.; Dick, L. Sea Otters, Aquapelagos & Ecosystem Services. *Shima Int. J. Res. Into Isl. Cult.* **2015**, *9*, 7.
58. Dayton, P.K. Ecology of Kelp Communities. *Annu. Rev. Ecol. Syst.* **1985**, *16*, 215–245. [CrossRef]
59. Springer, Y.; Hays, C.; Carr, M.; Mackey, M.M. *Ecology and Management of Bull Kelp (Harvest)*, *Nereocystis Luetkeana: A Synthesis with Recommendations for Future Research*; Lenfest Ocean Program: Santa Cruz, CA, USA, 2007.
60. Haida Marine Traditional Knowledge Study Participants; Council of the Haida Nation; Haida Oceans Technical Team; Winbourne, J. *Haida Marine Traditional Knowledge Volume II*; Council of the Haida Nation: Skidegate, BC, Canada, 2011.
61. Stekoll, M.S.; Deysher, L.E.; Hess, M. A Remote Sensing Approach to Estimating Harvestable Kelp Biomass. *J. Appl. Phycol.* **2006**, *18*, 323–334. [CrossRef]
62. Bell, T.W.; Cavanaugh, K.C.; Siegel, D.A. Remote Monitoring of Giant Kelp Biomass and Physiological Condition: An Evaluation of the Potential for the Hyperspectral Infrared Imager (HyspIRI) Mission. *Remote Sens. Environ.* **2015**, *167*, 218–228. [CrossRef]
63. Cavanaugh, K.C.; Kendall, B.E.; Siegel, D.A.; Reed, D.C.; Alberto, F.; Assis, J. Synchrony in Dynamics of Giant Kelp Forests Is Driven by Both Local Recruitment and Regional Environmental Controls. *Ecology* **2013**, *94*, 499–509. [CrossRef] [PubMed]
64. Reed, D.C.; Rassweiler, A.; Carr, M.H.; Cavanaugh, K.C.; Malone, D.P.; Siegel, D.A. Wave Disturbance Overwhelms Top-down and Bottom-up Control of Primary Production in California Kelp Forests. *Ecology* **2011**, *92*, 2108–2116. [CrossRef] [PubMed]
65. Mora-Soto, A.; Palacios, M.; Macaya, E.C.; Gómez, I.; Huovinen, P.; Pérez-Matus, A.; Young, M.; Golding, N.; Toro, M.; Yaqub, M.; et al. A High-Resolution Global Map of Giant Kelp (*Macrocystis pyrifera*) Forests and Intertidal Green Algae (Ulvophyceae) with Sentinel-2 Imagery. *Remote Sens.* **2020**, *12*, 694. [CrossRef]
66. Casal, G.; Sánchez-Rodríguez, E.; Freire, J. Remote Sensing with SPOT-4 for Mapping Kelp Forests in Turbid Waters on the South European Atlantic Shelf. *Estuar. Coast. Shelf Sci.* **2011**, *91*, 371–378. [CrossRef]
67. Ayoub, F.; Leprince, S.; Binet, R.; Lewis, K.W.; Aharonson, O.; Avouac, J.-P. Influence of Camera Distortions on Satellite Image Registration and Change Detection Applications. In Proceedings of the IGARSS 2008—2008 IEEE International Geoscience and Remote Sensing Symposium, Boston, MA, USA, 7–11 July 2008; Volume 2, pp. II-1072–II-1075.
68. Chang, K.-T. *Introduction to Geographic Information Systems*, 5th ed.; McGraw-Hill Higher Education: New York, NY, USA, 2009.
69. Matthew, M.W.; Adler-Golden, S.M.; Berk, A.; Richtsmeier, S.C.; Levine, R.Y.; Bernstein, L.S.; Acharya, P.K.; Anderson, G.P.; Felde, G.W.; Hoke, M.L.; et al. Status of Atmospheric Correction Using a MODTRAN4-Based Algorithm. In Proceedings of the Algorithms for Multispectral, Hyperspectral, and Ultraspectral Imagery VI, Orlando, FL, USA, 23 August 2000; International Society for Optics and Photonics. Volume 4049, pp. 199–207.
70. Lin, C.; Wu, C.-C.; Tsogt, K.; Ouyang, Y.-C.; Chang, C.-I. Effects of Atmospheric Correction and Pansharpening on LULC Classification Accuracy Using WorldView-2 Imagery. *Inf. Process. Agric.* **2015**, *2*, 25–36. [CrossRef]
71. Chavez, P.S. An Improved Dark-Object Subtraction Technique for Atmospheric Scattering Correction of Multispectral Data. *Remote Sens. Environ.* **1988**, *24*, 459–479. [CrossRef]
72. Sawaya, K. Extending Satellite Remote Sensing to Local Scales: Land and Water Resource Monitoring Using High-Resolution Imagery. *Remote Sens. Environ.* **2003**, *88*, 144–156. [CrossRef]
73. Wolter, P.T.; Johnston, C.A.; Niemi, G.J. Mapping Submergent Aquatic Vegetation in the US Great Lakes Using QuickBird Satellite Data. *Int. J. Remote Sens.* **2005**, *26*, 5255–5274. [CrossRef]
74. Druehl, L.D. The Distribution of *Macrocystis Integrifolia* in British Columbia as Related to Environmental Parameters. *Can. J. Bot.* **1978**, *56*, 69–79. [CrossRef]
75. Mumford, T.F. *Kelp and Eelgrass in Puget Sound*; Washington State Department of Natural Resources: Fort Belvoir, VA, USA, 2007.
76. Davies, S.C.; Gregr, E.J.; Lessard, J.; Bartier, P.; Wills, P. *Coastal Digital Elevation Models Integrating Ocean Bathymetry and Land Topography for Marine Ecological Analyses in Pacific Canadian Waters*; Fisheries and Oceans Canada: Ottawa, ON, Canada, 2019; p. 38, ISBN 978-0-660-31492-1.
77. Gregr, E.J.; Lessard, J.; Harper, J. A Spatial Framework for Representing Nearshore Ecosystems. *Prog. Oceanogr.* **2013**, *115*, 189–201. [CrossRef]
78. British Columbia Marine Conservation Analysis. *Marine Atlas of Pacific Canada: A Product of the British Columbia Marine Conservation Analysis (BCMCA)*; British Columbia Marine Conservation Analysis: Vancouver, BC, Canada, 2011; ISBN 978-0-9867511-0-3.
79. Tucker, C.J. Red and Photographic Infrared Linear Combinations for Monitoring Vegetation. *Remote Sens. Environ.* **1979**, *8*, 127–150. [CrossRef]
80. Kaufman, Y.J.; Remer, L.A. Detection of Forests Using Mid-IR Reflectance: An Application for Aerosol Studies. *IEEE Trans. Geosci. Remote Sens.* **1994**, *32*, 672–683. [CrossRef]
81. O'Neill, J.D.; Costa, M.; Sharma, T. Remote Sensing of Shallow Coastal Benthic Substrates: In Situ Spectra and Mapping of Eelgrass (*Zostera Marina*) in the Gulf Islands National Park Reserve of Canada. *Remote Sens.* **2011**, *3*, 975–1005. [CrossRef]

82. Whiteside, T.G.; Boggs, G.S.; Maier, S.W. Comparing Object-Based and Pixel-Based Classifications for Mapping Savannas. *Int. J. Appl. Earth Obs. Geoinf.* **2011**, *13*, 884–893. [\[CrossRef\]](#)
83. Weih, R.C.; Riggan, N.D. Object-Based Classification vs. Pixel-Based Classification: Comparative Importance of Multi-Resolution Imagery. *Int. Arch. Photogramm. Remote Sens. Spat. Inf. Sci.* **2010**, *38*, C7.
84. Gao, Y.; Mas, J.F. A Comparison of the Performance of Pixel-Based and Object-Based Classifications over Images with Various Spatial Resolutions. *Online J. Earth Sci.* **2008**, *2*, 27–35.
85. Kamal, M.; Phinn, S. Hyperspectral Data for Mangrove Species Mapping: A Comparison of Pixel-Based and Object-Based Approach. *Remote Sens.* **2011**, *3*, 2222–2242. [\[CrossRef\]](#)
86. Berry, B. Quantifying Impacts of Spatial Resolution on Pixel and Object-Based Methods of Image Classification. Bachelor's Dissertation, Dalhousie University, Halifax, NS, Canada, 2020.
87. Blaschke, T. Object Based Image Analysis for Remote Sensing. *ISPRS J. Photogramm. Remote Sens.* **2010**, *65*, 2–16. [\[CrossRef\]](#)
88. Gupta, N.; Bhaurauria, H.S. Object Based Information Extraction from High Resolution Satellite Imagery Using ECognition-ProQuest. *Int. J. Comput. Sci. Issues* **2014**, *11*, 139–144.
89. Olivero, J.; Ferri, F.; Acevedo, P.; Lobo, J.M.; Fa, J.E.; Farfán, M.Á.; Romero, D.; Amazonian Communities of Cascaradura, Niñal, Curimacare, Chapazón, Solano and Guzmán Blanco; Real, R. Using Indigenous Knowledge to Link Hyper-Temporal Land Cover Mapping with Land Use in the Venezuelan Amazon: “The Forest Pulse”. *Rev. Biol. Trop.* **2016**, *64*, 1661–1682. [\[CrossRef\]](#)
90. Boldt, J.L. *State of the Physical, Biological and Selected Fishery Resources of Pacific Canadian Marine Ecosystems in 2019*; Department of Fisheries and Oceans: Ottawa, ON, Canada, 2020; ISBN 978-0-660-34961-9.
91. Congalton, R.G. A Review of Assessing the Accuracy of Classifications of Remotely Sensed Data. *Remote Sens. Environ.* **1991**, *37*, 35–46. [\[CrossRef\]](#)
92. Nelson, M.D.; McRoberts, R.E.; Holden, G.R.; Bauer, M.E. Effects of Satellite Image Spatial Aggregation and Resolution on Estimates of Forest Land Area. *Int. J. Remote Sens.* **2009**, *30*, 1913–1940. [\[CrossRef\]](#)
93. Tian, J.; Zhu, X.; Wu, J.; Shen, M.; Chen, J. Coarse-Resolution Satellite Images Overestimate Urbanization Effects on Vegetation Spring Phenology. *Remote Sens.* **2020**, *12*, 117. [\[CrossRef\]](#)
94. Titus, J.; Geroge, S. A Comparison Study on Different Interpolation Methods Based on Satellite Images. *Int. J. Eng. Res.* **2013**, *2*, 4.
95. Berry, H.D.; Sewell, A.T.; Wylie-Echeverria, S.; Reeves, B.R.; Mumford, T.F.; Skalski, J.R.; Zimmerman, R.C.; Archer, J. *Puget Sound Submerged Vegetation Monitoring Project: 2000–2002 Monitoring Report*; Department of Natural Resources: Olympia, WA, USA, 2003; p. 170.
96. Gregr, E.J.; Palacios, D.M.; Thompson, A.; Chan, K.M.A. Why Less Complexity Produces Better Forecasts: An Independent Data Evaluation of Kelp Habitat Models. *Ecography* **2019**, *42*, 428–443. [\[CrossRef\]](#)
97. Markham, B.L.; Storey, J.C.; Williams, D.L.; Irons, J.R. Landsat Sensor Performance: History and Current Status. *IEEE Trans. Geosci. Remote Sens.* **2004**, *42*, 2691–2694. [\[CrossRef\]](#)
98. Thomson, R.E. *Oceanography of the British Columbia Coast*; Canadian Special Publication of Fisheries and Aquatic Sciences; Department of Fisheries and Oceans: Ottawa, ON, Canada, 1981; ISBN 978-0-660-10978-7.
99. Finger, D.J.I.; McPherson, M.L.; Houskeeper, H.F.; Kudela, R.M. Mapping Bull Kelp Canopy in Northern California Using Landsat to Enable Long-Term Monitoring. *Remote Sens. Environ.* **2021**, *254*, 112243. [\[CrossRef\]](#)
100. Alavipanah, S.K.; Matinfar, H.R.; Emam, A.R.; Khodaei, K.; Bagheri, R.H.; Panah, Y. Criteria of Selecting Satellite Data for Studying Land Resources. *Desert* **2010**, *15*, 83–102.
101. Nahirnick, N.K.; Reshitnyk, L.; Campbell, M.; Hessian-Lewis, M.; Costa, M.; Yakimishyn, J.; Lee, L. Mapping with Confidence: Delineating Seagrass Habitats Using Unoccupied Aerial Systems (UAS). *Remote Sens. Ecol. Conserv.* **2019**, *5*, 121–135. [\[CrossRef\]](#)
102. Cavanaugh, K.C.; Cavanaugh, K.C.; Bell, T.W.; Hockridge, E.G. An Automated Method for Mapping Giant Kelp Canopy Dynamics from UAV. *Front. Environ. Sci.* **2021**, *8*, 587354. [\[CrossRef\]](#)
103. Timmer, B.D. The Effects of Kelp Canopy Submersion on the Remote Sensing of Surface-Canopy Forming Kelps. Master's Dissertation, University of Victoria, Victoria, BC, Canada, 2022.
104. Young, N.E.; Anderson, R.S.; Chignell, S.M.; Vorster, A.G.; Lawrence, R.; Evangelista, P.H. A Survival Guide to Landsat Preprocessing. *Ecology* **2017**, *98*, 920–932. [\[CrossRef\]](#) [\[PubMed\]](#)
105. Bannari, A.; Morin, D.; Béné, G.B.; Bonn, F.J. A Theoretical Review of Different Mathematical Models of Geometric Corrections Applied to Remote Sensing Images. *Remote Sens. Rev.* **1995**, *13*, 27–47. [\[CrossRef\]](#)
106. Cooley, T.; Anderson, G.P.; Felde, G.W.; Hoke, M.L.; Ratkowski, A.J.; Chetwynd, J.H.; Gardner, J.A.; Adler-Golden, S.M.; Matthew, M.W.; Berk, A.; et al. FLAASH, a MODTRAN4-Based Atmospheric Correction Algorithm, Its Application and Validation. In Proceedings of the IEEE International Geoscience and Remote Sensing Symposium, Toronto, ON, Canada, 24–28 June 2002; Volume 3, pp. 1414–1418.
107. Pflug, B.; Main-Knom, M. *Validation of Atmospheric Correction Algorithm ATCOR*; Comérón, A., Kassianov, E.I., Schäfer, K., Picard, R.H., Stein, K., Gonglewski, J.D., Eds.; SPIE: Amsterdam, The Netherlands, 2014; p. 92420W.
108. Camacho, M. Depth Analysis of Midway Atoll Using QuickBird Multi-Spectral Imaging Over Variable Substrates. Master's Dissertation, Naval Postgraduate School, Monterey, CA, USA, 2006.

109. Yang, M.; Hu, Y.; Tian, H.; Khan, F.A.; Liu, Q.; Goes, J.I.; Gomes, H.d.R.; Kim, W. Atmospheric Correction of Airborne Hyperspectral CASI Data Using Polymer, 6S and FLAASH. *Remote Sens.* **2021**, *13*, 5062. [[CrossRef](#)]
110. Richter, R.; Schlapfer, D. *Atmospheric and Topographic Correction (ATCOR Theoretical Background Document)*; German Aerospace Centre: Weßling, Germany, 2019; p. 142.
111. Zhu, Z. Science of Landsat Analysis Ready Data. *Remote Sens.* **2019**, *11*, 2166. [[CrossRef](#)]
112. Frazier, A.E.; Hemingway, B.L. A Technical Review of Planet Smallsat Data: Practical Considerations for Processing and Using PlanetScope Imagery. *Remote Sens.* **2021**, *13*, 3930. [[CrossRef](#)]
113. Tarpley, J.D.; Schneider, S.R.; Money, R.L. Global Vegetation Indices from the NOAA-7 Meteorological Satellite. *J. Clim. Appl. Meteor.* **1984**, *23*, 491–494. [[CrossRef](#)]
114. Dierssen, H.M.; Chlus, A.; Russell, B. Hyperspectral Discrimination of Floating Mats of Seagrass Wrack and the Macroalgae Sargassum in Coastal Waters of Greater Florida Bay Using Airborne Remote Sensing. *Remote Sens. Environ.* **2015**, *167*, 247–258. [[CrossRef](#)]
115. Timmer, B.; Reshitnyk, L.Y.; Hessian-Lewis, M.; Juanes, F.; Costa, M. Comparing the Use of Red-Edge and Near-Infrared Wavelength Ranges for Detecting Submerged Kelp Canopy. *Remote Sens.* **2022**, *14*, 2241. [[CrossRef](#)]
116. Friedlander, A.M.; Ballesteros, E.; Bell, T.W.; Caselle, J.E.; Campagna, C.; Goodell, W.; Hüne, M.; Muñoz, A.; Salinas-de-León, P.; Sala, E.; et al. Kelp Forests at the End of the Earth: 45 Years Later. *PLoS ONE* **2020**, *15*, e0229259. [[CrossRef](#)]
117. McPherson, M.L.; Finger, D.J.I.; Houskeeper, H.F.; Bell, T.W.; Carr, M.H.; Rogers-Bennett, L.; Kudela, R.M. Large-Scale Shift in the Structure of a Kelp Forest Ecosystem Co-Occurs with an Epizootic and Marine Heatwave. *Commun. Biol.* **2021**, *4*, 298. [[CrossRef](#)] [[PubMed](#)]
118. Baraldi, A.; Boschetti, L. Operational Automatic Remote Sensing Image Understanding Systems: Beyond Geographic Object-Based and Object-Oriented Image Analysis (GEOBIA/GEOOIA). Part 1: Introduction. *Remote Sens.* **2012**, *4*, 2694–2735. [[CrossRef](#)]
119. Evans, T.L.; Costa, M.; Tomas, W.; Camilo, A.R. A SAR Fine and Medium Spatial Resolution Approach for Mapping the Brazilian Pantanal. *Geografia* **2013**, *38*, 19.
120. Uhl, F.; Bartsch, I.; Oppelt, N. Submerged Kelp Detection with Hyperspectral Data. *Remote Sens.* **2016**, *8*, 487. [[CrossRef](#)]
121. St-Pierre, A.P.; Gagnon, P. Kelp-Bed Dynamics across Scales: Enhancing Mapping Capability with Remote Sensing and GIS. *J. Exp. Mar. Biol. Ecol.* **2020**, *522*, 151246. [[CrossRef](#)]
122. Rowan, G.S.L.; Kalacska, M. A Review of Remote Sensing of Submerged Aquatic Vegetation for Non-Specialists. *Remote Sens.* **2021**, *13*, 623. [[CrossRef](#)]
123. Trishchenko, A.P.; Cihlar, J.; Li, Z. Effects of Spectral Response Function on Surface Reflectance and NDVI Measured with Moderate Resolution Satellite Sensors. *Remote Sens. Environ.* **2002**, *81*, 1–18. [[CrossRef](#)]
124. Teillet, P.M.; Ren, X. Spectral Band Difference Effects on Vegetation Indices Derived from Multiple Satellite Sensor Data. *Can. J. Remote Sens.* **2008**, *34*, 16.
125. Berry, H.D.; Mumford, T.F.; Christiaen, B.; Dowty, P.; Calloway, M.; Ferrier, L.; Grossman, E.E.; VanArendonk, N.R. Long-Term Changes in Kelp Forests in an Inner Basin of the Salish Sea. *PLoS ONE* **2021**, *16*, e0229703. [[CrossRef](#)] [[PubMed](#)]
126. Rogers-Bennett, L.; Catton, C.A. Marine Heat Wave and Multiple Stressors Tip Bull Kelp Forest to Sea Urchin Barrens. *Sci. Rep.* **2019**, *9*, 15050. [[CrossRef](#)] [[PubMed](#)]
127. Tanaka, K.; Taino, S.; Haraguchi, H.; Prendergast, G.; Hiraoka, M. Warming off Southwestern Japan Linked to Distributional Shifts of Subtidal Canopy-Forming Seaweeds. *Ecol. Evol.* **2012**, *2*, 2854–2865. [[CrossRef](#)] [[PubMed](#)]
128. Kumagai, N.H.; García Molinos, J.; Yamano, H.; Takao, S.; Fujii, M.; Yamanaka, Y. Ocean Currents and Herbivory Drive Macroalgae-to-Coral Community Shift under Climate Warming. *Proc. Natl. Acad. Sci. USA* **2018**, *115*, 8990–8995. [[CrossRef](#)]
129. Johnson, C.R.; Banks, S.C.; Barrett, N.S.; Cazassus, F.; Dunstan, P.K.; Edgar, G.J.; Frusher, S.D.; Gardner, C.; Haddon, M.; Helidoniotis, F.; et al. Climate Change Cascades: Shifts in Oceanography, Species' Ranges and Subtidal Marine Community Dynamics in Eastern Tasmania. *J. Exp. Mar. Biol. Ecol.* **2011**, *400*, 17–32. [[CrossRef](#)]
130. Vergés, A.; Doropoulos, C.; Malcolm, H.A.; Skye, M.; Garcia-Pizá, M.; Marzinelli, E.M.; Campbell, A.H.; Ballesteros, E.; Hoey, A.S.; Vila-Concejo, A.; et al. Long-Term Empirical Evidence of Ocean Warming Leading to Tropicalization of Fish Communities, Increased Herbivory, and Loss of Kelp. *Proc. Natl. Acad. Sci. USA* **2016**, *113*, 13791–13796. [[CrossRef](#)]
131. Carnell, P.E.; Keough, M.J. Reconstructing Historical Marine Populations Reveals Major Decline of a Kelp Forest Ecosystem in Australia. *Estuaries Coasts* **2019**, *42*, 765–778. [[CrossRef](#)]
132. Layton, C.; Coleman, M.A.; Marzinelli, E.M.; Steinberg, P.D.; Swearer, S.E.; Vergés, A.; Wernberg, T.; Johnson, C.R. Kelp Forest Restoration in Australia. *Front. Mar. Sci.* **2020**, *7*, 74. [[CrossRef](#)]
133. Coleman, M.A.; Reddy, M.; Nimbs, M.J.; Marshall, A.; Al-Ghassani, S.A.; Bolton, J.J.; Jupp, B.P.; De Clerck, O.; Leliaert, F.; Champion, C.; et al. Loss of a Globally Unique Kelp Forest from Oman. *Sci. Rep.* **2022**, *12*, 5020. [[CrossRef](#)]
134. Rinde, E.; Christie, H.; Fagerli, C.W.; Bekkby, T.; Gundersen, H.; Norderhaug, K.M.; Hjermann, D.Ø. The Influence of Physical Factors on Kelp and Sea Urchin Distribution in Previously and Still Grazed Areas in the NE Atlantic. *PLoS ONE* **2014**, *9*, e100222. [[CrossRef](#)]
135. Piñeiro-Corbeira, C.; Barreiro, R.; Cremades, J. Decadal Changes in the Distribution of Common Intertidal Seaweeds in Galicia (NW Iberia). *Mar. Environ. Res.* **2016**, *113*, 106–115. [[CrossRef](#)] [[PubMed](#)]

136. Casado-Amezúa, P.; Araújo, R.; Bárbara, I.; Bermejo, R.; Borja, Á.; Díez, I.; Fernández, C.; Gorostiaga, J.M.; Guinda, X.; Hernández, I.; et al. Distributional Shifts of Canopy-Forming Seaweeds from the Atlantic Coast of Southern Europe. *Biodivers Conserv.* **2019**, *28*, 1151–1172. [[CrossRef](#)]
137. Vega, J.M.A.; Broitman, B.R.; Vásquez, J.A. Monitoring the Sustainability of *Lessonia Nigrescens* (Laminariales, Phaeophyceae) in Northern Chile under Strong Harvest Pressure. *J. Appl. Phycol.* **2014**, *26*, 791–801. [[CrossRef](#)]

Disclaimer/Publisher's Note: The statements, opinions and data contained in all publications are solely those of the individual author(s) and contributor(s) and not of MDPI and/or the editor(s). MDPI and/or the editor(s) disclaim responsibility for any injury to people or property resulting from any ideas, methods, instructions or products referred to in the content.

MDPI
St. Alban-Anlage 66
4052 Basel
Switzerland
Tel. +41 61 683 77 34
Fax +41 61 302 89 18
www.mdpi.com

Remote Sensing Editorial Office
E-mail: remotesensing@mdpi.com
www.mdpi.com/journal/remotesensing





Academic Open
Access Publishing

www.mdpi.com

ISBN 978-3-0365-7521-6